Kharkiv National University of Radio Electronics

Academy of Sciences of Applied Radio Electronics

APPLIED RADIO ELECTRONICS

Scientific and technical journal

Editorial office:
Journal of Applied Radio Electronics
Kharkiv National University of Radio Electronics
14 Lenin Ave., 61166, Kharkov, Ukraine
Tel.: + 38 (057) 702 10 57
Fax: + 38 (057) 702 10 13
E-mail: are@kture.kharkov.ua
http://www.anpre.org.ua

CONTENTS

(Continued from front cover)

APPLIED RADIO ELECTRONICS. 2013. Vol. 12. № 1

ISSN 1727-1290

KHARKIV NATIONAL UNIVERSITY OF RADIO ELECTRONICS

ACADEMY OF SCIENCES OF APPLIED RADIO ELECTRONICS

APPLIED RADIO ELECTRONICS

Scientific and Technical Journal 2013 Volume 12 № 1

Special Issue on Third International Conference "Noise Radar Technology", NRT-2012

CONTENTS

EDITORIAL

This special issue of Applied Radioelectronics Journal is devoted to the Third International Conference on Noise Radar Technology, NRT-2012, being held in Yalta, Crimea, Ukraine on September 27-29, 2012. It has been organized by Laboratory for Nonlinear Dynamics of Electronic Systems (LNDES), IRE NASU with technical support by the Academy of Applied Radioelectronics, IEEE Kharkov Joint Chapter and National Antenna Association of Ukraine.

The first papers on range-measuring radar based upon noise signals have been published by R. Bourret in 1957 and B. Horton in1959. Employing noise signals can be traced back to 1904. At that time, noise pulses were used by C. Huelsmeyer in the "telemobiloscope", the radar precursor, which used a monostatic configuration and by A. Popov in the experiments on ships detection in bistatic configuration. In both cases, a discharge device played the role of a pulse-noise transmitter and a coherer was used as a detector to receive the noise pulses. Today's Noise Radar Technology (NRT) uses Noise (Random or Chaotic) Waveforms (NW) as a radar signal and *coherent* signal processing for noise radar returns reception.

In spite of rather long history, the concept of Noise Radar did not attract the radar engineers, mainly because of the lack of appropriate noise signals sources and essential difficulties in the correlation signal processing implementation using analogue circuits. Nevertheless, this concept has been rediscovered in the last decades as it follows from the recent conferences on NRT: Novel Radar session at "Advances in Radar" PIERS Conference, April 1998, Baveno, Italy; "The First International Workshop on NRT" (NRTW'2002), Yalta, Crimea, Ukraine; NRT-2003, Kharkov, October 21-23, 2003; and dedicated sessions on NRT at IRS-2006, Cracow, and IRS-2008, Wroclaw, Poland; IRS-2010, Vilnius, Lithuania. Besides, Noise Radar Workshop was held in November 2008 in Arlington, and dedicated NRT session at SPIE-2010 Conference in Orlando, USA. Dedicated session on "Applications of Random Signals for SAR" was organized at APSAR-2011, September 2011 Seoul, South Korea. All of them have drawn speakers and observers from many countries of America, Europe, Asia and Australia.

Actually Noise Radar has been under intensive development during the last 20 years in Ukraine, USA, Australia, Brazil, Canada, China, France, Italy, Poland, Russia, South Korea, Sweden, UK, and other countries. Noise Radar provides excellent potential capabilities for unambiguous and simultaneous range and Doppler measurements with high resolution and accuracy. Noise Radar Systems have the best Low Probability of Intercept (LPI) and Electromagnetic Compatibility (EMC) performance. They are suitable for implementing of covert operational mode of radar sensors and their high resistance against jamming, etc. All these and other properties enable design of cost-effective and affordable radar systems for various civil and military applications.

Ten year after the First NRT Conference, the NRTW-2002, we decided to gather noise radar engineers again in Yalta for the NRT-2012 Conference. NRT-2012 attendees from 13 countries had an excellent opportunity to present and discuss their recent R&D results in Noise Radar and related topics, exchange information and new ideas in the rapidly emerging Noise Radar Technology. Unlike previous NRT conferences we decided to extend the scope of the conference topics, including applications not pure random signals, but also pseudo random and even chirps and short pulses. Moreover, not only papers dealing with electromagnetic signals, but also papers devoted to applications of random signals in acoustic and seismic systems have been presented as well. All papers published in the present issue have been structured according to the following topics: **Random Waveform Design; Random Noise Signal Generation; Signal Processing in Noise Radar; Noise Radar Design; Noise Radar Performance; Noise Waveform SAR; Noise Radar Technique in Optics and Seismology.**

I hope that the papers presented in this issue will help radar engineers to understand better the advantages of Noise Radar for design of various radar systems. Application of noise waveforms and correlation processing of radar returns provides unique performance of noise radar systems which are not affordable when using other waveforms. We may recall some of them here: indoor measurements and imaging with Noise Radar, since reflections do not affect radar sensitivity that much; desirable limited working range of stepped-frequency noise radar due to disappearing of coherent reception beyond the correlation length of the transmitted random signal; partial reception/integration of long noise waveform pulses; Doppler frequency Noise Radar for range (!) estimation, etc.

I would like to emphasize that recently several Noise Radars have been designed, manufactured and delivered to customers in different countries for research and trials in both CW and pulse-coherent modes. However the first operational surveillance noise radar has been designed and manufactured by the ORBISAT Company in Brazil based on the noise radar concept suggested by LNDES IRE NASU, where the partial integration of the radar returns has been used to provide both a long working range and a short blind zone simultaneously. I am sure that Noise Radar will expand the area of realistic applications of radar systems due to the mentioned above and other unique properties of Noise Radar Technology.

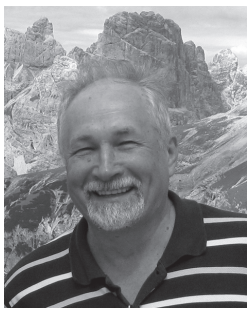

Konstantin Lukin,
Guest Editor
Chairman of the NRT-2012 Conference,
Fellow IEEE

RANDOM WAVEFORM DESIGN

UDK 621.37

ON THE DESIGN OF WAVEFORMS FOR NOISE-MIMO RADAR

G. GALATI AND G. PAVAN

Multiple-Input-Multiple-Output (MIMO) radar is an emerging technology that has significant potential for advancing the state-of-the-art of modern radar systems. Unlike standard phased-array radar, a MIMO Radar system can transmit, via its antennas, multiple signals that may be correlated or uncorrelated with each other. The orthogonal property is required for the transmitted signals to better separate them in reception. Although orthogonality may be imposed in the time, in frequency or in signals coding domain, to avoid changes in the radar cross-section of the target and undesirable Doppler effects, the waveforms have to be transmitted simultaneously and at the same carrier frequency. As a consequence, the orthogonality in the signals domain is the best choice and to successfully utilize such systems signal design plays a critical role. Good candidates as orthogonal signals for MIMO radar are the Phase Noise signals. In this paper, after an introduction to MIMO radar systems, we present the main characteristics of these signals through a statistical characterization, including an analysis of the autocorrelation, cross-correlation and spectral properties. Finally two novel methods to generate phase Noise signals will be proposed, i.e. a recursive method and non-recursive (closed form) one. Preliminary results will be presented.

Keywords: MIMO, Orthogonal Waveforms, Phase Noise.

1. INTRODUCTION

Recently a new field of radar research called Multiple Input Multiple Output (MIMO) radar has been developed [1], which can be thought as a generalization of the *multistatic radar* concept.

This kind of radar, as its name indicates, can be broadly defined as a radar system deploying multiple antennas to simultaneously transmit arbitrary waveforms and utilizing multiple antennas to receive the relevant echo signals.

The key ideas of MIMO radar concept has been picked up from communications, where the MIMO technique is used to increase data throughput and link range and to overcome the fading effects without neither additional bandwidth nor more transmission power. Conversely, a spatial diversity gain benefit is obtained in MIMO communications, often achieved by transmitting the same signal through different subchannels and combining the information at the receiver. Diversity gain is used against channel fading enhancing the link reliability of the system. Radar systems also suffer from fading (more precisely, fluctuation of the radar cross section) when there are complex and extended targets as it is the case very often.

It has long been understood that common radar targets are complex bodies, and large scintillations in the amount of energy back-scattered by a complex target can occur with very small changes (e.g. fractions of one degree) in the illuminating direction. If the antennas of MIMO radar are widely separated such that different antennas observe different aspects of the target, the target returns result from independent illuminations and can be combined together leading to a spatial diversity gain.

Diversity gain is only one of two key gains that MIMO communications can provide. The other gain is called spatial multiplexing, which expresses the ability to use the transmit and receive antennas to set up a multidimensional space for signaling. Then it is possible to form uncoupled, parallel channels that enable the rate of communication to grow in direct proportion to the number of such channels.

Similarly, in MIMO radar, a multidimensional signal space is created when returns from the multiple scatterers of a target combine to generate a rich backscatter. With proper design, transmit-receive paths can be separated and exploited for improving radar performance.

The transmit and receive antennas in a MIMO radar may be in the form of an array (see Fig. 1) and the transmit and receive arrays can be co-located (coherent MIMO) or widely separated (statistical MIMO).

Although MIMO radar system resembles phased-array radar system, there is a fundamental difference between these two approaches. In fact, unlike a standard phased-array, which transmits scaled, time-delayed version of a single waveform, MIMO radar systems transmits multiple signals and this waveform diversity enables superior capability and performance compared with standard phased-array radars.

In much of the current literature it is assumed that the waveforms coming from each transmit antenna are orthogonal. Although this is not a strict requirement for MIMO radar, orthogonality can facilitate the process of separation of the simultaneously received signals, avoiding the burden of further processing.

Orthogonality may be imposed in the time domain, in frequency domain or in the signals space. Time division or frequency division multiplexing are simple approaches but they both can suffer from potential performance degradation because the loss of coherence of the target response [15]. As a matter

of fact the scattering response of the target or of the background (clutter) is commonly time-varying or frequency selective, limiting the ability to coherently combine the information from the antenna elements. As a consequence obtaining the orthogonality in the signals domain is the best choice.

The paper is organized as follows. Chapter 2 describes the MIMO radar system, underlining its significant characteristics, classifications and the main differences with respect to the classical phased array radar. In addiction, a general model for the signals transmitted by the antenna array elements is proposed.

Chapter 3 underlines the importance of the orthogonal waveform design and presents the Phase Noise signals as a good solution to the problem. This chapter contains the description of a new technique to generate phase noise signals. It is based on an iterative procedure that permits to obtain low Peak-Side-Lobe-Ratio (PSLR) or Peak-to-Average Ratio (PAR), limiting the spectrum in a desired band. Chapter 4 contains the conclusions.

2. INTRODUCTION TO MIMO RADAR

MIMO radar is capable of significantly improving target detection, parameter estimation, tracking and recognition performance, using multiple transmit and multiple receive antennas (see Fig. 1). These antennas may be closely spaced in the form of an array or may be widely spaced forming a "netted radar like" structure. In this paper we refer to the former case.

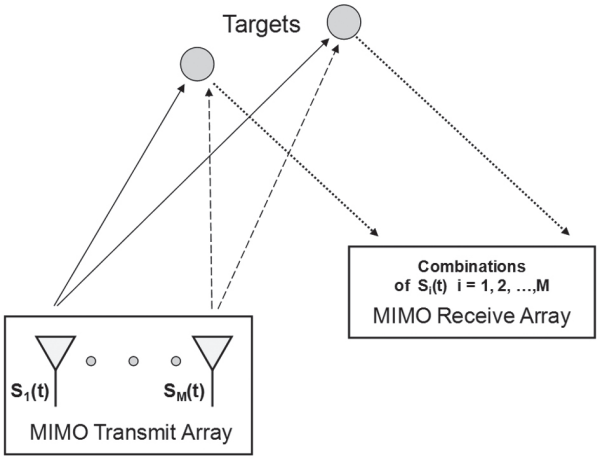

Fig. 1. Multiple transmit and multiple receive antennas for MIMO radar system

Every antenna element in a MIMO radar system (unlike standard phased-array radar which transmits delayed versions of a single waveform) can transmit different waveforms (waveform diversity). These may be orthogonal, mutually uncorrelated or linearly independent.

To benefit from this diversity, in the MIMO radar receiver there are as many matched filters as the number of transmitted signals. If the number of transmitting antenna elements is M and the number of receiving antenna elements is N, there are MN outputs of these matched filters totally (Fig. 2). MIMO radar processes these outputs jointly to decide whether a target is present or not.

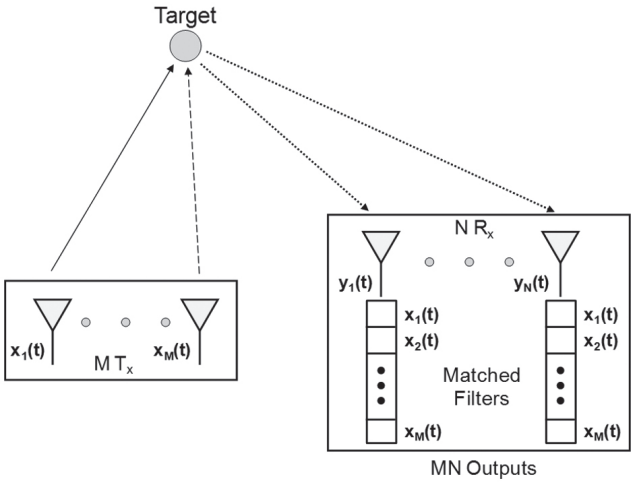

Fig. 2. Separation of different signals at the receiver: M matched filters to every transmitted signal in every receiver

As regards the kinds of MIMO radar systems, they can be classified into two categories according to their configurations and in particular to the distance between the antenna elements [1].

In the first category, referred to as *coherent* MIMO radar, the transmit and receive array elements are closely spaced so it is assumed that the target's scattering response is the same for each antenna pair, up to some small delay (the antennas are close enough such that all the elements view the same aspect of the target, or more precisely, are in the main lobe of the diffraction pattern of the target).

In the second category, referred to as *non-coherent* (or *statistical*) MIMO radar, the elements are broadly spaced, providing an independent scattering response for each antenna pair (the antennas are widely separated in order to capture the spatial diversity of the target's RCS).

2.1. Signal model

Consider a MIMO radar system that has a transmit and a receive array consisting of M and N elements respectively. Also, let denote the location parameter(s) of a generic target, for example, its azimuth angle and its range.

Under the assumption that the transmitted signals are narrowband and that the propagation is non-dispersive, the received signal can be written as [2]:

$$y(t) = diag(b(\theta)) \cdot A \cdot diag(a(\theta)) \cdot x(t-\tau) + w(t), \quad (1)$$

where the vectors $x(t)$ and $y(t)$ represent the transmitted and received signals:

$$x(t) = \left[x_1(t)x_2(t)...x_M(t)\right]^T \quad (2)$$

$$y(t) = \left[y_1(t)y_2(t)...y_N(t)\right]^T \quad (3)$$

and $w(t)$ denotes the interference-plus-noise term; A is a $N \times M$ matrix whose entries correspond to the bistatic RCS between each pair of transmitter and receiver; $a(\theta)$ and $b(\theta)$, which are some functions of the target

location θ, are the $M \times 1$ transmit steering vector and the $N \times 1$ receive steering vector, respectively:

$$a(\theta) = \left[e^{-j\psi_1} e^{-j\psi_2} .... e^{-j\psi_M} \right]^T , \quad (4)$$

$$b(\theta) = \left[e^{-j\varphi_1} e^{-j\varphi_2} .... e^{-j\varphi_N} \right]^T \quad (5)$$

where:

$$\tau = \tau_{t1}(\theta) - \tau_{r1}(\theta) , \quad (6)$$

$$\psi_m = 2\pi f_0 (\tau_{tm}(\theta) - \tau_{t1}(\theta)) , \quad (7)$$

$$\psi_n = 2\pi f_0 (\tau_{rn}(\theta) - \tau_{r1}(\theta)) , \quad (8)$$

with τ_{tm} time delay between the target and the m^{th} transmit antenna and τ_{rn} represents the time delay between the target and the n^{th} receive antenna.

2.2. Coherent MIMO Radar

Coherent MIMO radar resembles the phased array radar but every antenna element sends different waveforms (waveform diversity) and this diversity enables superior capabilities as compared to standard phased-array radar. For coherent MIMO radar the benefits are [3], [5]:

(*a*) *Higher resolution*: the performance of MIMO radar systems can be characterized by a virtual array constructed by the bi-dimensional convolution of the real transmit and receive antenna locations, assumed to belong to a common plane. This virtual array can be much larger than each constituting a real array. The aperture extension results in narrower beams and therefore in a higher angular resolution and a better detection performance. Moreover, some of the virtual sensor locations are identical, which can be interpreted as spatial tapering, and results in lower side lobes.

(*b*) *Extension of spatial coverage*: in conventional radar systems several directional beams are usually transmitted in order to scan a given region of interest and the time on target is equal to the total interval assigned for covering the region of interest divided by the required number of beams [4], while MIMO radar transmits orthogonal signals, with virtually omnidirectional beams and hence with an extended spatial coverage; therefore, the time on target for each beam increases, and may be set equal to the interval which is assigned to scan the whole area.

(*c*) *Transmit beam-pattern synthesis*: through the choice of a signal cross-correlation matrix, it is possible to create spatial beam-patterns ranging from the high directionality of phased-array systems to the omni-directionality of MIMO systems with orthogonal signals. In detail, by properly designing the cross-correlation matrix of the transmitted signals $R = a^H(\theta)\langle x(t)x^H(t)\rangle a(\theta)$, where $\langle\cdot\rangle$ denotes time average, it is possible to maximize the total spatial power at a number of given target locations, or more generally, to match a desired transmit beam-pattern and minimize the cross-correlation between the transmitted signals at a number of given target locations [6]. Two specific problems are addressed. On one hand there is the optimization problem of finding the matrix R which makes the transmit beampattern close to a desired beampattern. This is approached using convex optimization techniques. On the other hand there is the not easy problem of designing multiple constant-modulus waveforms with a given cross-correlation R.

(*d*) *Direct application of adaptive techniques for parameter estimation*: because of the different phase shifts associated with the different propagations path from the transmitting antenna to the targets, these independent waveforms are linearly combined at the target locations with different phase factors. As a result, the signals reflected form different targets are linearly independent of each other. Therefore the direct application of adaptive techniques becomes possible without the need for secondary range bins or even for range compression [3]. Example of adaptive array algorithms applied to MIMO radar are Capon and APES (Amplitude and Phase Estimation). The paper [7] discusses these adaptive radar algorithms.

Summing up, MIMO radar systems could have better (i) resolution, (ii) parameter estimation accuracy and (iii) interference rejection capability.

3. ORTHOGONAL WAVEFORM DESIGN

The waveform design and optimization is one of the main focuses of the research in multistatic and multifunction radar [8], [16]. In MIMO radar applications typically M codes are required in the set, where M is the number of transmit elements. The main requirements of a pair of signals with complex envelope s_i and s_j with $i, j = 1,..., M$, pulsewidth T and same power, are defined by:

- Peak Side Lobe Ratio $(< 30dB)$

$$PSLR = \frac{\max_l(s_i)}{\max_k(m_k)} , \quad (9)$$

where s_i = *sidelobe samples*, m_k = *mainlobe samples*.

– Crest Factor (C) or Peak-to-Average Ratio (PAR), i.e. the peak amplitude of the waveform divided by the *rms* value of the waveform $s(t)$:

$$C = \frac{\max(|s(t)|)}{\sqrt{\frac{1}{T}\int_0^T |s(t)|^2 \, dt}} . \quad (10)$$

– Mean Envelope-to-Peak Power Ratio:

$$MEPPR = \frac{\frac{1}{T}\int_0^T |s(t)|^2 \, dt}{\max(|s(t)|^2)} . \quad (11)$$

It results: $MEPPR = \frac{1}{C^2}$.

– Normalized cross-correlation:

$$r_{ij}(t) = \frac{|R_{ij}(t)|}{|R_{i(j)}(0)|} , \quad (12)$$

where $R_{ij}(t) = \int s_i^*(\theta) s_j(t+\theta) d\theta$, $i \neq j$ measures the orthogonality, the desired value is $r_{ij}(t) < -30dB$.

– Spectral band occupancy; sometimes this item is overlooked, especially when noise-like waveforms are concerned, but it is of paramount importance in most real-world radars.

As explained before, the MIMO radar waveforms orthogonality in the signal space is preferred. Thus orthogonal waveform design plays a critical role in determining the feasibility of MIMO radar.

A good candidates to design deterministic signals that satisfy the orthogonal requirements are the well-known *"up"* and *"down"* chirp (Linear-FM and Non-LFM) [9], but in this case only one pair of signals can be defined. To obtain *M* pairs of signals the Costas codes represents a possible solution [10]. In addition Alltop sequences can be considered [11].

More recent research on orthogonal signals proposed the use of normal or interleaved OFDM techniques [12]. The main limitation of the OFDM approach is due to the non-constant envelope of the signals, i.e. $MEPPR < 1$, the transmitter does not work at its maximum power.

Another class of waveforms, i.e. the Phase Noise signals [13], has two main advantages as compared to the signals introduced before. The former is the possibility to generate a large number of orthogonal signals, which is of great importance in MIMO radar systems. The latter is about the detectability; in fact they are random signals so they place limitation on the detection, the identification and the eventual spoofing of the signal, an element of great importance in many military applications which require low detectability of the active system. Finally the *MEPPR* can reach the unity.

For a phase noise signal the complex envelope can be written as:

$$s(t) = A \cdot \exp\{j\varphi(t)\} \cdot rect_T(t), \qquad (13)$$

where A is the constant amplitude, $rect_T$ is 0 outside the interval $[-T/2, +T/2]$ and 1 inside it (with T being the pulse length) and $\varphi(t)$ is the phase process modulating the noise signal $s(t)$.

In the following we present three methods to generate the phase noise signals highlighting their strengths and weaknesses.

3.1. Phase Noise Signals

In [13] Axelsson supposed for $\varphi(t)$ a zero-mean Gaussian process with root mean square (*rms*) σ and a given power with density spectrum within the band b. He showed that the normalized autocorrelation function of the signal $s(t)$ can be written in a closed-form expression as:

$$R(\tau) = \exp\left\{-\sigma^2[1-\rho(\tau)]\right\}, \qquad (14)$$

where $\rho(\tau)$ is the correlation coefficient of $\varphi(\tau)$. For example $\rho(\tau) = \dfrac{\sin(\pi b\tau)}{(\pi b\tau)}$ for a constant spectrum within the bandwidth b and zero outside.

Of course, $R(\tau)$ depends on the bandwidth b, on the pulse length T and on the *rms* phase fluctuation σ.

The bandwidth b is related to the width of the main peak and therefore, it determines the range resolution. An increase of *T*, and consequently of the compression ratio (the time-bandwidth product of the generated signal), causes a reduction of the range sidelobe level, whereas the mainlobe width remains fixed being independent of *T*. Finally the *rms* σ has two different effects. The former is on the sidelobe level: an increase of σ causes a decrease of the sidelobe level and an improvement of the PSLR.

The latter concerns the resolution. The *rms* value in fact establishes a connection between the bandwidth of the modulated signal and the bandwidth of the modulating signal. In detail, when σ increases the final bandwidth increases too. As a consequence a high *rms* value of σ gives an improved resolution (Fig. 3).

In [13] a simple relation between the *rms* bandwidth of the phase modulated signal (B_{rms}) and the *rms* bandwidth of the phase modulating noise (b_{rms}) has been found:

$$B_{rms} = \sigma \cdot b_{rms}. \qquad (15)$$

On the other hand, as regard the sidelobe suppression, the expression of the autocorrelation function introduced in [13] would show a progressive improvement of the sidelobe suppression as σ increases. However the periodic nature of $\varphi(t)$ with a folding in the $[-\pi, +\pi]$ interval has been neglected in [13], and in reality, the model can be used only for values of σ significantly smaller than π.

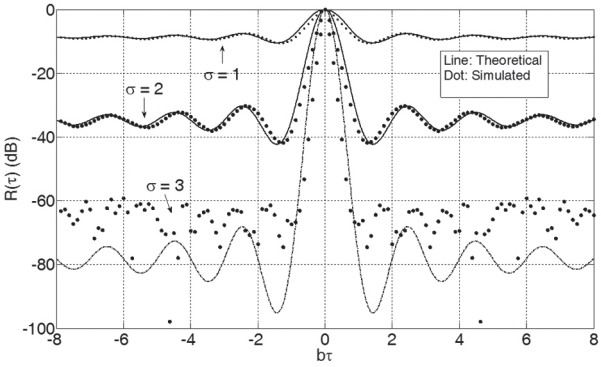

Fig. 3. Normalized autocorrelation for Phase Noise (compression ratio = 1000)

The Gaussian noise, used to modulate the signal phase, is to be compared with as a uniform distribution in the range $[-\pi, +\pi]$ with a standard deviation of $\pi/\sqrt{3} \cong 1.8 rad$. Therefore, if σ is too large $(\sigma > \pi/\sqrt{3})$, the resultant phase does not have a Gaussian distribution and the mathematical formulation introduced in [13] does not apply. This is shown, inter alia, in Fig. 3 where the difference between Axelsson's theory and experiments (by simulation) is clear for $\sigma = 3$.

On the other hand, considering simulations and the relation with a potential real application, it would be better to generate the signal through a white Gaussian process with its *in phase* and *in quadrature* components (I, Q) that are band-limited as desired. This is described in the ensuing section.

3.2. An iterative algorithm to generate Phase Noise Signals

To control the spectral width and to reduce the PSLR of the generated phase noise signals, we

propose an iterative algorithm as shown in Fig. 4. It is based on alternative projections in frequency and in time domain.

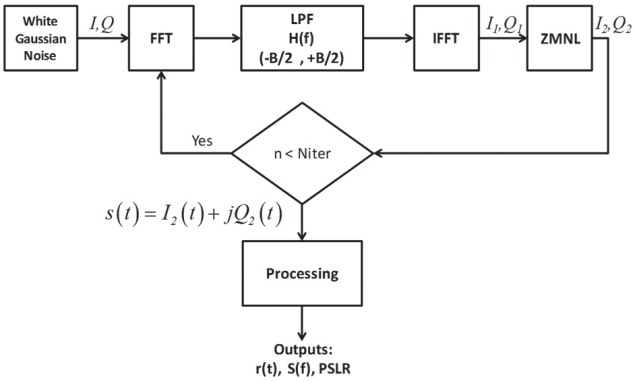

Fig. 4. Block diagram of the iterative algorithm to generate phase noise signals. *Legenda*: LPF = Low Pass Filter, ZMNL = Zero-Memory-Non-Linearity, N_{iter} = number of iterations

The filtering is implemented in frequency domain while the amplitude limitation (ZMNL = Zero-Memory-Non-Linearity) in time domain. The input to the algorithm is a *zero-mean white complex Gaussian process* $(I + jQ)$ with power $2\sigma^2$.

First we consider for ZMNL a *hard limiter*, i.e.:

$$I_2 = \frac{I_1}{\sqrt{I_1^2 + Q_1^2}}, \qquad Q_2 = \frac{Q_1}{\sqrt{I_1^2 + Q_1^2}}. \qquad (16)$$

Fig. 5 shows the obtained PSLR versus the number of iterations considering three different random sequences for the white Gaussian noise. The PSLR converges after some tens of iterations to –31 dB in the best case and it varies from –24 *dB* to –31 *dB*.

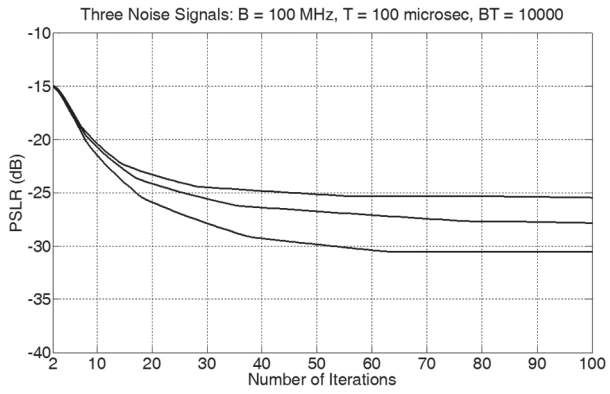

Fig. 5. PSLR versus the number of iterations. Three examples of convergence

Fig. 6 shows the normalized autocorrelation (around the main lobe) for two randomly generated phase noise signals.

Fig. 7 reports an example of density spectrum in comparison with them of Linear and Non-Linear *up* and *down* chirp. Due to the Low Pass Filter (LPF) of Fig. 4 the spectrum remains strictly band-limited as desired.

With respect to the orthogonality property, in Fig. 8 the cross-correlation is shown for a pair of generated phase noise signals. In comparison with the up and down chirp (LFM and NLFM), a degradation of 8-10 *dB* results.

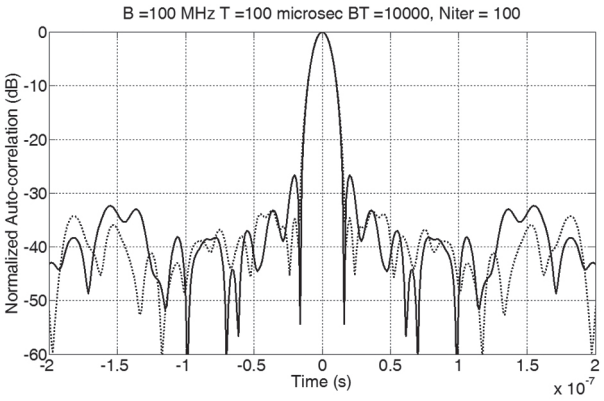

Fig. 6. PSRL near the mainlobe for two generated phase noise signals with a band of 100 MHz and a compression ratio of 10000

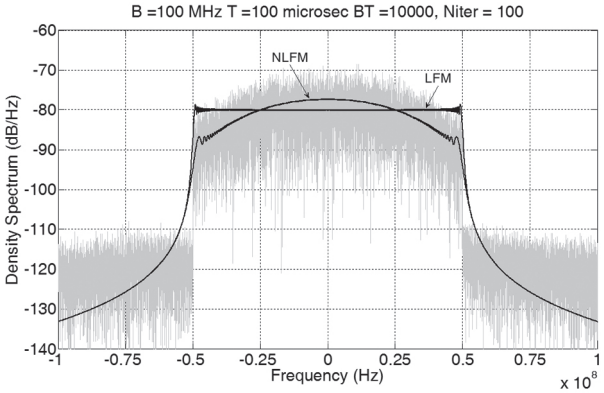

Fig. 7. Density spectrum of a phase noise signal with an allocated band of 100 MHz

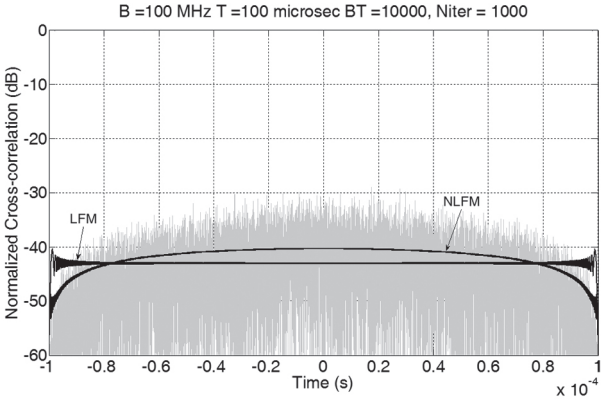

Fig. 8. Normalized cross-correlation of a pair of phase noise signal with a band of 100 MHz. Compression ratio of 10000. In black the cross-correlations of the pair up and down chirp (LFM and NLFM)

Considering now an *amplitude soft limiter* for the ZMNL (see Fig. 9 for the I/O characteristic):

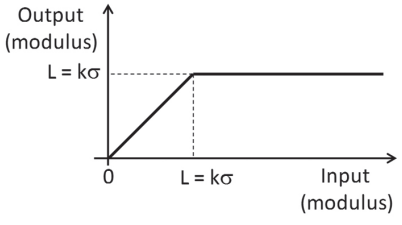

Fig. 9. Soft limiter I/O characteristic

and indicating with G_p the power gain of the Low Pass Filter (LPF) of Fig. 4, the Mean Envelope to Peak Power Ratio has been evaluated.

It depends on the number of iterations *m*, and on the ratio $k = \frac{L}{\sigma}$ being *L* the threshold of the soft limiter [17]. It results:

$$MEPPR = \frac{2(G_p)^{m-1}}{k^2}\left[1 - \exp\left(-\frac{k^2}{2(G_p)^{m-1}}\right)\right] \quad (17)$$

with $m = 1,2,\ldots$.

Fig. 10 shows that only four iterations (in the worst case when $L = 5\sigma$ and the effect of the limiter is negligible) are needed to obtain a MEPPR between -1 *dB* and 0 *dB*.

By increasing the number of iterations, as shown in the case of hard limiter, the PSLR decreases up to −30 *dB circa* as shown in Fig. 11 for two different values of the threshold *L*.

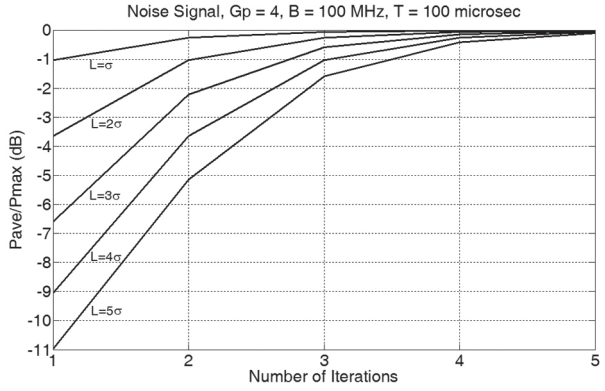

Fig. 10. Mean Envelope to Peak Power Ratio versus the number of iterations, varying the threshold $L = k\sigma$

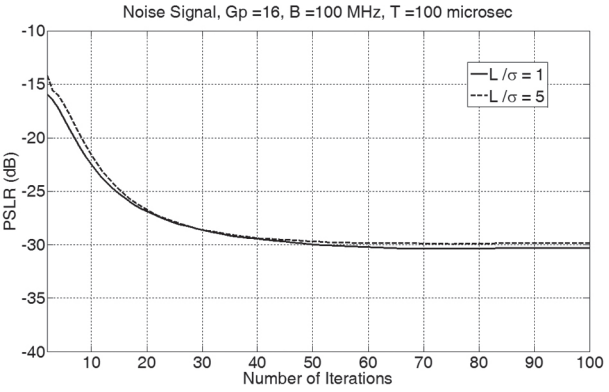

Fig. 11. PSLR versus the number of iterations considering a soft limiter. Two examples of convergence for $L = \sigma$ and $L = 5\sigma$

3.3. Closed-Form algorithm to generate Phase Noise Signals

A mathematical generation approach is based on the following considerations. For a real Gaussian process Van Vleck and Middleton [14] have shown that the autocorrelation coefficient (R_t with $t = t_2 - t_1$) of the output from a *hard limiter* is related with the input autocorrelation coefficient (here denoted r) by the well known *arcsine-law*:

$$R_t = \frac{2}{\pi}\arcsin(r). \quad (18)$$

Considering a complex Gaussian process, the correlation R_t after the *hard limiter* i.e. between: $\frac{z^*_1}{|z_1|} = \frac{x_1 - jy_1}{\sqrt{x_1^2 + y_1^2}}$ and $\frac{z_2}{|z_2|} = \frac{x_2 + jy_2}{\sqrt{x_2^2 + y_2^2}}$ is

$$R_t = E\left\{\frac{z^*_1 z_2}{|z_1||z_2|}\right\} = E\left\{\frac{x_1x_2 + y_1y_2 + j(x_1y_2 + x_2y_1)}{\sqrt{x_1^2 + y_1^2}\sqrt{x_2^2 + y_2^2}}\right\} = u + jv \quad (19)$$

where $E\{\cdot\}$ is the statistical *mean* operator. Supposing a symmetrical power density spectrum with respect to the origin, the correlation is real and $v = 0$. Equation (19) has been evaluated in [17] and it results:

$$R_t = b_0 r + \sum_{n=1}^{\infty} b_n \cdot r^{2n+1} \quad (20)$$

being:

$$b_n = \frac{(2n-1)^2}{4n(n+1)} \cdot b_{n-1}, \quad b_0 = \frac{2}{\pi} \quad n = 1,2,3, \quad (21)$$

Then R_t can be expressed as a sum of odd powers of r , where the coefficients b_n are very similar to those evaluated for the *arcsine-law*:

$$b_n = \frac{(2n-1)^2}{2n(2n+1)} \cdot b_{n-1}, \quad b_0 = \frac{2}{\pi} \quad n = 1,2,3, \quad (22)$$

Fig. 12 shows R_t versus the input correlation *r* for real and complex Gaussian process.

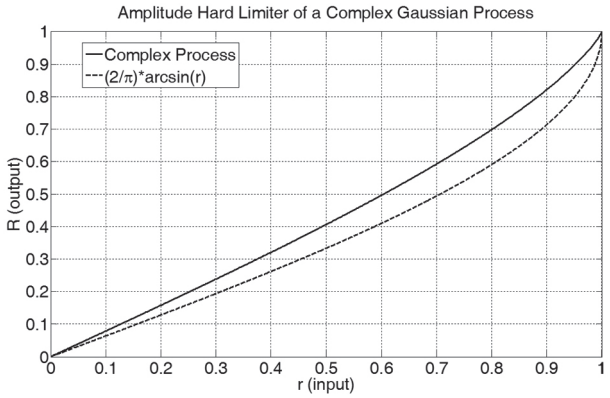

Fig. 12. Output autocorrelation (*R*) from a hard limiter versus the input autocorrelation (*r*)

Inverting eq. (20) it is possible to pre-distort the input autocorrelation to the hard limiter to obtain a desired R_t .

In such a way the requirements listed at the beginning of section 3 can be met with no need for iterations.

In fact, (*a*) the output autocorrelation is chosen in order to satisfy the PSLR requirement and the spectral band requirement, (*b*) the MEPPR requirement is satisfied by a suitable choice of the parameter *k* (ref. Fig. 9) of the limiter (the hard limiter being the situation $k \to 0$) and (*c*) the orthogonality is obtained by the randomness of the white Gaussian input

sequence, and may be enhanced by proper choices of the generated output sequences.

3.4. Comparison of the algorithms

A quantitative comparison of the generation methodologies is ongoing; the qualitative comparison is shown in the following Table 1.

Table 1

Comparison of the algorithms (TBC = To Be Checked)

	Algorithms to generate Phase Noise Signals		
Quality	Axelsson [13]	Iterative	Closed Form
PSLR	good only for $\sigma < 2rad$	$< -30dB$	TBC
Orthogonality	TBC	$< -30dB$	TBC
Band occupancy	non controlled	controlled	controlled
MEPPR	1	~ 1	~1

4. CONCLUSIONS

Coherent MIMO radars call for the design of sets of orthogonal waveforms with (*i*) large enough Peak-to-Side-Lobe-Ratio of the autocorrelation function, (*ii*) fairly good mean power to peak power ratio and (*iii*) an assigned spectral occupancy.

Having shown that there are conceptual drawbacks in the Axelsson's method [13], we have started investigating two novel methods, i.e. a recursive and non-recursive (closed form) one. Preliminary results have been presented, but they are not sufficient, at the moment, to define which one is preferable.

References

[1] Jian Li and Petre Stoica, "MIMO Radar Signal processing", John Wiley & Sons Inc., 2008.

[2] E. Fishler, A. Haimovich, R. Blum, L. J. Cimini, D. Chizhik and R. Valenzuela, "Spatial Diversity in Radars – Models and Detection Performance", IEEE Transactions on Signal Processing, vol. 54, n. 3, pp. 823-838, Mar. 2006.

[3] Jian Li and Petre Stoica, "MIMO Radar with Colocated Antennas", IEEE Signal Processing Magazine, vol. 24, no. 5, pp. 106-114, Oct. 2007.

[4] I. Bekkerman and J. Tabrikian, "Target Detection and Localization Using MIMO Radars and Sonars", IEEE Transactions on Signal Processing, vol. 54, no. 10, pp. 3873-3883, Oct. 2006.

[5] J. Li, P. Stoica, L. Xu and W. Roberts, "On Parameter Identifiability Of MIMO Radar", IEEE Signal Processing. Letters, vol. 14, no. 12, pp. 968-971, Dec. 2007.

[6] Petre Stoica, Jan Li and Yao Xie, "On Probing Signal Design For MIMO Radar", IEEE Transactions on Signal Processing, vol. 55, no. 8, pp. 4151-4161, Aug. 2007.

[7] L. Xu, J. Li, P. Stoica, "Radar Imaging via Adaptive MIMO Techniques", Proceedings of 14th European Signal Processing Conference, Sep. 2006.

[8] G. Galati, G. Pavan, "Orthogonal and Complementary Radar Signals for Multichannel Applications", Proc. EuRad 2011. Manchester (UK), 12-14 October 2011, pp. 178-181, 2011.

[9] G. Galati, G. Pavan, "Design Criteria for Multifunction Phased Array Radar Integrating Weather and Air Traffic Control Surveillance", Proceedings of the 6th European Radar Conference, Rome, Italy, 30 September - 2 October 2009, pp. 294-297, ISBN: 978-2-87487-014-9N.

[10] Levanon, E. Mozeson, "Radar Signals", IEEE Press, Wiley-Interscience, Jhon Wiley & Sons, 2004.

[11] W. O. Alltop "Complex sequences with low Periodic Correlations" IEEE Trans. on Information Theory, vol. IT-26, n. 3, May 1980, pp. 350-354.

[12] O. A. Krasnov, Z. Wang, R.F. Tigrek, P. van Genderen, "OFDM waveforms for a fully polarimetric weather radar", Proc. of ESAV'11, Capri 12-14 september 2011, pp. 69-75. ISBN 978890348235.

[13] R. J. Axelsson, "Noise Radar Using Random Phase and Frequency Modulation", IEEE Transactions on Geoscience and Remote Sensing, vol. 42, n. 11, November 2004, pp. 2370-2384.

[14] J. H. Van Vleck, D. Middleton "The Spectrum of Clipped Noise" Proceeding of the IEEE, vol. 54 n. 1, January 1966, pp. 2-19.

[15] G. Galati, G. Pavan "Range Sidelobes Suppression in Pulse-Compression Radar using Golay Pairs: Some Basic Limitations for Complex Targets" IEEE Trans. on Aerospace and Electronic Systems, Vol. 48, N. 3 July 2012, pp. 2756-2760.

[16] Lei Xu, Qilian Liang "Zero Correlation Zone Sequence Pair Sets for MIMO Radar" IEEE Trans. on Aerospace and Electronic Systems, Vol. 48, N. 3 July 2012, pp. 2100-2113.

[17] G. Galati, G. Pavan "Signal processing and waveforms design for Low-Probability-of-Intercept (LPI) noise radar", submitted paper.

Manuscript received November, 23, 2012

Gaspare Galati was with the company Selenia from 1970 till 1986, where he was involved in radar systems analysis and design. From March 1986 he has been associate professor (and full professor from November 1994) of radar theory and techniques at the Tor Vergata University of Rome, where he also teaches probability, statistics, and random processes. He is senior member of the IEEE, member of the IEE, and member of the AICT; within the AICT he is the chairman of the Remote Sensing, Navigation and Surveillance Group. He is the chairman of the SP and AES chapter of the IEEE. His main scientific interests are in radar, surveillance, navigation, and ATC/ASMGCS.

Gabriele Pavan received the Electronics Engineering Degree (Laurea) from the Tor Vergata University of Rome in 1993. After the Laurea he continued research on radarmeteorology. In 2001 he received a Ph.D. in Environmental Engineering. From 2007 he has been a researcher at the Tor Vergata University,where he currently teaches Probability Theory and Signal Processing. His focus of research is on the observation of atmospheric phenomena by radar systems.

УДК 621.37

Построение радиолокационных сигналов для шумового MIMO радара / Г. Галати, Г. Паван // Прикладная радиоэлектроника: науч.-техн. журнал. – 2013. – Том 12. – № 1. – С. 3–10.

Технология Multiple-Input-Multiple-Output (MIMO) является новым направлением в радиолокации, которое имеет значительный потенциал для улучшения характеристик современных радиолокационных систем. В отличие от обычных радиолокаторов с фазированной антенной решеткой, система MIMO может излучать через свои антенны несколько сигналов, которые могут быть коррелированы или не коррелированы друг с другом. Для лучшего разделения при приеме сигналы обязательно должны обладать свойством ортогональности. Хотя ортогональность может проявляться во временной, частотной областях или при кодировании сигналов, для предотвращения изменений в поперечнике рассеяния цели и нежелательных эффектов Доплера, сигналы должны передаваться одновременно и на одной и той же несущей частоте. Как следствие, ортогональность в сигнальной области наиболее предпочтительна, и для успешного использования такой системы ключевую роль играет качество построения сигналов. Хорошие результаты для радиолокационных систем с технологией MIMO показывают ортогональные сигналы со случайной фазой. В статье, после введения в MIMO технологии радиолокационных систем, представлено статистическое описание основных характеристик таких сигналов, в том числе анализ автокорреляционных, кросс-корреляционных и спектральных свойств. Наконец, предложено два новых метода для генерации сигналов со случайной фазой: рекурсивный и нерекурсивный (закрытая форма). Предварительные результаты будут представлены.

Ключевые слова: MIMO, ортогональные сигналы, фазовый шум.

Табл. 1. Ил. 12. Библиогр.: 17 назв.

УДК 621.37

Побудова радіолокаційних сигналів для шумового MIMO радара / Г. Галаті, Г. Паван // Прикладна радіоелектроніка: наук.-техн. журнал. – 2013. – Том 12. – № 1. – С. 3-10.

Технологія Multiple-Input-Multiple-Output (MIMO) є новим напрямком у радіолокації, який має значний потенціал для поліпшення характеристик сучасних радіолокаційних систем. На відміну від звичайних радіолокаторів з фазованими антенними решітками, система MIMO може випромінювати через свої антени кілька сигналів, які можуть бути корельовані або некорельовані один з одним. Для кращого поділу при прийомі сигнали обов'язково повинні мати властивість ортогональності. Хоча ортогональність може проявлятися в тимчасовій, частотної областях або при кодуванні сигналів, для запобігання змін у поперечнику розсіювання цілі і небажаних ефектів Доплера, сигнали повинні передаватися одночасно і на одній і тій самій несучій частоті. Як наслідок, ортогональність у сигнальній області найкраща, і для успішного використання такої системи ключову роль відіграє якість побудови сигналів. Хороші результати для радіолокаційних систем з технологією MIMO показують ортогональні сигнали з випадковою фазою. У статті, після введення в MIMO технології радіолокаційних систем, подається статистичний опис основних характеристик таких сигналів, в тому числі аналіз автокореляційних, крос-кореляційних і спектральних властивостей. Нарешті, запропоновано два нових методи для генерації сигналів з випадковою фазою: рекурсивний і нерекурсивний (закрита форма). Попередні результати будуть представлені.

Ключові слова: MIMO, ортогональні сигнали, фазовий шум.

Табл. 1. Іл. 12. Бібліогр.: 17 найм.

UDC 537.8

WAVEFORM DESIGN FOR MASKING EFFECT REDUCTION IN NOISE RADAR USING VITERBI ALGORITHM

E. TOHIDI, M. NAZARIMAJD, H. HAGHSHENAS, AND M.M. NAYEBI

Signal processing in noise radar is based on the calculation of the correlation between transmitted and received signals. Strong echoes of nearby targets present relatively high sidelobes in the correlation function, thus they can conceal weak echoes of far targets (masking effect). Therefore, finding methods to suppress this effect becomes important. These methods can be implemented at the transmitter or receiver side. There are many new methods developed for the receiver side and a few methods applicable at the transmitter side. The main idea of suppressing side lobes at the transmitter is to design a specific noise signal instead of using pure random noise. A new waveform design to reduce the masking effect is introduced in this paper, which is based on Viterbi algorithm and the produced signals are quantized.

Keywords: masking effect, noise radar, sidelobe, Viterbi algorithm.

I. INTRODUCTION

Pulse compression is an effective method for achieving medium- and high-range resolution in long-range radars.

For a long time, the desired range resolution has been obtained by means of linear frequency modulation (chirp) and matched filtering, in both pulsed and continuous wave (FMCW) radars. Recently, high resolutions are frequently achieved in ultra-wide band radars, often using noise or pseudo-noise signals for target illumination [1–3]. The noise radar technology is a radar technology which uses the noise continuous waveform as a probe signal and correlation (or double spectral) processing of the radar returns as its optimal reception (matched filtering) [4]. Having been considered as early as the 1950s, the concept of noise radar is not new [5]. Noise waveforms enable independent range and velocity resolution, which is regarded as a very significant attribute in the design of surveillance radar systems having moving target indicator (MTI) capabilities. In addition, noise radar guarantees high resolution, low cost, robustness to countermeasures and good electromagnetic compatibility.

Moreover, noise radar waveforms are of interest in LPI (low probability of intercept) radar and repeater jamming. These radars have been used for the measurement of range profiles [6], Doppler estimation [7], detection of buried objects [8], interferometry [9] and inverse synthetic aperture radar (ISAR) and synthetic aperture radar (SAR) imaging [10–12]. A more complete list of the literature on noise radars is provided in [13].

One of the major troubles that should be considered in radar design is weak target echo that may be masked by strong ones. This problem can be easily solved by utilizing range gain control in pulse radars, because of the time separation of near and far echoes. Also it is reduced in FMCW radars by using analogue filters benefiting from the frequency separation of near and far echoes. In contrast with pulse and FMCW radars, there is no frequency or time separation in continuous wave noise radars. Consequently, the sidelobes generated by range compression blocks may reduce radar sensitivity and detection range [14], and in the case of two close targets with significantly different RCS, it may also lead to masking the weak one. Moreover, crosstalk signal and clutter can be considered as important origins of masking effect. Several methods have been developed to counter the masking effect [15]. The crosstalk signal and the ground clutter can be adaptively removed from the received signal with an adaptive lattice filter [16, 17]. The non-zero Doppler clutter can also be removed by using a variation of the previous method [18, 19]. Since this method is not applicable to high-speed targets, stretch processing has been proposed by Misiurewicz and Kulpa [14] and Kulpa and Misiurewicz [20] to overcome the masking effect in noise radars. Another method of suppressing range sidelobe level (RSL), applied to random binary phase coded waveforms, has been introduced by Hong et al. [21]. An apodization filtering technique, developed in [22], achieves sidelobe suppression of greater than 20 dB. Nelander [23] has presented a sidelobe suppression algorithm based on inverse filtering. Sidelobe suppression can also be achieved using an iterative algorithm known as CLEAN [24]. Although all mentioned methods are based on signal processing at the receiver part, there are very few noticeable works focusing on the waveform design at the transmitter part of noise radars. In [25], it is shown that transmission of a sine wave, which is phase or frequency, modulated by random noise waveform leads to improved sidelobe suppression in comparison with transmission of a pure noise waveform. In [26], a method of waveform design with the goal of masking effect suppression has been developed. The proposed waveforms use many short codes to produce a code with the length of the product of the shorter codes lengths. The resulted long code can be arbitrarily long by introducing new shorter codes iteratively. A method for designing chaotic waveforms with parameter optimization for the purpose of complex target detection has been suggested by Carroll; however, it does not concern the masking effect [27]. As the review of noise radar literature shows, most of the algorithms that have been developed in order

to decrease the masking effect are applicable in the receiver end. Hence, it should first be clarified that whether masking effect reduction in noise radar is possible by concentrating on waveform design [28].

In this paper, a new waveform design based on Viterbi algorithm to reduce masking effect in random phase modulated radarsis introduced. Uniqueness of the developed algorithm comes from the quantized nature of designed signal which is another step to applicability. In previous waveform design methods which is presented in [29], the output signals are analog phases in range $[-\pi,\pi]$; however in practical radars, phases should be quantized with limited number of bits.

In the following sections, first of Viterbi algorithm is reviewed. second, all necessary parameters are defined. Next, waveform design using Viterbi Algorithm is introduced. Next, simulation results are discussed and eventually paper will be concluded.

II. VITERBI ALGORITHM

The Viterbi algorithm was proposed by Andrew Viterbi in 1967 as a decoding algorithm for convolutional codes over noisy digital communication links. The algorithm has found universal application in decoding the convolutional codes used in both CDMA and GSM digital cellular and etc.It is now also commonly used in speech recognition, keyword spotting, computational linguistics, and bioinformatics [30].

Since that time, it has been recognized as an attractive solution to a variety of digital estimation problems [30].

In its most general form, the VA may be viewed as a solution to the problem of maximum a posteriori probability (MAP) estimation of the state sequence of a finite-state discrete-time Markov process observed in memoryless noise [30].

In the presence of intersymbol interference in communication channels, using the whitening filter in system results [31]:

$$v_k = \sum_{n=0}^{L} f_n I_{k-n} + \eta_k \ . \qquad (1)$$

Where $\{\eta_k\}$ is a white Gaussian noise sequence, $\{f_k\}$ is a set of tap coefficients of an equivalent discrete-time transversal filter with length of L and $\{I_k\}$ s the information sequence.

MLSE of the information sequence $\{I_k\}$ is most easily described in terms of the received sequence $\{v_n\}$ at the output of the whitening filter. In the presence of intersymbol interference that spans $L+1$ symbols (L interfering components), the MLSE criterion is equivalent to the problem of estimating the state of a discrete-time finite-state machine [31]. The finite-state machine in this case is the equivalent discrete-time channel with coefficients $\{f_k\}$, and its state at any instant in time is given by the L most recent inputs, i.e., the state at time k is

$$S_k = (I_{k-1}, I_{k-2}.....I_{k-2}) . \qquad (2)$$

Where $I_k = 0$ for $k \le 0$. Hence, if the information symbols are M-ary, the channel filter has M^L states. Consequently, the channel is described by an M^L -state trellis and the Viterbi algorithm may be used to determine the most probable path through the trellis.

The metrics used in the trellis search are akin to the metrics used in soft-decision decoding of convolutional codes. In brief, we begin with the samples $v_1, v_2, ..., v_{L+1}$, from which we compute the M^{L+1} metrics

$$\sum_{k=1}^{L+1} In\rho(v_k | I_k, I_{k-1}, ...I_{k-L}) \qquad (3)$$

The M^{L+1} possible sequences of $I_{L+1}, I_L, ...I_2, I_1$ are subdivided into M^L groups corresponding to the M^L states $(I_{L+1}, I_L, ..., I_2)$ Note that the M sequences in each group (state) differ in I_1 and correspond to the paths through the trellis that merge at a single node. Form the M sequences in each of the M^L states, we select the sequence with the largest probability (with respect to I_1) and assign to the surviving sequence the metric

$$\begin{aligned} PM_1(I_{L+k}) &= PM_1(I_{L+1}, I_L, ..., I_2) \\ &= \max \sum_{k=1}^{L+1} In\rho(v_k | I_k, I_{k-1}, ..., I_{k-L}) \end{aligned} \qquad (4)$$

The $M-1$ remaining sequences from each of the M^L groups are discarded. Thus, we are left with M^L surviving sequences and their metrics.

Upon reception of v_{L+2}, the M^L surviving sequences are extended by one stage, and the corresponding M^{L+1} probabilities for the extended sequences are computed using the previous metrics and the new increment, which is $In\rho(v_{L+2} | I_{L+2}, I_{L+1}, ...I_2)$. Again, the M^{L+1} sequences are subdivided into M^L groups corresponding to the M^L possible states $(I_{L+2}, I_{L+1}, ...I_3)$ and the most probable sequence from each group is selected, while the other $M-1$ sequences are discarded.

The procedure continues with the reception of subsequent signal samples. In general, upon reception of v_{L+k}, the metrics

$$\begin{aligned} PM_k(I_{L+k}) = \max[&Inp(v_{L+k} | I_{L+k}, ..., I_k) + \\ &+ PM_{k-1}(I_{L+k-1})] \end{aligned} \qquad (5)$$

That are computed give the probabilities of the M^L surviving sequences. Thus, as each signal sample is received, the Viterbi algorithm involves first the computation of the M^{L+1} probabilities

$$Inp(v_{L+k} | I_{L+k}, ...I_k) + PM_{k-1}(I_{L+k-1})$$

corresponding of the M^{L+1} sequences that form the continuations of the M^L surviving sequences from the previous stage of the process. Then the M^{L+1} sequences are subdivided into M^L groups, with each group containing sequences that terminate in the same set of symbols $I_{L+k}, ...I_{k+1}$ and differ in the symbol I_k. From each group of M sequences, we select the one having the largest probability as indicated by (5), while the remaining M-1 sequences are discarded. Thus, we are left again with M^L sequences having the metrics $M_k(I_{L+k})$ [31].

III. DEFINITION OF ISLR

The transmitted and received signals are represented by x_k and y_k respectively. Assuming a maximum delay of N samples for farthest target, signals can be divided into N-sample blocks [32].

To extract information of targets at the receiver, a time correlation between these signals is calculated, which is between successive blocks. The time correlation between block m and m+1 is represented:

$$P(i,m)=\sum_{k=mN}^{(m+1)N-1} x_k y_{k+i}^{*} . \quad (6)$$

Where $i=0.1,...,N, m=0,1,...,M-1$, symbol * represents complex conjugate and M is the total number of blocks. Ignoring Doppler effect, received signal is a delayed version of transmitted one

$$y_k = x_{k-l} . \quad (7)$$

Suppose phase modulating signal:

$$x_k = e^{j\theta_k} . \quad (8)$$

Using (5), (6) and (7) results:

$$P(i,m)=\sum_{k=mN}^{(m+1)N-1} \theta^{j(\theta_k-\theta_{k+i-l})} . \quad (9)$$

Range main lobe take place, when i and l are equal and Range side lobe in other case. Sidelobes are divided into two groups based upon sign of $i-l$, show them with C_p and D_p respectively [32]:

$$C_p=\sum_{k=mN}^{(m+1)N-1} e^{j\theta_k-j\theta_{k+p}}, p=1.2....,N$$

$$D_p=\sum_{k=(m+1)N}^{(m+2)N-1} e^{j\theta_k-j\theta_{k-p}}, p=1.2....,N \quad (10)$$

In addition main lobe level is made up with C_0 and D_0 which are equal to N Fig. (1) represents a simple example of Masking weak target main lobe by strong target sidelobe [32].

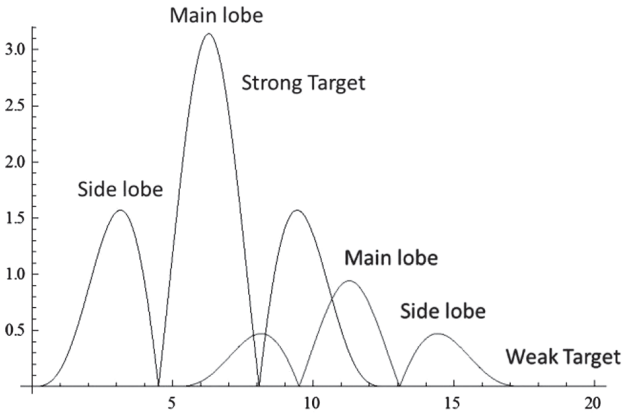

Fig. 1. Comparing magnitude of correlation of a strong and weak target

The Integrated side lobe ratio (ISLR) is defined as the total energy of sidelobes to total energy of main lobe, will equal

$$ISLR=\frac{2NJ}{|D_0|^2+|C_0|^2} . \quad (11)$$

And J is defined as below:

$$J=\frac{1}{2N}\sum_{p=1}^{N}(|C_p|^2+|D_p|^2) . \quad (12)$$

ISLR is an appropriate measurement of masking effect, from now on, the purpose is to minimize ISLR. Let's have a more detailed look on ISLR. As mentioned before, $|D_0|$ and $|C_0|$ are constant and equal to N, thus minimization of ISLR and J are equivalent. Expanding eq. (12):

$$J=\sum_{k=1}^{N}\sum_{i=1}^{N-1}\sum_{j=i+1}^{N}\{\cos(\theta_i+\theta_{j+k}-\theta_{i+k}-\theta_j)+ +\cos(\theta_{j+N}+\theta_{i+N-k}-\theta_{i+N}-\theta_{j+N-k})\} \quad (13)$$

Procedure of finding the appropriate phases for waveform design will be block by block, it means set first N-signal block randomly. Find the second N-signal block to minimize the ISLR due to these two blocks, and continue these progress up to end.

To find the transition coefficients among Markov process states, we rewrite J in a new form. That is

$$J=J_{cte}+J_{N+1}+J_{N+2}+...+J_{2N} . \quad (14)$$

Where, J_{cte} is the constant part of J due to the first N signal of first block which have been set and is independent of the second block that is in optimization process $J_m, m=N+1,...,2N$, is part of J which is affected by signals 1 to m.

$$J_m=\sum_{k=m-N}^{N}\sum_{i=1}^{m-k-1}\cos(\theta_m+\theta_i-\theta_{i+k}-\theta_{m-k})+ \sum_{k=1}^{N}\sum_{i=1}^{m-N-1}\cos(\theta_m+\theta_{i+N-k}-\theta_{i+N}-\theta_{m-k}) \quad (15)$$

Implementation of VA to minimize ISLR is discussed in subsequent section.

IV. ALGORITHM

In section II, a general discussion of VA was presented and important parameters were described. Let study this subject in detail.

The proposed waveform design method is based on VA, thus a Markov process, states, transition weights, decision criteria and all other parameters should be defined and a one-to-one correspondence between these parameters and the in hand problem should be made.

Suppose, signals of first block are chosen completely random. Now we are going to find the i^{th} block signals. More precisely, phase of i^{th} block signals. Clearly, due to quantized nature of produced signals, each phase can have 2^{nbits} different values, where $nbits$ is the number of quantization bits. As stated in previous section, ISLR is our criterion in designing the signals. In addition, equivalence of ISLR and parameter J was proved. Thus, the cost functions are chosen based on parameter J. For designing each new block signal, a new Markov process is synthesized, which has N steps (equal to number of signals in a block). It means, each step is matched with equivalent signal. In transition between step k to step $k+1,(k+1)^{th}$, signal is under investigation.

Ideally, number of states in each step, is number of all different cases of previous signals in the block. However, simple calculations show that is impossible in practical cases due to large consumption of memory and calculations. Thus, parameter L is defined, which is the memory (or buffer) size of algorithm. Parameter L means, in process of calculating different choices of θ_k, different cases of the last L signals are kept, however the other previous signals should have been determined up to that moment. i.e. θ_{k-L-1} should have been determined and costs for θ_k are calculated based on 2^{nbits} different values of θ_k and many different cases for θ_{k-L} to θ_{k-1}. Remember, these different cases are survived path of VA from previous step. Now, θ_{k-L} should be determined based on the θ_{k-L} of the minimum cost survived path of step *k*, and algorithm continues. Remember in step N, all the θ_{N-L} to θ_N should be determined based on the θ_{N-L} to θ_N of the minimum survived path of N^{tn} step.

A General description of proposed algorithm has been described so far. Now it's time to look in more detail to the algorithm. As discussed in section II, survived path in VA should be chosen based on a criterion. In section II it was probability, however as mentioned before, parameter *J* is our cost function and criterion for determining survived path. Due to parameters L and $nbits$, there are $2^{nbits\times L}$ states in each step. Each step is determined with a unique survived path. In addition, each state has a cost, which is sum of corresponding survived path, vectors cost. Let Illustrate the above parameters through an example. Again, suppose we are in transition of k^{tn} step to $(k+1)^{tn}$ step. Thus survived paths and costs of all the states in k^{tn} are determined and we should calculate these parameters for stats of $k+1$ step . There are 2^{nbits} different possibilities for θ_{k+1}. Vectors are the links, connecting states of k^{tn} step to states of $(k+1)^{tn}$ step. There are 2^{nbits} outgoing vectors from each state of k^{tn} step, and 2^{nbits} incoming vectors to each state of step $k+1$. Each state in k^{tn} step is one of the $2^{nbits\times L}$ different cases of θ_{k-L} to θ_{k-1} and each state in $(k+1)^{tn}$ step is one of the $2^{nbits\times L}$ different cases of θ_{k-L+1} to θ_k. Vectors cost of this transition is calculated by Eq. (15). Note that $m=k+N+1$ and θ_m is the corresponding value of θ_{k+1}. Now, each state of step $k+1$ has 2^{nbits} incoming vectors with different costs. If vectors cost are added to states cost of their sources, 2^{nbits} different total cost for each state is found. Clearly, the survived path is the path with minimum cost and the state cost is the minimum of the costs.

Note that the process depends on the parameters: N, L and $nbits$.

V. SIMULATION RESULTS

In this section, simulation results of developed method are presented. Variation of ISLR versus L of VA method for $N=8$ and different values of nbits is plotted in Fig. (2). As expected, increasing nbits leads to better ISLR (reduction in ISLR). In addition, note that ISLR decreases while L increases, which was predictable. This observation comes from the fact that, increasing L, is translated to increasing memory and including more cases that clearly result a better performance and of course imply more computational complexity.

Fig. (3) is similar to Fig. (2), however $N=16$. Those observations are confirmed in this plot again. Another interesting point is a negligible difference between the results of Fig. (2) and Fig. (3), which show a low relationship with N, number of signals in a block.

It should be emphasized that the ISLR improvement shown in following figures are in relative to pure noise sidelobe level. It means, to obtain sidelobe level of designed signal, these numbers should be added to pure noise sidelobe level.

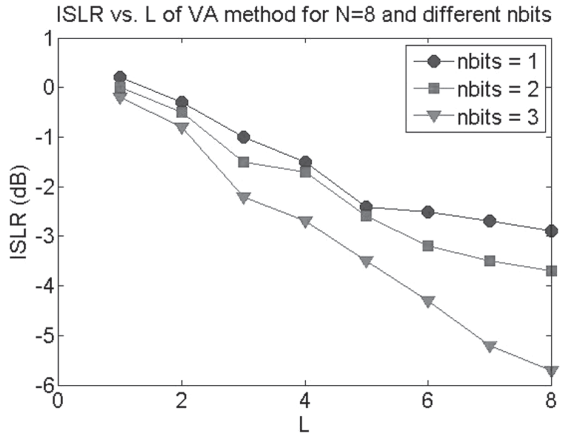

Fig. 2. ISLR vs. L of VA method for $N=8$ and different values of nbits.

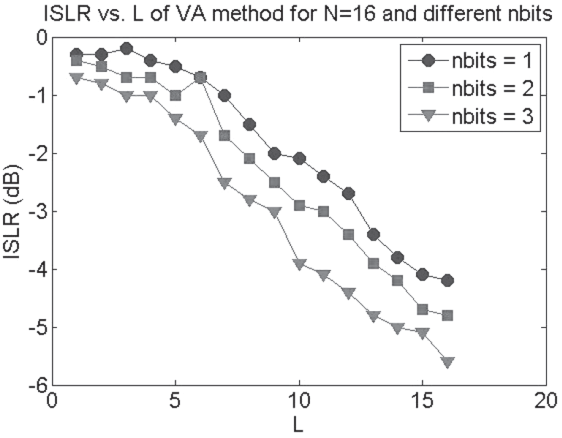

Fig. 3. ISLR vs. L of VA method for N=16 and different values of nbits

Few methods of waveform design for masking effect reduction have proposed till now. As mentioned before, all these methods make analog outputs. To have criterion of developed method performance, one of the best previous methods presented in [29] is compared with VA method, which is named Conventional method in tables in the following.

To have a fair comparison, output phases of Conventional method are quantized with similar number of bits for VA method and the results are represented in Table (1) for case $N=8$ and in Table (2) for $N=16$

Table 1

Performance comparison (ISLR) of VA and Conventional methods for $N = 8$

nbits	Conventional method	VA method
1	-1.1 dB	-2.9 dB
2	-2.7 dB	-3.7 dB
3	-4.5 dB	-5.7 dB

Table 2

Performance comparison (ISLR) of VA and Conventional methods for $N = 16$

nbits	Conventional method	VA method
1	-1.3 dB	-4.2 dB
2	-2.8 dB	-4.8 dB
3	-4.5 dB	-5.6 dB

ISLR of Conventional method is represented in second column of both tables and the third column is ISLR of VA method. First, second and third row of each table is for the cases of number of bits equal to one, two and three respectively. Better performance of developed method is visible for all the conditions and the results are similar for both cases $N = 8,16$.

VI. CONCLUSION

During the correlation process between transmitted and received signals, relatively high sidelobes of strong echoes of nearby targets can conceal weak echoes of far targets (masking effect). There has been a wide study on this subject which led to different methods. These methods can be implemented at the transmitter or receiver side.

There are many new methods developed for the receiver side and a few methods applicable at the transmitter side. The main idea of suppressing side lobes at the transmitter is to design a specific noise signal instead of using purely random noise.

In this paper a new waveform design to reduce the masking effect was introduced which is based on Viterbi Algorithm. The important difference of developed algorithm with other waveform design methods is the quantized nature of the produced signal that makes it more applicable. In addition, simulation results showed the higher performance of developed method in comparison with previous ones.

ACKNOWLEDGMENT

Special thanks go to Radar Laboratory group of Electrical Engineering Department at 'Sharif University of Technology'.

Financial supports from the National Elites Foundation to Ehsan Tohidi is gratefully acknowledged.

References

[1] Axelsson, S.R.J.: 'Noise radar for range/Doppler processing and digitalbeamforming using low-bit ADC', IEEE Trans. Geosci. Remote Sens.,2003, 41, (12), pp. 2703–2720.

[2] Salminen, V.J., Lensu, T., Eskelinen, P., Mertanen, S.: 'Noise modulatedmultistatic surveillance radar concept'. Proc. Int. Radar Symp., Krakow,Poland, May 2006, pp. 311–314

[3] Garmatyuk, D., Narayanan, M.: 'Ultra-wideband continuouswaverandom noise Arc-SAR', IEEE Trans. Geosci. Remote Sens., 2002,40, (12), pp. 2543–2552

[4] Lukin, K.A.: 'Millimeter wave noise radar technology'. Proc. MSMW-98 Symp., Kharkov, Ukraine, September 1998, pp. 94–975

[5] Horton, B.M.: 'Noise-modulated distance measuring systems', Proc.IRE, 1959, 47, (5), pp. 821–828

[6] Walton, E.K.: 'Use of the fixed range noise radar for moving vehicleidentification'. Proc. Sensors Electron Devices Symp., College Park,MD, 1997.

[7] Narayanan, R.M., Dawood, M., Mueller, R.D., Palmer, R.D.: 'Dopplerestimation using a coherentultrawideband random noise radar'. Proc.SPIE Conf. on Radar Processing Technology and Application II, SanDiego, CA, July 1997, vol. 3161, pp. 70–76

[8] Narayanan, R.M., Xu, Y., Hoffmeyer, P.D., Curtis, J.O.: 'Design,performance, and applications of a coherent ultrawideband randomnoise radar', Opt. Eng., 1998, 37, pp. 1855–1869

[9] Narayanan, R.M., Mueller, R.D., Palmer, R.D.: 'Random noise radarinterferometry'. Proc. SPIE Conf. on Radar Processing Technologyand Application, 2845, Denver, CO, August 1996, pp. 75–82

[10] Bell, D.C., Narayanan, R.M.: 'ISAR imaging using coherent randomnoiseradar techniques'. Proc. SPIE Conf. on Radar Processing Technology andApplication III, 3462, San Diego, CA, July 1998, pp. 284–265.

[11] Walton, E.K., Fillimon, V., Gunawan, S.: 'ISAR imaging using UWB noise radar'. Proc. Antenna Measurement Techniques Association(AMTA) Symp., 1996, pp. 167–171.

[12] Garmatyuk, D., Narayanan, R.M.: 'SAR imaging using a coherentultrawideband random noise radar'. Proc. SPIE Conf. on RadarProcessing Technology and Application IV, 3810, Denver, CO, July1999, pp. 223–230.

[13] Guosui, L., Hong, G., Weimin, S.: 'Development of random signalradars', IEEE Trans. Aerosp. Electron. Syst., 1999, 35, (3), pp. 770 -777.

[14] Misiurewicz, J., Kulpa, K.S.: 'Stretch processing for masking effectremoval in noise radar', IEE Proc. Radar Sonar Navig., 2008, 2, (4),pp. 274–283.

[15] Kulpa, K.S., Czekala, Z.: 'Short distance clutter masking effects in noiseradars', J. Appl. Radio Electron., 2005, 4, (1), pp. 96–98.

[16] Axelsson, S.R.J.: 'Improved clutter suppression in random noise radar'.Proc. URSI 2005 Commission F Symp. on Microwave Remote Sensingof the Earth, Oceans, Ice and Atmosphere, Barzad'Ispra, Italy, April 2005.

[17] Kulpa, K.S., Czekala, Z.: 'Ground clutter suppression in noise radar'.Proc. Int. Conf. on Radar, Toulouse, France, October 2004, p. 236.

[18] Kulpa, K.S.: 'Simple sea clutter canceller for noise radar'. Proc. Int.Radar Symp., Krakow, Poland, 2006, pp. 299–302.

[19] Kulpa, K.S., Czekala, Z.: 'Masking effect and its removal in PCL radar',IEE Proc. Radar Sonar Navig., 2005, 152, (3), pp. 174–178.

[20] Kulpa, K.S., Misiurewicz, J.: 'Stretch processing for long integrationtime passive covert radar'. Proc. CIE Int. Conf. on Radar, Shanghai,China, 2006, pp. 496–499.

[21] Hong, G., Guosui, L., Xiaohua, Z., Weimin, S., Li, X.: 'A new kind ofnoise radar – random binary phase coded CW radar'. IEEE NationalRadar Conf., Syracuse, NY, May 1997, pp. 202–206.

[22] Xu, X., Narayanan, R.M.: 'Range sidelobe suppression technique forcoherent ultra-wideband random noise radar imaging', IEEE Trans.Antennas Propag., 2001, 49, pp. 1836–1842.

[23] Nelander, A.: 'Inverse filtering for noise radar processing'. Proc. Int.Radar Symp., Krakow, Poland, 2006, pp. 421–424.

[24] Fry, R.D., Gray, D.A.: 'CLEAN deconvolution for sidelobesuppressionin random noise radar'. Proc. Int. Conf. Radar, September 2008,pp. 209–212.

[25] Axelsson, S.R.J.: 'Noise radar using random phase and frequencymodulation', IEEE Trans. Geosci. Remote Sens., 2004, 42, (11),pp. 2370–2384.

[26] Nelander,A.: 'Continuous codedwaveforms for noise radar'. Proc. Int.Conf.on Waveform Diversity and Design, Pisa, Italy, June 2007, pp. 438–442.

[27] Carroll, T.L.: 'Adaptive chaotic maps for identification of complextargets', IET Radar Sonar Navig., 2008, 2, (4), pp. 256–262.

[28] H. Haghshenas and M.M. Nayebi,'Suppressing masking effect in random signal radars by waveform design', IET Journals, Radar, Sonar & Navigation, 6, (3), pp. 137-148, 2012.

[29] H. Haghshenas, M. M. Nayebi, 'Waveform Design to Suppress Range Sidelobe in Random Phase Modulated Radar, in Electronic Proc Signal Processing Symp., SPS-2009, Jachranka, Poland, on CD-ROM, 28-30 May 2009.

[30] 11. Forney, G.D., Jr. 'The viterbi algorithm', Proceedings of the IEEE.61, (3), pp. 268-278, 1973.

[31] John Proakis, "Digital Communication", 4'th edition.

[32] E. Tohidi, M. NazariMajd, M. Bahadori, H. HaghshenasJariani, M. M. Nayebi, 'Periodicity in Contrast with Sidelobe Suppression in Random Signal Radars'. In Proceedings of 2011 IEEE CIE International Conference on Radar, Chengdu, China, pp. 442-445, 24-27 October 2011.

Manuscript received December, 12, 2012

Ehsan Tohidi was born in Iran on April 20, 1989. He received the B.Sc. degree in communication systems of electrical engineering, from Sharif University of Technology, Tehran, Iran in 2011. Since 2011, he has been working on his M.Sc. thesis on Array processing at thesame university. His research interests include Array processing, signal processing, Noise Radars, and detection theory.

M. Nazari Majd received the B.S. degree in communication systems of electrical engineering, from Sharif University of Technology, Tehran, Iran. He is now pursuing his M.S. at the same university. His research interests include MIMO Radars, Noise Radars, detection theory and Radar signal processing.

Hamed Haghshenas Jariani received the B.Sc degree from University of Tehran in 2004, and the M.Sc. degree from Sharif University of Technology in 2006. He is currently reading for his Ph.D degree in Telecommunication at Sharif University of Technology. His main Research interests are radar signal processing and image processing.

Mohammad M. Nayebi (S'89-M'94-SM'05) was born in IRAN in 1967. He received the B.S.E.E. and M.S.E.E. degrees, both with the honor of first rank, from Sharif University of Technology, Tehran, Iran, in 1988 and 1990, respectively, and the PhD. Degree in electrical engineering, with the same honor, from TarbiatModarres University, Tehran, Iran, in 1994. He joined the Sharif University of Technology faculty in 1994, and became an associate Professor in 1998, and Professor in 2003. His main research interests are radar signal processing and detection theory.

УДК 537.8

Получение сигнала для снижения маскирующего эффекта в шумовом радиолокаторе с использованием алгоритма Витерби / Е. Тохиди, М.Н. Мадж, Х.Х. Джариани, М. Наяби // Прикладная радиоэлектроника: науч.-техн. журнал. – 2013. – Том 12. – № 1. – С. 11–16.

Обработка сигналов в шумовой радиолокации основана на вычислении корреляции между передаваемым и принимаемым сигналами. Сильное эхо от близлежащих целей является причиной относительно высокого уровня боковых лепестков корреляционной функции, таким образом, они могут скрыть слабые отклики от далеко расположенных целей (эффект маскировки). Поэтому становится важным поиск методов для подавления этого эффекта. Эти методы могут быть реализованы на передающей или на приемной стороне. Существует много новых методов, разработанных для канала приемника, и несколько методов, применяемых в канале передатчика. Основная идея подавления боковых лепестков в передатчике заключается в формировании шумового сигнала со специальными свойствами вместо истинно случайного шума. Новый способ формирования сигнала с целью уменьшения эффекта маскировки, который предложен в статье, основан на алгоритме Витерби с квантованием получаемых сигналов.

Ключевые слова: маскирующий эффект, шумовой радиолокатор, боковые лепестки, алгоритм Витерби.

Ил. 03. Библиогр.: 32 назв.

УДК 537.8

Отримання сигналу для зниження маскуючого ефекту в шумовому радіолокаторі з використанням алгоритму Вітербі / Е.Тохіді, М.Н. Мадж, Х.Х.Джаріані, М.Наябі // Прикладна радіоелектроніка: наук.-техн. журнал. – 2013. – Том 12. – № 1. – С. 11–16.

Обробка сигналів в шумовій радіолокації заснована на обчисленні кореляції між переданим і прийнятим сигналами. Сильне відлуння від довколишніх цілей є причиною відносно високого рівня бічних пелюсток кореляційної функції, таким чином, вони можуть приховати слабкі відгуки від далеко розташованих цілей (ефект маскування). Тому стає важливим пошук методів для заглушення цього ефекту. Ці методи можуть бути реалізовані на передавальній або на приймальній стороні. Є багато методів, розроблених для каналу приймача, і кілька методів, які застосовуються в каналі передавача. Основна ідея заглушення бічних пелюсток в передавачі полягає у формуванні шумового сигналу зі спеціальними властивостями замість істинно випадкового шуму. Новий спосіб формування сигналу з метою зменшення ефекту маскування, який запропонований в статті, базується на алгоритмі Вітербі з квантуванням одержуваних сигналів.

Ключові слова: ефект маскування, шумовий радіолокатор, бічні пелюстки, алгоритм Вітербі.

Іл. 03. Бібліогр.: 32 найм.

UDC 621.396.2.018.424

NEW METHOD FOR GENERATION OF QUASI-ORTHOGONAL CHAOTIC SEQUENCES

K.A. LUKIN, V.Ye. SHCHERBAKOV AND D.V. SHCHERBAKOV

A new method for generation of quasi-orthogonal chaotic sequences for applications both in radars and communication systems has been suggested. The method is based upon a discrete chaotic map with two time delay parameters. The phase space structure of the suggested algorithm has been analyzed using computer simulation. The period spectrum of cyclic trajectories in the phase space for different values of the time delay parameters has been founded. The statistical and correlation characteristics of binary pseudorandom sequences, generated with the help of the suggested method have been studied in detail. It has been shown that for the properly chosen time delay parameters the suggested discrete chaotic algorithm generates binary pseudorandom sequences with a nearly uniform probability distribution. It has been shown that the correlation characteristics of binary pseudorandom sequences generated are rather similar to those of random process with a uniform probability distribution.

Keywords: quasi-orthogonal chaotic sequence, discrete chaotic algorithm, chaotic integer sequence, chaotic map, phase space, binary pseudorandom sequence, autocorrelation and cross-correlation function.

INTRODUCTION

One of the problems extant in design of radar and communication systems [1-5] lays in complexity of truly random sequences generation. The most appropriate generators of random sequences from the viewpoint of their quality are the generators, based on physical sources. However, they have number of drawbacks, such as: implementation difficulties of such generators in the required frequency band; complexity of their integration with other systems and subsystems, and also no possibility of random sequences reproducing using the same source.

That is why nowadays, pseudorandom sequences are widely used in various radars, communication and data transmission systems. A lot of algorithms for pseudorandom sequences (PR-sequences) generation are known to the date. Usually, recurrent algorithms are used for the PR-sequences generation. Binary PR-sequences on the basis of recurrent algorithms may be readily realized as a computer code or, otherwise, as a fast enough binary shift register. For example, so-called M-sequences generator may be implemented in this way. However, the main disadvantage of this approach consists in the absence of mathematical tool enabling derivation of algebraic polynomials for the arbitrary large power, generating the sequences of maximal period. In addition, their statistical properties, as a rule, are rather far from statistical properties of truly random signals.

The choice of proper binary PR-sequences is a very important stage of design and practical realization of both radars and communication systems. The chosen PR-sequence has to meet the requirements for both good auto (cross)-correlation properties and providing a large set for values of their lengths and, in particular, large number of sequences ensembles [2, 3, 5].

The known classes of both linear (M-sequences, Hadamard-sequences, Gold-sequences, Kasami-sequences and other) and nonlinear (Legendre-sequences, bent-sequences and other) PR-sequences do not meet some of the above requirements [5, 7].

Basic requirements to binary pseudorandom sequences (BPR-sequences), which can be used both in radar and communication systems are as follows [5, 7 and 10]:

1) binary sequence must be balanced, i.e. a number of «+1» differs from a number «-1» by no more than one unit;

2) occurrence probability of block from k identical symbols must be close to $p(k)=1/2^k$;

3) ensemble volume of binary sequences must be maximally large;

4) autocorrelation function of binary sequence must have one narrow peak and low side-lobes level;

5) it must be ensured a low level of cross-correlation between different binary sequences;

6) binary sequences must be reproduced on the receiving end of communication systems, i.e. it must be ensured a possibility for exact reiteration of the generated binary sequence for the same initial conditions;

7) it must be ensured an acceptable complexity of algorithm formula for its practical realization.

Nowadays, PR-sequences generated with a computer code are in a wide use both in radars and communication systems caused by resent advancing in digital electronics. In turn, development of computational mathematics methods resulted in elaboration of the special generation algorithms for so-called pseudorandom number sequences, in development of which a special role plays the methods for chaotic integer sequences generation in the limited interval of integers.

Basic requirements to *chaotic integer* sequences (CI-sequences) are as follows [6, 8]:

1) *high quality:* statistical properties of CI-sequence must be close to those of truly random process and it might have as long p|eriod as possible;

2) *efficiency:* algorithm for generation of CI-sequence must be quiet fast and occupy the minimal area in a computer memory;

3) *reproducibility:* the algorithm might generate exactly the same CI-sequence of any length for a chosen initial conditions, for arbitrary number of trials and minor changes in initial procedure must result in a generation of very different CI-sequences, still having a high-quality statistical properties;

4) *simplicity* – the algorithm formula must be as simple as possible in its realization and application.

In our opinion, random sequences generators based upon *multidimensional* chaotic systems may combine advantages of conventional random numbers generators used in computers and physical sources of noise signals.

In the paper we consider a new method for generation of quasi-orthogonal chaotic sequences, applicable in both radar and communication systems. Besides we investigate the period spectrum of binary pseudorandom sequences, generated according to the method suggested, and also study their statistical and correlation characteristics.

1. THE METHOD FOR GENERATION OF BINARY PSEUDORANDOM SEQUENCES BASED ON DISCRETE CHAOTIC ALGORITHM

On the basis of mathematical model of self-oscillatory modes in one-dimensional electromagnetic resonator with a nonlinear reflecting surface, the field dynamics in which obeys the system of functional-difference equations with *two* delays [9], the discrete chaotic algorithm for generating binary pseudorandom sequences has been developed and studied. This algorithm can be attributed to the class of recurrent parametric algorithms with two time delay parameters. The algorithms for PR-sequences generation using nonlinear difference equation with *one* delay have been derived in [11] from the model of nonlinear ring self-oscillatory system with filtration and delayed feedback.

The discrete chaotic algorithm suggested in our paper is based on the discrete nonlinear functional equation with two delay parameters, which in general case may be written as follows:

$$X_n = F\left(X_{n-q}, X_{n-Q}, q, Q, M\right), \qquad (1)$$

where X_n, X_{n-q} and X_{n-Q} are calculated and given terms of the generated chaotic integer sequence; n, q, Q, M are integer natural numbers; $M = 2,3,4...$; $Q = 2,3,4...$; $n \geq Q+1$; $1 \leq q < Q$; q and Q are the first and the second delay parameters, respectively.

$F(X)$ is the function describing nonlinear transformation (chaotic in general case) of initial values of the electromagnetic field either in the problem of self-oscillations in resonator with a nonlinear reflection [9] or in the time delay amplifying system [11], but with two delayed feedback channels.

For $q < Q$ the value of the delay parameter Q determines the number of terms in the integer sequence $X_{n-1}, X_{n-2} \ldots X_{n-Q}$. Using these values a new value of variables X_n is iteratively calculated according to Eq.(1). That is why they might be used as initial conditions for the iterative process of the PR-sequence generation.

The authors has considered here the most simple nonlinearity in the discrete chaotic algorithm Eq.(1), namely linear dependence of the result on the linear combination of two variables with two different delays, but limited by modulus M:

$$X_n = \begin{cases} X_{n-q} + X_{n-Q} & if \quad X_{n-q} + X_{n-Q} \leq M \\ X_{n-q} + X_{n-Q} - M & otherwise \end{cases} \qquad (2)$$

The theory of functional difference equations implies the Eq.(2) with two delays is equivalently to the system of Q equations with a single delay. Thus a discrete algorithm (2) is defined on the bounded set M of integer natural numbers, which belong to the closed numerical interval $[1, M]$. For $q < Q$ the phase space of the dynamical system (2) has a dimension Q. A number of system states in the phase space of the system (2) that is defined on the bounded discrete set, is finite and equals M^Q.

From Eq. (2) one can see that the return operation $X_n \to X_n - M$ is applied to the values X_n exceeding M when generating chaotic integer sequence $\{X_n\}$, realizing thereby a nonlinear transformation of the variable X_n similar to the known algorithm of 1D Bernoulli shift. Therefore the map (2) can be classified as multidimensional (MD) Bernoulli shift, operating in *multidimensional phase space*.

It is clear that in our case the algorithm for generation of chaotic integer sequences is the more rich and more efficient in generation of many varieties of quasi-orthogonal sequences suitable for applications in both radar and communication systems.

Generation of *binary* pseudorandom sequence has been implemented via clipping procedure of the multilevel chaotic integer sequence with respect to some threshold equals to $M/2$ according to the following rule:

$$Y_n = \begin{cases} -1, \ if \ X_n \leq \dfrac{M}{2} \\ 1, \ if \ X_n > \dfrac{M}{2} \end{cases} \qquad (3)$$

Since every state for the self-oscillatory system is defined on the finite and limited set of integers, the system sooner or later returns back to its primary state and process will be repeated. It means that a binary sequence $\{Y_n\}$ formed by the system has a limited length, representing a segment for pseudorandom sequence of the above length. This implies that a value M^Q determines a maximal theoretical cycle, but therefore a maximum possible duration of non-periodic realization $L_{\max} = M^Q$, formed by the algorithm of the given dimension. Appearance of a period in the sequence $\{Y_n\}$ has been fixed when iteration started with the exact values of initial conditions $X_{n-1}, X_{n-2} \ldots X_{n-Q}$.

2. RESULTS OF ALGORITHM STUDY

Phase space of the discrete dynamical system (2), consists of a set of isolated points with co-ordinates falling into the interval of integers $[1, M]$ and determine unambiguously the system state. Dynamics of the discrete dynamical system (2) may be described with the help of its representative point in the plane formed by the delayed coordinates which is, actually, an across-section of the phase space for the given parameters of the map (2). If to connect these points with solid lines we may get qualitative information on the CI-sequence length and chaotization rate of the system motion for each given set of the system parameters.

Two examples are shown in fig. 1 and 2 for different parameter sets of the map (2) .

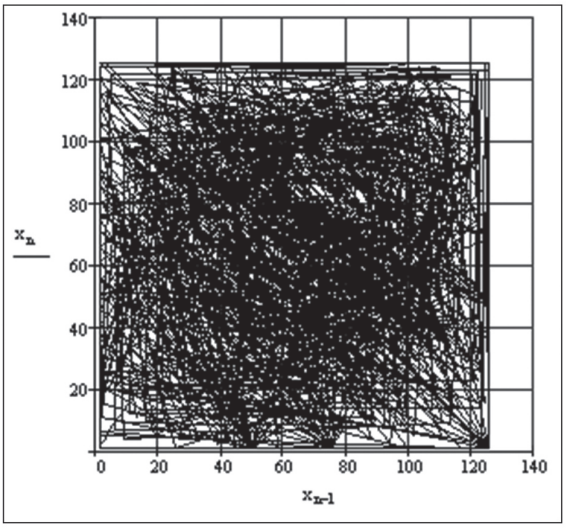

Fig. 1. Cross-section of the map (2) phase space in the delayed coordinates for the following parameter set of the map (2): M = 125, Q = 3, q = 1; and CI-sequence period = 775; representative points of the discrete dynamical system (2) are connected with solid lines at the neighboring instances of time

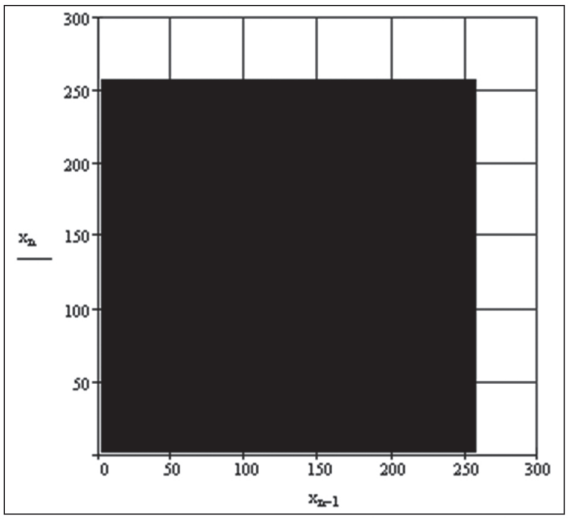

Fig. 2. Cross-section of the map (2) phase space in the delayed coordinates for the following parameter set of the map (2): $M = 125$, $Q = 3$, $q = 1$; $M = 257$, $Q = 3$, $q = 1$; and CI-sequence period = 66307; representative points of the discrete dynamical system (2) are connected with solid lines at the neighboring instances of time

One can see from these figures that the system path corresponds to the finite motion in the limited domain of the phase space. It is also seen, that the chaotization rate of any integer sequence strongly depends on the parameters M, Q, q. As a rule, with the increase of the parameters M and Q both the chaotiztion rate of the integer sequence and its period are increased.

Achievable values of the period of the binary pseudorandom sequences generated with the discrete chaotic algorithm (2) have been studied as functions of both the parameters q, Q, M and initial conditions.

Examples of the estimated period spectrum of binary pseudorandom sequences generated for various set of the parameters are represented in the Table 1.

The analysis of the above results has shown that there are some general laws in the periods estimations for the certain values of the M parameter. The most interesting cases take place for M parameter defined according to the following formulas:

a) $M = 2^k$, *where* $k = 1,2,3...$,
b) $M = 3^k$, *where* $k = 1,2,3...$,
c) $M = 5^k$, *where* $k = 1,2,3....$

Rather simple analytical expressions for calculation of all periods of binary pseudorandom sequences have been obtained for the above cases, respectively:

$$\text{a) } Period_{q,Q}^{M=2^k} = 2^{k-1} Period_{q,Q}^{M=2}, \quad (4)$$

$$\text{b) } Period_{q,Q}^{M=3^k} = 3^{k-1} Period_{q,Q}^{M=3}, \quad (5)$$

$$\text{c) } Period_{q,Q}^{M=5^k} = 5^{k-1} Period_{q,Q}^{M=5}. \quad (6)$$

Generalizing these formulas we may derive the analytical expression for calculation of large enough periods of binary pseudorandom sequences generated by discrete chaotic map (2) depending on the q, Q, and M parameters:

$$Period_{q,Q}^{M=m^k} = m^{k-1} Period_{q,Q}^{M=m}, \quad (7)$$

where m is an integer natural number; $m = 2,3,4....$

The period spectrums of binary pseudorandom sequences generated with algorithm (2) for the given values of the parameters q, Q, and M, and founded from the condition of exact reconstruction of the given initial conditions are presented in the Tables 2, 3 and 4.The periods obtained via simulation and calculated with formulas (4 - 6) have an absolutely exact coincidence. Increasing the values of the M, Q, and q parameters we may generate the binary pseudorandom sequences of the long enough length according to the Eq. (7).

In particular, certain laws have been found for the special case when M parameter equals to an *even number* and only parameters Q and q are varied. The related results of the period spectrums estimation for binary pseudorandom sequences for the above case are represented in the Table 5. Analyzing the Table 5 we may derive the followings laws:

1) The period spectrum of binary pseudorandom sequences, formed by the algorithm (2), is strictly symmetric with respect to the mean value of parameter q;

2) There are several different sequences with the same period in the phase space of the map (2).

Let denote as v the number of sequences with an identical period: $Period(v)_{Q,q}^{M}$. Then, for example, the writing $Period(2)_{4,q=1,3}^{256}=1920$ means that for $M=256$ and $Q=4$ there are two sequences with the period equal 1920. It follows from this consideration

Table 1

The period spectrum of binary pseudorandom sequences for the parameters set: $q=1$, $Q=2,3...12$ and $M=2,3...32$

	Period										
M/Q	2	3	4	5	6	7	8	9	10	11	12
2	3	7	15	21	63	127	63	73	889	1533	3255
3	4	8	40	26	364	728	3146	80	1640	8744	6560
4	6	14	30	42	126	254	126	146	1778	3066	6510
5	10	31	156	24	1562	19531	1116	390620	976562	487344	6781684
6	24	56	240	546	6552	92456	198198	5840	1457960	13404552	4270560
7	16	57	342	336	2400	48	1921600	2241867	1680600	4483734	117648
8	12	28	60	84	252	508	252	292	3556	6132	13020
9	12	24	120	78	1092	2184	9438	240	4920	26232	19680
10	60	217	1560	168	196812	2480437	15624	*	*	*	*
11	10	60	1330	120	118104	885775	*	590520	*	120	*
12	24	56	240	546	6552	92456	198198	5840	1457960	13404552	4270560
13	28	168	2196	366	371292	5198088	*	*	*	2613240	*
14	48	399	1710	336	50400	5096	*	*	*	*	*
15	40	248	3120	312	568568	14218568	3510936	1562480	*	*	*
16	24	56	120	168	504	1016	504	584	7112	12264	26040
17	36	288	96	288	88416	*	83520	*	*	*	*
18	24	168	240	546	6552	277368	198198	17520	4373880	13404552	4270560
19	18	381	14480	180	2476098	*	*	*	*	*	*
20	60	434	1560	168	196812	4960874	15624	*	*	*	*
21	16	456	13680	4368	218400	4368	*	*	*	*	*
22	30	420	3990	840	354312	*	*	*	*	61320	*
23	48	528	12166	1518	139920	6436342	*	*	*	*	*
24	24	56	240	1092	6552	92456	396396	5840	1457960	13404552	4270560
25	50	155	780	120	7810	97655	5580	1953100	4882810	2436720	33908420
26	84	168	10980	2562	7797132	*	*	*	*	*	*
27	36	72	360	234	3276	6552	28314	720	14760	78696	59040
28	48	798	1710	336	50400	6096	*	*	*	*	*
29	14	840	12194	5226	707280	731640	*	*	*	*	*
30	120	1736	3120	2184	5117112	*	*	*	*	*	*
31	30	920	61568	1986	476640	923520	*	*	*	*	*
32	48	112	240	336	1008	2032	1008	1168	14224	24528	52080

Note: * – more 16000000

Table 2

The period spectrum of binary pseudorandom sequences for the parameters set: $q=1$, $Q=2,3...15$ and $M=2^k$, *where* $k=1,2,3...11$

	Period										
Q/M	2	4	8	16	32	64	128	256	512	1024	2048
2	3	6	12	24	48	96	192	384	768	1536	3072
3	7	14	28	56	112	224	448	896	1792	3584	7168
4	15	30	60	120	240	480	960	1920	3840	7680	15360
5	21	42	84	168	336	672	1344	2688	5376	10752	21504
6	63	126	252	504	1008	2016	4032	8064	16128	32256	64512
7	127	254	508	1016	2032	4064	8128	16256	32512	65024	130048
8	63	126	252	504	1008	2016	4032	8064	16128	32256	64512
9	73	146	292	584	1168	2336	4672	9344	18688	37376	74752
10	889	1778	3556	7112	14224	28448	56896	113792	227584	455168	910336
11	1533	3066	6132	12264	24528	49056	98112	196224	392448	784896	1569792
12	3255	6510	13020	26040	52080	104160	208320	416640	833280	1666560	3333120
13	7905	15810	31620	63240	126480	252960	505920	1011840	2023680	4047360	8094720
14	11811	23622	47244	94488	188976	377952	755904	1511808	3023616	6047232	12094464
15	32767	65534	131068	262136	524272	1048544	2097088	4194176	8388352	16776704	33553408

Table 3

The period spectrum of binary pseudorandom sequences for the parameters set:

$q = 1$, $Q = 2,3...12$ and $M = 3^k$, *where* $k = 1,2,3...10$

	Period									
Q/M	3	9	27	81	243	729	2187	6561	19683	59049
2	4	12	36	108	324	972	2916	8748	26244	78732
3	8	24	72	216	648	1944	5832	17496	52488	157464
4	40	120	360	1080	3240	9720	29160	87480	262440	787320
5	26	78	234	702	2106	6318	18954	56862	170586	511758
6	364	1092	3276	9828	29484	88452	265356	796068	2388204	7164612
7	728	2184	6552	19656	58968	176904	530712	1592136	4776408	14329224
8	3146	9438	28314	84942	254826	764478	2293434	6880302	20640906	61922718
9	80	240	720	2160	6480	19440	58320	174960	524880	1574640
10	1640	4920	14760	44280	132840	398520	1195560	3586680	10760040	32280120
11	8744	26232	78696	236088	708264	2124792	6374376	19123128	57369384	172108152
12	6560	19680	59040	177120	531360	1594080	4782240	14346720	43040160	129120480

Table 4

The period spectrum of binary pseudorandom sequences for the parameters set:

$q = 1$, $Q = 2,3...12$ and $M = 5^k$, *where* $k = 1,2...5$

	Period				
Q/M	5	25	125	625	3125
2	10	50	250	1250	6250
3	31	155	775	3875	19375
4	156	780	3900	19500	97500
5	24	120	600	3000	15000
6	1562	7810	39050	195250	976250
7	19531	97655	488275	1441375	12206875
8	1116	5580	27900	139500	697500
9	390620	1953100	9765500	48827500	244137500
10	976562	4882810	24414050	122070250	610351250
11	487344	2436720	12183600	60918000	304590000
12	6781684	33908420	169542100	847710500	4238552500

that the Results of the Table 5 may be presented as follows:

$$Period(1)_{2,q=1}^{256} = 384,\ Period(4)_{11,q=1,4,7,10}^{256} = 196224,$$

$$Period(2)_{3,q=1,2}^{256} = 896,\ Period(4)_{7,q=1,3,4,6}^{256} = 16256,$$

$$Period(1)_{4,q=2}^{256} = 768,\ Period(2)_{4,q=1,3}^{256} = 1920.$$

One can see that with growth of the parameter Q the number of different sequences with an identical period is growing as well.

3. STATISTICAL AND CORRELATION CHARACTERISTICS OF BINARY PSEUDORANDOM SEQUENCES

Probability distribution uniformity (or equiprobability) of integers over a given interval $[1, M]$ is a very important issue in the problem of the generation of chaotic integer sequences. From this point of view the suggested discrete chaotic algorithm (2) is not perfect. Nevertheless computer simulation carried out have shown, that for the properly chosen values of the M, Q, q parameters the algorithm (2) generates practically uncorrelated chaotic integer sequences with nearly uniform probability distribution: $p(x) = 1/M$, provided the following condition is met:

Table 5

The period spectrum of binary pseudorandom sequences for the parameters set:

$M = 256$, $Q = 2,3...11$ и $q = 1,2,3...10$

	Period									
Q/q	1	2	3	4	5	6	7	8	9	10
2	384									
3	896	896								
4	1920	768	1920							
5	2688	3968	3968	2688						
6	8064	1792	1152	1792	8064					
7	16256	11904	16256	16256	11904	16256				
8	8064	3840	27776	1536	27776	3840	8064			
9	9344	59520	2688	65408	65408	2688	59520	9344		
10	113792	5376	130944	7936	1920	7936	130944	5376	113792	
11	196224	262016	249984	196224	76160	76160	196224	249984	262016	196224

$$Period_{Q,q}^{M} (\mathrm{mod}\, M) = 0 . \quad (8)$$

Among the chaotic integer sequences generated by discrete chaotic algorithm (2) there are sequences for which condition (8) is met exactly, as in the below example:

$$Period_{9,1}^{5} = 390620 / 5 = 78124 .$$

At the same time, there are many sequences for which condition (8) cannot be met exactly. Nevertheless, there are many sequences for which Eq. (8) is met approximately, and such sequences are also of a great practical interest. For example, chaotic integer sequences, generated with the suggested discrete algorithm (2), may be related to the sequences of that type:

$$Period_{7,1}^{125} = 488275 / 125 = 3906,2 ;$$

$$Period_{3,1}^{257} = 66307 / 257 = 258,004 .$$

The histograms of appearance frequency for generated integers in some chaotic integer sequences (CI-sequences) above mentioned are presented in fig. 3 and 4.

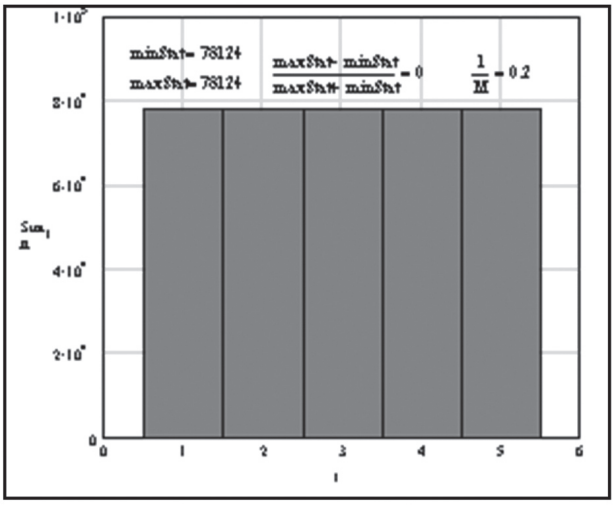

Fig. 3. Histogram of appearance frequency for different integers in CI-sequence for the following parameters: $M = 5$, $Q = 9$, $q = 1$; $Period = 390620$

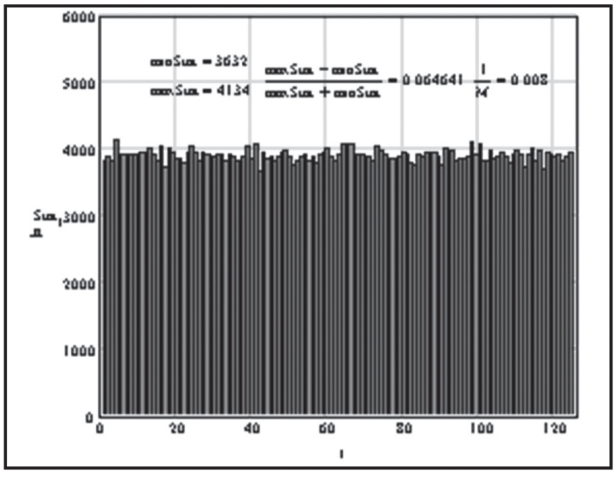

Fig. 4. Histogram of appearance frequency for different integers in CI-sequence for the following parameters: $M = 125$, $Q = 7$, $q = 1$; $Period = 488275$

We also analyzed the appearance frequency of the blocks of k identical characters in different realizations of binary pseudorandom (BPR) sequences generated via algorithm (2) and further application of the clipping operation (3). It is known that for ideal random process the appearance probability of blocks compound of k identical characters of binary process obeys the following probability distribution function $p(k) = 1/2^k$ [10]. Appearance frequencies of blocks of k identical characters in BPR-sequence obtained with the help of computer simulation using the algorithm (2) are presented in fig. 5 and 6.

Besides, estimations of correlation characteristics of BPR-sequences have been done for bulk enough BPR-sequences (a few hundred), generated via the algorithm (2) without any preferences in their balance characteristic.

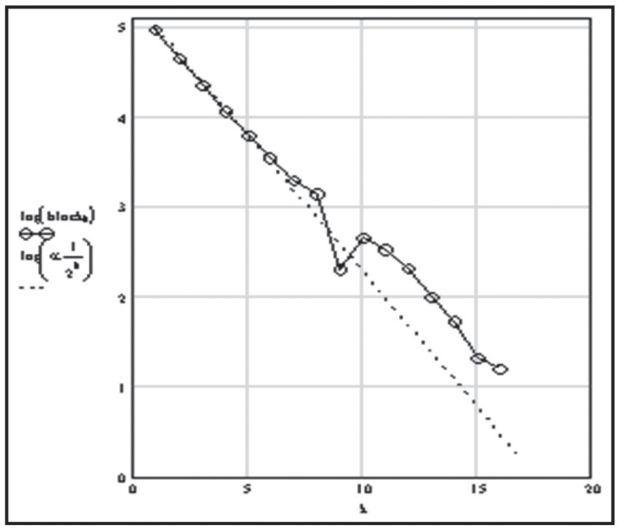

Fig. 5. Appearance frequency of blocks of k identical characters in BPR-sequence as function of parameter k; $M = 5$, $Q = 9$, $q = 1$; $Period = 390620$. Dashed line corresponds to the probability distribution $p(k) = 1/2^k$

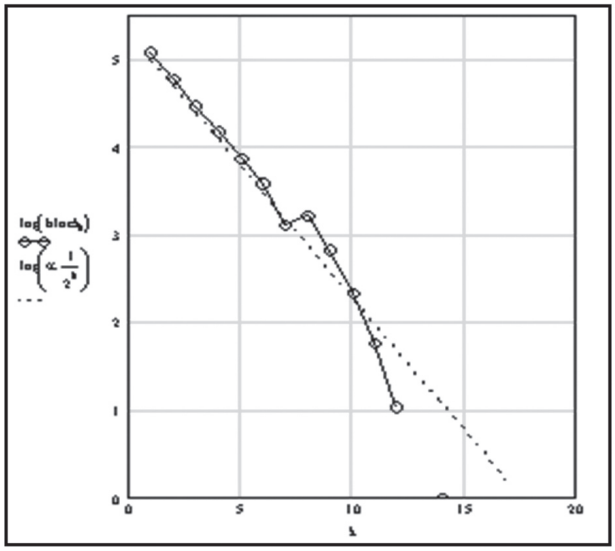

Fig. 6. Appearance frequency of blocks of k identical characters in BPR-sequence as function of parameter k; $M = 125$, $Q = 7$, $q = 1$; $Period = 488275$. Dashed line corresponds to the probability distribution $p(k) = 1/2^k$

Both autocorrelation and cross-correlation functions for the generated BPR-sequences of the length N equal to the period (*Period*) of the generated sequences according to the Tables 1...5, have been studied as well. Autocorrelation functions for two different realizations of BPR-sequences, generated via discrete chaotic algorithm (2) are presented in fig. 7 and 8. The maximal levels of the autocorrelation function side-lobes lay within the following range

$$R_{\max} = (2,4...4,6)/\sqrt{N}\,, \qquad (9)$$

where N is the length of the BPR-sequence.

The results obtained have shown that autocorrelation and cross-correlation functions of BPR-sequences generated via Eq.(2) are rather close to those of an ideal random process with the uniform distribution.

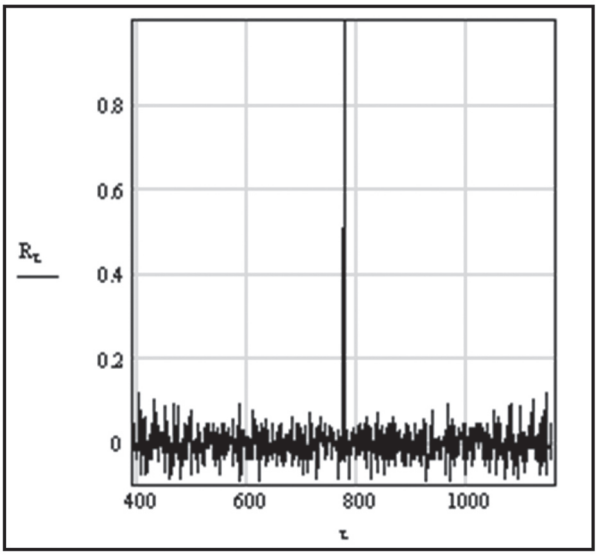

Fig. 7. Autocorrelation function of BPR-sequences for the following parameters: $M = 125$, $Q = 3$, $q = 1$; *Period* = 775

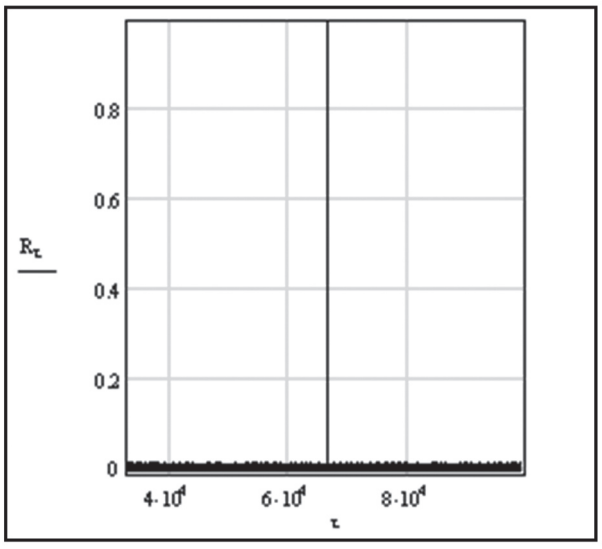

Fig. 8. Autocorrelation function of BPR-sequences for the following parameters: $M = 257$, $Q = 3$, $q = 1$; *Period* = 66307

The maximal outlier characteristics of the correlations are practically the same in all investigated auto- and cross-correlation functions and they are rather close to similar characteristics of the auto- and cross-correlations of random sequences with uniform probability distributions [7, 8 and 10].

CONCLUSIONS

1. A new method for generation of quasi-orthogonal chaotic sequences has been suggested for applications both in radars and communication systems. The method is based upon a discrete chaotic algorithm of a recurrent parametric type with two delay parameters. This algorithm allows generating a *rather wide* family of binary pseudorandom sequences.

2. Phase space structure of the suggested algorithm has been investigated and analyzed via computer simulation technique. The period spectrum of cyclic trajectories in phase space for different values of time delay parameters has been found. The analytical expression for calculation of rather long periods of BPR-sequences generated via discrete chaotic map with to delay parameters.

3. Statistical and correlation characteristics of BPR-sequences, generated according to the method suggested have been studied in detail. The computer simulation has shown that for the properly chosen values of the delay parameters the suggested discrete chaotic algorithm generates binary pseudorandom sequences with close to uniform probability distribution $p(x) = 1/M$. The correlation characteristics of BPR-sequences generated correspond to the correlation characteristics of the random process with uniform probability distribution.

4. It is shown that quasi-orthogonal binary sequences, generated according to the method suggested fulfill all the requirements to the signals used both in radars and communication systems.

References

[1] Konstantin Lukin, Valery Shcherbakov, Vladimyr Konovalov, Ryan Breed. Dedicated Short-Range Communication System for Vehicle-to-Vehicle Data Transmission on the Basis of Chaotic Waveform codes (DSRC-VVDT). // Proceedings of 16 International Conference on Microwaves, Radar and Wireless Communications – MIKON-2006, Krakow, Poland, May 22 – 24, 2006, Vol. 1, pp. 442 – 445.

[2] K.A. Lukin, V.Ye. Shcherbakov, V.M. Konovalov, D.S. Breed. Design Method of Self-Organizing Communication System for Vehicle-to-Vehicle Data Transmission on Highway. Radio-Electronic and Computer Systems, Kharkov «KhAI», 2007, №6 (25), pp. 238 – 244. (In Russian)

[3] K.A. Lukin, V.Ye. Shcherbakov, V.M. Konovalov, D.S. Breed. New Concept of Multiplex Broadband Wireless Communication for Vehicle-to-Vehicle Data Transmission on Highways. // Proceeding of the Sixth International Kharkov Symposium on Physics and Engineering of Microwaves, Millimeter and Submillimeter Waves – MSMW'07, Kharkov, Ukraine, June 25 – 30, 2007, Vol. 2, pp. 852 – 854.

[4] V.Ye. Shcherbakov, K.A. Lukin. The Modeling of System for Vehicle-to-Vehicle Data Transmission/Reception on Highway. Radio-Electronic and Computer Systems, Kharkov «KhAI», 2009, №7 (41), pp. 288 – 294. (In Russian)

[5] K.A. Lukin, V.Ye. Shcherbakov. A Forming Method of Quasi-Orthogonal Chaotical Codes for Data Transmission/Reception System between Vehicles on Highway. Applied Radio Electronics, 2012, Vol.11, №1, pp. 37 – 43. (In Russian)

[6] Knuth D.E. The Art of Computer Programming, vol.2, Seminumerical Algorithms. 2007. P. 832. (In Russian)

[7] Hayes Brian // American Scientists. 1999. V.87. №4. P. 296.

[8] Kahaner D., Moler C., Nash S. Numerical Methods and Software. 2001. P. 575.

[9] K.A. Lukin, Iu.L. Maistrenko, A.N. Sharkovskii, V.P. Shestopalov. Method of Difference Equations in a Resonator Problem with a Nonlinear Reflector. Reports of Academy of Sciences of the USSR, 1989, Vol. 309, pp. 327 – 331. (In Russian)

[10] Varakin L.Ye. Communication Systems with Noise-Like Signals. Moscow. Radio and Communication. 1985. (In Russian)

[11] Yu.V. Gulyaev, V.Ya. Kislov, V.V. Kislov, V.I. Kalinin, V.V. Kolesov, R.V. Belyaev, G.M. Vorontsov. Broadband Telecommunication Facilities with CDMA on the Basis of Chaotic Signals. Radiotekhnika, 2002, № 10, pp. 3 – 15. (In Russian)

Manuscript received December, 12, 2012

Konstantin A. Lukin, M. Sc. (1973), Ph. D. (1980), Doctor of Sc. in Physical Electronics (1989), Professor (2005), IEEE Fellow, a chief of Department for Nonlinear Dynamics of Electronic System, Institute for Radiophysics and Electronics of NAS of Ukraine. His current research interests are dynamical chaos, nonlinear microwave electronics, chaotic waveform generation, random signal processing, noise radar technology.

Valery Ye. Shcherbakov, M. Sc. (1976), a principal research engineer of Department for Nonlinear Dynamics of Electronic System, Institute for Radiophysics and Electronics of NAS of Ukraine. Current research interests: chaotic waveform generation, random and pseudo-random signal processing, short-range radar and spread spectrum communication system.

Dmytro V. Shcherbakov, M. Sc. (2003), M. Sc. (2005), Senior Software Engineer of Subsidiary Company «TOA Ukraine», TOA Technologies Inc., USA. Current research interests: Computer Science, Software Development, ICT Management, Business Intelligence, Business Administration.

УДК 621.396.2.018.424

Новый метод формирования квазиортогональных хаотических последовательностей / К.А. Лукин, В.Е. Щербаков, Д.В. Щербаков // Прикладная радиоэлектроника: науч.-техн. журнал. – 2013. – Том 12. – № 1. – С. 17–24.

Предложен новый метод формирования квазиортогональных хаотических последовательностей для применения как в радарах, так и в связных системах. Метод разработан на базе дискретного хаотического отображения с двумя параметрами запаздывания. Компьютерным моделированием проанализирована структура фазового пространства предложенного алгоритма. Найден спектр периодов циклических траекторий в фазовом пространстве, различающихся параметрами запаздывания. Проведено исследование статистических и корреляционных характеристик бинарных псевдослучайных последовательностей, сформированных согласно методу. Моделирование показало, что при соответствующем выборе параметров запаздываний предложенный дискретный хаотический алгоритм формирует бинарные псевдослучайные последовательности с распределением вероятностей, близким к равномерному. Показано, что корреляционные характеристики бинарных псевдослучайных последовательностей, сформированных дискретным хаотическим алгоритмом, соответствуют корреляционным характеристикам случайного процесса с равномерным распределением вероятностей.

Ключевые слова: квазиортогональная хаотическая последовательность, дискретный хаотический алгоритм, хаотическая целочисленная последовательность, хаотическое отображение, фазовое пространство, бинарная псевдослучайная последовательность, автокорреляционная и взаимнокорреляционная функция.

Табл. 5. Рис. 8. Библиогр.: 11 наим..

УДК 621.396.2.018.424

Новий метод формування квазіортогональних хаотичних послідовностей / К.О. Лукін, В.Є. Щербаков, Д.В. Щербаков // Прикладна радіоелектроніка: наук.-техн. журнал. – 2013. – Том 12. – № 1. – С. 17–24.

Запропонований новий метод формування квазіортогональних хаотичних послідовностей для застосування як в радарах, так і в системах зв'язку. Метод розроблений на базі дискретного хаотичного відображення з двома параметрами запізнювання. Комп'ютерним моделюванням проаналізована структура фазового простору запропонованого алгоритму. Знайдений спектр періодів циклічних траєкторій у фазовому просторі, що розрізняються параметрами запізнювання. Проведено дослідження статистичних і кореляційних характеристик бінарних псевдовипадкових послідовностей, сформованих згідно з методом. Моделювання показало, що при відповідному виборі параметрів запізнювань запропонований дискретний хаотичний алгоритм формує бінарні псевдовипадкові послідовності з розподілом ймовірностей, близьким до рівномірного. Показано, що кореляційні характеристики бінарних псевдовипадкових послідовностей, сформованих дискретним хаотичним алгоритмом, відповідають кореляційним характеристикам випадкового процесу з рівномірним розподілом ймовірностей.

Ключові слова: квазіортогональна хаотична послідовність, дискретний хаотичний алгоритм, хаотична цілочисельна послідовність, хаотичне відображення, фазовий простір, бінарна псевдовипадкова послідовність, автокореляційна та взаємокореляційна функція.

Табл. 5. Іл. 8. Бібліогр.: 11 найм.

UDK 621.37

GRAPH-BASED WAVEFORM DESIGN FOR RANGE SIDELOBE SUPPRESSION

HAGHSHENAS H. AND NAYEBI M. M.

The cross-correlation between transmitted and received signals is known as a common processing method in noise radars, but, it creates a lot of undesirable sidelobes which can mask weak echoes of far targets. A lot of receiver-based algorithms are developed due to masking effect suppression. In this paper, a transmitter-based method of waveform generation based on the graph theory is presented. First stage of this method tries to design a graph consisting of nodes each corresponds to a random subsequence. In Second stage, output sequence is generated by moving from one node to another based on the probability of each edge. First stage is done offline while the second one is performed online. The subsequences are designed in a way that the correlation sidelobe levels generated by two adjacent subsequences are reduced. The waveform randomness is measured and compared with purely random waveforms.

Keywords: Random waveform generator, Graph theory, Random walk.

1. INTRODUCTION

Random signal radar (RSR) is a kind of radar whose transmitted signal is generated by microwave noise source or modulated by the lower frequency white noise. Noise radar applications are very versatile [1], such as range profiles measurement, detection of buried objects, interferometry, collision warning, subsurface profiling, and ISAR and SAR imaging. One of the main problems is the masking effect of strong target echoes on weak ones. Several methods have been developed to counter the masking effect [2] such as adaptive lattice filter [3, 4], stretch processing [5, 6], apodization filtering [7], inverse filtering [8] CLEAN method [9, 10] and etc. Most of methods can be categorized as the receiver side methods. While there are various methods in this category, there are few methods focusing on the waveform design at the transmitter part of noise radars. In our previous works [11-13], it is clarified that masking effect reduction in noise radar is possible by concentrating on waveform design. The developed method is called "Forward-Design" method which can generate a random signal based on consecutive subsequences.

In this paper, we expand this method and combine it with the graph theory due to online generating unlimited-length noise-like waveform based on an offline design. The online generation of waveform from a given graph is handled by means of random walk. In this paper the method of generating and expanding a strongly connected graph is discussed. The way of designing subsequence of each node in a way that the correlation sidelobe levels are reduced is explained. Then the method of random walk is described. Finally, by means of computer simulation, the ability of the proposed method in decreasing masking effect is evaluated. Moreover, the randomness future of the generated waveform is taken into consideration.

2. CORRELATION PROCESS

Commonly, receiver unit of a noise radar performs correlation processing between reference signal and the received one [14], represented by x_k and y_k, respectively. In this paper phase-modulated (PM) signal is taken into consideration. The amplitude of signal, without loss of generality, is assumed to be one and its phase is the design object.

$$x_k = e^{j\theta_k}. \tag{1}$$

Since the maximum correlation shift is far less than the integration time, the correlation process can be done on N-point adjacent subintervals of the reference signal and corresponding $2N$-point subintervals of the received signal. This process is made in M parallel pulse compressors (PC), where M is the number of adjacent subsequences of the reference signal. Each PC unit outputs $N+1$ samples which correspond to radar range cells. The r^{th} output sample of m^{th} PC is shown by $p(r,m)$, where $r = 0,1,...,N$ and $m = 0,1,...,M-1$. Outputs of PC groups are then processed by Doppler processing which can be implemented by applying M-point FFT [9]. Using an appropriate CFAR detection algorithm, existing targets can be extracted from range-Doppler matrix $Q = [q(r,m)]$.

$$p(r,m) = \sum_{k=mN}^{(m+1)N-1} x_k y^*_{k+r} \tag{2}$$

$$q(r,m) = \sum_{k=0}^{M-1} p(r,k) e^{-jkm\frac{2\pi}{M}} \tag{3}$$

We suppose that the received signal is a delayed version of the transmitted one (d samples), the stretch of the signal envelope due to target movement during the integration time of one subinterval and also its Doppler effect are negligible.

$$p(r,m) = \sum_{k=mN}^{(m+1)N-1} x_k x^*_{k+r-d} \tag{4}$$

Range mainlobe is occurred when r and d are equal; in other cases, range sidelobes are produced. We divide sidelobes of Point Spread Function (PSF) into two groups based on the sign of $r-d$, represented by C_p and D_p ($p = 1,2,...,N$). We show both C_p and D_p together with S_p ($p = 1,2,...,2N$). S_0 (C_0 or D_0) represents the mainlobe level of PSF.

$$C_p^{(m)} = \sum_{k=mN}^{(m+1)N-1} x_k x^*_{k+p} \tag{5}$$

$$D_p^{(m)} = \sum_{k=(m+1)N}^{(m+2)N-1} x_k x_{k-p}^* \quad (6)$$

$$S_p = \begin{cases} C_p, & p = 1,2,...,N \\ D_{p-N}, & p = N+1, N+2,...,2N \end{cases} \quad (7)$$

The Integrated Sidelobe Ratio (ISLR) is used as the measure of range sidelobe effect evaluation. ISLR is defined as the ratio of total sidelobes energy to the mainlobe energy of the PSF.

$$J = \frac{1}{2N} \sum_{p=1}^{2N} \left| S_p \right|^2 \quad (8)$$

$$ISLR = 2NJ \Big/ \left| S_0 \right|^2 \quad (9)$$

It can be considered that the expectation value of ISLR equals to 2 in the case of purely random signals [11].

3. SUBSEQUENCES DESIGN

The methods presented in literature and discussed in section 1, try to decrease masking effect by applying an appropriate signal processing method on the received signal. In [11], it is shown that an alternative solution is usage of a well designed random waveform which leads to a better ISLR in comparison with pure random waveform. Moreover it is illustrated that obtaining a waveform with lower ISLR that can keep its randomness characteristics is possible by imposing some appropriate constraints on the waveform generator.

Considering (5)-(9), it is obvious that ISLR of each PC subinterval only depend on N-point reference signal of current and next subsequences. This property is the base of the proposed method in [11], called "Forward-Design" method. The main idea behind the Forward-Design method is to calculate each N-point subsequence of reference signal as a function of previous one with supposing ISLR minimization as the cost function. To begin the method, the first subsequence is selected randomly. The second subsequence is derived by minimizing the cost function of the first one. Applying the same procedure to the second subsequence leads to the generation of the third one and this process can be continued until the arbitrary length is reached. According to this method, a random sequence can be generated by attaching these subsequences.

The procedure of Forward-Design method can be modeled as a directed path graph [15]. The directed graph, generated by this method, has only one path. Actually, this directed graph is a weakly connected graph. It means that replacing all of its directed edges with undirected edges produces a connected (undirected) graph [16]. To generate a larger path in this method, it is necessary to add new nodes to the graph. Therefore, in order to generate unlimited length waveforms, design of new subsequences is required to be performed online. This characteristic imposes heavy computational expense on the transmitter. An alternative method to generate random waveform based on predesigned subsequences is developed in this paper. To develop a method for generating random waveform offline, we need to produce a strongly connected graph which contains at least one path from one node of the graph to every other node [16]. To generate and expand a strongly connected graph, we need to introduce a way to insert a node into an existing strongly connected graph. To fulfill this purpose, we should find a method of generating a subsequence which is placed between two existing subsequences and satisfy minimum ISLR condition. By reformulating the Forward-Design algorithm in reverse order (Backward-Design) and combining with forward order (Forward-Design), each N-point subsequence of the reference signal can be calculated as a function of the next and previous subsequences by minimizing ISLR as the cost function. This method is called "In-Between-Design" method. By applying this method, we can produce a subsequence which is laid between two known subsequences and has a reduced ISLR in correlation with its previous and next subsequences.

The cost function of In-Between-Design method is assumed to be the summation of the cost functions of Forward-Design (J_0) and Backward-Design methods (J_1).

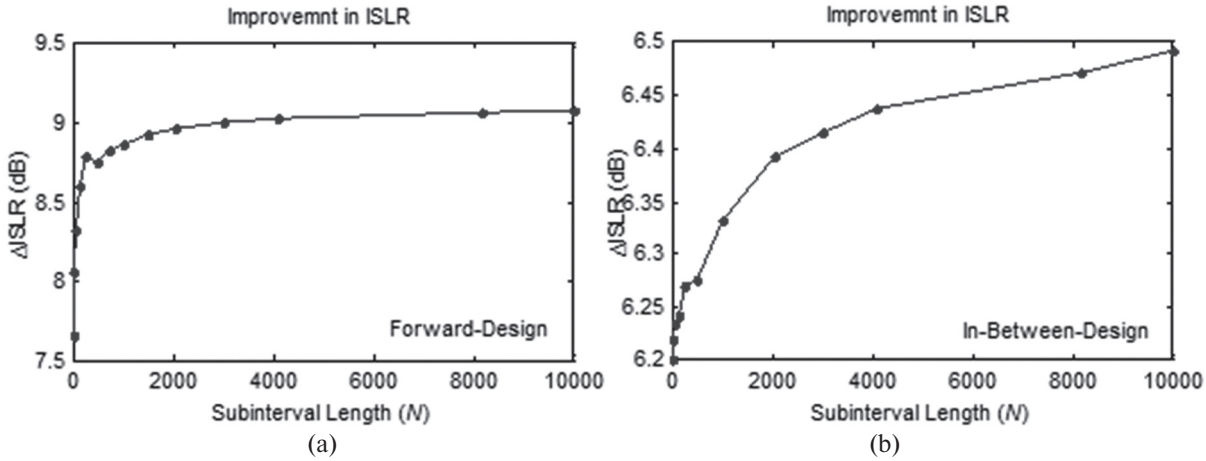

(a) (b)

Fig. 1. Improvement of ISLR in dB versus subinterval length for (a) Forward-Design method and (b) In-Between-Design method

$$J_T = J_0 + J_1. \quad (10)$$

Minimization of the above cost function is performed by means of numerical solutions such as Gradient Descent (GD) algorithm. To fulfill this purpose partial derivatives should be taken with respect to unknown variables, θ_k ($N \le k < 2N$).

$$\xi_0(\theta_k) = \sum_{p=k-N+1}^{N} C_p^{(0)*} e^{j\theta_{k-p}} + \sum_{p=1}^{N} D_p^{(0)} e^{j\theta_{k-p}} + \\ + \sum_{p=1}^{2N-k-1} D_p^{(0)*} e^{j\theta_{k+p}} \quad (11)$$

$$\xi_1(\theta_k) = \sum_{p=1}^{k-N} C_p^{(1)*} e^{j\theta_{k-p}} + \sum_{p=1}^{N} C_p^{(1)} e^{j\theta_{k+p}} + \\ + \sum_{p=2N-k}^{2N} D_p^{(1)*} e^{j\theta_{k+p}} \quad (12)$$

$$\frac{\partial J_T}{\partial \theta_k} = \frac{1}{N} \mathrm{Im}\left\{ \left(\xi_0(\theta_k) + \xi_1(\theta_k) \right) e^{-j\theta_k} \right\} \quad (13)$$

To evaluate the ability of the Forward-Design and In-Between-Design methods to generate a random subsequence with a lower ISLR, a lot of different simulations have been done and the achieved results prove the ability of the method to decrease the average power of sidelobes. For some different values of N (16, 32, 64, 128, 256, 512, 1024, 2048, 3000, 4096, 8192 and 10000), improvement of ISLR expectation value of the proposed waveform is compared with that of pure noise waveform ($\Delta ISLR(N)$). For each value of N , more than 100000 Monte Carlo replications, including 100 different waveforms with the length of 1000 subintervals, have been performed. Improvement of ISLR expectation value of the proposed waveforms generated by utilizing Forward-Design method and In-Between-Design one are shown in Fig. 1(a) and (b), respectively. As this figure shows, we achieved about 8dB and 6dB improvement in decreasing ISLR for Forward-Design and In-Between-Design methods respectively. Although the improvement achieved by In-Between-Design is less than Forward-Design method, this method can be applied to develop the random waveform generating based on the graph.

4. GRAPH GENERATION AND EXPANSION

According to previous section, one of the methods of offline generation of a waveform is using strongly connected graph (SCG). In this part, we introduce a way of producing a primitive SCG and expanding it. The method commences with a primitive SCG that could be a simple cycle graph [17] with L nodes. It is obvious that L must be at least 3.

Generating the cycle graph starts from choosing an arbitrary N-point subsequence which corresponds to the first node of the graph. Employing the Forward-Design method a directed path graph of length $L-1$ can be formed. Eventually, to obtain a cycle graph, L^{th} node is inserted between the last and the first nodes of the directed path graph. For expansion of the existing graph we need a tool which keeps the graph strongly connected. The procedure that can fulfill this requirement is In-Between-Design method. To insert a new node to the existing graph, two nodes are selected as initial and terminal nodes, respectively. Utilizing the In-Between-Design method, a new node will be added between the initial node and the terminal one. It is obvious that two edges, one from the initial node to the new one and another from the new node to the terminal one, are added to the graph. Q times repeating of the expansion procedure, a graph with $V = L + Q$ nodes and $E = L + 2Q$ edges is obtained. In Fig. 2 a random SCG is drawn. It can be easily proved that the achieved random graph shown by $RSCG(L, Q)$ remains strongly connected.

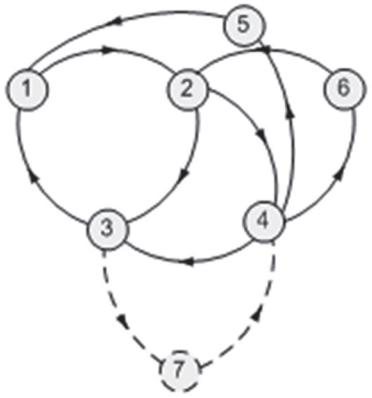

Fig. 2. A random strongly connected graph

Since we want to form a sequence by a random walk on the graph which meets each node with the same possibility (uniform stationary distribution); the regularity of the generated graph is preferable. To make the above graph regular there are two ways. Firstly, initial and terminal nodes in each expansion stage can be selected in a way that keeps the nodes degree the same as much as possible. Secondly, a suitable weight set of edges can be determined to make stationary distribution more uniform.

In q^{th} stage of expansion procedure ($1 \le q \le Q$), the existing directed graph contains $L + q - 1$ nodes and $L + 2q - 2$ edges. In this stage, the initial and terminal nodes are chosen from existing nodes according to the following probabilities:

$$p_i = \frac{1}{\sum_{k=1}^{L+q-1} \left(\frac{D_i}{D_k} \right)^{\alpha}}, \; i = 1,2,3,\ldots,L+q-1 \quad (14)$$

where parameter α is a non-negative number, i is node index and D_i denotes the outdegree and the indegree of i^{th} node for choosing initial node and terminal one, respectively. The number of incoming edges to a node and outgoing edges from a node are called indegree and outdegree, respectively. Using large value for α increases the possibility of being selected for low degree nodes.

Evaluation of the graph regularity is performed by measuring the standard deviation of node degrees (σ_d). The expectation value of σ_d versus α is depicted in Fig. 3 for four different size of graphs. For each size of graph, 1000 simulations have been performed. We can see that this method results in a non-zero standard deviation of node degrees, because nodes

selected early in the process will get more neighbors than nodes selected later on. As this figure shows, the generated graph becomes asymptotically regular for sufficiently large α and small ratio of L to Q. On the other hand, small value of α offers more choices to the expansion algorithm for selecting the initial and terminal nodes, and consequently increases the graph randomness. By making a trade-off between the regularity and randomness, a suitable value for α could be something like 5.

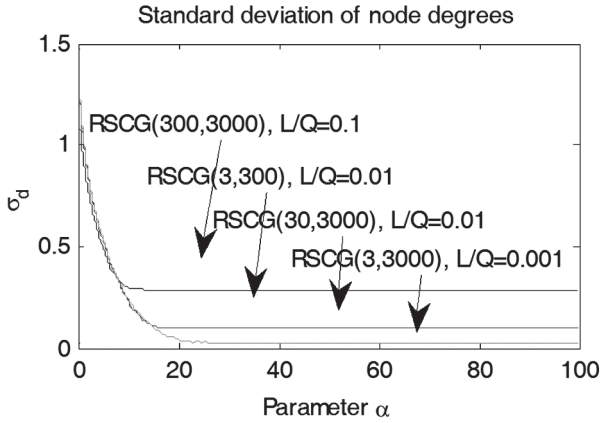

Fig. 3. Expectation value of the standard deviation of node degree versus parameter α, for four different graph sizes

However increasing the parameter α may make the stationary distribution closer to uniform distribution; it can limit the variety of the generated graphs. An alternative solution to make stationary distribution more uniform is determining a suitable weight set of edges. To optimize the uniformity of the stationary distribution of graph $G(V, E)$, the following 5-step iterative algorithm is suggested.

(1) Set the weight of all the edges equal to 1.

$$w_{uv} = \begin{cases} 1 & if\ uv \in E \\ 0 & otherwise \end{cases} \quad 1 \le u, v \le V \qquad (15)$$

(2) Calculate the transition probability matrix $\mathbf{P} = [P_{uv}]$ as follows:

$$P_{uv} = \frac{w_{uv}}{\sum_{i=1}^{V} w_{ui}}, \ 1 \le u, v \le V \qquad (16)$$

(3) Calculate the stationary distribution (row) vector $\mathbf{\Pi} = [\pi_i] : \mathbf{\Pi} \times \mathbf{P} = \mathbf{\Pi}$.

(4) Update the weight of all the edges:

$$w_{uv} = \begin{cases} (1-\xi) w_{uv}, & \pi_v > \dfrac{1}{V} \\ w_{uv}, & \pi_v = \dfrac{1}{V} \\ (1+\xi) w_{uv}, & \pi_v < \dfrac{1}{V} \end{cases} \qquad (17)$$

(5) Go to 2

The optimization procedure is terminated when no noticeable change in the stationary distribution is observed. The uniformity degree of the stationary distribution is measured by means of normalized root mean square deviation (NRMSD) of π_i from the ideal value of $1/V$.

$$NRMSD = \frac{\sqrt{\dfrac{1}{V}\sum_{i=1}^{V}\left(\pi_i - \dfrac{1}{V}\right)^2}}{\dfrac{1}{V}} = \sqrt{V \|\mathbf{\Pi}\|^2 - 1} \qquad (18)$$

where notation $\|\mathbf{\Pi}\|$ denotes the norm of vector $\mathbf{\Pi}$.

Table 1

Expectation value of NRMSD, in three conditions

Graph size	Expectation value of NRMSD		
	EW, $\alpha = 0$	EW, $\alpha = 5$	OW, $\alpha = 5$
RSCG(10,100)	1.08	0.46	0.23
RSCG(3,100)	1.14	0.51	0.2
RSCG(10,500)	1.14	0.51	0.22
RSCG(3,300)	1.17	0.52	0.21
RSCG(3,3000)	1.2	0.49	0.21

In Table 1, the expectation values of NRMSD in three conditions: equal weights (EW) with $\alpha = 0$, equal weights with $\alpha = 5$ and optimized weights (OW) with $\alpha = 5$ are tabulated. For each size of graph, 1000 simulations have been performed. By comparing the results, the effect of the parameter α and the ability of the described algorithm in making the stationary distribution more uniform are evident.

5. GENERATING RANDOM WAVEFORMS BY THE USE OF RANDOM WALK

Given a graph G and a starting node, we select a neighbor of it at random according to the transition matrix P, and move to this neighbor; then we select a neighbor of the new node at random, move to it and so on and so forth. The (random) sequence of nodes selected in this way is a random walk on the graph. A random walk is a memoryless Markov chain on graph G. Markov property implies that knowledge of previous states is irrelevant in predicting the probability of subsequent states. Therefore, the next state depends entirely on the current state.

Since each node corresponds to an N-point signal, attaching these signals according to the random walk can generate a random waveform. Although designing the finite random graph and the random subsequences of its nodes is done offline, the random walk is performed online with infinite (or arbitrary) length.

As the number of nodes of the generated graph is limited, same subsequences are possible to be repeated in the generated waveform which can be a potential threat to the LPI property. An effective solution is to vary the subsequence of each node during the random walk progression. It is desired that each time this procedure happens, the resultant node subsequence becomes more uncorrelated to the previous subsequence of that specific node and also we face minimum degradation in ISLR improvement, albeit as far as possible. In [18], we have developed a modulation-based method to update the subsequences on

each random walk state. Our suggested method makes a random linear change in phase and frequency of the subsequences in each step of the random walk. This method is equivalent to modulating the output sequence of random walk procedure with a random step frequency modulation (RSFM). By making change in phase and frequency of signal x, signal z is defined as follows:

$$z_k = x_k e^{j\left(2\pi\frac{k}{N}F_m+\phi_m\right)}, \quad m=\left[\frac{k}{N}\right] \tag{19}$$

where ϕ_m and F_m are phase shift and frequency shift of m^{th} subsequence, respectively. These parameters are selected according to a recursive equation

$$\begin{cases} F_m = F_{m-1} + \Delta_m \\ \phi_m = \phi_{m-1} - 2\pi\Delta_m \end{cases} \tag{20}$$

We suppose that in each step of the random walk, the frequency step (Δ_m) is selected randomly according to a normal distribution such as $N\left(\delta,\delta/\sqrt{3}\right)$, where δ is the distribution parameter.

$$\Delta_m \sim N\left(\delta,\delta/\sqrt{3}\right). \tag{21}$$

Appling RSFM with relatively small δ may lead to a few degradation in ISLR improvement of In-Between-Design method. where ϕ_m and F_m are phase shift and frequency shift of m^{th} subsequence respectively. Although using larger value for δ in RSFM results in further degradation in ISLR, it can increase the randomness of the output sequence. By making a trade-off between the performance and randomness, an appropriate value for δ should be selected.

5. RANDOMNESS

The quality of randomness can be measured in a variety of ways. To ensure that using the proposed waveforms retains the LPI characteristic, a well-known measure of randomness called spectrum flatness measure (SFM) are considered in this article. This criterion measures whiteness of the frequency spectrum of the test sequence. It is defined as the ratio of the geometric mean to the arithmetic mean of the power spectrum [19]. SFM is usually used for evaluating the amount of randomness that exists in a signal. A high SFM corresponds to a random signal in the sense that no significant information can be obtained by looking at longer blocks of signal samples [20]. Since the above measure is not zero mean in the case of random signals [21], a test of whiteness, which is a modified version of SFM, is used. This test is developed by Drouiche [22] and is implemented as follows:

$$W = \ln\left(\frac{1}{2\pi}\int_{-\pi}^{\pi}\left|X(\omega)\right|^2 d\omega\right) - \frac{1}{2\pi}\int_{-\pi}^{\pi}\ln\left(\left|X(\omega)\right|^2\right)d\omega - \gamma \tag{22}$$

where γ represents Euler-Mascheroni constant and $|X(\omega)|$ is the spectrum of a given sequence S with the length of L_S. It can be shown that $W \approx 0$ for a white noise and $W \to \infty$ if the sequence is maximally correlated. In practice, it will be assessed as the whiteness hypothesis if $W < \eta$ [23].

$$\eta = \sqrt{\frac{2\upsilon}{L_S}}\,\mathrm{erf}^{-1}(1-2\alpha), \tag{23}$$

where η is a threshold obtained for a test size α, $\upsilon = \pi^2/6 - 1$, and $\mathrm{erf}^{-1}(x)$ is the inverse of the standard error function.

$$\mathrm{erf}(x) = \frac{2}{\sqrt{\pi}}\int_0^x e^{-t^2}dt\,. \tag{24}$$

In this paper, we set $\alpha = 10^{-3}$ which results in $\eta = 2.48/\sqrt{L_S}$. In addition, calculation of the frequency spectrum in (22) is accompanied by Gaussian window. The SFM criterion for the proposed PM waveforms (with RSFM) with different lengths of sequence (L_S) and subinterval (N) is simulated and its average is tabulated in Table 2 in the case of graph size $RSCG(10,300)$. For each value of N and L_S, 1000 different waveforms are considered. As the table illustrates, SFM values are very close to zero, which confirms the randomness characteristics of the proposed waveforms. Furthermore, the probability of accepting whiteness hypothesis, listed in Table 3, demonstrates that the proposed waveforms are more likely to be random rather than periodic or predictable. To clarify this statement, the Average SFM of the proposed PM waveforms with the length of $N = 64$ is plotted as a function of the sequence length in Fig. 4 and is compared with purely random waveforms and periodic ones with the period of $N = 64$. To apply RSFM on the random walk process, value of δ in all simulations is assumed to be 0.1.

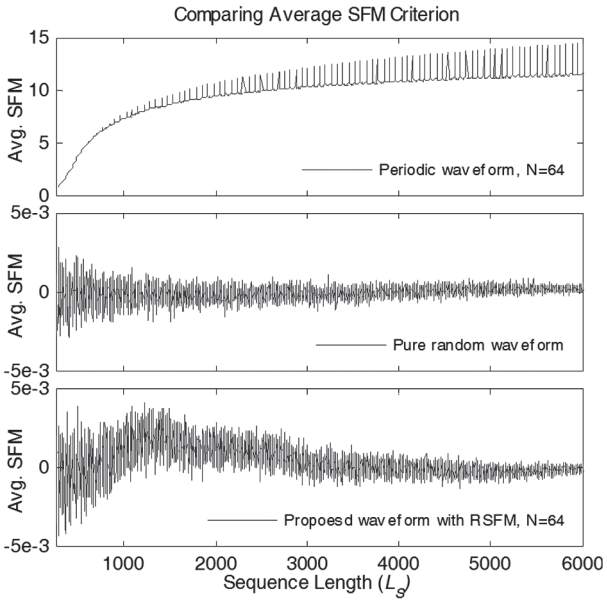

Fig. 4. The Average SFM versus the sequence length (L_S)

The obtained results reveal that the SFM values of the proposed waveforms and random ones are very close together and as the sequence length approaches higher values, the SFM values of the proposed waveforms tend to zero, similar to random sequences. Opposite to the SFM values of the proposed waveforms

and random waveforms, the SFM values of periodic waveforms are extremely large and increase with the length of sequence.

Table 2

The average SFM versus N and LS for graph size RSCG(10,300) with α=5 and optimized weights and RSFM with δ=0.1

L_S	N=64	N=512	N=2048
10N	-1.08E-3	4.31E-4	1.26E-4
100N	2.92E-4	4.39E-4	1.13E-4
300N	7.74E-5	1.61E-4	8.56E-5
500N	5.35E-5	9.8E-5	6.34E-5
1000N	3.25E-6	5.44E-5	7.55E-6
3000N	3.21E-6	6.33E-6	8.08E-7
5000N	3.14E-6	1.15E-6	6.91E-7

Table 3

The probability of whiteness hypothesis versus N and L_S for graph size RSCG(10,300) with α=5 and optimized weights and RSFM with δ=0.1

L_S	N=64	N=512	N=2048
10N	-1.08E-3	4.31E-4	1.26E-4
100N	2.92E-4	4.39E-4	1.13E-4
300N	7.74E-5	1.61E-4	8.56E-5
500N	5.35E-5	9.8E-5	6.34E-5
1000N	3.25E-6	5.44E-5	7.55E-6
3000N	3.21E-6	6.33E-6	8.08E-7
5000N	3.14E-6	1.15E-6	6.91E-7

6. CONCLUSION

We proposed a new method for designing waveforms in noise radars based on the graph theory in order to generate waveform with a lower correlation sidelobe online. According to the developed algorithm, a strongly connected graph with a finite (but arbitrary) number of nodes can be produced by minimizing the cost function over subsequences of adjacent nodes. In this method, output waveform is produced by applying a random walk process on the designed graph. Although designing the random graph and the random subsequences of its nodes is done offline, the random walk on the graph is executed online with infinite length which leads to arbitrary length of random waveform. This method has much less online computational complexity in comparison with Forward Design method.

References

[1] Guosui L., Hong G., and Weimin S. 1999, 'Development of random signal radars', *IEEE Trans. Aerosp. Electron. Syst.*, **35(3)**, 770–777.

[2] Kulpa K. S., and Czekala Z. 2005, 'Short distance clutter masking effects in noise radars', *J. Appl. Radio Electron.*, **4(1)**, 96–98.

[3] Axelsson S. R. J. 2005, 'Improved clutter suppression in random noise radar'. *Proc. URSI Commission F Symp. Microwave Remote Sensing of the Earth, Oceans, Ice and Atmosphere*, Italy.

[4] Kulpa K. S., and Czekala Z. 2004, 'Ground clutter suppression in noise radar'. *Proc. Int. Conf. Radar*, Toulouse, France, 236.

[5] Misiurewicz J., and Kulpa K. S. 2008, 'Stretch processing for masking effect removal in noise radar'. *IET Proc. Radar Sonar and Navigation*, **2(4)**, 274-283.

[6] Kulpa K. S., and Misiurewicz J. 2006, 'Stretch processing for long integration time passive covert radar'. *Proc. CIE Int. Conf. Radar*, Shanghai, China, 496–499.

[7] Xu X., and Narayanan R. M. 2001, 'Range sidelobe suppression technique for coherent ultra-wideband random noise radar imaging', *IEEE Trans. Antennas Propag.*, **49**, 1836–1842.

[8] Nelander A. 2006, 'Inverse filtering for noise radar processing'. *Proc. Int. Radar Symp.*, Krakow, Poland, 421-424.

[9] Fry, R. D., and Gray, D. A. 2008, 'CLEAN deconvolution for sidelobe suppression in random noise radar'. *Proc. Int. Conf. Radar*, 209-212.

[10] Bayat S., and et al. 2006 'Fast and high-resolution PCL radar detection in noisy environment', *Proc. Int. Radar Symp.*, Krakov, Poland, 245–249.

[11] Haghshenas H., and Nayebi M. M. 2012, 'Suppressing masking effect in random signal radars by waveform design', *IET Proc. Radar, Sonar and Navigation*, **6(3)**, 137-148.

[12] Haghshenas H., and Nayebi M. M. 2009, 'Waveform design for sidelobe suppression in noise radar'. *Proc. Int. Radar Symp.*, Hamburg, Germany, 281–285.

13] Haghshenas H., and Nayebi M. M. 2011, 'Comparing receiver-based and transmitter-based techniques to decrease masking effect in noise radars'. *Proc. Int. Radar Symp.*, Leipzing, Germany, 538-543.

[14] Guosui L., Hong G., Xiaohua Z., and Weimin, S. 1997, 'The present and the future of random signal radars', *IEEE Aerosp. Electron. Syst. Mag.*, 1997, **12(10)**, 35–40.

[15] Gross J. T., and Yellen J. 2006, 'Graph Theory and Its Applications', 2nd ed., Boca Raton, FL: CRC Press.

[16] Skiena S. 1990, 'Implementing discrete mathematics: Combinatorics and graph theory with mathematica', Addison-Wesley, Sec. 5.1.2: 'Strong and weak connectivity', 172-174.

[17] Diestel R. 2006, 'Graph Theory', 3rd ed., Germany: Springer Press.

[18] Haghshenas H., and Nayebi M. M. 2012, 'Online low-sidelobe waveform generator for noise radars based on the graph theory', *Submitted to IET Proc. Radar, Sonar and Navigation.*

[19] Gray Jr. A. H., and Markel J. D. 1974, 'A Spectral-Flatness Measure for Studying the Autocorrelation Method of Linear Prediction of Speech Analysis', *IEEE Trans. Acous. Speech Sig. Process.*, **3**, 207-217.

[20] Dubnov, S. 2004, 'Generalization of Spectral Flatness Measure for Non-Gaussian Linear Processes', *IEEE Signal Process. Lett.*, **11(8)**, 698-701.

[21] Gray Jr. A. H. 1974, 'Log spectra of Gausian signals', *J. Acoust. Soc. Am.*, **55(5)**, 1028-1033.

[22] Drouiche K. 2000, 'A new test for whiteness', *IEEE Trans. on Signal Processing*, **48(7)**, 1864–1871.

[23] Djermoune H., Kasalica G., and Brie D. 2007, 'Two-dimensional NMR signal analysis with an adapted subband decomposition', *22nd IAR annual meeting*, Grenoble, France, on CD-ROM.

Manuscript received January, 23, 2013

Hamed Haghshenas Jariani, for photograph and biography, see this issue, p. 16.

Mohammad M. Nayebi, for photograph and biography, see this issue, p. 16.

УДК 621.37

Метод уменьшения боковых лепестков, основанный на графах / А. Хагшенас, М. Найеби // Прикладная радиоэлектроника: науч.-техн. журнал. – 2013. – Том 12. – № 1. – С. 25–31.

Известно, что кросс-корреляция между переданным и опорным сигналами является общепринятым способом обработки сигналов в шумовых радарах. Однако такая обработка приводит к появлению большого числа нежелательных боковых лепестков, которые могут маскировать слабые отклики от удаленных целей. Разработано много алгоритмов приема для уменьшения эффекта маскирования. В данной работе представлен алгоритм генерации сигнала, основанный на теории графов и работающий на стороне передатчика. На первой стадии этого метода составляется граф, состоящий из точек, соответствующих случайным субпоследовательностям. На второй стадии генерируется выходная последовательность путем перехода от одной точки к другой согласно вероятности каждой грани. Первая стадия выполняется на этапе подготовки, вторая осуществляется в режиме реального времени. Субпоследовательности составлены в таком виде, что боковые лепестки корреляционной функции, производимые соседними субпоследовательностями, компенсируют друг друга. Степень случайности сигнала измерена и сравнена с чисто случайным сигналом.

Ключевые слова: генератор случайных сигналов, теория графов, случайный переход.

Табл. 2. Ил. 4. Библиогр.: 23 назв.

УДК 621.37

Метод зменшення бічних пелюсток, заснований на графах / А. Хагшенас, М. Найєбі // Прикладна радіоелектроніка: наук.-техн. журнал. – 2013. – Том 12. – № 1. – С. 25–31.

Відомо, що крос-кореляція між переданим і опорним сигналами є загальноприйнятим способом обробки сигналів у шумових радарах. Однак така обробка призводить до появи великого числа небажаних бічних пелюсток, які можуть маскувати слабкі відгуки від віддалених цілей. Розроблено багато алгоритмів прийому сигналів, покликаних зменшити ефект маскування. У даній роботі представлений алгоритм генерації сигналу, заснований на теорії графів, що працює на стороні передавача. На першій стадії роботи цього методу складається граф з точок, які відповідають випадковим субпослідовностям. На другій стадії генерується вихідна послідовність шляхом переходу від однієї точки до іншої згідно з ймовірностю кожної грані. Перша стадія виконується на етапі підготовки, друга здійснюється в режимі реального часу. Субпослідовності складені в такому вигляді, що бічні пелюстки кореляційної функції, вироблені сусідніми субпослідовностями, компенсують одина одну. Ступінь випадковості сигналу виміряна і порівняна з чисто випадковим сигналом.

Ключові слова: генератор випадкових сигналів, теорія графів, випадкових переход.

Табл. 2. Іл. 4. Бібліогр.: 23 найм.

UDC 537.862

FPGA BASED DESIGN OF RANDOM WAVEFORM GENERATORS FOR NOISE RADARS

O.V. ZEMLYANIY, AND S.K. LUKIN

The results on the use of arbitrary waveform generators that are based on FPGA technology for generation of complex signals in modern noise radars are presented. On the basis of these devices we propose a radar scheme with digital generation of noise waveforms for both sounding signal and reference and analog processing (stepped-delay method for noise radar). Experimental testing shows efficiency of FPGA-based application in radar with variety of sounding waveforms.

Keywords: noise radar, Field-Programmable Gate Array (FPGA), Arbitrary Waveform Generator (AWG), stepped-delay radar, cross-correlation function, noise/random/chaotic waveform.

1. INTRODUCTION

Nowadays, the development of digital methods of signal generation and processing gives the possibility of creation a pseudo-random/noise-like signal sources based on commercially available digital devices of different scale of integration. In this paper we present the results on the use of FPGA-based devices for generation of complex signals used in noise radars [1]. Two different methods for signal generation are applied. The first one is that the waveform samples with the given parameters, generated from the previously developed algorithm, are recorded in a binary file, which is then loaded into the memory of a digital device. Further these samples retrieved from memory with a clock frequency and are fed the input of the DAC, on output of which the analog signal with the desired properties is obtained. The second method uses a possibility having a programmable algorithm for obtaining the waveform samples directly in the FPGA and involves the calculation of each sample in real time. This method is more flexible, because allows storaging code for different algorithms in a program part of the FPGA and quickly switch between them without the need to reprogram the entire device for the desired type of signal.

2. PSEUDO-NOISE (PN) SEQUENCIES BASICS

Pseudo-random sequences is not truly random (deterministic) but they look randomly for the user who doesn't know the code. The larger the period of the PN spreading code, the binary sequence is more complicated and it is harder to detect it. A PN sequence is generated by a feedback shift register made up of flip-flops and a logic circuit [2]. The flip-flops in the shift register are clocked by a single timing generator. Binary sequences are shifted through the shift registers and the outputs of the various stages are logically combined and feed the input to the first stage (feedback loop). The initial states of the flip-flops are determined by the contents of the memory. The properties of generated PN sequence are defined by three factors that are the length m of the shift register, flip-flop's initial states and the feedback logic (taps numbering). The number of possible states of the shift register is 2^m for m flip-flops. So the generated PN sequence becomes periodic with a period of 2^m.

When the feedback logic consists of exclusive-OR gates, the shift register is called a linear and in such a case, the zero state is not permitted. Therefore the period of a PN sequence produced by a linear m - stage shift register can not exceed $2^m - 1$. When a sequence of period $2^m - 1$ generated, it is called a maximal-length sequence (Fig. 1, 2). Typical power spectrum density of m-sequences with chip duration T_c is depicted in Fig. 3.

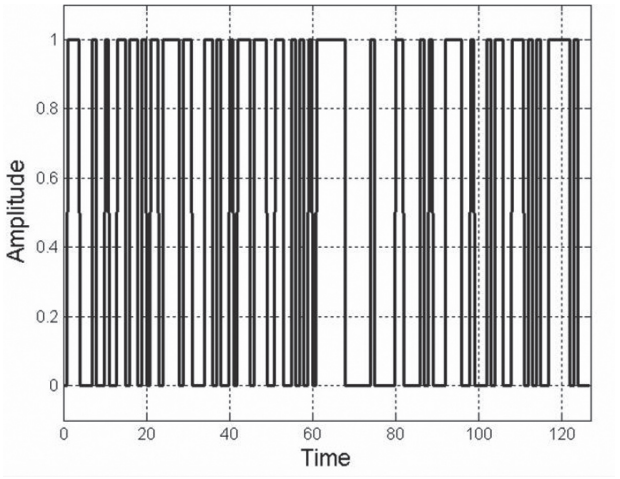

Fig. 1. M-sequence of length 128

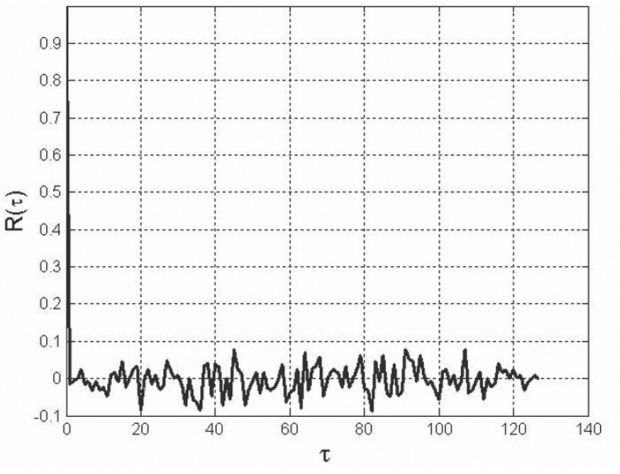

Fig. 2. Autocorrelation function of *m*-sequence of length 128

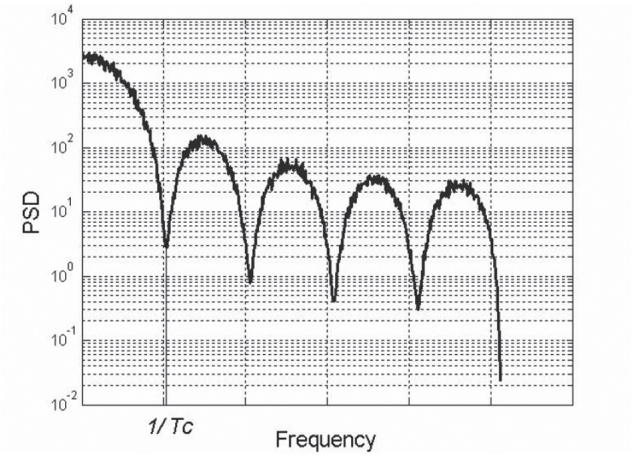

Fig. 3. Typical power spectrum density of m-sequences with chip duration T_c

3. LINEAR CONGRUENTIAL GENERATOR (LCG) AND ITS IMPLEMENTATION

We used the program generator, which is based on the realization of a linear congruential algorithm for obtaining pseudorandom sequence samples in real time [3].

The linear multiplicative or congruential algorithm generates a sequence of pseudo-random integers $X_i \in [0, m)$ based on the expression

$$X_{i+1} = (aX_i + c) \bmod m, \qquad (1)$$

where $a > 0$, $c \geq 0$, $m > 0$ are some integer constants. Properties of generated sequence are determined by the values a, c and m, but its particular type is given by starting value X_0.

The sequence of numbers generated by this algorithm is periodic with a period of not more than m. The length of the period is equal to m if and only if the following conditions are satisfied: c and m are coprime; $a-1$ is multiple of p for all primes p that are dividers of m; $a-1$ is multiple of 4, if m multiple of 4.

For 8-bit device the value of m can not exceed $2^8 = 256$, therefore the maximum length of the sequence is equal to 256. When choosing constant values according to the above conditions $a = 173$, $c = 163$, $m = 256$, $X_0 = 23$ we obtain the pseudorandom sequence shown in Fig. 4.

For justification of feasibility of LCG we used evaluation board which is built around a medium to large capacity FPGA device [4]. It hosts a ProASIC 3E FPGA chip (A3PE1500, FGG484), several peripheral interface controllers (LPT, RS-232, USB, Ethernet), an SDRAM Memory interface (256/512 MB), a JTAG interface for in-system programming and two expansion slots for daughter boards with ADC and DAC modules (Fig. 5). The frequency of on-board clock generator is 25 MHz. There are two types of daugherboards available: High Performance (14-bits 125 MSPS ADC + 16-bit 50 MSPS DAC) and Low Performance (Dual channel 10-bits 20 MSPS ADC, Dual channel 14-bit 1 MSPS DAC). There are also 4 pushbuttons, 4 LEDs for display/debug and a 4x7 Segment LED display.

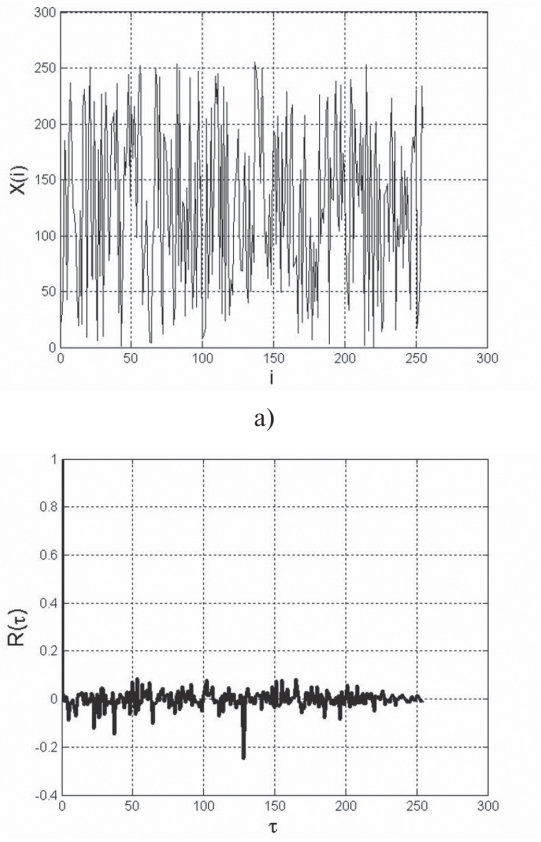

Fig. 4. Time series (a) and autocorrelation function (b) of pseudorandom sequence, generated using LCG with parameters $a = 173$, $c = 163$, $m = 256$, $X_0 = 23$

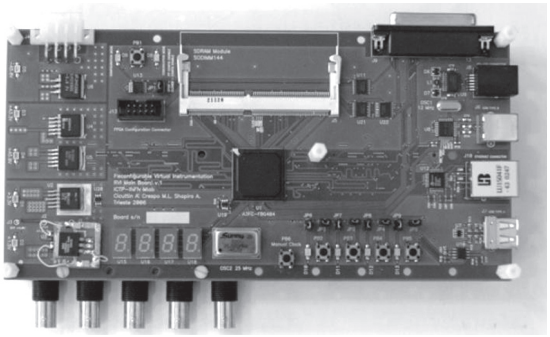

Fig. 5. Actel RVI FPGA development board

Using LCG we were able perform on-board generating of chaotic and pseudorandom sequences of different types. Fig. 6 shows output of FPGA-based generator producing pulsed waveform with pseudorandom filling, obtained via implementation of LCG algorithm (1) with parameters mentioned above.

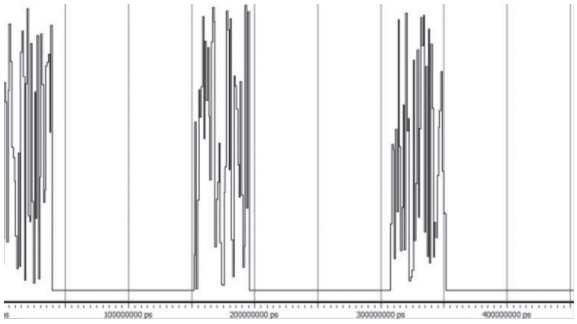

Fig. 6. Pulsed waveform with pseudorandom filling

It should be noted, that several simple techniques can be employed to improve this LCG in the future, for instance, increasing the m value up to 2^{32} and beyond, then use N most significant bits of the result as generator output, where N is the required result width in bits (this parameter is usually constrained by the DAC's resolution).

Generator developed utilizes the aforementioned LCG algorithm not only for generating pseudorandom filling for the pulses, but also for achieving random pulse repetition frequency (PRF) capability. The two LCG generators work independently in this case. Typical view of generated waveform of this type is shown in Fig. 7. The waveform were obtained using VHDL code simulation in ModelSim environment.

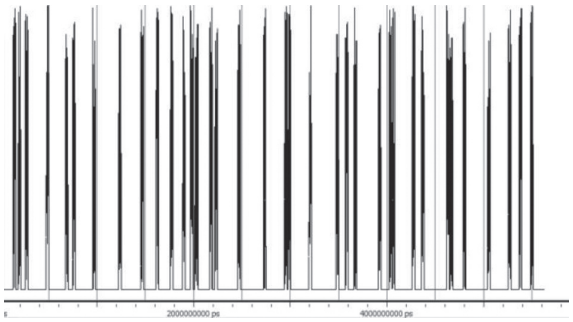

Fig. 7. Random PRF LCG-filled pulse generator output

The results presented here allow us making conclusion about versatility of the method, as it allows creating in a program part of FPGA memory a set of different algorithms and quickly switch between them without the need to reprogram the entire device for the desired type of signal.

4. AWG472 BOARD AND ITS KEY FEATURES

In our research we use 12-bit Dual-Channel Arbitrary Waveform Generator [5] for generation of different kinds of pre-programmed waveforms for noise radar. The AWG472 module (Fig. 8) allows generating dual channel arbitrary CW waveforms with sampling rates up to 4 GSPS. The on-board SRAMs provide 4Mx12-bit data memory to each channel.

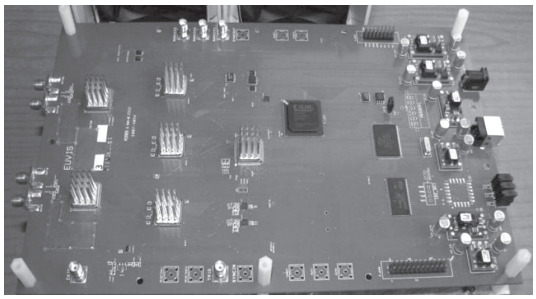

Fig. 8. General view of AWG472 board

The AWG472 is controlled by a PC via a USB interface. It also can work alone with pre-stored waveforms. The sole RF input is a single-ended clock source CKIP, which can be operated up to 4 GHz with minimum power of 12 dBm. The RF outputs of the module are comprised of two pairs of differential analog outputs, with 50-Ω back termination. The AWG472 consists of a high-speed MUXDAC, three QDR SRAMs, an ASIC memory controller, and an enhanced 8051 microcontroller with external RAM and EEPROM (Fig. 9). The key front-end component features up to 4GHz clock rate, 12-bit amplitude and 13-bit phase resolution. The differential analog outputs are 50-Ω terminated. The waveform data are stored in the QDR SRAMs, which provide 4Mx12-bit memory depth.

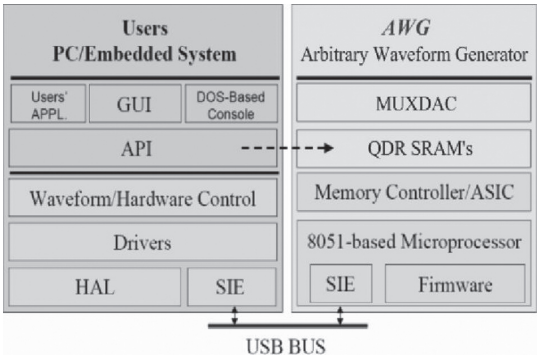

Fig. 9. Architecture of the AWG472

The ASIC memory controller performs reading/writing controls and data transfers. The microcontroller has an integrated USB 2.0 transceiver, a series interface engine (SIE) and an enhanced 8051 microprocessor, which provides a user friendly interface for the host PC or existing systems and general-purpose controls. The module accepts a high-speed trigger signal and generates synchronization outputs and three programmable marker signals. The module can be operated in three waveform generation modes: free-run/continuous mode, triggered free run mode and triggered burst mode: in free-run mode, the module starts waveform generation by a "Restart" command from the GUI or API-based applications. Once the waveform starts, the module repeats the waveform continuously. There is no latency between two consecutive waveforms. The following waveform starts right after the end of the preceding waveform. The waveform generation can be aborted by an "Abort" command from the GUI or API-based applications; in triggered free-run mode, the operation manner is similar to that in free-run mode except for the start of waveform. The waveform generation is initiated by a trigger signal. In order to accept the upcoming trigger signals, the module has to be armed prior the instance of the trigger signals. Trigger signals happening before the module is armed will be ignored. An "Arm" command from the GUI or API-based applications can be used to arm the module. Once the module is armed, it waits for the trigger signal. The waveform generation starts after the falling edge of the trigger signal. The trigger signal can be mainly applied via the TRIGGER SMA connector or provided by a command "Trigger" via the GUI or API-based applications; in triggered burst mode, the module starts waveform generation when it is armed and receives the trigger signal as in the triggered free-run mode. Instead of repeating continuously, the waveform starts, repeats, and stops after finite repetitions. The number of the repetitions can be specified by a property "Loop Count" via the GUI or

the API-based applications. The "Loop Count" can be set from 1 to 255. Similarly, trigger signals happening before the waveform stops will be ignored. Once the waveform stops, the module will arm itself automatically and wait for the next trigger signal.

The key features of the AWG472 module are as follows:

- two 12-bit DACs with 10-bit linearity;
- multiple waveform generation modes including Free Run, Triggered Free Run and Triggered Burst modes;
- in-phase or quadrature phase synchronization of outputs, which can be independently set;
- clock rate up to 4 GHz;
- 2 x 4M x 12-bit memory depth with multi-page configuration;
- up to 1 ms waveform at 4 GSPS output sample rate;
- Dynamic Paging – seamless waveform swapping;
- hi-speed hardware trigger and API software trigger;
- programmable cyclic waveform repetition;
- three marker signals;
- optional multi-module operations;
- USB 2.0 compliant interface (other interfaces available upon request);
- 25 W power consumption using on-board power modules with a 12 V power supply;
- various built-in waveforms, including pulse, multi-tone and FMCW linear chirping;
- companion API and software drivers for easy system development.

5. STEPPED-DELAY METHOD FOR NOISE RADAR

We present an approach to estimation in the radar the cross-correlation function between radiated signal and radar return, which uses combination of digital generation using AWG and analog processing of wideband noise signals. This procedure includes delaying of the transmitted signals with respect to the sampled reference with the help of digital signal generator, analog multiplication and integration. The design of such radar is based upon analog processing of wideband signals and digitizing of the results at relatively low frequency.

We have carried out experimental testing of the stepped-delay method (suggested by K.Lukin and presented in [6]) using propagation of noise sounding signal through a cable rather than its propagation in the open space. The data have been generated in a PC for both sounding and reference signal which have been uploaded into the corresponding channels of the arbitrary waveform generator AWG472. In this way, AWG472 continuously generates both sounding noise signal and its delayed copies. The reference signal was composed as a series of transmitted signal copies with the required delays and numbers of range bins. The signals have not been up converted since AWG472 clock frequency enabled direct generation of such signals (Fig. 10). Both signals have the maximal duration of 2 ms which is a limit for the AWG472 at the 2GHz clock frequency. In the experiment, the reference signal contained 20 copies of the transmitted signals with the delays which formed 20 range bins having 4 ns gaps between each of them. The 4 ns delay corresponds to ~80 cm length in the cable versus 120 cm length in air, since the dielectric constant of the cable material equals ~2.2. Duration of the signal for the each delay was 0.1 ms, which defined the value of integration time at each range bin. Overall duration of the measurement cycle was 2 ms. Spectrum bandwidth in this experiment was limited not by AWG472 device, but by the available mixer having bandwidth of ~190 MHz.

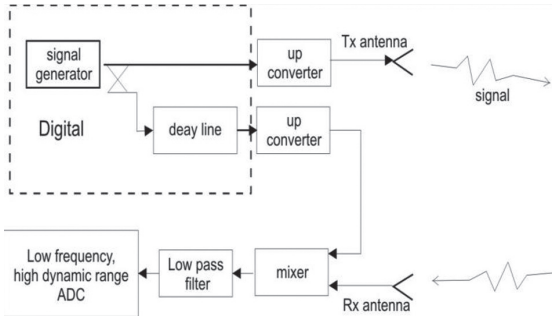

Fig. 10. Diagram of noise radar with digital generation and analog processing of signals, and slow ADC sampling of cross-correlation giving range profile

Fig. 11 shows results of the two target simulation experiment. Two targets at different ranges were modeled by two cables with different lengths connected in parallel. Difference in lengths of cables was 6 m.

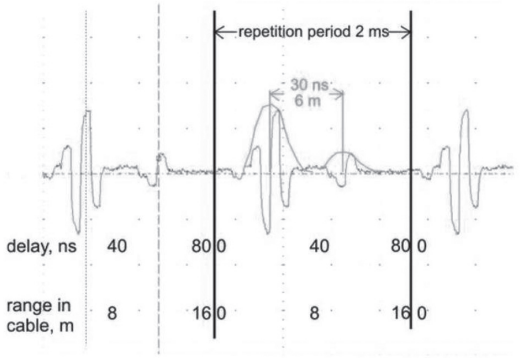

Fig. 11. Cross-correlation between transmitted signal and the reference, which gives the range profile, obtained with the help of stepped-delay method and AWG472: two targets case

In figure 10 the range profile obtained with the help of stepped-delay mode is presented. AWG472 signals and, consequently, range profiles are repeated with 2 ms period. The 4 ns delays in the signal enabled real-time integration in the mixer +amplifier +LPF, while further sampling with a slow ADC enabled range scan within 0...16 m (in cable). It is seen from the range profile obtained a good agreement between real and measured range differences of ~6 m.

6. CONCLUSIONS

The results on the use of FPGA-based devices for the generation of pseudo-random signals for noise radars are presented. Exploiting of m-sequencies and linear congruential algorithm for time series generating in real time using a FPGA evaluation board is demonstrated.

We present an approach for estimation of the radar cross-correlation which uses combination of digital generation using two-channel AWG and analog processing of wideband noise signals. This procedure includes delaying of the transmitted signals with respect to the sampled reference with the help of digital signal generator, analog multiplication and integration. We reported the parameters of available arbitrary waveform generators and described an approach enabling to form high resolution range profiles with arbitrary waveform generation and without need in having high sampling frequency of the ADC. Experimental validation has shown that the approach enables to generate range profiles and to digitize them in low frequency band. We also assured that digital scheme for noise signal generation allows controlling spectrum shape of sounding signal and is very attractive for use in modern noise radars.

7. ACKNOWLEDGEMENTS

The authors are grateful to professor K.A.Lukin for suggesting the problem, support and guidance in carrying out this work.

References

[1] *Lukin K. A.* Noise Radar Technology: the principles and short overview // Applied Radio Electronics. Vol. 4, No. 1. 2005. P. 4–13.

[2] *Varakin L. E.* The theory of complicated signals. M.: Sovetskoe Radio, 1970. 376 p. (in Russian).

[3] *Binder K.* Applications of Monte Carlo methods to statistical physics // Rep. Prog. Phys. 1997. Vol. 60, No. 5. P. 487-559.

[4] *Cicuttin A., Crespo M. L., Shapiro A., Abdallah N.* A Block-Based Open Source Approach for a Reconfigurable Virtual Instrumentation Platform Using FPGA Technology // IEEE International Conference on Reconfigurable Computing and FPGA's (ReConFig 2006), San Luis Potosi, Mexico, September 20-22, 2006. P. 39-46.

[5] http://www.euvis.com/

[6] *Lukin K. A., Vyplavin P. L., Zemlyaniy O. V., Palamarchuk V. P., Lukin S. K.* High Resolution Noise Radar without fast ADC // International Journal of Electronics and Telecommunications (JET). 2012. Vol. 58, No. 2. P. 135-140.

Manuscript received February, 6, 2013

Oleg V. Zemlyaniy M. Sc. (1990), Ph. D. (2009), Senior Research Fellow of Laboratory for Nonlinear Dynamics of Electronic Systems, Usikov Institute for Radiophysics and Electronics NAS of Ukraine. Areas of research: deterministic chaos in nonlinear dynamical systems with delayed feedback, pseudorandom/noise/chaotic waveform generation and processing, noise radars.

Sergiy K. Lukin was born in 1987. He graduated from Kharkiv National Aerospace University 2008 and joined Laboratory for Nonlinear Dynamics of Electronic Systems in Usikov Institute for Radiophysics and Electronics of NAS of of Ukraine. He currently holds the position of junior researcher. Field of interest: FPGA, signal processing, software-defined radar, software development.

УДК 537.862

Генераторы случайных сигналов на основе ПЛИС для шумовых радиолокаторов / О. В. Земляный, С. К. Лукин // Прикладная радиоэлектроника: науч.-техн. журнал. – 2013. – Том 12. – № 1. – С. 32–36.

Представлены результаты по применению генераторов сигналов произвольной формы, которые построены на основе ПЛИС для генерации сложных сигналов в шумовых радиолокаторах. Для генерации сигналов, представленных в цифровой форме в виде заранее запрограммированных последовательностей, предложено использовать генератор сигналов произвольной формы, позволяющий получать сигналы любого типа в реальном масштабе времени. На базе этого устройства предлагается схема построения радиолокатора с цифровой генерацией опорного и зондирующего шумовых сигналов (метод скачкообразного изменения задержки в шумовом радиолокаторе). Предложенный подход позволяет получать кросс-корреляционную функцию без использования быстродействующих АЦП и переключаемой линии задержки. Экспериментально на примере различных типов сигналов показана эффективность использования генераторов сигналов произвольной формы в радиолокаторах. В работе также использовался метод формирования сигналов с применением алгоритмов получения выборок непосредственно в ПЛИС, что подразумевает вычисление и выдачу отсчетов сигнала в реальном масштабе времени.

Ключевые слова: шумовой радиолокатор, программируемая логическая интегральная схема (ПЛИС), генератор сигналов произвольной формы, радиолокатор со скачкообразным изменением задержки, функция взаимной корреляции, шумовой / случайный / хаотический сигнал.

Ил. 11. Библиогр.: 6 назв.

УДК 537.862

Генератори випадкових сигналів на основі ПЛІС для шумових радіолокаторів / О.В.Земляний, С. К. Лукін // Прикладна радіоелектроніка: наук.-техн. журнал. – 2013. – Том 12. – № 1. – С. 32–36.

Представлені результати по застосуванню генераторів сигналів довільної форми, які побудовані на основі ПЛІС для генерації складних сигналів в шумових радіолокаторах. Для генерації сигналів, представлених у цифровій формі у вигляді заздалегідь запрограмованих послідовностей, запропоновано використовувати генератор сигналів довільної форми, що дозволяє отримувати сигнали будь-якого типу в реальному масштабі часу. На базі цього пристрою пропонується схема побудови радіолокатора з цифровою генерацією опорного і зондуючого шумових сигналів (метод стрибкоподібної зміни затримки в шумовому радіолокаторі). Запропонований підхід дозволяє отримувати крос-кореляційну функцію без використання швидкодіючих АЦП і лінії затримки, що перемикається. Експериментально на прикладі різних типів сигналів показана ефективність використання генераторів сигналів довільної форми в радіолокаторах. У роботі також використовувався метод формування сигналів із застосуванням алгоритмів отримання вибірок безпосередньо в ПЛІС, що має на увазі обчислення і видачу відліків сигналу в реальному масштабі часу.

Ключові слова: шумовий радіолокатор, програмована логічна інтегральна схема (ПЛІС), генератор сигналів довільної форми, радіолокатор із стрибкоподібною зміною затримки, функція взаємної кореляції, шумовий / випадковий / хаотичний сигнал.

Іл. 11. Бібліогр.: 6 найм.

RANDOM NOISE SIGNAL GENERATION

UDC 621.37

NONLINEAR DYNAMICS OF DELAYED FEEDBACK MICROWAVE OSCILLATORS

N.M. RYSKIN, V.V. EMEL'YANOV, O.S. KHAVROSHIN, S.A. USACHEVA AND A.V. YAKOVLEV

An overview of research activity on nonlinear dynamics of delayed feedback microwave oscillators in Saratov State University during the ten years passed since the first NRT Workshop is presented. The paper covers a broad range of problems. First, general picture of nonlinear dynamics in delayed feedback oscillators is described. Recent advance in generation of robust hyperbolic chaos in a klystron-type microwave oscillator is discussed. The problem of controlling chaos in delayed feedback oscillators, as well as forced synchronization of such oscillator by external harmonic driving is considered.

Keywords: Delayed feedback oscillator, microwaves, klystron, traveling wave tube, hyperbolic chaos, controlling chaos, synchronization.

1. INTRODUCTION

Development of sources of high-power noise-like microwave radiation with a relatively wide band is important for noise radar technology, chaos-based communication systems, microwave plasma heating, and a number of other applications [1-3]. The most common schematic of a source of chaotic microwave radiation is a ring-loop oscillator consisting of a power amplifier which output power is partly fed to input through an external delayed feedback transmission line. The first chaotic generator of such kind had been developed as far back as in 1960-ies by V.Ya. Kislov *et al.* using a wide-band traveling wave tube (see e.g. [4]). Note that delayed feedback systems are of great importance not only in electronics but also in nonlinear optics, biophysics, geophysics, etc.

In this paper, we summarize the results of research on nonlinear dynamics of delayed feedback microwave oscillators in Saratov State University during the ten years passed since the first NRT Workshop. The paper is organized as follows. In Sec. 2, general picture of nonlinear dynamics in delayed feedback oscillators is reviewed. Sec. 3 presents a new idea for generation of robust hyperbolic chaos in microwave band by a system of two coupled klystrons. In Sec. 4 application of controlling chaos technique for suppression of spurious self-modulation oscillations using an additional feedback loop is considered. Finally, forced synchronization of a delayed-feedback oscillator driven by an external harmonic signal is studied in Sec. 5.

2. MODEL OF A DELAYED-FEEDBACK OSCILLATOR

Consider a model of a ring-loop oscillator consisting of a nonlinear power amplifier, a bandpass filter and a feedback leg which contains a delay line, a variable attenuator and a phase shifter which provide control of the amplitude and the phase of the feedback signal (Fig. 1).

Since the filter is assumed to have narrow bandwidth it is convenient to use the slowly varying amplitude approximation. In this approximation dynamics of the oscillator obeys the following equation [5]:

$$\frac{dA}{dt} + \gamma A = \alpha e^{i\psi} F\left(A_\tau\right). \qquad (1)$$

Here A is the slow complex amplitude, γ is the parameter of losses, α is the parameter of excitation proportional to the gain factor of the amplifier, $F(A)$ is nonlinear transfer function of the amplifier, $A_\tau = A(t-\tau)$. Henceforth the delay time is accepted equal to unit that always can be achieved by renormalization of the variables.

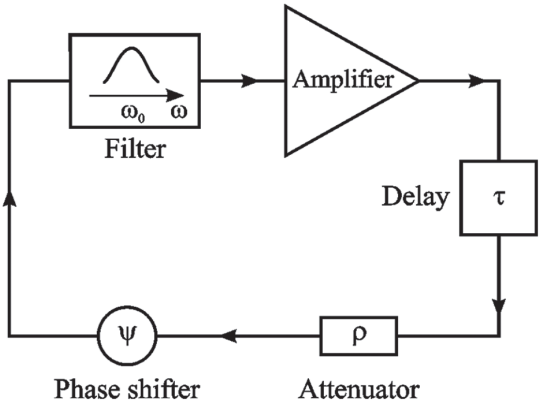

Fig. 1. Scheme of the delayed feedback oscillator

Consider oscillator with cubic nonlinearity, $F(A) = \left(1 - |A|^2\right)A$. Seeking for single-frequency solutions of (1), $A = A_0 \exp(i\omega t)$, we obtain the following equation for the eigenfrequencies:

$$\omega = -\gamma \operatorname{tg}(\omega\tau - \psi). \qquad (2)$$

Here ω is the detuning from the central frequency of the system passband ω_0. Eq. (2) has infinite number of complex roots, i.e. the time-delayed system with infinite-dimensional phase space has an infinite number of eigenmodes.

It is convenient to solve Eq. (2) graphically. If the roots are numbered as shown in Fig. 2a one can show that all the solutions can be divided into two classes. For the roots ω_n with even numbers $n=2k$ the amplitude of oscillations satisfies the equation

$$|A_0|^2 = 1 - \frac{\sqrt{\gamma^2+\omega_{2k}^2}}{\alpha}. \qquad (3)$$

These solutions exist when the parameter α exceeds the self-excitation threshold $\alpha > \alpha_{st} = \sqrt{\gamma^2+\omega_{2k}^2}$. The solutions with odd numbers $n=2k+1$ exist at any values of parameters, however they are always unstable. Nevertheless, they play an important role because self-modulation is caused by their excitation on the background of the fundamental mode with high amplitude [5]. Further we refer to them as self-modulation modes.

The self-excitation threshold is 2π-periodic in ψ and has a form of discrete domains called "oscillation zones" (Fig. 2b). In the centers of the zones, at $\psi = 2\pi k$, $\omega_{2k} = 0$ and threshold value of α is minimal. Near the boundaries of two adjacent zones, at $\psi = (2k+1)\pi$, there is a region of bistability and oscillation hysteresis, where either of the two eigenmodes can survive as a result of a mode competition process, depending on the initial conditions. In Fig. 2b, these domains are bounded by dashed lines.

When the parameter α increases well above α_{st} the single-frequency regime becomes unstable and self-modulation arises. Lowest self-modulation threshold α_{sm} is attained in the centre of a generation zone [5]. Further increase of α above the self-modulation threshold result in transition to chaos through a sequence of period doubling bifurcations [5].

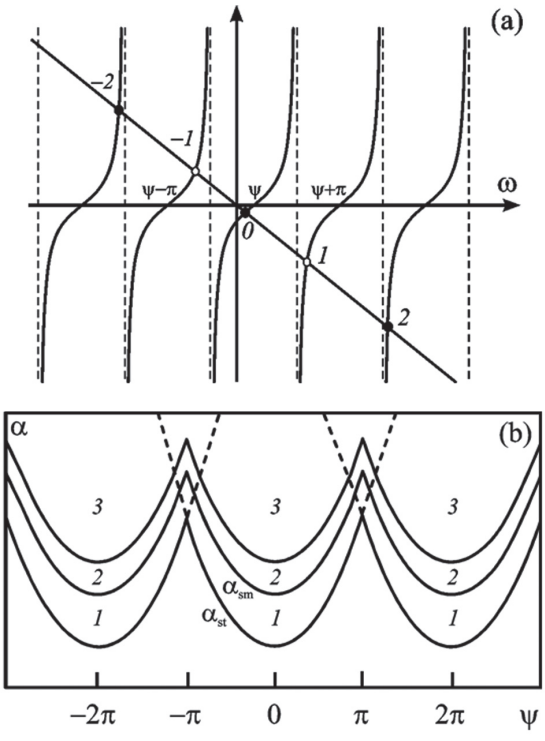

Fig. 2. (a) Graphical solution for eigenfrequencies. (b) Phase diagram on $\psi-\alpha$ plane: *1* — single-frequency oscillation; *2* — self-modulation; *3* — chaos

Delayed-feedback oscillators show the great variety of different chaotic regimes which are easy to control either by feedback parameters or by an external driving signal. Therefore, recently klystron [6] and traveling wave tube [7] oscillators driven by external signal have been considered as promising sources of chaotic radiation for chaotic-based communication systems at microwave frequencies.

3. KLYSTRON-TYPE MICROWAVE GENERATOR OF ROBUST HYPERBOLIC CHAOS

The hyperbolic chaos is known as the strongest type of the chaotic behavior when the strange attractor does not contain any stable periodic orbits and only comprises trajectories of saddle type [8]. These attractors possess the property of structural stability that implies insensitivity of the system dynamics and the attractor structure to variations of parameters and functions describing the system. Recently an approach for design of radio frequency oscillator with hyperbolic attractor has been proposed [9]. The operation principle of such system is alternating excitation of two coupled oscillators so that the transformation of the signal phase is described by chaotic Bernoulli map, which is a classical example of system with hyperbolic attractor [8]. Evidently, such generators are of practical interest for communication and radar systems using chaotic signals.

In [10, 11] we extended this principle to the microwave band using two coupled klystrons. Scheme of the oscillator is presented on Fig. 3. The input cavity of the first klystron is tuned to the frequency of ω, while the output one is tuned to frequency of 2ω. Thus, the first klystron doubles the frequency of the input signal. The output signal of the first klystron is fed to the input cavity of the second klystron via a wide-band dispersionless transmission line containing a phase shifter and an attenuator, which allow the signal phase and amplitude to be adjusted. In the second klystron, this signal is mixed with a reference signal, which represents a periodic sequence of pulses with carrier frequency of 3ω. Thus, in the second klystron there is a mixing of the signals of the second and third harmonics. In the output cavity of the second klystron a signal on a difference frequency of ω is separated and fed to the input cavity of the first klystron, thus closing the feedback circuit.

The dynamics of the oscillator is described by the following system of dimensionless delay-differential equations (DDEs) [10, 11]

$$\begin{aligned}
&\dot{F}_1^{\omega} + F_1^{\omega} = \rho_2 e^{i\psi_2} F_2^{\omega}/\sqrt{2},\\
&\dot{F}_1^{2\omega} + \delta F_1^{2\omega} = 4\alpha_1 J_2\left(2\left|F_{\tau,1}^{\omega}\right|\right) e^{2i\left(\varphi_{\tau,1}^{\omega}-\theta_0\right)},\\
&\dot{F}_2^{2\omega} + \delta F_2^{2\omega} = \sqrt{2}\rho_1 e^{i\psi_1} F_1^{2\omega},\\
&\dot{F}_2^{\omega} + F_2^{\omega} = 2\alpha_2 e^{-i\theta_0} \sum_{m=-\infty}^{\infty} i^m J_{3m+1}\left(\left|F_{\tau,2}^{2\omega}\right|\right)\times\\
&\times J_{2m+1}\left(\left|F_2^{3\omega}(t)\right|\right) e^{-i(3m+1)\varphi_{\tau,2}^{2\omega}}.
\end{aligned} \qquad (4)$$

Here $F_j^{k\omega}(t)$ are dimensionless slowly varying complex amplitudes of the signals in corresponding cavities, $\varphi_j^{k\omega} = \arg\left(F_j^{k\omega}\right)$, the subscripts $j = 1,2$ henceforth indicate the number of klystrons, the superscripts ω, 2ω denote the resonance frequencies of the cavities; τ is the normalized delay parameter; θ_0 is the unperturbed electron transit angle in the drift space; parameter $\delta = 2Q^{\omega}/Q^{2\omega}$ defines the ratio of Q-factors of the cavities operating at frequencies ω and 2ω; parameters ρ_j and ψ_j are attenuations and phase shifts in the coupling transmission lines, respectively; J_n is n^{th} order Bessel function of the 1st kind. The excitation parameters α_j which can be treated as the normalized dc electron beam currents most significantly influence the oscillator dynamics. The equations (4) are derived in a similar way as for other klystron-type delayed feedback oscillators (see e.g. [12]).

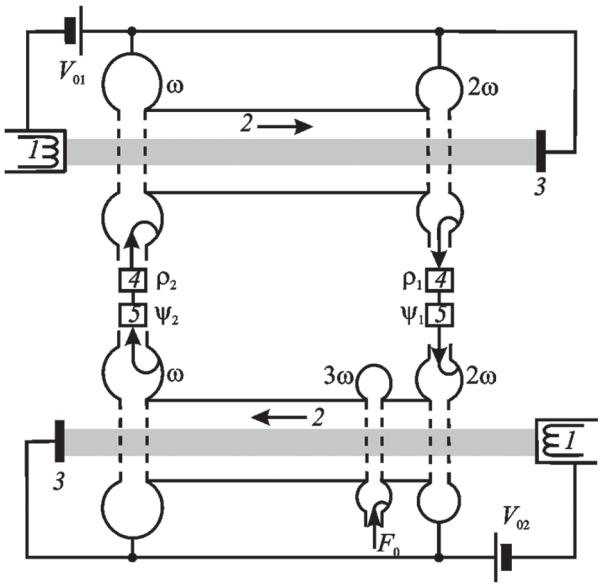

Fig. 3. Scheme of the proposed chaos generator based on coupled drift klystrons. *1* — electron guns, *2* — electron beams, *3* — collectors, *4* — variable attenuators, *5* — phase shifters

The reference signal at the third harmonic frequency is supplied from an external driving source in the form of a sequence of pulses with constant amplitude F_0 and a repetition period equal to the time of signal passage via the feedback circuit, 2τ.

Assuming that the oscillation build-up in the cavities is fast in comparison with delay time one can neglect the derivatives in (4) and consider the variables in discrete moments of time $t_n = 2n\tau$. As a result, after some mathematical transformations DDEs (4) are reduced to the 2-D iterative map

$$F_{n+1}e^{i\varphi_{n+1}} \approx rJ_2\left(2F_n\right)e^{i(\Delta-2\varphi_n)}, \qquad (5)$$

where $r = 4\alpha_1\alpha_2\rho_1\rho_2\delta^{-2}J_1\left(F_0\right)$, $\Delta = \psi_2 - \psi_1 + \theta_0$ [10,11]. From (5) one can see that the dynamics of the phase obeys the Bernoulli map $\varphi_{n+1} = \Delta - 2\varphi_n$ that demonstrates the hyperbolic chaotic dynamics with a positive Lyapunov exponent of $\Lambda = \ln 2$.

Numerical simulation of the DDEs (4) confirms that the generator is capable to produce robust hyperbolic chaotic oscillation. The values of parameters approximately correspond to the parameters of the millimeter band oscillators described in [12]. In Fig. 4, the plot of largest Lyapunov exponent of the hyperbolic attractor vs. the excitation parameter α_1 is shown. For comparison with the results for the map (5), we calculated the Lyapunov exponent for the stroboscopic Poincare map ($t = 2n\tau$). The largest Lyapunov exponent is almost independent from the parameter and approximately equal to $\ln 2$ that indicates structural stability of the chaotic attractor.

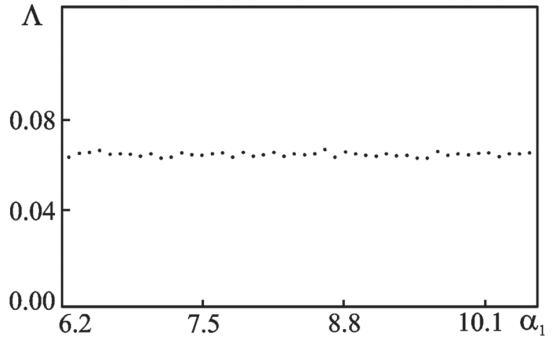

Fig. 4. Largest Lyapunov exponent of the hyperbolic attractor vs. α_1 at $\alpha_2 = 15.0$

Fig. 5 shows the typical waveform of the amplitude in the input cavity of the first klystron in the regime of hyperbolic chaos. One can see that the signal has the form of pulse sequence with nearly constant amplitude. However, the phase of the signal varies irregularly from pulse to pulse [9] providing robust chaotic signal. This is confirmed by Fig. 6 where typical examples of iterative diagram for the phase of subsequent pulses and projection of the attractor onto the $\mathrm{Re}\,F_1^{\omega} - \mathrm{Im}\,F_1^{\omega}$ plane are presented. For this plots we take the values of the variables at the moments of time when the amplitude $\left|F_1^{\omega}\right|$ reaches its local maximum. The attractor has a topology of the Smale–Williams solenoid, which is typical for the systems with hyperbolic chaos. The angular coordinate of the attractor obeys the Bernoulli map.

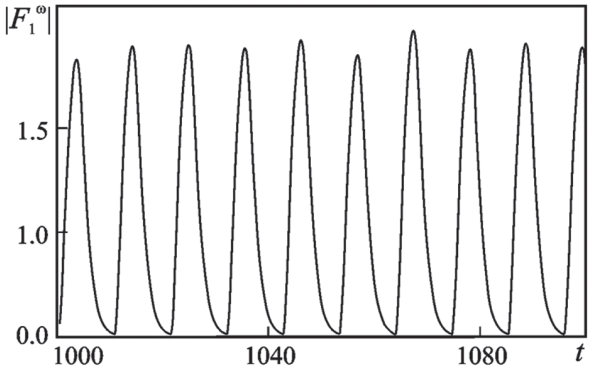

Fig. 5. Waveform of the field amplitude in the input cavity of the first klystron in the regime of hyperbolic chaos

Despite of the hypothesized hyperbolic nature of the chaotic attractor, the considered scheme of the generator is of interest itself, since it reveals an opportunity to obtain robust structurally stable chaos at

microwave frequencies. This property is very important for possible applications in chaos-based communication and radar systems.

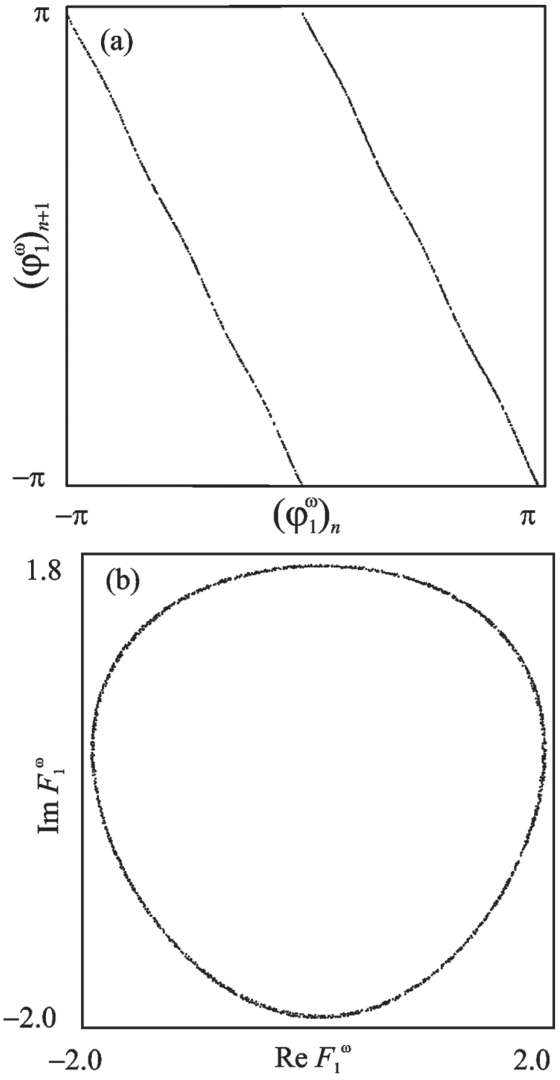

Fig. 6. The iterative diagram for the phase of the oscillations (a) and the projection of the phase portrait on $\mathrm{Re}\,F_1^{\omega} - \mathrm{Im}\,F_1^{\omega}$ plane (b)

4. SUPPRESSING SELF-MODULATION AND CONTROLLING CHAOS IN DELAYED FEEDBACK OSCILLATORS

As is mentioned in Sec. 2, self-modulation instability is typical for the oscillators with time delayed feedback. This instability results in generation of multiple frequencies or even spread spectrum chaotic signal. Thus the instability restricts the maximal output power and efficiency of an oscillator in the single-frequency regime.

In [13-15] a method for suppression of the self-modulation was proposed. This method expands the well-known idea of time-delayed feedback chaos control [16] on delayed feedback oscillators. It is based on adding an additional control feedback with the parameters chosen so that after passing through the two feedback legs the fundamental waves appear in the same phase, while the self-modulation sidebands appear in anti-phase, and thus, suppress each other.

Consider the general scheme of a ring-loop oscillator which consists of an amplifier and a delayed feedback path. To stabilize single frequency generation regimes we split the feedback leg into two paths as shown in Fig. 7. Let parameter k define relative power level of the signals passing through the two feedback legs. Assume that we are able to adjust the delay times $\tau_{1,2}$ and phase shifts $\psi_{1,2}$. Considering propagation of a modulated signal with fundamental frequency ω and modulation frequency Ω one can show [13-15] that for suppression of the sidebands the parameters should satisfy the following relations:

$$\psi_1 - \psi_2 - \omega(\tau_1 - \tau_2) = 2\pi n\,, \tag{6}$$

$$\Omega(\tau_1 - \tau_2) = 2\pi m + \pi\,. \tag{7}$$

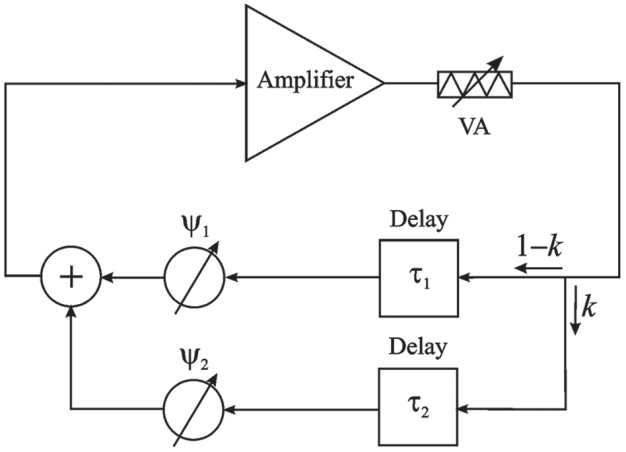

Fig. 7. Scheme of an oscillator with double delayed feedback loop

We demonstrate successful application of the method on two examples. We performed numerical simulations for a generalized model of a delayed-feedback oscillator (1) [13], as well as for klystron [15] and TWT [14] oscillators. For example, the Eq. (1) for the case of two feedback loops should be modified as follows

$$\frac{dA}{dt} + \gamma A = \\ = \alpha\left[(1-k)e^{i\psi_1}F(A_{\tau 1}) + ke^{i\psi_2}F(A_{\tau 2})\right]. \tag{8}$$

Numerical results show that the application of the additional control feedback allows suppression of self modulation including chaotic spread spectrum oscillation. Fig. 8 shows a typical example of steady-state output signal amplitude F_{out} vs. the excitation parameter α for a two-cavity klystron oscillator. The circles denote stable steady states while the squares denote unstable steady states that are stabilized by applying the control feedback. One can see that the self-modulation threshold increases from $\alpha = 24.06$ to $\alpha = 44.01$. Suppose that we keep the amount of feedback constant and increase α by increase of the beam current. In the steady-state regime output power $P \sim |F_{out}|^2$. So from Fig. 8 one can estimate that the beam current at which the single frequency regime is stable can be increased in approximately in 1.83 times, and this

result in 1.5 increase of the output power. However, the electronic efficiency $\eta \sim F_{out} J_1(F_{out})$ decreases approximately in 1.25 times.

By adjusting the phase of the controlling feedback to $\psi_2 \approx \psi_1 + \pi$ the power can be increased by a factor of 3 or more [15].

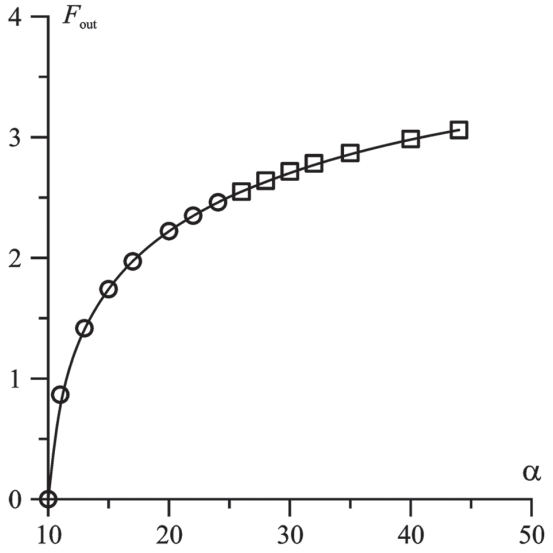

Fig. 8. Typical example of output signal amplitude vs. α for the two-cavity klystron oscillator

Similar results were obtained for the TWT oscillator. Basic equations and details of nonstationary simulations are described in [14]. Fig. 9 shows a typical plot of output power and electronic efficiency vs. normalized length $L = 2\pi CN$ where C is the Pierce gain parameter and N is the phase length of the tube [17].

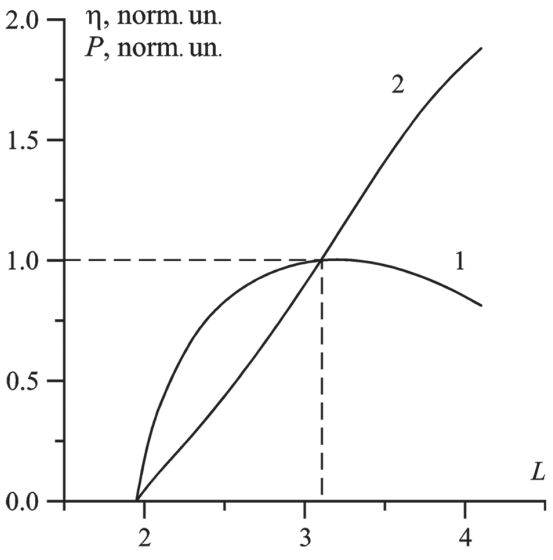

Fig. 9. Normalized TWT efficiency (*1*) and output power (*2*) vs. normalized length $L = 2\pi CN$. Self-modulation in a system without control arise at $L = 3.1$

Power and efficiency are normalized to the values at $L = 3.1$, that is the self-modulation threshold in the oscillator without the control. Again we suppose that the amount of feedback is kept constant while the beam current, and thus, L increases. Nearly twice increase of the threshold beam current and output power is observed, with simultaneous decrease of the efficiency. Similar to the klystron oscillator, maximal efficiency is reached near the self-modulation threshold in the oscillator without the control. However, in the TWT oscillator it is possible to stabilize not only fundamental mode, but also higher-order modes which interact with the beam more efficiently. In that case, efficiency enhancement becomes possible [14].

5. FORCED SYNCHRONIZATION OF A DELAYED FEEDBACK OSCILLATOR

Investigation of forced synchronization of a delayed feedback oscillator by an external harmonic driving is important in connection with recent projects of using non-autonomous klystron and TWT oscillators in chaos-based communication systems [6, 7]. Owing to multimode nature of delayed-feedback systems one can expect that processes of synchronization will have a number of special features in comparison with systems with low number of degrees of freedom. The picture of forced synchronization of a general model of the delayed-feedback oscillator (1) was thoroughly investigated in [18].

Consider oscillator (1) with cubic nonlinearity driven by an external harmonic signal

$$\frac{dA}{dt} + \gamma A = \alpha e^{i\psi}\left(1 - |A_\tau|^2\right)A_\tau + Fe^{i\omega t}. \qquad (9)$$

Let us start from the case $\psi = 0$ that corresponds to the centre of a generation zone that is optimal conditions for self-excitation, and choose the other parameters $\gamma = 0.3$ and $\alpha = 0.9$. Such a value of α exceeds the generation threshold $\alpha_{st} = 0.3$ but lies below the self-modulation threshold $\alpha_{sm} = 1.33$, so the free-running system exhibits stable single-frequency oscillations.

Solutions of (9) $A_0 \exp(i\omega t)$ correspond to the forced synchronization mode. We studied the stability of these solutions analytically and numerically. In Fig. 10a the picture of frequency responses (resonant curves) $\rho(\omega)$ where $\rho = |A_0|^2$ is presented. The bottom part of the Fig. 10a is similar to a classical picture of resonance curves for synchronization of a system with one degree of freedom [19]. However in the domain of high amplitudes there exist significant differences. First of all, one should notice the domains of phase locking at frequencies of self-modulation modes. Second, the resonance curves become unstable in the domain of high amplitudes. This instability is caused by excitation of sidebands with frequencies of self-modulation modes. Despite there is no self-modulation in the free-running oscillator for the chosen values of parameters, excitation of self-modulation modes is possible when intensive external driving is applied. We name this regime as *drive-induced self-modulation*. Fig. 10b shows a corresponding synchronization tongue on the ω-F plane. Lines of saddle-node (SN) and Andronov–Hopf (AH) bifurcations are shown. These lines contact with each other in Bogdanov–Takens (BT) points marked by circles. Domain of stable synchronous operation is shown in white color, unstable domains are shaded.

Notice that in the free-running oscillator self-modulation is caused by excitation of two sidebands which are equidistant from the fundamental frequency (modes with numbers $n=\pm1$ in Fig. 2a). Accordingly, the boundary of drive-induced self-modulation in Fig. 10 consists of two intertwined curves which correspond to excitation of mode with either $n=1$ or $n=-1$.

It is well known that SN bifurcation corresponds to phase-locking of the free-running oscillator [19]. Note that there exist two kinds of SN bifurcations, one corresponding to phase-locking of the fundamental mode near $\omega=0$ (SN_1) and the others near $\omega\approx\pm0.55\pi$ (SN_2) corresponding to the self-modulation modes (see Sec. 1) which are always unstable. There also exist domains of phase-locking of higher-order self-modulation modes not shown in Fig. 10. Similarly, there are two kinds of AH bifurcations: one (AH_1) corresponds to synchronization via suppression of natural dynamics, while the other (AH_2) one corresponds to drive-induced self-modulation. Therefore, there are two kinds of BT points marked by light and dark circles respectively.

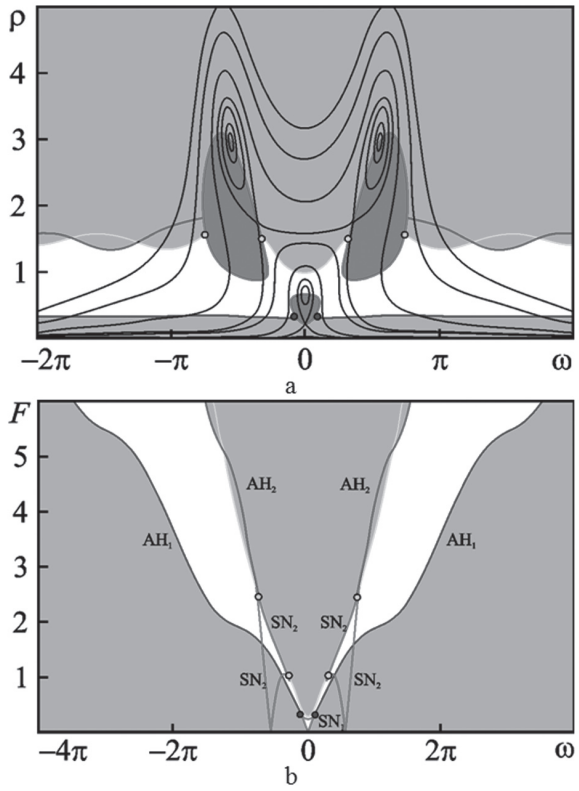

Fig. 10. (a) The picture of resonance curves in the center of generation zone, $\psi=0$, $\gamma=0.3$, $\alpha=0.9$; (b) Synchronizations tongue on $\omega-F$ plane. SN — saddle-node bifurcations; AH — Andronov–Hopf bifurcations. Bogdanov–Takens points are shown by circles

We also investigated transformation of resonant curves and synchronization tongues with the approaching to the self-modulation threshold. With the increase of α, the phase-locking domains formed at the fundamental and two self-modulation modes merge, breaking the domain of stability into three separated parts. Accordingly, the synchronization tongue also breaks into three partly overlapping parts that corresponds to bistability. While parameter α approaches to the self-modulation threshold the central part of synchronization tongue decreases in size. Finally, when $\alpha>\alpha_{sm}=1.33$, the central domain of synchronization vanishes (Fig. 11). Now the tongue consists of two separate parts and the synchronization tongue does not touch the $F=0$ axis, i.e. synchronization threshold appears. This occurs since the free-running oscillator generates quasiperiodic self-modulated oscillation with two independent frequencies.

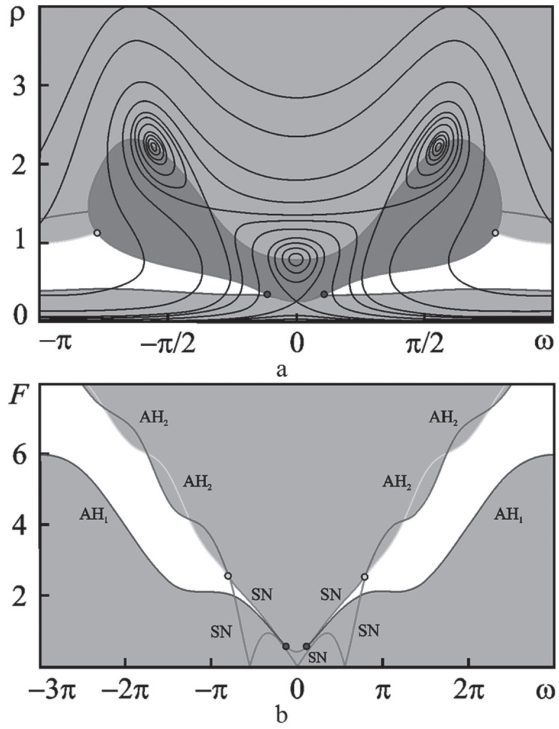

Fig. 11. The picture of resonance curves (a) and synchronizations tongue (b) above the self-modulation threshold: $\psi=0$, $\gamma=0.3$, $\alpha=1.45$

The analytical results presented above were verified by direct numerical simulation of the Eq. (9). Simulation of the process of transition to synchronous regime with increasing of the driving force detected the very complicated picture of dynamical regimes. When the driving frequency is close to the natural frequency of the oscillator, synchronization via phase locking occurs similar to system with one degree of freedom. However, the mode-locking process is accompanied by periodic excitation and decay of self-modulation modes [18].

When the driving frequency shifts off the natural frequency, synchronization occurs via suppression of the natural frequency. In that case, period-doubling cascade and transition to chaos precedes transition to the synchronous mode. Such a behavior can be explained as follows. The free-running system operates close to the self-modulation threshold, i.e. with the increase of the excitation parameter α the sequence of period doublings is observed. External driving increases the amplitude of oscillation thus stimulating the sequence of bifurcations observed in the free-running system.

When the driving frequency is close to the frequency of a secondary eigenmode hard transition to the synchronous regime is observed. The hard transition is accompanied by hysteresis and a narrow band of bistability appears near the boundary of the domain of synchronization.

The mechanisms described above are illustrated in Fig. 12 where the phase diagram on the $\omega - F$ plane is presented. The lines of different bifurcations which form the boundary of a synchronization tongue (similar to Figs. 10,11) are also shown. Domain of synchronization is shown by white, domain of bistability is hatched. Domains of period doublings (T2) and chaotic dynamics (C) are also shown. One can see that the domain of chaotic dynamics is located close to the self-modulation frequency ($\omega \approx 0.6\pi$). Inside this domain there exist a lot of narrow windows of periodic motion which are not shown in Fig. 12.

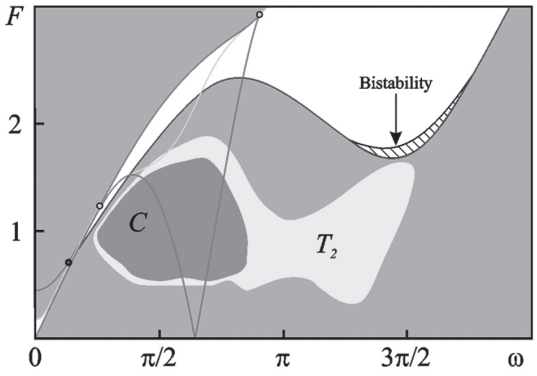

Fig. 12. Phase diagram on $\omega - F$ plane at $\psi = 0$, $\gamma = 1.0$, $\alpha = 2.5$

6. CONCLUSION

In this paper, we presented an overview of research activity on nonlinear dynamics of delayed feedback microwave oscillators in Saratov State University. The delayed feedback oscillators are distributed systems with infinite number of degrees of freedom and demonstrate a very complicated behavior including multiple transitions between regular and chaotic regimes. By that reason, they have good prospects as sources of chaotic microwave radiation for communication and radar systems.

In particular, the ring-loop oscillator consisting of two coupled klystrons with resonators tuned to fundamental and second harmonic frequencies is proposed. This oscillator is capable to generate structurally stable hyperbolic chaos at microwave frequencies. Structural stability means insensitivity of the system dynamics and the attractor structure to variations of parameters of the system.

The method to suppress self-modulation instability based on an additional delayed feedback circuit is proposed. It allows substantial increase in the beam current that corresponds to the stability of the stationary single-frequency generation and nearly threefold increase in the generation power.

The picture of forced synchronization in delayed feedback systems is investigated. In the domain of the small amplitudes the picture of synchronization is similar to the classical one of the oscillator with one degree of freedom. However, with growth of amplitude there are a lot of differences caused by excitation of different self-modulation modes.

ACKNOWLEDGMENTS

The work is supported by Russian Foundation for Basic Research No. 12-02-00541 and 12-02-31493.

References

[1] Kennedy M.P., Rovatti R. and Setti G. (eds.) 2000. *Chaotic Electronics in Telecommunications*, CRC Press, Boca Raton. FL.

[2] Vladimirov S.N., Izmailov V.V. and Poizner B.N. 2009. *Nonlinear Dynamical Cryptology: Radio-physical and Optical Systems*, Fizmatlit, Moscow.

[3] Lukin K.A. 2005. 'The principles of noise radar technology' *Appl. Radio Electron.* **4**, 4-13.

[4] Kislov V.Ya., Myasin E.A. and Zalogin N.N. 1980. 'On the nonlinear stochastization of self-oscillations in the electron-wave oscillator with delayed feedback', *Radiotekh. Electron.* **25**, 2160-2168.

[5] Ryskin N.M., Shigaev A.M. 2002. 'Complex dynamics of a simple distributed self–oscillatory model system with delay', *Tech. Phys.* **47**, 795-802 [Zh. Tech. Fiz., **72**(7), 1-8].

[6] Shigaev A.M., Dmitriev B.S., Zharkov Y.D. and Ryskin N.M. 2005. 'Chaotic dynamics of delayed feedback klystron oscillator and its control by external signal', *IEEE Trans. Electron Devices* **52**, 790-797.

[7] Marchewka C., Larsen P., Bhattacharjee S., Booske J., Sengele S., Ryskin N.M. and Titov V.N. 2006. 'Generation of chaotic radiation in a driven traveling wave tube amplifier with time-delayed feedback', *Phys. Plasmas* **13**, 013104.

[8] Katok A. and Hasselblatt B. 1995. *Introduction to the Modern Theory of Dynamical Systems*, Cambridge University Press. Cambridge.

[9] Kuznetsov S.P. 2005. 'Example of a physical system with a hyperbolic attractor of the Smale-Williams type' *Phys. Rev. Lett.* **95**, 144101.

[10] Emel'yanov V.V., Kuznetsov S.P. and Ryskin N.M. 2009. 'Hyperbolic chaos generator based on coupled drift klystrons', *Tech. Phys. Lett.* **35**, 773–776.

[11] Emel'yanov V.V., Kuznetsov S.P., Ryskin N.M. 2010. 'Hyperbolic chaos in the klystron-type microwave vacuum tube oscillator', *Chaos* **20**, 043104.

[12] Shin Y.M., Ryskin N.M., Won J.H., Han S.T. and Park G.S. 2006. 'Theoretical analysis of cross-talking signals between counter-streaming electron beams in a vacuum tube oscillators', *Phys. Plasmas* **13**, 033104.

[13] Emel'yanov V.V., Ryskin N.M. and Khavroshin O.S. 2009. 'Suppression of self-modulation in the self-oscillator with delayed feedback using the method for chaos control', *J. Comm. Technol. Electron.* **54**, 685–691.

[14] Ryskin N.M., Khavroshin O.S. 2008. 'Suppressing self-modulation instability in a delayed feedback traveling wave tube oscillator using controlling chaos technique', *IEEE Trans. Electron Devices* **55**, 662-667.

[15] Ryskin N.M., Khavroshin O.S. 2011. 'Self-modulation suppression in the delayed feedback klystron-type oscillator via the chaos control method' *J. Comm. Technol. Electron* **56**, 690–698.

[16] Pyragas, K. 1992. 'Continuous control of chaos by self-controlling feedback', *Phys. Lett. A* **170**, 421-428.

[17] Pierce J.R. 1950. *Traveling Wave Tubes,* Van Nostrand, Toronto.

[18] Usacheva S.A., Ryskin N.M. 2012. 'Forced synchronization of a delayed-feedback oscillator', *Physica D* **241**, 372-381.

[19] Pikovsky A., Rosenblum M., Kurths J. 2001. *Synchronization: A Universal Concept in Nonlinear Science*, Cambridge University Press, Cambridge.

Manuscript received December, 7, 2012

Nikita M. Ryskin was born in Saratov, Russia, in 1966. He received the Diploma degree, Ph.D. degree, and D.Sc. degree from Saratov State University (SSU), Saratov, Russia, in 1991, 1996, and 2005, respectively. From 1991 to 1997, he was engaged as a Research Scientist at the Research Institute for Mechanics and Physics, SSU. Since 1997 he has been with the Faculty of Nonlinear Processes, SSU, where he is currently a Professor at the Department of Nonlinear Physics. He has been a Senior Member of IEEE since 2010. Dr. Ryskin has co-authored many journal and conference papers and two student textbooks, "Nonlinear waves" (Moscow, Fizmatlit, 2000) and "Nonlinear oscillations" (Moscow, Fizmatlit, 2002). His current research interests include nonlinear phenomena in vacuum microwave electron devices, vacuum microelectronics, as well as nonlinear waves, solitons and chaos.

Valeriy V. Emelianov was born June 18, 1987 in Pugachov, Saratov region, Russia. In 2009 he received the Diploma degree from Saratov State University (SSU). He is currently working towards his PhD degree at the Department of Nonlinear Physics, SSU. Already he has been with "Almaz" R&D Company, Saratov, since 2009. His research interest is in modeling of nonlinear phenomena in vacuum microwave devices. V.V. Emelianov is a co-author of 4 journal papers.

Oleg S. Khavroshin was born in Lutsk, Ukraine, in 1983. He received the Diploma degree in physics and PhD degree from Saratov State University, Saratov, Russia in 2006 and 2009 respectively. His research interests are in computer simulation of nonlinear dynamics of oscillators with delayed feedback as well as propagation of electromagnetic waves in nonlinear media.

Svetlana A. Usacheva was born in Saratov, Russia (1987). She received Diploma degree and PhD degree in Radio physics from Saratov State University in 2009 and 2012, respectively. She has been IEEE Member since 2011. Her research interests are in nonlinear dynamics of delayed feedback systems and multimode microwave oscillators. S.A. Usacheva has co-authored 5 papers in peer-reviewed journals.

Anton V. Yakovlev received the Diploma degree from the Faculty of Nonlinear Processes, Saratov State University (SSU), Saratov, Russia in 2009. He is currently working towards his PhD degree at the Department of Nonlinear Physics, SSU. His research interest is in theoretical analysis and numerical modeling of microwave electron devices such as klystrons and coupled cavity traveling wave tubes.

УДК 621.37

Нелинейная динамика микроволновых генераторов с запаздывающей обратной связью / Н.М. Рыскин, В.В. Емельянов, О.С. Хаврошин, С.А. Усачева, А.В. Яковлев // Прикладная радиоэлектроника: науч.-техн. журнал. – 2013. – Том 12. – № 1. – С. 37–44.

Представлен обзор исследований в области нелинейной динамики микроволновых автогенераторов с запаздыванием, выполненных в Саратовском государственном университете в течение последних десяти лет. В статье затрагивается широкий круг вопросов. Описана общая картина нелинейной динамики генераторов с запаздыванием. Обсуждаются последние достижения в области разработки микроволновых генераторов грубого гиперболического хаоса клистронного типа. Рассматриваются проблемы управления хаосом в генераторах с запаздыванием, а также синхронизации таких генераторов внешним гармоническим сигналом.

Ключевые слова: генератор с запаздывающей обратной связью, микроволны, клистрон, лампа бегущей волны, гиперболический хаос, управление хаосом, синхронизация.

Ил. 12. Библиогр.: 18 назв.

УДК 621.37

Нелінійна динаміка мікрохвильових генераторів із запізнілим зворотним зв'язком / Н.М. Рискін, В.В. Ємел'янов, О.С. Хаврошин, С.А. Усачова, А.В. Яковлев // Прикладна радіоелектроніка: наук.-техн. журнал. – 2013. – Том 12. – № 1. – С. 37–44.

Представлено огляд досліджень в галузі нелінійної динаміки мікрохвильових автогенераторів із запізненням, виконаних у Саратовському державному університеті протягом останніх десяти років. У статті порушується широке коло питань. Описана загальна картина нелінійної динаміки генераторів з запізненням. Обговорюються останні досягнення в галузі розробки мікрохвильових генераторів грубого гіперболічного хаосу клістронного типу. Розглядаються проблеми управління хаосом в генераторах з запізненням, а також синхронізації таких генераторів зовнішнім гармонійним сигналом.

Ключові слова: генератор із запізнілим зворотним зв'язком, мікрохвилі, клістрон, лампа біжучої хвилі, гіперболічний хаос, управління хаосом, синхронізація.

Іл. 12. Бібліогр.: 18 найм.

UDC 517.862

TIME-DOMAIN SIMULATION OF SHORT-PULSE OSCILLATIONS IN A GUNN DIODE SYSTEM WITH TIME-DELAY MICROSTRIP COUPLING

L.V. YURCHENKO AND V.B. YURCHENKO

Time-domain simulations of active systems with Gunn diodes connected by sections of microstrip transmission lines (TL) are carried out. Self-generation of Gunn diodes mounted in various ways in the TL circuits has been investigated. Complex dynamics of electromagnetic field radiated into an open end of the TL are observed. Trains of high-frequency pulses are shown to emerge when active devices are separated from compact resonant circuits by extended sections of the TL providing a time-delayed feedback.

Keywords: high-frequency pulses, Gunn diode, delay line, time delay system.

1. INTRODUCTION

We perform time-domain computer simulations of nonlinear self-oscillations in distributed microstrip transmission line systems with active devices specified by negative differential resistance (NDR) of current-voltage characteristics such as of Gunn diodes and similar structures. There are two main goals of this research which concern both the theoretical and practical aspects of the problem:

1) Developing mathematical models, numerical techniques and computer codes for the efficient self-consistent time-domain simulation of high-frequency excitation in distributed systems with a strong time-delayed coupling between active devices connected by sections of transmission lines;

2) Investigating available options of microstrip implementation of nonlinear power combining (superlinear in the number of devices) and non-conventional spectral effects (ultra-wideband chaotic oscillations etc) for possible practical applications in high-frequency electronic systems (ultra-short pulse generation, noise radars, etc).

Microwave power combining has been investigated for a long time. Initially, there were lumped circuits being considered. Later on, waveguide network [1, 2] and quasi-optical array systems [3, 4] have been proposed. Despite numerous achievements [4, 5], efficient power combining remains a challenging problem. There are important physical reasons for this, such as the distributed character of systems whose size is large compared to the wavelength (especially, when considering open radiating systems), broadband and multi-frequency dynamics of oscillations, etc.

Nowadays, the major goal is the power combining in the THz bands where the power output of individual devices is intrinsically limited by the physical processes involved (the main relaxation channels in both the devices and the environment occur precisely in this domain). In the meantime, conventional design and simulation techniques (e.g., the impedance analysis method) are insufficient for these systems [6, 7], being only valid in a small-signal approximation for narrow-band applications. On the other hand, exact numerical methods (such as finite-difference time-domain ones [8]) require huge computational resources and are inappropriate in many cases.

The active character of devices characterized by instability and nonlinearity makes common simulation tools (e.g., Flomerics Micro-Strips, etc) inadequate for the rigorous modeling of such systems. Other software, such as SPICE, cannot cope with distributed systems where the wave propagation between the devices is an essential part of system operation. A promising approach is the use of hybrid numerical methods [9] that combine both the frequency-domain and the time-domain computations, though they also suffer from various limitations (narrow-band approximation etc).

For these reasons, the design of active structures is usually split in two separate stages dealing with either linear or nonlinear parts of the system. In this method, the attention is focused on passive components whose design is carried out in much detail. As a price for this simplification, some assumptions are supposed to be met such as the operation of the system in the narrow band or in a given set of a few narrow bands, etc.

In this work, we choose an alternative approach and focus our attention on the nonlinear part of the problem, while the linear part is chosen to be relatively simple. In this approach, the aim is the accurate self-consistent modeling of nonlinear effects through rigorous solutions of governing equations and, specifically, accurate time-domain simulations of nonlinear oscillations and non-conventional dynamics (chaos, pulses) emerging in various conditions [10-13]. As a practical issue, nonlinear power combining is investigated in a rigorous manner.

By reducing the linear part of the problem to the simplest form, we arrive at a set of discrete devices connected by sections of one-dimensional transmission lines, e.g., microstrips. Microstrips excited by solid-state devices are rather practical solutions for various applications. A study of one-dimensional models provides also a benchmark for testing various computational methods ranging from analytic approximations to advanced numerical tools.

In quasi-optical applications, parallel coupling of active devices in a single array is used for increasing the power output [4] (in microwaves, similar ideas were implemented in the waveguides by K. Kurokawa [1]). A one-dimensional analogue of this system is the parallel connection of transmission line circuits, with microwave power being radiated into an open infinite

section of the line (the latter models the radiation of the electromagnetic waves from the antennas into free space in three-dimensional open systems).

As an alternative system, a series connection of active devices in a sufficiently long transmission line (a ladder-type oscillator) represents a simplified model of an open active structure with distributed elements that could be used for the spectrum modification of THz radiation. Our simulations of a chain of Gunn diodes [10] revealed complicated dynamics of the electromagnetic field in this system, though more detailed analysis of this structure is needed.

The interest in the systems of this kind is justified by their potential applications as the sources of chaotic signals for the emerging field of the noise radar technology [14]. This technology provides a number of benefits such as an ultra-wideband spectrum of radiation, simultaneous detection of the position and the velocity of the target, operation below the noise level of the environment, and other advantages. For these reasons, THz applications and, especially, MMIC implementations of these systems are of particular interest.

2. SIMULATION OF PARALLEL TIME-DELAY NETWORK OF ACTIVE DEVICES

Simulation approach outlined above was applied earlier to a few kinds of time-delay circuits with active devices (Gunn diodes) of relatively simple configurations [10-13]. They were mostly series networks of a few devices with time-delay microstrip coupling or single-diode systems with time-delay feedback where complicated dynamics of high-frequency radiation field have been predicted [10-13].

Here we consider another system, which is a parallel time-delay network of active devices as shown in Fig. 1, a. All active blocks in this network ($n=1,...N$) are identical, being of the kind shown in Fig. 1, b. A common passive block ($n=0$) is of the kind shown in Fig. 1, c. The block operates as a remote resonator for the given set of active devices and, in the same time, as a resonant antenna that transmits electromagnetic radiation into an open (infinite) section of microstrip line as shown in Fig. 1, a.

Microstrip lines of length d_n and d_{S_n} provide time-delay coupling and feedback in this system. They are supposed to be sufficiently long as compared to characteristic wavelength of emerging radiation.

Formulation of the problem is provided by the set of equations consisting of

– the wave equations for the current $i_n(\tau,x)$ and voltage $e_n(\tau,x)$ in each section of the microstrip transmission line;

– the circuit equations for each circuit n written in terms of the current $i_n(\tau)$ and voltage $e_n(\tau)$ defined appropriately for each circuit as shown in Figs. 1 (e.g. for active circuits the circuit currents and voltages are

$$i_n = i_n^- = i_n^+, \quad e_n = e_n^- - e_n^+,$$

$$i_n = i_{L_n} = i_{G_n} + i_{C_n}, \quad e_n = e_{C_n} + e_{L_n} - e_{B_n});$$

– the boundary conditions for the wave equations at the points of microstrip connections to the circuits ($x_n^{\pm} = x_n \pm 0$) which establish the link between the microstrip currents and voltages at the points $x_n^{\pm}$ ($i_n^{\pm}(\tau) = i_n(\tau, x_n^{\pm})$, $e_n^{\pm}(\tau) = e_n(\tau, x_n^{\pm})$) and the circuit currents and voltages $i_n(\tau)$, $e_n(\tau)$ as shown in Fig. 1.

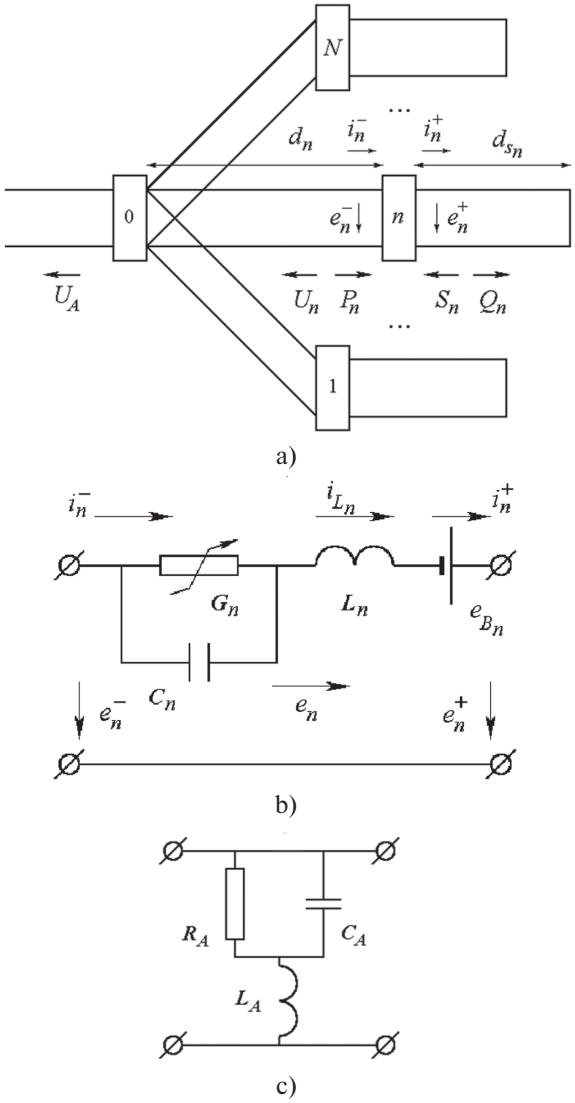

Fig. 1. (a) A network of active circuits connected by sections of microstrip transmission lines and schematics of (b) active circuits used in the network and (c) a resonant circuit used as an antenna node $n=0$

The set of equations is completed by the radiation condition at $x=-\infty$ (no incoming waves from the open end of the transmission line) and the short-circuit condition that leads to the occurrence of reflected waves from the ends of the stub sections d_{S_n}.

Despite apparent simplicity of circuits considered, self-consistent time-domain modelling of these distributed systems is a complicated problem.

In case of a small spatial dispersion of microstrip line the linear part of the problem is simplified significantly so as the wave propagation in the waveguide sections is described by a well-known Riemann-D'Alembert solution to the one-dimensional wave equation. In our modelling, we use this approach for time-domain simulation of linear part of the problem while the nonlinear part is modelled in full, in distinction from a more traditional approach. It allows us to reduce the problem described with complicated partial differential equations to a problem with an equivalent

set of ordinary differential-difference equations with time delay (the equations with deviating argument).

Despite the remaining complexity caused by delay, the equations can be solved by available numerical methods [15]. In the explicit form, differential-difference equations for electromagnetic waves in a network of transmission lines with active blocks ($n=1...N$) described above are presented as follows:

$$U_n''(\vartheta_n) = -P_n''(\vartheta_n - d_n) + \\ +\omega_{L_n} e'_{B_n}(\tau) + 2\omega_{L_n}[S_n'(\vartheta_n - 2d_{S_n}) - \\ -U_n'(\vartheta_n)] - \omega_{0_n}^2[U_n(\vartheta_n) + P_n(\vartheta_n - d_n) - G_n(e_{C_n})], \quad (1)$$

where

$$P_n(\vartheta_n - d_n) = U_n(\vartheta_n - 2d_n) - e_{C_A}(\tau - d_n) - U_A(\tau - d_n); \quad (2)$$

$$S_n(\vartheta_n) = U_n(\vartheta_n) + P_n(\vartheta_n - d_n) - S_n(\vartheta_n - 2d_{S_n}); \quad (3)$$

$$e_{G_n} = e_{B_n} + 2[S_n(\vartheta_n - 2d_n) - U_n(\vartheta_n)] - \\ -\tau_{L_n}[U_n'(\vartheta_n) + P_n'(\vartheta_n - d_n)]. \quad (4)$$

In these equations, $U_n(\vartheta_n)$, $P_n(\vartheta_n)$, $Q_n(\vartheta_n)$, $S_n(\vartheta_n)$ and $U_A(\tau)$ are the amplitudes of the waves propagating in the corresponding sections of the line (Fig. 1a) presented as functions of time variables $\vartheta_n = \tau + d_n = \tau + x_n$, $\vartheta_{S_n} = \vartheta_n + d_{S_n} = \tau + x_{S_n}$ and the current time τ in such a manner that

$$i_n^+(\tau) = S_n(\vartheta - 2d_{S_n}) + S_n(\vartheta_n), \\ e_n^+(\tau) = -S_n(\vartheta - 2d_{S_n}) + S_n(\vartheta_n), \\ i_n^-(\tau) = U_n(\vartheta_n) + P_n(\vartheta_n - d_n), \\ e_n^-(\tau) = -U_n(\vartheta_n) + P_n(\vartheta_n - d_n), \quad (5) \\ i_{A_n}^+(\tau) = U_n(\vartheta_n - d_n) + P_n(\vartheta_n), \\ e_{A_n}^+(\tau) = -U_n(\vartheta_n - d_n) + P_n(\vartheta_n), \\ i_A^-(\tau) = U_A(\tau), \\ e_A^-(\tau) = -U_A(\tau).$$

The index A designates the variables associated with the antenna element (see designations on Figs. 1a, 1c), and the value $U_A(\tau)$ describes the wave radiated into the open section of TL towards the infinity.

Notice that all the equations in this work are written in terms of dimensionless normalized variables such as the relative coordinate $x = X/a,$, time $\tau = ct/a,$, voltage $e_n = V_n/V_0$ and current $i_n = Z_0 I_n / V_0$, where a is the spatial scale used for normalization, c is the speed of wave in the transmission line, Z_0 is the intrinsic impedance of the line, V_0 is the normalization voltage. In a similar way, we introduce other dimensionless parameters such as $\tau_{C_n} = cZ_0 C_n / a$, $\tau_{L_n} = cL_n/(Z_0 a)$, $\tau_{0_n} = 2\pi(\tau_{L_n}\tau_{C_n})^{1/2}$, $\omega_{C_n} = 1/\tau_{C_n}$, $\omega_{L_n} = 1/\tau_{L_n}$ and $\omega_{0_n} = (\omega_{L_n}\omega_{C_n})^{1/2}$, etc.

The Gunn diodes are simulated in terms of the given current-voltage characteristics with negative differential resistance (NDR) as shown in Fig.2. This approximation assumes the limited space-charge accumulation (LSA) mode of operation of Gunn diodes. This allows a rather broadband functioning of the devices, with the maximum-to-minimum frequency ratio exceeding a decade. The approximation means an instant response of the diodes to the external field neglecting the modelling of strong-field domains in the diode structures. Instead, characteristic times of intrinsic processes specific for the diodes are represented by the equivalent capacitance C_n and the inductance L_n of the devices and their connections to the circuits. The current-voltage characteristic of the diodes is given by the approximation [16] typical for GaAs and GaN structures

$$G_n = G_n(e) = G_{0_n}[(e + 0.2e^4)/(1 + 0.2e^4) + 0.05e], \quad (6)$$

where $G_{0_n} = Z_0 I_{0_n}/V_0$ is the dimensionless diode current parameter, I_0 and V_0 are the characteristic absolute current and voltage specifying the diodes (e.g., for the L-band GaN THz Gunn diodes described in [17], we have $I_0 \approx 8A$, $V_0 \approx 30V$), and, finally, $e = |e_{G_n}|$ is the dimensionless voltage applied to the diode (Fig.2).

The model of this kind became an engineering norm for the time-domain calculations and applied, for example, in the well-known circuit design software *HSPICE*.

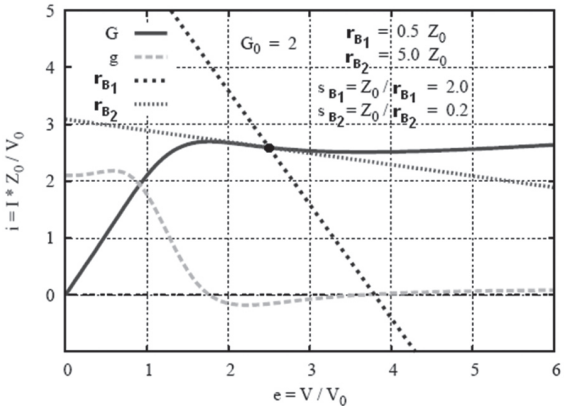

Fig. 2. The Gunn diode current-voltage characteristic $G_n = G_n(e)$, $g_n(e) = dG_n(e)/de$ — the differential conductance, and the load lines at the bias resistance r_B

The electromagnetic self-excitation appears in the system when the Gunn diodes are biased to the NDR region. The oscillations develop in response to a small fluctuation of the bias voltage, once the voltage is in this region, or as a result of switching the bias from the stable to this unstable domain.

The bias voltage $e_B(\tau)$ is specified by the function

$$e_B(\tau) = e_{B_0} + \delta e_B f_B(\tau/\tau_S) - \delta e_B f_B((\tau - \tau_F)/\tau_S),$$

where e_{B_0} is the steady-state voltage in the "off" position below the threshold $e_{B_{th}}$ when no self-oscillations are excited (the oscillations appear if $e_B > e_{B_{th}}$), $e_{B_1} = e_{B_0} + \delta e_B$ is the steady-state voltage in the "on" position when self-oscillations are being developed ($e_{B_1} > e_{B_{th}}$), $f_B(\tau/\tau_S)$ is the bias switch function which describes the switching on and off process beginning at the moment $\tau = 0$ and $\tau = \tau_F$, respectively, and developing during the characteristic time τ_S ($0 \le f_B \le 1$, $f_B = 0$ at $\tau \le 0$, $f_B = 1$ at $\tau \ge \tau_S$).

As a switch function, we choose $f_B = (\tanh(u) + 1)/2$, with the substitution $u = s/(1 - s^2)$, $s = 2\tau/\tau_S - 1$, defined in the interval

$|s|<1$ where $0 \le f_B \le 1$ ($f_B = 0$ at $s = -1$, $f_B = 1$ at $s = 1$), while outside of this interval we assign $f_B = 0$ at $s < -1$ ($\tau < 0$) and $f_B = 1$ at $s > 1$ ($\tau > \tau_S$).

This definition of the switch function f_B allows us to confine the duration of switching on and off within the finite time interval $0 \le \tau \le \tau_S$, with both $df_B / d\tau$ and $d^2 f_B / d\tau^2$ being zero at $\tau \le 0$ and $\tau \ge \tau_S$. Notice, the condition $df_B / d\tau = d^2 f_B / d\tau^2 = 0$ at $\tau \le 0$ is necessary for the consistency of time-delay equations at $\tau \le 0$ with the trivial initial conditions on the unknown functions at the time-delayed intervals while assuming no time variations before the switching on begins.

In a similar way, we write the equations for the resonant antenna circuit ($n = 0$) schematically shown in Fig. 1, a and c. As a result, we obtain a complete system of $N+1$ second-order differential-difference equations, which describe the electromagnetic field evolution in the given microwave circuit of transmission lines with active Gunn-diode devices. They account for both the nonlinearity of devices and the delay of coupling between the devices due to the time needed for the wave propagation along the transmission lines. This property makes the system prone to non-conventional dynamics such as the dynamical chaos and other nonlinear effects that could be useful for various applications.

3. NUMERICAL REZULTS

We obtain numerical solutions of the equations in by using the integration methods presented in [15], particularly, the Dormand-Prince method of the 8(5+3) order, which we extended for the case of time-delay equations specific for our problem. Being direct time-domain computations, accurate solutions of these nonlinear equations are rather time-consuming. Time sequences of the field evolution were, typically, found for many thousands of intrinsic periods T_n as defined by the system parameters, with the accuracy of solutions specified at the level $\varepsilon = 10^{-7}...10^{-12}$ [15] sufficient for obtaining stable and reproducible solutions as verified by more accurate test simulations.

When considering a network with a single active circuit ($N = 1$), we found a possibility for the system to generate a train of high-frequency pulses radiated into an open section of microstrip line (Fig. 3). The pulses are excited when the bias voltage E_{B_n} is increased above a threshold value (the system is turned on) and cease when E_{B_n} is reduced below the threshold.

A characteristic feature of the effect is that the pulse duration t_P equals to the time interval between the pulses Δt_P and each of them is close to the duration of the round trip of a signal from the active device ($n = 1$) to the remote resonator ($n = 0$) and back to the active device ($n = 1$). Thus, the spatial length of each pulse in an infinite microstrip line $L_p = ct_p$ (c is the speed of wave in the line) is about twice the length of the microstrip section, $L_p = 2d_n$.

The carrier frequency of each pulse ω is determined by the intrinsic frequency of active circuits, and the optimal condition for the formation of a clear sequence of pulses is the coincidence of intrinsic frequencies of the remote resonator ($n = 0$) and the active circuit ($n = 1$), while the length of microstrip section d_n that provides a time-delay coupling is required to be large enough for the pulse duration t_p to be much greater than the oscillation period $\tau = 2\pi\omega$.

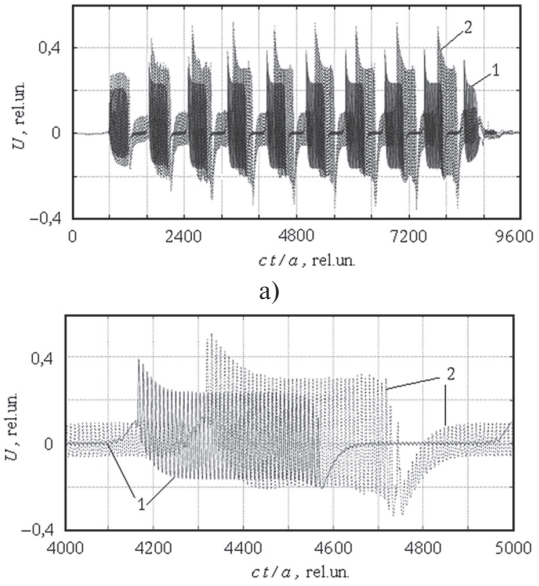

Fig. 3. A train of high-frequency pulses radiated from the system of one Gunn-diode active circuit (curves 1) and two identical active circuits (curves 2) when the circuits are connected to the antenna node $n = 0$ by microstrip transmission lines of length $d_n = 200$ (in relative units where the pulse radiation wavelength is $\lambda = 9.0$)

The formation of train of pulses and the main conditions for this could be explained as follows. If the active circuit is designed so that oscillations are excited when no resonator is present at the antenna node n=0, the oscillations arise and exist for the duration of time t_P until the feedback signal returns from the remote resonator ($n = 0$) to the active node ($n = 1$). Then, if the design of the entire system including both the active circuit and the remote resonator is of such a kind that oscillations cannot exist in the entire system, the oscillations cease for the period of time Δt_p when active circuit receives a feedback from the node $n = 0$ and, in this way, "feels" the presence of remote resonator. After that time, the feedback disappears, the active circuit does not "feel" any remote resonator again, and a new pulse of oscillations arises.

When connecting two identical branches of active circuits in parallel to the antenna node, we obtain a similar train of pulses radiated from the system, though of slightly different parameters (Fig. 3, b). With increasing the number of branches, the oscillations may not cease completely between the pulses and the entire process becomes more complicated.

Keeping in mind the explanation of the effect given above, we may consider the networks of multiple time-delay branches of different length of microstrip sections. With account of different times of arriving time-delay feedbacks from different circuits and nonlinear mixing of oscillations in active devices, we can expect the development of complicated and, potentially, chaotic or quasi-chaotic oscillations that could be of interest for certain applications [14].

Consider now the network of two branches of identical active circuits of the kind shown in Fig. 1, though of different and, preferably, non-commensurable length of time-delay microstrip sections d_n.

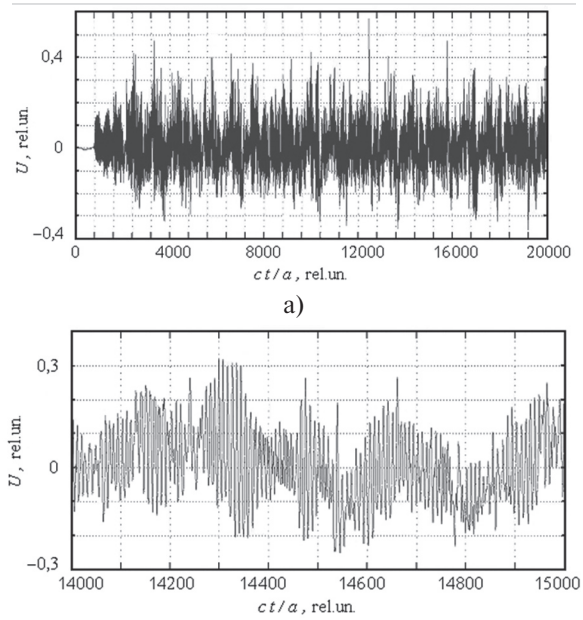

Fig. 4. A quasi-chaotic signal radiated from a system of two active circuits connected to the antenna node by transmission lines of length $d_1 = 200$ and $d_2 = 266.67$, respectively, when the basic radiation wavelength at the emerging carrier frequency is $\lambda = 8.6$

In this case, despite the relative simplicity of active system, there will be a complicated mixing of time-delay feedbacks in different branches of active devices, thus, providing a complicated (virtually, quasi-chaotic in the lower frequency bands) nonlinear oscillations as shown, e.g., in Fig. 4 (a similar effect should also arise in the networks of dispersive transmission lines because of different propagation time of different frequency components).

In this example, even though there is a certain carrier frequency due to intrinsic oscillations of active circuits, the entire waveform that corresponds to the lower frequency band as compared to the carrier frequency, is rather chaotic and remains so for a long period of time being simulated (here we choose the length parameters $d_1 = 200$ and $d_2 = 266.67$ in relative units, while the carrier oscillation period is $\tau = 8.6$.

Quasi-chaotic character of low-pass-band signal radiated from the system is well illustrated by the plots of auto-correlation function and Poincare section computed for the emerging oscillations (Figs. 5–6).

When comparing auto-correlation functions (Fig. 5) of train of pulses and quasi-chaotic signal, one can see a reversal of correlation over the period of pulse repetition (at $\tau \sim 840$ in Fig. 5) and a significant loss of correlation in quasi-chaotic signal at all times exceeding the period of oscillations ($\tau = 8.6$).

In a similar way, Poincare sections (Fig. 6) clearly show the presence of periodicity in the train of pulses over a long period of time and the lack of long-term periodicity in quasi-chaotic signal of Fig. 4. The frequency spectrum of the quasi-chaotic signal is shown in Fig. 7.

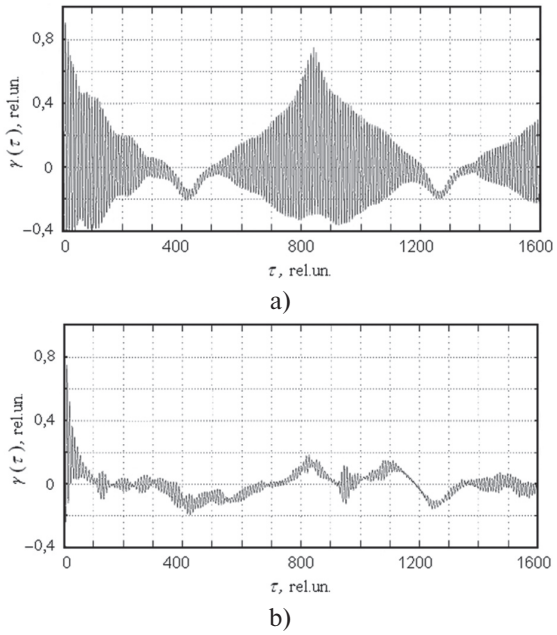

Fig. 5. Auto-correlation function of (a) train of pulses of Fig. 3 and (b) quasi-chaotic signal of Fig. 4 computed over the time interval $t = 1000 - 9000$ and $t = 2000 - 20000$, respectively

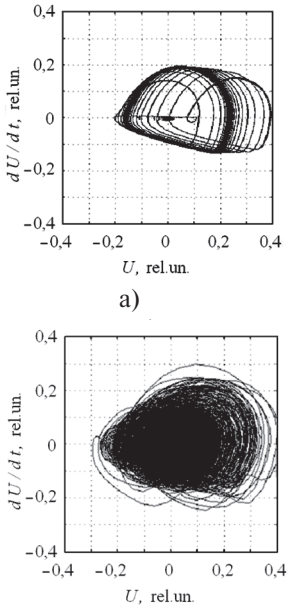

Fig. 6. Poincare section U vs dU/dt of (a) train of pulses of Fig. 3 and (b) quasi-chaotic signal of Fig. 4 computed over the time interval $t = 4000 - 8000$

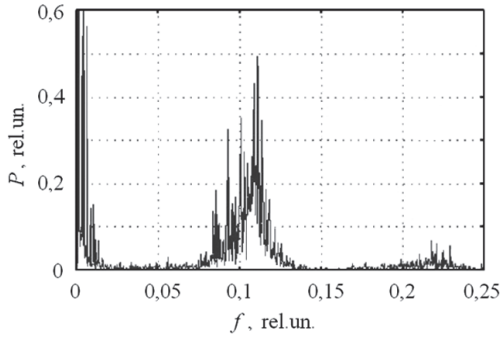

Fig.7. Frequency waveform radiated from time-delay TL circuit ($N = 2$) with $d_n \gg 1$

4. CONCLUSIONS

Time-domain simulations of distributed networks of active circuits connected by sections of microstrip transmission lines have shown a possibility of generation of trains of high-frequency pulses radiated into an open section of transmission line. The trains of pulses can emerge when active devices are separated from compact resonant circuits by extended sections of transmission lines providing a time-delay feedback. When using a few branches of active circuits with different length of time-delay transmission lines, a complicated quasi-chaotic signal can be generated by the system that could be of interest for emerging applications.

References

[1] *Kurokawa K.* The Single-Cavity Multiple-Device Oscillator // IEEE Trans. Microwave Theory Techn. 1971. Vol. MTT-19. P. 793–801.

[2] *Russell K. J.* Microwave Power Combining Technique // IEEE Trans. Microwave Theory Techn. 1979. Vol. MTT-27, P. 472–478.

[3] *Mink J. W.* Quasi-Optical Power Combining of Solid-State Millimeter-Wave Sources // IEEE Trans. Microwave Theory Techn. 1986. Vol. MTT-34. P. 273–279.

[4] *DeLisio M. P. and York R. A.* Quasi-Optical and Spatial Power Combining // IEEE Trans. Microwave Theory Techn. 2002. Vol. MTT-50. P. 929–936.

[5] *Siegel. P. H.* Terahertz Technology // IEEE Trans. Microwave Theory Techn. 2002. Vol. MTT-50. P. 910–928.

[6] *Liao S. Y.* Microwave Circuit Analysis and Amplifier Design. New Jersey. Prentice-Hall, 1987. 325 p.

[7] *Lee C. A. and Dalman G. C.* Microwave Devices, Circuits and their Interaction. New York. John Willey and Sons, 1994. 280 p.

[8] *Taflove A. and Hagness S. C.* Computational Electrodynamics: the Finite-Difference Time-Domain Method. New York. Artech House, 2000. 425 p.

[9] *Erturk, V. B., Rojas R. G. and Roblin P.* Hybrid Analysis/Design Method for Active Integrated Antennas // IEE Proc. Microw. Antennas Propag. 1999. Vol. 146. P. 131–137.

[10] *Yurchenko L. V. and Yurchenko V. B.* Time-Domain Simulation of Power Combining in a Chain of THz Gunn Diodes in a Transmission Line // Int. J. Infrared and Millimeter Waves. 2004. Vol. 25. No. 1. P. 43-54.

[11] *Yurchenko L. V. and Yurchenko V. B.* Multi-frequency generation in microstrip lines with Gunn diodes // Radioelectronika i Informatika (in Russian). 2007. No.2. P.24-29.

[12] *Yurchenko L. V. and Yurchenko V. B.* Modeling of self-oscillations in a series chain of Gunn diodes in a microstrip line // Applied Radio Electronics. (in Russian). 2007. Vol. 6. No. 4. P. 555-560.

[13] *Yurchenko L. V. and Yurchenko V. B.* Chaotic generation in an extended microstrip line with a chain of Gunn diodes // Radioelectronika i Informatika. 2009. (in Russian). No. 3. P. 14-20.

[14] *Lukin K. A, Mogyla A. A., Palamarchuk V. P. et al.* Ka-band bistatic ground-based noise waveform SAR for short-range applications // IET Radar, Sonar & Navigation. 2008. Vol. 2. No. 4. P. 233-243.

[15] *Hairer E. and Wanner G.* Solving Ordinary Differential Equations II: Stiff and Differential-Algebraic Problems. Berlin. Springer-Verlag, 1991. 354 p.

[16] *Shur M.* GaAs Devices and Circuits. London. Plenum Press, 1987. 452 p.

[17] *Alekseev E., Pavlidis D.* GaN Gunn diodes for THz signal generation // IEEE MTT-S Int. Microwave Symposium Digest. 2000. Vol. 3. P.1905-1908.

Manuscript received February, 12, 2013

Yurchenko Lidiya Valerievna, MSc (1980), PhD (1991), Senior Research Fellow, Department of Nonlinear Dynamics of Electronic Systems, Usikov Institute of Radiophysics and Electronics, NAS of Ukraine, Kharkov, Ukraine. Research interests: computer simulations of the electromagnetic dynamical chaos in electronic systems, self-generation of ultra-short pulses, chaos, multi-frequency oscillations, spatial power combining and multi-channel nonlinear feedback in open distributed systems with arrays of active microwave devices.

Yurchenko Vladimir Borisovich, MSc (1980), PhD (1984), DSc (1994), Senior Research Fellow, Department of Solid State Radiophysics, Institute of Radiophysics and Electronics, NAS of Ukraine, Kharkov, Ukraine. Research interests: theory of electronic devices, hot electrons in semiconductors, nonlinear dynamics, EM wave propagation and scattering, millimeter-wave photonic structures, antenna simulations.

УДК 517.862

Моделирование во временной области колебаний высокочастотных импульсов в микрополосковых линиях задержки с диодами Ганна / Л.В. Юрченко, В.Б. Юрченко // Прикладная радиоэлектроника: науч.-техн. журнал. – 2013. – Том 12. – № 1. – С. 45–50.

В статье было выполнено моделирование во временной области активных систем с диодами Ганна, соединенных секциями микрополосковой линии передачи. Было исследовано самовозбуждение диодов Ганна, вмонтированных различными способами в цепь линии передачи. Обнаружена сложная динамика электромагнитного поля, излученного в открытую секцию микрополосковой линии. Показана возможность появления серии высокочастотных импульсов в случае, когда активные блоки отделены от компактных резонансных элементов протяженными секциями линии передачи с задержкой обратной связи.

Ключевые слова: высокочастотные импульсы, диод Ганна, линии задержки, система с запаздыванием.

Ил. 07. Библиогр.: 17 назв.

УДК 517.862

Моделювання у часовому просторі коливань високочастотних імпульсів у мікросмуговій лінії затримки з діодами Ганна / Л.В. Юрченко, В.Б. Юрченко // Прикладна радіоелектроніка: наук.-техн. журнал. – 2013. – Том 12. – № 1. – С. 45–50.

У статті було виконано моделювання у часовому просторі активних систем з діодами Ганна, з'єднаних секціями мікросмугової лінії передачі. Було досліджено самозбудження діодів Ганна, вмонтованих різним чином у ланцюжок лінії передачі. Знайдена складна динаміка електромагнітного поля, що випромінюється у відкриту секцію мікросмугової лінії. Показана можливість появи серії високочастотних імпульсів у випадку, коли активні блоки відділені від компактних резонансних елементів подовженими секціями лінії передачі з затримкою зворотного зв'язку.

Ключові слова: високочастотні імпульси, діод Ганна, лінія затримки, система з запізнюванням.

Іл. 07. Бібліогр.: 17 найм.

UDC 621.385.6

MODE INTERACTION FOR RANDOM SIGNAL GENERATION IN MM-WAVEBAND VACUUM OSCILLATORS

E. M. KHUTORYAN

We consider transformation of single frequency oscillations to multi-frequency and to the chaotic ones in Smith-Purcell radiation (SPR) multiplier. It consists of grating with upper mirror that enables both BWO and diffraction radiation oscillator (DRO) modes excitation. We consider the case when fundamental frequency oscillation corresponds to backward wave oscillator mode. The SPR condition holds for nth harmonic (3rd in our case). When operating-to-starting current ratio exceeds unit value for both modes the auto-modulation process takes place, which leads to generation of oscillations with multifrequency spectrum. The reason for this is BWO and DRO modes interaction. When operating current exceeds starting one many times both for BWO and DRO mode the oscillation spectrum becomes a continuous one. The spectrum behavior has been studied for various system parameters such as electron beam current, grating length, OR quality factor, etc.

Keywords: Backward wave oscillator, Diffraction radiation oscillator, Smith-Purcell radiation multiplier, mode interaction, stochastic oscillations.

INTRODUCTION

The electron vacuum oscillators can generate stochastic oscillations when electron beam (EB) is overbunched and there is time delay of wave propagation. One of the most known examples are backward wave oscillator (BWO) and reflection diffraction radiation oscillator (R-DRO) [1, 2]. Also reason for stochastic oscillation can be the mode interaction in overmoded resonant devices such as gyrotron, resonant BWO, DRO, etc. Mode interaction is possible also for different types of feedback. In [3] the mode competition between BWO and DRO modes has been studied both theoretically and experimentally. It was shown that for moderate operating current single frequency oscillatory mode is established: for low EB velocity BWO when coupling impedance is rather low the DRO oscillations are excited; for higher EB velocities BWO oscillations occur. Later experimentally was shown possibility of BWO and DRO simultaneous oscillations [4]. It can lead to stochastic oscillatory mode. Another case of BWO and DRO modes interaction is Smith-Purcell multiplier [5]. In this case BWO mode self-excites on the fundamental frequency and SPR condition holds for n^{th} harmonic. If it coincides with the open resonator resonant frequency the DRO mode is excited [6, 7]. Here we consider the case when operating-to-starting current ratio exceeds unit value for both modes that can lead to generation of EM oscillations with continuous spectrum.

THEORY

As it is known, for BWO mode the phase shift φ over grating period l is between π and 2π. If the EB velocity is v then oscillation frequency will be close to $f = vl/\varphi$. The n^{th} harmonic frequency is nvl/φ and $n\varphi = 2\pi m$. This gives certain values of phase shift φ for SPR. Since BWO wavelength approximately equals quarter of grating depth λ~h/4 the effective SPR takes place for odd harmonics. Let's consider the case when $n = 3$ and $m = 2$ (Fig. 1). Then BWO electric field may be represented as superposition of forward and backward wave:

$$\vec{E}_{BWO} = C^{+}(y,t)\vec{E}_{p}(y,z,k)e^{i(ky-\omega t)} + C^{-}(y,t)\vec{E}_{-p}(y,z,k)e^{i(-ky-\omega t)}$$

whose amplitudes have been governed by following excitation equations:

$$\begin{cases} \dfrac{1}{v_{gr}}\dfrac{\partial C^{-}}{\partial t} - \dfrac{\partial C^{-}}{\partial y} + \gamma C^{-} = \dfrac{1}{\tilde{N}_{-p}}\displaystyle\int_{S}\overline{\vec{j}_1(t)\vec{E}_p e^{i\omega t}}\,dS \\ \dfrac{1}{v_{gr}}\dfrac{\partial C^{+}}{\partial t} + \dfrac{\partial C^{+}}{\partial y} + \gamma C^{+} = 0 \\ C^{+}(0,t) = R_1 C^{-}(0,t) \\ C^{-}(L,t) = R_2 C^{+}(L,t)e^{i2kL} \end{cases} \quad (1)$$

The vortex field DRO of high Q cavity can be represented as an expansion by cavity eigenmodes:

$$\vec{E}_{DRO} = \sum_{m} C_m(t)\vec{E}_m(y,z)e^{i(4\pi y/l - 3\omega t)}$$

where $\vec{E}_m(r)$ is electric field of the cavity eigenmode. If resonator is not overmoded the only single DRO mode is assumed to be excited. Then, in a weakly non-stationary approximation the equation for the DRO complex mode amplitudes becomes

$$-\frac{dC}{dt} + i(3\omega - \omega_{DRO})C = \frac{1}{N_m}\int_{V}\overline{\vec{j}_3(r,t)\vec{E}_m(r)e^{i3\omega t}}\,dV, \quad (2)$$

where $N_m = \dfrac{1}{4\pi}\displaystyle\int_{V}\varepsilon\vec{E}_m^2 dV$ is the m^{th} mode norm, $\vec{j}_{1,3}$ is the current density of first and third harmonic, respectively, which are to be found from the motion equation.

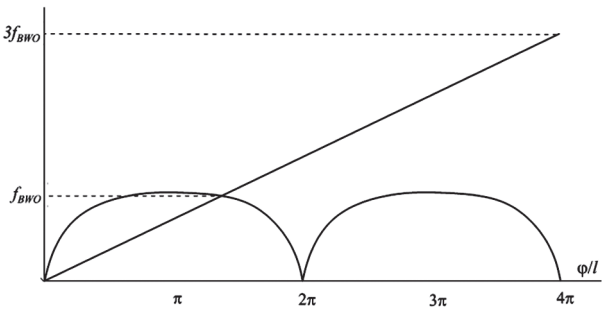

Fig. 1. Dispersion of BWO

RESULTS

Solving the equations (1) and (2) together with EB motion equation we obtain time dependence of BWO and DRO amplitudes. Let's note that for case [3, 4] when $\omega_{DRO} \neq n\omega$ the solution for single frequency regime occurs when $C^{\pm} \neq 0$, $C = 0$ or $C^{\pm} = 0$, $C \neq 0$. At SPR multiplier $\omega_{DRO} = n\omega$ both amplitude non-equal to zero. Therefore for arbitrary frequency ratio the following regimes have been observed [4]: 1) single frequency; 2) two-frequency with different frequency steepness: 3) BWO frequency spectrum enrichment due to auto-modulation; 4) stochastic mode interaction; 5) mutual mode synchronization for $f_{BWO}/f_{DRO} = 5/6$ with the same frequency steepness for both modes.

For case of SPR multiplier the parameters to be varied are resonator Q-factor, EB current, reflection factors, grating length, frequency mismatch, EB inclination angle.

Amplitude time dependences and corresponding FT for matched BWO ($R_{1,2} = 0$) have been shown in Fig. 2. EB current-to-starting one ratio for BWO equals 6 and for DRO is 2.3; frequency mismatch is 0 and Q = 200. Let's note that even for exact relation between 'cold' frequencies ($\omega_{DRO} = 3\omega$) the electron frequency shift for BWO mode results in some mismatch. Additional BWO mode automodulation (appearing additional frequencies in BWO spectrum) makes DRO dynamics much more complex. From Fig. 2 one can see that DRO automodulation is deeper than that for BWO. If frequency shift is more than DRO resonator bandwidth there is DRO mode collapse. In this case near DRO modes should be considered.

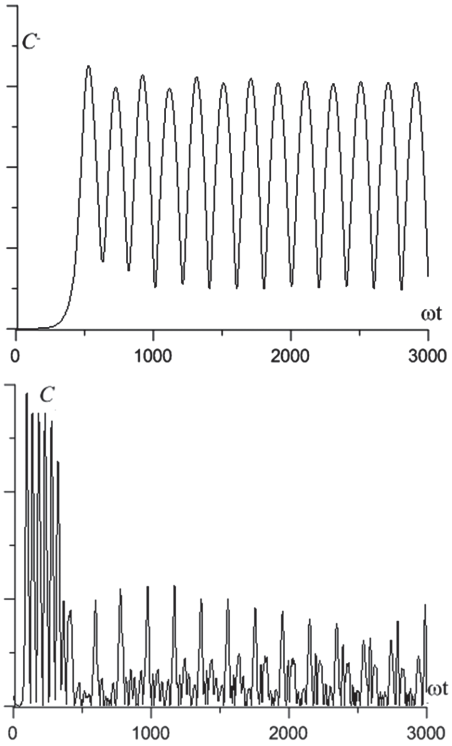

Fig. 2. Amplitudes time dependence EB current-to-starting one ratio for BWO equals 6 and for DRO is 2.3

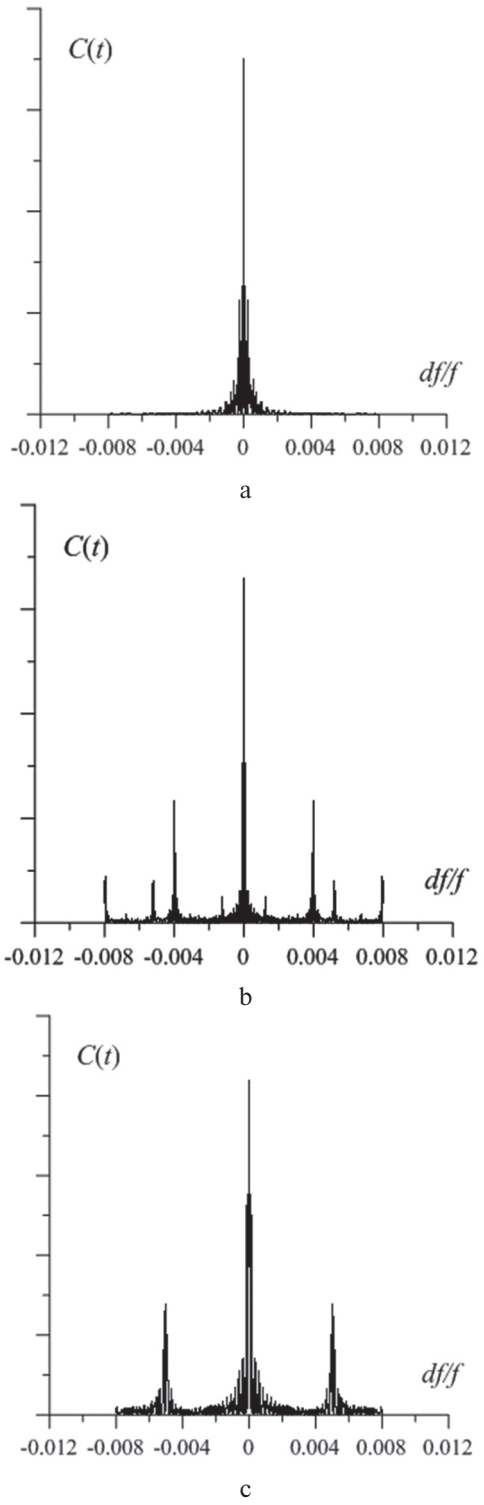

Fig. 3. DRO amplitudes FT for EB current-to-starting one ratio for DRO equals a) 0.7; b) 2; c) 3.5

FT evolution at EB current change shown in Fig.3 indicates enrichment of oscillation spectrum due to deep automodulation.

CONCLUSIONS

The mechanism for stochastic oscillation generation in SPR multiplier has been considered. It is shown that BWO and DRO modes interaction leads to deep automodulation and multifrequency spectrum and there is feasible possibility for stochastic oscillations. The variation of large quantity of both

modes parameters enables different ways of oscillation spectrum transformation.

Author would like to thank Konstantin Lukin for the suggested topic and useful discussions and suggestions.

References

[1] Ginzburg, N. S., Kuznetsov, S. P., Fedoseeva, T. N., 'Transition processes in BWO', *Radiophysics & Quantum Electronics* **21**, 728-739 (1978).

[2] Vertiy, A. A., Ermak, G. P., Skrinnyk, B. K., Tsvyk, A. I., 'Generators of Diffraction Radiation', edited by V. P. Shestopalov, Naukova Dumka, Kiev, 1991.

[3] Ermak G. P., Lukin K. A., Shestopalov V. P., "Mode interaction in DRO", *Radiophysics and Quantum Electronics*, 1986, Vol.29, #5, pp.458-465.

[4] Efimov, B. P., Lukin, K. A., Rakityanskiy, V. A., Shestopalov, V. P., 'Stochastic mode interaction in an electron-wave self-oscillating system with two feedback channels', *Pis'ma v Zhurnal Tekhnicheskoi Fiziki (ISSN 0320-0116)*, **15**, 1989, 9-12. (in Russian).

[5] D. Li, Z. Yang, K. Imasaki, Gun-Sik Park "Particle-in-cell Simulation of coherent and superradiant Smith-Purcell radiation", *Phys. Rev. ST Accel. Beams* 9, 040701 (2006).

[6] V. L. Bratman, A. E. Fedotov, P. B. Makhalov, 'Experimental demonstration of Smith–Purcell radiation enhancement by frequency multiplication in open cavity', Appl. Phys. Lett. **98**, 061503, 2011.

[7] Lukin, K. A., Khutoryan, E. M., Park, G. S., 'Interaction of evanescent wave and Smith-Purcell radiation modes in resonant BWO-DRO device', *Proc. of IVEC 2009*, Roma, Italy, pp. 388-389.

Manuscript received February, 22, 2013

Eduard Khutoryan received his diploma in Radiophysics & Electronics from Kharkov National University in Ukraine in 2000. Since 2000, he has been with the Institute for Radiophysics and Electronics, National Academy of Sciences of Ukraine, IRE NASU, Kharkov. He completed his Ph.D. thesis at IRE NASU in 2011. He is currently working on microwave and terahertz vacuum electron devices. He is the author/coauthor of more than 25 publications in peer-reviewed journals and conferences.

УДК 621.385.6

Взаимодействие мод в вакуумных генераторах миллиметрового диапазона для генерации случайных сигналов/ Э. М. Хуторян // Прикладная радиоэлектроника: науч.-техн. журнал. – 2013. – Том 12. – № 1. – С. 51–53.

Рассматривается преобразование одночастотных колебаний в многочастотные и хаотические в умножителе на эффекте Смита-Парселла (СП), состоящем из гребенки и верхнего зеркала и поддерживающем возбуждение режимов ЛОВ и ГДИ. Рассматривается случай возбуждения режима ЛОВ на основной гармонике. Режим излучения СП при этом наблюдается на третьей гармонике. Когда рабочий ток превышает стартовый для обоих режимов, наблюдается многочастотная генерация, причиной которой является взаимодействие мод ЛОВ и ГДИ. Когда рабочий ток намного превышает стартовый для обоих режимов, спектр колебаний становится непрерывным. Исследуется поведение спектра в зависимости от различных параметров, таких как ток, длина гребенки, добротность резонатора и т.д.

Ключевые слова: взаимодействие мод, ЛОВ, ГДИ, многочастотные колебания, высшие пространственные гармоники.

Ил. 03. Библиогр.: 07 назв.

УДК 621.385.6

Взаємодія мод у вакуумних генераторах міліметрового діапазону для генерації випадкових сигналів / Е. М. Хуторян // Прикладна радіоелектроніка: наук.-техн. журнал. – 2013. – Том 12. – № 1. – С. 51–53.

Розглянуто перетворення одночастотних коливань в багаточастотні і хаотичні в помножувачі на ефекті Сміта-Парселла (СП), що складається з гребінки і верхнього дзеркала, які підтримують збудження режимів ЛЗХ і ГДВ. Розглядається випадок збудження режиму ЛЗХ на основній гармоніці. Режим випромінювання СП при цьому спостерігається на третій гармоніці. Коли робочий струм перевищує стартовий для обох режимів, спостерігається багаточастотна генерація, причиною якої є взаємодія мод ЛЗХ і ГДВ. Коли робочий струм набагато перевищує стартовий для обох режимів, спектр коливань стає безперервним. Досліджується поведінка спектра в залежності від різних параметрів, таких як струм, довжина гребінки, добротність резонатора і т. д.

Ключові слова: взаємодія мод, ЛЗХ, ГДВ, багаточастотні коливання, вищі просторові гармоніки.

Іл. 03. Бібліогр.: 07 найм.

UDC 621.37

EFFECT OF REFLECTION FROM THE REMOTE LOAD ON MODE COMPETITION IN MULTIMODE RESONANT ELECTRON OSCILLATORS

S.A. USACHEVA, M.M. CHUMAKOVA, M.YU. GLYAVIN, YU.V. NOVOZHILOVA AND N. M. RYSKIN

Effect of reflection from the remote load on the mode competition in a two-mode electronic maser is considered. A system of two coupled equations for slowly varying amplitudes of the modes with time delayed coupling is investigated analytically and numerically. It is shown that the reflections can, under the certain conditions, strongly affect the operation regime. Special attention is paid to a gyrotron with build-in quasioptical mode convertor where the radiation after reflection from the window is converted into oppositely rotating mode.

Keywords: reflections, mode competition, maser, gyrotron, delayed feedback.

1. INTRODUCTION

Reflections from a remote load can strongly affect the dynamics of microwave oscillators, especially gyrotrons [1-7]. Not only reflection from the output window but also reflection from the plasma in electron-cyclotron plasma heating experiment may play a significant role [7]. Moreover, this effect is used in autodyne (self-mixing) detection. In particular, autodyne chaotic oscillators for noise radar systems had been developed in IRE NASU [8,9].

In Refs. [10-12], we studied a general model of a single-mode oscillator with delayed reflection from a remote load. The conditions of stability of steady states were derived analytically. Numerical simulation of transient processes was performed in the most interesting case of large delay and low reflections. Good agreement between theory and simulations was observed. However, most of modern microwave resonant masers, especially gyrotrons, utilize oversized resonators where excitation of different eigenmodes and strong mode-competition phenomena are typical. We believe that delayed reflections from the remote load should strongly affect the mode competition processes.

In this paper, we investigate two different models of resonant multi-mode oscillators with reflections. In Sec. 2, a system of two competing modes described by the well-known equations for slowly varying amplitudes is presented and the influence of additional delayed feedback due to reflections is investigated. In Sec. 3, a gyrotron with build-in quasioptical mode convertor is considered, where the radiation after reflection from the window is converted into oppositely rotating mode.

It is shown that the reflections can, under the certain conditions, strongly affect the operation regime. Complicated sequence of transitions from one regime to another which takes place with the increase of reflection factor is investigated.

2. REFLECTION EFFECT ON MODE COMPETITION IN A TWO-MODE MASER

Consider a model of a two-mode electronic oscillator, which is described by the equations for slowly varying complex amplitudes of the modes $A_{1,2}$ in the quasi-linear approximation of the electron susceptibility by cubic polynomial:

$$\dot{A}_1 = \left(\sigma_1 - \beta_1 |A_1|^2 - \gamma_1 |A_2|^2\right) A_1 + \rho_1 e^{i\psi_1} A_{1\tau}, \quad (1)$$

$$\dot{A}_2 = q\left(\sigma_2 - \beta_2 |A_2|^2 - \gamma_2 |A_1|^2\right) A_2 + \rho_2 e^{i\psi_2} A_{2\tau}. \quad (2)$$

In (1), (2) parameter q is a relation of start-oscillation currents of the two modes. Coefficients σ_j β_j, γ_j are complex functions of electron transit angle; details of derivation are presented in [13]. For simplicity, we assume that these coefficients are real, i.e. the effects of reactive phase nonlinearity are negligible. The last terms in right-hand side of Eqs. (1), (2) describe an influence of delayed reflections, $\rho_{1,2}\exp\left(i\psi_{1,2}\right)$ are complex parameters of reflection, τ is the delay time, $A_{j\tau} \equiv A_j\left(t-\tau\right)$. In the case of zero reflections, Eqs. (1), (2) are converting into well-known equations of competing modes [14].

Without reflections dynamics of the system is determined by parameters $\chi_j = \gamma_j\sigma_i/\beta_i\sigma_j$, $i \neq j$. Consider the situation when $\chi_1 < 1$, $\chi_2 > 1$. In that case, the first mode survives in the competition process and suppresses the second one. Let us investigate how the reflections affect the operation of the oscillator.

Consider a single-mode solution of Eqs. (1), (2): $A_1 = A_0\exp\left(i\omega t\right)$, $A_2 = 0$ where amplitude and frequency obey the following equations

$$|A_0|^2 = \left(\sigma_1 + \rho_1\cos\theta\right)/\beta_1', \quad (3)$$

$$\omega = -\left(\beta_1''|A_0|^2 + \rho_1\sin\theta\right), \quad (4)$$

where $\theta = \omega\tau - \psi_1$. With growing of reflections, there appear new solutions of the transcendental characteristic equation (4), thus, higher-order steady-state modes arise [10-12]. Frequencies of these modes depend on reflections in such a way that $\cos\theta \to 1$ with the increase of ρ_1.

Detailed analysis of stability of the single-mode solutions with respect to perturbations of the first mode is presented in [10-12]. However, apart from the mechanisms of instability described in [10-12], in the two-mode oscillator there exists one more mechanism caused by excitation of the second mode.

We performed numerical simulation of the mode-competition processes with the increase of

reflections assuming that both modes have equal reflection coefficients: $\rho_1 = \rho_2$. The most significant impact of reflections takes place when the phase of the first mode reflection parameter is close to π, and phase of parameter of second mode reflection is close to zero. In that case, reflections result in decrease of the amplitude of the first mode and increase of the second one. Thus, reflections facilitate excitation of the second mode.

In Fig. 1, domains of different regimes on the $\psi_2 - \rho_{1,2}$ plane are presented. One can see, that even when rather small reflections are entered, transition to the regime of two-mode oscillations is observed. With the increase of $\rho_{1,2}$, the second mode completely suppressed the first one. However, with further increase of the reflections, excitation of higher-order steady states of the first mode becomes possible. Since frequencies of these solutions differ from that of the fundamental one (see [10-12]), the value of phase $\psi_1 = \pi$ does not provide suppression of the first mode. Therefore, a backward sequence of transitions to the two-mode regime and then the regime of the first mode generation is observed.

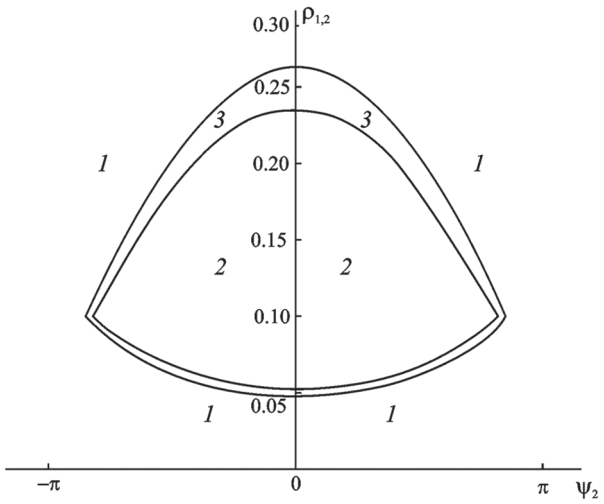

Fig. 1. Domains of regimes of generation of the first mode (1), second mode (2), and two-mode generation (3) on $\psi_2 - \rho_{1,2}$ plane of parameters for $\chi_1 = 0.9$, $\chi_2 = 1.1$, $\psi_1 = \pi$, $\tau = 10$, $q = 1$

However, the picture described above is quite sensitive to the value of ψ_1. Numerical simulation shows that when ψ_1 shifts off the value $\psi_1 = \pi$, at which reflections suppresses the first mode, the domains of two-mode and second mode oscillations quickly decrease in size. This is illustrated by Fig. 2 where boundaries of the domains of the different regimes are plotted for three different values of ψ_1. On the contrary, with decreasing of the delay time τ, domains of the second mode generation and of the two-mode oscillation grow.

We also studied the case $\chi_{1,2} < 1$, when without the reflections regime of two-mode generation is stable. When small reflections appear, the second mode suppresses the first one, since the chosen values of the phases $\psi_{1,2}$ provide decrease of the amplitude of the first mode and increase of the amplitude of the second one. However, with further increase of $\rho_{1,2}$ excitation of a higher-order steady state of the first mode occurs. Frequency of this state shifts off the fundamental one, and, similar to the previous case, a backward transition to the two-mode regime takes place.

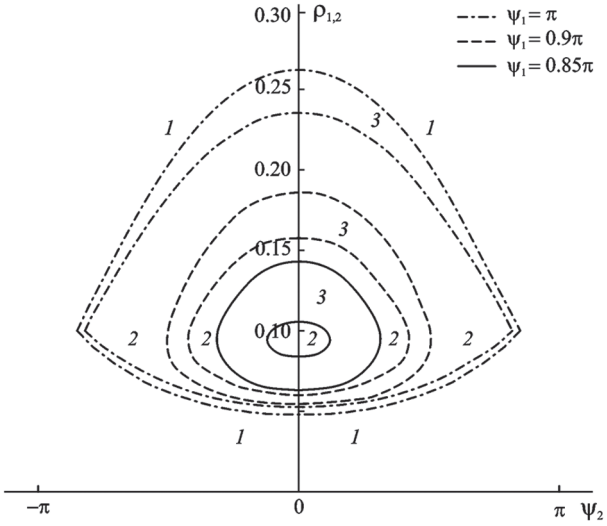

Fig. 2. Domains of regimes of generation of the first mode (1), second mode (2), and two-mode generation (3) for different values of the phase ψ_1. Other parameters are the same as in Fig. 1

3. REFLECTIONS IN A GYROTRON WITH RADIAL OUTPUT

Modern gyrotrons designed for operation at high power levels and high frequencies, especially in subterahertz and terahertz region, are operating at very high-order modes, $TE_{m,n}$, $m,n \gg 1$. For instance, the gyrotron developed for the International Thermonuclear Experimental Reactor (ITER), operates at the $TE_{34,19}$ mode; here 34 and 19 are the azimuthal and radial indices, respectively (see e.g. [5,6]). For such gyrotrons, a build-in quasioptical mode convertor is used to convert high-order cavity mode radiation into a Gaussian wave beam. The radiation, after leaving the cavity and propagating through the output waveguide, hits the launcher in which an individual rotating mode loses its identity and with the use of a quasiparabolic reflector is converted into an approximately linearly polarized Gaussian wave beam. This beam is guided by means of phase correcting mirrors to the output window. When, for some reasons, the window is not perfectly matched for this wave beam, the reflected radiation follows the reverse path. On this way, the beam is transformed inside the launcher into the oppositely rotating mode, which returns to the cavity. This means that, in contrast with the situation considered in Sec. 2, in a gyrotron with a radial output one has to consider the competition between oppositely rotating modes with the same azimuthal and radial indices, $TE^{\pm}_{m,n}$ [5,6]. Here the superscripts "+" and "−" denote positively and negatively rotating modes, respectively.

For the case of competition of the $TE^{\pm}_{m,n}$ modes, Eqs. (1), (2) can be simplified. First, for the modes with the same azimuthal and radial indices, coefficients

β_j and γ_j are equal. Moreover, one can show that $\gamma_j = 2\beta_j$ [13,15]. Thus, Eqs. (1), (2) become

$$\dot{A}_1 = \left(\sigma_1 - \beta|A_1|^2 - 2\beta|A_2|^2\right)A_1, \quad (5)$$

$$\dot{A}_2 = q\left(\sigma_2 - \beta|A_2|^2 - 2\beta|A_1|^2\right)A_2 + \rho e^{i\psi}A_{1\tau}. \quad (6)$$

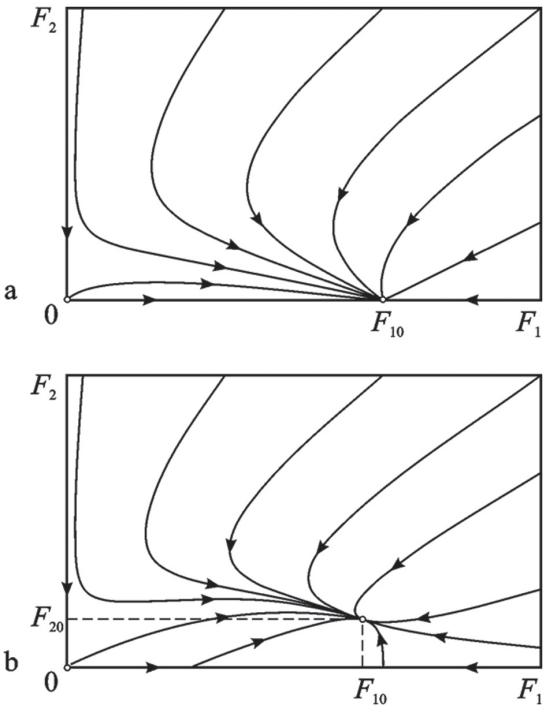

Fig. 3. Phase portraits without (a) and with (b) reflections

Here, A_1 is the amplitude of the fundamental mode and A_2 is that of the spurious mode with opposite rotation. It is assumed that the first mode, after leaving the cavity, is partly reflected from the window, changes the direction of its rotation and returns to the cavity affecting the second mode. The secondary mode with opposite rotation usually does not reach the window and the effect of its reflection on the primary mode can be neglected [5,6].

Introducing real amplitudes and phases, $A_j = F_j/\sqrt{\beta'}\cdot\exp\left(i\varphi_j\right)$, one can rewrite Eqs. (5), (6) as follows:

$$\dot{F}_1 = \left(\sigma_1' - F_1^2 - 2F_2^2\right)F_1, \quad (7)$$

$$\dot{F}_2 = q\left(\sigma_2' - F_2^2 - 2F_1^2\right)F_2 + \rho F_{1\tau}\cos\left(\varphi_{1\tau} - \varphi_2 + \psi\right), \quad (8)$$

$$\dot{\varphi}_1 = \sigma_1'' - \lambda\left(F_1^2 + 2F_2^2\right), \quad (9)$$

$$\dot{\varphi}_2 = q\left(\sigma_2'' - \lambda\left(F_2^2 + 2F_1^2\right)\right) + \rho\left(F_{1\tau}/F_2\right)\sin\left(\varphi_{1\tau} - \varphi_2 + \psi\right), \quad (10)$$

where $\sigma_j' = \mathrm{Re}\,\sigma_j$, $\sigma_j'' = \mathrm{Im}\,\sigma_j$, $\beta' = \mathrm{Re}\,\beta$, $\beta'' = \mathrm{Im}\,\beta$, $\lambda = \beta''/\beta'$.

Consider the case when $\sigma_1' > 0$, $\sigma_2' < 0$. In that case, excitation of the oppositely rotating mode in the gyrotron with perfectly matched window ($\rho = 0$) is impossible. Steady-state solutions of the Eqs. (7)–(10) – are

$$F_j = F_{j0},\ \varphi_j = \Omega_j t + \varphi_{j0}, \quad (11)$$

where F_{j0}, φ_{j0} and Ω_j are constants. Without reflections there exist two steady-state solutions: the unstable zero solution $F_{j0} = 0$ and the stable one

$$F_{10} = \sqrt{\sigma_1'},\ F_{20} = 0,\ \Omega_1 = \sigma_1'' - \lambda\sigma_1', \quad (12)$$

which corresponds to generation of the fundamental mode. Phase portrait on the $F_1 - F_2$ plane is plotted in Fig. 3a.

When small reflections appear, $\rho \ll \sigma_1'$, they induce excitation of the secondary mode and two-mode oscillation arises. The stable fixed point on the $F_1 - F_2$ plane shifts off the horizontal axis $F_2 = 0$ (Fig. 3b). One can find approximate steady-state solution accurate within $O(\rho)$:

$$F_{10} \approx \sqrt{\sigma_1'},\ F_{20} \approx \frac{\rho\sqrt{\sigma_1'}\cos\vartheta_0}{q\left(2\sigma_1' - \sigma_2'\right)}, \quad (13)$$

$$\Omega_1 = \Omega_2 \approx \sigma_1'' - \lambda\sigma_1'. \quad (14)$$

Note that frequencies of both modes in the steady state should be equal, $\Omega_1 = \Omega_2 = \Omega$. In Eq. (13)

$$\vartheta_0 = \varphi_{10} - \varphi_{20} - \psi - \Omega\tau \quad (15)$$

which can be found from (7)–(10), (13):

$$\mathrm{tg}\,\vartheta_0 = \frac{\sigma_1''(1-q) - \lambda\sigma_1'(1-2q)}{q\left(2\sigma_1' - \sigma_2'\right)}. \quad (16)$$

Since we consider the case of small reflections, higher-order steady-state solutions discussed in Sec. 2 do not appear.

Thus, even at very small reflections, at the same time with excitation of fundamental mode, in a gyrotron cavity stable forced oscillation of the mode of opposite rotation arise. We believe that this effect is responsible for distortion of the transverse pattern of radiation discovered in [16] where a gyrotron with modulated reflection from an oscillating membrane was studied.

ACKNOWLEDGMENTS

The work is supported by Russian Foundation for Basic Research grants No. 11-02-01411a and 12-02-01298a.

References

1. Antonsen T.M., Cai S.Y., and Nusinovich G.S. 1992. 'Effect of window reflection on gyrotron operation', *Phys. Fluids B* **4**, 4131-4139.
2. Dumbrajs O., Glyavin M., Zapevalov V.E., and Zavolsky N. 2000. 'Influence of reflections on mode competitions in gyrotrons' *IEEE Trans. Plasma Sci.* **28**, 588-596.
3. Airila M.I., Kall P. 2004. 'Effect of reflections on nonstationary gyrotron oscillations', *IEEE Trans. Microwave Theory and Techniques* **52**, 522-528.
4. Dumbrajs O., Idehara T., Watanabe S., Kimura A., Sasagawa H., Agusu L., Mitsudo S., and Piosczyk B. 2004. 'Reflections in gyrotrons with axial output', *IEEE Trans. Plasma Sci.* **32**, 899-902.
5. Dumbrajs O., Nusinovich G.S., and Piosczyk B. 2004. 'Reflections in gyrotrons with radial output: Consequences for the ITER coaxial gyrotron', *Phys. Plasmas* **11**, 5423-5429.
6. Dumbrajs O. 2010. 'Influence of Possible Reflections on the Operation of European ITER Gyrotrons', *J. Infrared Millim. Terahz. Waves* **31**, 892-898.

7. Batanov G.M., Kolik L.V., Novozhilova Yu.V. *et al.* 2001. 'Response of a gyrotron to small-amplitude low-frequency-modulated microwaves reflected from a plasma', *Tech. Phys.* **46**, 595-600.
8. Kulik V.V., Lukin K.A., and Rakityansky V.A. 1998. Autodyne effect in weak-resonant BWO with chaotic dynamics', *Int. J. Infrared Millim. Waves* **19**, 427-440.
9. Lukin K.A., 2002. 'The principles of noise radar technology' *Proc. First Int. Workshop NRTW*, Yalta, Ukraine, 13-22.
10. Novozhilova Yu.V., Ryskin N.M., and Usacheva S.A. 2011. 'Nonstationary processes in an oscillator with delayed reflection from the load', *Tech. Phys.* **56**, 1235-1242.
11. Novozhilova Yu.V. 2011. 'Parametric instability in an oscillator with delayed reflection from a load. Theory', *Appl. Nonli. Dyn.* **19** (2), 122-127.
12. Novozhilova Yu.V., Sergeev A.S., and Usacheva S.A. 2011. 'Parametric instability in an oscillator with delayed reflection from a load. Numerical results', *Appl. Nonli. Dyn.* **19** (2), 128-140.
13. Nusinovich G.S. 1981. 'Mode interaction in gyrotrons', *Int. J. Electron.* **51**, 457-474.
14. Rabinovich M.I., Trubetskov D.I. 1996. *Oscillations and Waves in Linear and Nonlinear Systems*, Kluwer, Dordrecht.
15. Nusinovich G.S., Sinitsyn O.V., and Antonsen T.M. 2007. 'Mode switching in a gyrotron with azimuthally corrugated resonator', *Phys. Rev. Lett.* **98**, 205101.
16. Kharchev N.K., Batanov G.M., Bondar Yu.V. *et al.* 2011. 'Gyrotron affected by modulated reflection: new experiments', *Proc. 8th Int. Workshop "Strong Microwaves and Terahertz Waves: Sources and Applications".* IAP RAS, Nizhny Novgorod, Russia, 90-91.

Manuscript received February, 28, 2013

Svetlana A. Usacheva, for photograph and biography, see this issue, p. 44.

Maria M. Chumakova was born October 14, 1991 in Saratov, Russia. She is a student at the Faculty of Nonlinear Processes, Saratov State University. Her research interest is in studying of microwave oscillators with delayed reflection from remote load.

Mikhail Yu. Glyavin, Head of Laboratory of microwave processing of materials, Gyrotron Group Plasma Physics and High Power Electronics Department, Institute of Applied Physics RAS, Nizhny Novgorod, Russia (IAP RAS). He was born in Nizhny Novgorod (former Gorky), Russia, in 1965. He received the B.S. degree from Gorky Polytechnic Institute and since 1988 has been working at the IAP RAS. He received the Ph.D. and D.Sc. degrees in physics in 1999 and 2009, respectively. At 1999-2008 he partly joined FIR FU, Fukui, Japan as visiting professor. His scientific interests were aimed at developing high power, high efficiency millimeter and submillimeter wave gyrotrons. His current research includes gyrotron development, the study of application of high power electromagnetic radiation for material processing and diagnostics of various media. He has more than 100 publications on the theoretical and experimental topics. M. Glyavin is a member of GYCOM team — the leading Russian producer of generators and amplifiers at (10–1000) GHz frequencies, as well as relevant wave transmission and control electrodynamics structures.

Yulia V. Novozhilova, Senior Reseacher of Plasma Physics and High Power Electronics Department, Institute of Applied Physics RAS, Nizhny Novgorod, Russia. She was born in Nizhny Novgorod (former Gorky), Russia, in 1960. She graduated from Gorky University and since 1982 has been working at the IAP RAS. She received the Ph.D. in physics in 1995. Her research interests are in the theory and development of electron microwave radiation sources, especially millimeter and submillimeter wave gyrotrons. She has co-authored more than 50 journal papers.

Nikita M. Ryskin, for photograph and biography, see this issue, p. 44.

УДК 621.37

Влияние отражений от удаленной нагрузки на конкуренцию мод в многомодовых резонансных электронных генераторах / С.А. Усачева, М.М. Чумакова, М.Ю. Глявин, Ю.В. Новожилова, Н.М. Рыскин // Прикладная радиоэлектроника: науч.-техн. журнал. – 2013. – Том 12. – № 1. – С. 54–57.

Рассматривается влияние отражений от удаленной нагрузки на конкуренцию мод в двухмодовом электронном мазере. Аналитически и численно исследуется система двух связанных уравнений для медленно меняющихся амплитуд мод, в которую входят слагаемые, содержащие запаздывание. Показано, что при определенных условиях отражения сильно влияют на режим генерации. Особое внимание уделяется гиротрону со встроенным квазиоптическим преобразователем мод, где излучение после отражения от окна преобразуется в моду встречного вращения.

Ключевые слова: отражения, конкуренция мод, мазер, гиротрон, запаздывающая обратная связь.

Ил. 3. Библиогр.: 16 назв.

УДК 621.37

Вплив відбиттів від віддаленого навантажування на конкуренцію мод в багатомодових резонансних електронних генераторах / С.А. Усачова, М.М. Чумакова, М.Ю. Глявін, Ю.В. Новожилова, Н.М. Рискін // Прикладна радіоелектроніка: наук.-техн. журнал. – 2013. – Том 12. – № 1. – С. 54-57.

Розглядається вплив відбиттів від віддаленого навантаження на конкуренцію мод у двухмодовому електронному мазері. Аналітично і чисельно досліджується система двох зв'язаних рівнянь для повільно мінливих амплітуд мод, в яку входять доданки, що містять запізнювання. Показано, що при певних умовах відбиття сильно впливають на режим генерації. Особлива увага приділяється гіротрону з вбудованим квазіоптичних перетворювачем мод, де випромінювання після відбиття від вікна перетворюється в моду зустрічного обертання.

Ключові слова: відбиття, конкуренція мод, мазер, гіротрон, запізненний зворотний зв'язок.

Іл. 3. Бібліогр.: 16 найм.

UDC 621.385.62

COMPUTER SIMULATION OF NOISE GENERATION IN MAGNETRON

G.I. CHURYUMOV, A.V. GRITSUNOV AND A.I. EKEZLY

This paper describes possible approaches to the computer simulation of fluctuation processes in a magnetron operating in π-mode. The use of computer simulation (TULIP particle-in-cell simulation code) allows carrying out comparative analysis of output spectrum and phase focusing of electron flow in different operating conditions of the magnetron. It is shown that the regularization of electron flow motion associated with decreasing its turbulence, leads to minimizing the noise level in the range of up to - 60 dB relative to a level of operating signal. A circuitry model of the magnetron is established for more detailed study of physical processes and understanding the influence of fluctuation processes in re-entrant electron flow on the quality of the output spectrum.

Keywords: magnetron, simulation, noise, fluctuation, PIC method, circuit method, output spectrum.

I. INTRODUCTION

Various magnetrons as the most popular vacuum tubes keep attracting attention of the researchers in vacuum electronics worldwide (see, e.g., [1–4]). Traditional research and developments of magnetrons are focused on the following topics: enhancement of energy efficiency, increase of output power and working frequency; advancing technologies for anode & cathode and magnetron magnet systems, etc. Nowadays, one may see increasing interest to the research focused on improvements in frequency characteristics of the magnetrons, including enhancement of frequency stability and quality of the output spectrum; suppression of the spurious oscillations and both the amplitude and phase noise, etc. [2, 5–7]. On the other hand, the idea of using magnetrons for generation of oscillations with increased level of the noises and design on this basis the microwave noise generators did not lost its relevance yet [8].

The main objective of this paper is to make choice of a method for computer simulation of the fluctuation processes in the magnetrons for adequate describing the chaotic behavior of electron flow and the study of existing regularities between the space charge spokes form and levels of the spurious oscillations in the output spectrum of the magnetron.

II. STATEMENT OF THE PROBLEM

For understanding the need of investigation of the fluctuation processes in the magnetrons we might study in details the output waveform of the magnetron and features of its frequency spectrum.

Fig. 1 shows the distributions of instantaneous values of the RF amplitudes for the ideal (a) and actual (b) the output waveform in the time and frequency domains.

As is seen, in case of the actual waveform we have spurious amplitude and frequency (phase) modulations of the output signal. As a result, at the output of the magnetron instead of the ideal monochromatic oscillation

$$\tilde{U}(t) = \tilde{U}_m \cdot \cos\omega_0 t\,, \qquad (1)$$

where $\tilde{U}(t)$ is the instantaneous RF amplitude; $\tilde{U}_m$ is the voltage of microwave oscillation in the steady state operation of the magnetron; ω_0 is the oscillation frequency of the magnetron, we have randomly modulated oscillation

$$\tilde{U}(t) = \tilde{U}_m \cdot \left[1 + \alpha(t)\right] \cdot \cos\left[\omega_0 t + \varphi(t)\right], \qquad (2)$$

where $\alpha(t)$ is the dimensionless coefficient that determines the instantaneous depth of the chaotic amplitude modulation ($\alpha(t) << 1$); $\varphi(t) = \int_0^t \Delta f(\tau) d\tau$ is the function that determines the variations of the output signal phase; $\Delta f(\tau)$ is the instantaneous frequency deviation.

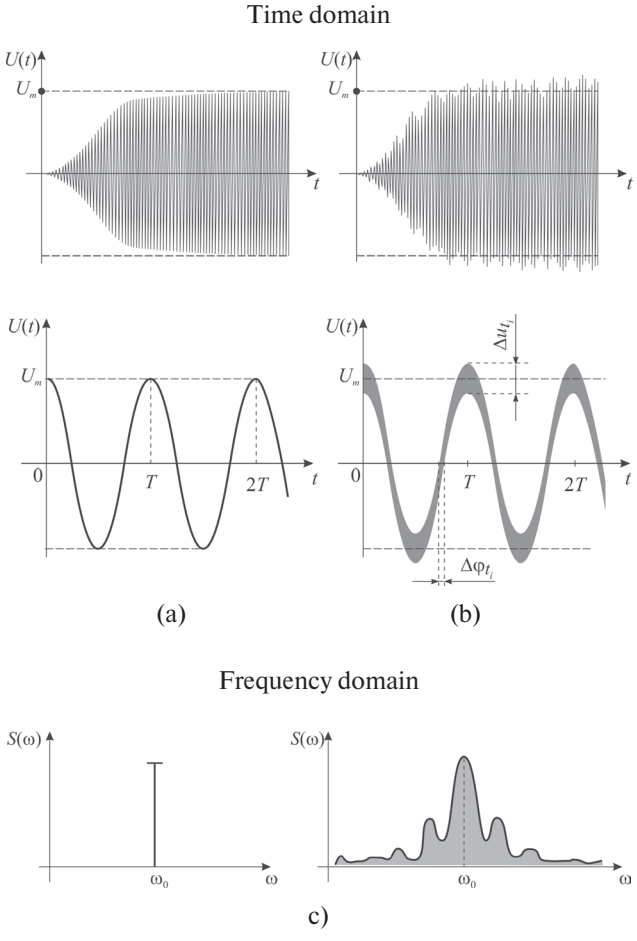

Fig. 1. The ideal (a) and actual (b) waveform output signals and their spectrum (c)

Analysis of the expression (2) shows that the availability of amplitude modulation of the output signal leads to expansion of its spectrum. With increasing complexity of waveform $\tilde{u}(t) = \tilde{U}_m \cdot \alpha(t)$ increases the number of spectral components in the output spectrum $\tilde{U}(t)$ and its quality deteriorates. Stochastic fluctuations of the phase in (2) are determined by the type of dependence $\varphi(t)$ (phase noise) and are one of the criteria for frequency stability of the magnetron.

For determining a spectrum of the output signal (2) necessary to analyze the waveform $\tilde{u}(t)$. In the case when the waveform is periodic we can represent it as a Fourier series

$$\tilde{u}(t) = U_0 + \sum_{k=1}^{\infty} \tilde{U}_{mk} \cdot \sin(k\Omega t + \psi_k), \qquad (3)$$

where U_0 is the constant component of the voltage ($U_0 = 0$); $\Omega = \frac{2\pi}{T}$ is the fundamental frequency; $\tilde{U}_{mk}$ and ψ_k are the amplitude and phase of the k-th harmonic of the fundamental signal. The set of values $\tilde{U}_{mk}$ is defined as the amplitude spectrum of the output signal.

For spectral decomposition of a non-periodic waveform $\tilde{u}(t)$ we use a Fourier integral

$$\tilde{u}(t) = \frac{1}{2\pi} \cdot \int_{-\infty}^{\infty} S(\omega) \cdot e^{j\omega t} d\omega , \qquad (4)$$

where

$$S(\omega) = \int_{-\infty}^{t} \tilde{u}(t) \cdot e^{-j\omega_0 t} dt . \qquad (5)$$

The value $S(\omega)$ is the spectral density, and its absolute value $|S(\omega)|$ determines the output frequency spectrum of the magnetron.

The presence of random fluctuations of the voltage $\Delta\tilde{U}_{t_i}$ and the phase $\Delta\varphi_{t_i}$ of the RF output signal can be considered as demonstration of the noise caused by the influence of internal and external destabilizing factors (stochastic fluctuations).

The main sources of the intrinsic destabilizing factor (noise) in the magnetrons are re-entrant electron flow with inherent discrete nature of electric charge and probabilistic nature of electron emission from the cathode. This causes an appearance of the fluctuation noise including the shot noise, distribution noise as well as secondary electron emission noise. Besides, the stochastic local changes of work function of cathode material and consequent the spontaneous modulation of the space charge are the reasons for electron emission current fluctuations (flicker noise) and noise associated with the presence of positive ions in the electron flow near a cathode of the magnetron [5, 7, 9]. Among external destabilizing factors affecting the magnetron operation one has to note the deterministic fluctuations or noise caused by an influence of magnetron power supply circuits, vibrations, temperature changes, etc.

Level of the noise in magnetrons is the result of composition of all the above mentioned sources of. For a quantitative assessment and comparative noise analysis of the noise level we use the dimensionless parameter as the ratio of signal power to noise power (signal/noise)

$$SNR(dB) = 10 \cdot \lg\left[\frac{P_{signal}}{P_{noise}}\right] = 20 \cdot \lg\left[\frac{U_{signal}}{U_{noise}}\right]. \qquad (6)$$

III. RESULTS OF COMPUTER SIMULATION

The computer simulation of fluctuation processes in the magnetrons is usually performed using both analytical methods (see, e.g. [4]) and numerical methods based on the FTTD technique for an electromagnetic field simulation and particle-in-cell (PIC) method for the simulation of electron flow [3]. It should be noted that the computer simulation allows studying the various noise sources. However, the computational experiment has a significant drawback that limits its application for studying electron-wave processes in low field operation. This is because high level of the so-called "computing noise" inherent in this approach due to calculation errors of the electrical and magnetic components of electromagnetic field and the coordinates and velocities of charged particles as well as value of space-charge field at the points of discrete space-time grid. Therefore, the use of computational experiment to study the noise processes is possible in a case when the level of physical noise will dominate compared to "computational noise". As it is shown in [3], it is possible to analysis the noise in high-power microwave tubes, such as the magnetron amplifiers. On the other hand, this ability is achieved by increasing the accuracy of calculations and related to the use of computational algorithms that provide programmable level of the calculation errors as well as available hardware capabilities of the computers (for example, carrying out calculations with double precision).

Fig. 2 shows the results of the computer simulation of the electron bunching and output spectrum for different operating conditions of the 4J33 magnetron. These results have been obtained with 2D PIC simulations using the TULIP code created for full-format and spectral computer simulation of the magnetrons [10].

As illustrated in Fig. 2, the quality of the output spectrum of the magnetron is largely dependent on conditions of its operation. Regularization of motion of the electron flow associated with decreasing its turbulence is achieved by choosing the optimal anode voltage. As a result we have a significant reduction of the noise level in the output spectrum (Fig. 2, b). Analysis of kinematic characteristics of the electron flow shows that in optimal conditions operating reduces velocities spread of electrons and increases laminar nature of its motion in area of the electron spokes relative to the fixed coordinate system. Unfortunately, in the case of the noise process studying via the computational experiment it is difficult (and in some cases impossible) to understand and define the role of specific factors and their effects on a noise level

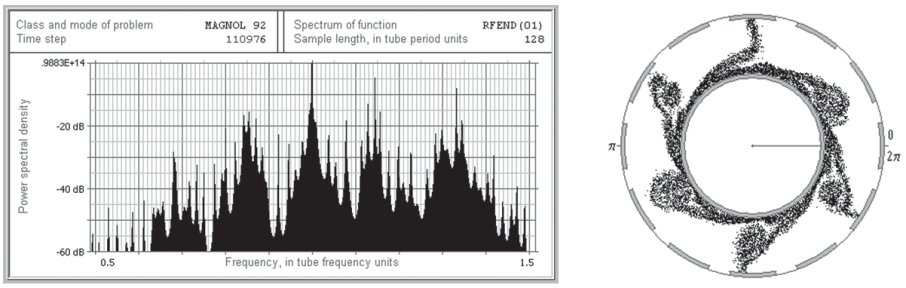

a)

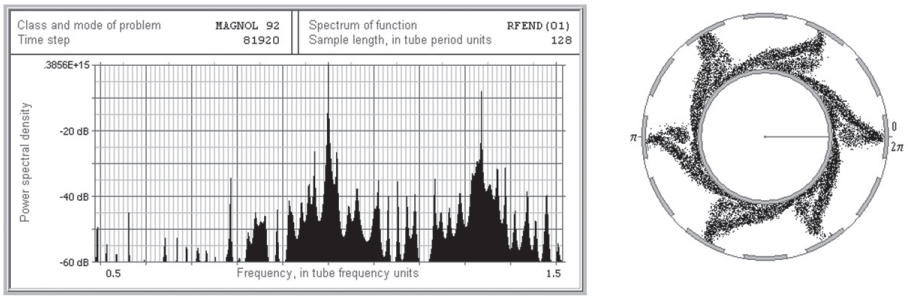

b)

Fig. 2. The distribution of space charge and output spectrum of the 4J33 magnetron at $B_0 = 0.25$ T; $U_a = 24{,}0$ kV (a) and $U_a = 28{,}0$ kV (b)

taking into account that all factors are interrelated and it is not possible unambiguously to determine the causes of these changes. Therefore, there is a need for further development of more simple and physically adequate mathematical models for studying the noise processes in the magnetrons.

IV. CIRCUITRY MODEL OF MAGNETRON

When studying the fluctuation processes in steady state mode of the 4J33 magnetron we assumed that π–mode is the main operating mode for which the space charge distribution in the interaction space can be presented as $N/2$ formed electron spokes. The general view of the formed electron spokes in the moving coordinate system is shown in Fig. 2, b. For analytical calculations of induced current let us consider a more simple form of the electron spokes representation in the interaction space.

Fig. 3 shows two electron spokes over one period of the anode resonant system: 1 denotes the form of electron spoke that is used for the analytical model of the magnetron and 2 denotes the electron spoke obtained with the help of the PIC method. The electron spokes revolve around the cathode and induce current on the segments of the anode resonant system in accordance with the Shockley-Ramo theorem. In the two-dimensional approximation, we obtain that

$$i(t) = h\int_S \rho(r,\varphi)\vec{v}(r,\varphi)\vec{E}(r,\varphi)dS\,, \qquad (7)$$

where $\vec{E}(r,\varphi) = \tilde{E}_r\vec{r}_0 + \tilde{E}_\varphi\vec{\varphi}_0$ is the expression for π–mode field intensity [11]; $\rho = \rho(r,\varphi)$ is the distribution of the space charge density; $\vec{v} = \vec{v}(r,\varphi)$ is the distribution of the velocities in the electron bushing and spokes of space charge; h is the height of the anode block of the magnetron.

In order to determine the dependencies $\rho = \rho(r,\varphi)$ and $\vec{v} = \vec{v}(r,\varphi)$ we use the results of numerical simulation of bunching processes of the space charge which have been described in [12]. These dependencies (curves 1) and the results of their more simple approximation (curves 2) are shown in Fig. 4.

The expression for the radial distribution of the space charge density in electron spoke can be written as

$$\rho(r) = \rho_{\max} e^{-\alpha(r-r_c)}\,, \qquad (8)$$

where

$$\alpha = \frac{1}{(r_a - r_c)}\cdot\ln\left(\frac{I_{em}}{I_a}\right), \qquad (9)$$

$\rho_{\max}$ is the maximal electron flow density near the cathode (in area of virtual cathode); I_{em} is the total current from the cathode, providing a space-charge-

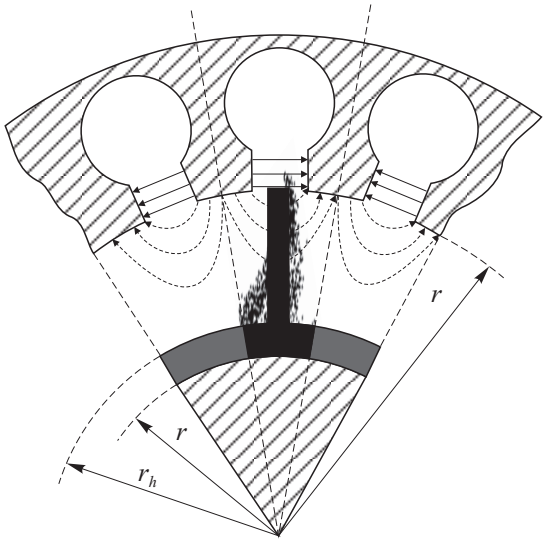

Fig. 3. The distribution of space charge and output spectrum of the 4J33 magnetron at $B_0 = 0.25$ T; $U_a = 24{,}0$ kV (a) and $U_a = 28{,}0$ kV (b)

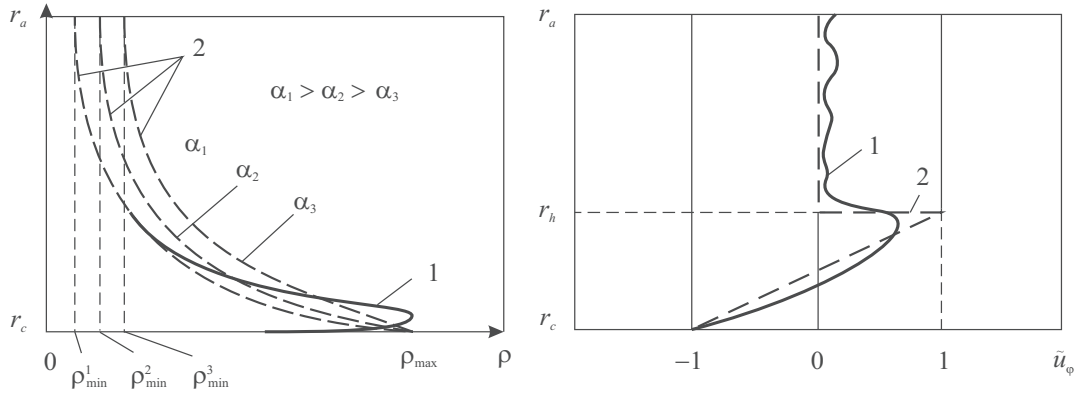

Fig. 4. The radial distributions of space charge density and azimuthal velocity of the electron cloud

limited emission regime; I_a is the anode current of the magnetron.

Analysis of the electron flow in the magnetron shows that in the steady-state operation exist two stable regions in the flow. These are two region of the electron bushing: in the first one $r_c < r < r_h$, predominates double-flow state of the electron flow, while in the second one $r_h < r < r_a$ the electrons motion is close to laminar one (quasi-laminar electron flow) [12]. The results obtained via computer simulation showed that in the area of the electron bushing linear azimuthal velocity increases from zero at the $r = r_c$ to $(1.1 - 1.3) \cdot \bar{v}_e$ on the top of the electron bushing at the $r = r_h$, where $\bar{v}_e = \dfrac{U_a}{r_a \cdot B_0 \cdot \ln(r_a / r_c)}$ is the average drift velocity of the electron flow at the anode. In the area of the electron spokes in the area of $r_h < r < r_a$, as illustrated in Fig. 4, b, predominates quasi-laminar motion of the electron flow. For this area the azimuthal velocity is equal

$$v_\varphi = \bar{v}_e + \Delta\tilde{v}_e , \qquad (10)$$

where $\Delta\tilde{v}_e$ is oscillation of the azimuthally velocity related to radial motion of the electrons.

The expression for the current induced by the one electron spoke on the segments of the anode resonant system can be written as

$$i(t) = h \cdot \rho_{max} \cdot \bar{v}_e \cdot \left\{ \int_{r_c}^{r_a} \int_{-\frac{\pi}{2}}^{+\frac{\pi}{2}} r \cdot e^{-\alpha(r-r_c)} \cdot \tilde{E}_\varphi d\Phi dr + \right. \qquad (11)$$

$$+ \int_{r_c}^{r_a} \int_{-\pi}^{-\frac{\pi}{2}} r \cdot \left\{ 1 - \cos\left[\frac{(r-r_c)}{(r_h - r_c)} \right] \cdot \pi \right\} e^{-\alpha(r-r_c)} \cdot \tilde{E}_\varphi d\Phi dr +$$

$$\left. + \int_{r_c}^{r_h} \int_{+\frac{\pi}{2}}^{+\pi} r \cdot \left\{ 1 - \cos\left[\frac{(r-r_c)}{(r_h - r_c)} \right] \cdot \pi \right\} e^{-\alpha(r-r_c)} \cdot \tilde{E}_\varphi d\Phi dr \right\} .$$

In the steady state operation of the magnetron the current to be induced by the electron spokes on the anode are periodic sequence of the current pulses, which can be expanded in Fourier series

$$i(t) = I_0 + \sum_{n=1}^{\infty} I_n e^{jn\Omega_e t} , \qquad (12)$$

where n is the number of current harmonic; I_0 is the dc component of the induced current (anode current); $\Omega_e = \dfrac{\omega}{\gamma}$ is the angular velocity of rotation of the electron spokes (condition for re-entrant electron flow); $\gamma = \dfrac{N}{2}$ is the propagation constant corresponding π-mode.

The expression for a synchronous harmonics of the induced current can be written as

$$I_n = \frac{1}{2\pi} \cdot \int_{-\pi}^{+\pi} i(t) \cdot e^{-jn\Omega_e t} dt , \qquad (13)$$

Fig. 5 shows the equivalent circuit of the magnetron corresponding the excitation of the π-mode. This equivalent circuit comprises current sources $I_\omega(t)$ and voltage sources $U_a(t)$ and $\tilde{U}_\pi(t)$. The number of the current sources corresponds to the number of the electron spokes, i.e. $\dfrac{N}{2}$, where N is the number of the cavities (in our case $N = 12$). The value of the current which induces by the current sources $I_\omega(t)$ corresponds to the synchronous harmonic of the induced current (13).

The value $I_\omega(t)$ can be written as

$$I_\omega(t) = \bar{I}_\omega + \Delta\tilde{I}_\omega(t) , \qquad (14)$$

where $\bar{I}_\omega$ is the value of the induced current corresponding the constant emission current from the cathode; $\Delta\tilde{I}_\omega(t)$ is the fluctuations of the induced current associated with influence of oscillatory processes in the electron flow (shot effect, the phenomenon of the current distribution and the secondary emission).

As the sources of voltage in Fig. 5 we consider the source of anode voltage $U_a(t)$ and the synchronous voltage source $\tilde{U}_\pi(t)$ that excites the mode oscillations in the anode resonant system of the magnetron, i.e.

$$U_a(t) = U_a + \Delta U_a(t) , \qquad (15)$$

$$\tilde{U}_\pi(t) = \tilde{U}_{\pi m} \cos\left[\omega t + \psi(t)\right] , \qquad (16)$$

where U_a is the constant anode voltage; $\Delta U_a(t)$ is the anode voltage fluctuations caused by an instability of the power supply; $\tilde{U}_{\pi m}(t)$ is the instantaneous

amplitude of the π-mode in the steady state of the magnetron; $\psi(t)$ is the parameter determining the phase shift between the voltage of the π-mode and the synchronous harmonic of the current (13).

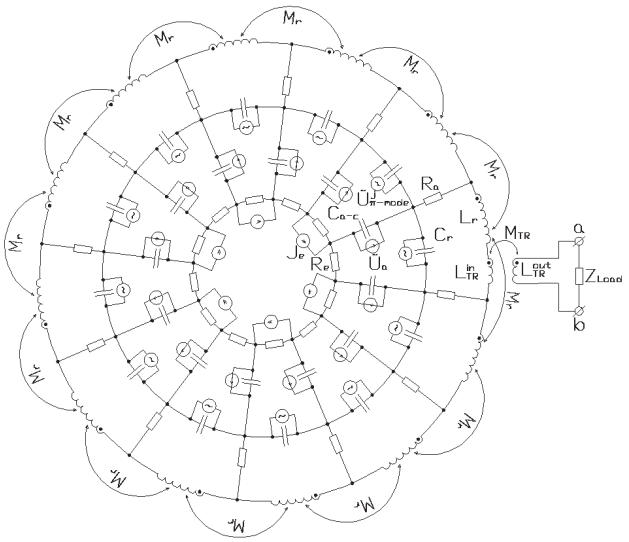

Fig. 5. Equivalent circuit of "hot" magnetron

For determining the values of the capacitances of the interaction space $C_{a-c}(t)$ and resonators $C_r(t)$ we use the expression for a capacitance of the parallel-plate capacitor, i.e.

$$C_{a-c}(t) = \frac{\varepsilon_e^{a-c}(t) \cdot S_{a-c}}{4\pi d_{a-c}}, \quad (17)$$

$$C_r(t) = \frac{\varepsilon_e^{r}(t) \cdot S_r}{4\pi d_r}, \quad (18)$$

where S_{a-c} is the cross-sectional area of a vane; S_r is the slit area of a resonator; $d_{a-c} = r_a - r_c$ is the distance between the cathode and anode; d_r is the distance between the vanes at the $r = r_a$; r_a and r_c are the anode and cathode radiuses; $\varepsilon_e^{a-c} = \overline{\varepsilon}_e^{a-c} + \Delta\tilde{\varepsilon}_e^{a-c}(t)$ and $\varepsilon_e^{r} = \overline{\varepsilon}_e^{r} + \Delta\tilde{\varepsilon}_e^{r}(t)$ is the dielectric constant of the electron flow in cathode-anode space and between the vanes; $\overline{\varepsilon}_e^{a-c}$ and $\overline{\varepsilon}_e^{r}$ is the average values of dielectric constants of the electron flow; $\Delta\tilde{\varepsilon}(t)$ is the fluctuations of the dielectric constant of the electron flow resulting from oscillations in the electron density of the space charge.

In general, it should be noted that the capacitance values $C_{a-c}(t)$ and $C_r(t)$ have a non-linearly dependence on the anode voltage U_a. The nature of the nonlinearity depends on the state of the electron flow and distribution of the space charge density in the space between the cathode and anode.

To convert the equivalent circuit of "hot" magnetron to the form convenient for calculations it is necessary to exclude the magnetic coupling between the inductances L_r of the coupled cavities of the anode resonator system as well as input L_{tr}^{in} and output L_{tr}^{out} inductances of output linear transformer which provides matching the anode resonant system with the output load

$$Z_{load} = R_{load} + jX_{load}. \quad (19)$$

The matching condition of the magnetron is given by the

$$R_{load} = \mathrm{Re}\left(Z_{in}^{a-b}\right), \quad (20)$$

where Z_{in}^{a-b} is the value of input impedance of the anode resonant system of the magnetron (Fig. 5).

In order to describe the electrical circuit we apply Kirchhoff's laws, writing equations for the instantaneous values of the induced currents using the mesh-current method. Consequently, the numerical solutions of the equations we get the complex values of the instantaneous induced current in the each circuit of the electrical network.

The instantaneous value of the active power at the matched load equal

$$P_a(t) = \frac{I_{\omega load}^{\ 2}(t) \cdot R_{load}}{2}, \quad (21)$$

where $I_{\omega\, load}$ is the instantaneous value of the induced current in the output circuit of the magnetron to be found from solution of the set of equations for the loop currents

V. SUMMARY

A novel approach for investigation of the noise processes in magnetrons has been proposed. This approach is based on a combination of numerical and analytical simulation of deterministic and stochastic fluctuation processes. The use of numerical methods (computational experiment) showed that the noise level depends on the operating conditions of the magnetron and decreases for the electron flow available lower parameter of turbulence (quasi-laminar electron flow). At the same time the possibility of computational experiment for analyzing an interaction of the electron flow with lower electromagnetic fields are limited. This is due to the errors of calculation that accumulate ("computational noise") and can become a cause of the appearance of "non-physical" effects (e.g., the spurious generation of additional components in the output spectrum of the magnetron). In order to carry out analytical simulation of the fluctuation processes in the magnetrons proposed an analytical model based on the equivalent circuits method. This model allows studying the influence of fluctuations of electron emission parameters (emission current density, including a secondary electron emission), the characteristics of electron flow (coordinates and velocities of electrons, space-charge density) as well as the parameters of external electric circuit (power supply voltage and induced external electromagnetic signals) into the operation mode of the magnetron (π-mode).

References

[1] O.A. Morozov, and other, The second born of magnetron direction. Electronnaya Technika. Ser.1. SVCh Technika, No 3 (496), 2008, pp. 3–9 (in Russian).

[2] I. Tahir, A. Dexter, R. Carter, "Noise Performance of Frequency and Phase Locked CW Magnetrons Operated as Current Controlled Oscilators," IEEE Trans. on Electron Devices, vol. ED-52, November, 2005.

[3] Cherrnin D.P. Computer Simulation of Low Noise States in a High-Power Crossed-Field Aplifer. IEEE Trans. On Electron Devices. Vol. 43, # 11, November 1996, pp. 2004 -2010.

[4] Li D., Chen X. Study of Non-Linear Dynamics in Magnetron by Using Circuitry Model. Physics of Plasma 19, 2012, pp.2004 – 2010.

[5] K. Yamamoto, H. Kuronumo, T. Koinumo, and N. Tashiro, A Study of Magnetron Noise. IEEE Trans. On Electron Devices. Vol. ED-34, No 11, May 1987, pp. 1223-1226.

[6] G.I. Churymov, O.M. Nikitenko, and V.N. Zin'kovski, Noise in Crossed-Field Devices. Proceedings of NRT - 2002. Yalta. Ukraine, 2002.

[7] G.I. Churyumov and other, Magnetron – EMI Sources: Computer Modeling and Experimental Investigations. Proceedings of EMC Europe. Eindhoven. Netherlands, 2004.

[8] Yu.V. Anisimova and other, Shumotron, Radiotechnika, № 2, 2000, pp. 19–22 (in Russian).

[9] A.N. Malahov, Fluctuatsii v avtokolebatel'nych sistemach. – Moscow: Nauka. 1968, 660 p. (in Russian).

[10] A.V. Gritsunov, Exitation of Electromagnetic Oscillations of Arbitrary Spectral Contents by Re-entrant Electron Beams in Crossed-Field Systems. Thesis for a doctor's degree. – Institute of Radiophysics and Electronics of National Academy of Science of Ukraine, Kharkov, 2005 (in Russian).

[11] G. B. Collins, Microwave Magnetrons. New York: McGraw-Hill, 1948, ch. 19.

[12] G.I. Churyumov, Ways and Methods of Increase of Interaction Efficiency of of Electron Beam with Slowed Electromagnetic Waves in the Crossed-Field Systems. Thesis for a doctor's degree. – Institute of Radiophysics and Electronics of National Academy of Science of Ukraine, Kharkov, 2005 (in Russian).

Manuscript received February, 28, 2013

Gennadiy I. Churyumov (M'96, SM'00) received the Cand. Sc. degree (Ph.D.) in 1981 from the Kharkov State Technical University of Radio Electronics, Kharkov, Ukraine; and the Doctor of Sc. degree in 1997 from Institute of Radio Physics and Electronics of NASU, Kharkov. He is currently a Professor and the Head of the Microwave & Optoelectronics Laboratory at the Department of Electronics Engineering, Kharkov National University of Radio Electronics. His general research interests lie in the area of 2-D and 3-D computer modeling of electron-wave processes in vacuum tubes, simulation techniques of electromagnetic problems and nonlinear phenomena, electromagnetic compatibility. His current activity concentrates on the practical aspects of application of the vacuum tubes. Prof. Churyumov is a member of the European Microwave Association.

Gritsunov Alexander Valentinovich received the M.S. degree in electronic engineering in 1979, the Ph.D. degree in radio physics in 1984, and the D.Sc. degree in physical electronics in 2006, all from the Kharkiv National University of Radio Electronics. Since 1977, he deals with the computer simulations of crossed-field devices. Now he also introduce his spectral methodic into the numerical modeling of signal spectra in TWT's and klystrons.

Andrew I. Ekezly is a junior researcher of the Kharkov National University of Radio Electronics. His research work is focused on computer modeling of microwave devices.

УДК 621.37

Математическое моделирование генерации шума в магнетроне / Г.И. Чурюмов, А.В. Грицунов, А.И. Экезли // Прикладная радиоэлектроника: науч.-техн. журнал. – 2013. – Том 12. – № 1. – С. 58–63.

В данной статье рассматриваются возможные подходы к моделированию флуктуационных процессов в стационарном режиме работы магнетрона на основном виде колебания. Применение вычислительного эксперимента (программа TULIP) позволяет провести сравнительный анализ выходного спектра магнетрона и состояния фазовой группировки электронного облака в различных режимах работы магнетрона. Показано, что регуляризация движения электронного потока, связанная с уменьшением его турбулентности, приводит к минимизации уровня шума в диапазоне значений до –60 дБ по отношению к уровню основного сигнала. Описана математическая модель магнетрона на основе метода эквивалентных схем для более детального изучения и понимания влияния флуктуационных процессов в электронном облаке на качество спектра выходного сигнала.

Ключевые слова: магнетрон, моделирование, шумы, колебания, PIC метода, метода цепи, выходной спектр.

Ил. 5. Библиогр.: 11 назв.

УДК 621.37

Математичне моделювання генерації шума в магнетроні / Г.І. Чурюмов, О.В. Грицунов, А.І. Екезлі // Прикладна радіоелектроніка: наук.-техн. журнал. – 2013. – Том 12. – № 1. – С. 58–63.

У даній статті розглядаються можливі підходи до моделювання флуктуаційних процесів у стаціонарному режимі роботи магнетрона на основному виді коливання. Застосування обчислювального експерименту (програма TULIP) дозволяє провести порівняльний аналіз вихідного спектра магнетрона та стану фазового групування електронного потоку в різних режимах роботи магнетрона. Показано, що регуляризація руху електронного потоку, пов'язана зі зменшенням його турбулентності, призводить до мінімізації рівня шуму в діапазоні значень до –60 дБ по відношенню до рівня основного сигналу. Описано математичну модель магнетрона на основі методу еквівалентних схем для більш детального вивчення та розуміння впливу флуктуаційних процесів у електронному потоці на якість спектра вихідного сигналу.

Ключові слова: магнетрон, моделювання, шуми, коливання, PIC методу, методу ланцюга, вихідний спектр.

Іл. 5. Бібліогр.: 11 найм.

SIGNAL PROCESSING IN NOISE RADAR

UDC 621.396.96:551.501.815

ON METHODS FOR ESTIMATION OF RANDOM PROCESSES SPECTRA

D. I. LEKHOVYTSKIY, D. S. RACHKOV, A. V. SEMENIAKA, AND D. V. ATAMANSKIY

We analyze the quality of reproduction of random processes' continuous energy spectra by classical nonparametric (periodogram and correlogram) spectral estimation (**SE**) methods based on Fourier transform and by modern (parametric) **SE** methods. The unified approach to their synthesis is proposed. In its framework, along with the known methods the new ones with practically useful features are obtained. The well-known and new quality criteria of continuous spectra reproduction are discussed. On these criteria, we compare the "extreme" capabilities of classical and parametric **SE** methods under hypothetic conditions of exactly known covariance matrix (**CM**) of analyzed mixture consisting of Gaussian random process and internal receiver noise. These methods' statistical characteristics in real "adaptive" situation, when different **CM** estimates formed on finite-size training sample are used instead of *a priori* unknown **CM**, are also compared. The rational ways of practical implementation of perspective parametric **SE** methods on the basis of adaptive lattice filters are proven.

Keywords: continuous energy spectrum, statistical analysis, accuracy of spectral estimation, integral criterion, adaptive lattice filter.

1. INTRODUCTION

Estimation of random processes' power spectral density (energy spectrum) is one of the major tasks of various informational (first of all, radio engineering) systems. The information derived from the spectra is used for determination of properties and parameters of these processes' sources, diagnosis and forecast of their state, detection and coordinates measurement, protection from the interference, recognition etc. In this connection, in the literature of the last several decades, the huge attention is paid to the development and improvement of methods for spectral estimation (**SE**) of random processes with different physical nature. Such a development was intensively stimulated by the rapid progress of digital computing machinery. Intensive research held in many countries has resulted in today's arsenal of **SE** methods being substantially wider as compared with classical periodogram (correlogram) discrete-Fourier-transform-based (**DFT-FFT**) methods, which appeared as far back as the early twentieth century. The new methods were developed to solve "different spectral analysis problems, corresponding to different kinds of prior information about the phenomenon being observed, different kinds of data, different kinds of perturbing noise, and different objectives. It is, therefore, quite meaningless to pass judgment on the merits of any proposed method unless one specifies clearly: "In what class of problems is this method intended to be used?" [1]".

This paper considers the problems of **reproduction** of **continuous** spectra of random processes with different nature, particularly, corresponding to reflections from meteorological formations (**MF**) and clutter from ground objects in pulse Doppler weather radars (**PDWR**), geophysical, speech, medical and other signals. Such processes have specific peculiarities as compared to the processes with discrete spectra. In this connection, quasi-harmonic spectral analysis methods based on fundamentally discrete nature of analyzed spectra (particularly, widely-known "eigen-structural" methods like **MUSIC**) could be non-applicable for their **SE**.

It is planned to take up a number of important theoretical and practical questions of **SE** of processes with continuous power spectra, namely: generalized spectrum analyzers, whose structure includes the majority of well-known **SE** methods, their common properties and peculiarities; test autoregressive (**AR**) models being used for comparative evaluation of various **SE** methods; unified approach to the synthesis of different **AR**-parametric **SE** methods, which allows to obtain both practically useful modifications of known methods and their new variants with improved characteristics; well-known and new **SE** quality criteria taking into account the specificity of continuous spectra of analyzed input signals; numerical evaluation and comparison of "extreme" capabilities of classical "nonparametric" and "parametric" **SE** methods on considered integral criteria under hypothetical conditions with exactly known covariance matrix (**CM**) of analyzed mixture of receiver noise and external **AR**-processes of different order; methodology and numerical results of analytical and experimental investigation and comparison of statistical characteristics of classical and "parametric" **SE** methods under real "adaptive" situation, when the different-kind **CM** estimates formed on finite-size training samples are used instead of *a priori* unknown **CM**; gains in **SE** quality, which could be achieved at the expense of taking into account the **CM** specificity, which is caused, particularly, by the specificity of sounding principle being used in **PDWR**; rational ways of practical implementation of prospective "parametric" **SE** methods on unified basis of adaptive lattice filters (**ALF**); practical recommendations on choice, construction and improvement of **SE** systems for processes with

continuous power spectra, particularly, for estimation of weather echoes spectra in **PDWR**.

2. GENERALIZED ANALYZERS OF RANDOM PROCESSES SPECTRA

A. Fig. 1 shows two kinds of generalized spectrum analyzer (**GSA**) for the random vector (burst) $\mathbf{u}=\{u_\ell\}_{\ell=1}^{M}$ with $M\times M$ **CM** $\mathbf{\Phi}=\overline{\mathbf{u}\cdot\mathbf{u}^*}$ being *a priori* unknown. In this paper, the bar and asterisk are symbols of statistical averaging and Hermitian conjugation, respectively.

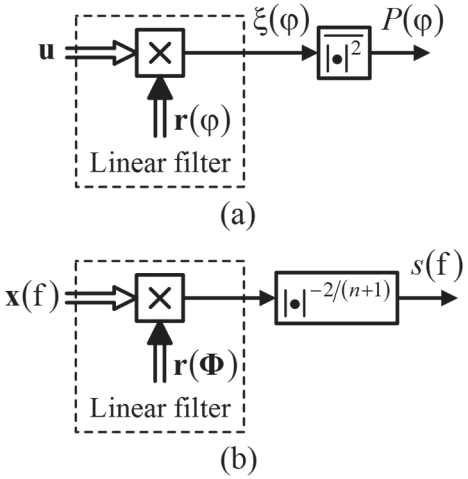

Fig. 1. Generalized spectrum analyzers

Elements of the analyzed vector (burst) **u** could correspond to complex amplitudes of signals at an output of receiving channels spaced in space or (and) in time. To be specific, we use "time" interpretation here. A generalization on "space" ("space-time") one is quite obvious albeit has specific peculiarities.

B. In the first **GSA** (Fig. 1a), the analyzed vector **u** is transformed in a linear filter with impulse response (**IR**) $\mathbf{r}(\varphi)=\{r_\ell\}_{\ell=1}^{M}$. Next, vector **u** spectrum $s(\varphi)$ in specified frequency band $\varphi\in(\varphi_{\min},\varphi_{\max})$ is obtained in a process of filter's **IR** reconfiguration in this band, and identified with an estimate $\hat{P}(\varphi)$ of power

$$P(\varphi)=\overline{\left|\xi(\varphi)\right|^2}=\mathbf{r}^*(\varphi)\cdot\mathbf{\Phi}\cdot\mathbf{r}(\varphi) \qquad (1)$$

of linear filter output signal

$$\xi(\varphi)=\mathbf{r}^*(\varphi)\cdot\mathbf{u}=\sum_{\ell=1}^{M}r_\ell^*(\varphi)\cdot u_\ell. \qquad (2)$$

Such a procedure completely corresponds to the definition of "spectrum" as a function which describes the power distribution on frequencies [2, 3].

The second **GSA** (Fig. 1b) is based on the well-known connection [4, 5] of the spectrum

$$s_{out}(\mathrm{f})=s(\mathrm{f})\cdot\mathrm{k_p}(\mathrm{f}) \qquad (3)$$

at linear filter output with the spectrum *s*(f) at its input. Here

$$\mathrm{k_p}(\mathrm{f})=\left|\mathbf{x}^*(\mathrm{f})\cdot\mathbf{r}\right|^2 \qquad (4)$$

is the squared absolute value of filter's frequency response (energy frequency response (**EFR**)), and $\mathbf{x}(\mathrm{f})=\{x_\ell(\mathrm{f})\}_{\ell=1}^{M}$ is *M*-variate vector consisting of samples of complex harmonic with the frequency f. These samples are taken at time moments determined by time intervals between pulses of sounding signal burst.

In this case, for the output spectrum of a kind

$$s_{out}(\mathrm{f})=1/s^n(\mathrm{f}),\ n\ge 0 \qquad (5)$$

the sought input spectrum

$$s(\mathrm{f})=1/\mathrm{k_p}(\mathrm{f})^{1/(n+1)} \qquad (6)$$

is completely determined by the **EFR** (4) of filter which performs transform (5).

Particularly, for $n=0$ and $n=1$

$$s(\mathrm{f})=1/\mathrm{k_p}(\mathrm{f}) \quad\text{and}\quad s(\mathrm{f})=1/\mathrm{k_p}(\mathrm{f})^{1/2}. \qquad (7)$$

The first situation ($n=0$) corresponds to the **whitening** filter with **EFR**

$$\mathrm{k_p}(\mathrm{f})=1/s(\mathrm{f}), \qquad (8a)$$

which transforms nonuniform, in general case, spectrum $s(\mathrm{f})$ to the uniform spectrum $s_{out}(\mathrm{f})=1$ of white noise. The second situation ($n=1$) corresponds to the **inverse** filter with **EFR**

$$\mathrm{k_p}(\mathrm{f})=1/s^2(\mathrm{f}), \qquad (8b)$$

which transforms an input process with spectrum $s(\mathrm{f})$ to an output process with the spectrum $s_{out}(\mathrm{f})=1/s(\mathrm{f})$ being inverse to the input one.

C. The procedure of Fig. 1a includes classical periodogram (correlogram) **SE** methods, which are referred to as **nonparametric** [4, 5]. The last term means that these methods do not use any *a priori* information about functional form of sought spectrum or, equivalently, about structure and parameters of forming filter for input process. Formally, due to this fact filter's (Fig. 1a) **IR** $\mathbf{r}=\mathbf{r}(\varphi)$ does not depend on these parameters concentrated in the **CM** $\mathbf{\Phi}=\{\phi_{ij}\}_{i,j=1}^{M}$ elements.

As contrasted to this, **SE** methods, which could be included to the procedure of Fig. 1b, are usually referred to as **parametric** [4, 5]. This is caused by the fact that here one postulates a structure of input process' forming filter (**FF**). The structure determines a functional form of this process spectrum, which depends on a finite-dimensional vector of the **FF** parameters. In this case, the main stage of **SE** is to find these parameters' estimates, which are concentrated in elements of the estimate $\hat{\mathbf{\Phi}}=\{\hat{\phi}_{ij}\}_{i,j=1}^{M}$ of process' **CM** $\mathbf{\Phi}$. Based on its key elements (parameters) the estimate $\hat{\mathbf{r}}=\mathbf{r}(\hat{\mathbf{\Phi}})$ of **IR** $\mathbf{r}=\mathbf{r}(\mathbf{\Phi})$ and the estimate $\hat{\mathrm{k}}_\mathrm{p}(\mathrm{f})=\left|\mathbf{x}^*(\mathrm{f})\cdot\mathbf{r}(\hat{\mathbf{\Phi}})\right|^2$ of **EFR** $\mathrm{k_p}(\mathrm{f})$ (4) are calculated. These estimates are used in the second-kind **GSA** (Fig. 1b) to form the spectrum *s*(f) (6) estimate $\hat{s}(\mathrm{f})=s(\mathrm{f},\hat{\mathbf{\Phi}})=1/\hat{\mathrm{k}}_\mathrm{p}(\mathrm{f})^{1/(n+1)}$.

In the both procedures of Fig. 1, the scalar products in (2), (4) could be calculated by identical linear filters, for example, classical transversal filter (Fig. 2) based on tapped-delay line with coefficients, which

determine the elements r_ℓ of filter's **IR** $\mathbf{r}=\{r_\ell\}_{\ell=1}^{M}$ of size M. Other structures, being more suitable under real "adaptive" situation, are considered further.

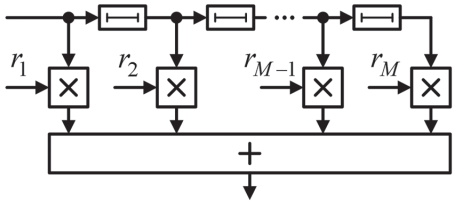

Fig. 2. Linear transversal filter

D. Many kinds of parametric **SE** methods are known [4, 5]. They were synthesized using various criteria, approaches and assumptions, what often do not allow to compare advantages and drawbacks of methods. Based on Fig. 1 **GSA**s, a unified methodology is proven below. In its framework, one can derive well-known parametric **SE** methods as well as their modifications and new kinds with practically useful properties. Their common basis is a representation of analyzed process as a stationary discrete autoregressive (**AR**) process of integer order $p\geq 1$ [3 – 5]. In this connection, these methods are hereinafter referred to as **AR**-parametric.

Input process samples are supposed to be spaced by intervals, which determine time intervals between the taps of taped-delay line of filter in Fig. 2. These intervals are supposed to be constant and equal to T. Therefore, in (1) – (8) and further, f and φ have a sense of normalized (dimensionless) frequencies connected with true frequency f by the equalities $\mathrm{f}=f\cdot T$ and $\varphi=f\cdot T$. Considered spectra are periodical with unit period on such normalized frequency axis. This allows to limit oneself with their analysis in the interval φ, $\mathrm{f}\in(-0.5, 0.5)$. The effects connected with differences (staggering) of pulse repetition intervals are subject for special analysis.

3. AR-PARAMETRIC METHODS FOR SPECTRAL ESTIMATION

A. Let samples y_k of stationary discrete **AR**-process of order $p\geq 1$ (hereinafter, for short, **AR**-p process) have zero mean $\overline{y_k}=0$ and unit variance (power)

$$\sigma_{y_k}^2=\overline{y_k\cdot y_k^*}=\sigma_y^2=1,\ k=0,\pm1,\pm2,\ldots \qquad (9)$$

Based on the definition of **AR**-p process [3 – 5], they satisfy the differential equation (recurrent relation)

$$y_k=\xi_k+\sum_{i=1}^{p}\phi_i\cdot y_{k-i},\ \ k=0,\pm1,\pm2,\ldots \qquad (10)$$

with parameters vector $\boldsymbol{\varphi}=\{\phi_i\}_{i=1}^{p}$. Here,

$$\xi_k\sim CN(0,C),\ \overline{\xi_k\cdot\xi_\ell^*}=C\cdot\delta_{k\ell},\ \delta_{k\ell}=\begin{cases}1, & k=\ell\\ 0, & k\neq\ell\end{cases} \qquad (11)$$

are independent samples of complex normal stationary white noise with zero mean and variance C, which ensure a fulfillment of normalization (9).

Fig. 3 shows the scheme of forming filter for **AR**-p process; the scheme corresponds to (10). When the elements of complex, in the general case, vector of parameters $\boldsymbol{\varphi}=\{\phi_i\}_{i=1}^{p}$ are properly chosen, this filter can form processes with continuous $n\leq p$-modal spectra with arbitrary width, speed of roll-off, and location of modes on normalized frequency axis $\mathrm{f}\in(-0.5, 0.5)$. These parameters have clear physical meaning and completely define the spectrum and **CM** of formed process. Parametric **SE** methods being considered below significantly use this fact.

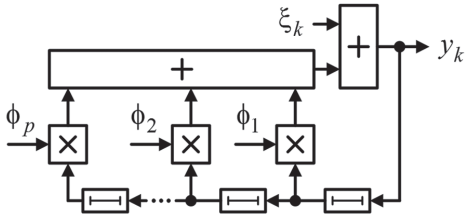

Fig. 3. Forming filter for **AR**-p process

B. As it follows from the definition (10), for a set of $p+1$ adjacent samples of **AR**-p process following equality is true

$$y_k-\sum_{i=1}^{p}\phi_i\cdot y_{k-i}=\boldsymbol{\alpha}^*\cdot\mathbf{y}_k=\xi_k,\ \ \boldsymbol{\alpha}^*=\{\alpha_i\}_{i=1}^{p+1},$$
$$\alpha_1=1,\ \ \alpha_{i+1}=-\phi_i,\ \ \mathbf{y}_k=\{y_{k-i}\}_{i=0}^{p}. \qquad (12)$$

Equation (12) can be realized, particularly, by a transversal filter shown in Fig. 4. This filter input signals are samples of **AR**-p process with parameters ϕ_i ($i\in 1,p$), and its output signals are samples ξ_k (11) of stationary white noise. Therefore, the Fig. 4 filter with the **IR** $\boldsymbol{\alpha}^*$ (12) of size $p+1$ is a whitening filter for **AR**-p process with parameters ϕ_i ($i\in 1,p$). By virtue of (4), (8a), its **EFR**

$$\mathrm{k_p}(\mathrm{f})=\left|\boldsymbol{\alpha}^*\cdot\mathbf{x}_{p+1}(\mathrm{f})\right|^2=C/s(\mathrm{f}) \qquad (13)$$

defines a spectrum $s(\mathrm{f})$ of input process.

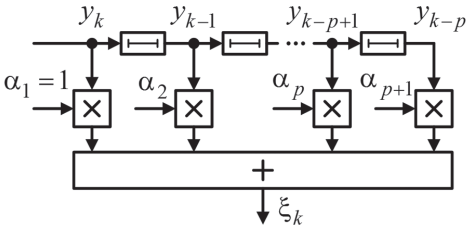

Fig. 4. Whitening filter for **AR**-p process

Hereinafter, $\mathbf{x}_L(\mathrm{f})=\{x_\ell(\mathrm{f})\}_{\ell=1}^{L}$ denotes a vector consisting of $L\leq M$ adjacent components of vector $\mathbf{x}(\mathrm{f})=\{x_\ell(\mathrm{f})\}_{\ell=1}^{M}$.

C. The essence of **IR** $\boldsymbol{\alpha}^*$ follows from the equation

$$\boldsymbol{\alpha}^*\cdot\overline{\mathbf{y}_k\cdot\mathbf{y}_k^*}=\overline{\xi_k\cdot\mathbf{y}_k^*} \qquad (14a)$$

obtained by a multiplication from the right of both parts of (12) on $(p+1)$-variate row $\mathbf{y}_k^*$ and subsequent statistical averaging. Since the input process is stationary one and intervals between samples are equal, its $(p+1)\times(p+1)$ normalized **CM**

$$\boldsymbol{\rho}^{(p+1)} = \left\{ \rho_{ij} \right\}_{i,j=1}^{p+1} = \overline{\mathbf{y}_k \cdot \mathbf{y}_k^*}, \quad \rho_{ii} = \sigma_y^2 = 1, \ i \in 1, p+1 \tag{14b}$$

is **Toeplitz** [6] one and does not depend on k, and the row-vector in the right part of (14a)

$$\overline{\xi_k \cdot \mathbf{y}_k^*} = C \cdot \mathbf{e}_1^{(p+1)^*}, \tag{14c}$$

where $\mathbf{e}_\ell^{(m)}$ is the ℓ th column of $m \times m$ identity matrix $\mathbf{I}_m$.

The last equality follows from that all the components of vector $\mathbf{y}_k^*$, except the first one, are formed by "preceding" noise samples ξ_ℓ, $\ell < k$, being uncorrelated with the kth noise sample, which has the variance C and enters to the first component of vector $\mathbf{y}_k^*$. That is why, a solution of equation (14a) is the vector

$$\boldsymbol{\alpha}^* = C \cdot \mathbf{e}_1^{(p+1)^*} \cdot \boldsymbol{\Omega}^{(p+1)} = C \cdot \boldsymbol{\Omega}_1^{(p+1)^*}, \quad C = 1 \big/ \omega_{11}^{(p+1)}. \tag{14d}$$

It is proportional to the first row of the matrix

$$\boldsymbol{\Omega}^{(p+1)} = \left\{ \omega_{ij}^{(p+1)} \right\}_{i,j=1}^{p+1} = \left(\boldsymbol{\rho}^{(p+1)} \right)^{-1}, \tag{14e}$$

being inverse to the **CM** (14b), with the coefficient C (14d) obtained from the equality $\alpha_1 = 1$ (12).

D. The Fig. 4 filter with **IR** (14d), being proportional to the first row $\boldsymbol{\Omega}_1^{(p+1)^*}$ of matrix (14e), defines the spectrum (5) with parameter $n=0$. For $M>p$ it is also defined by the first row of $M \times M$ matrix

$$\boldsymbol{\Omega} = \left\{ \omega_{ij} \right\}_{i,j=1}^{M} = \boldsymbol{\rho}^{-1}, \quad \boldsymbol{\rho} = \left\{ \rho_{ij} \right\}_{i,j=1}^{M} = \overline{\mathbf{y} \cdot \mathbf{y}^*}, \ \ \mathbf{y} = \left\{ y_\ell \right\}_{\ell=1}^{M}. \tag{15}$$

Other rows of this matrix or this matrix powers define the spectra (5) with parameter $n>0$. Choosing them as an **IR** leads to respective variants of Fig. 1b **GSA** and **AR**-parametric **SE** methods on their basis.

E. These methods can be derived in following way. Due to a fact that matrix $\boldsymbol{\Omega}$ is Hermitian positively definite (**h.p.d.**), it is true **Cholesky** representation [6]

$$\mathbf{n} \cdot \mathbf{n}^* = \boldsymbol{\Omega} = \mathbf{h}^* \cdot \mathbf{h} \tag{16a}$$

of this matrix as a product of triangular multipliers

$$\mathbf{n} = \left\{ n_{ij} \right\}_{i,j=1}^{M}, \quad \mathbf{h} = \left\{ h_{ij} \right\}_{i,j=1}^{M}, \quad n_{ij} = h_{ij} = 0, \ j > i; \ \ n_{ii} > 0, \ h_{ii} > 0. \tag{16b}$$

When, in addition, $M \times M$ **h.p.d. Toeplitz** matrix $\boldsymbol{\rho} = \left\{ \rho_{ij} \right\}_{i,j=1}^{M}$ (15) is a **CM** of **AR**-$p<M$ process, the representation (16) is transformed to the form [3]

$$\mathbf{n}_b \cdot \mathbf{n}_b^* = \boldsymbol{\Omega}_b = \mathbf{h}_b^* \cdot \mathbf{h}_b, \tag{17}$$

where $\mathbf{h}_b$ and $\mathbf{n}_b$ are lower triangular band [6, 7] $M \times M$ matrices with band width $zz = p+1$ and real positive diagonal elements, and $\boldsymbol{\Omega}_b$ is **h.p.d.** band $M \times M$ matrix with band width $z = 2 \cdot p + 1$ (Fig. 5).

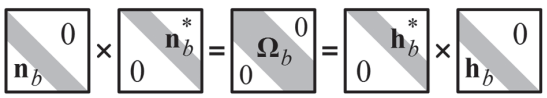

Fig. 5. Cholesky factorization of **h.p.d.** matrix $\boldsymbol{\Omega}_b$

The connection between matrices $\boldsymbol{\Omega}_b$ (17) and $\boldsymbol{\rho}$ (15) is described in details in [3, 8]. Particularly, it is shown that for **h.p.d.** Toeplitz matrix $\boldsymbol{\rho}$ matrix $\boldsymbol{\Omega}_b$ is **h.p.d.** persymmetrical, i.e. satisfies the equality [7]

$$\boldsymbol{\Omega}_b = \boldsymbol{\Pi} \cdot \boldsymbol{\Omega}_b^T \cdot \boldsymbol{\Pi} = \boldsymbol{\Pi} \cdot \boldsymbol{\Omega}_b^{\sim} \cdot \boldsymbol{\Pi}, \ \ \boldsymbol{\Pi} = \boldsymbol{\Pi}^T = \boldsymbol{\Pi}^{-1} \tag{18}$$

and coincides with a result of its "rotation" with respect to the secondary diagonal.

Here, $\boldsymbol{\Pi}$ is symmetrical orthogonal permutation matrix with units occupying its secondary diagonal and zeros occupying other positions, superscripts (~) and (T) are symbols of complex conjugation and transposition, respectively.

The consequent from (18) are the equalities

$$\mathbf{h}_b = \boldsymbol{\Pi} \cdot \mathbf{n}_b^T \cdot \boldsymbol{\Pi}, \quad \mathbf{n}_b = \boldsymbol{\Pi} \cdot \mathbf{h}_b^T \cdot \boldsymbol{\Pi}, \tag{19}$$

which mean that matrix $\mathbf{h}_b$ ($\mathbf{n}_b$) coincides with a result of matrix $\mathbf{n}_b$ ($\mathbf{h}_b$) "rotation" with respect to its secondary diagonal. In this connection, matrix $\mathbf{h}_b$ defines unambiguously all matrices in (17).

The "genesis" of many known [4, 5] and new parametric **SE** methods is explained by rigorously proven in [9] properties of matrices (17). These properties can be formulated as follows.

1. The lower triangular corner $(p+1) \times (p+1)$ submatrix of matrix $\mathbf{h}_b$ is the lower triangular multiplier $\mathbf{h}^{(p+1)}$ of matrix (14e)

$$\boldsymbol{\Omega}^{(p+1)} = \mathbf{h}^{(p+1)^*} \cdot \mathbf{h}^{(p+1)} = \left(\boldsymbol{\rho}^{(p+1)} \right)^{-1}. \tag{20}$$

2. All the rows located within a band of width $(p+1)$ are identical and coincide with the last row of corner submatrix $\mathbf{h}^{(p+1)}$.

3. This last row coincides with the **IR** of whitening filter for **AR**-$p<M$ process.

This can be verified, using persymmetry of **CM** $\boldsymbol{\rho}^{(p+1)} = \boldsymbol{\Pi} \cdot \boldsymbol{\rho}^{(p+1)^{\sim}} \cdot \boldsymbol{\Pi}$, which allows to rewrite the equation (14a) in the form

$$\boldsymbol{\beta}^* \cdot \boldsymbol{\rho}^{(p+1)} = C \cdot \mathbf{e}_{p+1}^{(p+1)^*}, \quad \boldsymbol{\beta}^* = \left\{ \beta_\ell \right\}_{\ell=1}^{p+1} = \boldsymbol{\alpha}^T \cdot \boldsymbol{\Pi} = C \cdot \mathbf{e}_{p+1}^{(p+1)^*} \cdot \boldsymbol{\Omega}^{(p+1)}. \tag{21}$$

The **EFR** of filer with **IR** $\boldsymbol{\beta}^*$ equals to

$$\mathrm{k_p}(\mathrm{f}) = \left| \boldsymbol{\beta}^* \cdot \mathbf{x}_{p+1}(\mathrm{f}) \right|^2 = \left| \boldsymbol{\alpha}^* \cdot \boldsymbol{\Pi} \cdot \mathbf{x}_{p+1}^{\sim}(\mathrm{f}) \right|^2 = \left| \boldsymbol{\alpha}^* \cdot e^{-j \cdot 2 \cdot \pi \cdot \mathrm{f} \cdot (p+2)} \cdot \mathbf{x}_{p+1}(\mathrm{f}) \right|^2 = \left| \boldsymbol{\alpha}^* \cdot \mathbf{x}_{p+1}(\mathrm{f}) \right|^2, \tag{22}$$

i.e. coincides with (13). Therefore, Fig. 6 filter with **IR** $\boldsymbol{\beta}^*$ is also the whitening one.

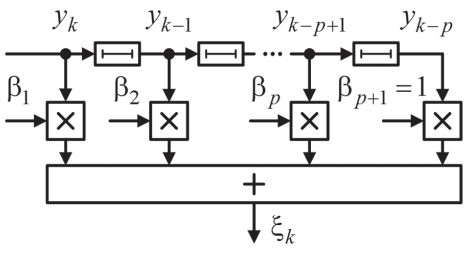

Fig. 6. Whitening filter for **AR**-p process

By virtue of (20), its **IR** is associated by equality

$$\boldsymbol{\beta}^{*} = C \cdot \mathbf{e}_{p+1}^{(p+1)^{*}} \cdot \mathbf{h}^{(p+1)^{*}} \cdot \mathbf{h}^{(p+1)} = \\ = C \cdot h_{p+1}^{(p+1)} \cdot \mathbf{h}_{p+1}^{(p+1)^{*}} \quad (23)$$

with $(p+1)$-variate last row $\mathbf{h}_{p+1}^{(p+1)^{*}} = \left\{ h_{\ell}^{(p+1)} \right\}_{\ell=1}^{p+1}$ of lower triangular matrix $\mathbf{h}^{(p+1)}$. Due to persymmetry of the matrix $\boldsymbol{\Omega}^{(p+1)}$ (20), (14e)

$$h_{p+1}^{(p+1)} = \sqrt{\omega_{p+1,p+1}^{(p+1)}} = \sqrt{\omega_{11}^{(p+1)}} = 1/\sqrt{C}, \quad (24)$$

and, therefore, the last row of matrix $\mathbf{h}^{(p+1)}$ equals

$$\mathbf{h}_{p+1}^{(p+1)^{*}} = 1/\sqrt{C} \cdot \boldsymbol{\beta}^{*} = \sqrt{C} \cdot \mathbf{e}_{p+1}^{(p+1)^{*}} \cdot \boldsymbol{\Omega}^{(p+1)}. \quad (25)$$

The filter with the **IR** (25) has the **EFR**

$$\mathrm{k_p}(\mathrm{f}) = \left| \mathbf{h}_{p+1}^{(p+1)^{*}} \cdot \mathbf{x}_{p+1}(\mathrm{f}) \right|^{2} = 1/s(\mathrm{f}), \quad (26a)$$

what proves the property **3** of the matrix $\mathbf{h}_b$ (17).

By virtue of this property and property **2**,

$$\left| p_{\ell}(\mathrm{f}) \right|^{2} = 1/s(\mathrm{f}), \quad \ell \in p+1, M, \quad (26b)$$

where $p_{\ell}(\mathrm{f})$, $\ell \in 1, M$ is the ℓth element of vector

$$\mathbf{p}(\mathrm{f}) = \left\{ p_{\ell}(\mathrm{f}) \right\}_{\ell=1}^{M} = \mathbf{h} \cdot \mathbf{x}(\mathrm{f}). \quad (26c)$$

Thereby, the filter with $M \times M$ matrix impulse response (**MIR**) $\mathbf{h} = \mathbf{h}_b$ (17) contains $M - p$ whitening filters of size $(p+1)$ (Fig. 6) for **AR**-$p < M$ process. The **IR**s of these filters are equal to the rows $\mathbf{h}_{\ell}^{*}$ of matrix $\mathbf{h}$ with numbers $\ell \in p+1, M$. Considered situation is equivalent to that, when a single $(p+1)$-variate filter is available, which processes whole M-element burst in a "sliding window" mode.

Analogously, by virtue of (19),

$$\left| q_{\ell}(\mathrm{f}) \right|^{2} = 1/s(\mathrm{f}), \quad \ell \in 1, M-p, \quad (26d)$$

where $q_{\ell}(\mathrm{f})$, $\ell \in 1, M$ is the ℓth element of vector

$$\mathbf{q}(\mathrm{f}) = \left\{ q_{\ell}(\mathrm{f}) \right\}_{\ell=1}^{M} = \mathbf{n}^{*} \cdot \mathbf{x}(\mathrm{f}). \quad (26e)$$

F. The properties **1 – 3** of the matrix $\mathbf{h}_b$ define also the important properties of band matrix $\boldsymbol{\Omega}_b$ (17) (Fig. 5). They consist in following [9].

1. The first ($\boldsymbol{\Omega}_{b1}^{*}$) and the last ($\boldsymbol{\Omega}_{bM}^{*}$) rows of matrix $\boldsymbol{\Omega}_b$ are proportional to **IR**s of whitening filters with **EFR**

$$\mathrm{k_p}(\mathrm{f}) = \left| \boldsymbol{\Omega}_{b1}^{*} \cdot \mathbf{x}(\mathrm{f}) \right|^{2} = \left| \boldsymbol{\Omega}_{bM}^{*} \cdot \mathbf{x}(\mathrm{f}) \right|^{2} = c/s(\mathrm{f}), \\ c = \omega_{MM}^{(b)} = \omega_{11}^{(b)} = 1/C. \quad (27)$$

2. The rows $\boldsymbol{\omega}_{p+\ell}^{*} = \left\{ \omega_{p+\ell,i} \right\}_{i=\ell}^{2 \cdot p+\ell}$, $\ell \in 1, M-2 \cdot p$ of matrix $\boldsymbol{\Omega}_b$ (17) from the $(p+1)$st to $(M-p)$th inclusive, being located within the band of width $(2 \cdot p+1)$, are identical:

$$\boldsymbol{\omega}_{p+\ell}^{*} = \boldsymbol{\omega}_{p+1}^{*} = \left\{ \omega_{p+1,i} \right\}_{i=1}^{2 \cdot p+1}, \quad \ell \in 1, M-2 \cdot p. \quad (28)$$

3. These rows coincide with **IR** of **inverse** filter with **EFR**

$$\mathrm{k_p}(\mathrm{f}) = \left| \boldsymbol{\omega}_{p+\ell}^{*} \cdot \mathbf{x}_{2 \cdot p+1}(\mathrm{f}) \right|^{2} = 1/s^{2}(\mathrm{f}). \quad (29a)$$

By virtue of this property and property **2**,

$$\left| r_{\ell}(\mathrm{f}) \right|^{2} = 1/s^{2}(\mathrm{f}), \quad \ell \in p+1, M-p, \quad (29b)$$

where $r_{\ell}(\mathrm{f})$, $\ell \in 1, M$ is the ℓth element of vector

$$\mathbf{r}(\mathrm{f}) = \left\{ r_{\ell}(\mathrm{f}) \right\}_{\ell=1}^{M} = \boldsymbol{\Omega} \cdot \mathbf{x}(\mathrm{f}). \quad (29c)$$

This result is quite natural, because transition from **MIR** $\mathbf{h}_b$ to **MIR** $\boldsymbol{\Omega}_b = \mathbf{h}_b^{*} \cdot \mathbf{h}_b$ is equivalent to consecutive connection of Fig. 6 filters and so to multiplication of their equal **EFR**s (26a). This effect leads also to consecutive connection of two filters, shown in Fig. 4, with $(p+1)$-variate **IR**s, which are the nonzero elements of the first row of upper triangular matrix $\mathbf{n}_b^{*}$ (Fig. 5).

The effect of spectrum inversion could be achieved also by consecutive connection of whitening filters shown in Fig. 4 and Fig. 6. It results from application of connections (19) in (17).

Thereby, the filter with $M \times M$ **MIR** $\boldsymbol{\Omega}_b$ (17) contains two whitening filters for **AR**-$p < M$ processes with $(p+1)$-variate **IR**s $\boldsymbol{\Omega}_{b1}^{*}$ and $\boldsymbol{\Omega}_{bM}^{*}$, and $M - 2 \cdot p$ inverse filters for **AR**-$p \le (M-1)/2$ processes with $(2 \cdot p+1)$-variate **IR**s (28). When $M \ge 2 \cdot p+1$, the rest rows of matrix $\boldsymbol{\Omega}_b$ have a sense of **IR**s of "over-whitening" ("sub-inverse") filters with **EFR**

$$\mathrm{k_p}(\mathrm{f}) = \left| r_{\ell}(\mathrm{f}) \right|^{2} \approx 1/s^{\gamma}(\mathrm{f}), \\ 1 < \gamma < 2; \quad \ell \in 2, p, \quad \ell \in M-p+1, M-1. \quad (30)$$

Such **EFR**s belong to two consecutively connected filters of Fig. 4 or (and) Fig. 6, such that the size zz of one of them is less than $p+1$.

It is obvious, that increasing further the number of whitening or inverse filters one can obtain **EFR**s of kind (8), which are inversely proportional to arbitrary power of input process spectrum.

G. The foregoing consideration allows to disclose from unified positions the essence of majority of known parametric non-eigenstructural **SE** methods, which were synthesized previously based on various approaches, to prove their correction caused by the specificity of problems of continuous spectra reproduction, and to propose new modifications with practically useful properties.

For all the diversity of spectral functions (**SF**) of **SE** methods under consideration, their common feature is a combining of squared absolute values of elements of the vectors

$$\mathbf{p}(\mathrm{f}) = \left\{ p_{\ell}(\mathrm{f}) \right\}_{\ell=1}^{M} = \mathbf{h} \cdot \mathbf{x}(\mathrm{f}), \\ \mathbf{q}(\mathrm{f}) = \left\{ q_{\ell}(\mathrm{f}) \right\}_{\ell=1}^{M} = \mathbf{n}^{*} \cdot \mathbf{x}(\mathrm{f}), \\ \mathbf{r}(\mathrm{f}) = \left\{ r_{\ell}(\mathrm{f}) \right\}_{\ell=1}^{M} = \boldsymbol{\Omega} \cdot \mathbf{x}(\mathrm{f}). \quad (31)$$

The way of combination distinguishes one method from the other. At stages of disclosure of these combinations' essence, their correction and rationale of new variants, we suppose, without special reservations, that for respective elements of these vectors the equalities (26b), (26d), (29b) are true. The real distinctions from them belong to the mismatch factors of filter and input process. Their impact is analyzed separately.

H. For all the **SE** methods under consideration, a basic method is the "**linear prediction**" (**LP**) one [1, 4, 5] with **SF**

$$s_{\mathrm{LP}}(\mathrm{f}) = 1 \Big/ \left| r_{\ell}(\mathrm{f}) \right|, \quad \ell = \left[(M+1)/2 \right]. \qquad (32a)$$

Two kinds of **LP** method have **SF**s $s_{\mathrm{ME1}}(\mathrm{f}) = \omega_{MM} \Big/ \left| r_M(\mathrm{f}) \right|^2$ and $s_{\mathrm{ME2}}(\mathrm{f}) = \omega_{11} \Big/ \left| r_1(\mathrm{f}) \right|^2$, and are referred to as "**maximum entropy**" (**ME**) **Burg** method.

Since $r_M(\mathrm{f}) = \sqrt{\omega_{MM}} \cdot p_M(\mathrm{f})$, $r_1(\mathrm{f}) = \sqrt{\omega_{11}} \cdot q_1(\mathrm{f})$ these **SF**s could be rewritten in more simple form

$$s_{\mathrm{ME1}}(\mathrm{f}) = 1 \Big/ \left| p_M(\mathrm{f}) \right|^2, \; s_{\mathrm{ME2}}(\mathrm{f}) = 1 \Big/ \left| q_1(\mathrm{f}) \right|^2. \quad (32b)$$

The essence of **SF**s (32a), (32b) is obvious. In accordance with properties (26), (29), they represent the input process spectrum, being formed by Fig. 1b **GSA** with different **IR**s – the central ($\ell = \left[(M+1)/2 \right]$) row of matrix **Ω**, and "edge" ($\ell = M$, $\ell = 1$) rows of matrices **h** and $\mathbf{n}^*$ (16).

Note, that, in quasi-harmonic **SE** problems, more computationally simple square of **SF** $s_{\mathrm{LP}}(\mathrm{f})$ (32a) is usually understood as the **SF** of **LP** method [5]. Such a representation increases a contrast between the peaks in analyzed spectrum of harmonics and, therefore, is completely permissible in these problems. However, it is unacceptable in problem of reproduction of continuous spectra of reflections from **MF**, because it potentially corresponds not to the spectrum, but to the square of sought input process spectrum.

Now, let's consider the combinations of basic **SF**s. The best known is the "**minimum variance**" (**MV**) **Capon** method [4, 5] with **SF**

$$s_{\mathrm{MV}}(\mathrm{f}) = M \Big/ \left(\mathbf{x}^*(\mathrm{f}) \cdot \mathbf{\Omega} \cdot \mathbf{x}(\mathrm{f}) \right),$$

which, due to (16), (26), is representable as [10, 11]

$$s_{\mathrm{MV}}(\mathrm{f}) = \left(\frac{1}{M} \cdot \sum_{m=1}^{M} \left| p_m(\mathrm{f}) \right|^2 \right)^{-1} = \left(\frac{1}{M} \cdot \sum_{m=1}^{M} \left| q_{M+1-m}(\mathrm{f}) \right|^2 \right)^{-1}. \qquad (32c)$$

The denominators of these **SF**s are the arithmetic mean of **EFR**s of filters with **IR**s, which equal to all rows of triangular matrices **h** and $\mathbf{n}^*$. Thereby, the **EFR**s of whitening ($m \in p+1, M$) filters as well as **EFR**s of "sub-whitening" ($m \in 1, p$) ones are averaged here. In this connection, **SF** (32c) differs from the spectrum of input process and therefore reproduces it potentially worse than previous **SF**s. However, this does not mean that such relation between these **SF**s will remain in "adaptive" situation.

It is true also for "**thermal noise**" (**TN**) method with **SF**

$$s_{\mathrm{TN}}(\mathrm{f}) = M \Big/ \left(\mathbf{x}^*(\mathrm{f}) \cdot \mathbf{\Omega}^2 \cdot \mathbf{x}(\mathrm{f}) \right),$$

whose variants for continuous spectra reproduction are

$$s_{\mathrm{TN1}}(\mathrm{f}) = \left(\sqrt{\frac{1}{M} \cdot \sum_{m=1}^{M} \left| r_m(\mathrm{f}) \right|^2} \right)^{-1}, \qquad (32d)$$

$$s_{\mathrm{TN2}}(\mathrm{f}) = \left(\frac{1}{M} \cdot \sum_{m=1}^{M} \left| r_m(\mathrm{f}) \right| \right)^{-1}. \qquad (32e)$$

The first of them contains in its denominator the square root from arithmetic mean of **EFR**s of filters with **IR**s, which are equal to all rows of matrix **Ω**. Since, in this case, the **EFR**s of inverse ($m \in p+1, M-p$), "sub-inverse" ($m \in 2, p$, $m \in M-p+1, M-1$) and whitening ($m = 1$, $m = M$) filters are averaged, the radical expression differs from inverse filter **EFR**, and its square root differs from whitening filter **EFR**. Due to this fact, the **SF** (32d) potentially will reproduce input spectrum worse than **SF**s (32a), (32b).

The denominator of the second **SF** (32e), being the arithmetic mean of **EFR**s of "sub-whitening" and whitening ($m \in p+1, M-p$) filters, potentially will reproduce input spectrum worse than the basic **SF**s.

For the **SF** of **Borgiotti – Lagunas** (**BL**) method

$$s_{\mathrm{BL}}(\mathrm{f}) = \frac{\mathbf{x}^*(\mathrm{f}) \cdot \mathbf{\Omega} \cdot \mathbf{x}(\mathrm{f})}{\mathbf{x}^*(\mathrm{f}) \cdot \mathbf{\Omega}^2 \cdot \mathbf{x}(\mathrm{f})} = \frac{s_{\mathrm{TN}}(\mathrm{f})}{s_{\mathrm{MV}}(\mathrm{f})},$$

following representations are allowable

$$s_{\mathrm{BL}}(\mathrm{f}) = \frac{\sum_{m=1}^{M} \left| p_m(\mathrm{f}) \right|^2}{\sum_{m=1}^{M} \left| r_m(\mathrm{f}) \right|^2} = \frac{\sum_{m=1}^{M} \left| q_m(\mathrm{f}) \right|^2}{\sum_{m=1}^{M} \left| r_m(\mathrm{f}) \right|^2}. \qquad (32f)$$

Here, accurate within factor M, the numerator is a rough approximation of whitening filter **EFR** (being inverse to input process spectrum), and the denominator is a rough approximation of inverse filter **EFR**. Therefore, the whole fraction also approximates a sought spectrum, but with a quality being potentially inferior to the quality of basic **SF**s.

Higher quality could be potentially expected from the "**modified Capon**'s **algorithm**" (**MCA**) [10, 11] with **SF**

$$s_{\mathrm{MCA}}(\mathrm{f}) = \frac{s_{\mathrm{LP}}^2(\mathrm{f})}{s_{\mathrm{MV}}(\mathrm{f})} = \frac{\frac{1}{M} \cdot \sum_{m=1}^{M} \left| p_m(\mathrm{f}) \right|^2}{\left| r_{(M+1)/2}(\mathrm{f}) \right|^2} = \frac{\frac{1}{M} \cdot \sum_{m=1}^{M} \left| q_m(\mathrm{f}) \right|^2}{\left| r_{(M+1)/2}(\mathrm{f}) \right|^2}, \qquad (32g)$$

whose numerator approximates the whitening filter **EFR** (being inverse to input process spectrum) with the same accuracy as the numerator of **SF** (32f) of **BL** method provides; at the same time, the denominator here theoretically exactly coincides with the inverse filter **EFR** (being inverse to square of this spectrum).

I. The **SF**s of parametric **SE** methods are not limited to cited above ones. Their names reflect the variety of approaches, based on which each method could be synthesized and interpreted. This could be clearly observed in many literary sources, where the same **SF**s are synthesized in different ways, have various names and interpretations.

Above, the approach is developed, which is based on purposeful taking into account of connections between sought spectrum of input process and **IR**s being the rows of **CM**-inverse matrix or its triangular multipliers. This approach does not contradict in any way with the known approaches, but supplements them, enables

uniform and quite simple explanation of properties of various **SF**s, and, what is more important, allows to "see" practically useful modifications of these **SF**s.

Particularly, one can attribute to them the "**intermediate**" **SF**s [11]

$$s_{\text{int}1}(\text{f}) = \frac{M_e}{\sum\limits_{m=\chi\cdot M}^{M} \left| p_m(\text{f}) \right|^2}, \quad M_e = M\cdot(1-\chi)+1, \quad (32\text{h})$$

$$s_{\text{int}2}(\text{f}) = \frac{M_e}{\sum\limits_{m=\chi\cdot M}^{M} \left| q_{M+1-m}(\text{f}) \right|^2}, \quad (32\text{i})$$

$$M_e = M\cdot(1-\chi)+1,$$

$$s_{\text{int}3}(\text{f}) = \frac{1}{\sqrt{\frac{1}{N_e}\cdot\sum\limits_{m=beg}^{end} \left| r_m(\text{f}) \right|^2}},$$

$$beg = \left[\tau\cdot\frac{M+1}{2}\right], \quad end = M - beg + 1, \quad (32\text{j})$$

$$N_e = end - beg + 1.$$

Here, M_e and N_e are the numbers of accumulated elements of vectors (31). Their values are regulated by the "factors of burst size utilization"

$$\chi \in 1/M, 1 \quad \text{and} \quad \tau \in 2/(M+1), 1. \quad (33)$$

For minimum values $\chi = 1/M$ and $\tau = 2/(M+1)$, $M_e = N_e = M$, so the **SF**s (32h), (32i) are transformed to **SF** (32c) of **MV Capon** method, and the **SF** (32j) is transformed to **SF** (32d) of **TN** method. For maximum values $\chi = \tau = 1$, $M_e = 1$ and $N_e = 2$ (1) for even (odd) M values. In this case, **SF**s (32h), (32i) are transformed to **SF** (32b) of **ME Burg** method, and the **SF** (32j) is transformed to **SF** (32a) of **LP** method.

The "intermediate" variants of **SF**s (32e) – (32g) could be constructed in the same way.

The essence of "intermediate" **SF**s consists in increasing of relative part of "homogeneous" **EFR**s, which form the resultant spectrum. At this expense, one can expect higher "extreme" possibilities of **SE** than at maximum number of summable "heterogeneous" **EFR**s, and lower, than at minimum number of these **EFR**s, level of fluctuations in "adaptive" situation.

J. The assumptions about input process, which are used to synthesize considered known and new parametric **SE** methods, are fulfilled in practice with one or another accuracy only. Particularly, the process of main interest is always observed in a mixture with receiver noise. Such a mixture is not the **AR**-process, even when external process is **AR** one. The *a priori* unknown order p of **AR**-process could exceed the size M of whitening or inverse filter, what will additionally increase the **SE** errors. Under real conditions of *a priori* uncertainty, the errors of spectrum reproduction will be much higher due to the errors of estimation of input process' parameters, which are caused by the finite size of training sample, being used for the estimation. Therefore the level of practical acceptability of **SE** methods will essentially depend on their sensitivity to the impact of listed and a number of other factors typical for real conditions.

CONCLUSIONS

1. The known and new parametric spectral estimation (**SE**) methods have spectral functions (**SF**) being inversely proportional to respective degrees of energy frequency responses (**EFR**) of whitening (inverse) filters or to different-kind combinations of such an **EFR**s.

2. Linear whitening and inverse filters for order $p \geq 1$ autoregressive processes, which approximate the reflections from meteorological formations (**MF**), have impulse responses (**IR**), which are determined by respective rows (columns) of matrix **Ω**, being inverse to covariance matrix (**CM**) of M-variate vector consisting of **MF** samples, or by rows of matrix **Ω** **Cholesky** multipliers. If **IR**s of filters of size $M > p$ are proportional to the $(p+1)$st ... Mth (1 st ... $(M-p)$ th) rows of lower (upper) right triangular multiplier of matrix **Ω**, then such a filters "whiten" input process' spectrum. If **IR**s of filters of size $M > 2\cdot p$ are proportional to the first or the last rows of matrix **Ω**, then such a filters "whiten" input process' spectrum also. Moreover, if **IR**s of filters of size $M > 2\cdot p$ are proportional to the $(p+1)$st ... $(M-p)$ th rows of matrix **Ω**, then such a filters "invert" input process' spectrum. When filter size is another or when other rows of considered matrices are used as the filter's impulse response, then a resultant filter "quasi-whitens" or "over-whitens" ("sub-inverts") **MF** spectrum.

3. Transforming a vector, whose elements are samples of complex harmonic of analyzed frequency, in a whitening or inverse filter with matrix impulse response (**MIR**), being proportional to triangular **Cholesky** multiplier of **CM**-inverse matrix or this inverse matrix in whole, and combining squared absolute values of elements of the transformed vector, one can obtain spectral functions for different parametric **SE** methods. The distinction between these methods is captured by a way, in what the elements of vector of filter's output signal are combined. Particularly, averaging all the components of vector of whitening filter output signals, one can obtain the **SF** of "minimum variance" **Capon** method. Using only the last component of this vector, one can obtain the **SF** of "maximum entropy" **Burg** method.

4. The filter reproduces practically precisely an input process spectrum, when their parameters are fully matched. In practice, the parameters mismatch is inevitable. It could be caused by the unconformity of filter size M and order p of its input signal, internal receiver noise, and errors in estimation of parameters of input signals' **CM**. The filters, which imply spectrum inversion, are the most sensitive to the mismatches of the first two kinds. It is planned to prepare a separate publication devoted to investigation of impact of mismatches of the most important kind, namely, errors of filter parameters estimation caused by finite size of training sample available for this purpose.

References

[1] Jaynes E. T. 1982, 'On the rationale of maximum-entropy methods', *IEEE Proc.* vol. 70, no. 9, 939–952.

[2] Yaglom A. M. 1981, *Correlation Theory of Stationary Random Functions with Examples from Meteorology*, Gidrometeoizdat, Leningrad, in Russian.

[3] Jenkins G. M., and Watts D. G. 1969, *Spectral Analysis and Its Applications*, Holden-Day, London.

[4] Stoica P., and Moses R. L. 1997, *Introduction to Spectral Analysis*, Prentice Hall, Upper Saddle River, NJ.

[5] Marple S. L., Jr. 1987, *Digital Spectral Analysis with Applications*, Prentice Hal.

[6] Strang G. 1976, *Linear Algebra and Its Applications*, Academic Press.

[7] Voevodin V. V., and Kuznetsov Yu. A. 1984, *Matrices and Computations*, Nauka, Chief editorial office of physical and mathematical literature, Moscow, in Russian.

[8] Lekhovytskiy D. I. 1992, 'Generalised Levinson algorithm and universal lattice filters', *Proc VUZ Radiophysics* vol. 35, no. 9–10, 790–808, in Russian.

[9] Lekhovytskiy D. I., Rachkov D. S., Semeniaka A. V., and Atamanskiy D. V. 2011, 'Parametric methods for spectrum estimation of reflections from meteorological formations', *Information Processing Systems* no. 5 (95), 67–78, in Russian.

[10] Lekhovytskiy D. I., Flexer P. M., Atamanskiy D. V., and Kirillov I. G. 2000, 'Statistical analysis of superresolving methods for direction finding of noise radiation sources in antenna arrays under finite size of training sample', *Antennas* no. 2 (45), 23–39, in Russian.

[11] Lekhovytskiy D. I., Atamanskiy D. V., and Kirillov I. G. 2000, 'Kinds of superresolving space-time spectrum analyzers of random signals on the basis of whitening adaptive lattice filters', *Antennas* no. 2 (45), 40–54, in Russian.

Manuscript received January, 23, 2013

David I. Lekhovytskiy, Doctor of Technical Sciences, Professor, Chief research scientist in Research-and-development centre of Kharkiv National University of Radio Electronics. Field of scientific interests – adaptive space-time signal processing against the background of interferences in information systems of different purpose.

Dmytro S. Rachkov, junior research scientist in Research-and-development centre of Kharkiv National University of Radio Electronics. Field of scientific interests – primary interperiod signal processing in Doppler weather radars, unified processors and systems of adaptive signal processing against the background of interferences.

Andrii V. Semeniaka, junior research scientist in Research-and-development centre of Kharkiv National University of Radio Electronics. Field of scientific interests – unified processors and systems of adaptive signal processing against the background of interferences.

Dmytro V. Atamanskiy, Candidate of Technical Sciences, Associate Professor, Doctoral Candidate in Kharkiv Air Force University named after Ivan Kozhedub. Field of scientific interests – adaptive space-time signal processing against the background of interferences in information systems of different purpose.

УДК 621.396.96:551.501.815

О методах оценивания спектров случайных процессов / Д.И. Леховицкий, Д.С. Рачков, А.В. Семеняка, Д.В. Атаманский // Прикладная радиоэлектроника: науч.-техн. журнал. – 2013. – Том 12. – № 1. – С. 64–71.

Анализируется качество воспроизведения непрерывных энергетических спектров случайных процессов классическими непараметрическими (периодограммными, коррелограммными) методами на основе преобразования Фурье и современными (параметрическими) методами спектрального оценивания (СО). Предлагается единый подход к их синтезу, в рамках которого наряду с известными получаются новые методы с практически полезными свойствами. Обсуждаются известный и новый критерии качества воспроизведения непрерывных спектров. По этим критериям сравниваются «предельные» возможности классических и параметрических методов СО в гипотетических условиях точно известной корреляционной матрицы (КМ) анализируемой смеси гауссового случайного процесса и собственного шума приемника, а также их статистические характеристики в реальной «адаптивной» ситуации использования вместо априори неизвестной КМ ее оценок различного вида, формируемых по обучающим выборкам конечного объема. Обосновываются рациональные способы практической реализации перспективных параметрических методов СО на основе адаптивных решетчатых фильтров (АРФ).

Ключевые слова: непрерывный энергетический спектр, статистический анализ, точность оценивания спектра, интегральный критерий, адаптивный решетчатый фильтр.

Ил. 6. Библиогр.: 11 назв.

УДК 621.396.96:551.501.815

Про методи оцінювання спектрів випадкових процесів / Д.І. Леховицький, Д.С. Рачков, А.В. Семеняка, Д.В. Атаманський // Прикладна радіоелектроніка: наук.-техн. журнал. – 2013. – Том 12. – № 1. – С. 64–71.

Аналізується якість відтворення неперервних енергетичних спектрів випадкових процесів класичними непараметричними (періодограмними, кореляграмними) методами на основі перетворення Фур'є та сучасними (параметричними) методами спектрального оцінювання (СО). Пропонується єдиний підхід до їхнього синтезу, в рамках якого поряд із відомими отримані нові методи з практично корисними властивостями. Обговорюються відомий і новий критерії якості відтворення неперервних спектрів. За цими критеріями порівнюються «граничні» можливості класичних і параметричних методів СО в гіпотетичних умовах точно відомої кореляційної матриці (КМ) суміші гаусового випадкового процесу та власного шуму приймача, а також їхні статистичні характеристики в реальній «адаптивній» ситуації використання замість апріорі невідомої КМ її оцінок різного виду, які формуються за навчаючими вибірками кінцевого об'єму. Обґрунтовуються раціональні способи практичної реалізації перспективних параметричних методів СО на основі адаптивних решітчастих фільтрів (АРФ).

Ключові слова: неперервний енергетичний спектр, статистичний аналіз, точність оцінювання спектра, інтегральний критерій, адаптивний решітчастий фільтр.

Іл. 6. Бібліогр.: 11 найм.

UDC 621.396.96

NON-PARAMETRIC SIGNAL PROCESSING IN NOISE RADAR

R. B. SINITSYN AND F. J. YANOVSKY

Noise radar is one of the most interesting technical and scientific ideas implemented in modern radar design. Nonparametric methods of signal processing, with some loss in efficiency, give us the opportunity of providing the synthesis of procedures that are invariant to changes in the signal form and changes of the interference situation. The use of statistical methods for the noise signal processing is closely linked with the latest digital signal processing achievements, which give us the possibility of simplifying the technical implementation of the noise radar as well as signal processing. Thus the use of digital processing techniques can technically implement the idea of noise radar.

Keywords: Noise radar, permutation statistics, copula, rank, permutations, ambiguity function.

1. INTRODUCTION

Noise radar is one of the most interesting technical and scientific ideas implemented in modern radar design.

Scientific interest in the noise radar is associated with the form of the sounding signal (waveform). Typically, the properties of the sounding signal are connected with its shape, which is characterized by its radar ambiguity function. The form of the ambiguity function is connected with the possibility of simultaneous measurement of spatial coordinates and velocity of the target.

If we use a random process with uniform spectrum (a white noise) as a sounding signal, we can obtain almost a unique form of the ambiguity function, which tends to a delta function. This allows us to make simultaneous measurement of distance and speed with maximum resolution. Certainly, such results can also be obtained by using other signals, but in our opinion, it is essentially more complicated. The selection of the waveform creates a coordinate system in which the radar measurements exist. The choice of a rational system of coordinates simplifies obtaining the necessary resolution.

Radar targets are always observed on the background of random noise, and this requires the use of statistical methods for signal processing. Only the statistical approach allows us to implement scientifically optimal signal processing with a fixed level of error.

Nonparametric methods of signal processing, with some loss in efficiency, give us the opportunity of providing the synthesis of procedures that are invariant to changes in the signal form and changes of the interference situation.

In recent years, these methods have been based on the use of the rank procedures, as well as some relatively new methods, such as kernel estimates of the probability density and on such notion as the copula.

The use of statistical methods of processing for a random sounding signal is natural for the noise radar. This allows us to obtain the most efficient use of statistical and non-parametric methods with a random coordinate system and the random noise generated by the radar.

In this paper we will discuss all possible statistical methods of noise radar signal processing. Among them there are the following.

Classical parametric methods of signal processing. Rank signal processing techniques. Processing methods based on permutation statistics. Processing methods, based on kernel estimates of the probability density, as well as methods using copulas, which enable us to generalize the concept of the ambiguity function.

The use of statistical methods for the noise signal processing is closely linked with the latest digital signal processing achievements, which give us the possibility of simplifying the technical implementation of the noise radar as well as signal processing. Thus the use of digital processing techniques can technically implement the idea of noise radar.

2. GENERAL DETECTION PROBLEM DEFINITION

We can divide the signal space observed by the radar into two areas. In one area, as supposed, there is a useful signal, in the other there is interference: noise or clutter. Signal detection is achieved by using a difference of a multivariate probability density in observed areas. Thus, the task of detection is reduced to checking the hypothesis H_0 about the equality of probability density functions and alternative hypothesis H_1:

$$H_0 : f_S(\mathbf{x}) = f_N(\mathbf{x}) \quad (1)$$

$$H_1 : f_S(\mathbf{x}) \neq f_N(\mathbf{x}), \quad (2)$$

where $f_S(\mathrm{x})$ is a probability density function of a signal in the area where we are trying to find a target, $f_N(\mathrm{x})$ is a probability density function of a received signal in the area where there is no target.

Let us assume that from the samples received from signal and noise (or clutter) areas, it is possible to generate the mixed sample

$$\mathbf{x} = \{x_1, x_2, \ldots, x_m, \ldots, x_n\} \quad (3)$$

where $x_1, x_2, \ldots, x_m$ are samples received from the noise or clutter area, and $x_{m+1}, \ldots, x_n$ are samples received from the signal area. We will suppose that the signal and noise (or clutter) samples are statistically independent.

Then the task of testing the hypothesis is reduced to checking the hypothesis about the form (shape) of the density function of the mixed sample

$$H_0:\ f_0(\mathbf{x})=\prod_{i=1}^{n} f_N(\mathbf{x}) \qquad (4)$$

$$H_1:.\ f_1(\mathbf{x})=\prod_{i=1}^{m} f_N(x_i)\prod_{i=m+1}^{n} f_S(x_i).$$

The problem of the signal detection in this case is reduced to the problem of the form of the probability density function.

3. RANK AND PERMUTATION ALGORITHMS

3.1. Similar Test

If we compare the likelihood function $f_1(\mathrm{x})$ with the solution threshold obtained with the help of the empirical permutation distribution, which is derived by substituting all permutations of the vector x in the likelihood function, we will obtain the most powerful similar test. Such a test has the property of similarity, i.e. a fixed level of error of the first kind. The detection algorithm built on the basis of this test has stability of the false alarm probability.

However, it has an essential disadvantage. The number of all permutations is too great, it increases with the increase of a number of samples and is equal to $n!$. This fact hampers the practical use of the devices, which have been designed on the basis of using the permutation test.

3.2. Permutation Algorithm

Thus, the suggested algorithm for detecting signals is reduced to the following procedure:

The likelihood function from the accepted signal is computed

$$l(\mathbf{x})=\prod_{i=1}^{m} f_N(x_i)\prod_{i=m+1}^{n} f_S(x_i), \qquad (5)$$

which, after some of identical conversions, can be reduced to the following expression

$$l(\mathbf{x})=\prod_{i=1}^{m} f_N(x_i)\prod_{i=m+1}^{n} f_S(x_i)\prod_{i=m+1}^{n}\frac{f_N(x_i)}{f_N(x_i)}= =\prod_{i=1}^{n} f_N(x_i)\prod_{i=m+1}^{n}\frac{f_S(x_i)}{f_N(x_i)} \qquad (6)$$

Let us take into account only those permutations of samples x_i, which require the modification of the statistic $l(\mathbf{x})$. We will remark, that for all permutations of the statistics **x**, the product $\prod_{i=1}^{n} f_N(x_i)$ remains constant. Therefore in the procedure of decision making it is possible not to take into account the whole set of $n!$ permutations, it is enough to consider $\binom{n}{m}=\frac{n!}{m!(n-m)!}$ permutations and the following statistics

$$L(\mathbf{x})=\prod_{i=m+1}^{n}\frac{f_S(x_i)}{f_N(x_i)}=\prod_{i=m+1}^{n}\lambda(x_i), \qquad (7)$$

where $\lambda(x_i)=\frac{f_S(x_i)}{f_N(x_i)}$ are partial likelihood ratios.

Using the statistics $\lambda(x)$, we will suggest the rank test, which is based on permutations of the partial likelihood ratios $\lambda_i=\lambda(x_i)$. We will use the vector statistic

$$\boldsymbol{\lambda}=\{\lambda_1,\lambda_2,\ldots,\lambda_m,\ldots,\lambda_n\}.$$

Variables λ_i are independent and have the same distribution if the hypothesis H_0 is true. We can construct a permutation test using permutations of the variables λ_i but not x_i.

Ranking the variables λ_i we obtain the vector of ranks of variables λ_i

$$\mathbf{r}=\{r_1,r_2,\ldots,r_m,\ldots,r_n\}$$

On the basis of statistic **r** many different rank hypothesis tests and corresponding to them signal detection algorithms can be constructed. For example, a rank test which is similar to the Vilkokson criteria

$$Q_1=\sum_{i=m+1}^{n} r_i.$$

This statistic is not optimal, but has sufficient efficiency, and an algorithm, based on this statistic is attractively simple.

Rank tests are using the empirical distribution function as a functional transform. We suggest using smoothed estimates of this function, among them kernel estimates.

The kernel estimate of a cumulative distribution function is constructed by using of the partial likelihood ratios $\lambda_i=\lambda(x_i)$. The following functions will be used as the kernels

$$K_i(\lambda)=\frac{1}{n}W(\lambda-\lambda_i), \qquad (8)$$

where $W(\lambda)$ is some cumulative distribution function, λ_i is a value of the partial likelihood ratio.

The estimate of a cumulative distribution function for noise area is determined by the expression

$$\widehat{F}(\lambda)=\sum_{i=1}^{n} K_i(\lambda). \qquad (9)$$

After the functional transform we obtain the vector of transformed partial likelihood ratios

$$\mathbf{l}=\{l_1,l_2,\ldots,l_m,\ldots,l_n\},$$

where $l_i=\widehat{F}(\lambda_i)$. Density function of transformed statistics for hypotheses H_0 and H_1 can be calculated, using following approach.

The density function of the vector of the initial samples can be represented as

$$f_l(l_1,l_2,\ldots,l_m,\ldots,l_n)=\prod_{i=1}^{m} f_{Nl}(l_i)\prod_{i=m+1}^{n} f_{Sl}(l_i).$$

The density function of the vector l coordinates l_i is described by the integral

$$f_l(l_i)=\int_{-\infty}^{\infty}\ \ldots\ \int_{-\infty}^{\infty}\prod_{j=1}^{m} f_N(\lambda_j)\cdot f_S(\widehat{F}^{-1}(l_i;\lambda_1,\ldots,\lambda_m))\cdot \frac{1}{\widehat{f}(\widehat{F}^{-1}(l_i;\lambda_1,\ldots,\lambda_m))}d\lambda_1\ldots d\lambda_m, \qquad (10)$$

where $\hat{F}^{-1}(\mathbf{l})$ is the function, inverse to $\hat{F}(\lambda)$, $\hat{f}(\lambda)$ is the derivative of the $\hat{F}(\lambda)$.

When $N \to \infty$ estimate $\hat{F}(\lambda) \to F(\lambda)$

$$f_l(l_i) = \frac{f_S\left\{F^{-1}(l_i)\right\}}{f_N\left\{F^{-1}(l_i)\right\}}.$$

This vector can be used as a statistic for designing an ordinary Neyman-Pearson test and a signal detection algorithm.

For hypothesis H_0 the distribution $f_l(l_i)$ asymptotically tends to the uniform distribution. In the case of the alternate hypothesis H_1 validity the statistics distribution $f_l(l_i)$ of the signal aria elements differs from the distribution of the elements of the noise area. It is determined by the presence of the desired signal.

The decision statistics is defined by the likelihood ratio, which is in this case equal to the likelihood function (Fig. 1.)

$$\ell(l) = \prod_{i=n+1}^{n} f_l(l_i). \qquad (11)$$

If the density function of reflections from the guessed target coincides with the density function of the interference, the density function of references l is asymptotically uniform. Thus, in the case of validity of the hypothesis H_0, i.e. in the no-signal condition the density function is equal to 1. In the case when the hypothesis H_1 is valid (when the desired signal is available) the density function of converted references l also lies in the interval [0,1], but it is not uniform.

The solution about a desired signal is made by comparing $\ell(l)$ with the solution threshold (Fig. 2). This threshold has a constant value and depends only from the false alarm probability for all signal and interference probability densities.

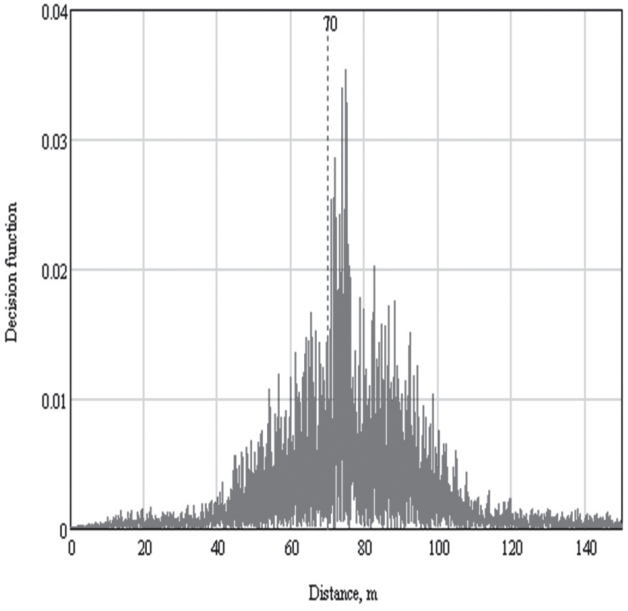

Fig. 1. Dependence of the decision function for the algorithm, based on the kernel estimate from distance. Number of samples is 111891

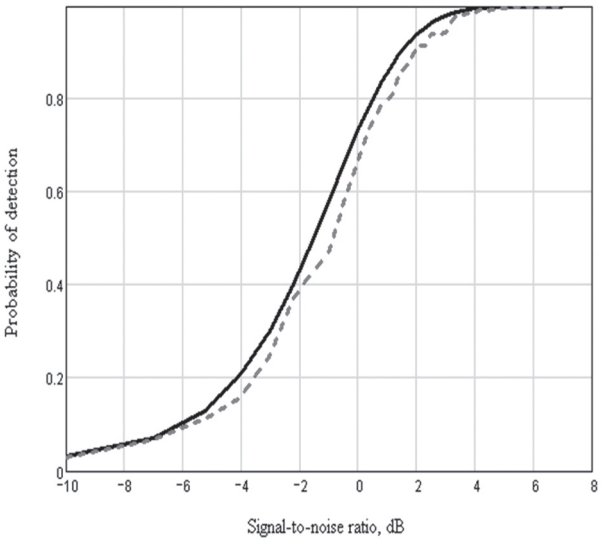

Fig. 2. Dependence of the detection probability on SNR for the algorithm, based on permutations of partial likelihood ratios (the dashed curve) and the optimal algorithm (the solid curve). Number of samples is 16. Size of the noise area is 128. False alarm probability is 0.01

4. COPULA DETECTION ALGORITHM

4.1. Copula Transform

We can transform the vector (x,y) to a new a random variable (x_T, y_T), using two marginal cumulative distribution functions $x_T = F_x(x)$, $y_T = F_y(y)$ as functional transforms. It is easy to prove that vector (x_T, y_T) has uniform distribution if random variables x and y are independent. The bivariate cumulative distribution function of the transformed variables (x_T, y_T) is called a copula of these variables [2] and according to the Sklar's theorem

$$F(x,y) = C(F_x(x), F_y(y)),$$

where $F(x,y)$ is a bivariate cumulative distribution function of (x,y).

The density function, corresponding to the copula $C(x_T, y_T)$ is

$$c(x_T, y_T) = \frac{\partial C(x_T, y_T)}{\partial x_T \partial x_T}.$$

If a useful signal is absent the copula density function has a uniform distribution on $[0, 1]^2$.

If a useful signal is present a copula density function has some other distribution on $[0, 1]^2$.

A copula density function can be estimated using kernel estimates.

Let us replace the cumulative distribution functions $F_x(x)$ and $F_y(y)$ by their estimates $\hat{F}_x(x)$ and $\hat{F}_y(y)$. It is assumed, that if the size of a sample is increased, the estimate converges to a cumulative distribution function. Transformations of the sounding and reflected signals

$$x_{Ti} = \hat{F}_x(x_i), \; y_{Ti} = \hat{F}_y(y_i)$$

will be used later.

4.2. Copula Estimates

The kernel estimates of the cumulative distribution functions will be used as this transform [3], [4].

Thus the estimate of a bivariate copula density function $c(x_T, y_T)$ will look like the total of the kernels $K_i(x_T, y_T)$

$$\hat{c}(x_T, y_T) = \sum_{i=1}^{n} K_i(x_T, y_T), \quad (12)$$

where n is the sample size, which is the basis for finding an estimate.

Let's assume, that the kernels look as follows

$$K_i(x_T, y_T) = \frac{1}{n}\omega(x_T - x_{Ti}, y_T - y_{Ti}), \quad (13)$$

where $\omega(x_T, y_T)$ is some probability density, for example, normal, (x_{Ti}, y_{Ti}) is the sample unit i, which is the basis for an estimate.

For the estimate $\hat{F}_x(x)$ of one-dimensional cumulative distribution function the kernels look as follows

$$P_i(x) = \frac{1}{n}\int_{-\infty}^{x}\int_{-\infty}^{\infty}\omega(u - x_i, v - y_i)dudv. \quad (14)$$

4.3. Decision Rule

To synthesise the decision rule on the basis of **x** and y statistics it is necessary to obtain the density function of these statistics under competing hypotheses H_0 and H_1. The detection procedure is based on testing the hypotheses about the density function of transformed signals on the basis of Neyman – Pearson criterion. In this case, the distribution of a transformed statistics tends to be uniform if we increase a sample size. Thus the distribution of the converted statistics $(\mathbf{x_T}, \mathbf{y_T})$ under the hypothesis H_0 (no target) is asymptotically uniform. Thus testing the hypothesis about the presence of the target is reduced to testing the hypothesis about uniformity of distribution of the transformed statistics and likelihood ratio - to the likelihood function of the statistics $(\mathbf{x_T}, \mathbf{y_T})$. The likelihood function is substituted by its estimate (12) obtained with the help of the kernels, such as (13) and (14)

$$\lambda_T(\mathbf{x}_T, \mathbf{y}_T) = \prod_{i=1}^{n}\hat{c}(x_{Ti}, y_{Ti}), \quad (15)$$

where

$$\hat{c}(x_{Ti}, y_{Ti}) = \sum_{j=1}^{m} K_j(x_{Ti}, y_{Ti}),$$

where m is a sample size of the test statistics obtained on the basis of reflections from the target. After taking the logarithm of expression (15) we obtain the final formula of decision rule enabling us to detect the target

$$\lambda_T(\mathbf{x}_T, \mathbf{y}_T) = \sum_{i=1}^{n}\ln(\hat{c}(x_{Ti}, y_{Ti})). \quad (16)$$

This result can be simply extended to MIMO [8] variant

$$\lambda_T(\mathbf{x}_T, \mathbf{y}_T) = \sum_{k=1}^{m}\sum_{j=1}^{m}\sum_{i=1}^{n}\ln(\hat{c}(x_{Tij}, y_{Tik})).$$

For making a decision $\lambda_T(\mathbf{x}_T, \mathbf{y}_T)$ is compared with the invariable threshold C. The invariability of the threshold for decision making providing stable error probability of first kind, is ensured by the uniform distribution of statistics under the hypothesis H_0. In particular, to simplify the practical realization of the method the kernels are decomposed into a trigonometric series, and the algorithm of fast Fourier transform is used.

The relationship between the detection probability and signal to noise ratio expressed in power units is represented in Fig. 3. These characteristics are obtained as a result of Monte-Carlo simulation, α is the false alarm probability, the sample size is 100.

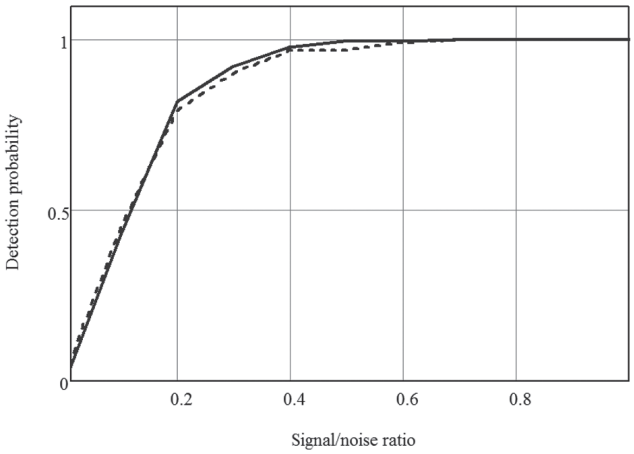

Fig. 3. Performance of detection as a dependence from signal-to-noise ratio . Signal and noise with Gaussian distribution. Solid curve – parametric algorithm, dashed curve – nonparametric algorithm ($\alpha = 0.01, \quad N = 100$)

In Fig. 3 parametric and nonparametric algorithms are presented. As we can see the results for parametric signal processing algorithm are slightly better. But we must understand that simulation was made in the case of the prior certainty of the signal and noise probability densities. In the real situation for unknown signals and noises the nonparametric algorithm must be better.

5. COPULA AMBIGUITY FUNCTION

5.1. Ambiguity Function

The cross-ambiguity function [1] for two random processes $X(t)$ and $Y(t)$ can be defined as an average

$$\chi(\tau, \alpha) = \sqrt{|\alpha|}E\left\{(X(t)) - m_x)(Y^*(\alpha(t-\tau)) - m_y)\right\},$$

where $\alpha = \frac{c-v}{c+v}$ is a scale coefficient, c is the velocity of the wave, v is the target velocity, $Y^*(t)$ is a complex conjugate of the random process $Y(t)$, m_x and m_y are mathematical expectations of $X(t)$ and $Y(t)$. This variant of the ambiguity function can be simply recalculated in the range/velocity coordinates. For the ergodic process we can consider, that the cross-ambiguity function is (17). This expression looks like an ordinary wideband ambiguity function definition for deterministic signals

$$\chi(\tau, \alpha) = \lim_{T\to\infty}\frac{\sqrt{|\alpha|}}{T}\int_0^T (x(t) - m_x)(y^*(\alpha(t-\tau)) - m_y)dt. \quad (17)$$

The example of the calculation of the cross-ambiguity function estimate for the noise acoustic radar is presented in Fig. 4.

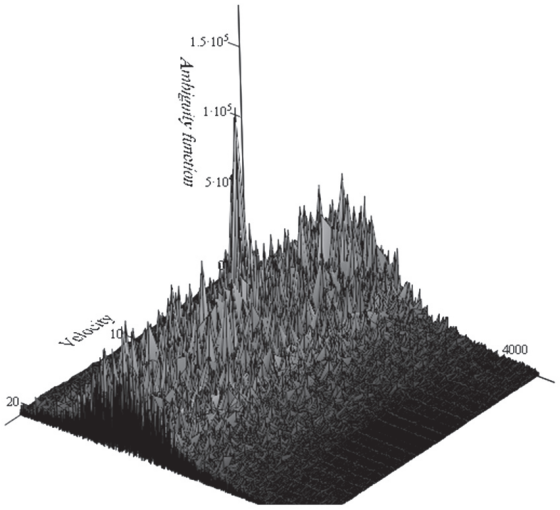

Fig. 4. Estimate of the cross-ambiguity function for the acoustic radar. Range in distance samples and velocity in ADC digits. One digit for velocity is 1 m/s, number 11 corresponds to zero velocity, one digit for distance is equal to 0.0038820862 m

The sounding signal in this radar is a discrete white noise with a normal distribution. The ambiguity function is calculated in range/velocity coordinates. The sampling frequency is 48 kHz.

5.2. Estimates

The kernel estimates of the cumulative distribution functions will be used as this transform. Thus the estimate of a bivariate copula density function $c(x_T, y_T)$ will look like the total of the kernels $K_i(x_T, y_T)$

$$\hat{c}(x_T, y_T) = \sum_{i=1}^{n} K_i(x_T, y_T),$$

where n is the sample size, which is the basis for finding an estimate [3].

The copula kernel estimate, calculated for the signal of the acoustic noise radar(which samples which are shown in Fig. 5), is presented in Fig. 6.

Let's assume, that the kernels look as follows

$$K_i(x_T, y_T) = \frac{1}{n} w(x_T - x_{Ti}, y_T - y_{Ti}),$$

where $w(x_T, y_T)$ is some probability density, for example, normal, (x_{Ti}, y_{Ti}) is the sample unit i, which is the basis for an estimate.

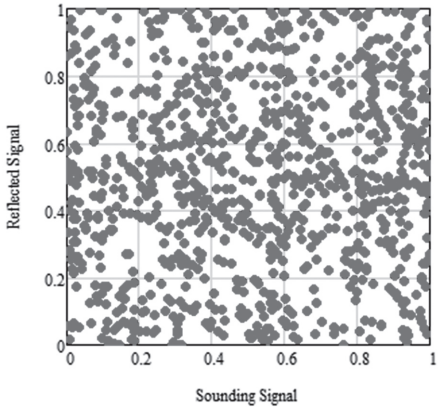

Fig. 5. Sounding and reflected signal samples

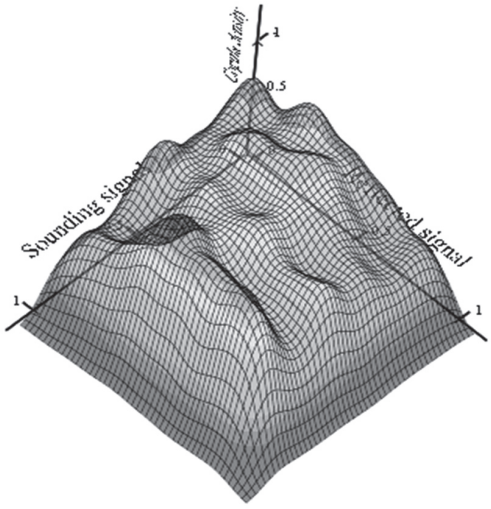

Fig. 6. The kernel estimate of a bivariate copula density for the acoustic radar signal

For the estimate $\hat{F}_x(x)$ of one-dimensional cumulative distribution function the kernels look as follows

$$P_i(x) = \frac{1}{n} \int_{-\infty}^{x} \int_{-\infty}^{\infty} w(u - x_i, v - y_i) du dv .$$

The kernel estimate for the copula itself is presented in Fig. 7.

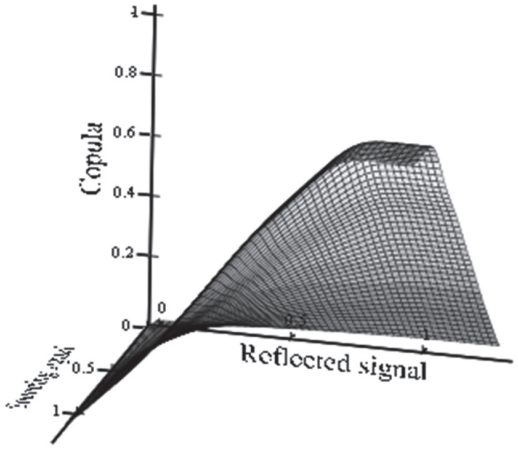

Fig. 7. The kernel estimate of a bivariate copula for acoustic radar signal

5.3. Copula Ambiguity Function

Using the copula density function we can define its copula ambiguity function [9] as a second mixed central moment of the copula density

$$\chi(\tau, \alpha) = \sqrt{|\alpha|} E\{(F_x(X(t)) - m_x)(F_y(Y^*(\alpha(t-\tau))) - m_y)$$

or for the ergodic process

$$\chi(\tau, \alpha) = \lim_{T \to \infty} \frac{\sqrt{|\alpha|}}{T} \int_0^T (F_x(x(t)) - m_u)(F_y^*(y(\alpha(t-\tau))) - m_v) dt.$$

Using the kernel estimates of the cumulative density function we can obtain the copula ambiguity function kernel estimate in some finite time interval

$$\chi(\tau, \alpha) = \sqrt{|\alpha|} \int_{t_1}^{t_2} (\hat{F}_x(x(t)) - m_u)(\hat{F}_y^*(y(\alpha(t-\tau))) - m_v) dt . \quad (18)$$

The authors also are suggesting in heuristic variant of the function (19). In this formula we are using

an estimate of the moment of the second order for the uniform distribution. For obtaining the statistics, which depends from two parameters, we will use an additional functional transform, transforming the copula statistic to a normal distribution

$$\chi(\tau,\alpha)=\sqrt{|\alpha|}\int_{t_1}^{t_2} F_N^{-1}(\hat{F}_x(x(t)))F_N^{-1}(\hat{F}^*_y(y(\alpha(t-\tau))))dt \ ,(19)$$

where F_N^{-1} is an inverse cumulative function of a normal distribution.

With the help of the noise acoustic radar, designed and constructed by authors [4, 5, 6, 7], the copula ambiguity function was measured for real signals. The acoustic radar sounding signal is a wideband random signal with a normal distribution. The signal reflected from the solid object at the distance equal to 70 m from the radar. For this signals the copula ambiguity functions were calculated. The results are presented in Fig. 8 and in Fig. 9.

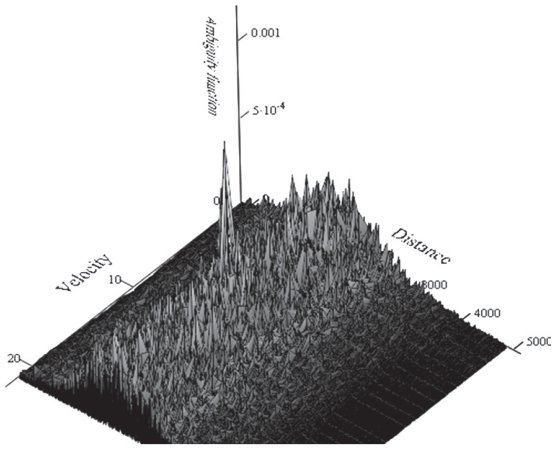

Fig. 8. Estimate of the copula cross-ambiguity function for the acoustic radar. Range in distance samples and velocity in ADC digits. One digit for velocity is 1 m/s, 11 corresponds to zero velocity, one digit for distance is equal to 0.0038820862 m

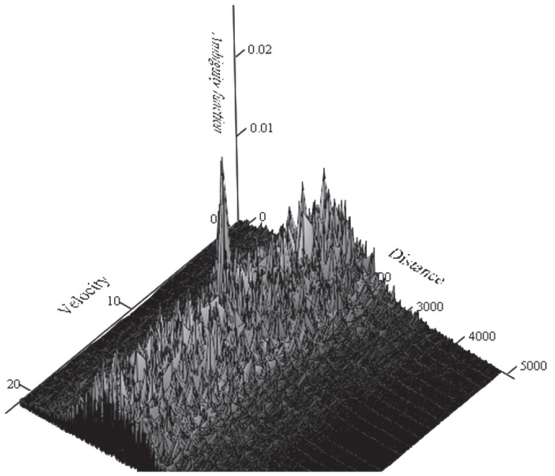

Fig. 9. Estimate of the copula cross-ambiguity function (with an aditional functional transform) for the acoustic radar

The cross section of the ambiguity function in time area (or in distance area) for zero velocity of the target propagation is the correlation function. The result of the calculations is presented in Fig. 10. The same calculations were done for the cross section of the copula ambiguity function. The result is presented in Fig.11.

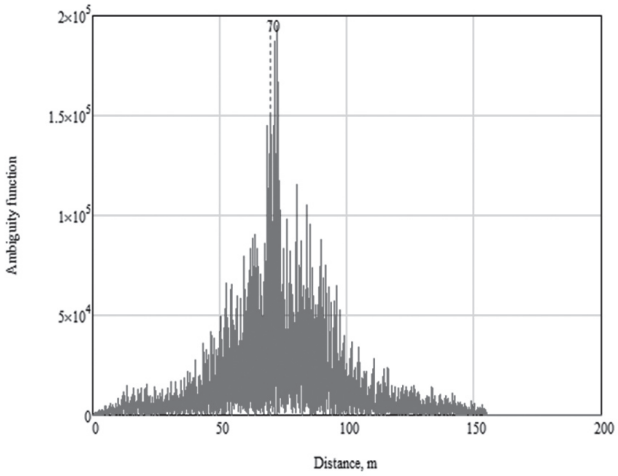

Fig. 10. Estimate of the cross-ambiguity function cross section (cross-correlation function) for the acoustic radar

The shape of the suggested variant of the ambiguity function does not depend on the probability density functions of the sounding and reflected signals. That is why signal detection algorithms, which are based on this notion are distribution free and have a constant level of the false alarm probability. The detection can be done with the help of the simple threshholding of the copula ambiguity function.

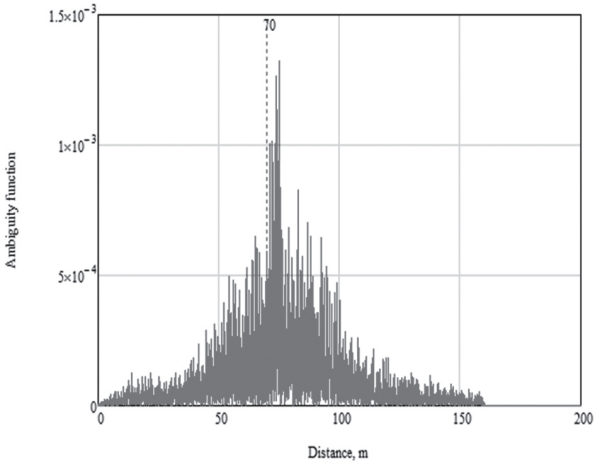

Fig. 11. Estimate of the copula cross-ambiguity function cross section (cross-correlation function) for the acoustic radar

CONCLUSION

In this paper different aspects of the signal processing algorithms for random signal radars were discussed.

We believe that the random signal radar is one of the most interesting types of radar. It combines properties of UWB radar with some additional features, based on random nature of the sounding waveform. This new properties allows us to simplify signal detection algorithms and measure a distance, an azimuth and a target velocity simultaneously with high resolution and accuracy because of the noise sounding waveform. Nonparametric algorithms have wonderful properties of invariance to the group of the noise and signal transforms and stable level of the false

alarm probability. It is important to remember that all these good properties exist only in the case when we have independent samples. The noise signal forms the independent samples because of its nature.

The generalization of the radar ambiguity function has been suggested. In contrast to classically defined ambiguity function, new one does not dependent on the signal PDF. It can be used as a pure measure of the relation between sounding and reflected signals as well as for the analysis of potential properties of waveforms.

References

[1] L. Sibul, L. Ziomek, "Generalised wideband crossambiguity function", *IEEE Int. Conf. on Acoustics, Speech, and Signal Processing, ICASSP'81*, 01/05/1981; 6: pp. 1239–1242.

[2] I. Gijbels, J. Mielniczuc, Estimating the density of a copula function, Comm. Stat. Theory Meth. 19, 2, 1990, pp.445–464.

[3] Zh.M. Bokal, R.B. Sinitsyn, and F.J. Yanovsky, "Generalized Copula Ambiguity Function Application for Radar Signal Processing", *Proc. Microwaves, Radar and Remote Sensing Symposium,* August 25–27, 2011, Kiev, Ukraine, pp. 313 – 316.

[4] R.B. Sinitsyn, F.J. Yanovsky. "Kernel Estimates of the Characteristic Function for Radar Signal Detection", *Proc. 2nd European Radar Conference*, 2005, Paris, pp. 53-56.

[5] R.B. Sinitsyn, F.J. Yanovsky, "Acoustic Noise Atmospheric Radar with Nonparametric Copula Based Signal Processing", *Proc. Statistical Methods of Signal and Data Processing Conf. SMSDP-2010*, Kiev, 2010, pp. 91-94.

[6] R.B. Sinitsyn, "Copula based detection algorithm for MIMO ultrawideband noise radars", *Proc. 6th European Radar Conference*, Rome, 2009, pp. 121-124.

[7] R.B. Sinitsyn, A.J. Beletsky, F.J. Yanovsky, "Noise signal for sodar application" , *Applied Radio Electronics*, Vol. 4, No 1, Kharkov, 2005, pp. 107-110.

[8. J. Li, P. Stoica, MIMO Radar Signal Processing, John Wiley & Sons, 2008, p. 448

[9] R.B. Sinitsyn and F.J. Yanovsky, Copula Ambiguity Function for Wideband Random Radar Signals, The International IEEE Conference on Microwaves, Communications Antennas and Electronic Systems, Tel-Aviv, Israel, November 7-9, 2011, 5 pp.

Manuscript received February, 14, 2013

Rustem B. Sinitsyn, PhD, IEEE Member is Associate Professor at Electronics Department of the National Aviation University, Kiev, Ukraine. His research interests are in statistical processing signals of different nature including noise radar, acoustics, and weather radar, and particularly development and modeling non-parametric algorithms.

Felix J. Yanovsky, PhD, DSc, Professor, Fellow IEEE, Ukraine State Prize Winner is currently Head of Electronics Department of the National Aviation University, Kiev, Ukraine. His current research interests include radar, signal processing, avionics, meteorology, spectral polarimetry, remote sensing and diagnostics of objects and environment, and in particular parametric and nonparametric algorithms of detection, measurement and recognition.

УДК 621.396.96

Непараметрическая обработка сигналов в шумовом радаре / Р.Б. Синицын, Ф.И. Яновский // Прикладная радиоэлектроника: науч.-техн. журнал. – 2013. – Том 12. – № 1. – С. 72–78.

Рассмотрены различные алгоритмы обработки сигнала шумового радиолокатора. Разработана теория и алгоритмы непараметрической обработки сигналов, которые с некоторой потерей эффективности дают возможность обеспечить синтез процедур, обладающих свойством инвариантности по отношению к изменениям формы сигнала и помеховой обстановки. Синтезированные непараметрические алгоритмы обеспечивают также стабильный уровень вероятности ложной тревоги. Указанные свойства существуют только в случае независимых выборок, что в шумовом локаторе обеспечивается естественным образом в силу характера генерируемого шумового сигнала. В работе также предложено обобщение функции неопределенности, которая, в отличие от классической, не зависит от плотности вероятности сигнала и может быть использована как чистая мера связи между зондирующим колебанием и отраженным сигналом. Она также обеспечивает анализ потенциальных свойств зондирующего сигнала. Предложенные статистические методы обработки шумового сигнала в сочетании с новейшими достижениями цифровой обработки обеспечивают упрощение технической реализации шумовой радиолокации.

Ключевые слова: шумовой радиолокатор, статистики перестановок, копула, ранжирование, функция неопределенности.

Ил. 11. Библиогр.: 09 назв.

УДК 621.396.96

Непарамертична обробка сигналів у шумовому радарі / Р.Б. Сініцин, Ф.Й. Яновський // Прикладна радіоелектроніка: наук.-техн. журнал. – 2013. – Том 12. – № 1. – С. 72–78.

Розглянуто різні алгоритми обробки сигналу шумового радіолокатора. Розроблено теорію і алгоритми непараметричної обробки сигналів, які з деякою втратою ефективності дають можливість забезпечити синтез процедур, що мають властивість інваріантності по відношенню до змін форми сигналу і завадової обстановки. Синтезовані непараметричні алгоритми забезпечують також стабільний рівень ймовірності хибної тривоги. Зазначені властивості існують лише в разі незалежних вибірок, що в шумовому локаторі забезпечується природним чином в силу характеру генерованого шумового сигналу. В роботі також запропоновано узагальнення функції невизначеності, яка, на відміну від класичної, не залежить від щільності ймовірності сигналу і може бути використана як чиста міра зв'язку між зондувальним коливанням і відбитим сигналом. Вона також забезпечує аналіз потенційних властивостей зондувального сигналу. Запропоновані статистичні методи обробки шумового сигналу в поєднанні з новітніми досягненнями цифрової обробки забезпечують спрощення технічної реалізації шумової радіолокації.

Ключові слова: шумовий радіолокатор, статистики перестановок, копула, ранжування, функція невизначеності.

Іл. 11. Бібліогр.: 09 найм.

NOISE RADAR DESIGN

UDC 621.37

ULTRA-WIDEBAND PSEUDO-NOISE SENSORS

SACHS, J.; KMEC, M.; FRITSCH, H. C.; HELBIG, M.; HERRMANN, R.; SCHILLING, K.; RAUSCHENBACH, P.

The ultra-wideband (UWB) pseudo-noise (PN) technique merges the circuit simplicity of the pulse technique and the precision of the sine wave method with the LPI performance (low probability of intercept) of noise radar. Binary PN sequences of large bandwidth may be generated and captured with high precision and temporal stability by comparatively simple means. This opens up new high-resolution short-range radar applications. The article introduces the basic working principle, summarizes the state of recent devices, and introduces some key parameters as assistance for device parameterization that is appropriate for an intended application.

Keywords: ultra-wideband, pseudo-noise, M-sequence, Golay-sequence, sub-sampling, Hadamard-transform, impulse response function, frequency response function.

1. INTRODUCTION

The aim of this paper is to give an overview of the recent development state of ultra-wideband (UWB) sensing devices based on pseudo-noise (PN) codes. Since the radio emission of UWB devices is restricted by radio regulation to a very low power level, such sensors are typically found in short range applications, i.e. their range coverage is barely more than some tens or hundreds of meters.

The use of ultra-wideband PN-codes for stimulation of the test scenario brings some advantages, which will be summarized in what follows.

• Binary PN-codes such as an M-sequence have a crest-factor relatively close to unity. Hence, they carry a large amount of energy even if their magnitude is quite small. Thus, PN-codes provide best conditions for large suppression of random perturbations while protecting the sensor electronics and the test objects from strong electric fields. This is especially important, since one often deals with very near field measurements involving e.g. biologic tissue. Furthermore, it also enables monolithic integrated RF-circuits manufactured in a low-cost semiconductor technology.

• Some binary UWB PN-codes may be **easily generated** by high-speed digital shift registers with an appropriate feedback structure (for details on PN-sequences see [1]). The bandwidth of the sounding signal depends on the clock rate of the shift register. The generation of the wideband signal is controlled by a single tone RF-generator which pushes the shift register. Single tone generators can be built very precisely with respect to short time frequency fluctuations (phase noise) and with respect to the absolute frequency value (e.g. atomic clock as ultimate solution). In consequence, UWB-sensors based on PN-signals may have available very precise internal time reference if required. Firstly, this allows very precise range measurements due to the absolute frequency precision. Secondly, the sensors are very sensitive for weak range variations (often named micro Doppler) due to low phase noise of the timing reference. For details on corresponding aspects see [2].

• **PN-signals are periodic**. Hence, we can apply sub-sampling and synchronous averaging. Sub-sampling (stroboscopic sampling) will reduce the technical effort of data capturing and handling. Needless to say, that high sub-sampling factors must be traded against receiver efficiency leading to lower noise suppression or extended recording time (see [3] for comprehensive discussions). Consequently, one has to find a compromise between technical effort/device costs and degradation of measurement speed.

Synchronous averaging serves as noise suppression and reduction of data amount. It can be applied if the speed of data capturing is higher than required from the measurement scenario. The period length of the PN-code and capturing speed should be selected according to the requirements of the test scenario (see below for details). In order to reduce the data amount to be handled, the PN-code should be as short as possible.

Short sequences will however degrade the LPI (low probability of intercept) performance. In order to approach the LPI behavior of random noise, the PN-code and/or the clock rate of the shift register may be irregularly switched in time intervals comprising an integer multiple of periods.

The periodicity of the sounding signal avoids any truncation effects if appropriately captured. Furthermore, an expectation procedure for variance reduction as in case of random noise sounding signals is not necessarily required. Thus, the measurement approach is basically suited for high speed UWB-measurements.

• In case of radar applications, the **receive signals have to be compressed** in time in order to achieve an interpretable impulse response function. The impulse compression leads to a coherent energy accumulation of the measurement signal in favor of

random perturbations as additive noise, jitter, or jammers which are only non-coherently accumulated. Hence, an excellent suppression of various perturbation signals is inherent.

In what follow, we will start with a short introduction of the basic functioning of an UWB PN-sensor and we will summarize the key parameters of a PN-device in order to have some design guide lines for specific applications. In a further section, we will present a family of PN-devices for short range radar applications as well as general purpose time or frequency domain measurements. Finally, we will give an overview over some useful data pre-processing steps.

2. M-SEQUENCE PRINCIPLE

The design and technical implementation of an UWB-sensing concept should respect three key issues. These are the generation of the sounding signal, the capturing of the response signal, and the optimization of data throughput. We will discuss these points on the basis of Fig.1 which was firstly introduced by [4] and thoroughly analyzed in [3].

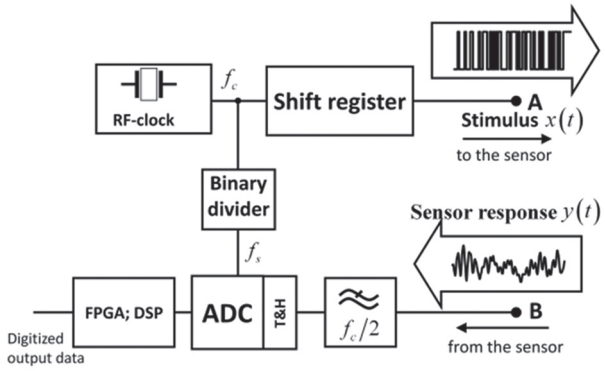

Fig. 1: Basic concept of UWB PN sensor head

The aim of this circuit is either the determination of the impulse response function (IRF) or the estimation of the frequency response function (FRF) related to the transmission path between the points A and B of Fig. 1. The measurement of the IRF is usually of interest in radar or TDR (Time Domain Reflectometry) operation mode, while the capturing of the FRF is applied in the network analyzer operation mode. Both methods only differ in the kind of processing the captured data.

The measurement of the IRF or FRF of a device or scenario under test requires a stimulation signal of sufficiently large bandwidth. In the simplest and most reliable case, one applies M-sequences (maximum length binary sequence). They are generated by linear feedback shift registers. Fig. 2 gives an example of one of its canonical structures. A second option would be the Fibonacci structure. It is not shown here since the Galois structure is usually preferred due to higher possible operational frequencies. The upper limit of the clock rate is determined by the toggle time of the individual flip-flops in the shift register and the delay of the feedback paths. In order to keep both as short as possible, the shift register must be monolithically integrated. A list of appropriate feedback structures is given in the online annex of [3]. The unit delay is provided by flip-flops which are pushed by an RF-clock $f_c = 1/t_c$. The state $Q_v(nt_c)$ of any flip-flop may act as the stimulation signal $x(t)$.

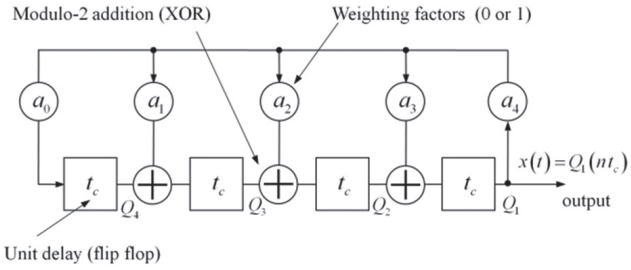

Fig. 2: Galois-structure of 4th order linear feedback shift register

Some characteristic functions – exemplified for an ideal M-sequence of 4th order – are depicted in Fig. 3. Time evolution and spectrum of a realistic M-sequence are shown in Fig. 4 and 5. The M-sequence is a periodic time signal having a discrete spectrum whose power envelope has a sinc^2-shape. Within the spectral band $[0, f_c/2]$, the stimulus power can be considered as nearly frequency independent which makes it suitable for IRF and FRF measurements of test objects having an operational band within this range. Above $f_c/2$, the signal power will rapidly decay so that random noise will more and more dominate the signal if the measurement bandwidth is extended beyond that limit.

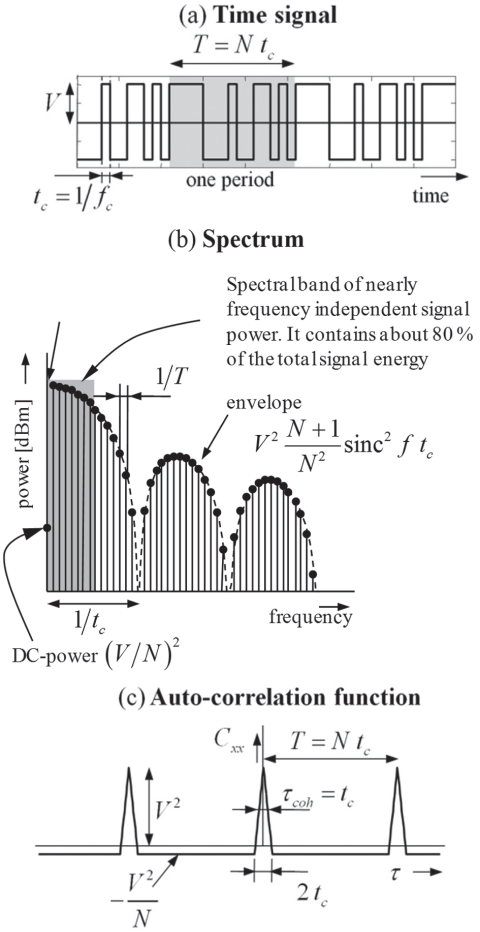

Fig. 3: Characteristic functions of the band unlimited M-sequence: time signal (a), power spectrum (b) and auto-correlation function (c)

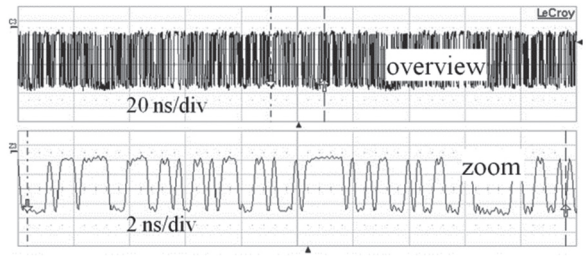

Fig. 4: Time evolution of a real M-sequence (9th order; clock rate 5 GHz). The clock rate was chosen to meet the bandwidth of the digital real-time oscilloscope

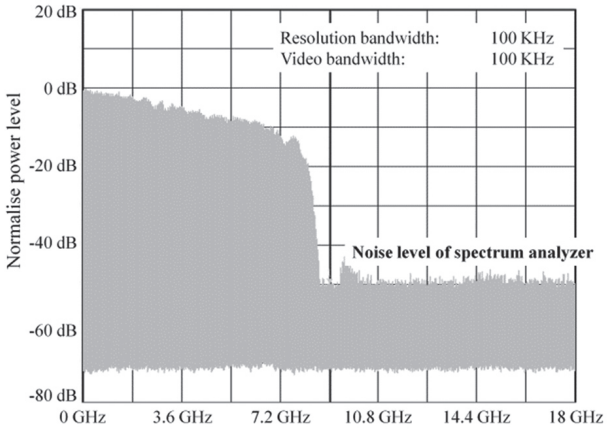

Fig. 5: Band limited spectrum of an M-sequence (9th order; clock rate 18 GHz)

The determination of the IRF $h(t)$ is based on the following relation:

$$C_{yx}(t) = h(t) * C_{xx}(t) \qquad (1)$$

in which $C_{xx}(t) = x(t) * x(-t)$ is the auto-correlation function of the stimulus and $C_{yx}(t) = y(t) * x(-t)$ represent the cross-correlation between receive signal and stimulus. The symbol $*$ means convolution. Obviously, the triangular shape of the auto-correlation function approaches a Dirac-delta with increasing clock rate of the shift register. Thus, we can roughly approximate for sufficiently large f_c: $C_{yx}(t) \sim h(t)$ (see also annex B9 of [3]).

The DC-offset of $C_{yx}(t)$ can mostly be ignored since we usually deal with AC-coupled systems and furthermore the DC-value of the measured signal is often affected by the offset voltage of the measurement receiver. If the DC-offset from $C_{xx}(t)$ is of importance, one can use complementary Golay sequences [3, 5-8] which will, however, complicate the device implementation – especially for a large bandwidth.

Since we like to process our data in the numerical domain, we first have to digitize the response signal $y(t)$. In order to relax the conditions to meet the Nyquist criterion, we apply sub-sampling. This is allowed since the response signal is periodic. Sub-sampling may drastically reduce the actual sampling rate as well as the data throughput and therefore it will decrease the device costs and the power consumption of the circuits.

A very simple and extremely stable approach to control the sub-sampling procedure follows from the band limitation to $f_c/2$ as depicted in Fig. 1 and Fig. 3 (b). For this case, the Nyquist criterion leads to a minimum (equivalent) sampling rate of $f_{eq}=f_c$, i.e. we only need one sample per chip of the PN-sequence whereat the capturing of these data points may be scattered over many periods of the response signal due to its periodicity (therefore the term "equivalent" sampling rate). The simplest way to control the data capturing exploits binary dividers (refer to Fig. 1). It assumes a signal length of $N = 2^m - 1$ chips (as valid for an M-sequence) per period. If we apply a binary divider of one stage, the actual sampling rate will be $f_s=f_c/2$ and we need two signal periods to capture the whole data set: the odd sample numbers during the first period and the even sample numbers during the second period. A binary divider of two stages reduces the sampling rate further to $f_s=f_c/4$. But now, we already need 4 periods to gather all data. This principle works for all orders of the binary divider.

In the case of Golay-sequences, the approach has to be slightly modified. The length of a Golay-sequence is 2^m which interdicts the use of a simple binary divider. If however the dividing factor is modified to $2^n \pm 1$, it works as before.

The use of the binary divider for sub-sampling control has some essential advantages:

- It provides very sharp trigger edges leading to sampling events which are robust against random jitter.
- The divider runs through all its states before it releases a new sampling event. Hence, any asymmetries of the internal flip flops will not affect the timing precision.
- The timing precision is determined by the single tone RF clock generator. If its frequency is stable within the recording time, the device internal time reference will be absolutely linear and stable. This guarantees very precise time measurements (also for long propagation times) and allows a practically unlimited number of synchronous averages for noise suppression when the test scenario/object is time invariant.
- The data capturing deals with Nyquist sampling. It provides the lowest possible data throughput which is required to correctly reconstruct waveform (in case of no prior knowledge). The visualization of a Nyquist sampled signal is less comprehensible for the human eye. Therefore, visualized waveform should be $\sin x/x$-interpolated for display. Note, non-ideal low-pass filters (namely due to their limited stop band attenuation) will cause some errors within the interpolated signal.

Except for the low-pass filter in Fig. 1, all device components may be monolithically integrated (compare Fig. 10 below). If one removes the analog RF-low pass, the involved electronic components will give a "natural" band limitation. Since it will certainly be beyond $f_c/2$, one has to increase the equivalent sampling rate – i.e. one has to take more than only one sample per M-sequence chip.

As depicted in Fig. 6, this can be achieved by a slight extension of the circuit from Fig. 1 [9]. The basic sampling approach remains the same as before. But it will be q-fold repeated whereat each time the sampling cycle is shifted by the q-th fraction of the clock period (i.e. $\Delta t_q=(qf_c)^{-1}$). This is managed with the additionally inserted steerable phase shifter.

By this approach, the equivalent sampling rate is increased to $f_{eq}=qf_c$ (which can be selected high enough to meet the Nyquist criterion if no artificial spectral cutting is applied) but also the recording time is extended by the factor of q. The captured noise power will also grow much stronger with increasing factor q than the energy of the response signal (due to the spectral decay of the stimulus signal). However, both effects may be neutralized, if the q-fold oversampled signal is band limited to $f_c/2$ by digital low-pass filtering now. This is quite more flexible but also requires more power for signal processing. With digital $f_c/2$ filtering, the same noise performance as a q-fold synchronously averaged signal from the basic concept according to Fig.1 with the analog low-pass filter can be obtained. Hence, the same recording time is needed for both cases. Since digital low-pass filtering may be joined with decimation, we will finally get the same data amount in both systems.

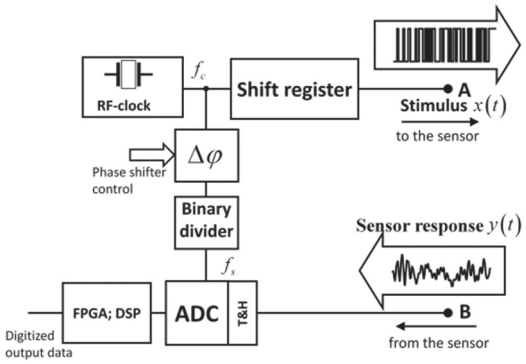

Fig. 6: Modified UWB PN-sensor head for equivalent time oversampling

3. ILMSENS PN-DEVICE LINE

Based on the working principle described in section 2, ILMsens develops a toolbox of wideband PN-devices and components for application-specific wideband measurements within the low-frequency, the radio frequency, and the microwave range. The intended scope of the toolbox is symbolized in Fig. 7. Herein, we distinguish between the baseband units which are the key component of every PN-device, the various options of RF-frontends and the basic software to operate the devices with standard computers.

The basic hardware structure is depicted in Fig. 8. It shows a baseband unit and an RF-frontend as two separated modules so that the sensor can be flexibly adapted to user requirements. The baseband unit constitutes from two parts, the RF-unit and a digital board containing the electronics for digitizing, high-speed pre-processing, and data transfer.

For the RF-unit, there are three realization options:

- The multi-chip RF-unit contains several custom-made SiGe-chips. This implementation provides high flexibility to modify the device structure concerning specific application requirements. Furthermore, it has the best RF-performance due to careful shielding between transmitter and receivers. An implementation example is shown in Fig. 9.
- In the case of the single-chip baseband unit shown in Fig. 10, the whole RF-part is merged in a single SiGe-chip while the digital board may be the same as before. This realization requires less supply power and less electronic components. Furthermore, the small size of the integrated RF-part – possibly including the RF-frontend, too – permits to place the measurement ports directly into the intended measurement plane. Hence, one can omit RF-cables. This will give additional degrees of freedom in the applicator design (antennas, coaxial probes, electrode configurations) since impedance matching is of less importance under this condition.
- The real-time baseband unit completely renounces the RF-part. Test signal generation and data capturing is entirely organized by the digital board which is identical for all three types of baseband implementation. Its bandwidth is mainly limited by the FPGA performance and the sampling rate f_s of the ADCs.

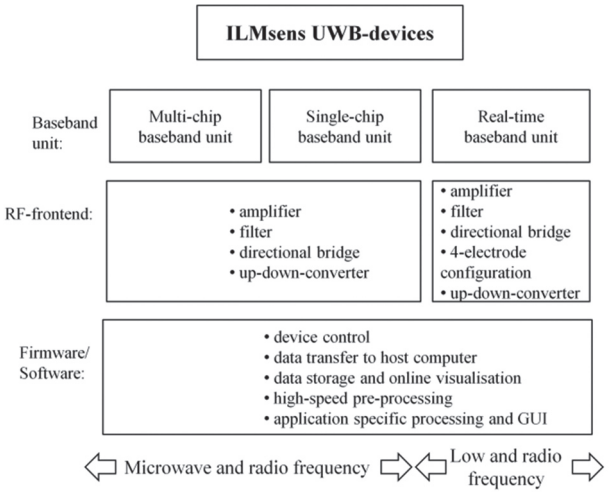

Fig. 7: PN-device toolbox

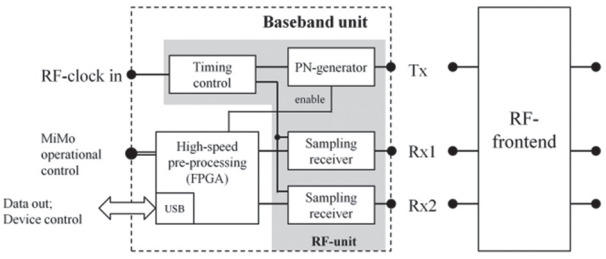

Fig. 8: Basic PN-device structure

Independent from the actual technical implementation, every baseband unit covers one PN-generator (which may be enabled or disabled during the operation of the measurement head) and two parallel working receiver channels. This configuration permits several measurement arrangements:

• The device may be operated as a wideband radar interferometer (e.g. used in Through-Wall-Radar) or as polarimetric radar.

• One channel may be used to capture the stimulus signal for reference.

• The device is able to capture one-port scattering parameters since it is able to stimulate a port and to measure the incident and emanating wave if directional bridges are inserted (see Fig. 10).

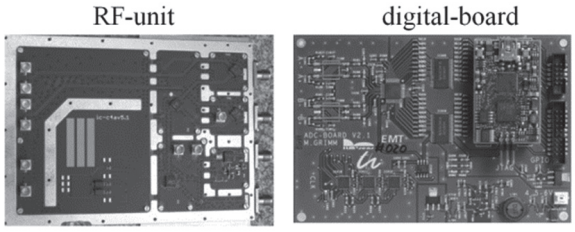

Fig. 9. Disassembled multi-chip baseband unit showing the RF-unit and the digital board which are stacked when in operation

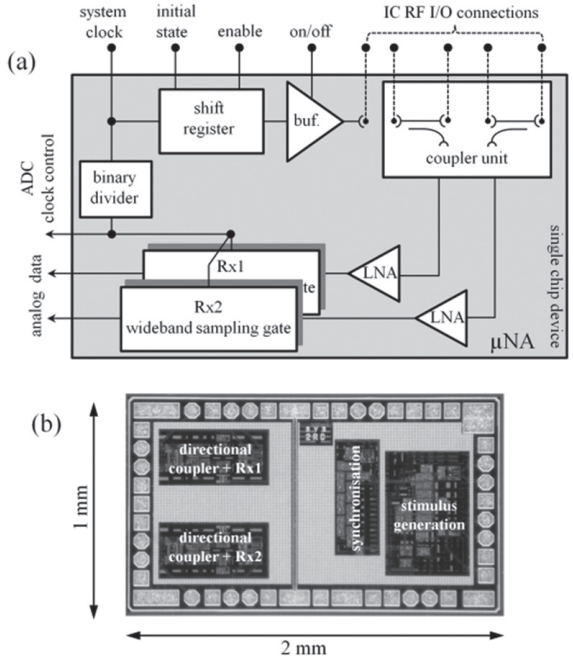

Fig. 10. Monolithically integrated M-sequence RF-unit with two reflectometer inputs: circuit schematic (a) and chip micrograph (b)

• The device is able to capture one-port impedance parameters since it is able to stimulate a port and to measure current and voltage.

• The device may act as a receiver only by disabling the PN-source.

• Several devices may be cascaded to form MiMo-Systems as depicted in Fig. 11. This permits the construction of MiMo-radars and multi-port S-parameter or Impedance-parameter measurement systems.

The optional RF-frontends provide the interface for application specific applicators or measurement circuits. They may contain filters, amplifiers, directional bridges, current-voltage converts, up-down-converters etc.

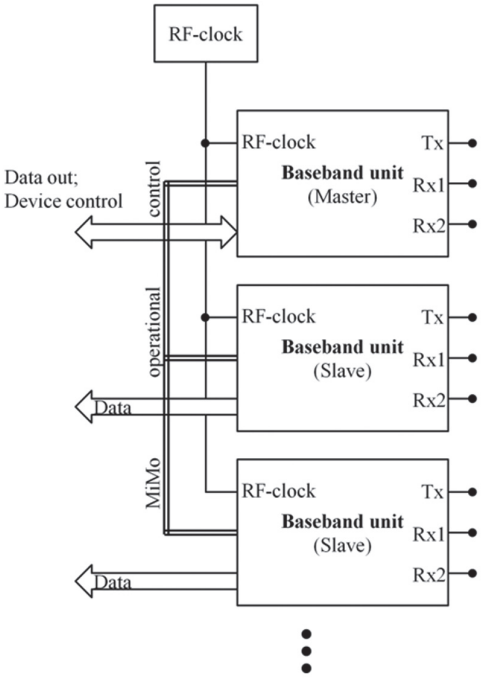

Fig. 11. MiMo-device structure

Fig. 12–16 exemplify implemented devices, their respective device extensions, and frontends.

Fig. 12. Standard baseband unit

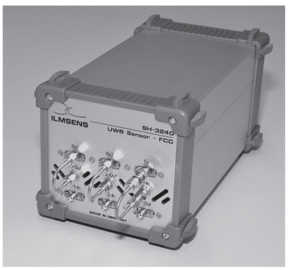

Fig. 13. FCC respectively ECC compatible device. These devises provide a complex valued IRF

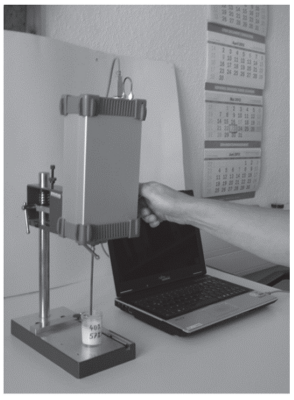

Fig. 14. Baseband unit extended with an active directional bridge for impedance spectroscopy and mono-static radar applications

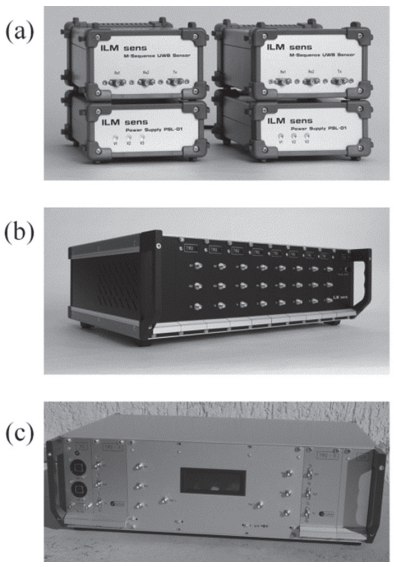

Fig. 15. Several options of MiMo-devices: (a) 2Tx/4Rx-system built from two basic modules. (b) 8Tx/16Rx-system. (c) 2Tx/4Rx-system with build-in reflectometers for scattering parameter measurements

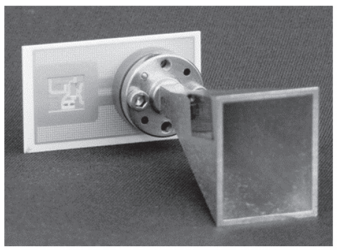

Fig. 16. Experimental wideband 60 GHz-frontend based on monolithically integrated SiGe-up-down converters extending the FCC-compatible PN-device for mm-wave channel sounding and radar [10]

The firmware to operate the devices pursues a corresponding modular concept as the hardware. Depending on the requirements and the skill of the user, two strategies are supported. In the first case – i.e. ultraANALYSER as shown in Fig. 17 – the software modules are designed to work stand alone for a set of well specified measurement tasks (e.g. short range radar and microwave imaging, Time Domain Reflectometry, vector network analyzer, impedance spectroscopy, ...). In the second case (see Fig. 18), the user has to implement the data processing on its own. Only the basic functionalities such as data transfer, data storage, device parameterization, and on-line visualization are available. Currently, it is based on MATLAB, but it will be extended to e.g. LabView in the future.

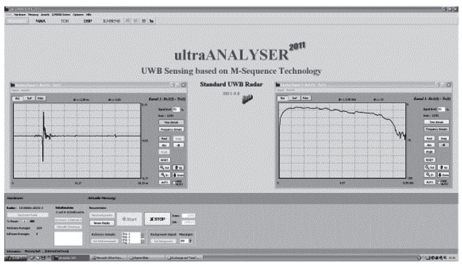

Fig. 17: ultraAnalyser GUI for standard stand-alone applications

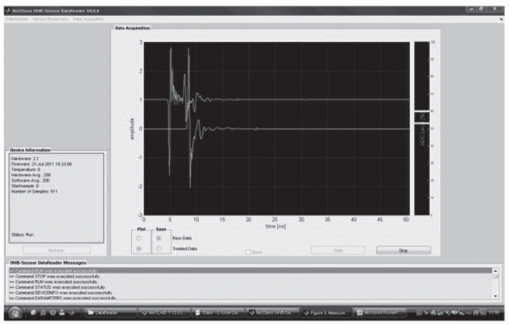

Fig. 18: MATLAB GUI for visualization, storage, and integration of a user function enabling user specific processing

4. KEY PARAMETERS

The most important quantities influencing the performance of a PN-sequence unit according to Fig. 1 are symbolized by the design tetrahedron in Fig. 19.

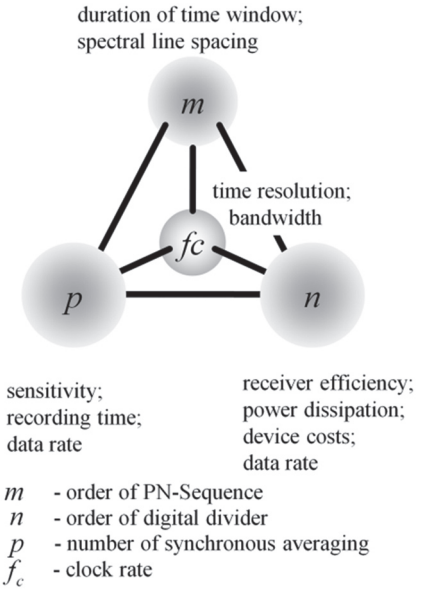

Fig. 19: Design tetrahedron of a PN-sequence system

Usually, one can select among four quantities to optimize the device performance for a specific application. These are the RF-clock rate f_c, the shift register length m, the length n of the binary divider and the number p of synchronous averaging. From this, we can roughly estimate the main features of the sensing unit (c_0 – speed of light; b – effective number of bits of the ADC and T&H):

Bandwidth:

$$B \cong 0 \cdots f_c/2 \tag{2}$$

Range resolution:

$$\delta_r \cong \frac{c_0}{f_c}. \tag{3}$$

Observation time window length:

$$T \cong \frac{2^m}{f_c}. \tag{4}$$

Spectral line spacing: $\Delta f = T^{-1} \cong 2^{-m} f_c$ (5)

Unambiguity range: $R \cong 2^{m-1} \frac{c_0}{f_c}$ (6)

Recording time per IRF or FRF:

$$T_R \cong \frac{p2^{m+n}}{f_c}. \quad (7)$$

Effective data amount per measurement:

$$H[\text{bit}] \cong \left(b + \frac{1}{2}\,\text{lb}\,p\right)2^m \quad (8)$$

(note, the word length of a data sample increases to $(b+\text{lb}p)$ bits by p-fold synchronous averaging. But half of the "new" bits are noise affected, so that finally the effectively utilizable resolution gain will be $(\text{lb}\,p)/2$ bit).

Effective bit rate for continuous operation:

$$R_b = \frac{H}{T_R} \cong \frac{2b + \text{lb}\,p}{p2^{n+1}} f_c. \quad (9)$$

Eq. (8) and (9) assumes that no time compression was performed. It would increase the word length per sample by m bit.

In case of non-stationary test scenarios, the maximum recording time is either restricted by the bandwidth of the scenario variations (i.e. $2B_{TS}T_R \le 1$ – Nyquist theorem of the test scenario) or by the Doppler Effect. The latter provokes de-correlation between transmitted and received signals for high speed targets. In order to keep the de-correlation negligible, the recording time should not exceed the maximum target speed of [3]:

$$v_{\max} \cong \frac{\delta_r}{T_R} \cong \frac{c_0}{p2^{m+n}}. \quad (10)$$

Please note, in the case of UWB PN-sequences, we will not observe Doppler ambiguity as is n the case for narrowband signals.

The dynamic range of the sampling receivers D_{R_x} is limited by different effects (see [3] for a detailed discussion). For the sake of shortness, we will refer only to limitations by electronic and quantization noise here. For time (superscript (TD)) and frequency (superscript (FD)) domain data, it can be approximated by:

$$\begin{aligned} D_{R_x}^{(TD)}[\text{dB}] &\cong 6b + 3m + 10\lg p \\ D_{R_x}^{(FD)}[\text{dB}] &\cong 6b + 10\lg p \end{aligned} \quad (11)$$

which leads to a recording time referred dynamic range (specific dynamic range DT) of:

$$\begin{aligned} D_{R_x}^{(TD)}[\text{dBs}] &= 10\lg(D_{R_x}^{(TD)}/T_R[\text{s}]) \\ &\approx 6b - 3n + 10\lg f_c[\text{Hz}] \\ D_{R_x}^{(FD)}[\text{dBs}] &= 10\lg(D_{R_x}^{(FD)}/T_R[\text{s}]) \\ &\approx 6b - 3(m+n) + 10\lg f_c[\text{Hz}] \end{aligned} \quad (12)$$

[dBs] – read dB per second; $D_{R_x}^{(\ldots)}$ – in linear scale.

The time domain related dynamic range refers the peak value of the time compressed signal to noise while the frequency domain related dynamic range compares the strength of an individual sine wave component with the noise power.

All these equations have shown the large room that exists to adapt the properties of the sensing device to the actual requirements. In standard configurations, the clock rate f_c is fixed to 125 MHz (real time unit only) or 5, 7, 9, 13, and 18 GHz for the RF units, respectively. The length m of the shift register is either 9 or 12 and the binary divider in our sensors is of order 9. The recently achieved specific dynamic range is about $DT^{(TD)} \approx 114$ dBs.

5. BASIC PRE-PROCESSING

Pre-processing is used to treat the captured data in such a way that it may be used by the subsequent main processing like microwave imaging, target detection, parameter extraction, and so forth. The pre-processing is mainly aimed at providing the IRF or FRF of the test object and at reduction of captured data volume to a manageable amount. The different procedures of pre-processing are distributed between the sensor internal processor (typically an FPGA and/or DSP) and the host computer. As long as the procedures deal with linear operations (e.g. correlation, Fourier transform, low-pass filtering, averaging, etc.), their sequence can be arbitrary selected due to the law of commutation. Hence, one is well advised to start with simple and fast procedures which additionally lead to a reduction of the data amount. Such procedures should run in the FPGA of the UWB-device in order to disburden the data interface to the host computer (e.g. USB2) which is often the bottleneck within the processing chain. Consequently, algorithms which increase the amount of data (e.g. time compression by correlation or imaging) should run after transmission to a computer. In what follows, some useful pre-processing approaches will be shortly summarized.

Data reduction by blind measurements: The minimum recording time of recent PN-sequence devices (which uses a 9th order binary divider for sampling control) ranges between 14 μs and 420 μs (i.e. about 2.400 to 71.000 response functions per second) depending on the clock rate and the order of the M-sequence (for details see datasheets at www.ilmsens.com). Usual Windows PCs may reliably handle only about 200 (9th order M-sequence) or 25 (12th order M-sequence) response functions per second. This gap may be bridged in the simplest case by ignoring most of the measurements. This approach will be the method of choice if the recording time is limited by physical reasons as e.g. for tracking of high speed targets (see eq. 10).

Data reduction by synchronous averaging: In most of the intended applications of UWB PN-sensors, the motions and variations of the scenario under test are slow compared to the measurement speed. Hence, we can increase the recording time. This opens up the opportunity to apply synchronous averaging by which the noise performance of the measurement will be considerably improved and additionally the data throughput will be reduced (refer to (8), (9), and (11)). If the required update rate of the measurements may be handled by the host computer, this approach will not cause any data losses.

Data reduction by background removal: in many cases, the UWB-sensor observes a scenario in which only minor variations appear (e.g. in case of through-wall radar, vital sign detection, supervision of a space etc.). Under such conditions, a new measurement will provide only minor new information. Therefore, the data amount can be drastically reduced by updating only the small variations of the captured data relative to the previous measurements. A simple realization of such background removal may be achieved by exponential filtering as expressed by (13).

$$\begin{aligned} \bar{y}_k(t) &= \alpha\, y_k(t) + (1-\alpha)\,\bar{y}_{k-1}(t) \\ \Delta y_k(t) &= y_k(t) - \bar{y}_{k-1}(t) \end{aligned} \tag{13}$$

Herein, $y_k(t)$ represents the captured signal of the k-th measurement cycle. $\bar{y}_k(t)$ is the background which is updated by every new measurement whereat the update speed is controlled by the forgetting factor $\alpha \in (0,1)$. The remaining signal $\Delta y_k(t)$ contains the variations (new information) gained by the k-th measurement. It has to be considered by the subsequent processing steps.

IRF and FRF determination: Typically the measurement should provide either the IRF (in case of radar or TDR) or the FRF (in case of the network analyzer operation mode) of the investigated transmission path. Since their calculation from the captured data is numerically more expensive than the previously mentioned procedures, it should be done at the end of the pre-processing chain. Depending on the required measurement precision, we have several options:

Option 1: Here, we assume that the sounding signal corresponds to an ideal M-sequence $m(t)$. That is, we disregard all deviations of a real M-sequence (as illustrated in Fig. 4 and 5) from the ideal one (as shown in Fig. 3). Under this condition, we can proceed as proposed by eq. (1), i.e. we calculate the cross-correlation between receiving signal and ideal M-sequence. The result can be interpreted as a first order approximation of the IRF of the transmission path:

$$h^{(1)}(t) \sim y(t) * m(-t) \tag{14}$$

Since the ideal M-sequence constitutes only from +1 or -1, the algorithm behind (14) can be implemented by a very fast and efficient way [3, 11]. It is called the fast Hadamard-transform (FHT) which has some structural similarity to the fast Fourier-transform (FFT). But in contrast to the FFT, it only requires summing and difference operations which can be handled extremely fast by modern FPGAs. The calculation of tens of thousands of IRFs per second should be feasible which could be applied to detect and track very fast objects. Note however, that (14) is linked with a time compression of the received signal which leads to an increased word length of the data (see also (8), (9) and related discussion). Therefore, the FHT should only run at the FPGA if it also performs target detection in order to reduce the data amount to be transferred.

Transforming $h^{(1)}(t)$ into the frequency domain, we would also get a first order approximation of the FRF $\underline{H}^{(1)}(f)$ of the device under test (DUT).

Option 2: This approach respects the actual time evolution or spectrum of the sounding signal. In order to get this signal, one either needs a second receiver for reference measurements or one performs a calibration measurement with a direct connection of generator and receiver (it is often called "response calibration" in network analyzer terminology). Now, we can de-convolve the actual sounding signal out of the captured one to get a better approximation of the DUT behavior. De-convolution can be done by several ways (see e.g. [12]). Here, we will only refer to a simple method which uses a frequency domain approach and a window function $w(f)$ for suppression of ill-conditioned parts of the spectrum. From this, we get a second order approximation of the DUT response in time or frequency domain.

$$\begin{aligned} & x(t) \xrightarrow{FFT} \underline{X}(f); \quad y(t) \xrightarrow{FFT} \underline{Y}(f) \\ & \underline{H}^{(2)}(f) = \frac{\underline{Y}(f)}{\underline{X}(f)} w(f) \xrightarrow{IFFT} h^{(2)}(t) \end{aligned} \tag{16}$$

Option 3: Unfortunately, option 2 of FRF or IRF determination does not respect all imperfections of the measurement device as e.g. cross-talk, port mismatch, multiple reflections etc. In order to remove these errors from the measurement, one needs a device calibration comparable to the approaches used for network analyzers. Deeper discussions of this topic would go beyond the scope of this article. But the interested reader can find the theoretic basis for network analyzer calibration in [13, 14] and corresponding considerations related to PN-devices including some examples are given in [3, 9, 15, 16].

The basic prerequisites to allow such error corrections are twofold. Firstly, one has to capture the complete set of signals at any port of the DUT, i.e. in case of S-parameter measurements one needs to know all ingoing waves a_n as well as all emanating waves b_n. Equivalently, one can also measure the current and the voltage at all ports. This is one of the reasons why ILMsens PN devices have two receive channels. The second assumption concerns the time stability of the measurement devices since their behavior must not change between repetitions of calibration and the time point of the measurement. Details of these issues are discussed in [2].

SUMMARY

The UWB PN-technique joins the circuit simplicity of the pulse technique and the precision of the sine wave method with the LPI performance of the noise radar. Binary PN sequences of large bandwidth may be generated by comparatively simple means. The selection of appropriate PN-codes depends on several aspects such as their auto-correlation and cross-correlation properties as well as the technical challenges of their generation. In order to determine a reliable estimation of the impulse response function of a DUT, the auto-correlation function of the PN-sequence should approach a Dirac-delta. This is best fulfilled by Maximum Length Binary Sequences

(M-sequence) and complementary Golay-codes. In both cases, the auto-correlation function represents a comb of triangular peaks having a base width of double the chip duration and a period according to code length. Hence, by increasing the code generating clock rate f_c, the wanted Dirac-delta is approximated better and better.

A family of M-sequence devices for high-resolution short-range sensing was introduced and the key parameters of the devices where summarized.

References

[1] H. J. Zepernick, and A. Finger, *Pseudo Random Signal Processing – Theory and Application*: John Wiley & Sons, 2005.

[2] J. Sachs, M. Kmec, and R. Herrmann, "Time and Range Accuracy of Short-Range Ultra-Wideband Pseudo-Noise Radar," in Noise Radar Technology, Yalta, Cremia (Ukraine), 2012.

[3] J. Sachs, *Handbook of Ultra-Wideband Short-Range Sensing - Theory, Sensors, Applications*, Berlin: Wiley-VCH, November 2012.

[4] J. Sachs, P. Peyerl, and M. RoЯberg, "A New Principle for Sensor-Array-Application.," in IEEE Instrumentation and Measurement Technology (IMTC), Venice (Italy), 1999, pp. 1390-1395.

[5] T. H. Andres, and R. G. Staton, "Golay Sequences," *Lecture Notes in Mathematics;Combinatorial Mathematics V*, C. H. C. Little, ed., Berlin, Heidelberg, New York: Springer, 1977.

[6] S. Foster, "Impulse response measurement using Golay codes," in Acoustics, Speech, and Signal Processing, IEEE International Conference on ICASSP '86., 1986, pp. 929-932.

[7] A. Vazquez Alejos, D. Muhammad, and H. Ur Rahman Mohammed, "Ground Penetration Radar Using Golay Sequences," in Region 5 Technical Conference, 2007 IEEE, 2007, pp. 318-321.

[8] A. V. Alejos, M. G. Sбnchez, I. Cuicas *et al.*, "Wideband Noise Radar based in Phase Coded Sequences," *Radar Technology*, G. Kouemou, ed.: InTech, 2010.

[9] R. Herrmann, "M-sequence based ultra-wideband radar and its application to crack detection in salt mines," Faculty of Electrical Engineering and Information Technology, Ilmenau University of Technology (Germany), Ilmenau, 2011.

[10] A. P. Garcia Ariza, R. Mьller, R. Stephan *et al.*, "60 GHz Polarimetric MIMO Sensing: Architectures and Technology," in EUCAP 2012, Prague, 2012.

[11] M. Cohn, and A. Lempel, "On fast M-sequence transforms (Corresp.)," *Information Theory, IEEE Transactions on,* vol. 23, no. 1, pp. 135-137, 1977.

[12] T. G. Savelyev, L. Van Kempen, and H. Sahli, "Deconvolution techniques," *Ground Penetrating Radar*, D. Daniels, ed., London: Institution of Electrical Engineers, 2004.

[13] D. K. Rytting, "Network Analyzer Error Models and Calibration Methods," in RF & Microwave Measurements for Wireless Applications (ARFTG/NIST Short Course Notes), 1996.

[14] D. K. Rytting, "Network Analyzer Accuracy Overview," in ARFTG Conference Digest-Fall, 58th, 2001, pp. 1-13.

[15] R. Herrmann, J. Sachs, and P. Peyerl, "System evaluation of an M-sequence ultra wideband radar for crack detection in salt rock," in International Conference on Ground Penetrating Radars (GPR), Ohio (Columbus), 2006.

[16] R. Herrmann, J. Sachs, K. Schilling *et al.*, "12-GHz Bandwidth M-Sequence Radar for Crack Detection and High Resolution Imaging," in International Conference on Ground Penetrating Radar (GPR), Birmingham, UK, 2008.

Manuscript received December, 20, 2012

Juergen Sachs is Senior Lecturer at Ilmenau University of Technology, Germany. He teaches "Basics of Electrical Measurement Technology", "Measurements in Communications" and "Ultra-Wideband Radar Sensing". He is head of several research projects, and inter alia coordinator of European projects for humanitarian demining and disaster relief. His research areas cover RF-signal analysis and RF-system identification; Surface Penetrating Radar for non-destructive testing and medical engineering, ultra wideband methods and their application in high resolution radar and impedance spectroscopy, digital processing of ultra wideband signals, array processing; and design and implementation of new RF device approaches.

Marko Helbig received the Dipl.-Ing. and Dr.-Ing. degrees in Electrical Engineering (Biomedical Engineering and Signal Processing) from Ilmenau University of Technology in 1996 and 2007. Currently, he is working as a research assistant at the Electronic Measurement Research Lab, Ilmenau University of Technology. His research interests include biomedical signal processing and high resolution ultra-wideband imaging for medical applications, especially for breast cancer detection.

Ralf Herrmann was born on 19.09.1978 in Germany. He started a course on engineering for computer science at the Ilmenau University of Technology in 1998 and graduated with an Eng. degree in 2004. After an internship at the Tohoku University in Sendai (Japan) he returned to Ilmenau in 2005 and has been working as a research assistant in the Electronic Measurement Research Lab of TU Ilmenau where he received his Dr. Eng. degree in 2011. Research focus is on system design of novel UWB pseudo-noise sensors and embedded electronics systems.

Martin Kmec received the Ing. degree in electronics and telecommunication technology from the Technical University Košice, Slovakia in 2000. In 2000 and 2001 he was with Meodat GmbH, Ilmenau, Germany, where his work has included the analysis and design of ultra-wideband current mode integrated circuits. Since 2001, he is with Electronic Measurement Laboratory on the Technical University Ilmenau in Germany as research assistant. His research interests are in the design and characterization of SiGe BiCMOS based circuits for novel UWB sensor systems. Hi is currently pursuing the Dr. degree in the field of monolithically integrated M-Sequence based UWB systems.

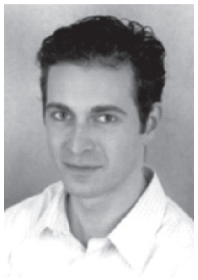

Kai Schilling received his diploma in Engineering Informatics with focus on Measurement and Telecommunication Technologies from Ilmenau University of Technology, Germany in 07/2007. He works since 08/2007 at the Institute for Information Technology Ilmenau as research assistant. His research activities cover the design and implementation of UWB Sensor Systems with focus on mixed signal and RF-hardware.

Peter Rauschenbach received his Eng. degree in electronics and telecommunication engineering from Ilmenau University of Technology, Germany in 1993. After his university studies, he was dealing with optical communication and microwaves. Since 1997, he is employee of MEODAT GmbH (Germany) where he is responsible for RF-technology, Filter and PCB design, and chip housing.

Hans-Christian Fritsch received the Master of Science in Business Informatics from Ilmenau University of Technology in 2010. In 2008 he completed the Bachelor of Science degree in Media Management. He is employed at the TU Ilmenau Service GmbH where he is charged with project management and the commercialisation of UWB-Technology.

УДК 621.37

Сверхширокополосные псевдошумовые сенсоры / Ю.Сакс, М. Кмец, Х.К. Фритч, М. Хелбиг, Р. Херрманн, К. Шиллинг, П.Раушенбах // Прикладная радиоэлектроника: науч.-техн. журнал. – 2013. – Том 12. – № 1. – С. 79–88.

Технология сверхширокополосных псевдошумовых (ПШ) сигналов объединяет простоту схем импульсной технологии и точность метода синусоидальных сигналов с низкой вероятностью перехвата шумовых радаров. Бинарные ПШ последовательности с широкой полосой могут быть достаточно просто сгенерированы и оцифрованы с высокой точностью и временной стабильностью. Это открывает новые применения радаров с высоким разрешением, работающих на малых дальностях. В данной работе описаны базовые рабочие принципы СШП ПШ радаров, приведен обзор новых устройств, представлены основные параметры как помощь в параметризации устройства, подходящего для применения метода.

Ключевые слова: сверхширокополосный, псевдошумовой, М-последовательность, последовательность Голай, субдискретизация, преобразование Адамара, импульсная функция отклика, амплитудно-частотная характеристика.

Ил. 19. Библиогр.: 16 назв.

УДК 621.37

Надшироковсмугові псевдошумові сенсори / Ю. Сакс, М. Кмец, Х.К. Фритч, М. Хелбіг, Р. Херрманн, К. Шиллінг, П.Раушенбах // Прикладна радіоелектроніка: наук.-техн. журнал. – 2013. – Том 12. – № 1. – С. 79-88.

Технологія надширокосмугових псевдошумових (ПШ) сигналів об'єднує простоту схем імпульсної технології і точність методу синусоїдальних сигналів з низькою імовірністю перехоплення шумових радарів. Бінарні ПШ послідовності з широкою смугою можуть бути досить просто згенеровані і оцифровані з високою точністю і стабільністю у часі. Це відкриває нові застосування радарів з високим розрізненням, працюючих на малих відстанях. У даній роботі описані базові робочі принципи СШП ПШ радарів, наведено огляд нових пристроїв, представлені основні параметри, як допомога в параметризації пристрою, придатного для застосування методу.

Ключові слова: надширокосмуговий, псевдошумовий, М-послідовність, послідовність Голай, субдискретізація, перетворення Адамара, імпульсна функція відгуку, амплітудно-частотна характеристика.

Іл. 19. Бібліогр.: 16 найм.

UDC 621.37

FPGA BASED SOFTWARE DEFINED NOISE RADAR

K.A. LUKIN, J.R. MOREIRA, P.L. VYPLAVIN, S.K. LUKIN, AND O.V. ZEMLYANIY

Software Defined Radar concept which supposes realization of all radar units as digital circuits, has been applied to implementation of noise radar having such attractive performance as covertness, absence of range ambiguities, high electromagnetic compatibility, etc. This novel concept requires design of digital random signal generators and digital correlators in fast digital circuit such as FPGA. We present the results of our evaluation of the software defined noise radar design and demonstrate the corresponding digital sub-units development on the basis of various FPGA boards. In the experiments we generate noise signals in digital generator implemented in the FPGA, convert it to analog form and transmit it to propagation medium. Noise radar returns have been sampled using onboard ADC and fed into a digital correlator, also realized inside FPGA, along with the sounding signal copy as the reference. The correlator output is processed using algorithms on hosted PC. Design of noise software defined radar using FPGA based SPOS board from ORBISAT company has been evaluated.

Keywords: Noise Radar Technology, Software Defined Noise Radar; FPGA, noise waveform, random signal generator, cross-correlation function, SPOS, correlator.

1. INTRODUCTION

Software Defined Radar concept supposes to leave for a computer or Digital Signal Processor (DSP) as much "work" as possible. In Noise Radar, coherent reception of noise radar returns is performed via estimation of cross-correlation between the sampled reference and radar returns [1-3]. Application of Field Programmable Gate Arrays (FPGA) based devices is one of the ways of implementation of rather fast digital signal processing. Actually, FPGAs allow realization of truly parallel calculations which enables realization of real-time signal processing. Besides, their application in noise radar design provides rather high performance and simplicity of the radar design. That is why FPGA is a most appropriate platform for implementing of signal processing in Software Defined Noise Radar. This concept implies both random waveform generation and radar returns processing be implemented in FPGA designs. In this case signal can be generated digitally, transformed into analog signal using Digital-to-Analog Converter (DAC), and converted up to the working frequency band, amplified, and transmitted. After reception of radar returns, they are to be digitized with ADC for primary and secondary processing realized in the same FPGA crystal. In this way, we have a good platform for design of operational Noise Radar within the frame of software defined radar concept.

In the paper we present some preliminary results of the design and implementation of FPGA-based correlator for coherent reception of radar returns and its application to software defined noise radar. Conventional approach to evaluation of cross-correlation function consists in performing of all calculations in spectral domain: applying Fourier transform to both signals, multiplication of the obtained Fourier spectra and inverse Fourier transform of the result giving all the range gates in parallel. Parallelization of computations in FPGA enabled realization of efficient time-domain algorithms for evaluation of cross-correlations in time domain comparable with the frequency-domain algorithm in efficiency. We present comparison of performance and limitations of different designs considered and test results of a proof-of-concept for software defined noise radar.

2. TIME DOMAIN CORRELATOR FOR CONTINUOUS SIGNALS

Correlator is a device intended for estimation of the correlation functions of any two signals. Having two input signals in digital forms, the above estimation in time domain could be simplified to this:

$$K_\tau = \sum_{n=1}^{N} A_{n-\tau} B_n \qquad (1)$$

where A and B are input signals, n is integer delay between input signals, N is the number of integrated samples.

Normally, in most of the applications it is necessary to find correlation function values on multiple range bins. For example, in radars it enables to obtain range profile, showing dependency of reflected signal level on the range. It is clearly seen from Eq.(1) that computation load depends on N and number of range bins τ. Cross-correlation function estimation consists of three operations: shifting of signals in time, their multiplication and integration. Each of the operations can be easily implemented in FPGA. There are several approaches to building a time domain correlator and we have chosen the one which is optimal for continuous signals. Block diagram of such correlator for three channels is shown in fig. 1. This correlator computes cross-correlation function simultaneously for multiple range bins. It has many equal channels operating in parallel, each for certain range bin. On a clock cycle each channel integrates one more pair of samples (A and B signals).

Delay line is intended for providing delays for one of the signals. It is made using serially connected registers. Each successive register contains signal delayed for one clock cycle. Each correlator channel consists of multiplier, adder and register. Multiplier performs

multiplication of A and B signals. Adder and register act as an integrator: the adder adds the result to the previous value and register keeps the result from the previous cycle.

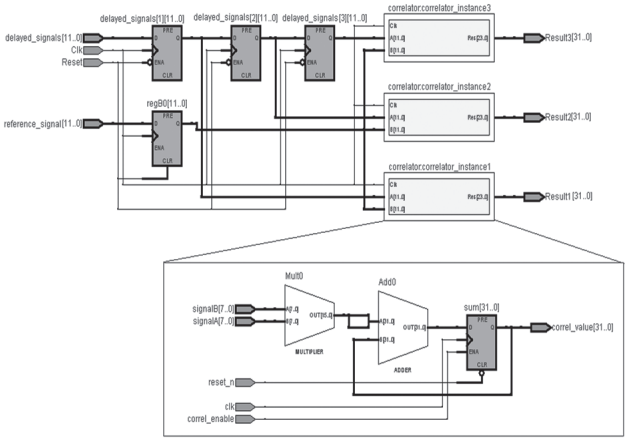

Fig. 1. Block diagram of time domain correlator for continuous signals

The correlator operates in the following way: reference signal comes to delay line (line of registers) and from delay line to channels. Radar return comes to all the channels at the same time. The radar return is multiplied with delayed reference; the result is added to the value contained in register of correlator channel. After several cycles of operation overflow may occur in the registers of correlator channels.. Then the results from adders are transferred to results bank (line of registers) for subsequent operation and all the channels are reset for processing the next set of data.

Fig. 2 shows the flow diagram of test design for such multichannel correlator implemented in FPGA. The realized correlator enables calculation of the correlation function at the fixed number of range bins for a certain integration time. The integration time is limited by number of bits used in the digital integrator of the FPGA-based correlator. We have realized 64-channel correlator with 32-bits integrator. This correlator operates at the frequency of up to 300 MHz. In these conditions correlator can make about 1280 additions thus it can integrate during more than 4 seconds. After that the data are to be delivered to a buffer and transferred serially to personal computer through Ethernet port. It is assumed that the correlator will be connected to the outputs of ADC. But for testing we transferred input signals through the Ethernet port from the computer.

A TCP sever was run on NIOS II processor of the FPGA board in order to provide connection to the computer. A client program running on PC was connected to this server and was used for transmission of initial data, reception of correlation results and their comparison with theoretical ones.

Data for computing from PC comes to FPGA via Ethernet to Ethernet controller. Nios II processor manages the data streams. Data from Ethernet controller comes to Delay and directly to correlator channels. After processing results through the Results bank come back to Ethernet controller and from there – to PC for displaying and analyzing.

The correlator test results as seen in the PC client program, are shown in fig. 3.

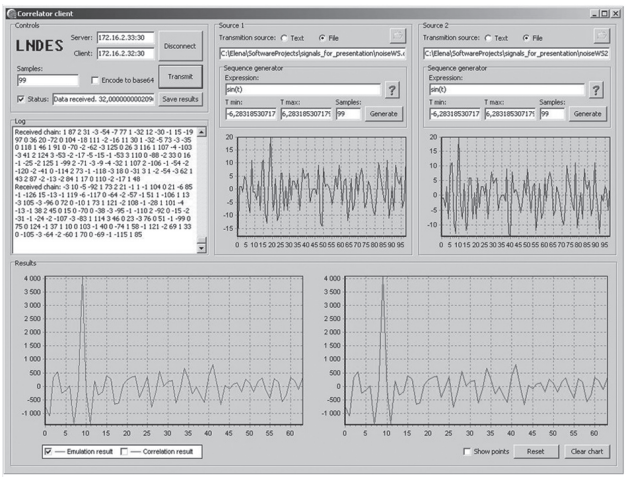

Fig. 3. The PC client program window with correlator test results

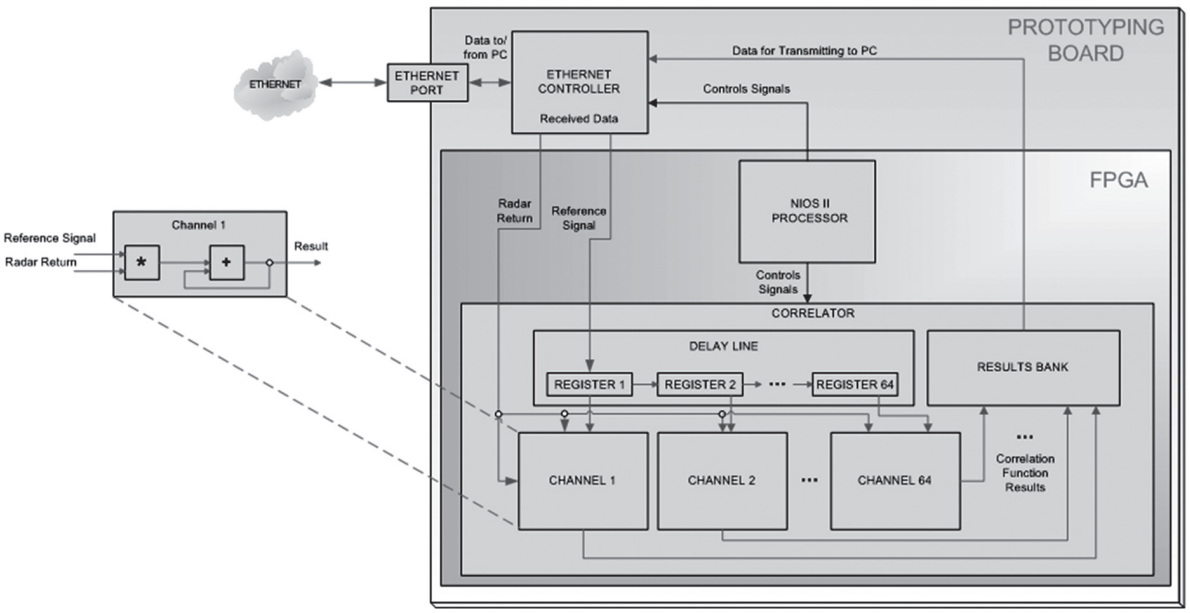

Fig. 2. Flow diagram of multichannel correlator using FPGA

3. SOFTWARE-DEFINED NOISE RADAR

The successful development and tests of the FPGA-based time domain correlator allowed us to prove the concept further by developing a software-defined noise radar (SDNR) for continuous signals. For this project we used the RVI Development Board, developed at the ICTP M-LAB.

It is based on the Actel ProASIC 3E FPGA chip [4]. Fig. 4 shows the flow diagram of the SDNR for continuous signals. The sampling frequency of the 10-bit on-board ADC is 20 MHz. The update rate of the 14-bit on-board DAC is 1 MHz. Thus, the output dataflow is small enough to let us use the COM-port. The maximum frequency of the on-board chip is 57600 bits per second, which suits our purposes.

The Random signal generator uses a common pseudo-random signal generation algorithm – linear congruential algorithm. Its output is fed to the DAC through the output buffer, which stores the output as the reference signal. The buffer length can be adjusted to evaluate various range bins. After the signal is amplified, transmitted, received, and amplified again, it is digitized by the ADC and fed into the correlator together with the reference signal. The result from the correlator is serialized by a FIFO-module and transmitted to the COM-controller, which sends it to the PC.

The results of a cable-medium test of the software-defined radar, as shown by the COM-client program, are presented in fig. 5. The generated pseudo-random reference signal is shown in fig. 6.

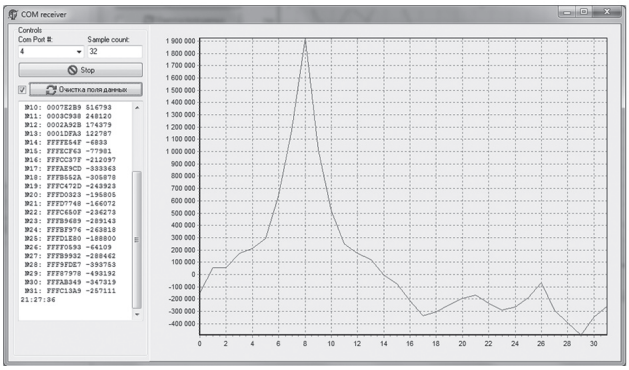

Fig. 5. Cross-correlation estimation in Software Defined Radar

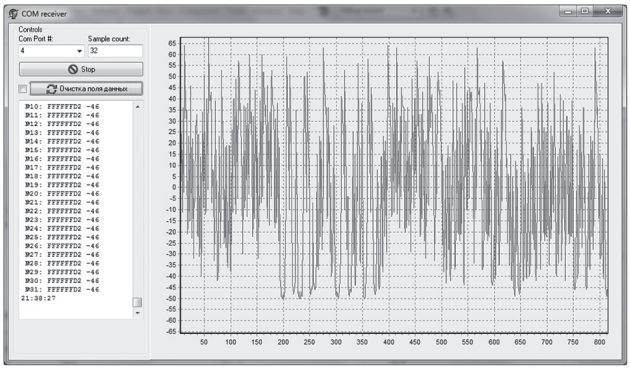

Fig. 6. Reference signal in the COM-client

4. RADAR SIGNAL GENERATOR

For generation of radar waveforms of different types we use the approach, that supposes having a programmable algorithm for obtaining the waveform samples directly in the FPGA and involves the calculation of each sample in real time. This method is extremely versatile, because it allows storing the code for different algorithms in the program part of the FPGA and quick switching between them without the need to reprogram the entire device for the desired type of signal.

HDL coder (version 3.0) was used for generating of portable VHDL code from Simulink (MATLAB ver.7.14.0.739 R2012a) models for the following types of radar waveforms: spreading pseudo-noise binary sequence of maximal length generated by LFSR of arbitrary word length; periodic pulsed LFM waveform (validated for the linear case; nonlinear frequency varying can be distinguished via replacing in the model the linear block by a nonlinear function); periodic pulsed waveform with prescribed duty cycle (this is the basic model for any pulsed waveforms with random or another type of filling); random stepped frequency waveform. Simulink models for above waveforms were created using a library of Simulink blocks (fig. 7), each of them is compatible with HDL code generation routine.

For justification of feasibility of the suggested method we used evaluation board which is built on around a medium to large capacity FPGA device [5]. It hosts a ProASIC 3E FPGA chip (A3PE1500, FGG484), several peripheral interface controllers (LPT, RS-232, USB, and Ethernet), SDRAM Memory interface (256/512 MB), JTAG interface

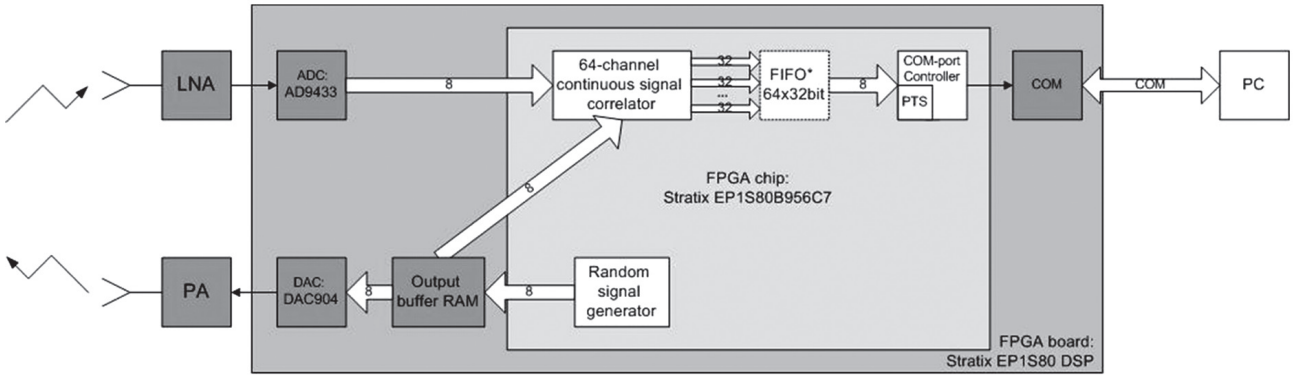

Fig. 4. Flow diagram of the software-defined noise radar for continuous signals

for in-system programming and two expansion slots for daughter boards with ADC and DAC modules. Also, generated VHDL models have been tested using ModelSim test bench. Validation of developed VHDL codes is in progress using Actel Fusion Embedded Development Kit based on M1AFS1500-FGG484 FPGA device and Spartan-3E Embedded Processing development board based on Spartan-3E FPGA device. Fig. 8 shows output of Simulink model for RSG in random stepped frequency mode. Fig. 9 shows output from FPGA device received by PC through RS-232 interface.

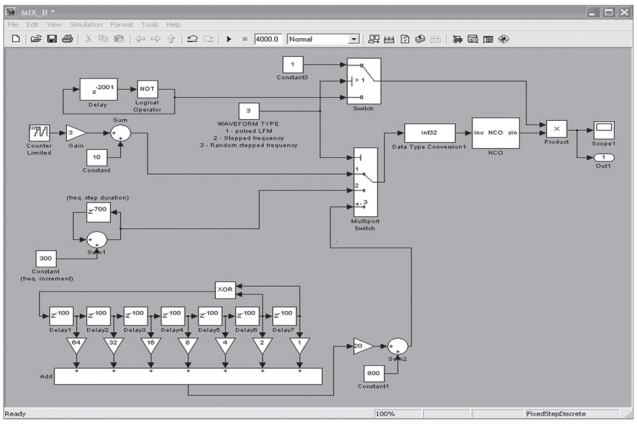

Fig. 7. Simulink model for Radar Signal Generator (RSG)

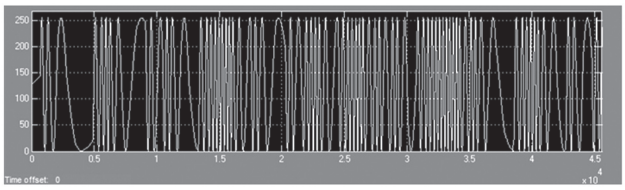

Fig. 8. Output of Simulink model for RSG in random stepped frequency mode

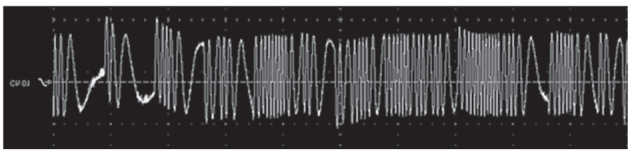

Fig. 9. RSG output in random stepped frequency mode from FPGA device received by PC through RS-232 interface

5. SPOS FPGA BOARD

Signal Processing OrbiSat (SPOS) is a robust single-board FPGA based system for realization of software-defined radar and other applications. It was developed by OrbiSat da Amazonia S.A company [6]. The block diagram of SPOS board is shown in fig. 10.

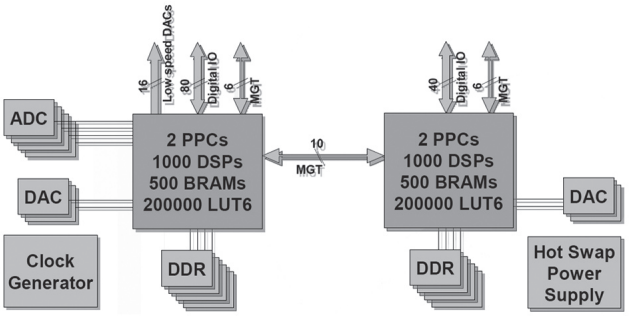

Fig. 10. SPOS FPGA Board Architecture

The board hosts four 14-bit ADCs with up to 400 MHz sampling rate, five 12-bit DACs with up to 800 MHz sampling rate and 5 digital up-converters integrated in the DACs with a bandwidth of 160 MHz, programmable synchronized clock generation with 7 output channels including independent phase shifts, PLL for synchronization to an external clock or direct external clocking. The board itself is shown in fig. 11. The computational capabilities of the board are provided by 2 Xilinx Virtex 5 FPGAs (option: FX200T, FX130T, FX100T, SX240T).

Each FPGA chip contains:

– up to 2112 DSP48E blocks;

– up to 1032 dual port 36 kbit BRAMs;

– up to 400000 FPGA lookup tables with 6 inputs (LUT6).

Each FPGA chip can host up to 4 PPC440 processors (see fig. 12). The capabilities listed above are more than enough to host the core and interfaces of real-time multichannel time-domain correlator.

Memory and interfaces:

• 32 multiple Gigabit transceivers (MGT) up to 6.5 Gbits/s;

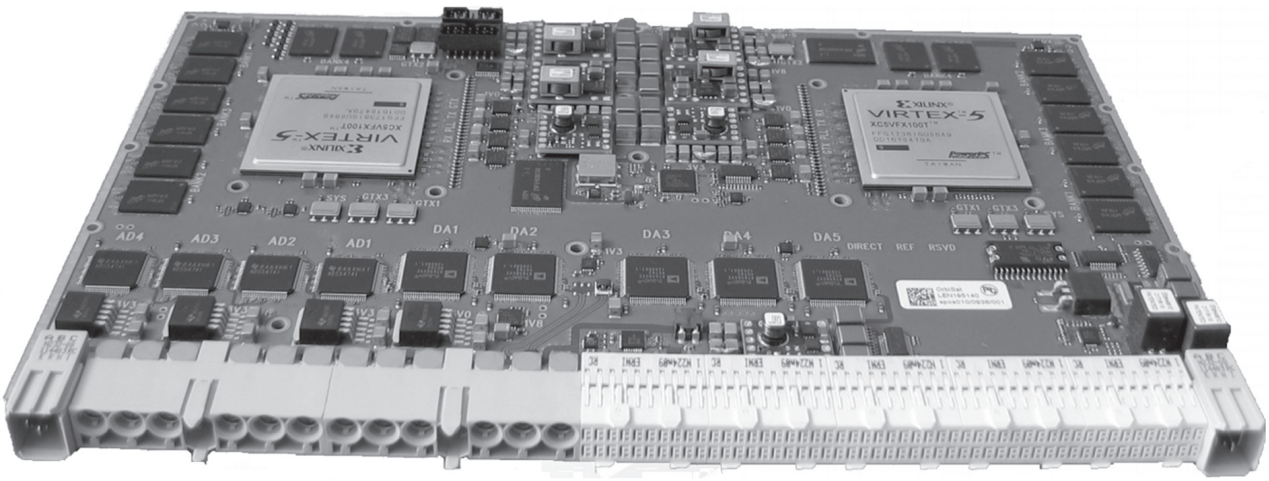

Fig. 11. SPOS FPGA Board

• 12 MGT links for inter-board`, 10 MGT links for inter FPGA communication (these can be used for interfacing in case we need to use multiple FPGA boards);

• MGT protocols: PCI-Express, Gbit Ethernet, SATA, Aurora.

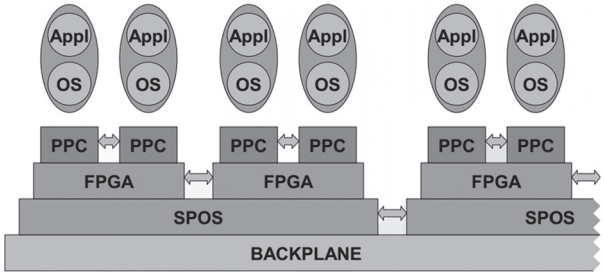

Fig. 12. SPOS FPGA Board Intercommunication

Thus the board can be connected to a PC through PCI-Express for control, data transfer & display. We can use Gbit Ethernet for the same purpose as well. This allows us to build the SDNR as a more autonomous system. The SATA interface can be used for storage of radar data, computation results and long pre-generated sounding signals in case we want to use this approach instead of on-the-fly signal generation.

• 16 DAC output channels at up to 1 MHz sampling rate, 12 bits resolution. These can be used for control of analog elements of the system RF part.

• 8 independent DDR2 DRAM banks, each 512 Mbytes. The memory is needed to store the generated sounding signals, radar returns, results from the correlator and further processing, if it is also implemented in the FPGA.

• 2 independent NAND FLASH memories, each 8 GBytes. They will be used for hosting the OS files should we require one and, more importantly, pre-generated sounding signals.

• 2 SPI flash memories for multiple FPGA configurations;

• 120 digital input/output ports for single ended or differential use.

Other characteristics:

• Power supply and temperature monitoring (built-in test);

• Real time clock with programmable alarm and watchdog;

• Unique board identifier;

• All input/ output channels routed to backplane connectors for easy board exchange (hot swap);

• Single power supply;

• Rugged board for conduction or air cooling;

• Industrial temperature range;

• Impedance controlled 20 layer board.

Software capabilities include:

• Native or embedded Linux operation (very useful for sequential signal processing, network capabilities and creating an independent radar system with graphical user interface);

• High level software library for board configuration and operation;

• Each PPC with 4 hardware DMA engines and crossbar for peripheral access;

• Multi transfer architecture in FPGA for signal generation and acquisition;

• Programmable DMA controllers for DRAM access;

• Ideally suited for high efficient real-time processing.

6. CONCLUSIONS

Algorithms for correlation processing in FPGA in time domain have been implemented. The analysis shows that all correlators have rather good performance and each of them can be used for specific applications. The correlator has been implemented in the Altera/Stratix evaluation board having 1 million gates and up to 300 MHz clock frequency. For testing of the correlator designed we used the noise signal and model of radar returns generated in a PC and transmitted to FPGA via Ethernet interface. After evaluation of the cross-correlation function the data from the FPGA are transmitted back to the PC for display and analysis using the same channel. Software defined continuous wave noise radar on the basis of RVI Development Board from ICTP M-LAB has been realized. It utilizes the Actel RVI's onboard ADC & DAC (1 MSPS), computes the 32-rangebin estimation of cross-correlation function at 25 MHz and transmits the results to PC via COM-port at 576 kbit/s.

We have also regarded the possibility of developing real-time software defined noise radar based on SPOS FPGA Board and find the board highly suitable for this application.

References

1. K.A.Lukin, "Noise Radar Technology", *Radiophysics and Electronics*, Kharkov, Institute for Radiophysics and Electronics of NAS of Ukraine, 1999, Vol.4, #3, pp.105-111.
2. *Lukin K. A.* Noise Radar Technology: the principles and short overview // Applied Radio Electronics. Vol. 4, No. 1. 2005. P. 4-13.
3. *Lukin K. A., Vyplavin P. L., Zemlyaniy O. V., Palamarchuk V. P., Lukin S. K.* High Resolution Noise Radar without fast ADC // International Journal of Electronics and Telecommunications (JET). 2012. Vol. 58, No. 2. P. 135-140.
4. http://mlab.ictp.it/microlab/research/rvi.html
5. Cicuttin A., Crespo M. L., Shapiro A., Abdallah N. A Block-Based Open Source Approach for a Reconfigurable Virtual Instrumentation Platform Using FPGA Technology // IEEE International Conference on Reconfigurable Computing and FPGA's (ReConFig 2006), San Luis Potosi, Mexico, September 20-22, 2006. P. 39-46.
6. http://www.orbisat.com.br/novo/index.php

Manuscript received January, 17, 2013

Joao Roberto Moreira Neto, graduated from the Aeronautical Technological Institute ITA, Sao Jose de Campos, in 1982, the Dipl.-Ing. degree in electrical engineering from the Technical University of Munich, Germany, in 1985, and the Dr.-Ing. degree in microwave engineering, also from the Technical University of Munich,

in 1992. In 1983 he joined the Institute for Radio Frequency Technology at the German Aerospace Research Establishment, DLR, in Oberpfaffenhofen, Germany. Since 1983 he has been engaged in the design and development of the experimental SAR system of DLR. In 1987-1996 he has been leading the SAR Simulation and Processing Group. In 1996-2001 he was Head of Director of Radar Systems Remote Sensing at Aerosensing Radarsysteme GmbH, Germany. Since 2002 he is Head of OrbiSat Ind. e Aerolevantamento S.A., Brazil.

Konstantin Lukin, for photograph and biography, see this issue, p. 24.

Oleg V. Zemlyaniy, for photograph and biography, see this issue, p. 36.

Vyplavin Pavel Leonidovich, Ph.D. physics and mathematics, scientist of Laboratory for Nonlinear Dynamics of Electronic Systems of Usikov Institute for Radiophysics and Electronics NAS of Ukraine. The field of scientific interests: noise radar technology, chaotic waveform generation and processing, SAR imaging.

Sergiy K. Lukin, for photograph and biography, see this issue, p. 36.

УДК 621.37

Программно-определяемый шумовой радар на основе ПЛИС / К.А. Лукин, Дж. Морейра, П.Л. Выплавин, С.К. Лукин, О.В. Земляный // Прикладная радиоэлектроника: науч.-техн. журнал. – 2013. – Том 12. – № 1. – С. 89–94.

Концепция программно определяемого радара, которая предполагает реализацию всех радарных блоков в цифровом исполнении, была применена для разработки шумового радара, имеющего такие привлекательные характеристики, как скрытность, отсутствие неоднозначности измерений дальности, высокая электромагнитная совместимость и т.д. Эта концепция требует проектирования цифровых генераторов случайных сигналов и цифровых приемников на базе корреляторов на основе быстрой цифровой техники типа FPGA. В работе представлены результаты нашей оценки возможности разработки программно определяемого шумового радара и приводятся результаты разработки соответствующих цифровых блоков на основе различных FPGA. В экспериментах мы генерируем шумовые сигналы в цифровом генераторе, осуществленном в FPGA, преобразуем его в аналоговую форму и излучаем сигнал в направлении цели. Отраженные сигналы оцифровывались в бортовом АЦП и подавались в цифровой коррелятор, также реализованный в FPGA, наряду с копией переданного сигнала, используемого в качестве опоры. Выход коррелятора обрабатывался в ПК с помощью соответствующих алгоритмов. Приведены оценки создания программно определяемого шумового радара с использованием цифровой платы SPOS, разработанной компанией ORBISAT на основе FPGA фирмы XILINX.

Ключевые слова: шумовая радарная технология, программно определяемый радар, ПЛИС, шумовой сигнал, генератор случайных сигналов, цифровая обработка сигналов, кросс-корреляция, коррелятор.

Ил. 12. Библиогр.: 6 назв.

УДК 621.37

Шумовий радар, що визначається програмно на основі ПЛІС / К.А. Лукін, Дж. Морейра, П.Л. Виплавін, С.К. Лукін, О.В. Земляний // Прикладна радіоелектроніка: наук.-техн. журнал. – 2013. – Том 12. – № 1. – С. 89–94.

Концепція радара, що визначається програмно, яка передбачає реалізацію всіх радарних блоків у цифровому виконанні, була застосована для розробки шумового радара, що має такі привабливі характеристики, як скритність, відсутність неоднозначності вимірювань дальності, висока електромагнітна сумісність, тощо. Ця концепція потребує проектування цифрових генераторів випадкових сигналів і цифрових приймачів на базі кореляторів на основі швидкої цифрової техніки типу FPGA. У роботі представлені результати нашої оцінки можливості розробки шумового радара, що визначається програмно, і наводяться результати розробки відповідних цифрових блоків на основі різних FPGA. В експериментах ми генеруємо шумові сигнали в цифровому генераторі, здійсненому в FPGA, перетворюємо його в аналогову форму і випромінюємо сигнал у напрямку цілі. Відбиті сигнали оцифровувалися в бортовому АЦП і подавалися в цифровий корелятор, також реалізований в FPGA, разом з копією переданого сигналу використовуваного як опора. Вихід корелятора оброблявся в ПК за допомогою відповідних алгоритмів. Наведено оцінки створення шумового радара, що визначається програмно, з використанням цифрової плати SPOS, розробленої компанією ORBISAT на основі FPGA фірми XILINX.

Ключові слова: шумова радарна технологія, радар, що визначається програмно, ПЛІС, шумовий сигнал, генератор випадкових сигналів, цифрова обробка сигналів, крос-кореляція, корелятор.

Іл. 12. Бібліогр.: 6 найм.

UDC 621.37

COMPRESSION AND INTERPERIOD PROCESSING OF SIGNALS IN SURVEILLANCE RADARS

V.V. RODIONOV

This article considers the formation of probing signal with low-level side lobes of the range uncertainty function, algorithms for detection of moving targets among passive interferences, and a possibility for their implementation by means of digital signal processing modules.

Keywords: signal, radar, compression.

1. INTRODUCTION

Any modern ATCRBS's signal processing functions are as follows:

• Formation and compression of signal with low-level side lobes of the range uncertainty function;

• Interperiod processing of reflected signal in order to detect moving targets among passive interferences;

• Detection of moving targets, their coordinates' estimation (including their azimuth and range estimation), plots formation, and their transmission to the air traffic control tower (ATCT) via the relevant communication channel;

• Targets tracking; and

• Information imaging on the radarscope.

All the functions above may be performed by means of modern digital signal processing modules.

There are many companies these days that manufacture digital modules with various architectures, which employ various types of digital signal processors (DSP's) and programmable integrated circuits (PIC's). Let us consider the algorithm for signals processing used in ATCRBS's before we make a reasonable choice between various digital modules' architectures.

It becomes obvious from Fig. 1 that the information processing is performed consecutively in an RBS. That was the reason why we chose a signal processing digital module employing 4 ADSP-21160 digital signal processors (DSP's) manufactured by Analog Devices, and integrated into an ADP160QPCIv2.2 circuit board in conjunction with the ADMDD-C2WB-L digital receiving sub-module manufactured by Instrumentalnye Systemy Company, Moscow.

Please consult Fig. 2 for the layout of the digital module employing a ADP160QPCIv2.2 circuit board.

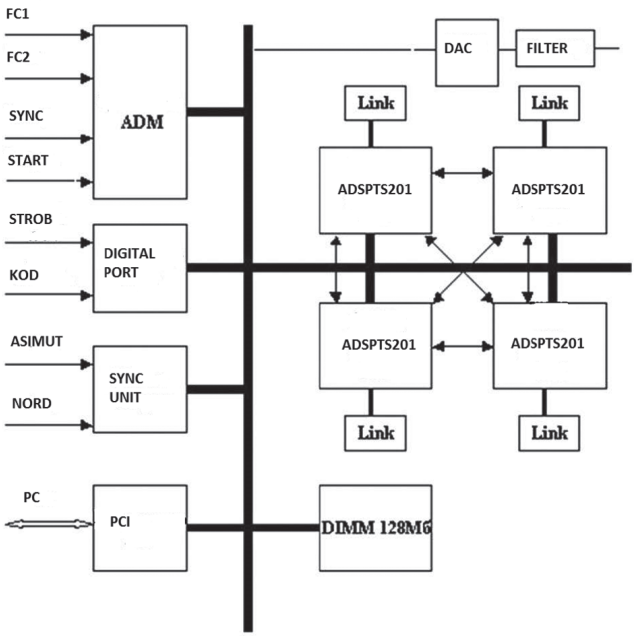

Fig. 2. Layout digital module employing a ADP160QPCIv2.2 circuit board

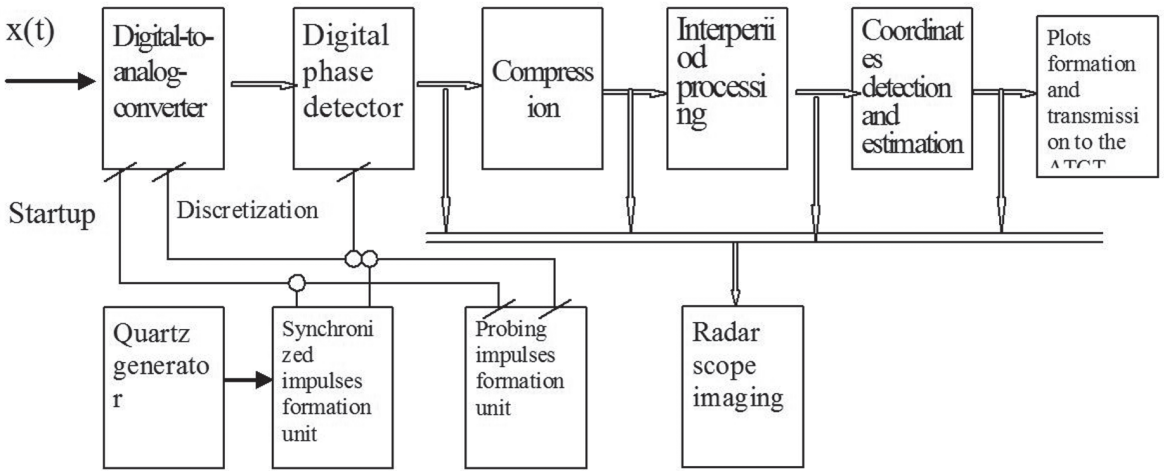

Fig. 1. The algorithm for signals processing used in ATCRBS's

The intermediate frequency amplifier's output signals are converted into digital countdowns by means of the DAC. Subsequently, the digital phase detector performs the digital operation of quadratures detection. The operations in question are performed by the digital receiving sub-module. The resulting complex digital signal is compressed by the third signal processor, to transmit the compression result to the second processor via the two links. The second processor performs the interperiod processing, employing the interferences chart that is stored in the external RAM. The processing results are transmitted to the first processor via the link. The first processor performs the incoherent accumulation, the detection, and the estimation of the coordinates, and represents the processed information in analog form via the DAC in the shape of so called "raw video". The resulting estimations are transmitted to the ATCT via the communication line together with the additional information (the plots). The fourth signal processor employs the algorithm for the information processing of the secondary locator that operates in ATC and RBS modes.

The computerized radarscope may represent the information at various processing stages, including the uncompressed signals, the compressed signals, the signals after interperiod processing, and the fully processed signals with the plots being transmitted to the ATCT represented. The personal computer can also be used to control the information processing, the receipt, and the detection of accidents and errors.

2. FORMATION AND COMPRESSION OF SIGNALS WITH LOW-LEVEL SIDE LOBES OF THE RANGE UNCERTAINTY FUNCTION

When an RBS's range is extended while the transmitter's peak power remains limited, complex signals have to be used. As a result, the side lobe' level of the signal's range uncertainty function begins to affect the resistance to interference when passive interference takes place.

A problem arises when it comes to choosing a probing signal and such an algorithm for its processing, which will guarantee a preset low level of the side lobes in the uncertainty function, as well as small losses in the signal-to-noise ratio caused by uncoordinated processing.

Amplitude frequency correction of the received signals is one of the methods to reduce the side lobes' level in compressed signals [1, 2].

It is the fundamental concept of amplitude frequency correction that the received signals are to be passed through such a filter that the output signals do not have any phase modulation, while its amplitude frequency spectrum coincides with the preset function of the frequency window whose profile guarantees a preset side lobes' level. In [1], this method to reduce the side lobes' level is referred to as the reverse pulsations method.

It was demonstrated in [2] that for signals with nonlinear frequency modulations, whose complex envelope spectrum has the form

$$S(f,a)=\int_{-T/2}^{T/2} e^{j2\pi\left(ft+\sum_{i=0}^{n-1} a_i\left(\frac{t}{T}\right)^{2i+2}\right)}dt,$$

the frequency characteristics of the correction filter is equal to $H(f)=\frac{X(f)}{S(f,a)}$, while the modulation parameters are derived from the extremum problem

$$\min_a \int_{-\infty}^{\infty}\left|\frac{X(f)}{S(f,a)}\right|^2 df.$$

Here, $X(f)$ is the desired form of the amplitude frequency characteristics of the output signal produced by the compression filter.

We chose Nuttall window as the frequency window, where the side lobes' maximum level was -98 dB and the side lobes' decrease rate was 6 dB/octave. It was proven in [2] that for a signal with the duration of 32 μs, the signal-to-noise ratio losses were equal to -0.097 dB. The signal's frequency modulation parameters were a_0= 8.692, a_1=-5.353, a_2= 47.9. The frequency deviation was 0.9373 mHz.

Fig. 3 and 4 shows signal's responses with nonlinear frequency modulation at the matched filter's output and at the correction filter's input.

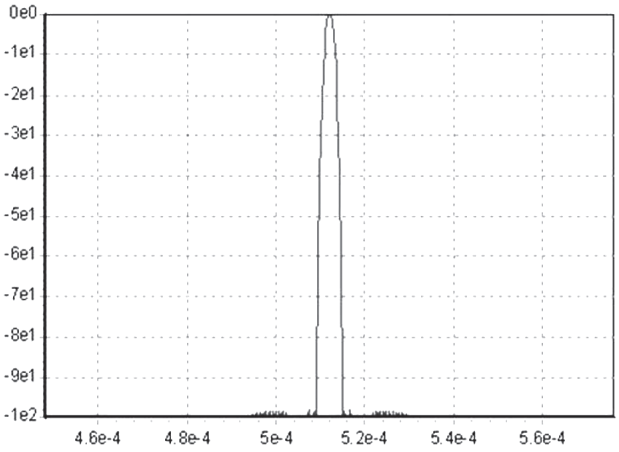

Fig. 3. Filter's response output

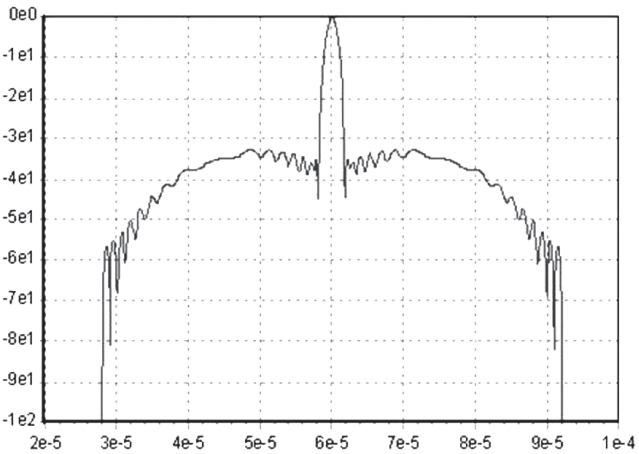

Fig. 4. Correction filter's response output

3. INTERPERIOD PROCESSING OF REFLECTED SIGNALS TO DETECT MOVING TARGETS AMONG PASSIVE INTERFERENCE

Methods to synthesize optimal algorithms for detection of moving point targets have been widely described in literature.

In coherent RBS's, a signal reflected by a target can be in most cases represented as a slowly fluctuating Gaussian process (as a model of a quasi-determined signal).

When it comes to synthesizing a detection algorithm within the conceptual framework of this model, the reflected signal's Doppler frequency is assumedly known. Moreover, an algorithm for both signals and interferences, synthesized from a comprehensive a priori information is optimal, while its detection characteristics are limitedly achievable.

In RBS detection problems (e.g., those for ATCRBS's), the reflected signal's Doppler frequency is unknown, and, in most cases, is not required. Besides, in reality, the passive interference's correlation function, on which the detection algorithm depends, is unknown either.

When it comes to the detection of a point target among a long-range interference, there is a good chance that we can estimate the interference's unknown correlation function, and to realize the adaptive detection algorithm.

The algorithm in question can be synthesized by substituting the interference's unknown parameters in the algorithm that has been synthesized from comprehensive a priori information, for the estimations derived form the classified training sample.

When information about the reflected signals' Doppler frequency is required (e.g., in an ATCRBS), a signal burst's model with independently fluctuating pulses may be used as a reflected signal's model.

It is not impossible to demonstrate [3] that the detection algorithm represented as an independently fluctuating pulses burst with wobulation of the repetition period among a passive Gaussian interference and Gaussian white noise assumes the form:

$$\sum_{k=0}^{N-1} \frac{1}{\left(\lambda_k + d_{sh}^2\right)\lambda_k} \left| \sum_{i=0}^{N-1} x_i \psi_{ki} \right|^2 >< c$$

where ψ_{ki} and λ_k are the eigenvectors and the eigenvalues of the correlation matrix **(K)** of interference-and-noise mixture; d_{sh}^2 is the signal-to-noise ratio, and N is the number of pulses per burst.

It is obvious that when the signal is weak ($d_{sh}^2 << \lambda_k$), the algorithm in question is the known algorithm for optimal filtration with incoherent accumulation, while when the signal is strong ($d_{sh}^2 >> \lambda_k$), this algorithm is the algorithm for detection with the passive interference's decorrelation and subsequent incoherent accumulation.

The analysis has proven [3] that when the number of pulses per burst is less than 20, the signal-to-noise ratio losses in the algorithms above do not exceed 3.6 dB in comparison with the optimal ones, but the algorithm employing interference decorrelation takes lesser amount of calculations.

When it comes to practical realization of the adaptive algorithms based on the detection algorithms above, the estimations of the unknown values ψ_{ki} and λ_k have to be calculated.

Let us set the class of the interference for which the adaptation is to be performed.

It has been proven in the course of studies that in L-band RDS's, the interperiod correlation index is, in most cases, close to 1 ($\approx 0.97..0.99$). Moreover, weather fronts as whole objects can have such a displacement rate that causes Doppler frequency shifts in the interference's correlation matrix.

When the correlations is so high, the form that the fluctuations correlation matrix's eigenvectors assume (without the Doppler frequency shift taken into account) is little dependent on the fine structure of the matrix in question, and can be predetermined.

That is why it is not impossible to determine the interference class that admits the following notation for the fluctuations correlations: $K_{ij} = \sum_{k=0}^{N-1} \lambda_k \psi_{ki} \psi_{kj}^* C_i C_j^*$.

Here, $C_i = \exp(j2\pi f_g t_i)$; the orthonormal vectors' system $\vec{\psi}_k$ was selected in advance, while the parameters λ_k *and* f_g stand for the interference's Doppler frequency and may vary.

The parameters in question are estimated be means of the interference's training sample $\left(\vec{x}_1, \vec{x}_2, ..., \vec{x}_n\right)$.

It is obvious that the estimations of the maximum likelihood of the values $C_0 C_j^*$ and λ_k are as follows:

$$\hat{C_0 C_j} = \frac{\sum_{i=1}^{n} x_{0i} x_{ji}^*}{\left| \sum_{i=1}^{n} x_{0i} x_{ji}^* \right|}, \quad \lambda_k = \frac{1}{n} \sum_{i=1}^{n} \left| \sum_{j=0}^{N-1} x_{ji} \psi_{kj}^* \hat{C_0 C_j^*} \right|^2.$$

It is noteworthy that the algorithm's computational complicity does not depend on the training sample's volume, because the respective maximally likely estimations can be calculated recurrently.

The experience of designing and operating the digital module that employed the ADP160QPCIv2.2 circuit board in conjunction with the ADMDD-C2WB-L digital receiving sub-module demonstrated not only its strengths but also revealed some weaknesses caused by the circuit board's versatility.

In particular, it turned out that the implementation of the same internal bus for both the receipt of digital data from the digital receiver and the data transmission to the RAM, to the host computer, and to the DAC considerably slowed down the operation, and prevented us from using more complex processing algorithms that required more intense exchange with the external memory.

Nonetheless, the processing algorithms above were realized when using the circuit board integrated into the АОРЛ-1АС, an air route surveillance radar at

the Polyot Radio Plant's testing ground, and yielded good results.

Figure 5, 6 shows the radarscope images before and after an interperiod processing. The target disguised by a weather front on the Before picture is clearly seen on the After picture, while the weather clutter and the ground clutter are suppressed.

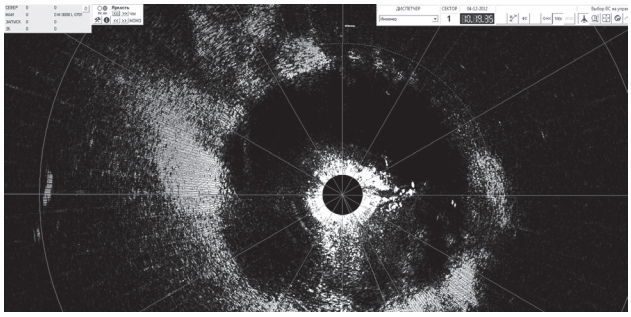

Fig. 5

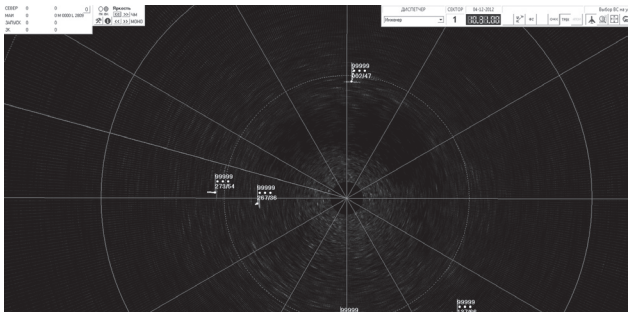

Fig. 6

References

[1] *Оконешников В.С., Кочемасов В.Н.* Сжатие частотно-модулированных сигналов с небольшим произведением девиации частоты на длительность импульса // Зарубежная радиоэлектроника. – № 1. – 1987. – С. 82-94.

[2] *Родионов В.В., Рукавишников В.М., Филонов Ю.В. и др.* Способ обработки радиолокационного сигнала. – Патент на изобретение №2212683 от 20.09.2001

3. *Родионов В.В.* Адаптивный алгоритм обнаружения точечных целей на фоне протяженных по дальности помех // Прикладная радиоэлектроника. – науч.-техн. журнал. – 2002. – Т. 1. – № 2 . – С. 205-209.

Manuscript received January, 30, 2013

Rodionov Vladimir Valentinovich, doctor of the technical sciences, professor, chief of the research centre JSC «Chelyabinsk radio plant «Polet». The Area scientific interest: Game-theoretical models of the interaction radar station and systems electromagnetic countermeasures and radar systems for air traffic control

УДК 621.37

Сжатие и межпериодная обработка сигналов в обзорных радарах / В.В. Родионов // Прикладная радиоэлектроника: науч.-техн. журнал. – 2013. – Том 12. – № 1. – С. 95–98.

В работе рассматриваются формирование зондирующего сигнала с низким уровнем боковых лепестков в дальностном сечении функции Вудворда, алгоритмы обнаружения движущихся целей на фоне пассивных помех и возможность их реализации посредством модулей цифровой обработки сигнала.

Ключевые слова: сигнал, радар, компрессия сигналов.

Ил. 06. Библиогр.: 3 назв.

УДК 621.37

Компресія та міжперіодна обробка сигналів в оглядових радарах / В.В. Родіонов // Прикладна радіоелектроніка: наук.-техн. журнал. – 2013. – Том 12. – № 1. – С. 95-98.

У роботі розглянуті формування зондуючого сигналу з низьким рівнем бічних пелюсток в дальністному перерізі функції Вудворда, алгоритми виявлення цілей, що рухаються на фоні пасивних перешкод, та можливість їх реалізації за допомогою модулів цифрової обробки сигналів.

Ключові слова: сигнал, радар, компресія сигналів.

Іл. 06. Бібліогр.: 3 найм.

UDC 537.874

PARTIAL DIELECTRIC LOADED TEM HORN AND REFLECTOR ANTENNA DESIGNS FOR ULTRAWIDE BAND GROUND PENETRATING RADAR SYSTEMS

A.S. TURK, A.K. KESKIN, M. ILARSLAN

This paper deals with ultra-wide band (UWB) TEM horn antenna designs and their usage as feeder of parabolic reflector, which are suitable for down-looking and forward-looking vehicle-mounted impulse GPR systems, respectively. On this scope, partial dielectric loaded, Vivaldi form and array configurations of the TEM horn structure are investigated, designed, simulated and measured. Vivaldi shaped TEM horn fed parabolic reflector antenna prototype is proposed to reach hyper-wide band impulse radiation performances from 300 MHz up to 15 GHz for multi-band GPR operation that can provide both deep and high resolution imaging. The gain and input reflection performances are demonstrated with measurement results.

Keywords: Ultra-wide band antenna, TEM horn, Parabolic reflector, Ground penetrating radar, Impulse radiation.

I. INTRODUCTION

Ultra wide band (UWB) antennas have been using increasingly in many applications of high-speed wireless communication, high resolution noise radar, RF jamming and EMC test systems. The operational frequency bands of the impulse and UWB radar systems can be very broad starting from VHF band up to millimeter waves. The UWB operation provides some critical advantages, such as improved detection, adaptive ranging and target resolution performances. There are a few types of UWB antennas which operate at various frequency bands, such as horn, spiral, bi-conical and log-periodic arrays [1].

In recent years, ground-penetrating radar (GPR) has become a leading non-destructive testing and through-wall imaging technology for the detection, identification, and imaging of subsurface structures and buried objects such as pipes, mines, gaps, water channels, tunnels, roads and concealed bodies [2]. The central frequency and bandwidth of the GPR signal are the key factors for the detection performance. The higher frequencies are needed for better resolution, nevertheless the lower frequency bands are preferred to detect something buried too deep due to the dramatically increased wave attenuation in the soil with increasing frequency. Thus, UWB GPR systems are proposed to benefit from both low and high frequencies. For impulse GPR, the impulse durations can vary from a few nanoseconds to hundred picoseconds corresponding to a broad spectrum from 100 MHz to 10 GHz. It can be extended up 15 GHz for stepped-frequency GPR systems, which use microwave tomography methods for high resolution imaging [3].

The target detection and identification performance of the GPR depends significantly on the proper design of the UWB transmitter and receiver (T/R) antennas, which should have high gain, narrow beam, low side lobe and input reflection levels over the wide operational frequency band [2]. On this scope, TEM horn and double-ridged horn antennas (DRHA) are one of most favorites due to their high gain, narrow beam and low input reflection characteristics over 20:1 bandwidth ratio [3]. The TEM horn antenna consists of a pair of triangular or circular slice shaped conductors forming some V-dipole [4]. The partial dielectric loading (PD) techniques can be applied to improve the UWB gain performances [5]. For instance, the PD-TEM horn was introduced by Turk as an efficient UWB impulse radiator over 20:1 frequency band [6-7]. Furthermore, its array combination was designed to obtain extended UWB characteristics up to 50:1 [8].

The DRHA operates at very wide frequency band by using ridges inside the horn that adjust the upper and lower cut-off frequencies of the propagating modes [9]. The antenna gain is sufficiently high and almost stable over the wide band. Dielectric aperture loading methods (i.e. hemispherical lenses) can be applied to improve the gain performance at high frequencies. Nevertheless, such big lenses increase the physical dimensions and weight of the antenna. Hence, the partial dielectric lens loading has also been proposed for DRHA to improve the gain performance and to eliminate radiation pattern deterioration without significant changes on the antenna sizes and weight [10].

This paper starts with a generic survey for UWB TEM horn antenna types, which are most suitable design models for multi-sensor adaptive, stepped-frequency and impulse mode UWB GPR systems. For example, the partial dielectric loaded TEM (PDTEM) horn, Vivaldi shaped TEM horn (PDVA) and array combinations have been introduced by Turk, as efficient UWB impulse radiators operating from 150 MHz up to 10 GHz [6-8]. A novel version of Vivaldi shaped TEM horn design is proposed as feeder of the parabolic reflector (PR) to obtain hyper-wide band antenna characteristics from 200 MHz up to 15 GHz. The partially loaded transmission line antenna method (PLTLM) and the analytical regularization method (ARM) are used for proper designs of TEM horn feeder and reflector antennas, respectively. The antenna models were designed and measured between 0.1–15 GHz. The antenna gain, VSWR and radiation pattern performances are presented and compared with standard 1-18 GHz DRHA. It is shown that PDTEM and PDTEM-PR designs are highly suitable for multi-band GPR operations, due to advantages of up to 10 dB enhanced gain performances over 1:100 bandwidth ratio.

II. PLTLM PROCEDURE FOR TEM HORN ANALYSIS

TEM horn is a kind of travelling wave antenna. Hence, its structure can be considered as combination of micro-strip transmission line segments, which are characterized by their local geometrical and constitutional structure parameters. The staircase modelling is used for the analysis. 3D antenna geometry is firstly divided into N number of elementary cells, which are chosen locally homogeneous and sufficiently small in wavelength. Then, the structure is reduced to the equivalent 1D transmission line with corresponding characteristic impedance definitions. The input impedance of each line segment and its characteristic impedance are expressed as [6]:

$$Z_{in}^n = Z_0^n \frac{Z_{in}^{n+1} + jZ_0^n \tan\beta_n l_n}{Z_0^n + jZ_{in}^{n+1} \tan\beta_n l_n};\ n=1,2,...,N \quad (1)$$

$$Z_0^n = 138\sqrt{\frac{\mu_r^n}{\varepsilon_r^n}} \log\frac{8}{(w_n/d_n)};\ \text{for } (w_n/d_n) \le 1 \quad (2)$$

where, β_n is propagation constant, l_n is segment length, w_n is segment width, d_n is segment height, L is the total arm length, $\beta_n = \frac{2\pi f}{c}\sqrt{\mu_r^n \varepsilon_r^n}$ and Z_{in}^{N+1} is the equivalent antenna line output impedance. The input and local reflection coefficients of the n*th* segment line are given by Eqs. (3) and (4):

$$\Gamma_{in}^n = \frac{Z_{in}^n - Z_0^{n-1}}{Z_{in}^n + Z_0^{n-1}};\ n=1,2,...,N \quad (3)$$

$$\Gamma^n(z) = \Gamma_{in}^{n+1} e^{-j2\beta_n(l_{n+1}-z)};\ z \in l_n; 0 \le z \le L \quad (4)$$

Using the Eq. (4), the discrete voltage and current distribution functions over the antenna line are determined as follows:

$$\begin{aligned} V^n(z) &= V_{0+}^n e^{-j\beta_n z}\left[1+\Gamma^n(z)\right] \\ I^n(z) &= I_{0+}^n e^{-j\beta_n z}\left[1-\Gamma^n(z)\right] \end{aligned};\ z \in l_n; n=1,2,...,N \quad (5)$$

V_{0+}^n and I_{0+}^n coefficients are calculated iteratively using the initial values, such as the excitation voltage at the antenna line feed and the source impedance. The integral equation techniques are used to compute radiated field. This method is faster than direct numerical techniques [7].

III. PARTIAL DIELECTRIC LOADED TEM HORN ANTENNA DESIGNS

TEM horn structure consists of a pair of triangular or circular slice shaped conductors forming some V-dipole structure and characterized by L, d, α and θ parameters which correspond to the arm length of antenna, feed point gap, conductor plate angle and elevation angle, respectively [4]. The conventional TEM horn shows band pass filter-like gain behavior due to the arm length that limits the lower cut-off frequency of the radiated pulse. Thus, dielectric filling and partial dielectric loading techniques are employed to broaden the operational band up to twice [5-6].

Some TEM horn, PDTEM horn, PDVA and PDTEM horn array design configurations are given in Table 1 and Fig. 1, with the gain and VSWR measurement results shown in Fig. 2. It is seen that partial dielectric loading approach used in PDVA-10 can attain two times broadened gain characteristics than VA-10 with a VSWR level less than 2. The grating arm model PDVA structure in Fig. 1c, which is basically Vivaldi shaped wing version of the PDTEM horn is a special design proposal for metal detector adaptive operation of GPR [7].

Table 1

UWB GPR antenna designs

Fig	Model	Physical Descriptions
1a	TEM-10	$\alpha = 20°$, $\theta = 60°$, $d = 0.15$ cm, $L = 10$ cm, $\varepsilon_r = 1$, air-filled
	PDTEM-10	$\alpha = 20°$, $\theta = 60°$, $d = 0.15$ cm, $L = 10$ cm, $\varepsilon_r = 3$, dielectric loaded
1b	VA-10	$\alpha = 20°$, $\theta \in (0°–160°)$, $d = 0.4$ cm, $L = 10$ cm, $\varepsilon_r = 1$, air-filled
	PDVA-10	$\alpha = 20°$, $\theta \in (0°–160°)$, $d = 0.4$ cm, $L = 10$ cm, $\varepsilon_r = 3$, dielectric-loaded
1c	PDTE-MA-45	$\alpha_1 = 20°$, $\theta_1 = 90°$, $d_1 = 0.25$ cm, $L_1 = 45$ cm, *aperture*: 10 cm × 15 cm; $\alpha_2 = 20°$, $\theta_2 = f(l) \in (0°–120°)$, $d_2 = 0.2$ cm, $L_2 = 25$ cm, Dielectric profile: $\varepsilon_r = 3.5$, $a_1 = 4$ cm, $a_2 = 13$ cm, $b_1 = 3$ cm, $b_2 = 9$ cm, $b_3 = 7$ cm, $t = 5.5$ cm
2	PDVA-30	$\alpha = 20°$, $\theta \in (0°–160°)$, $d = 0.5$ cm, $L = 30$ cm, $\varepsilon_r = 2.1$, dielectric-loaded

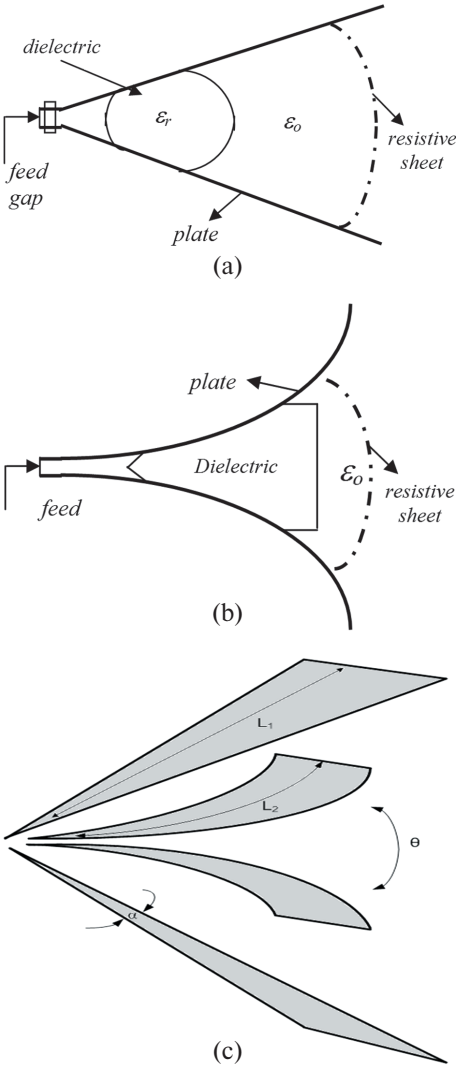

Fig. 1. TEM horn design illustrations: (a) PDTEM horn geometry (side view); (b) Vivaldi form TEM horn (side view); (c) PDTEM horn array (3D view, adapted from [8])

For vehicle mounted systems, the array combination of PDVA with TEM horn antenna can be proposed (see Fig. 1c) for hyper-wide band GPR operations to extend bandwidth ratios up to 50:1 (150 MHz to 10 GHz) [8]. Moreover, partial dielectric loading method can also yield about 5 dB gain increment for standard double-ridged horn antenna structures [10].

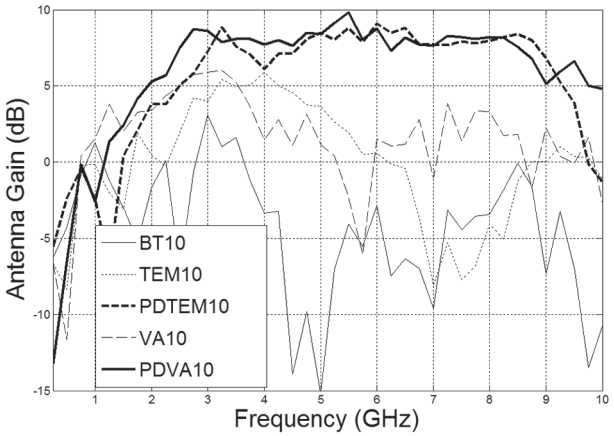

Fig. 2. Antenna gain characteristics of TEM horn designs

The geometrical view of the Vivaldi shaped TEM horn designed as an UWB feeder for parabolic reflector is shown in Fig. 3. The near field illumination of this antenna is calculated by PLTLM (see Section II) and then, the ARM procedure described in Section IV is used for computation of the UWB reflector radiation.

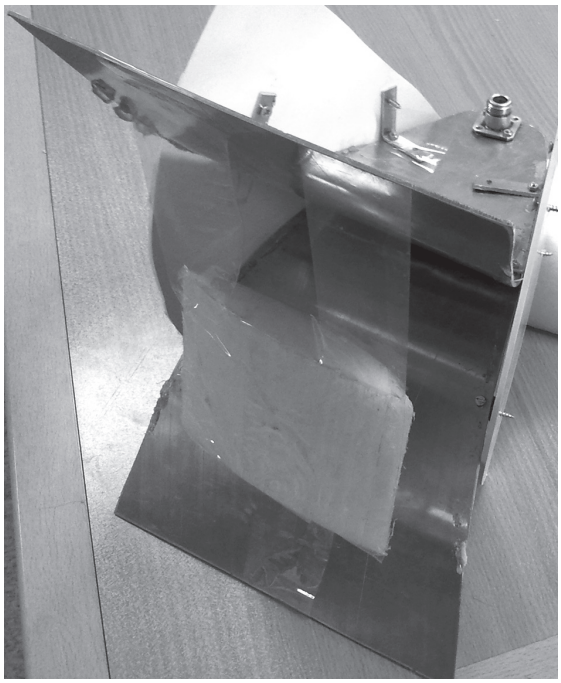

Fig. 3. Designed PDTEM horn feeder for parabolic reflector

IV. ARM FORMULATION FOR PARABOLIC REFLECTOR

Scalar diffraction problem of an infinitely long, smooth, longitudinally homogeneous and perfectly conducting cylindrical obstacle corresponds to the Dirichlet boundary condition for E-polarized incident wave. Considering that XOY plane cross section is denoted by the closed contour S, the incident and scattered scalar wave functions ($u^i(p)$ and $u^s(p)$) must satisfy the Helmholtz equation given in Eq. (6) and the Dirichlet boundary condition in Eq. (7) [11].

$$\left(\Delta + k^2\right)u^s(p) = 0, \quad p \in R^2 \setminus S \tag{6}$$

$$u^{s(+)}(p) = u^{s(-)}(p) = -u^i(p), \quad p \in S \tag{7}$$

where, S smooth contour of the domain D in 2D space R^2 that belongs to the smoothness class $C2,\alpha$ [11]. $u^{s(+)}(p)$ and $u^{s(-)}(p)$ are limiting values of $u^s(p)$ in the inner and the outer sides of S, respectively. The solution of the BVP is written in Eq. (8) using Green's formula and the boundary condition in Eq. (7).

$$-\frac{i}{4}\int_S \left[H_0^{(1)}(k\,|q-p|)Z(p)\right]dl_p = -u^i(q), \quad q,p \in S \tag{8}$$

where, $Z(p) = \dfrac{\partial u^{s(-)}(p)}{\partial n} - \dfrac{\partial u^{s(+)}(p)}{\partial n}$, $p \in S$; n is the unit outward with respect to S normal of the point p. The unknown function $Z(p)$ is constructed by solving Eq. (8), and using parameterization of the S contour specified by the function $\eta(\theta)=(x(\theta), y(\theta))$ that smoothly parameterizes the contour S by the points of $\theta \in [-\pi,\pi]$. The integral equation representation of the first kind in Eq. (8) can be equivalently rewritten by means of the $\eta(\theta)$ parameterization as follows:

$$\frac{1}{2\pi}\int_{-\pi}^{\pi}\left\{\ln\left|2\sin\frac{\theta-\tau}{2}\right| + K(\theta,\tau)\right\}Z_D(\tau)d\tau = g(\theta), \quad \theta \in [-\pi,\pi] \tag{9}$$

with the unknown function $Z_D(\tau)$ and the given function $g(\theta)$, where,

$$Z_D(\theta) = l(\theta)Z(\eta(\theta)),\ g(\theta) = -u^i(\eta(\theta)); \quad \theta \in [-\pi,\pi] \tag{10}$$

$$l(\theta) = \left([x'(\theta)]^2 + [y'(\theta)]^2\right)^{1/2} > 0,$$

$$x(\theta), y(\theta) \in C^\infty\left(Q^1\right) \tag{11}$$

Here $K(\theta,\tau)$ function is rather smooth section of the Green's function in comparison with $\ln\left|2\sin\dfrac{\theta-\tau}{2}\right|$ part that represents the main singularity of the Eq. (4). The functions in Eq. (9) are represented by their Fourier series expansions with ks,m, zm, gm coefficients. Subsequently, one can obtain an infinite system of the linear algebraic equations of the second kind [11]:

$$\hat{z}_s + \sum_{m=-\infty}^{\infty}\hat{k}_{s,m}\hat{z}_m = \hat{g}_s, \quad s = \pm1,\pm2,.. \tag{12}$$

where,

$$\hat{k}_{s,m} = -2\tau_s\tau_m\left[k_{s,-m} + \frac{1}{2}\delta_{s,0}\delta_{m,0}\right],$$

$$\hat{z}_n = \tau_n^{-1}z_n, \hat{g} = -2\tau_s g_s$$

$$\tau_n = \max(1,|n|^{1/2}), \quad n = 0,\pm1,\pm2,.. \tag{13}$$

and $\delta_{s,0}$ is the Kronecker delta function. Finally, the scattered field $u^s(q)$ for $q \in R^2$ are obtained by the

integral equation representation of the Eq. (9) with any required accuracy by the truncation method [12].

The ARM procedure is derived for analysis of scattering from parabolic reflector antenna. The 2-D cylindrical reflector structure illustrated in Fig. 4 is considered. The cross-section of the reflector is a parabolic arc of the outer focus *b*, inner focus *a* and thickness *c*. It is modeled in ARM as a closed contour *L* goes from point *A* to point *D* and back to *A* which corresponds to $\theta\in[-\pi,\pi]$. The total contour *L* which consists of four parts is defined as:

$$L = L_{AB} + L_{BC} + L_{CD} + L_{DA}\text{; Total contour length} \quad (14)$$

$$L_{AB} = b\tan\left(\frac{\psi_{02}-\psi_{01}}{2}\right)\text{; Outer contour length} \quad (15)$$

$$L_{CD} = a\tan\left(\frac{\psi_{02}-\psi_{01}}{2}\right)\text{; Inner contour length} \quad (16)$$

$$\left.\begin{aligned} L_{BC} &= R\pi c_1 \\ L_{DA} &= R\pi c_2 \end{aligned}\right\}\text{; Edge contour lengths} \quad (17)$$

where

$$c_1 = \frac{b-a}{1+\cos\psi_{01}},\ c_2 = \frac{b-a}{1+\cos\psi_{02}} \quad (18)$$

$\psi_{02} = -\psi_{01} = 44^\circ$ and the edge-rolling coefficient *R* is 1.

The parameterization of the contour line is separately implemented from *A* to *D* and back to *A* by means of the variable $l\in[A,D]$ as follows [13]:

$$x = -\frac{2b\cos\phi_1}{1+\cos\phi_1}\quad y = \frac{2b\sin\phi_1}{1+\cos\phi_1};\ l\in[A,B] \quad (19)$$

$$x = -\frac{2a\cos\phi_2}{1+\cos\phi_2}\quad y = \frac{2a\sin\phi_2}{1+\cos\phi_2};\ l\in[C,D] \quad (20)$$

$$\left.\begin{aligned} x &= c_2\cos[(-l+L_{AB})/c_2+\pi-\psi_{02}]- \\ &-\frac{(a+b)\cos\psi_{02}}{1+\cos\psi_{02}}-(R-1)c_2\cos\psi_{02} \\ y &= c_2\sin[(-l+L_{AB})/c_2+\pi-\psi_{02}]+ \\ &+\frac{(a+b)\sin\psi_{02}}{1+\cos\psi_{02}}-(R-1)c_2\sin\psi_{02} \end{aligned}\right\};$$

$$l\in(B,C) \quad (21)$$

$$\left.\begin{aligned} x &= c_1\cos[(-l+L_{CD})/c_1+\pi-\psi_{01}]- \\ &-\frac{(a+b)\cos\psi_{01}}{1+\cos\psi_{01}}-(R-1)c_1\cos\psi_{01} \\ y &= c_1\sin[(-l+L_{CD})/c_1+\pi-\psi_{01}]+ \\ &+\frac{(a+b)\sin\psi_{01}}{1+\cos\psi_{01}}-(R-1)c_1\sin\psi_{01} \end{aligned}\right\};$$

$$l\in(D,A) \quad (22)$$

where

$$l = (\theta+\pi)L/(2\pi)\ ;\quad l\in[0,L]\to(\theta,\tau)\in[-\pi,\pi] \quad (23)$$

$$\varphi_1 = \psi_{01} + [(\psi_{02}-\psi_{01})l/L_{AB}] \quad (24)$$

$$\varphi_2 = \psi_{02} - [(\psi_{02}-\psi_{01})(l-L_{BC})/(L_{CD}-L_{BC})] \quad (25)$$

The PDVA model TEM horn feeder is assumed to be located on the focus of the reflector. The near field illumination of the PDVA-30 on the reflector is defined as the incident wave at ARM algorithm.

V. UWB REFLECTOR DESIGN AND PERFORMANCES

The geometry of the designed reflector antenna with PDVA-30 feeder is given in Fig. 4, with the numerical ARM results shown in Fig. 5. This structure can also be adapted for offset feeding, which is more suitable in forward-looking GPR applications due to low tilt angle.

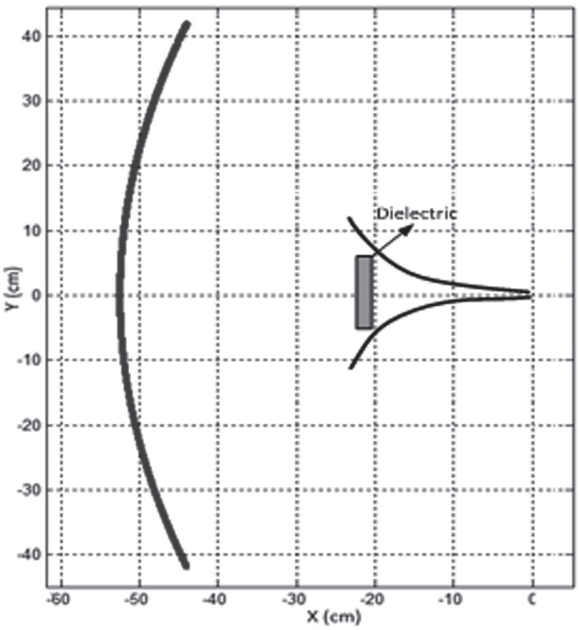

Fig.4. 2D cross-section geometry of parabolic reflector antenna with PDTEM horn feeder

The measurement results plotted in Figs. 6-7 show that radiated impulse signal has highly narrow beam widths and 10 dB improved gain performances can be achieved over 50:1 bandwidth, from 300 MHz up to 15 GHz.

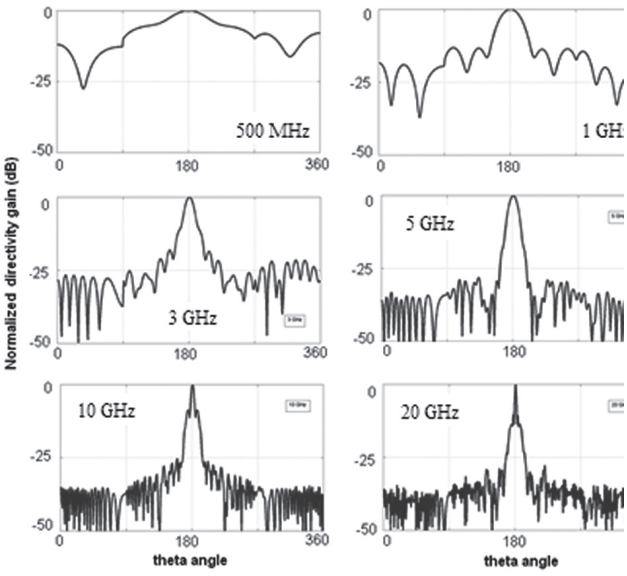

Fig. 5. ARM simulation results of the normalized radiation patterns

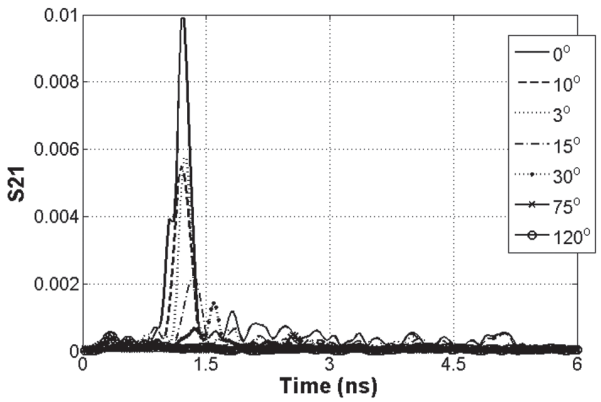

Fig. 6. Time domain transformations of 15 GHz impulse radiation gain measurements for different observation angles

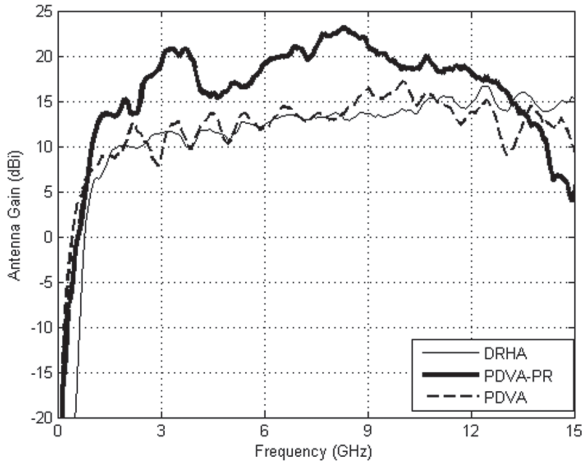

Fig. 7. Antenna gain measurement results; (**Bold**) PDVA fed parabolic reflector, (Solid) 1-18 GHz double ridged horn antenna, (Dashed) PDVA

VI. CONCLUSION

In this study, different design forms of TEM horn antennas, which are dielectric loaded, Vivaldi shaped and array versions, were surveyed for UWB GPR systems. The partial dielectric loaded Vivaldi shaped TEM horn (PDVA) combined with parabolic reflector was introduced to achieve high antenna gain and narrow beam width characteristics over an ultimate wide band greater than 50:1. The PLTLM and ARM algorithms are used to make pre-design of the PDVA-PR in a fast way.

It is shown that antenna attains highly efficient UWB radiation performances, which is suitable for multi-band forward-looking ground-penetrating radar operations.

ACKNOWLEDGMENT

This work was supported by grant 110E222 of TUBITAK (The Scientific and Technological Research Council of Turkey) research fund.

References

[1] *R. J. Fontana,* "Recent system applications of short-pulse ultra-wide band technology", IEEE Trans. Microwave Theory Tech., Vol. 52, No. 9, Sept. 2004.

[2] *D.J. Daniels,* Surface Penetrating Radar, IEE press, London, 1996.

[3] *A. S. Turk, A. K. Hocaoglu*, "Buried Object Detection", Encyclopedia of RF and Microwave Engineering, vol. 1, pp. 540-559, Wiley-Interscience, New Jersey, 2005.

[4] *B. Scheers, M. Acheroy and A.V. Vorst*, "Time-domain simulation and characterization of TEM horns using a normalized impulse response", IEE Proc. Microwave Antennas Propagation, vol. 147, no. 6, 463-468, 2000.

[5] *A. G. Yarovoy, A. D. Schukin, I. V. Kaploun, L. P. Ligthart,* "The dielectric wedge antenna", IEEE Trans. on Antennas and Propagation, vol. 50, no. 10, 1460-1472, 2002.

[6] *A. S. Turk, D. A. Sahinkaya,* "Partial Dielectric Loaded TEM Horn Design for Ultra-Wideband Ground Penetrating Impulse Radar Systems", Ultra-Wideband Short-Pulse Electromagnetics Series 7, chapter 34, Springer, Berlin, 2007.

[7] *A. S. Turk,* "Ultra-wideband Vivaldi antenna design for multi-sensor adaptive ground-penetrating impulse radar", Microwave and Optical Technology Letters, 48, (5), 834-839, 2006.

[8] *A. S. Turk, H. Nazli,* "Hyper-wide band TEM horn array design for multi band ground-penetrating impulse radar", Microwave and Optical Technology Letters, 50 (1), 76-81, 2008.

[9] *C. Bruns, P. Leuchtmann, R. Vahldieck,* "Analysis and simulation of a 1–18-GHz broadband double-ridged horn antenna", IEEE Trans. Electromagn. Compat., 45, pp. 55–60, 2003.

[10] *A. S. Turk., A. K. Keskin,* "Partially dielectric-loaded ridged horn antenna design for ultrawide band gain and radiation performance enhancement", IEEE Antennas and Wireless Propagation Letters, vol. 11, pp. 921-924, 2012.

[11] *Y. A. Tuchkin, E. Karacuha, A. S. Turk,* "Analytical regularization method for E-polarized electromagnetic wave diffraction by arbitrary shaped cylindrical obstacles", 7th Int. Conference on Mathematical Methods in Electromagnetic Theory (MMET 1998), 733-735, Kharkov-Ukraine, 1998.

[12] *E. Karacuha, A. S. Turk,* "E-polarized scalar wave diffraction by perfectly conductive arbitrary shaped cylindrical obstacles with finite thickness", Int. J. Infrared and Millimeter Waves, 22, 1531-1546, 2001

[13] *O. M. Yucedag., A. S. Turk.,* "Parametric design of open ended waveguide array feeder with reflector antenna for switchable cosecant-squared pattern", Applied Computational Electromagnetics Society (ACES) Journal, vol. 27, Issue 8, pp. 668-675, 2012.

Manuscript received February, 13, 2013

Ahmet Serdar Turk received the B.S. degree in Electronics-Communication Engineering from Yıldız Technical University, Istanbul, Turkey in 1996. He received M.S. and Ph.D. degrees in Electronics Engineering from Gebze Institute of Technology, in 1998 and 2001, respectively. He joined the Scientific and Technical Research Council of Turkey (TUBITAK) in 1998. He has worked on land mine detection systems as impulse radar RF system and antenna designer till 2008. He is currently working as professor at Yıldız Technical University Electronics Engineering Department. His research interests include

horn, reflector, array and ultra-wide band antenna designs in RF and microwave bands, numerical methods in electromagnetic wave scattering, high frequency surface wave radar, ground penetrating radar, and microwave and millimeter wave radar systems.

Ahmet Kenan Keskin received B.S. degree in Electronics-Communication Engineering from Yıldız Technical University, Istanbul-Turkey in 2010. He is currently working as research assistant at Yıldız Technical University Electronics Engineering Department. His research interests are ultra-wide band antenna design, ground penetrating radar, RF and microwave circuit design.

Mustafa Ilarslan was graduated from the Middle East Technical University of Ankara in 1989, with a B.Sc. degree in Electrical & Electronics Engineering. He served in various TurAF (Turkish Air Force) units at different positions that include avionics maintenance officer, project officer and IFF systems engineer at NATO till 2003. He received M.Sc. degree in Electronics Engineering from the Osmangazi University of Eskisehir, Turkey. He joined the academic staff of TurAF Academy in 2008 and held the positions of Planning Division chief and the head of Electronics Engineering department. He has been the director of Aeronautics and Space Technologies Institute of TurAFA located in Istanbul, Turkey since March 2011. His research interests are aircraft and spacecraft avionics, systems engineering, radar and EW systems and technologies.

УДК 537.874

Применение частично заполненных диэлектриком антенн рупорного и рефлекторного типов для сверхширокополосных подповерхностных радиолокаторов / А.С. Турк, А.К. Кескин, М.Иларслан // Прикладная радиоэлектроника: науч.-техн. журнал. – 2013. – Том 12. – № 1. – С. 99–104.

Статья посвящена разработке сверхширокополосных (СШП) ТЕМ-антенн рупорного типа и их использованию в качестве облучателя для параболического отражателя, которые предназначены для установленных на транспортных средствах смотрящих вниз и вперед импульсных георадаров, соответственно. С этой целью были исследованы, сконструированы, промоделированы и измерены частично заполненные диэлектриком антенны Вивальди и конфигурации массива ТЕМ-рупоров. С использованием антенны Вивальди в форме ТЕМ-рупора в качестве облучателя параболической зеркальной антенны предлагается достичь гиперширокой полосы импульсного излучения от 300 МГц до 15 ГГц для работы в составе многодиапазонного георадара, что может обеспечить получение изображения на глубине с высоким разрешением. Усиление и отражение по входу соответствуют результатам измерений.

Ключевые слова: сверхширокополосная антенна, ТЕМ-рупор, параболический отражатель, георадар, импульсное излучение.

Ил. 07. Библиогр.: 13 назв.

УДК 537.874

Застосування частково заповнених діелектриком антен рупорного та рефлекторного типів для надширокосмугових підповерхневих радіолокаторів / С. Турк, А.К. Кескін, М.Іларслан // Прикладна радіоелектроніка: наук.-техн. журнал. – 2013. – Том 12. – № 1. – С. 99–104.

Стаття присвячена розробці надширокосмугових ТЕМ-антен рупорного типу та їх використанню як опромінювача для параболічного відбивача, які призначені для встановлених на транспортних засобах таких, що дивляться вниз і вперед імпульсних георадарів, відповідно. З цією метою були досліджені, сконструйовані, промоделювані та виміряні частково заповнені діелектриком антени Вівальді та конфігурації масиву ТЕМ-рупорів. З використанням антени Вівальді у формі ТЕМ-рупора як опромінювача параболічної дзеркальної антени пропонується досягти гіперширокі смуги імпульсного випромінювання від 300 МГц до 15 ГГц для роботи в складі багатосмугових георадарів, що може забезпечити отримання зображення на глибині з високою роздільною здатністю. Посилення і віддзеркалення по входу відповідають результатам вимірювань.

Ключові слова: надширокосмугова антена, ТЕМ-рупор, параболічний відбивач, георадар, імпульсне випромінювання.

Іл. 07. Бібліогр.: 13 найм.

NOISE RADAR PERFORMANCE

UDC 621.37

TIME AND RANGE ACCURACY OF SHORT-RANGE ULTRA-WIDEBAND PSEUDO-NOISE RADAR, NRT-2012

J. SACHS, R. HERRMANN, AND M. KMEC

Time and range estimations based on ultra-wideband (UWB) measurements need to be carefully considered with respect to their accuracy, since range, propagation delay and time position can often not be uniquely defined. The paper illustrates these issues and shows some common approaches for UWB range and time position estimation. Ranging errors provoked from the sensor device are introduced and the performance of pseudo-noise radar concepts is shown. They provide excellent time axis accuracy due to a stable clock reference and cause random timing errors in the fs-range which is a consequence of a robust synchronization concept and jitter suppression by correlation. The impact of frequency aliasing onto time position measurements is considered as well.

Keywords: PN-sequence, jitter, time position, range accuracy, correlation, aliasing.

1. INTRODUCTION

The target range or time of flight are the most important parameters gained from a radar measurement. The goal of this paper is to discuss the achievable precision and some error sources of such measurements using ultra-wideband (UWB) radar devices. Specifically, we will focus on UWB pseudo noise (PN) radar for short range applications.

Precise and stable time or range measurements are important for applications involving super-resolution techniques [1], micro motion detection [2], target localization [3], system calibration [4, 5], hidden target detection [6] and others. The attached references refer to corresponding examples.

In what follows, we start with an introduction of range measurements and the general challenges one is faced in case of UWB sounding. Furthermore, we consider some methods and errors of pulse position estimation. In our discussion, we mainly refer to a PN-radar principle and investigate its robustness against deterministic and random errors.

2. STATEMENT OF THE PROBLEM

2.1. Experimental setup

Here we are mainly interested in two points. Firstly, it refers to the question how precise we can determine the range of a target.

This point is identical with the question how precise we can measure a time delay $\Delta\tau$ (propagation speed of the sounding waves is supposed to be exactly known). We will focus our consideration to a single target scenario, i.e. the issues of range resolution and the separation of two closely located targets will be not within the scope of the paper. The second point relates to the detection of weak targets closely located behind a penetrable but strongly reflecting interface. We refer to the issues related to range measurements by the term scenario A and for hidden target detection we take scenario B.

Range estimation based on radar sensing is illustrated in Fig. 1. A sounding wave is emitted by an antenna, reflected by the target and collected by the same (compare Fig. 1a) or a second antenna. The roundtrip time is determined from the mutual delay $\Delta\tau$ between received and transmitted signals. The relation

$$\hat{R} = \frac{1}{2}\Delta\tau\, c_0 \quad \text{with} \quad \Delta\tau = \tau_y - \tau_x - 2\tau_0 \tag{1}$$

(c_0 – speed of light; τ_0 – antenna internal propagation delay) is then usually taken as an estimation for the target's distance R_0, i.e. one assumes $R_0 \triangleq \hat{R}$.

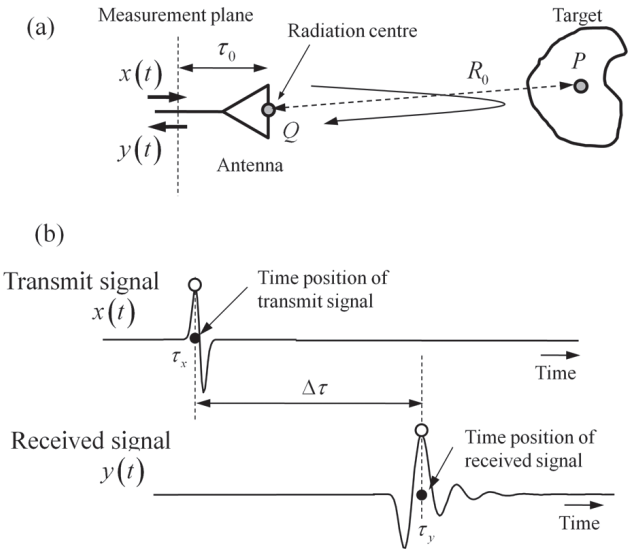

Fig. 1. Principle of range estimation based on radar measurements for scenario A: (a) measurement setup; (b) simplified UWB signals

Hidden target detection (scenario B) is symbolized in Fig. 2. If the target is located close to a boundary, the surface reflex (also denoted as surface clutter) will overwhelm the target return and the question is, to what extend we can remove the strong reflex from the captured signal and detect the target. In two cases

this would be at least theoretically perfectly possible – namely if we can take a reference measurement from the interface without target or if the target shows some temporal variations (movement, shape variation, permittivity) while the interface stays time invariant.

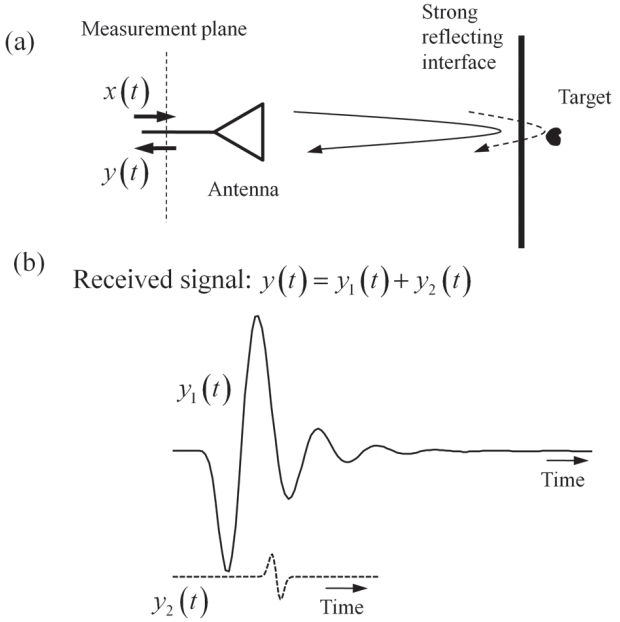

Fig. 2. Hidden target detection in scenario B: (a) measurement setup; (b) returned UWB signals

By considering these scenarios more profoundly under the aspect of ultra-wideband sensing, we will become aware of some shortcomings and insufficiencies which are discussed below.

2.2. Range definition

In case of scenario A, it already starts with the definition of the target range. Mathematically correct, the range assigns the distance between two points, i.e. two infinitesimal small "objects". By introducing a side condition as "shortest range", we can still define uniquely the distance between a point and a straight line (e.g. a thin wire or a "knife" edge) or a point and a flat plane. Hence, the prerequisite for a unique range measurement is only given if the involved objects (i.e. antenna and target) are at least in one dimension infinitesimal small. But practically, this will be commonly not the case.

Since the achievable range resolution of UWB sensors is often better than the geometric size of the involved objects, these issues have to be appropriately respected. In case of the antenna, this can be done by introducing a centre of radiation (refer to point Q in Fig. 1) by prior calibration [7, 8]. It "merges" the properties of a real object with finite dimensions in a virtual point. The determination of a more or less objective "scattering centre" for the target (exemplified by point P in Fig. 1) is barely possible since the scattering object is usually not known a-priori.

2.3. Definition of Roundtrip time

The determination of the roundtrip or delay time $\Delta\tau$ is linked to a similar problem. $\Delta\tau$ is a time interval which is defined by the elapsed time between two time points. Thus, we need again "points", but what we have are signals of finite duration (or finite coherence time) due to limited bandwidth. Hence, we either have to define the time positions τ_x, τ_y of two pulses (transmitted and received one) or we have to estimate the time position of the cross-correlation maximum from $x(t)$ and $y(t)$.

Both approaches face the same problem since an exact time delay may only be defined between two signals of identical shape (i.e. the fidelity [8, 9] of both signals must be one). While $x(t)$ may be obtained from a calibration or reference measurement, $y(t)$ usually remains unpredictable due to the unknown scatterer (except when the scatterer approximates a small point, an infinite line, or infinite plane where exact mathematical models are known). Hence, we have to anticipate increasing systematic errors if the fidelity departs from one.

Further challenges arise if the return signal of the target is affected by noise, multipath signals, or other clutter. The interested reader can find some discussions on these topics in [10, 11]. Since our main aim is to investigate the role of the measurement device in range measurements, we will not go deeper into issues from above since they are mainly motivated by the conditions of the test scenario. That is, we assume in our following consideration that we have measurement conditions which allow defining uniquely the radar rage. An example scenario could e.g. be the scattering from an infinite metal sheet.

2.4. Pulse Position

Independently on how delay time measurements are performed or on how strong they are affected by different signals and perturbations, they are always connected with the determination of at least one pulse position.

There are multifold options to define the pulse position. The most popular strategies are

1) to use the intersection of the rising or falling pulse edge with an absolute or normalized threshold (e.g. normalized to the pulse peak)

2) to take the maximum position of the pulse. This approach is a special case of 1) since the maximum position is achieved if the first derivative of the pulse form crosses the zero line. Note that this method may be extended to complex valued impulse waveforms as they appear after IQ-down-conversion of band-pass signals (complex envelope).

3) to take the zero crossing of the strongest half-cycle in the case of a band-pass pulse. The selection of the correct half-cycle may be based on the maximum position of the pulse envelope.

4) to determine one of the centers of gravity:

$$\tau_p = \frac{\int t\left|x(t)\right|^p dt}{\int \left|x(t)\right|^p dt}; \quad p \geq 1 \tag{2}$$

It follows from eq. (2) that τ_1 relates to the gravity centre of the pulse area, τ_2 represents the energetic centre of the pulse, and τ_∞ offers a second possibility to define the maximum position.

The pros and cons of the different definitions of pulse position are compared in [8]. In summary of the discussion there, we can state that threshold crossing of either the first derivative (i.e. maximum position) or of the original pulses or cross-correlation function provides the best performance in case of baseband signals (pulse or pseudo noise). The integral values of pulse position corresponding to point 4 are prone to biased estimations if the signal is affected by noise.

Using the "maximum approach" (point 2), we find for the variance φ_0^2 of time delay estimation [8]:

$$\varphi_0^2 = \frac{\underset{\cdot\cdot}{B}_n^2}{3(4\pi)^2 \, SNR \, \underset{\cdot\cdot}{B}_{eff}^4}, \qquad (3)$$

$\underset{\cdot\cdot}{B}_n$ — noise bandwidth of the receiver (double sided); SNR — SNR value of the receiving signal; $B_{eff}^2 = \int f^2 \underset{\cdot\cdot}{\Psi}_{yy}(f) df \Big/ \int \underset{\cdot\cdot}{\Psi}_{yy}(f) df$ — effective bandwidth of the receiving signal; $\underset{\cdot\cdot}{\Psi}_{yy}(f)$ — power spectrum of receiving signal (double sided).

For optimum noise suppression, the receiver bandwidth should be matched to the bandwidth of the input signal. If this is of constant power spectral density within the spectral band $\pm \underset{\cdot\cdot}{B}/2$ which equals the receiver noise bandwidth, eq. (3) modifies to:

$$\varphi_0^2 = \frac{1}{\left(2\pi B_{eff}\right)^2 SNR} = \frac{3}{\pi^2 \underset{\cdot\cdot}{B}^2 SNR} \qquad (4)$$

$$for \quad \underset{\cdot\cdot}{\Psi}_{yy}(f) = \begin{cases} \Psi_0 & |f| \le \underset{\cdot\cdot}{B}_n/2 \\ 0 & |f| > \underset{\cdot\cdot}{B}_n/2 \end{cases} \Rightarrow B_{eff}^2 = \frac{\underset{\cdot\cdot}{B}_n^2}{12}$$

In what follows, we will investigate the role of the sensing device for the correct determination of the pulse position corresponding to scenario A as well as the conditions allowing precise suppression of the interface reflex from scenario B.

3. PRECISE AND STABLE DEVICE TIMING

It is obvious from the discussions of section 2.4, that imperfections of the device internal time representation as well as additive random noise will be the major sources of time position errors. Since nowadays the captured signals are usually digitized, we have to anticipate following timing errors:

- an erroneous value of the sampling interval (e.g. caused from an unreliable clock generator)
- systematic deviations from an equidistant sampling interval. Such deviations may have a global tendency leading to a non-linear time axis of the device or they are arbitrary so that they generate a kind of "systematic" jitter. The first effect may be observed in e.g. sequential sampling oscilloscopes which use a dual ramp approach for sampling control. The second effect appears if the dual ramp approach is replaced by digitally controlled stepped delay lines whose delay steps are not ideally identical [8].
- random deviations of the sampling points (sampling jitter)
- random fluctuations of stimulus launch (trigger jitter).

Fig. 3 (a) represents a sensor concept which defeats these timing errors. It is based on the generation of UWB PN-signals to stimulate the device under test (DUT) and a sub-sampling receiver [12].

The timing of the whole device is controlled by a single tone RF-clock operating commonly in the 2-20 GHz range. Such a generator can be built for very precise frequency values and low phase noise. This provides one of the prerequisites for absolute timing accuracy and low random timing errors.

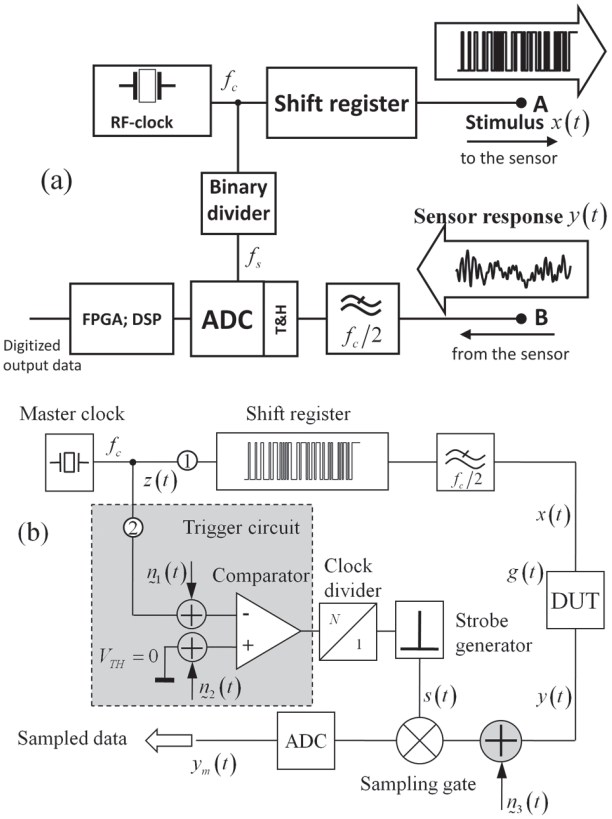

Fig. 3. Block schematic (a) of a PN-sequence ultra-wideband sensor and its simplified system model (b)

A major issue is to trigger the signal generator (i.e. the shift register) and the Track and hold circuit (T&H) as reliable as possible. We will discuss this point with help of Fig. 3 (b). For the sake of shortness, we only refer to a single jitter source, namely the aperture jitter of the strobe signal $s(t)$. We model it by the grey box of Fig. 3 (b). Two noise voltages $\underset{\sim}{n}_1(t) \sim N\left(0, \sigma_1^2\right)$ and $\underset{\sim}{n}_2(t) \sim N\left(0, \sigma_2^2\right)$ are transformed into jitter by the comparator. The binary divider is then assumed to be jitter free.

The noise signals $\underset{\sim}{n}_1(t)$ and $\underset{\sim}{n}_2(t)$ provoke a random temporal fluctuation $\Delta\underset{\sim}{\tau}_j$ of comparator switching which we regard as a zero mean random process having the probability density function (PDF) $p_{\Delta\tau}(t)$. The period should be placed into the previous line. Hence, we have for the expected value:

$$\mathrm{E}\left\{\Delta\tau_j\right\} = \int_{-\infty}^{\infty} t\; p_{\Delta\tau}(t)\,\mathrm{d}t = 0 \tag{5}$$

The variance of the fluctuations follows from simple considerations to be:

$$\begin{aligned}\mathrm{var}\left\{\Delta\tau_j\right\} = \varphi_T^2 &= \int_{-\infty}^{\infty} t^2\; p_{\Delta\tau}(t)\,\mathrm{d}t \\ &\approx \frac{\sigma_1^2+\sigma_2^2}{\left(\left.\dfrac{\mathrm{d}\,z(\xi)}{\mathrm{d}\xi}\right|_{\xi=t_0}\right)^2}\end{aligned} \tag{6}$$

whereat t_0 represents the nominal trigger point at which the unperturbed trigger signal $z(t)$ crosses the threshold V_{TH}.

In our case, we have a sine wave generator as trigger source and the threshold level is zero $V_{TH} = 0$. Hence we get from (6):

$$\varphi_T^2 = \frac{\sigma_1^2+\sigma_2^2}{(2\pi f_c)^2} \tag{7}$$

Now, we can model the captured signal as a random process (for the sake of convenience, we will stay at time continuous signals and consider the DUT as a simple delay, i.e. $g(t) = \delta(t-\Delta\tau)$):

$$\begin{aligned}\underset{\sim}{y}_m(t) &= \underset{\sim}{y}\left(t+\Delta\tau_j\right) + \underset{\sim}{n}_3\left(t+\Delta\tau_j\right) \\ &= \sum_{\nu}\frac{1}{\nu!}\left(\frac{\mathrm{d}^\nu y(\xi)}{\mathrm{d}\xi^\nu}+\frac{\mathrm{d}^\nu n_3(\xi)}{\mathrm{d}\xi^\nu}\right)\Bigg|_{\xi=t}\Delta\tau_j^\nu \\ &\approx y(t) + \left.\frac{\mathrm{d}\,y(\xi)}{\mathrm{d}\xi}\right|_{\xi=t}\Delta\tau_j + \underset{\sim}{n}_3(t) \\ &\approx x(t-\Delta\tau) + \left.\frac{\mathrm{d}\,x(\xi)}{\mathrm{d}\xi}\right|_{\xi=t-\Delta\tau}\Delta\tau_j + \underset{\sim}{n}_3(t)\end{aligned} \tag{8}$$

The order of Taylor series expansion in eq. (8) can be drastically reduced if jitter and noise do not dominate the deterministic part of the signal.

We will use this relation, to estimate the jitter φ_T^2 of an M-sequence device [13]. For that purpose, we need to know the signal derivative at any time point. Since M-sequence devices are Nyquist sampled, the equivalent sampling rate has to be increased in order to permit reliable derivation. Therefore, we introduced a mechanical precision delay line at points ①, ② (see Fig. 3 (b)) or as a DUT. The delay steps are 0.2 ps allowing an equivalent sampling rate of 5 THz. Thus, the realizations of $\underset{\sim}{y}_m(t)$ can be considered as quasi continuous in time. Furthermore, the random perturbations have to be suppressed before the derivation can be determined. This was done by synchronous averaging of about $N = 100$ realizations of $\underset{\sim}{y}_m(t)$:

$$\begin{aligned}\bar{y}_m(t) &= \frac{1}{N}\sum_{n=1}^{N}\underset{\sim}{y}_{m,n}(t) \\ &= \frac{1}{N}\sum_{n=1}^{N}\left(x_n\left(t-\Delta\tau+\Delta\tau_{j,n}\right)+\underset{\sim}{n}_{3,n}\left(t+\Delta\tau_{j,n}\right)\right)\end{aligned} \tag{9}$$

Its expected value leads to the relation:

$$\begin{aligned}\mathrm{E}\left\{\bar{y}_m(t)\right\} &= x(t-\Delta\tau) * p_{\Delta\tau}(t) \\ &\approx x(t-\Delta\tau) \quad \textit{if} \quad \varphi_T\, B \ll 1\end{aligned} \tag{10}$$

such that $\bar{y}_m(t)$ can be considered as a reasonable source to calculate the signal derivative in particular if the convolution may be omitted. This is allowed if the temporal width φ_T of $p_{\Delta\tau}(t)$ is short compared to any variations in $x(t)$ which we have expressed by the side condition $\varphi_T\, B \ll 1$.

Using eq. (8), the variance of the captured signal can be written as:

$$\begin{aligned}\mathrm{var}\left\{\underset{\sim}{y}_m(t)\right\} &= \sigma_y^2(t) = \sigma_\varphi^2(t) + \sigma_3^2 \\ &= \left(\left.\frac{\mathrm{d}\,x(\xi)}{\mathrm{d}\xi}\right|_{\xi=t-\Delta\tau}\right)^2\varphi_T^2 + \sigma_3^2\end{aligned} \tag{11}$$

with $\underset{\sim}{n}_3 \sim N\left(0,\sigma_3^2\right)$

If we plot for all samples of the signal the standard deviation $\sigma_y(t_0)$ versus the slope of the signal $\mathrm{d}\bar{y}_m(t)/\mathrm{d}t\big|_{t=t_0}$ ($t_0 \in [0,T)$; T — signal period), we can expect behaviour as depicted in Fig. 4.

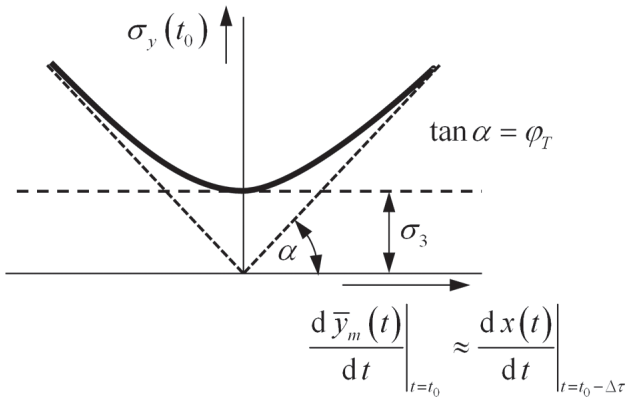

Fig. 4. Illustration of signal variance as function of signal slope under the presence of jitter

The real behavior of the data is shown in Fig. 5. Since the M-sequence has many locations with identical slopes and we only respect a finite number of experiments in our calculation, we get a cloud of data samples. By fitting (11) to this cloud, we finally arrive at the wanted rms jitter value φ_T of the device. Fig. 5 (a) relates to an example where the additive noise dominates while Fig. 5 (b) also shows some jitter induced effects.

The two examples show that the timing concept according to Fig. 3 provides very low jitter values owed to the high-speed/steep edge binary divider and the large clock rates f_c.

Moreover, the binary divider also provides perfectly equidistant strobe pulses of $s(t)$ (random jitter not respected) since it is running through all its states before it releases a new sampling event. Hence, any asymmetry of the internal flip-flops impacts all sampling pulses in the same fashion. Thus, a precise device

internal time axis is guaranteed also for a very long signal if the clock-generator is sufficiently time stable.

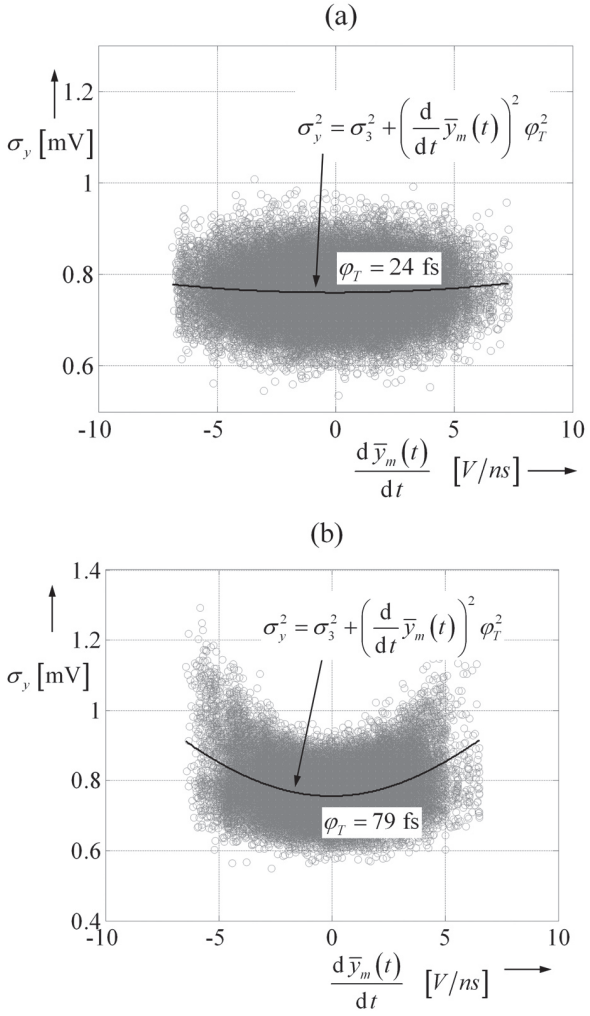

Fig. 5. Variance of measured data samples as a function of signal slope for two different RF-clock generators: (a) – High-quality RF-laboratory generator SMP04 (R&S); (b) – free running DRO

4. SUPPRESSION OF NOISE AND JITTER

Since the involved UWB signals are expanded in time (Fig. 3 (a)), the estimation of the delay time $\Delta\tau$ of a DUT requires the determination of the peak position of the correlation function between input- and output signal. In the best case, the statistical confidence in this peak position may be estimated from eq. (4). This still requires the evaluation of the SNR-value of the correlation function $C_{y_m,x}(\tau)$ which we consider as a random process while the stimulus signal $x(t)$ is supposed to be perfectly known:

$$\underset{\sim}{C}_{y_m x}(\tau) = \frac{1}{T}\int_T \underset{\sim}{y}_m(t)\, x(t+\tau)\, dt \tag{12}$$

The SNR-value of the correlation function can be defined by the relation between its peak value and its variance according to:

$$SNR_C(\tau) = \frac{\left\| \mathrm{E}\left\{\underset{\sim}{C}_{y_m x}(\tau)\right\}\right\|_\infty^2}{\mathrm{var}\left\{\underset{\sim}{C}_{y_m x}(\tau)\right\}} \tag{13}$$

whereat $\|\cdots\|_p$ means the Lp-norm.

Inserting eq. (8) into eq. (12), we get for the expected value of the correlation function:

$$\begin{aligned}\mathrm{E}\left\{\underset{\sim}{C}_{y_m x}(\tau)\right\} &= \frac{1}{T}\int_T x(t-\Delta\tau)\, x(t+\tau)\, dt \\ &= C_{xx}(\tau-\Delta\tau)\end{aligned} \tag{14}$$

and its maximum value equals the power of the sounding signal:

$$\left\| \mathrm{E}\left\{\underset{\sim}{C}_{y_m x}(\tau)\right\}\right\|_\infty = C_{xx}(0) = \|x(t)\|_2^2 = x_{rms}^2 \tag{15}$$

In Lp-norm notation, the variance of the correlation function may be expressed as follows (see [8] for details):

$$\begin{aligned}&\mathrm{var}\left\{\underset{\sim}{C}_{y_m x}(\tau)\right\} \\ &= \frac{1}{T\ddot{B}_n}\left(\sigma_3^2 \|x(t)\|_2^2 + \varphi_T^2 \|x(t+\tau)\,\dot{x}(t)\|_2^2\right) \\ &\quad using\ \frac{\mathrm{d}x(t)}{\mathrm{d}t} = \dot{x}(t)\end{aligned} \tag{16}$$

$\ddot{B}_n$ is the double sided noise bandwidth of the receiver and T is the time over which the integration is performed. Insertion of eqs. (15) and (16) into eq. (13) results in:

$$SNR_C(\tau) = \frac{T\ddot{B}_n \|x(t)\|_2^4}{\sigma_3^2 \|x(t)\|_2^2 + \varphi_T^2 \|x(t+\tau)\,\dot{x}(t)\|_2^2} \tag{17}$$

After some manipulations, we can rewrite eq. (17) in the form:

$$SNR_C(\tau) = \frac{T\ddot{B}_n}{\frac{CF^2}{SNR_0} + \frac{SAF^2(\tau)}{RJR}} \tag{18}$$

This equation is valid for compact as well as time extended UWB-signals. The involved parameters describe characteristic properties of the test signal as well as of the measurement procedure. The crest or peak factor is defined as:

$$CF = \frac{\|x(t)\|_\infty}{\|x(t)\|_2} \tag{19}$$

It may tend towards 1 for time extended signals. An ideal M-sequence has $CF = 1$. An $f_c/2$ band limited M-sequence has $CF \approx 2...3$ depending on the filter. For short pulse signals it tends to large values (the same is true for Gaussian noise). The slope amplitude factor $SAF(\tau)$ describes the coincidences of strong signal variations at large magnitude. It is defined as:

$$SAF(\tau) = t_r \frac{\|x(t+\tau)\,\dot{x}(t)\|_2}{\|x(t)\|_2^2} \tag{20}$$

Usually it depends on the time lag τ. In the case of short pulse signals, it takes high values where signal edges appear and it becomes zero at the pulse base [8, 14]. In contrast, it is nearly constant at $SAF \approx 3$ for a band limited M-sequence. The SNR-value of the captured signal with additive noise, we write as:

$$SNR_0 = \frac{\|y(t)\|_\infty^2}{\sigma_3^2} \quad (21)$$

Note that we take the peak power of the signal but not the average power for this definition. And finally, we still have the rise-time jitter ratio (t_r – rise time), which reads as:

$$RJR = \frac{t_r^2}{\varphi_T^2} \quad (22)$$

It represents a kind of "signal to noise ratio" of the time axis.

We can observe from eq. (18) that for short, pulse like sounding signals the correlation gain TB_n will be compensated by large CF - and SAF -values. The correlation will not bring any profit for noise and jitter suppression. In the case of PN-sequences, CF and SAF take small and constant values. That means, the correlation performs a suppression of additive noise and jitter as well. The jitter energy is equally distributed over the whole correlation function such that its steep edges are not more severely affected by random perturbations than flat regions. In consequence, we get a strong reduction of positions errors according to eqs. (3) or (4). The examples listed in sections 5 and 6 of this paper indicate values of 3...5 fs time position variation, i.e. a 1...1.6 μm range uncertainty in air.

This temporal stability of the measurements is the prerequisite to subtract in a stable and precise way the surface reflex according to Fig. 2 in order to make visible the weak hidden scatterer. Supposing the surface reflex must be reduced by the factor N when subtracting a reference signal, the temporal uncertainty φ_T of time position has to meet the condition:

$$\frac{\varphi_T}{t_r} \approx \varphi_T \; \ddot{B} \le \frac{1}{N} \quad (23)$$

Herein, $\ddot{B}$ is the two sided bandwidth of the surface reflex and t_r is its rise time.

5. SUPPRESSION OF DRIFT

Time drift is a long-term fluctuation which is not respected by the consideration in sections 3 and 4. It may be provoked by biased threshold voltages or trigger signals whereat the bias typically depends on temperature, aging, etc. In order to suppress drift effects, it is recommended to perform relative measurements between two receivers of identical construction and identical temperature level. These conditions are best met by integrated circuits.

Further, we should also take the temperature sensitivity of feeding cables into account. If we simply consider the coefficient of thermal expansion of copper ($\alpha \approx 16 \cdot 10^{-6}\ K^{-1}$) as an equivalent for the cable expansion and omit the temperature dependency of the dielectric insulator etc., we already get a time drift of $\Delta t \approx 100\ fs/m\,K$ for a cable of 1 m length and 1 Kelvin temperature variation. We can learn from this estimation that simply the geometric dimension of a measurement device or arrangement may limit the achievable measurement precision.

Fig. 6 shows a practical example. During the warming up phase of a device the length of its cable was measured whereat only the temporal fluctuations of the input and output signal was registered. If we only refer to the pulse position captured by the two measurement channels, we can observe a variation of about 2 ps during the observation time. This corresponds to a range uncertainty of several hundred μm in air. As expected, the variations in both channels are nearly coherent. Hence, if we account only for their differences, we get a considerable improvement of the delay time measurement to about 5 fs rms value of short time variations.

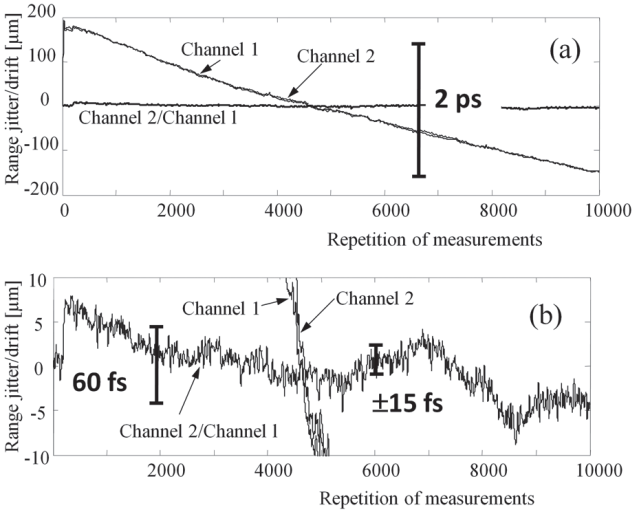

Fig. 6. Pulse position drift of an M-sequence device (9th order M-sequence, clock rate 9 GHz) during warming up observed over about 10 min. (a) – overview (b) zoom

6. DENSITY OF DATA SAMPLING

There is often the argument to sample the data very densely in order to get high range precision. This statement is not valid if it is expressed in that generic way. As we have seen in eqs. (3) and (4), bandwidth and noise are the key issues. Basically, Nyquist sampling is sufficient to reach full precision since interpolation to an arbitrary fine degree can be done in the numerical domain. However, this supposes that aliasing components must be fully suppressed. If one cannot sufficiently suppress aliasing components, the sampling rate has to be increased at least to such a degree where the aliasing components fall below the noise level. Fig. 7 demonstrates how aliasing affects the delay time measurement. For demonstration, a mechanical delay line increases the propagation path length in 2 mm steps. The measurement device was based on a 9th order M-sequence and 18 GHz clock rate using insufficient suppression of aliasing frequencies. The standard deviation of the individual distance measurements was about 1.0 ... 1.2 μm, i.e. it is more than two orders better than the systematic deviations caused by aliasing as shown in Fig. 7. The annex gives a simplified consideration about the creation of time position errors due to aliasing.

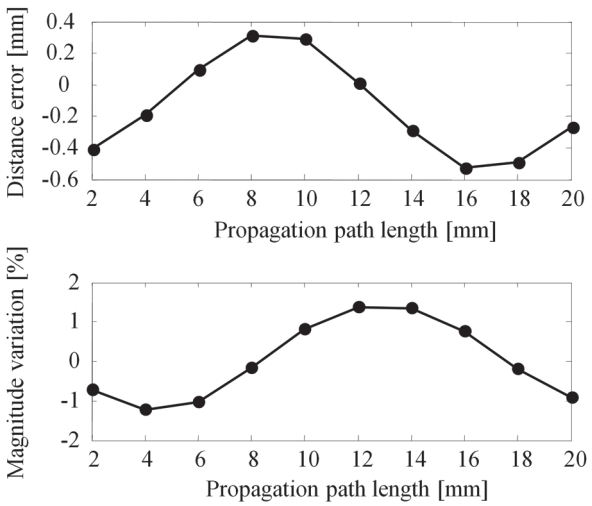

Fig. 7. Effect of aliasing onto systematic range deviations and onto the maximum value of the correlation function in dependence from the propagation path length

7. SUMMARY

Time and range accuracy should be considered with some care under UWB conditions since geometric dimensions of the object and temporal duration of signals make unique definitions of points and distances difficult. This may cause systematic deviations exceeding even the range resolution predicted by the classical formula $\delta_R = c/2B$.

The short time instabilities of an M-sequence device allow to resolve motions of a single target down to 1 μm being about 10.000 times better than the range resolution δ_R. In order to exploit this sensitivity in practical applications, the issues of mechanical precision and stability of sensor elements as well as questions of thermal expansion will become more and more important for sensor design. Aliasing effects should be properly suppressed in order to reduce systematic deviations of the device down to the level of random errors. The quality of the RF-clock generator decides about the precision of the device internal time axis with respect to absolute and random deviations. Its phase noise becomes as more influence as longer the DUT delay is.

References

[1] *M. Helbig, M. A. Hein, U. Schwarz et al.*, "Preliminary investigations of chest surface identification algorithms for breast cancer detection," in International Conference on Ultra-Wideband, Hannover (Germany), 2008.

[2] *J. Sachs, M. Helbig, R. Herrmann et al.*, "Remote Vital Sign Detection for Rescue, Security, and Medical Care by Ultra-Wideband Pseudo-Noise Radar," *Ad Hoc Networks*, 2012.

[3] *J. Rovňáková, and D. Kocur*, "TOA Estimation and Data Association for Through-Wall Tracking of Moving Targets," *EURASIP Journal on Wireless Communications and Networking,* vol. 2010, 2010.

[4] *R. Herrmann, J. Sachs, K. Schilling et al.*, "12-GHz Bandwidth M-Sequence Radar for Crack Detection and High Resolution Imaging," in International Conference on Ground Penetrating Radar (GPR), Birmingham, UK, 2008.

[5] *R. Herrmann, J. Sachs, and P. Peyerl,* "System evaluation of an M-sequence ultra wideband radar for crack detection in salt rock," in International Conference on Ground Penetrating Radars (GPR), Ohio (Columbus), 2006.

[6] *R. Herrmann*, "M-sequence based ultra-wideband radar and its application to crack detection in salt mines," Faculty of Electrical Engineering and Information Technology, Ilmenau University of Technology (Germany), Ilmenau, 2011.

[7] *J. Sachs, P. Peyerl, P. Rauschenbach et al.*, "Characterizing Impulse radiating Antennas by an Intuitive Approach," *Ultra-Wideband, Short-Pulse Electromagnetics 7*, F. Sabath, E. L. Mokole, U. Schenk *et al.*, eds., pp. 334-41: Springer, 2007.

[8] *J. Sachs,* Handbook of Ultra-Wideband Short-Range Sensing - Theory, Sensors, Applications, Berlin: Wiley-VCH, November 2012.

[9] *D. Lamensdorf, and L. Susman,* "Baseband-pulse-antenna techniques," Antennas and Propagation Magazine, IEEE, vol. 36, no. 1, pp. 20-30, 1994.

[10] *M. R. Hoseini, X. Wang, and M. J. Zuo,* "Estimating ultrasonic time of flight using envelope and quasi maximum likelihood method for damage detection and assessment," Measurement, vol. 45, pp. 2072–2080, 2012.

[11] *S. Guowei, R. Zetik, Y. Honghui et al.,* "Time of arrival estimation for range-based localization in UWB sensor networks," in Ultra-Wideband (ICUWB), 2010 IEEE International Conference on, 2010, pp. 1-4.

[12] *J. Sachs, H. C. Fritsch, M. Helbig et al.,* "Ultra-Wideband Pseudo-Noise Sensors," in Noise Radar Technology, Yalta, Crimea (Ukraine), 2012.

[13] *B. Streng,* "Entwicklung und Implementierung eines Messplatzes zur Charakterisierung des HF-Teils von M-Sequenzmesskцpfen in MATALB," Faculty of Electrical Engineering and Information Technology, Ilmenau University of Technology, Ilmenau, 2009.

[14] *J. Sachs, M. Helbig, R. Herrmann et al.*, "On the Range Precision of UWB Radar Sensors," in IRS 2010 International Radar Symposium, Vilnius (Lithuania), 2010.

ANNEX: POSITION ERROR CAUSED FROM ALIASING COMPONENTS

We assume the test signal

$$x_0(t) = \mathrm{sinc}(\ddot{B}_0 t), \tag{24}$$

having a rectangular spectrum of width $\ddot{B}_0$. Our measurement system is designed for this bandwidth, i.e. the sampling rate is selected to $f_s = \ddot{B}_0$. Sub-sampling is omitted here for the sake of brevity.

In order to emulate aliasing, we insert a second signal exceeding the given band limitation:

$$x(t) = (1-\eta)\mathrm{sinc}(t\ddot{B}_0) + \eta\,\mathrm{sinc}(2t\ddot{B}_0) \tag{25}$$

Its spectrum is depicted in Fig. 8. Part A represents the wanted signal and the parts B refer to the aliasing components after the signals is sampled with frequency f_s. The orginal spectrum of $x(t)$ spectrum is:

$$X(f) = \frac{1}{\ddot{B}_0}\left((1-\eta)\mathrm{rect}\left(\frac{f}{\ddot{B}_0}\right) + \frac{\eta}{2}\mathrm{rect}\left(\frac{f}{2\ddot{B}_0}\right)\right). \tag{26}$$

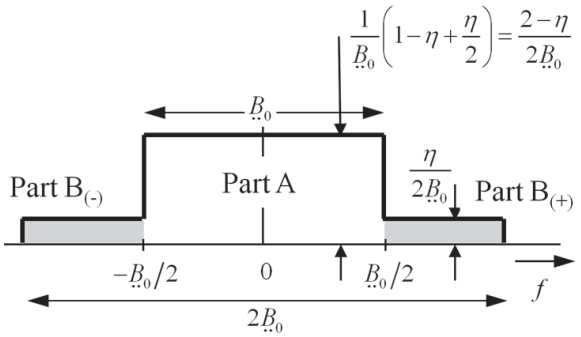

Fig. 8. Spectrum of the idealized signal

The maximum of $x(t)$ is $\|x(t)\|_\infty = 1$ and it is located at $t = 0$. Further this signal is subjected to a time delay τ, so that its maximum is now placed at time position $t = \tau$. Time signal and spectrum are:

$$\begin{aligned} y(t) &= x(t-\tau) \\ &= (1-\eta)\,\mathrm{sinc}\left((t-\tau)\underline{B}_0\right) + \eta\,\mathrm{sinc}\left(2\underline{B}_0(t-\tau)\right) \end{aligned} \tag{27}$$

$$\begin{aligned} \underline{Y}(f) &= X(f)\,e^{-j2\pi f\tau} \\ &= \frac{e^{-j2\pi f\tau}}{\underline{B}_0}\left((1-\eta)\,\mathrm{rect}\left(\frac{f}{\underline{B}_0}\right) + \frac{\eta}{2}\,\mathrm{rect}\left(\frac{f}{2\underline{B}_0}\right)\right) \end{aligned}$$

The sampled signal is then written as:

$$\begin{aligned} z(t) &= \sum_n y(n\,\Delta t_s) \\ \underline{Z}(f) &= f_s \sum_m \underline{Y}(f - m f_s) \end{aligned} \tag{28}$$

Hence, we get for our simple example:

$$\begin{aligned} \underline{Z}(f) &= \frac{f_s}{\underline{B}_0}\sum_m e^{-j2\pi(f-mf_s)\tau}\cdots \\ \cdots &\left((1-\eta)\,\mathrm{rect}\left(\frac{(f-mf_s)}{\underline{B}_0}\right) + \frac{\eta}{2}\,\mathrm{rect}\left(\frac{(f-mf_s)}{2\underline{B}_0}\right)\right). \end{aligned} \tag{29}$$

If the sampling rate is $f_s = \underline{B}_0$, the spectral components beyond $|f| \geq \underline{B}/2$ (parts B) will overlap with the central part (part A) of the spectrum. The spectrum of the sampled signal is illustrated for $m = -1, 0, 1$ in Fig. 9 for the case $f_s = \underline{B}_0$:

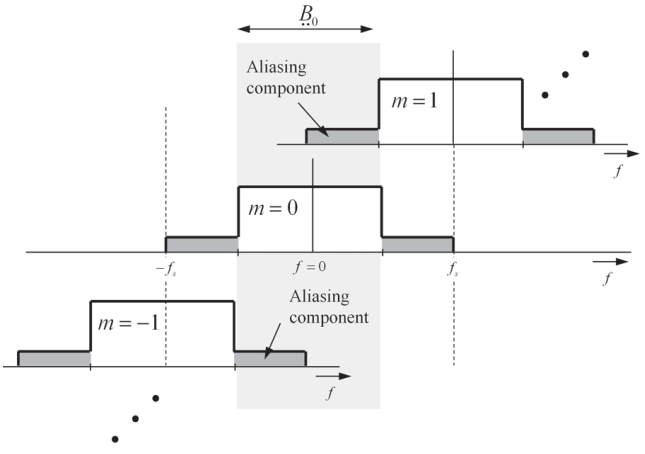

Fig. 9. Amplitude spectrum of the sampled signal fragmented in its individual part

Note, that in case of a discrete Fourier transform, only the spectral components covered by area $\pm\underline{B}_0/2$ around $f = 0$ are involved. Here, the parts $B_{(+)}$ and $B_{(-)}$ (gray) (compare Fig. 8) of the spectrum represent aliasing components caused from the spectral power exceeding the band limits $\pm f_s/2$. They are convolved into the main spectral part. The overall spectrum within this area may be written as:

$$\begin{aligned} \underline{\hat{Z}}(f) = &\underbrace{\frac{2-\eta}{2\underline{B}_0}e^{-j2\pi f\tau}}_{\text{part A effect - wanted}} + \underbrace{\frac{\eta}{2\underline{B}_0}e^{-j2\pi\tau(f-f_s\,\mathrm{sgn}(f))}}_{\text{part B effect - aliasing}} \\ &f \in \left[-\frac{f_s}{2};\frac{f_s}{2}\right] \end{aligned} \tag{30}$$

In time domain, eq. (30) gives after inverse Fourier transform:

$$\begin{aligned} \hat{z}(t) &= \int_{-f_s/2}^{f_s/2} \underline{\hat{Z}}(f)\,e^{j2\pi ft}\,df = \hat{z}_A(t) + \hat{z}_B(t) \\ &= \left(1-\frac{\eta}{2}\right)\mathrm{sinc}\left(\underline{B}_0(t-\tau)\right)\cdots \\ &\cdots + \frac{\eta}{2}\cos\frac{\pi\underline{B}_0(t+3\tau)}{2}\,\mathrm{sinc}\frac{\underline{B}_0(t-\tau)}{2} \end{aligned} \tag{31}$$

The maximum position of this signal is determined from the zero-crossing of its derivative:

$$\left.\frac{\mathrm{d}\,\hat{z}(t)}{\mathrm{d}\,t}\right|_{t=\tau} = 0 \tag{32}$$

In order to simplify the calculation, we develop $\hat{z}(t)$ into a Taylor series around the expected maximum $t \approx \tau$:

$$\begin{aligned} \hat{z}(\tau+\Delta t) &\approx a_0 + a_1\Delta t + a_2\Delta t^2 \\ a_0 &= 1 + \frac{\eta}{2}\left(\cos(2\pi\underline{B}_0\tau) - 1\right) \\ a_1 &= -\frac{\eta\pi\underline{B}_0\sin(2\pi\underline{B}_0\tau)}{4} \\ a_2 &= -\frac{(\pi\underline{B}_0)^2}{12}\left(\eta\left(\cos(2\pi\underline{B}_0\tau) - 1\right) + 2\right) \end{aligned} \tag{33}$$

whereat Δt represents the difference to τ. This gives for the maximum location:

$$\begin{aligned} \frac{\mathrm{d}\,\hat{z}(\tau+\Delta t)}{\mathrm{d}\,\Delta t} &= a_1 + 2a_2\Delta t = 0 \\ \Rightarrow \Delta t_{\max} &= -\frac{a_1}{2a_2} \\ &= -\frac{3\eta\sin(2\pi\underline{B}_0\tau)}{2\pi\underline{B}_0\left(\eta\left(\cos(2\pi\underline{B}_0\tau) - 1\right) + 2\right)} \\ &\approx -\frac{3\eta}{4\pi\underline{B}_0}\sin(2\pi\underline{B}_0\tau) \quad \textit{since} \quad \eta \ll 1 \end{aligned} \tag{34}$$

$\Delta t_{\max}$ represents the measurement error of roundtrip time provoked by the aliasing effects. As we can observe, the aliasing effect will cause a systematic error which oscillates around the actual value in dependence of the propagation time τ. The magnitude of the oscillation depends on the bandwidth and the suppression of the aliasing components.

The amplitude of the maximum is also affected by an oscillation of the same kind. Usually, the condition $\eta \ll 1$ is met, so that we can write:

$$\tilde{z}\left(\Delta t_{\max}\right)\Big| \approx 1 + \frac{\eta}{2}\left(\cos\left(2\pi \ddot{B}_0 \tau\right) - 1\right) \qquad (35)$$

Manuscript received November, 29, 2012

Juergen Sachs, for photograph and biography, see this issue, p. 87.

Ralf Herrmann, for photograph and biography, see this issue, p. 87.

Martin Kmec, for photograph and biography, see this issue, p. 88.

УДК 621.37

Точность по времени и дальности сверхширокополосного псевдошумового радара для малых дальностей / Ю. Сакс, Р. Херманн, М. Кмец // Прикладная радиоэлектроника: науч.-техн. журнал. – 2013. – Том 12. – № 1. – С. 105–113.

Оценка времени и дальности, основанная на измерениях с использованием сверхширокополосных (СШП) сигналов, должна быть внимательно рассмотрена с учетом точности, поскольку дальность, время распространения и позиция во времени часто не могут быть однозначно оценены. Данная работа иллюстрирует эти особенности и показывает некоторые общие подходы к оценке времени и дальности в СШП измерениях. Представлены ошибки измерения дальности, вызываемые сенсором, и показаны возможности, предоставляемые концепцией псевдо-шумового радара. Они обеспечивают отличную точность по оси времени благодаря использованию стабильного генератора тактовой частоты. Случайные ошибки оценки времени составляют величины порядка фемтосекунд благодаря использованию принципа устойчивой синхронизации и уменьшению дрожания с помощью корреляции. Кроме того, рассмотрено влияние дискретности спектра на точность измерения времени.

Ключевые слова: псевдослучайный сигнал, джиттер, временная позиция, точность по дальности, корреляция, влияние дискретности.

Ил. 9. Библиогр.: 14 назв.

УДК 621.37

Точність за часом та дальністю надширокосмугового псевдошумового радару для малих дальностей / Ю. Сакс, Р. Херманн, М. Кмец // Прикладна радіоелектроніка: наук.-техн. журнал. – 2013. – Том 12. № 1. – С. 105–113.

Оцінка часу і дальності, заснована на вимірах з використанням надширокосмугових (НШС) сигналів, повинна бути уважно розглянута з урахуванням точності, оскільки дальність, час поширення та позиція в часі часто не можуть бути однозначно оцінені. Дана робота ілюструє ці особливості і показує деякі загальні підходи до оцінки часу і дальності в НШС вимірах. Представлено помилки виміру дальності, що викликаються сенсором, і показано можливості, що надаються концепцією псевдошумового радара. Вони забезпечують відмінну точність по осі часу завдяки використанню стабільного генератора тактової частоти. Випадкові помилки оцінки часу складають величини порядку фемтосекунд завдяки принципу стійкої синхронізації та зменшення тремтіння за допомогою кореляції. Крім того, розглянуто вплив дискретності спектра на точність вимірювання часу.

Ключові слова: псевдовипадковий сигнал, джіттер, часова позиція, точність за дальністю, кореляція, вплив дискретності.

Іл. 9. Бібліогр.: 14 найм.

UDC 621.37

RADARS WITH LOW PROBABILITY OF INTERCEPTION

A. G. STOVE

The arrival of wide band, high duty cycle radars has made it practical to design radars with enough processing gain to detect their targets at greater ranges than those at which their transmissions can be intercepted. This paper looks at the principles of such Low Probability of Intercept (LPI) Radars and illustrates this with a simple quantitative example, comparing the performance of a pulse radar with an Frequency-Modulated Continuous Wave radar. The paper takes as its baseline a receiver using the Instantaneous Frequency Measurement technique, but discusses other possible receiver types, leading to a brief examination of the trade-off between interception sensitivity and intercept time. It is argued that coherent matched filtering is not a good way of trying to intercept an LPI radar and, instead, the virtues of the Matched Incoherent Receiver are discussed, where the pre-detection bandwidth and post-detection integration time are matched to the radar's signals, but the detection is incoherent rather than coherent. The additional strengths which are potentially offered in this area by noise waveforms are also discussed. The importance of the military scenario for the significance of an LPI radar and particularly for the complementary principle of 'Low Probability of Exploitation' are also emphasized.

Keywords: Low Probability of Intercept Radar, Intercept Receiver, ESM.

1. INTRODUCTION

The designation 'Low Probability of Intercept' (LPI) for a radar is intimately connected with the 'contest' between radars and Electronic Support Measures (ESM, Intercept) receivers in a tactical military environment, which was well illustrated in reference 1. The way in which this battle plays out and how it is affected by the design of the equipment, both the radar and the intercept receiver, is best explained by way of typical quantitative examples, but before these are introduced, some points which will define the problem more clearly will be examined.

The description above used the terms 'tactical' and 'military.' This paper is not concerned with 'strategic' (electronic intelligence) issues, such as knowing that a given type of radar exists and what its modes are. Given time, a radar can always be detected. The question is whether the radar can be designed so that it can remain undetected for long enough to give its users a significant tactical advantage. For this reason, the baseline intercept receiver is considered to be an ESM receiver.

This can also be called a 'military' issue since interception is not a concern to civil radars. More significant, is the fact that 'military' operations should now also include actions against smugglers and pirates, who can potentially afford radar detectors, which are manufactured for mariners to detect other radar-equipped craft. There are also low cost marine radars which are readily available which have considerable LPI potential as a side-effect of using waveforms compatible with solid-state transmitters. The term 'military' should thus be taken also to include 'paramilitary' users.

The term 'Low Probability of Exploitation' is sometimes preferred to 'Low Probability of Intercept,' since what is often required by the interceptor is not just to know that the emitter is there, but to be able to do something with the information obtained from it, either to obtain tactically-useful information from its presence or to be able, for example, to jam it. This paper, however, will continue to use the term 'Interception' because this is amenable to more general quantitative analysis. 'Exploitation,' whilst it better describes what is militarily significant, is much more dependent on the operational scenario, which then has as much effect on a technique's effectiveness as does its scientific characteristics.

Other methods of reducing the probability of exploitation, which should be mentioned for completeness, are bistatic operation, where detecting the transmissions does not give us the location of the receiver, or disguising the radar's waveform so that it looks as if its purpose is other than it is. An example of this is the desire to be able to use conventional civil marine radar waveforms for military purposes.

This paper, however, will concentrate on what can be done with the design of the radar itself to minimise its detectability, although the user of such techniques will always be aware of other operational and scenario-dependent approaches which can be used to help achieve the same end.

2. LPI TECHNIQUES

This section and the next compare the relative range at which the radar can detect a given target with that at which a given intercept receiver can detect the radar's transmissions. It will then look at how the radar can design its waveform to minimise the range at which it can be intercepted. Fig. 1 show a sketch of a typical scenario to which this might apply:

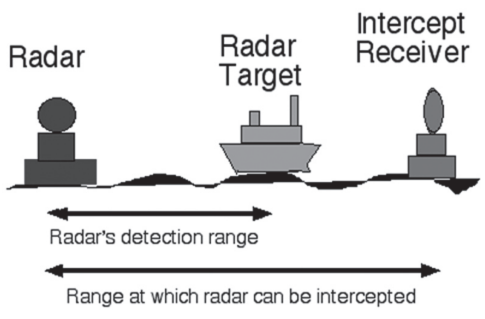

Fig. 1. Simple LPI Scenario

The sensors are assumed to be mounted on ships. One favoured application of LPI techniques, but by no means the only one, is for marine navigation. In a typical tactical scenario the intercept receiver might be carried on the 'target' platform, in which case if the detection range can be made greater than the interception range, the radar will be able 'To See Without Being Seen.'[1] Note that it is not essential to the analysis presented here that the intercept receiver should actually be on the radar target.

This baseline example is also analyzed in reference 2. Reference 3 treats the propagation in more detail, including effects due to multipath and the curvature of the earth, whilst reference 4 considers a number of different scenarios. The latter treats the argument in a slightly different way, so several of its numerical results are slightly different from those presented here, but the principles are the same.

2.1 Interception Range

The basic sensitivity equation for interception of a radar's transmissions is the same as for a simple radio link:

$$SNR = P_p G_t A_r / [4\pi r^2 k T B_i N_i L_i F], \quad (1)$$

where SNR is the signal to noise ratio seen by the intercept receiver; P_p is the peak transmitted power of the radar; G_t — is the gain of the transmitter (radar) antenna; r — is the range; k — is Boltzmann's constant; T is the temperature of the receivers; N_i is the noise figure of the intercept receiver; B_i is the effective bandwidth of the intercept receiver; L_i represents the losses in the intercept receiver and F is the propagation factor.

The propagation factor is taken to include interference due to multipath reflections, which will usually be predominantly from the earth's surface, as well as factors such as attenuation through clear air and through any precipitation which may be present. For the purposes of this discussion this factor can be ignored and the analysis will look only at the free-space numbers, although, as mentioned above, reference 3 includes a more sophisticated treatment of multipath for one particular scenario.

The product $P_p G_t$ is the peak effective radiated power of the radar and is the basic measure of the power which is available to the intercept receiver when the latter is in the main beam of the radar's antenna.

The peak power is used to calculate the sensitivity of the ESM receiver because it cannot be matched to the waveform of a specific radar for two reasons: if the radar is 'hostile' the intercept receiver will not be able to know its waveforms a priori and, in any case, because it has to be able to detect all the radars in the scenario, its processing cannot be matched to any particular one of them.

The beamwidth of the antenna of the intercept system must also be wide in order to detect signals coming from all directions, and its bandwidth must be wide in order to detect signals at different frequencies. We will see later that all these factors make the ESM receiver much less sensitive than the radar receiver, an inefficiency which, however, in many cases is more than countered by the fact that the propagation to the intercept receiver is only one-way, i.e. there is an r^2 term in the dominator of the equation, unlike the radar case where we will see the familiar r^4 term in the corresponding equation.

In order to reduce the signal to noise ratio which the intercept receiver can obtain against it, or equivalently, to reduce the range at which the intercept receiver can obtain the signal to noise ratio necessary to be able to exploit it, the radar must minimise its effective radiated power and maximize the bandwidth over which the intercept receiver will have to look in order to be sure of intercepting the radar's signals.

2.2 Radar Detection Equation – Mean Power Form

The simplest form of the equation for the radar's detection performance is probably:

$$SNR = P_m G_t^2 \lambda^2 \sigma \tau / [(4\pi)^3 r^4 \times k T N_r L_r], \quad (2)$$

where P_m is the mean power of the radar; λ is the wavelength; σ is the Radar Cross Section (RCS) of the target; N_r is the noise figure of the radar receiver; L_r represents the losses is the radar receiver and τ is the integration time of the radar receiver.

This form differs slightly from the more familiar form of this equation, in terms of the radar's peak power and the receiver bandwidth, which is introduced as equation (3) below, but brings out more clearly that the sensitivity of the radar is a function of the energy ($P_m\tau$) which it can direct towards the target.

Note that the two receivers are assumed to be at the same temperature.

Apart from the term σ/r^4, the key difference between the two equations is that the mean transmitted power replaces the peak power and the integration time replaces the inverse of the receiver bandwidth. This is because one consequence of the matched filter theorom[5] is that, since the radar knows its own waveform, it can use an optimal receiver which coherently integrates energy over all the frequency components in the signal and yields a sensitivity which is only dependent on the total energy (mean power × integration time) received from the target. As mentioned above, the ESM receiver must be mismatched to the signal and so cannot achieve this gain.

This version of the radar power budget does not include the bandwidth of the signal, because the matched filter in the receiver can coherently integrate all the received power over the whole of the signal bandwidth.

Of course, the radar cannot increase its integration time without limit because this is limited by the rate at which it must be able to deliver information.

The special cases where the intercept receiver can try to approach the processing gain possessed by the radar are discussed briefly in section 6.

The factor $G_t\lambda^2/(4\pi)$ in equation 2 is the effective aperture of the radar antenna, and the equation makes the assumption that the radar's transmit and receive antennas have the same gain - the same antenna

would, of course, normally be usually be used for both functions.

The loss term is assumed to include both RF and processing losses. The transmission losses are assumed to be included within P_m, i.e. the latter is assumed to be the power actually radiated from the antenna, because and losses in the transmission feed path will affect the sensitivity of the radar and its ability to be intercepted to the same extent and so it is best to use definitions which avoid the need to consider such losses.

Although the best way to design the radar antenna for LPI is to maximize its gain (strictly, to maximize its receiver aperture) it is also usually desirable to minimise its sidelobes, to inhibit interception of the radar signals when the radar is not actually looking at the intercept receiver. This makes it harder to exploit any interceptions, since they will become intermittent.

2.3 Radar Detection Equation – Peak Power Form

The radar range equation can also, of course, be written in terms of the peak power levels. Although less 'fundamental' than the mean power from, this version is often used and is also closer to the form of the interception equation (equation 1). It takes the form:

$$\mathrm{SNR} = P_p G_t^2 \lambda^2 \sigma G_{PC} / [(4\pi)^3 r^4 \times k T B_r N_r L_r], \qquad (3)$$

where G_{PC} is the processing (pulse compression) gain of the matched receiver and B_r is the effective bandwidth of the radar signal.

This version is more directly comparable with the 'interception' budget in that it includes the peak power and the bandwidth, but the radar still possesses the processing gain of the matched filter, which, by comparison with equation 2, can be seen to be equal to the time-bandwidth product of the signals, i.e. the product of the bandwidth and the integration time. A more detailed analysis of the two forms will show that the processing losses (within the term L_r) are slightly different when using the two models, but these relatively minor differences do not affect the general principles. A concise way of expressing a key LPI design goal, derived from comparing equations 1 and 3, is to maximize the time-bandwidth product of the radar.

3. POWER BUDGETS

3.1. Sensitivity of a typical Intercept Receiver

The sensitivity of ESM receivers is usually quoted in terms of the minimum detectable signal divided by the antenna gain:

$$S = kTB_i N_i L_i . SNR_{min} / G_r, \qquad (4)$$

where SNR_{min} is the minimum signal to noise level required for detection.

This minimum signal to noise ratio is usually controlled in the receiver by dynamically setting the detection threshold this far above the noise floor. This measure is thus related to the power density at the ESM antenna which is necessary to detect the signal. Since the signal level at the receiver input is equal to the power density multiplied by the effective aperture of the antenna, which is equal to $G_r\lambda^2/4\pi$, the minimum power density which can be detected is actually,

$$P_{min} = 4\pi S/\lambda^2. \qquad (5)$$

The detection range deduced from equations (1) and (5) is thus:

$$r_{max} = \sqrt{(P_p G_t / S)}\lambda/(4\pi). \qquad (6)$$

We will now consider a 'classic' case of an Instantaneous Frequency Measurement (IFM) receiver[6]. Although this is no longer the 'state of the art' for receiver sensitivity, it will serve to show how LPI became a 'battle' between the radar and the intercept receiver. Fig. 2 shows a sketch of a block diagram of an IFM receiver.

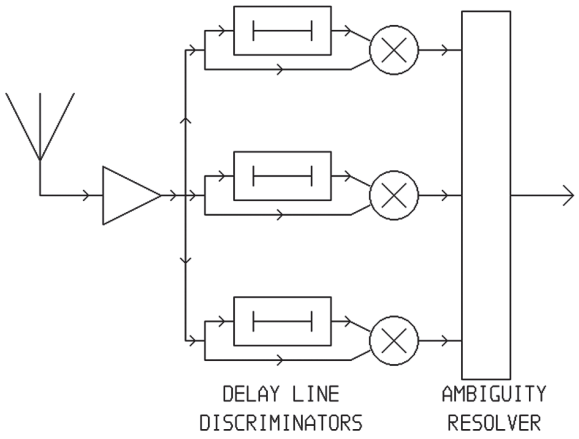

Fig. 2. IFM The Principle of the IFM Receiver

The IFM measures frequency using delay line discriminators. The phase between the direct and delayed paths is a measure of frequency, but is ambiguous as the phase can only be measured modulus 2π. A set of delay lines is therefore used, long ones with a narrow unambiguous range but high resolution and shorter, lower resolution, lines to resolve the ambiguities. The desirable combination of wide frequency coverage and high accuracy is obtained by combining the phase measurements using appropriate logic. Since the set of phase measurements is available from a single pulse, the frequency can be measured within the period of a single pulse, i.e. effectively instantaneously. The noise figure can be defined by the amplifier at the input of the receiver, but the Radio Frequency (RF) bandwidth must be high in order to capture emitters over the whole range of frequencies and will be at least 2GHz. However, the bandwidth after the phase detectors (the video bandwidth) needs only to be fast enough to capture the shortest pulses of interest, and may typically be 10MHz.

This mismatch between the RF and video bandwidths gives the ESM receiver an approximate effective bandwidth of

$$B_{eff} \approx \sqrt{(2 B_{RF} B_v)}, \qquad (7)$$

where B_{RF} is the RF bandwidth and B_v is the video bandwidth.

Using the example bandwidths quoted above the effective bandwidth of the receiver will be 200MHz.

In our baseline scenario, the ESM receiver may be assumed to have an antenna gain of 0dBi, so the aperture will be $\lambda^2/(4\pi)$. In fact the antenna will not be omnidirectional, but it will have a wide field of view, so its directive gain will be low. The need for a wide frequency coverage will add further losses, so the net gain will be close to that of an omnidirectional antenna.

The other parameters of the intercept receiver may be assumed to be:

Table 1

Components of the Sensitivity Calculation for an IFM-based Receiver

Noise Figure:	10 dB
Processing Losses:	4 dB
Minimum Signal-to-noise for detection:	17 dB

Inserting these values into equation 4 gives a sensitivity of -60dBmi.

3.2. Detection range of the baseline radar

We consider first how such a receiver can intercept a 'typical' pulse-modulated marine radar. The radar is assumed to have the following key parameters:

Table 2

Parameters of the Pulse Radar

Peak transmitter power:	10 kW
Antenna Gain:	30 dB
Frequency:	9 GHz
(wavelength	3.3 cm)
Pulse Width:	100 ns
(Receiver Bandwidth:	10 MHz)
Noise Figure	4 dB
Losses	4 dB
Pulse Repetition Frequency:	1 kHz
Azimuth beamwidth:	1.2°
Scan rate:	40 r.p.m.
(Dwell Time	5 ms)

The wavelength, the receiver bandwidth and the dwell time are in brackets because they are derived parameters.

The radar's receiver bandwidth has been taken to be approximately the reciprocal of the pulse length. The radar is has a lower system noise figure than the intercept receiver because it has a narrower bandwidth and is generally better 'tuned' to its signals.

The dwell of 5ms allows five pulse to be integrated across the beam. This is assumed to lead to an incoherent gain of 4dB, which lowers the effective bandwidth to 4MHz. Putting these figures into equation 3 show that the radar can detect a target with an RCS of $100m^2$ (such as a small ship) at a free-space range of 20km. with 15dB signal to noise ratio.

3.3. Baseline Intercept Range

Inserting the parameters of the pulse radar into equation 5 gives an intercept range of 250km, i.e. more than an order of magnitude greater than the range at which the radar can detect its target.

3.4. LPI Radar Intercept Range

If we follow the principle outlined above and change the radar design to increase the duty cycle to 100% this will allow us to reduce the peak power from 10kW to 1W without changing the mean power and hence without changing the detection performance, so the radar will still be able to detect the ship at 25km range.

The radar can be assumed, for convenience, to use Frequency-Modulated Continuous Wave (FMCW) modulation, although this is not critical to these high-level sensitivity calculations. The full set of parameters of the this radar are listed in table 3 for convenience:

Table 3

Parameters of the FMCW Radar

Mean transmitter power:	1W
Antenna Gain:	30dB
Frequency:	9GHz
(wavelength	3.3cm)
[Sweep Bandwidth	10MHz]
Noise Figure	4dB
Losses	4dB
Sweep Repetition Frequency:	1kHz
(Coherent Integration Time	1ms)
Azimuth beamwidth:	1.2°
Scan rate:	40 r.p.m.
(Dwell Time	5ms)

As in table 2, the wavelength and the dwell time are in brackets because they are derived parameters. The coherent integration time is also in brackets because it is derived from the sweep repetition frequency. The sweep bandwidth is in square brackets because it is not used in the calculations in this section of the paper.

Five sweeps can be integrated incoherently over the dwell, in a process analogous to the incoherent integration of the pulses for the pulse radar. The detection range can be calculated using either equation 3 or, more conveniently, using equation 2 and will, of course, be the same as that of the pulse radar. Although there may be practical difficulties in achieving this performance with some CW radar designs, it has been shown[2,3] that an FMCW radar can achieve this performance and this may also be possible in the future for with radars using noise waveforms for example.

Although it has no effect on the sensitivity of the radar, the change in modulation has a dramatic effect on the range at which its transmissions can be intercepted. The reduction in peak power from 10kW to 1W means that the intercept range is reduced by a factor of 100 to only 2.5km, i.e. the LPI radar can indeed detect its targets at much greater ranges than those at which its own transmissions can be intercepted.

The general principle of minimizing the probability of intercept is therefore to spread the radar signal as widely in time and frequency as possible in order to minimise the power density at the intercept receiver. It is also, of course, valuable to maximize the uncertainty of its bearing, to prevent the intercept receiver from using a directional antenna, with a relatively large receiver aperture, which would increase the receiver's sensitivity.

4. NARROW-BAND INTERCEPT RECEIVERS

It will be appreciated that the sensitivity of the intercept receiver has been severely limited by making it 'wide open' in frequency and bearing. This is needed

in order to retain a high 'Probability of Intercept' so that the receiver can be sure of rapidly detecting all the signals which are in the environment. However, in some cases it might be worth trying to increase the sensitivity, i.e. increase the intercept range, even if the probability of being able to intercept the signal over any given time period has to be reduced as a result.

4.1. Superheterodyne receiver

As an example of a receiver which trades probability of intercept for sensitivity is the superheterodyne (superhet) receiver. This uses a relatively narrow band receiver which is swept in frequency to look for the radar. A typical superhet might have a bandwidth of 2MHz, giving it 20dB better sensitivity than our IFM. This would mean that the free-space range at which our LPI radar could be intercepted would be increased by an order or magnitude, to 25km, i.e. to a value which is very similar to the range at which the radar can detect its target. If the superhet is to dwell for long enough to be able to characterize the radar, however, i.e. for several milliseconds, it will now take several seconds to cover the bandwidth of 2GHz which our IFM could cover instantaneously. A faster scan could cover the band much more quickly, but the shorter 'dwell' on each frequency would not allow the signals to be characterized, i.e. we would be trading 'Probability of Intercept' against 'Probability of Exploitation' as well as trading both against intercept range.

If the radar is agile from sweep to sweep within the dwell, or if it is agile from scan to scan but the intercept receiver cannot cover the whole of its agile band within a single dwell, then the interception of the radar's signals become a probabilistic process. The process of intercepting the radar in this case can be modelled by a Poisson distribution, for which the probability of failing to make an interception is

$$(1 - p_i) = e^{-n\psi} \quad (8)$$

therefore

$$p_i = 1 - e^{-n\psi}, \quad (9)$$

where p_i is the probability of intercepting the radar, n is the number of opportunities for interception and ψ is the probability of interception on one opportunity. For example if the superhet dwelt for 1ms, its probability of being on the right frequency to intercept the radar at some time within its dwell would be approximately the ratio between the bandwidth of the radar signals (10MHz) and the superhet's search bandwodth (2GHz) i.e. about 0.005, whereas if it dwelt for only 10μs it would cover about a hundred 10MHz-wide 'windows' during the radar's sweep time, so the probability of intercept would become $1\text{-}e^{-0.5} \approx 0.4$.

There is a steep trade-off between detection probability and sensitivity. The general shape of this trade-off is shown in fig. 3.

The effect of an increase in intercept time is multiplied because if the receiver can only intercept the radar's main beam, then if it cannot detect the radar during the 5ms for which the radar is illuminating it, it will not have another chance to do so until the next scan, 1.5 seconds later.

The two cases shown in figure 3, for 90% and 10% cumulative PoI illustrate the times until the interceptor can be reasonably sure of finding the radar, and that for which the radar can be reasonably sure that it has not been detected. The separation between these lines (approximately a factor of 20 in time) highlights the important tactical difference which can arise as a consequence of deciding which criterion is appropriate in a particular scenario.

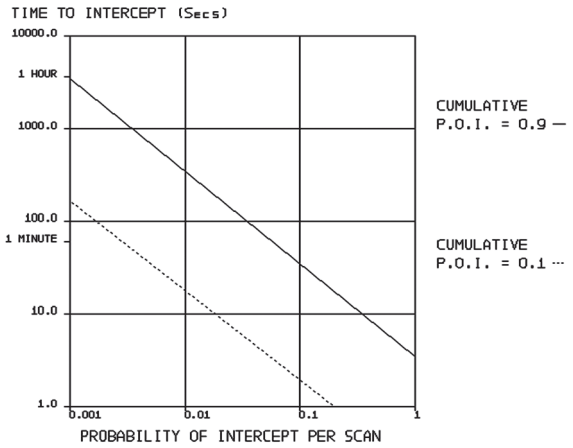

Fig. 3. Effect of Probability of Intercept on Time to Intercept the Radar

4.2. Channelized Receivers

The ideal is, of course, to obtain the sensitivity of a narrow-band receiver with the probability of intercept of a wide-open receiver. The only known way to do this is to create a series of receivers in parallel. Figure 4 shows an outline sketch of a channelized receiver architecture.

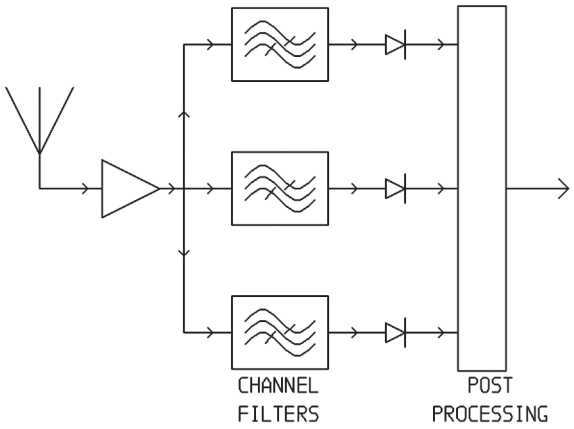

Fig. 4. Outline of a Channelized Receiver

Each 'channel' is a narrowband receiver, with the sensitivity appropriate to such a receiver, but the multiplicity of such channels in parallel give the coverage of a 'wide open' receiver. Non-trivial logic is required after detection to 'pull together' all the information on the scenario and to suppress potential artifacts such as those which can occur when signals straddle several channels. This sort of architecture has been popular since the late 1980's where high sensitivity and wide bandwidth are required simultaneously. Some of the early implementations used analogue

filters, but modern implementations predominantly used Fourier transform based techniques to create the required parallel channels. Such a receiver would typically have a channel bandwidth, and hence a sensitivity and interception range, equal to that of the superhet, but with 100% probability of intercept against the main beam of the radar.

As well as providing better sensitivity, the channelized receiver also allows multiple signals on different frequencies to be seen simultaneously. This was difficult with an IFM, but it has become more necessary as the duty cycles of conventional radars have increased, so that it is now quite likely that signals from several radars will be present simultaneously in the receiver.

5. INTERCEPT RECEIVER PROCESSING GAIN

It was mentioned in section 3 that a general-purpose intercept receiver will not have any processing gain against the radar signals because it does not know *a priori* what processing it should apply. Various attempts, have, however, been made to overcome this limitation. Attempts have been made to obtain coherent processing gain against LPI radars, but these generally fail either if the signal to noise ratio is low (which is just when the gain is needed), because the signals are then too corrupted by noise, or else they are too vulnerable to relatively minor changes in the radar waveform.

Other approaches have used non-linear processing, but this is easily upset when multiple signals are present. This is a problem since the LPI signals will be the weakest of those present and hence the ones most likely to be lost amongst any spurious signals introduced by the processing.

The relative failure of attempts to create intercept receivers using coherent processing has led instead to the idea that one should try to do as well as one could to match the receiver to the bandwidth and duration of the signal being intercepted, but without attempting any coherent processing of it. This is the idea behind the Matched Incoherent Receiver (MIR). This is a radiometric receiver, i.e. it attempts only to detect the presence of RF energy but not its characteristics. It is designed with an RF bandwidth equal to the radar's agile bandwidth and a video bandwidth equal to the reciprocal of its dwell time. Although the details of such a receiver become specific to the particular radar, the rule can be applied to the detection of any radar waveform. It probably represents the 'worst case' intercept scheme against the radar and although such a receiver is unlikely to exist for any particular radar, it represents a good baseline against which the practical robustness of a radar's the LPI performance can be assessed.

The name 'Matched Incoherent Receiver' is therefore used for this receiver because it is matched both to the RF bandwidth of the signals to their information bandwidth, but not to the details of the waveform. Its use would mean that the radar would no longer have the advantage of a mismatch between its bandwidths and those of the intercept receiver, but only the advantage of knowing its own waveforms. This principle allows the intercept receiver to recover the square root of the radar's time-bandwidth product, and it is, of course, the time bandwidth product which gives the radar its LPI characteristics. Shirman et al.[7] have also reported that the performance of this receiver is very insensitive to errors in the estimates of the time and bandwidth of the signals.

To detect the FMCW radar described in section 3.3 and in table 3, for example, the MIR would have an effective bandwidth of 200kHz, making it 30dB more sensitive than our baseline IFM-based receiver, giving it a free-space detection range of about 80km against the main beam of our 'LPI' radar design.

5.1 Trade-off between sensitivity and information

It is noteworthy that in order to maximize its sensitivity as a detector, this radiometric receiver destroys all the information about the signal. There is an interesting analogy between this behaviour and the true, coherent, matched filter[5]. In the latter case, the matched filter has a frequency response which is the complex conjugate of the spectrum of the signal, so the filtering process removes all the phase information from the signal and hence destroys the information about the 'shape' of the signal in the time domain.

It is speculated that an efficient detector, by 'gathering together' as much as possible of the energy in the signal will always tend to destroy the information which an intercept receiver might otherwise want to retain in order to identify it.

6. NOISE WAVEFORMS FOR LPI

The design principle of the Matched Incoherent Receiver implies that the LPI performance is independent of the details of the waveform, being driven entirely by its overall integration time and its overall bandwidth. From that point of view, noise waveforms would be expected to have the same LPI characteristics as other CW waveforms such as FMCW.

6.1. Security from Potential Interception Strategies

There are, however, two other benefits of using random waveforms. The first of these comes from the consideration that it may in fact be possible to design practical receivers for deterministic high-duty-cycle waveforms which can exploit their deterministic properties, even though, as was argued in the previous section, no practical scheme for doing this has yet been implemented. No such improvement in sensitivity over the radiometric receiver is possible, against noise, however, unless the particular noise sequence is known, and this is not possible if the sequence is generated at random in real time. The use of random waveforms thus gives protection against any exploitation of the characteristics of the signal which might become possible in the future.

6.2. Security from Range-Gate Pull-Off Jamming

The other advantage possessed by a noise waveform is that it will defeat the attempt to use a Digital Radio Frequency Memory (DRFM) to achieve range-gate pull-off.

The significance of range-gate pull off as a jamming technique, and the way in which increasingly

more sophisticated jamming and counter-jamming techniques have developed over successive generations of equipment is in itself a very good example of the continuing 'battle' between radar and electronic countermeasures systems, as well as being of practical relevance for noise radar in particular.

Range-gate pull-off relies on placing a false target close to the return from the real target, and persuading the radar to track the false target instead of the real one. As illustrated in figure 5, older jammers could place the false target behind the real one, by retransmitting the signal received at the target.

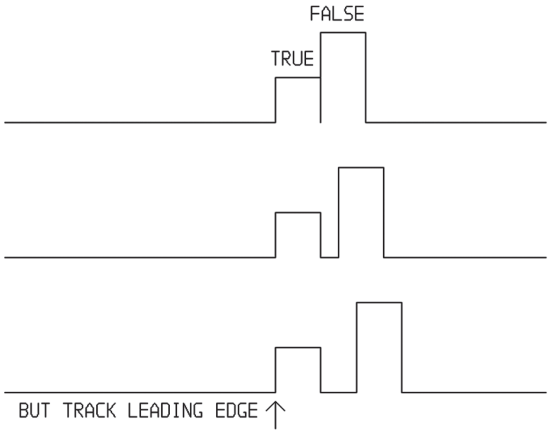

Fig. 5. Principle of Range-Gate Pull-Off

The plots illustrate three successive 'A-scope' images showing the 'true' signal reflected from the target and the 'false' signal re-transmitted by the jammer.

The false target is bigger than the real one and is slowly moved away from the real one by increasing the delay before retransmission. When the two signals are well enough separated, the false target is removed, leaving the radar with nothing to track.

As noted in the text of the lowest 'A scope,' however, a newer generation of radars countered this technique by tracking the 'leading edge' return. This would, of course, ignore a false target behind the true one and this was done specifically to defeat range-gate pull off.

If the jammer is on the platform to be protected, as is frequently the case, the principle of causality prevents it from creating a false copy of the true signal which can reach the radar before the 'true' return, so the next step in the battle has been to 'counter' the leading edge tracker by exploiting the repetitive nature of the radar signals and delay the received signal by slightly less than the pulse repetition interval (or equivalently, the sweep repetition interval for an FMCW radar) so that the false signal appears slightly before the true reflected signal from the next pulse as illustrated in fig. 6.

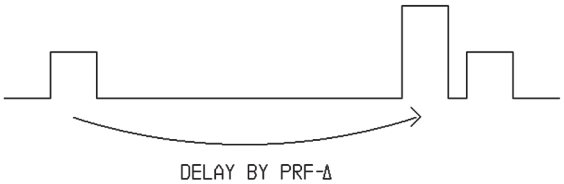

Fig. 6. Principle of a DRFM - Used to Create An Up-Range False Target

The 'leading-edge' tracker will then still be deceived into following the false signal. This does not work against a noise waveform however, because the signal is non-repetitive, and non-deterministic, so delaying the signal can never be equivalent to moving the signal 'forward' in time.

It is worth remarking about this is not an 'LPI' feature so much as a way of preventing exploitation of the radar. This can be illustrated by considering the fact that the repeater jammer can in principle jam the radar with false targets without being able to detect the signals . It can repeat a signal which is buried within the jammer's own receiver noise and rely on the radar which is being jammed to use its own signal processing gain to extract the false signal from the noise. - Of course it would need information from somewhere, possibly from the known characteristics of the signal, in order to know the repetition period.

It is important to note that these strengths are based on the unpredictability of the signals and, at least in principle, they will be compromised if pseudo-noise waveforms, using pseudo-random sequences or the outputs of chaotic systems, are employed instead of pure noise, although their practical exploitation would still be very difficult

CONCLUSION

This paper has illustrated how an intercept receiver can easily detect the signals from a conventional radar at long range, even though its receivers are relatively insensitive due to the need for them to be wide open in both frequency and bearing, because the intercept path uses only one-way propagation (r^2) whereas the radar's detection of its targets requires two way (r^4) propagation.

LPI radars can overcome the effect of this r^4 path loss by using high processing gains which the intercept receiver cannot match. The current interest in LPI techniques and methods of countering them has arisen since modern radar hardware has made it practical to use waveforms with very high time-bandwidth products.

Classical intercept receiver designs can only overcome the radar's processing gain at the expense of a reduced probability of intercepting the radar, which may make them tactically ineffective.

More sophisticated channelized receivers, or special-purpose 'matched incoherent receivers' can recover most of the intercept receiver's range advantage. It should be noted however, that this is only the case when the main beam of the radar points at the intercept receiver. Achieving high intercept ranges is still difficult against the radar's sidelobes. The issues associated with this go beyond what can be discussed in this paper, but are considered in reference 4.

Noise radars have a theoretical immunity to 'clever' interception schemes, and a practical immunity to up-range false target jamming, but these benefits may be compromised if pseudo-random waveforms are used, rather than those which are truly random.

Low Probability of Intercept can be a genuine and important feature of a radar, but its significance is scenario dependent.

The 'battle' between designing radars to exploit increasingly-sophisticated waveforms and intercept receivers of increasing sensitivity and sophistication has been played out over many decades in the past and will doubtless continue into the future.

References

[1] Fuller, K. L., 'To See and Not be Seen,' Proc. IEE **137**, Pt F., pp1-9, (1) February 1990.

[2] Stove, A. G., Beasley, P. D. L., Reits, B. J. and Ås, B-O, 'Das PILOT-Radar,' Proceedings of MIOP '90, Stuttgart, 1990.

[3] Ås, B.-O., 'The PILOT, A Quiet Naval Tactical Radar,' proceedings of Radarcon 90, Adelaide, 1990, pp. 165-71, published by DSTO.

[4] Stove, A. G., Hume, A. L. and Baker, C. J., 'Low Probability of Intercept Radar Strategies,' IEE Proc. Radar Sonar & Navig, 151 (5), pp249-60, October 2004

[5] Cook, C. E. and Bernfeld, M., 'Radar Signals,- an Introduction to Theory and Application,' New York, 1967, Academic Press, Library of Congress Catalog 66-30803, Chapter 2

[6] East, P. W., 'Fifty Years of Instantaneous Frequency Measurement,' IET Proc. Radar Sonar & Navig. **6**, pp112-122, (2) February 2012

[7] Y. D. Shirman, V. M. Orlenko and S. V. Seleznev, "Passive Detection of Stealth Signals," Proceedings of European Radar Conference 2004, pp. 321-4, October 2004

Manuscript received December, 10, 2012

Dr Andy Stove received a BA degree in Engineering Science in 1977 and a DPhil degree in 1981 for work on surface acoustic wave devices, both degrees being received from Oxford University. He then joined Philips Research Laboratories, working principally on the application of FMCW techniques to naval navigation radars and low-level air defence radars, on guided ammunition and on automotive radar. This work included the research which led to the development of the PILOT Low Probability of Intercept FMCW navigation radar. After a short period working on ways to enable computers to understand their users' mental states, he joined Racal Radar Defence Systems, now Thales Defence and Mission Systems Domain, in 1996. Since then he has worked on the system design and proving of the Searchwater 2000 family of Maritime Surveillance and AEW radars. He has also worked on target classification and discrimination for microwave and VHF radars and has continued to work on FMCW techniques, including their application to low cost phased array radars and further studies of their detectability. He has also worked on calibration techniques and systems concepts for advanced, low cost, phased array radars, on techniques for modelling the operation and performance of radar systems and on their use in multi-function and multi-static systems. He is co-Chairman of the NATO SET-184 group "Capabilities of Noise Radar". Dr Stove is also a senior member of the IEEE and a fellow of the IET.

УДК 621.37

Радары с низкой вероятностью обнаружения / А.Г. Стоув // Прикладная радиоэлектроника: науч.-техн. журнал. – 2013. – Том 12. – № 1. – С. 114–121.

Появление широкополосных радаров с большими относительными длительностями включения привело к тому, что стало практичным создавать радары с коэффициентом усиления обработки достаточно высоким для работы на дальностях, на которых сигналы этих радаров не могут быть перехвачены. Данная работа рассматривает принципы таких радаров с низкой вероятностью перехвата и иллюстрирует их простыми количественными примерами, сравнивая характеристики с импульсными радарами с линейной частотной модуляцией сигналов. В качестве базы в данной работе рассматривается приемник с использованием техники измерения моментальной частоты, но обсуждаются и другие возможные варианты радаров, и исследуется противоречие между чувствительностью перехвата и временем перехвата. Приводятся аргументы в пользу того, что согласованная фильтрация – не лучший способ перехвата радара с низкой вероятностью перехвата. Рассматриваются достоинства согласованного некогерентного приемника, где время предетектирования и ширина полосы пост-детектирования согласованы с радиолокационным сигналом, но обнаружение некогерентно. Кроме того, обсуждаются дополнительные достоинства в этой сфере, потенциально доступные для шумовых радаров. Подчеркнута важность в военном сценарии низкой вероятности перехвата и, в частности, дополнительного принципа низкой вероятности использования сигнала.

Ключевые слова: низкая вероятность обнаружения, приемник-перехватчик, радиоперехват.

Ил. 6. Библиогр.: 7 назв.

УДК 621.37

Радари з малою імовірністю перехоплення / А.Г. Стоув // Прикладна радіоелектроніка: наук.-техн. журнал. – 2013. – Том 12. – № 1. – С. 114–121.

Поява широкосмугових радарів з великою відносною тривалістю включення призвела до того, що стало практичним створювати радари з коефіцієнтом посилення обробки достатньо високим для огляду відстаней, на яких сигнали цих радарів не можуть бути перехоплені. Дана робота розглядає принципи таких радарів з низькою ймовірністю перехоплення та ілюструє їх простими кількісними прикладами, порівнюючи характеристики з імпульсними радарами з лінійною частотною модуляцією сигналів. Як база у даній роботі розглядається приймач з використанням техніки вимірювання моментальної частоти, але обговорюються й інші можливі варіанти радарів, досліджується протиріччя між чутливістю перехоплення і часом перехоплення. Наводяться аргументи на користь того, що узгоджена фільтрація — не кращий спосіб перехоплення радара з низькою ймовірністю перехоплення. Розглядаються переваги узгодженого некогерентного приймача, де час попереднього детектування і ширина смуги пост-детектування узгоджені з радіолокаційним сигналом, але детектування є некогерентним. Крім того, обговорюються додаткові переваги в цій сфері, потенційно доступні для шумових радарів. Підкреслено важливість у військовому сценарії низької ймовірності перехоплення і, зокрема, додаткового принципу низької ймовірності використання сигналу.

Ключові слова: мала імовірність детектування, приймач-перехоплювач, радіоперехоплювання.

Іл. 6. Бібліогр.: 7 найм.

UDC 621.37

RADAR WITH RANDOM VARIATION OF PROBING SIGNAL PARAMETERS

V.V. RODIONOV

This paper utilizes game-theoretic principles in detecting of Gaussian signals against background of Gaussian noise. We propose the payoff function generalizing signal-to-noise ratio to casual signals. It is found that potential immunity of radar to electronic countermeasure strategies is only achievable through random variation in parameters of sounding signals. Performance limits of radar depend on the product of probing signal bandwidth and its duration. The coherent integration time is to be 2-10 times less than full processing time of the received signal.

Keywords: jammer, radar, game theory, signal.

1. INTRODUCTION

Statistical Hypothesis Testing theory provides a basis for procedures of synthesis of optimum detection algorithms [1,2], the theory gives a principal opportunity to work out optimum detection algorithms for any kind of jamming, irrespective of whether detailed statistical characteristics of signals and jamming are known, or whether under a priori uncertainty conditions [3, 4].

As current methods of algorithm synthesis use a model of signal environment allowing the only active party, that is a radar, the theory is not applicable to synthesis of detection algorithms, if electromagnetic countermeasures (ECM) are employed. When there are electromagnetic countermeasures then there are at least two active parties, a radar trying to improve signal detection and countermeasure systems trying to prevent a radar from operating as well as it might.

Although there isn't an appropriate theoretical framework experts have proposed anti-jam techniques. Note that these techniques don't follow from solution of any classical synthesis problem. For example, there are random changing in signal-carrier frequency, changing of pulse recurrence interval, changing of signal waveform etc. Most every modern radars deploy random variation in parameters of sounding signals against active jamming. Modern communication systems also use random variation in parameters of sounding signals (a.k.a. frequency hopping) to improve noise immunity. Although these anti-jam techniques have proved to be practical, developing of new methods of synthesis and guaranteed immunity resistance to jamming still attract great interest.

The theory of algorithms synthesis for detecting signals in electronic countermeasures based on the model of a game between a radar and jammer can help to meet these goals. [5,6,7,8,9,10].

2. GAME-THEORETIC MODEL OF GAUSSIAN SIGNALS DETECTION

A game-theoretical model consists of two players at least, in our case these are a target and a radar, with the target always trying to prevent the radar from fulfilling its task. Since there are two players and the target and the radar form an adversarial system, their interaction is modelled as a two-person zero-sum game, a.k.a. antagonistic game. On the first stage needed to choose a function of advantage of game.

For example we have an interaction between a radar and a target, where the former tries to locate the target in any kind of bin. The radar operates with variation in parameters of sounding signals and algorithm of processing of the received signals. The target, which carries jamming equipment, tries to generate jamming that could confuse the radar. Thus, this interaction can be represented as a two-person zero-sum game.

We assume that:

player 1 (radar) has a set of **X** possible actions to choose from (pure strategies);

player 2 (jammer) has a set of **Y** pure strategies to pick from;

stands for payoff function for player 1: $H: X \times Y \to R$ (This is criterion for detection efficiency).

The payoff function is critical to choose. On the one hand the payoff function is one of the ECM-resistance properties and on the other hand it is supposed to allow the game to have the solution and non-trivial results.

The quality of detection is normally expressed as the probability of detection for a given conditional probability of false alarm (Neumann-Pearson criterion). Since Neumann-Pearson criterion is a special case of more general average risk criterion the game was formalized and solved, where average risk is the payoff function [1].

The solution of the game shows that the most unfavourable jammer is to come from the detectable signal [5]. Multivariate density of probability of the most unfavourable jammer is expressed as multivariate density of probability of the detectable signal:

$$W_y(\mathrm{x}) = (1-\lambda)\sum_{k=0}^{\infty}\lambda^k W_s^{(k)}(\mathrm{x}). \qquad (1)$$

Where $\lambda < 1$ reciprocal to comparison threshold of likelihood ratio of Bayes optimal algorithm:

$$\frac{W_s(\mathrm{x}) \otimes W_y(\mathrm{x}) \otimes W_n(\mathrm{x})}{W_y(\mathrm{x}) \otimes W_n(\mathrm{x})} \gtrless \frac{1}{\lambda},$$

$$W_s^{(k)}(\mathrm{x}) = \underbrace{W_s(\mathrm{x}) \otimes W_s(\mathrm{x}) \otimes \cdots \otimes W_s(\mathrm{x})}_{k}$$

denote convolution of k of probability density $W_s(x)$ of the detectable signal; $W_n(x)$ probability density function of noise.

Correlation function of this kind of jammer and correlation function of the suppressed signal agree within constant multiplier. When the jammer tries to mask Gaussian signal, the radar gets multi-component Gaussian distribution.

Let us compare characteristics of a finite-state masking jammer and characteristics of Gaussian masking jammer with the equal power when Gaussian signal is suppressed (Fig. 1). The diagram shoes that the lines of these two types of jammers are almost coincide. This lets us make a feasible conclusion that the most unfavourable jammers are to be found the range of Gaussian noise.

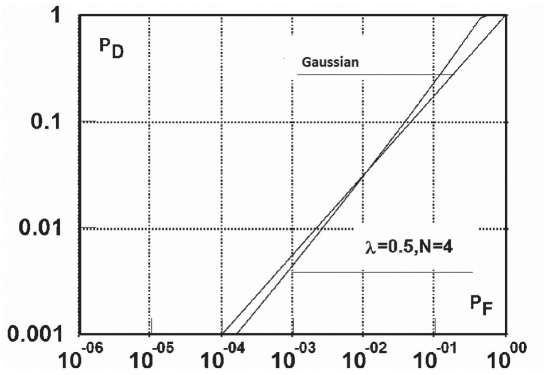

Fig. 1. The performance of detection

We assume that the radar system in operation can use signals of some set: $S_1 = \{s_1(t;a): a \in A\}$ with that the received signals are random and can be presented as a model of a Gaussian process. Correlation function of the signal reflected from the target $K_s(t,u;a)$ depends on parameters chosen by the radar. For example, these parameters can be carrier frequency, code phase modulation or some other signal parameters. In this case the received signals belong to the set:

$$S = \left\{ s(t;a): \int_0^T K_s(t,t;a)dt = E_s,\ a \in A \right\}, \qquad (2)$$

which we denote as the set of detectable signals

Where: E_s denote average energy of the received signal in a time T; **a** stands for the n-dimensional vector of non-power controlled signal parameters; **A** stands for the set of possible values of signal parameters; s(t,**a**) stands for complex random Gaussian process with zero mean and correlation function $K_S(t,u;\mathbf{a})$.

Assume that a choice of any of the signal parameters $a \in A$ in (2) and of algorithm for its processing is a strategy for the radar.

The strategy for the jammer is the ability to generate any Gaussian jammer with zero mean and finite mean energy E_n in a time T. Since Gaussian process is completely determined by its mean and the correlation function, the strategy for the jammer is to choose any of the jammer correlation function from the set: $K_n(t,u)$

$$\left\{ K_n(t,u): \int_0^T K_n(t,t)dt \le E_n \right\}.$$

The jammer has pure strategy since if the jammer has mixed strategies (that is selection of the correlation function $K_n(t,u)$ in relation to some probability measure) this generalizes potential interference to multy-Gaussian interference.

In order to determine the payoff function it should be kept in mind that for every round of the game the goal is to locate Gaussian signal $s(t;a)$ (with parameter $a \in A$, which is known to the receiving end) against the background of Gaussian jammer with correlation function $K_n(t,u)$ and white Gaussian noise with spectral density $N_0/2$.

It is common knowledge that against background of white noise and Gaussian jammer with correlation function $K_n(t,u)$ optimum Gaussian detector with correlation function $K_s(t,u;a)$ calculates statistics for L(**x**) and compares it with threshold **c** [2]:

$$L(x) = \sum_k \frac{\alpha_k}{1+\alpha_k} \left| \int_0^T x(t)\phi_k^*(t)dt \right|^2 \gtrless c. \qquad (3)$$

Where: x(t) stands for realization of the detectable signal; α_k and $\phi_k(t)$ denote eigenvalues and eigenfunctions of the integral equation:

$$\int_0^T K_s(t,u;a)\phi_k(u)du = \alpha_k \int_0^T K_\Sigma(t,u)\phi_k(u)du, \qquad (4)$$

$\phi_k(t)$ which incorporates the complex conjugate function $\phi_k(t)$. The eigenfunctions are normalized with the condition:

$$\int_0^T \int_0^T K_\Sigma(t,u)\phi_k(u)\phi_k^*(t)dudt = 1,$$

where $K_\Sigma(t,u) = K_n(t,u) + \frac{N_0}{2}\delta(t-u)$.

Keep in mind that the eigenvalues and eigenfunctions of the integral equation (4) are equal to the eigenvalues and eigenfunctions of the integral operator. $K_\Sigma^{-1}K_s$. Where K_Σ denotes the integral operator whose kernel is equal to the sum of correlation function of the signal $K_n(t,u)$ and the correlation function of the interference of white noise: $\frac{N_0}{2}\delta(t-u)$, K_s denotes the integral operator whose kernel is equal to the correlation function of the signal $K_s(t,u;a)$; K_Σ^{-1} stands for the operator which the converse of K_Σ.

Account for x (t) stands for complex Gaussian process for both hypotheses we define the characteristic function of L(x) with no signal (hypothesis H0) and having the signal (hypothesis H1) as:

$$\Theta(v/H_0) = \prod_k \left(1 - \imath v \frac{\alpha_k}{1+\alpha_k}\right)^{-1},$$
$$\Theta(v/H_1) = \prod_k \left(1 - \imath v \alpha_k\right)^{-1} \qquad (5)$$

($\imath$ denotes imaginary unit)

In relation to the expression (3) infinite number of channels is required for realization of optimal algorithm. If the channels are restricted to some finite number then performance calculation for detection parameters is based on the characteristic functions with finite number of multipliers (5) and the probability calculation of false and successful detection based on these formulas can make use of the technique proposed here: [11].

As it follows from (5) detection characteristics are completely determined by distribution of the eigenvalues α_k of the integral equation (4). See that α_k is signal-to-noise ratio at the output of the k-th processing channel (symbol ξ_k in Fig. 2).

Then we define $\sum_k \alpha_k$ as the total signal-to-noise ratio on all channels of processing. The higher this value is, the better is detection and vice versa.

This gives us the reason to propose the sum of eigenvalues of the operator as the payoff function $\mathrm{K}_\Sigma^{-1}\mathrm{K}_s$ (the trace of the operator), the payoff function generalizes signal-to-noise ratio to casual Gaussian signals and agrees with signal-to-noise ratio at the output of the linear part of the optimal detector when detecting quasideterministic signals.

Thus we assume the trace of the operator $\mathrm{K}_\Sigma^{-1}\mathrm{K}_s$ as the payoff function is given as:

$$H(a,K_n)=\int_0^T\int_0^T K_\Sigma^{-1}(t,u)K_s(u,t;\mathrm{a})dudt\,, \qquad (6)$$

where $K_\Sigma^{-1}(t,u)$ stands for the kernel of the integral operator $\left(\mathrm{K}_n+\mathrm{I}\right)^{-1}$, I – for the unity operator.

The electronic countermeasures system tries to reduce (6) by make a selection from the jammers with the correlation function. $K_n(t,u)$ By contrast, the radar tries to find probing-signals $\mathrm{a}\in A$ which are able to increase (6). The processing algorithm (3) remains optimal in the process.

3. GAME SOLUTION AND CONSIDERATION

In the general case game with the payoff function (6) hasn't got a saddle point in pure strategies. We always have:

$$\min_{K_n}\max_a H(a,K_n) > \max_a\min_{K_n} H(a,K_n)$$

Specifically, this means that if the parameters of the detectable signal are known to the jammer, then there exists the Gaussian jammer with the correlation function to make the smallest signal-to-noise ratio at the output of the linear part of the receiver.

This game has a saddle point in mixed strategies. Under given conditions, only player 1 (radar) has the mixed strategy, and pure strategy is always the optimal one for player 2 (jammer).

The payoff function in mixed strategies is given as:

$$H(\mu_a,K_n)=\int_0^T\int_0^T K_\Sigma^{-1}(t,u)K_s(u,t)dudt\,,$$

where: $K_s(t,u)=\int_A K_s(t,u;\mathrm{a})d\mu_\mathrm{a}$, μ_a stands for probability measure defined on the set **A**. This is mixed strategy of the radar. The correlation function $K_s(t,u)$ we shall call the correlation function of the set of detectable signals.

Subject to the limitation (2) the correlation function $K_s(t,u)$ can be expanded to series of eigenfunctions

$$K_s(t,u)=E_s\sum_k \gamma_k\psi_k(t)\psi_k^*(u)\,,$$

where $\sum_k \gamma_k=1$.

The minimum value $H(\mu_a,K_n)$ is achieved when the jammer's correlation function can be expanded by the same system of eigenfunctions

$$K_n(t,u)=\sum_k \lambda_k\psi_k(t)\psi_k^*(u),\ \ \sum_k\lambda_k\le E_n\,. \qquad (7)$$

where:

$$H(\mu_a,K_n)=E_s\sum_k\frac{\gamma_k}{\lambda_k+N_0/2}\,. \qquad (8)$$

Minimizing (8) λ_k subject to the limitation $\sum_k\lambda_k\le E_n,\ \lambda_k\ge 0$ we obtain

$$\lambda_k^0=\begin{cases}\left(E_n+m\dfrac{N_0}{2}\right)\dfrac{\gamma_k^{1/2}}{\sum_{i=1}^m\gamma_i^{1/2}}-\dfrac{N_0}{2}, & k\le m\\ 0, & k>m.\end{cases} \qquad (9)$$

The eigenvalues γ_k are in descending order of their values, m stands for the largest integer for which the inequality $\lambda_m^0>0$ is true, viz $\gamma_m^{1/2}>\sum_{k=1}^m\gamma_k^{1/2}\Big/\left(\dfrac{2E_n}{N_0}+m\right)$.

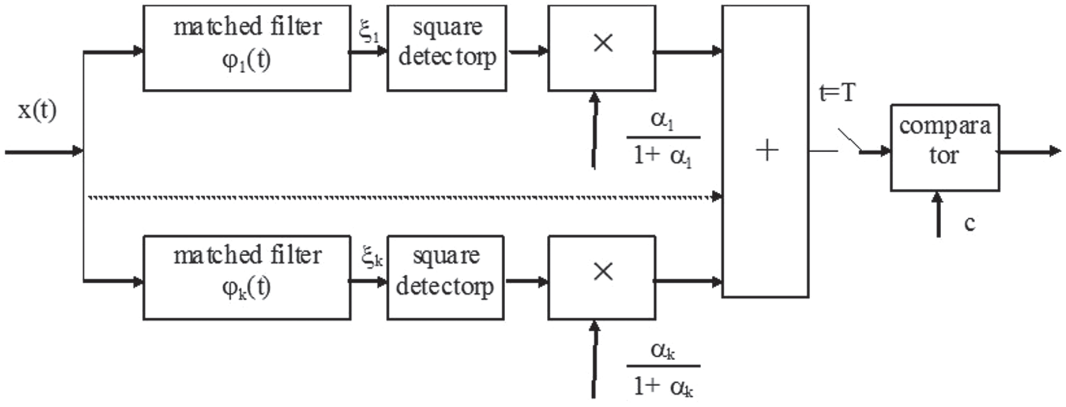

Fig. 2. Optimal detector diagram

Account for (7) and (9) we shall get that the correlation function of the jammer is given as the finite series:

$$K_n^0(t,u)=\sum_{k=1}^{m}\lambda_k^0\psi_k(t)\psi_k^*(u),$$

and the price of the game is:

$$H(\mu_a^0,K_n^0)=\frac{E_s}{E_n+mN_0/2}\left(\sum_{k=1}^{m}\sqrt{\gamma_k}\right)^2+$$
$$+\frac{2E_s}{N_0}\left(1-\sum_{k=1}^{m}\gamma_k\right).$$

The expression for the correlation function of the worst-case jammer agrees with the similar expression which was proposed in [6], where the game-theoretic was used assuming that the signal is known. It implies that optimal strategy for the jammer doesn't depend on the type of signals randomness, whether it is determined by radar, whether it is determined by the medium or both.

In many cases the signal is random due to multiplicative noise, and the correlation function is given as:

$$K_s(t,u;\mathrm{a})=E_s\rho(t,u)s(t,\mathrm{a})s^*(u,\mathrm{a}),$$

where $\rho(t,u)$ stands for the correlation function of the fluctuation of the complex envelope of the detectable signal, which is independent from **a**; $s(t,\mathrm{a})$ denotes the final complex function; $s^*(t,\mathrm{a})$ denotes complex conjugate function $s(t,\mathrm{a})$.

It is found in [7] that if controlled parameters of the signal $\mathrm{a}\in A$ are nonpower kind then selection of this parameter with equal probability is the optimal mixed strategy for the radar.

In this case the eigenvalues and the eigenfunctions of the integral equation (4) are given as:

$$\alpha_k=\begin{cases}\dfrac{E_s}{q}\nu_k^{1/2}\sum\limits_{j\in J}\beta_j^{1/2}+\dfrac{2E_s\nu_k}{N_0}\left(1-\sum\limits_{j\in J}\beta_j\right), & k\in I,\\ \dfrac{2E_s}{N_0}\nu_k, & k\notin I.\end{cases} \quad (10)$$

$$\phi_k(t)=\begin{cases}\psi_k(t)h(t;a), & k\in I,\\ \psi_k(t)s(t;a), & k\notin I.\end{cases}$$

Where ν_k and $\psi_k(t)$ denote the eigenvalues and the eigenfunctions of the correlation function of the fluctuations; $\rho(t,u)$, β_k and $f_k(t)$ stand for the eigenvalues and the eigenfunctions of the correlation function. $\int_A s(t,\mathrm{a})s^*(u,\mathrm{a})d\mu_\mathrm{a}$.

Arrange the outcomes of eigenvalues $\nu_i\beta_j$ in decreasing order and give then numbers 1,2, .., k, in such a way, that $\nu_{i_k}\beta_{j_k}$ will be the k-th member of the sequence.

Then

$$q=\frac{E_n+m\dfrac{N_0}{2}}{\sum\limits_{k=1}^{m}\nu_{i_k}^{1/2}\beta_{j_k}^{1/2}},\ I=\{i_1,i_2,...,i_m\},\ J=\{j_1,j_2,...,j_m\},$$

m stands for the largest integer for which the inequality

$$\nu_{i_m}^{1/2}\beta_{j_m}^{1/2}>\sum_{k=1}^{m}\nu_{i_k}^{1/2}\beta_{j_k}^{1/2}\Big/\left(\frac{2E_n}{N_0}+m\right).$$

is true: Function h(t;**a**) agrees with:

$$h(t;\mathrm{a})=s(t;\mathrm{a})-\sum_{j\in J}\left(1-\frac{N_0}{2q\beta_j^{1/2}}\right)s_j(\mathrm{a})f_j(t).$$

See that this is the weight of the optimal detector of deterministic signals s(t;**a**) with random variation of parameter $\mathrm{a}\in A$ against background of worst-case Gaussian noise [8].

Hence the algorithm for the optimal detector of random Gaussian signals against background of worst-case Gaussian noise is as given:

$$L(x)=\sum_{k\in I}\frac{\alpha_k}{1+\alpha_k}\left|\int_0^T x(t)\psi_k^*(t)h^*(t;\mathrm{a})dt\right|^2+$$
$$+\sum_{k\notin I}\frac{2E_s\nu_k/N_0}{1+2E_s\nu_k/N_0}\left|\int_0^T x(t)\psi_k^*(t)s^*(t;\mathrm{a})dt\right|^2>c. \quad (11)$$

With a view to simplification of the algorithm the second item of the sum (11) can be omitted. This is tantamount to eliminating of the lower line in the brace in the expression (10) The technique proposed in [9] allows developing corresponding performance characteristics. In case of long-term fluctuations when the eigenvalues of α_k don't agree the formulas for probabilities of false alarm and successful detection are as given:

Successful detection:

$$P_D=1-\sum_{i\in I}\frac{1-\exp(-c/\alpha_i)}{\prod\limits_{j\neq i,j\in I}\left(1-\dfrac{\alpha_j}{\alpha_i}\right)}.$$

False alarm probability:

$$P_F=\prod_{i\in I}(1+\alpha_i)\sum_{i\in I}\frac{\exp\left(-c\cdot(1+\alpha_i)/\alpha_i\right)}{(1+\alpha_i)\prod\limits_{j\neq i,j\in I}(1-\dfrac{\alpha_j}{\alpha_i})}.$$

Where c denotes the relative detection threshold

4. POTENTIAL NOISE-IMMUNITY OF RADAR WITH A RANDOM VARIATION OF THE PROBING SIGNALS

We ask, not whether there is an optimal type of signal which provides the highest of radar noise-immunity?

To search for such signals, it is desirable not to limit their set parametric representation, and enter only significant limitations, implementation of which necessarily from physical considerations.

Such restrictions can be considered a frequency band in which the radar can operate, the time of coherent and incoherent accumulation.

Signals received by the radar are random due to fluctuations the reflecting surface of the target.

These fluctuations are multiplicative noise:

$$s(t,\mathrm{a}) = \xi(t) s_s(t,\mathrm{a}),$$

where $\xi(t)$ — Gaussian random process; $s_s(t,\mathrm{a})$ — probe signal; $\xi(t)$ varies slowly compared to $s_s(t,\mathrm{a})$.

We approximate the multiplicative interference by sequence pulse (Figure 3):

$$\xi(t) = \sum_i \xi_i \quad (t - iT_0), \qquad (t) = \begin{cases} 1, & t \in [0, T_0] \\ 0, & t \notin [0, T_0] \end{cases}.$$

Then

$$s(t,\mathrm{a}) = \sum_i \xi_i s_i (t - iT_0, \mathrm{a}_i).$$

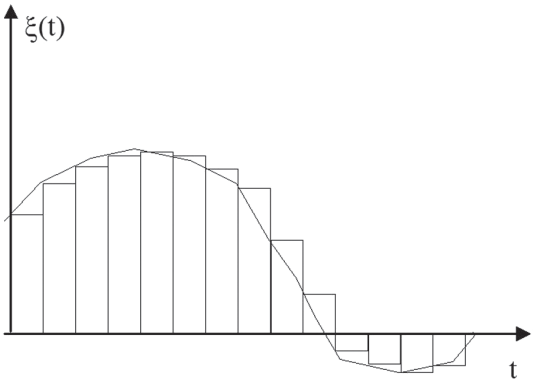

Fig. 3

It is known that the signal can be represented as a series of orthogonal functions. These functions are eigenfunctions of the integral equation:

$$\int_0^{T_0} \frac{\sin(2\pi\Delta f(t-u))}{2\pi\Delta f(t-u)} \phi_i(u)du = \lambda_i \phi_i(t), \ t \in [0, T_0]$$

and are called circular spheroidal. They have a greater concentration of the spectrum in the band Δf.

As shown in [10] is enough to choose the length of the series $n = [\Delta f T]$ ([x] — integer part of x).

Thus, the set of probing signals of duration T and the width of the spectrum Δf is of the form of:

$$\mathrm{S} = \left\{ s(t,\mathrm{a}) : s(t,\mathrm{a}) = \sum_{i=0}^{N-1} \sum_{k=0}^{n-1} a_{ik} \Psi_k (t - iT_0) \right\}.$$

Here a_{ik} — the parameters selected on the side of the radar.

In [10] is shown that, the parameters are selected independently for each piece of the signal in the time interval $[iT_0, (i+1)T_0]$.

The parameters are selected inside track equally likely from ensemble: $\left\{ \mathrm{a} : \sum_{i=0}^{N-1} |a_i|^2 = 1 \right\}$.

Parameter detection α_k can be written as:

$$\alpha_k = \frac{P_s}{P_n + \dfrac{\Delta f N_0}{2}} \Delta f T \nu_k. \qquad (10)$$

Here P_s is the signal power, P_n is the jammer power, ν_k — the eigenvalues of the correlation matrix of sequence ξ_i.

Detection characteristics depend only on the multiplicative noise and on the product width of the spectrum of signals on duration. The parameters of the partition into intervals of duration T0 only affect the precision of the multiplicative noise.

Equation (10) determines the optimal noise immunity of radar when using continuous signals. If you are using pulsed signals, parameter of the detect will take type:

$$\alpha_k = \frac{P_s}{P_n + \dfrac{\Delta f N_0}{2}} \Delta f T \frac{\tau}{T_n} \nu_k.$$

Here $\dfrac{T_n}{\tau}$ — pulse on-off time ratio.

Thus, the potential noise immunity of a pulsed radar inversely proportional to the pulse on-off time ratio.

It is consider the case when the observation time can be divided into n non-overlapping intervals. In each interval can be a coherent accumulation, and fluctuations in the adjacent intervals between themselves independent. If the duration of coherent accumulation is *Tkog* then $n = T / T_{kog}$.

In this case $\alpha_k = d^2 = d_0^2 \dfrac{1}{n}$.

Working feature of detection is easily determined in terms of the chi-square distribution with 2n degrees of freedom: $F(x;2N) = \int_0^x \dfrac{t^{N-1}}{2^N (N-1)!} e^{-t/2} dt$:

$$P_D = 1 - F\left(\frac{F^{-1}(1 - P_F; 2n)}{1 + d^2}; 2n \right).$$

Here P_d — detection probability; P_F — false alarm, $F^{-1}(x;2n)$ — the inverse $F(x;2n)$.

The value of parameter detection d_0^2, required to provide a given probability of correct detection and false alarm can be obtained from the expression:

$$d_0^2 = \left(\frac{F^{-1}(1 - P_F; 2n)}{F^{-1}(1 - P_D; 2n)} - 1 \right) n.$$

On Fig. 4 shows the parameter detection d_0^2 on the ratio between the total accumulation time and time coherent integration n for the probability of false alarm $P_F = 10\text{-}8$.

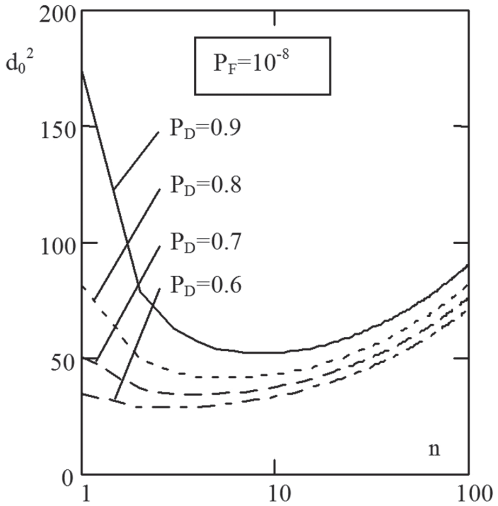

Fig. 4

From the figures it is clear that for a fixed probability of false alarm, there is an optimal ratio between the total accumulation time and time coherent integration n, which requires minimum value detection d_0^2 to provide the required detection probability. This optimum is the more pronounced the greater the required probability of correct detection.

On the other hand the optimum is not sharp and close to optimal values are obtained in the range. $2 \le n \le 10$.

References.

[1] E., Leman, Proverka statisticheskikh gipotez (Statistical Hypothesis Testing), Moscow: Nauka, pp. 500, 1964. [in Russian]

[2] Levin, B. R., Teoreticheskije osnovi statisticheskoy radiotehniky (Theory of Statistical Radio Engineering), Book 2, Sovetskoe Radio, Moscow, pp. 504, 1968. [in Russian]

[3] P. S., Akimov, P. A., Bakut, V. A., Bogdanovich in: P. A. Bakuta (Ed.), "Teoria signalov" (The Theory of Signal Detection), Moscow, Radio i sviaz', pp. 440, 1984. [in Russian]

[4] A. P., Trifonov, A. V., Zakharov, and E. V., Pronyaev "Adaptive Detection of a Stochastic Signal under Parametric a priori Uncertainty", Voronezh, VSU, pp. 246, 1991.[in Russian]

[5] V. V. Rodionov, Yu. T. Karmanov, V. M. Rukavishnikov, "Synthesis of interference which maximally masks a signal" (in Russian), Radiotekhnika i Elektronika, vol. 19, no. 8, pp. 1646, 1974.

[6] V. V. Rodionov, "Game-theoretical approach to the detection of radar signals on a background of unknown noise" (in Russian) Radiotekhnika i Elektronika, vol. 27, no. 9, pp. 1754, 1982.

[7] V. V. Rodionov "Detection of signals from coherent pulsed radars with random variation in parameters of sounding signals from pulse to pulse against background of worst-case Gaussian noise" (in Russian), Radiotekhnika i Elektronika, vol. 29, no. 7, pp. 1339 -1346, Jul. 1984.

[8] V. V. Rodionov, "Effective detection of a radar with a random change of the sounding-signal parameters from pulse to pulse against background of worst-case Gaussian noise" (in Russian), Radiotekhnika i Elektronika, vol. 40, no. 12, pp. 1850, 1995.

[9] V. V. Rodionov. "Optimal Detection of Fluctuating Pulse Burst Against Background of Worst-case Gaussian Noise by Radar with Random Variation of Probing Signal Parameters from pulse to pulse", Radiotekhnika i Elektronika, vol. 43, no. 10, pp. 1207, 1998.

[10] V. V. Rodionov "Potential Immunity of Radar with Random Variation of Probing Signal Parameters against background of electronic countermeasure", Radiotehnika, no. 3, pp. 9, 1999. [in Russian]

[11] J. G. Sosulin "The Theory of Detection and Estimation of Stochastic Signals", Moscow, Sovetskoe Radio, 1978. [in Russian]

Manuscript received January, 25, 2013

Rodionov Vladimir Valentinovich, for photograph and biography, see this issue, p. 98.

УДК 621.37

Радар со случайной вариацией параметров зондирующего сигнала / В.В. Родионов // Прикладная радиоэлектроника: науч.-техн. журнал. – 2013. – Том 12. – № 1. – С. 122–127.

В статье рассмотрено обнаружение гауссовых сигналов на фоне гауссова шума с использованием принципов теории игр. Предложена функция компенсации, обобщающая отношение сигнал-шум на случайные сигналы. Показано, что потенциальная устойчивость радара к стратегиям радиоэлектронного противодействия достижима только при случайном изменении параметров зондирующего сигнала. Потенциальные возможности радара определяются произведением полосы частот и длительности зондирующего сигнала. Время когерентного накопления должно быть в 2–10 раз меньше полного времени обработки принятого сигнала.

Ключевые слова: постановщик помех, радар, теория игр, сигнал.

Ил. 04. Библиогр.: 11 назв.

УДК 621.37

Радар з випадковою зміною параметрів зондувального сигналу / В.В. Родіонов // Прикладна радіоелектроніка: наук.-техн. журнал. – 2013. – Том 12. – № 1. – С. 122-127.

У статті розглянуто виявлення гаусових сигналів на тлі гаусової перешкоди за використання принципів теорії ігор. Запропоновано функцію компенсації, що узагальнює відношення сигнал-шум на випадкові сигнали. Показано, що потенційна опірність радару до стратегій радіоелектронної протидії досяжна тільки за випадкової зміни параметрів зондуючого сигналу. Потенційні можливості радара визначаються добутком смуги частот і тривалості зондуючого сигналу. Термін когерентного накопичення має бути в 2–10 разів менший від повного часу обробки прийнятого сигналу.

Ключові слова: постановник завад, радар, теорія ігор, сигнал.

Іл. 04. Бібліогр.: 11 найм.

UDC 621.37

INTEGRATED AND MAXIMAL SIDELOBE LEVELS OF NOISE SIGNAL

P.L. VYPLAVIN

One of the most important characteristics of a radar signal is sidelobes level. It is known that it is possible to build a noise signal generator with power spectrum shape close to Gaussian. Such signal can provide rather low sidelobe level. On the other hand, it is well known that randomness of noise signals leads to randomness of resulting range profiles which is observed as residual fluctuations of autocorrelation also called as processing noise or noise floor. Increase of signal time-bandwidth product leads to decreasing of such residual fluctuations. Residual fluctuations can be a big drawback of noise signal for some applications and can be neglected in other ones. Current work is dedicated to numerical and experimental investigation of properties of noise signal. Because residual fluctuations are spread over the range profile, we have chosen such parameter as integrated sidelobe ratio of the signal (ISLR) to be used for analysis of the signal performance. We estimated ISLR for modeled noise signal with various parameters. Besides, through analysis of reference channel of existing noise radars we estimated ISLR for real systems.

Keywords: sidelobes, noise signal, residual fluctuations.

1. INTRODUCTION

Main characteristics of radar signal are range resolution and sidelobe ratio. Normally, resolution is specified by width of autocorrelation function of the signal. Resolution describes the minimal distance between targets responses at which they can be detected separately. Sidelobe level is measured as amplitude difference between the main peak and side peaks of the autocorrelation function. In practice low sidelobe level enables detection of weaker targets in the presence of stronger ones. In the case of correlation receiver both resolution and sidelobes level are specified by the frequency spectrum shape of the signal. There are numerous approaches to making signals having low sidelobe levels [1]. One of the possible solutions among them is generation of noise signal having power spectrum shape close to Gaussian [2]. This can be achieved by generation of low frequency noise signal with Gaussian probability distribution and using it for modulation of voltage controlled oscillator. This gives random signal with smooth frequency spectrum having low sidelobes. Besides low sidelobes level such noise waveform gives additional benefits to the radar such as best electromagnetic compatibility, high interference immunity, low probability of interception. On the other hand, noise signals suffer from residual fluctuations in range profiles [2, 3]. Those residual fluctuations are caused by randomness of the signal. They have noise-like structure and depend on the time-bandwidth product of the sounding signal rather than on spectrum shape. Nevertheless, their influence on the resulting performance of the radar is similar to influence of sidelobes: they lead to masking of weak responses by the strong ones. Current work is devoted to numerical and experimental investigation of sidelobes of noise waveform. In order to characterize the sidelobe levels over the range profile we have chosen such parameter as integral sidelobe ratio (ISLR). It is given as ratio between energies of mainlobe and sidelobes. We analyze variation of the ISLR as function of signal base. We start by description of basic principles through numerical simulation and then give some results of experimental investigation. The latter has been done using noise signal taken from channels of Ground-based Noise waveform SAR systems operating in Ka-band and X-band [4, 5]. In the first system noise signal is generated using frequency modulation of VCO by thermal noise. In the second one it is made using generator based upon dynamical chaotization of microwave oscillations. As the result we find parameters of the radar under which ISLR is limited by residual fluctuations and under which it is determined by the autocorrelation function sidelobes.

2. ISLR OF NOISE SIGNAL

ISLR is relation of total energy of the sidelobes to the energy of the mainlobe. Normal sidelobe ratio describes how effective the signal is for detection of two targets with various amplitudes. ISLR describes properties of the signal for conditions when multiple objects are likely to be present in the range profile. We evaluated it as sum of squares of all corresponding discrete values. It must be noted that integration is done for the limited time period which cuts off part of the sidelobes energy. This simplification was used because in most practical applications ranges of observable targets with significant response amplitude are limited by physical factors.

Fig. 1 shows example of modeling of ISLR for noise signal for various numbers of integrated pulses and ISLR for chirp and windowing function. Pulses are assumed to be independent from each other. It can be seen that integration of large numbers of pulses lead to approach of the resulting ISLR to that of the window. Residual fluctuations at lower widths of the window are caused by decrease of the time-bandwidth product of the signals.

3. EXPERIMENTAL INVESTIGATION OF NOSE RADAR ISLR

We estimated ISLR using the described above approach for two radar systems designed in LNDES. An X band coherent pulse radar uses chaotic oscillator for generation of noise signal with bandwidth of

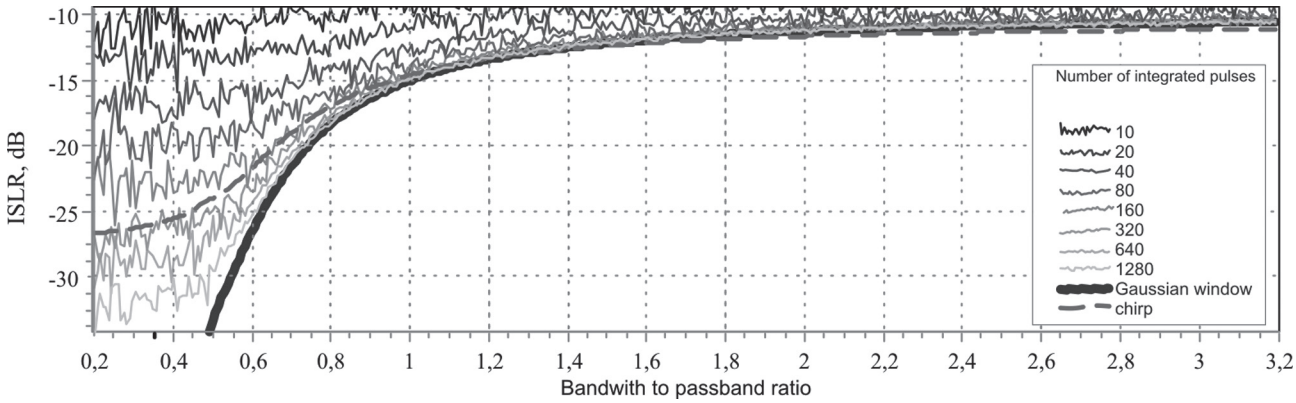

Fig. 1. ISLR for noise signal with various numbers of integrated pulses

250 MHz. This signal is used to form succession of 100 ns pulses filled up with noise. The number of radiated pulses can be varied in order to tune between low residuals and fast acquisition. Part of the transmitted signal is coupled, down-converted and fed to ADC as a reference. We used this reference signal in order to estimate the ISLR. It has to be noted that this approach doesn't take into account the influence of non ideal receiver to the signals. Figure 2 shows example of autocorrelation function estimated over 9400 pulses (time-bandwidth product of the signal is about 235000). It can be seen that the first sidelobe has quite high amplitude (about -12 dB with respect to the maximum). Besides, there is a peak in the autocorrelation at 39 ns which is caused by reflections of the signal in antenna feeding path and not ideal isolation.

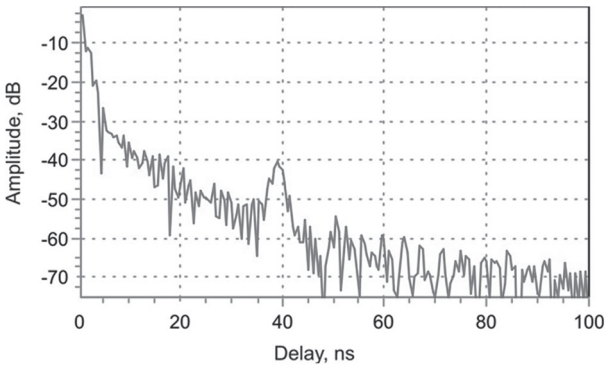

Fig. 2. Autocorrelation of pulsed noise radar signal

Figure 3 shows dependency of the ISLR on the number of integrated pulses. Maximum time-bandwidth product of the signal in the plot (at number of pulses equal to 94) is 2350. ISLR sets at value of -8 dB at 15 integrated pulses and doesn't get lower at higher numbers. This is caused by high level of sidelobes inherent to the radiated signal shape so that noise residuals doesn't make strong impact on the ISLR when integration time exceeds 2 μs.

In a Ka-band noise radar low frequency noise signal is generated using thermal noise, this signal is used for modulation of high frequency VCO oscillations. Parameters of the modulation can be adjusted leading to changes in the frequency spectrum of the signal such as central frequency and bandwidth. The shape of the spectrum is determined by both amplitude distribution of the modulating signal and by high frequency filters of the transmitter. In the case of relatively narrow low amplitude of the modulating signal the spectrum has bell-like shape and low bandwidth, otherwise, the spectrum has complex shape and higher bandwidth. The radar operates in continuous regime. As in the previous case, we used only the reference signal for the estimations.

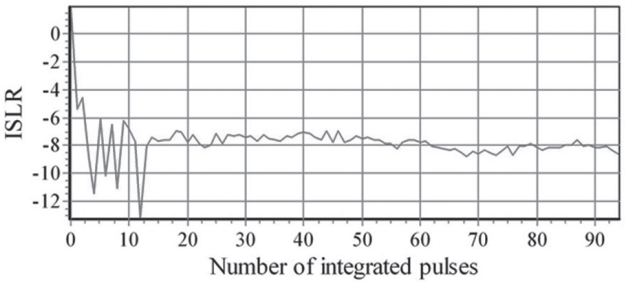

Fig. 3. Dependence of ISLR on the number of integrated pulses

We fixed the integration period for ISLR at 2 μs which corresponds to scene length of 300 m (this value is practical for our radar). The data were divided into chunks each containing 2 μs of sounding signal. Autocorrelation was estimated using each chunk and such estimations were integrated. Fig. 4 shows example of autocorrelation for the case of signal bandwidth 385 MHz and 96 MHz for and integration time 0.1 s (Time-bandwidth product of the signal is about 38500000 and 9600000, respectively). It can be seen that the signal with higher bandwidth has much higher sidelobes. This is explained by the shapes of the spectra shown in fig. 5: signal with narrower band has smoother power spectrum shape and, consequently, has lower sidelobes of correlation function.

Fig. 6 shows dependence of ISLR on the amount of integrated data (or integration time) for various bandwidths of the sounding signal. Corresponding power spectra are shown in figure 5. Linear in logarithmic coordinates part on the plot starting at integration time 10000 ns corresponds to the improving of signal to noise ratio with increase of integration time (at this level ISLR is limited by the random residuals in the response). Above the certain integration time the random residuals are not the limiting factor and the ISLR is determined by the sidelobes of the signal.

This is seen as a horizontal part on the plots at higher integration times. This means that we observe influence of two factors on the ISLR level.

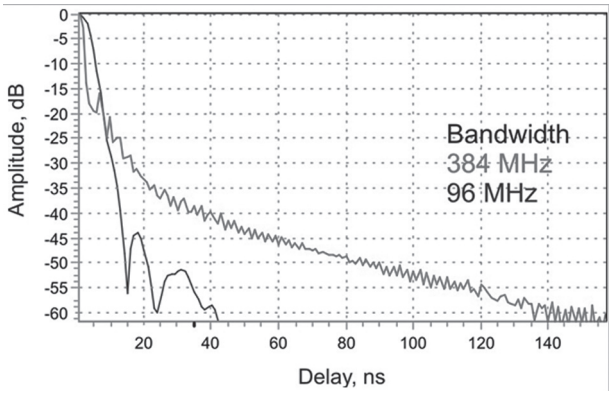

Fig. 4. Autocorrelation of CW noise radar signal

CONCLUSIONS

In the work, we have carried out experimental investigation of integrated sidelobe level of noise signal using example of two noise waveform radars operating in X-band and in Ka-band. It has been shown that in practice both the sidelobes and residual fluctuations can be limiting factor for the ISLR level. Increasing of signal time-bandwidth product enables to decrease influence of the residual fluctuations. Besides, it has been shown that noise waveform generator using noise modulation of voltage controlled oscillator can generate noise with frequency spectrum rather similar to Gaussian shape and as the result having low ISLR. The results can be used for specifying practical regimes of noise radar operation whereas integrated levels of residual fluctuations and sidelobes are of the same order.

References

[1] S.Lawrence Marple, "Digtal Spectral Analysis with Applications", Prentice-Hall Signal, Inc., Englewood Cliffs, New Jersey, 1987, 492 p.

[2] Lukin, K. A., "Noise Radar Technology", Telecommunications and Radio Engineering, 55(12), pp. 8-16 (2001).

[3] Stove A.G. Using noise modulation in practical radar systems: Including a comparison with FMCW modulation / A.G. Stove // Proc. 11th International Radar Symposium (IRS). – Vilnius, Lithuania, 2010. – P.1-4.

[4] K. Lukin. "Ground Based Noise-Waveform-SAR for Monitoring of Chernobyl Sarcophagus", Proceedings of International Radar Symposium, IRS-2005, 06-08 September 2005, Berlin, Germany, pp. 655-659.

[5] D. Tarchi, K. Lukin, J.Fortuny-Guasch, A.Mogila, P.Vyplavin and A. Sieber. "SAR Imaging with Noise Radar", IEEE Transactions on Aerospace and Electronic Systems, 46(3), pp.1214 – 1225 (2010).

Manuscript received January, 30, 2013

Vyplavin Pavel Leonidovich, for photograph and biography, see this issue, p. 94.

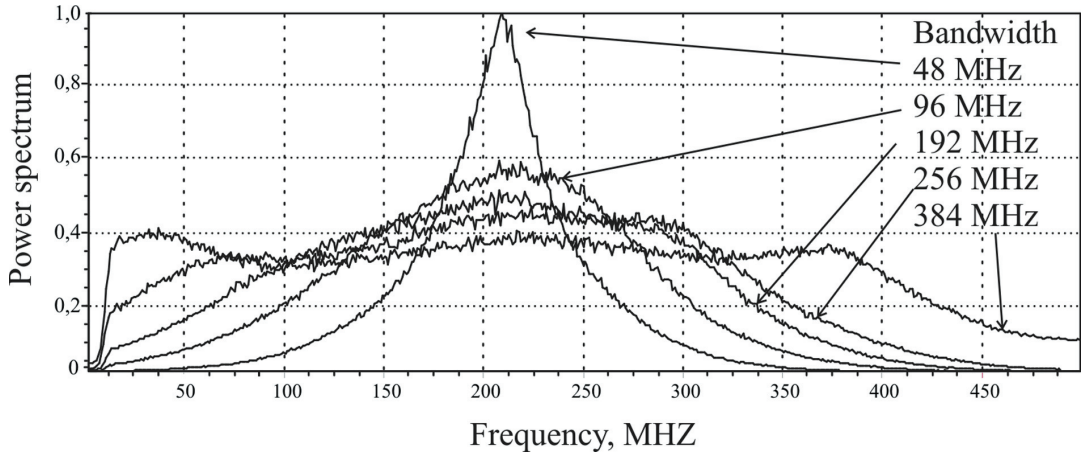

Fig. 5. Frequency spectra of sounding signal of Ka-band noise radar for various bandwidths

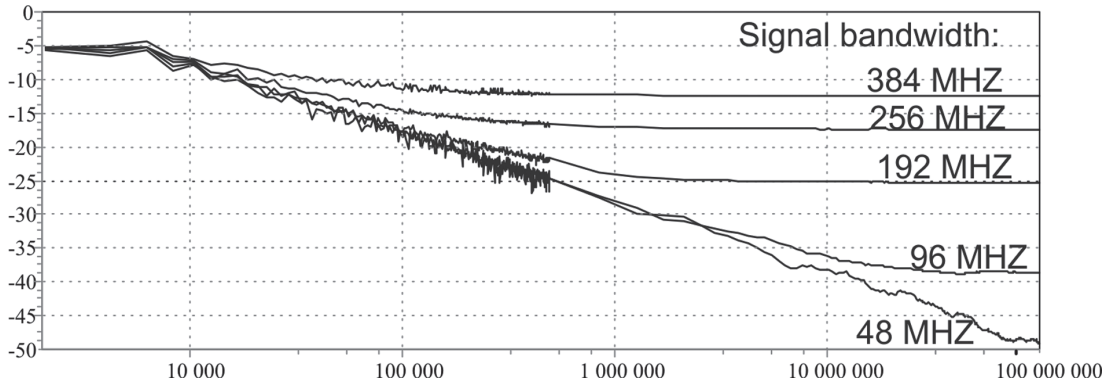

Fig. 6. ISLR sounding signal as a function of integration time for various bandwidths

УДК 621.37

Интегральный и максимальный уровни боковых лепестков шумового сигнала / П.Л. Выплавин // Прикладная радиоэлектроника: науч.-техн. журнал. – 2013. – Том 12. – № 1. – С. 128–131.

Уровень боковых лепестков является одной из наиболее важных характеристик радиолокационных сигналов. Известно, что возможно создание генераторов шума с формой спектра, близкой к гауссовой. Такой сигнал обеспечивает малый уровень боковых лепестков. С другой стороны, известно, что случайная природа шумового сигнала приводит к случайности результирующих профилей дальности, наблюдаемых в виде остаточных флуктуаций автокорреляции, называемых также шумом обработки, или фоновым шумом. Повышение произведения длительности сигнала на ширину полосы приводит к уменьшению таких остаточных флуктуаций. В одних радарах остаточный шум может быть большой проблемой, в других он может быть, наоборот, пренебрежимо мал. Данная работа посвящена численному и экспериментальному исследованию свойств шумового сигнала. Поскольку остаточные флуктуации распределены по профилю дальности, мы использовали такой параметр, как интегральный уровень боковых лепестков (ИУБЛ), для анализа свойств сигнала. Мы оценили ИУБЛ для моделированного шумового сигнала с различными параметрами. Кроме того, посредством анализа опорного сигнала существующих шумовых радаров мы оценили ИУБЛ реальных систем.

Ключевые слова: боковые лепестки, шумовой сигнал, остаточные флуктуации.

Ил. 6. Библиогр.: 5 назв.

УДК 621.37

Інтегральний та максимальний рівні бокових пелюсток шумового сигналу / П.Л. Виплавін // Прикладна радіоелектроніка: наук.-техн. журнал. – 2013. – Том 12. – № 1. – С. 128–131.

Рівень бічних пелюсток є однією з найбільш важливих характеристик радіолокаційних сигналів. Відомо, що можливо створення генераторів шуму з формою спектра, близькою до гаусової. Такий сигнал забезпечує малий рівень бічних пелюсток. З іншого боку, відомо, що випадкова природа шумового сигналу призводить до випадковості результуючих профілів дальності, спостережуваних у вигляді залишкових флуктуацій автокореляції, званих також шумом обробки, або фоновим шумом. Підвищення добутку тривалості сигналу на ширину смуги призводить до зменшення таких залишкових флуктуацій. В одних радарах залишковий шум може бути великою проблемою, в інших він може бути, навпаки, зневажно малий. Дана робота присвячена чисельному та експериментальному дослідженням властивостей шумового сигналу. Оскільки залишкові флуктуації розподілені за профілем дальності, ми використовували такий параметр, як інтегральний рівень бічних пелюсток (ІРБП), для аналізу властивостей сигналу. Ми оцінили ІРБП для модельованого шумового сигналу з різними параметрами. Крім того, за допомогою аналізу опорного сигналу існуючих шумових радарів ми оцінили ІРБП реальних систем.

Ключові слова: бокові пелюстки, шумовий сигнал, залишкові флуктуації.

Іл. 6. Бібліогр.: 5 найм.

UDC 621.37

ON A COMPARISON OF RADAR SYSTEM PERFORMANCE BETWEEN RANDOM AND LINEAR FREQUENCY MODULATION CONSIDERING SIDELOBE SUPPRESSION TECHNIQUES

B. POMPEO, L. PRALON, G. BELTRAO, H. CIOQUETA, B.COSENZA AND J.R. MOREIRA

In order to improve sidelobe suppression, to increase processing gain and range resolution at the receiver filter's output, many techniques based on transmit waveform and receiver's filter design have already been proposed. This paper addresses a comparison on the performance of pulse compression radar systems that apply random frequency modulated transmitted signals, commonly used in noise radars, and linear frequency modulated transmitted signals. For the latter, it will also be analyzed pulse compression's sidelobes reduction techniques, more precisely, it is investigated window functions techniques and mismatched receiver filter design using the Lp- norms minimization techniques. Peak to sidelobe ratio, range resolution, compression gain and signal to noise ratio will be evaluated for all cases by means of mathematical analyses and simulations.

Keywords: noise radar, LFM, sidelobes.

I. INTRODUCTION

Many techniques related to transmit waveform design [3] and receiver filter design [2] emerged in order to increase the detection performance, to improve sidelobe suppression, to increase processing gain and range resolution in pulse compression radar systems. Pulse compression is a signal processing technique widely used in modern radar systems. A pulse compression radar involves the transmission of a long coded (modulated) pulse and the processing of the received echo to obtain a relatively narrow pulse. The increased detection capability of a long-pulse radar system is achieved while retaining the range resolution capability of a narrow- pulse system [1].

Studies to improve radar performance when this technique is employed have been a research subject since it's inception in mid 1950s[2]. However, the pursuit to achieve all the previously reported goals simultaneously is a never-ending challenge, because almost in every proposed scheme a requirement has to be relaxed in order to satisfy another.

A well known waveform generation procedure is based on linear frequency modulation. Transmitted signals of this nature have been more employed than any other coded waveform in radar systems due to it's great popularity, easy generation and it's insensibility to Doppler shifts [1]. Traditionally, matched filtering is then applied in the receiver's signal processing chain when pulse compression technique is employed, maximizing signal to noise ratio, for AWGN, at the filter's output [4]. This technique, however, introduces high levels of sidelobes, which can significantly increase the false alarm rate.

In order to eliminate the previously mentioned drawback, sidelobe suppression techniques can be applied. In the present paper, windowing function along with matched filtering and mismatched filtering are taken into consideration in order to improve the proposed comparison. The former reduces sidelobes to an acceptable level, but do not make use of any optimization algorithm. The latter has gain notoriety in radar society due to recent presented research results. It is a method based on a minimization of Lp norms of the sidelobes seeks to achieve not only low sidelobe levels but also a constant value over all non-zero time shifts [2].

A more widespread approach to solve high levels of sidelobes at pulse compression output relays on waveform design. Nonlinear frequency modulation, phase coded pulses generation, which range from analytical techniques [5] to exhaustive searches and random waveforms are examples of such approach. However, the first two methods mentioned are limited in use and development due to computational complexity and time computing [1,2].

Random waveforms present some advantages when used as transmitted waveform: low probability of interception [10], suppression of range ambiguity and low range sidelobe levels [6]. However, until a few years ago, such transmitted signals could be left aside due to generation complexity. Nowadays, with the advances made in hardware as well as the rise of software defined noise radar concept [7] many works have been published in this area referred to: system modelling [8], waveform generation [9] and optimal detectors design [10].

In the present work, random waveforms are taken into consideration on a comparison between linear frequency modulation waveforms, the latter with and without the usage of the sidelobes suppression techniques previously mentioned. Lukin [11] and Axelson [6] published recent works describing the phase/frequency randomly modulated signal's power spectral density and autocorrelation function for employment as transmitted signal in noise radar systems which will be directly used in the discussion.

This paper is organized in 6 more Sections. In Section II, a brief discussion about radar coherent reception is performed, highlighting the importance of pulse compression. The Section III describes the linear frequency modulated signal's characteristics. Section IV presents two distinct methods widely disseminated in radar systems to reduce pulse compression output's sidelobe level. In Section V, the specific features of Noise Radar coherent reception are taken into consideration and randomly frequency modulated signal's properties are presented when a Gaussian, unit power

and with rectangular power spectral density modulating signal is used. In Section VI, the results of software simulations are showed and finally Section VII presents the conclusion about the results obtained.

II. PULSE COMPRESSION

Pulse compression is a signal processing technique applied in radar systems that enables the transmission of a long pulse, achieving higher energy without jeopardizing range resolution. Furthermore, it is also possible to extract the exact position of the target based on the delay of the returning signal when this method is employed.

Let us consider a radar emitting a time limited signal $s(t)$. Furthermore, we shall assume that a single point scatterer is located at the range r_0. According to this assumption, the received signal, $r(t)$ can be written as $r(t) = A(t)s(t-T_0)+v(t)$ where v(t) is associated to external interferences; $A(t)$ denotes the fading function of the signal; $T_0 = \frac{2r_0}{c}$ is the time spent by the echo signal to return to the radar and c is the vacuum light speed. Usually radar systems perform signal processing digitally using signal's complex envelope. Therefore, the mathematical analysis was performed under this perspective. The delayed reference signal's complex envelope is correlated with the actual target echo's complex envelope. The peak position value of the correlation output indicates the round-trip delay of the electromagnetic wave, resulting in a measure of distance. The output of the coherent receptor that has an equivalent impulse response $\tilde{h}(t), \tilde{y}(t)$, is given by

$$\tilde{y}(t) = \int_0^{T_{\text{int}}} \tilde{r}(\tau)\tilde{h}(t-\tau)d\tau , \quad (1)$$

where T_{ind} denotes the integration time and $\tilde{r}(t)$ denotes the received signal's complex envelope.

Matched filtering has simple implementation and maximizes signal to noise ratio associated to the pulse compression output, increasing the system's probability of detection. Hence it is preferred by most radar designers. Matched filter's impulse response is given by $\tilde{h}(t) = \tilde{s}^*(-t)$, where $\tilde{s}^*(t)$ is the complex conjugate of the transmitted signal's complex envelope. In the next sections it is analyzed the behaviour of two different frequency modulated transmit waveforms when employed in pulse compression systems.

III. LINEAR FREQUENCY MODULATION

Frequency modulated waveforms complex envelope are given by

$$\tilde{s}(t) = \sqrt{2P}\, e^{K_p \int_{-\infty}^{t} a(\alpha)d\alpha} , \quad (2)$$

where P is signal's mean power, K_p is the modulation constant and $a(t)$ is the modulating signal.

When the modulating signal is given by a linear function, the transmitted signal is said to be linear modulated and it's complex envelope is given by

$$\tilde{s}(t) = \sqrt{2P}\, e^{\left[\frac{K_p t^2}{2} - \frac{K_p \tau_s t}{2}\right]} , \quad (3)$$

where ts is the pulse duration.

When matched filtering is applied and when $A(t) = A$, pulse compression's output can be showed to be given by

$$\tilde{y}(t) = 2AP\tau_s sinc\left(\frac{K_p \tau_s \tau}{2}\right) e^{j\left[-\frac{K_p t^2}{2} - \frac{K_p \tau_s t}{2}\right]} e^{j\frac{K_p \tau_s \tau}{2}} . \quad (4)$$

Range resolution of such systems are associated with the 3dB width of the pulse compression's output and the signal to noise ratio associated to the pulse compression output is given by the relation between it's peak instantaneous power and the noise power. For linear frequency modulated waveforms along with matched filtering the range resolution is given by [12]

$$\Delta\tau_{3dB} = \frac{0.9}{B_s} , \quad (5)$$

where B_s is signal's bandwidth. The instantaneous power of the pulse compression's output peak is given by $P(T_0) = \left|\tilde{y}(T_0)\right|^2 = 4A^2P^2\tau_s^2$

It can be observed from (4) that the absolute value of the pulse compression output, when linear frequency modulated signals are employed as transmit waveforms and matched filtering is performed at the receptor chain, has high levels of sidelobes. They are spaced in time by $\tau = \frac{1}{B}$ and the sidelobe with higher intensity is just 13.2 dB below the pulse compression peak [1].

A. Sidelobe Suppression Techniques

Sidelobes can severely deteriorate radar performance since it can induce a false alarm or, if any sidelobe suppression technique is employed it can mask nearby targets. Many methods for sidelobe suppression have been proposed in the scientific community. Next we take into consideration a widespread windowing approach and a mismatched filtering approach.

1) Windowing: Windowing technique consists in multiplying the reference signal for a window function prior to the pulse compression. Some windows function are represented in Table I where the column PSLR stands for peak to side lobe ration achieved and G stands for the peak value gain.

TABLE I

Window functions properties

window	PSLR(dB)	G
Uniform	-13	1.00
Hamming(0.54)	-43	0.54
Gaussian(a=3.0)	-55	0.43
Blackman	-58	0.42
Dolph-Chebyshev(a=4.0)	-80	0.42

In the present work it is used the Hamming(0.54) window [1], which is the most popular in radar systems. It's digital implementation is given by

$$\omega(t) = 0.54 - 0.46\cos\left(\frac{2\pi t}{N-1}\right) , \quad (6)$$

where N stands for the size of the window in samples.

Even though this technique reduces the sidelobe significantly, achieving nearly 40dB of peak to sidelobe ratio, the tradeoffs that it introduce are not always bearable. Pulse compression's output peak power is

reduced, deteriorating the signal to noise ratio associated and the 3dB width is expanded decreasing range resolution.

2) Mismatched Filters: In the present work mismatched filter design was carried out by means of minimization of L_{p}- norms of the sidelobes [2]. The signal to noise ratio associated to the pulse compression's output when any mismatched filter is always lower than the obtained when matched filter is employed and is usually called mismatch loss. Furthermore, the 3dB mainlobe width of the pulse compression output that employ mismatched filtering is slightly wider than for the corresponding matched filter [2]. Filter length is usually higher than transmitted pulse length thus filter coefficients calculation and mismatched filtering operation introduce a level of computational complexity that is not inherent to the corresponding matched filter operation.

IV. RANDOM FREQUENCY MODULATION

Random frequency modulated waveforms are generated from (2) using a modulating signal characterized by stochastic process. In the present work, the modulating signal, is here represented by a Gaussian wide sense random process with unit power and rectangular power spectral density. Hence, the transmitted signal is also represented by a stochastic process and therefore a better way to evaluate performance of this sort of signal is trough the analysis of the expected value of the output of coherent receptor, $\tilde{y}(t)$. When $A(t) = A$, and when the transmitted signal and thermal noise are considered independent processes, it is given as [9]

$$E\left[y(t)\right] = T_{\text{int}} A R_{ss}(t - T_0) \tag{7}$$

where $R_{ss}(t)$ is the autocorrelation function of the transmitted signal and T_{int} is the total integration time. It can be seen that the transmitted signal's autocorrelation function plays an important row in radar systems that use random signals, since the target detection is directly obtained from the maximum of this function.

If $K_p \gg B_a$, the modulation is said to be wideband and approximations lead to an autocorrelation function given by

$$R_{\tilde{s}}(\tau) = 2Pe^{-\left[\frac{K_p^2\tau^2}{2B_a}B_a\right]} = 2Pe^{-\left[\frac{\tau^2}{2\frac{1}{K_p^2}}\right]} \tag{8}$$

The instantaneous power of the pulse compression's output peak is given by

$$P(T_0) = E\left[\left|\tilde{y}(T_0)\right|^2\right] = 4A^2P^2\tau_s^2 .$$

The same as the one obtained when linear frequency modulation is employed along with matched filtering. It can also be showed that the signal to noise ratio associated to the pulse compression's output is the same as the one obtained when linear frequency modulation is employed along with matched filtering.

The $3dB$ width of the pulse compression's output from which it's derived system's range resolution can be showed to be given by

$$\Delta\tau_{3dB} = \frac{0.869}{B_s} \tag{9}$$

It can be noticed from (9) that the range resolution of system's that employ random frequency modulated signals as transmit waveforms is slightly narrower than the one obtained when linear frequency modulated signals are chosen as transmit waveforms.

Since the transmitted signal is here characterized by a wide sense stationary random process, each sample of the pulse compression output will be a random variable. Therefore, even though the expected value of the pulse compression output (7) does not predict sidelobes, Axelsson [6] reported that this sidelobes are related to the variance of each random variable and is given by $T_p B_s N$ where T_p is the pulse duration, B_s is the signal's bandwidth and N is the number of pulses coherently integrated. Thus, the radars designers ought to increase the number of pulses integrated in order to achieve less sidelobe levels.

V. SIMULATION

In this section, a numerical example is presented. Two distinct 2MHz transmitted signal were generated: (i) a linear frequency modulated signal; (ii) a random frequency modulated signal. Pulse compression was performed on both signals. For case (i), matched filter with and without windowing and mismatched filtering were performed. For case (ii) only matched filtering was applied however it was considered two distinct scenarios: only one pulse compression's output and an average of 1000 pulse compression's output.

At first, a comparison of pulse compression's output using linear frequency modulated signal was realized. This simulation is illustrated on Figure 1. It can be seen that windowing technique causes an increase of the 3dB width and a decrease of the peak value. Eventhough PSLR increases, the achieved sidelobe levels are higher than when mismatched filtering is applied. Thus, it was concluded that mismatched filtering has a better performance regarding sidelobe levels when compared to simple matched filtering and matched filtering along with windowing technique.

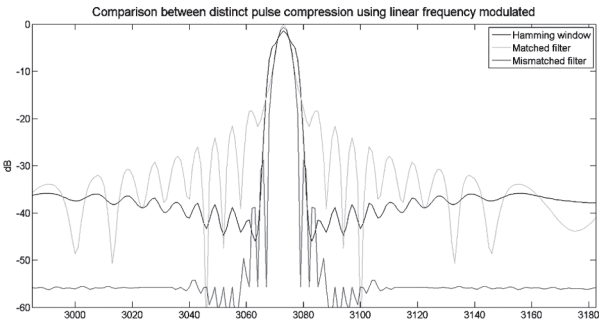

Fig. 1. Comparison between distinct pulse compression using linear frequency modulated

The next simulation consists of a comparison between mismatched and matched filtering when linear frequency modulated are employed and matched filtering when random frequency modulated are employed as transmitted waveforms. Since the transmitted signal is represented by a stochastic process, a better way to evaluate the performance of such signals is trough the analysis of the expected value of the output of the coherent receptor. This affirmative is confirmed

in figure 2, where a single pulse is compressed. Note that the sidelobe level of the pulse compression output is too high, approximately -15dB.

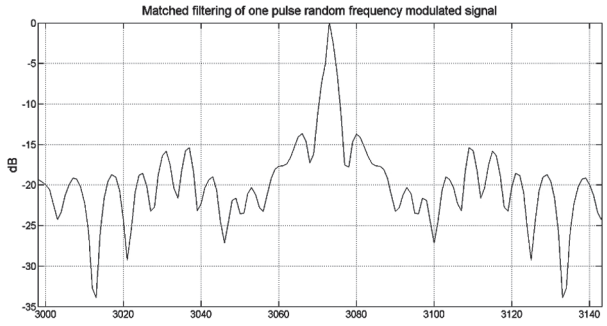

Fig. 2. Pulse compression's output of a single random frequency modulated signal

The comparison between the three different pulse compression methods above mentioned, considering an average of 1000 pulse compression's output for random waveforms, is shown in figure 3 while figure 4 highlights the main lobe and the sidelobes with higher intensity.

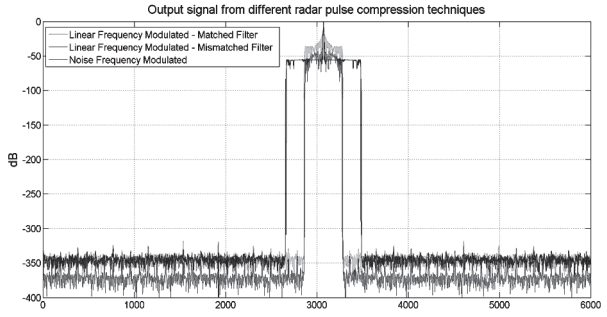

Fig. 3. Power spectral density of transmitted signal

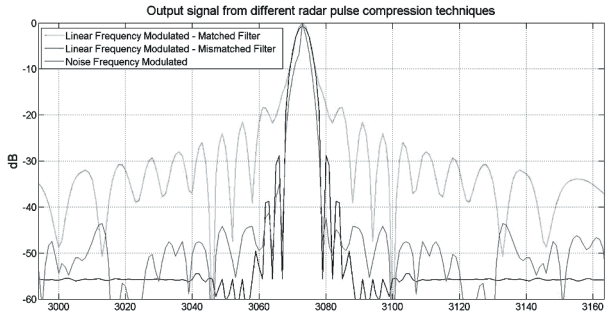

Fig. 4. Power spectral density of transmitted signal

CONCLUSION

In this paper, we have presented a comparison on the performance of radar systems that employ linear frequency modulated and random frequency modulated transmit signals. It was also taken into consideration two distinct techniques of peak-to-side lobe ratio improvement when using linear frequency modulation.

It was taken into consideration a wideband randomly frequency modulated signal, which features a bell shaped autocorrelation function, more specifically a Gaussian distribution shape, very attractive for radar systems. It was shown that aside from the intuitive advantages that arise when random signals are employed as radar transmit waveform, such as low probability of interception, immunity to similar systems interference, intentional or not [10] and suppression of range ambiguity, other performance related advantages of such systems can be highlighted.

Mathematical analysis and simulations results showed that when the application requires low sidelobe levels, random frequency modulation systems have better performance then classical linear frequency modulation systems, despite of any improvement technique applied. It was shown that not only optimal peak signal to side lobe ratio can be achieved through coherent integration, but also signal to noise ratio remains unchanged when compared to classical linear frequency modulation.

Furthermore, for applications that require the higher resolution as possible for a given bandwidth, random frequency modulation should also be employed. It was shown that random frequency modulation matched filter's output is narrower than deterministic linear frequency modulation response to such detectors for a given signal's bandwidth.

The two linear frequency modulation sidelobe suppression techniques analyzed had significant tradeoffs involving side- lobe levels, signal to noise ratio and range resolution, not to mention the considerable increase in signal processing complexity when mismatched filters are applied. Therefore, the performance of radar systems that employ linear frequency modulation along with any of the analyzed sidelobes suppression techniques will never overcome random frequency modulation systems performance, despite of the analysis perspective.

References

[1] Skolnik M., Radar Handbook, Second Edition, McGrawHill, 1990

[2] Cilliers, JE Smit, JC. Pulse Compression Sidelobe Reduction by Minimization of L p-Norms . IEEE Transactions on Aerospace and Electronic Systems, VOL 43, NO.3 July 2007.

[3] Mow, W. H. Best quadriphase codes up to length 24. IEE Electronic Letters, 29, 10 (May 1993), 923-925.

[4] North, D. O. An analysis of the factors which determine signal-noise discrimination in pulsed carrier systems. RCA Laboratory, Report PTR-6C; reprinted in Proceedings of IEEE, 51 (July 1963), 1016—1027.G.

[5] Coxson and J. Russo, "Efficient exhaustive search for binary codes," IEEE Trans. Aerospace and Electronic Systems, vol. 41, no. 1, pp. 302-308, January 2005.

[6] Axelsson, S. R. J. Noise radar using random phase and frequency modulation. IEEE Transactions on Geoscience and Remote Sensing, 42, 11 (Nov. 2004), 2370—2384.

[7] Moreira, J.R., Spilbauer, R., Lukin, K., Lukin, S. "Software Defined Noise Radar on the Basis of FPGA based SPOS board", Synthetic Aperture Radar (APSAR), 2011 3rd International Asia-Pacific Conference on

[8] Narayanan, Ram M., Dawood, M., "Ambiguity Function of an Ultrawideband Random Noise Radar"

[9] K. A. Lukin, V. V. Kulyk, O. V. Zemlyaniy, "Application of dynamical chaos for design of random waveform generators" - First International Workshop on the Noise Radar Technology : int. conf., 18-20 Sept. 2002 : conf. proc. - Yalta, Crimea, Ukraine, 2002. - P. 127-135.

[10] T. Thayaparan, C. Wernik, "Noise Radar Technology Basics" - Defence R and D Canada - ottawa. Technical Memorandum - DRDC ottawa TM 2006-266, December 2006

[11] K. A. Lukin, V. N. Skresanov, O. V. Zemlyaniy, "Frequency modulation technique for generation of millimeter wave noise signals" - First International Workshop on the Noise Radar Technology : int. conf., 18-20 Sept. 2002 : conf. proc. - Yalta, Crimea, Ukraine, 2002. - P. 171-176.

[12] Wang, B, "Digital Signal Processing Techniques and Applications in Radar Image Processing", John Wiley and Sons, Inc., Publication, 2008.

Manuscript received February, 5, 2013

Leandro Pralon graduated from Brazilian Military Institute of Engineering in 2007 receiving his B.S. degree in Electrical Engineering. He received the M.Sc degree in Electrical Engineering from Pontifical Catholic University of Rio de Janeiro. Since 2008 he has been with the Radar Development Group of the Brazilian Army as an active researcher and developer.

Bruno Pompeo graduated from Brazilian Military Institute of Engineering in 2008 receiving his B.S. degree in Electrical Engineering. He received the M.Sc degree in Electrical Engineering from State University of Campinas. Now, he is an undergraduate student in Physics at the Federal University of Rio de Janeiro and since 2009 he has been with the Radar Development Group of the Brazilian Army as an active researcher and developer.

Bruno Cosenza, Electronic Engineer from Polytechnical School at Federal University of Rio de Janeiro (1986), master's at Electric Engineering from Brazilian Military Institute of Engineering (1993) and doctorate at Electric Engineering from Pontifical Catholic University of Rio de Janeiro (2002). Since 2010 project manager of the Radar SABER M200 (a medium range radar).

Gabriel Beltrão received B.S. degrees in Telecommunications Technology and Electrical Engineering from Salvador University (UNIFACS) and University of Campinas (UNICAMP), both in Brazil, in 2007 and 2010, respectively. He received the M.Sc. degree in Electrical Engineering from the Faculty of Electrical and Computer Engineering, at the University of Campinas (UNICAMP), Brazil, in 2012. Since 2010, he works as a Signal Processing Engineer with the Radar Division, at Orbisat Industria e Aerolevantamento S/A. He is also a researcher in the Visual Communications Laboratory at the University of Campinas (UNICAMP).

Higor Cioqueta received B.S. degrees in Electronic Engineering from Minas Gerais Federal University (Brazil) and Technische Universitaet Berlin (Germany) in 2004. He received the M.Sc. degree in Electronic Engineering at the Technological Institute of Aeronautics, Brazil, in 2006. Since 2005, he has been working as a Signal Processing Engineer in projects related to weather radars, surveillance radars, and air traffic control systems at Atech S/A and Orbisat S/A, both in Brazil.

Joao Roberto Moreira Neto, for photograph and biography, see this issue, p. 93.

УДК 621.37

Сравнение характеристик радарной системы при использовании шумовых сигналов и сигналов с линейной частотной модуляцией с точки зрения подавления боковых лепестков / Б. Помпео, Л. Пралон, Г. Белтрао, Х. Чикуета, Б. Косенза, Дж. Морейра // Прикладная радиоэлектроника: науч.-техн. журнал. – 2013. – Том 12. – № 1. – С. 132–136.

Существует много методов улучшения подавления боковых лепестков, увеличения коэффициента усиления обработки и повышения разрешения по дальности на выходе фильтра приемника. Эти методы основаны на выборе формы зондирующего сигнала или характеристик приемного фильтра. В данной работе представлено сравнение производительности радиолокационных систем со сжатием импульсов, со случайной частотной модуляцией передаваемых сигналов, используемой в шумовых радарах, и с линейной частотной модуляцией сигналов. В отношении последнего проведен анализ методов уменьшения боковых лепестков сжатых по дальности импульсов, а именно, исследованы оконные функции и неоптимальные фильтры, использующие минимизацию Lp-норм. Путем моделирования оценены уровень боковых лепестков, разрешение по дальности, коэффициент усиления обработки и отношение сигнал-шум.

Ключевые слова: шумовой радар, ЛЧМ сигнал, боковые лепестки.

Табл. 1. Ил.4. Библиогр.: 12 назв.

УДК 621.37

Порівняння характеристик радарної системи при використанні шумових сигналів і сигналів з лінійною частотною модуляцією з точки зору заглушення бічних пелюсток / Б. Помпео, Л. Пралон, Г. Белтрао, Х. Чикуета, Б. Косенза, Дж. Морейра // Прикладна радіоелектроніка: наук.-техн. журнал. – 2013. – Том 12. – № 1. – С. 132-136.

Існує багато методів поліпшення заглушення бічних пелюсток, збільшення коефіцієнта посилення обробки та підвищення роздільної здатності за дальністю на виході фільтра приймача. Ці методи засновані на виборі форми зондуючого сигналу або характеристик приймального фільтра. В даній роботі представлено порівняння продуктивності радіолокаційних систем зі стискуванням імпульсів, з випадковою частотною модуляцією переданих сигналів, використовуваної в шумових радарах і з лінійною частотною модуляцією сигналів. Щодо останнього проведено аналіз методів зменшення бічних пелюсток стислих за дальністю імпульсів, а саме, досліджені віконні функції і неоптимальні фільтри, що використовують мінімізацію Lp-норм. Шляхом моделювання оцінені рівень бічних пелюсток, роздільна здатність за дальністю, коефіцієнт посилення обробки і відношення сигнал-шум.

Ключові слова: шумовий радар, ЛЧМ сигнал, бічні пелюстки.

Табл. 1. Іл. 4. Бібліогр.: 12 найм.

UDC 621.396.96

CLUTTER COMPENSATION PROBLEM IN THE LPI RADAR

S.Y. SEDYSHEV, S.A. GORSHKOV, AND M.N. VORONTSOV

Noise probing signals and noise radar technology is one of perspective directions in the radar systems theory and techniques. Detection of moving targets in background clutter environment by noise radar is discussed in this paper. Some questions of pseudorandom quasi-continuous signals processing in surveillance radar are also considered.

Keywords: LPI Radar, clutter, noise-like signals, autocorrelation function, cross-correlation function, «range-rate» matrix.

1. INTRODUCTION

Lowing of radar signal interception probability is an important way to improve the noise interference immunity and survivability of radars. Radars with the low level of the signals interception probability are called as Low Probability of Intercept Radar (LPI Radar) [1], [2], [3], [9], [12], [15]. Usually the time-frequency structure of radar signals is to be rather close to that of the noise waveform to provide improvement of radar LPI performance [5], [8], [9], [15].

Digitally generated random signals are to be called as noise-like signals (NLS). The term «noise-like signals» is due to their random properties, but actually these signals are generated with the help of mathematical algorithms. Noise-like signals are also called as pseudo-random signals (PRS) or pseudo-noise ones.

Number of theoretical and practical problems of the LPI radar has been solved [1], [2], [3], [5]. At present the following issues have been studied:

Formation rules for coherent sequences of pseudo-random signals [5], [8], [9], [12], [15];

Generation methods for high power probing pseudo-noise signals;

Pseudo-random signals compression principles.

Use of the sophisticated probing signals (PS) in radar made it possible to resolve the conflict between radar resolution and radar operation range, improve their immunity, and reduce the radiation peak power of the transmitters. Application of the pseudo-random sequences for complex noise-like signals formation allowed increasing of radar electromagnetic compatibility, improving the efficiency of the radio spectrum use by the code separation of PS.

There is one more important issue in the active LPI radar design to be studied in more details: the moving targets detection on the background clutter. Random modulation law (ML) of the NLS has a different structure of compressed pulse sidelobes at different pulse repetition periods. In this case the clutter correlation rate may decrease from period to period and, as a result, the quality of clutter suppression may reduce.

Mathematical modeling results of pseudorandom signals and device for their processing in surveillance radar at the presence of passive interferences are presented in the paper.

2. APPLICATION OF QUASI-CONTINUOUS SIGNALS IN LPI SURVEILLANCE RADAR LIGHTING

Improving of the quality of the passive interferences suppression can be achieved by increasing the pulse repetition frequency (PRF) of the radar. Furthermore, coherent integration (CI) of the reflected signals (RS) will reduce probability of the radar radiation interception [5]. Use of the quasi-coherent sequences NLS with ML change from pulse to pulse (Fig. 1) allows to save the unambiguous range r_{unq} with simultaneous expanding of the unambiguous determination range of radial velocity V_{runq} [13], [14].

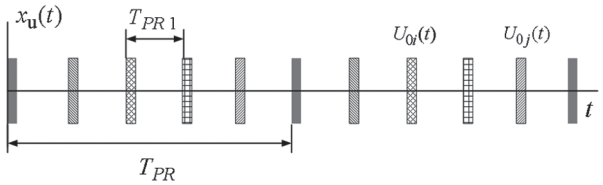

Fig. 1. Real component of the infinite coherent sequence of five mutually orthogonal signal

According to Fig.1 infinite coherent sequence of composite ML $U_0(t)$

$$U(t) = \sum_{k=-\infty}^{+\infty} U_0(t - kT_{PR}), \quad (1)$$

contains N repetitive mutually orthogonal signals

$$U_0(t) = \sum_{j=0}^{N-1} U_{0j}(t - kT_{PR1}), \quad (2)$$

$$\int_{-\infty}^{+\infty} U_{0i}(t)U_{0j}^*(t)dt = 0 \quad \forall i \neq j \quad i,j = \overline{0,N-1}. \quad (3)$$

The unique range for the probe sequence (1) with (2) and (3) is defined by the pulse repetition period T_{PR}:

$$r_{unq} = 0.5cT_{PR}, \quad (4)$$

and unique radial velocity range is defined by the repetition period T_{PR1}:

$$V_{r_{unq}} = \pm\lambda / 4T_{PR1}, \quad (5)$$

where c is a light velocity, λ is a wavelength.

The ambiguity function of signal (1) is shown in the Fig. 2, b in comparison with the ambiguity function of the conventional PS sequence (without mutual orthogonality) (Fig. 2, a).

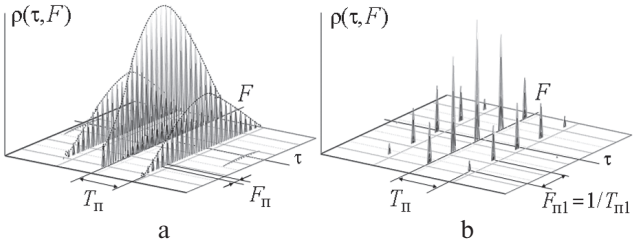

Fig. 2. Ambiguity function: a – conventional PS sequence; b – sequences of three PS consisting of five mutually orthogonal LNS

3. SIGNAL PROCESSING WITHIN THE PERIOD IN CASE OF COMPOUND MODULATION LAW

The impulse response of the matched filter (MF) is described by the mirror image of the complex-conjugate PS ML $U_0(t)$ [10], [11]. For the compound ML (2)

$$v_0(t) = U_0^*(t_0 - t) = \sum_{j=0}^{N-1} U_{0j}^*(t_0 - t - kT_{n1}), \qquad (6)$$

where t_0 is minimum delay value that is to be taken from the condition of the filter implementation assumption [9].

Digital implementation of the device (6) for processing within the period of the compound modulation law (PPML) will be considered further. The structural scheme of this device with the buffer random access memory (RAM) for the case $N = 5$ is shown in the Fig. 3.

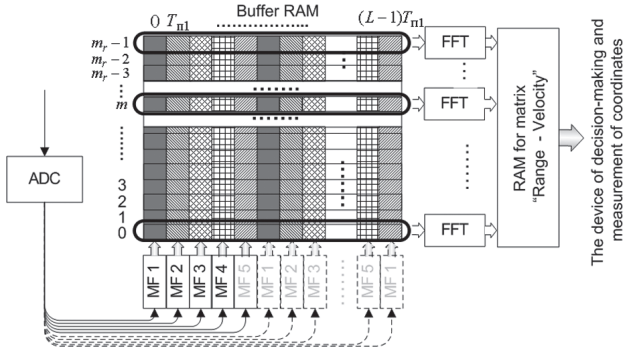

Fig. 3. Processing device of the compound ML

In figure (3) L is the number of coherently accumulated complex samples over a period T_{PR1} in every m radar resolution element for the range; m_r is the number of the range radar elements,

$$m_r = r_{unq} / \Delta r, \qquad (7)$$

where Δr is the radar range resolution of the radar.

4. PULSE-TO-PULSE SIGNAL PROCESSING

Pulse-to-pulse signal processing of the received radar returns consists of the following three stages [10], [11]:

Coherent compensation of the clutter;

Coherent integration of the signals;

Incoherent integration of the reflected signals.

Coherent compensation of the clutter is realized with the help of the following hardware :

Devices of the subtraction through a period (STP) or notch filters with fixed parameters;

Clutter adaptive automatic compensators with the correlation feedback;

Adaptive lattice filters (ALF);

Other ways of the coherent compensation.

STP is used for the coherent compensation of the clutter in this article. Coherent integration of the L complex samples through a period T_{PR1} is realized by the discrete Fourier transform (DFT) application for every m-th column of the buffer memory (Fig. 3). In case of L is defined by the number of power 2, then fast Fourier transform (FFT) may be used instead DFT.

The results of the DFT algorithm are stored in the output 2D memory buffer having $m_r \times L$ elements (RAM of the «Range-Velocity» matrix), which contains the square modules of the coherently integrated signals complex amplitudes in radar range resolution cells. It enables to evaluate the radial velocities of targets detected in these range elements within unambiguous velocity range (5). Examples of the coherent integration parameters have been considered in [5], [13], [14], [16].

Thus, the coherent integration of the matched filtration results in every m-th line of the buffer RAM (Figure 3) allows to organize a radar space surveillance over both range and radial velocity.

5. THE MODELING RESULTS

Mathematical model of the quasi-continuous sequences of five mutually orthogonal cyclically recurring ML based on Gold codes was used as an input signal for processing devices (Fig. 3). Mismatch function and mutual mismatch function of the Gold codes are shown in Fig. 4, 5.

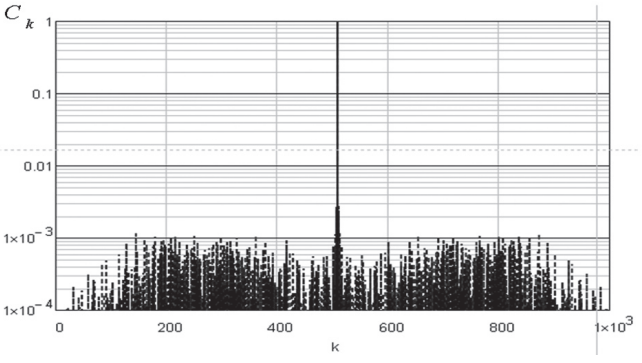

Fig. 4. Autocorrelation function of the Gold code sequences LM

$L = 16$ repetition periods with $T_{PR1} = 200$ μs were used for modeling. The following PS characteristics were used: wavelength is $\lambda = 0.23$ m, discrete value duration is $T_d = 0.15 \cdot 10^{-6}$ s, discrete value amount is $N_d = 255$, sampling step in the model is $\Delta t = T_d / 2$. To reduce amount of computation the processing sample was modeled for 2048 range samples.

Clutter with zero Doppler frequency, ΔF_n =50 Hz spectrum width of the inter period fluctuations and clutter/noise ratio γ_{cl} = 30 dB (or γ_{cl} =37 дБ) held samples for the range with numbers 510-th up to 660-th after MF. Reflected signal with output MF signal/noise ratio γ = 10 dB and Doppler frequency F_D =2.4 kHz (V_r = 280 m/s) was located on 555-th sample for the range.

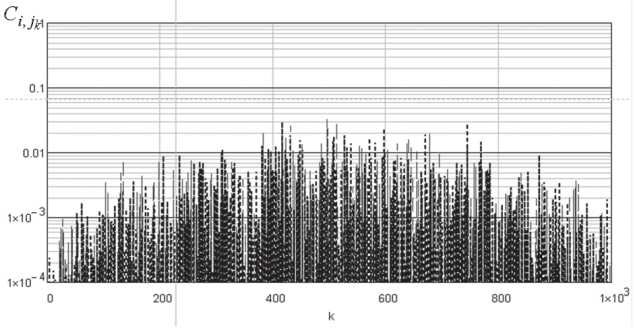

Fig. 5. Cross-correlation function of the Gold code sequences LM

Square modulus of the received signal MF result are shown in Figure 6 in dashed line. Solid line in Fig. 6 shows the output signal square modulus of the MTD device.

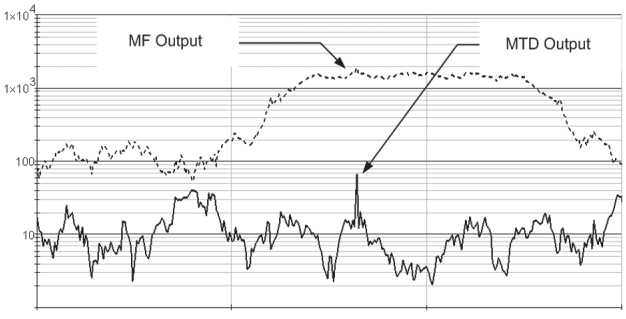

Fig. 6. Output signals of the MF and MTD device

Usual sequence clutter suppression coefficient on the output MTD device is defined as [10]:

$$K_{cl} \approx 0.023(F_{PR1} / \Delta F_{cl})^3 = 2.3\times10^4 \approx 44 \text{ дБ}, \quad (8)$$

where $F_{PR1} = 1 / T_{PR1} = 5000$ Hz.

Coherent sequence of mutually orthogonal probing signals leads to the reduction of the interperiod clutter correlation coefficient. Partial clutter decorrelation is caused by amplitude-phase differences of compressed pulses sidelobes in adjacent repetition periods. It was found in the mathematical modeling process of the clutter coherent compensation for mutually orthogonal PS sequences and different ratios interference/noise, that output clutter suppression coefficient of the STP device can be represented as:

$$K_{cl1} \approx \left(\frac{1}{K_{cl}} + \nu_{sb} \right)^{-1}, \quad (9)$$

where ν_{sb} is the sidelobe average level of mutually orthogonal PS ML mismatch functions.

The sidelobe average level of Gold codes sequences used in the mathematical modeling is –30 dB. The resulting output clutter suppression coefficient of the twice STP device with (8) and (9) is

$$K_{cl1} = (10^{-4} / 2.3 + 10^{-3})^{-1} \approx 960 \approx 30 \text{ дБ}. \quad (10)$$

Thus, the influence of the sidelobe average level of the mutually orthogonal PS ML begins to affect when ratio interference/noise is $\gamma_{cl} > 1 / \nu_{sb}$.

The coherent signal storage results after STP device for different ratio values interference/noise are shown in the Figure, a, b. In both cases the output ratio signal/noise of the MF devise was set = 4 dB.

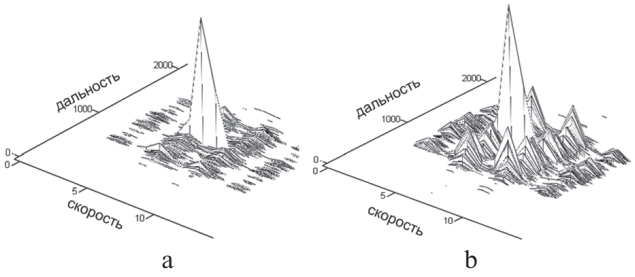

Fig. 7. CA results in the «range-rate» matrix:
a – ratio signal/noise is γ_{cl} =30 dB;
b – ratio signal/noise is γ_{cl} =37 dB

Fig. 7, b shows the growth of clutter compensation balances in «range-velocity» matrix in Figure 7,b compared with the Figure 7. This is due to the fact that the receiver internal noise level is less then sidelobes of the compressed signals.

6. CONCLUSIONS

The modeling results of the processing of the signals sequence reflected from target and clutter in the form of Gold codes sequence with ML change from pulse to pulse in the device shown in Figure 3 confirm the decreasing of the passive interference inter period correlation coefficient because the pseudorandom modulation law varies from period to period. For Gold codes sequence considered in the paper, the clutter suppression coefficient is less than the value inverse to sidelobes average level of the correlation function, i.e. -30 dB level.

Further quality improvement of the clutter coherent compensation can be achieved by:

Increasing number of QPSK signal discrete with simultaneous spectrum expansion at preserving PS duration $T_0 = T_d N_d$. «Blind» range sizes are not increased in this case;

Selecting of the better ways to form mutually orthogonal modulation law based on Frank and , Welch-Costas codes, signals with orthogonal frequency of channels division [3], etc.

References

[1] Pace P.E. Detecting and Classifying Low Probability of Intercept Radar. – Boston-London, Artech House, 2004.

[2] Richard G. Wiley., ELINT The Interception and Analysis of Radar Signals, Canton Street Norwood, MA Artech House, 2006. – 451 p.

[3] Levanon, Nadav. Radar signals / Nadav Levanon, Eli Mozeson. Published by John Wiley & Sons, Inc., Hoboken, New Jersey, 2004. – 411 p.

[4] Lukin K.A. Noise Radar Technology: the Principles and Short Overview.- Applied Radio electronics.- Kharkov: IASARE, 2005, No 1.

[5] Gorshkov S.A., Sedyshev S.Yu., Vorontsov M.N. Analysis of the characteristics of random probing signals to solve the problem of target detection on the background clutter. 3rd International Conference Noise Radar Technology, NRT-2012. Yalta, Ukraine, September 27-29, 2012, p.p. 68-69.

[6] V. Borisov Immunity and other radio systems with spread spectrum signals using pseudorandom adjustment frequency. - M.: Radio and communication, 2000. - 384 p.: Ill.

[7] LE Varakin Communication system with noise-like signals / L. Varakin, Sov. Radio, 1985. - 380 p.

[8] Gantmakher VE, Bystrov, NE, Chebotarev DV. Noise-like signals. Analysis, synthesis, processing - St.: Science and Technology, 2005. - 400: ill.

[9] VA Kotelnikov Signals with minimum and maximum probability of detection / VA Kotelnikov, Technology and Electronics. - 1959. - № 3, pp. 354-358.

[10] Okhrimenko, AE Fundamentals of radar and the radar fight / AE Okhrimenko. M. "DoD Military Press" CH1 1983. - 285 p.

[11] Radio Electronic Systems: Fundamentals of the theory. Handbook. Ed. 2nd, revised. and add. / JD Shearman, Gorshkov S., Lehovitsky DI Malyarenko SA Leshchenko SP, Orlenko VM Moskvitin SV Ed. JD Shirman. Moscow Radio, 2007. - 512s.

[12] Tkachenko VP Complex solution of detection, identification, target recognition, radar jamming protection and survivability of weapons based on the synthesis of noise-like signals / VP Tkachenko, St. Petersburg.: MVAA. 2008. -206

[13] Sedyshev SY, Vorontsov MN Extending the range of unique determination of the radial velocity of the pulse-Doppler radars. Fourth International radio-electronic forum MRF-2011, KHNURE, Kharkov, Ukraine. October 18-21, 2011.

[14] Sedyshev SY Expansion slot unambiguous determination of radial velocity radar survey at a given interval unique range / SY Syedyshev, MN Vorontsov Reports BSUIR. 2012. № 6. Pp. 76-81.

[15] Shearman JD, Orlenko VM Broadband active radartion with the signals of varying degrees completely chaotic / JD Shearman, VM Orlenko, Applied Electronics. Kharkov, Volume 8-2009.-№ 4. Pp. 426-443.Device signal processing unambiguous definition range and radial velocity: pat. 8233 Resp. Belarus, IPC G01S 13/52 / SA Pots.

[16] SJ Sedyshev, MN Vorontsov, the applicant EE "Warbah» № u20110635; appl. 11.08.08, publ. 12.02.15 / / Afitsyyny bulletin. / Nat. tsentr intelektual. ulasnastsi. - 2012. - S. 4.

Manuscript received February, 20, 2013

S. Gorshkov is a Member of the Academy of Sciences of Applied Radio Electronics (Ukraine, Russia and Belarus). PhD, chief of the Department of Radiolocation and Transceivers of the Military Academy of Republic of Belarus, Minsk. His current research involves modeling, detection, measurement and recognition of radar signals, as well as radar data processing.

S. Sedyshev is a Member of the Academy of Sciences of Applied Radio Electronics (Ukraine, Russia and Belarus). PhD, the professor, the senior lecturer of the Department of Radiolocation and Transceivers of the Military Academy of Republic of Belarus, Minsk. His current research involves modeling, detection, measurement and recognition of radar signals, as well as radar data processing.

M. Vorontsov is a master of engineering science. Now the post-graduate student of the Department of Radiolocation and Transceivers of the Military Academy of Republic of Belarus, Minsk. His current research involves modeling, detection, LPI radar data processing.

УДК 621.396.96

Проблема компенсации мешающих отражений в LPI РЛС обзора / С.Ю. Седышев, С.А. Горшков, М.Н. Воронцов // Прикладная радиоэлектроника: науч.-техн. журнал. – 2013. – Том 12. – № 1. – С. 137–140.

Случайный закон модуляции шумоподобных сигналов обладает случайной структурой боковых лепестков сжатого импульса. В этом случае происходит снижение коэффициента межпериодной корреляции пассивных помех, и, как следствие – снижается качество их подавления. В настоящей статье рассматривается возможность обнаружения движущихся целей на фоне пассивных помех. Приводятся результаты математического моделирования квазинепрерывной последовательности из пяти взаимно ортогональных циклически повторяющихся кодов Голда и устройств их обработки на фоне пассивных помех для РЛС обзора.

Ключевые слова: LPI РЛС, шумоподобные сигналы, пассивные помехи, коэффициент подавления, матрица «дальность-скорость».

Ил. 7. Библиогр.: 16 назв.

УДК 621.396.96

Проблема компенсації відбитків, що заважають, у LPI РЛС огляду / С.Ю. Седишев, С.А. Горшков, М.Н. Воронцов / / Прикладна радіоелектроніка: наук.-техн. журнал. – 2013. – Том 12. – № 1. – С. 137-140.

Випадковий закон модуляції шумоподібних сигналів має випадкову структуру бічних пелюсток стисненого імпульсу. У цьому випадку відбувається зниження коефіцієнта міжперіодної кореляції пасивних перешкод, і, як наслідок – знижується якість їх заглушення. У цій статті розглядається можливість виявлення рухомих цілей на фоні пасивних перешкод. Наводяться результати математичного моделювання квазі-неперервних послідовностей з п'яти взаємно ортогональних циклічно повторюваних кодів Голда і пристроїв їх обробки на фоні пасивних перешкод для оглядових РЛС.

Ключові слова: LPI РЛС, шумоподібні сигнали, пасивні перешкоди, коефіцієнт заглушення, матриця «дальність-швидкість».

Іл. 7. Бібліогр.: 16 найм.

NOISE WAVEFORM SAR

UDC 621.37

SAR IMAGING WITH STEPPED FREQUENCY NOISE RADAR

K.A. LUKIN, J.P. KIM, P.L. VYPLAVIN, AND V.P. PALAMARCHUK

In the paper, a radar scheme combining benefits of noise and stepped frequency waveforms is considered. Noise signal provides the best electromagnetic compatibility, LPI performance and interference robustness but design of conventional noise radar requires expensive high speed ADCs. Stepped frequency radar uses narrowband signals for sounding. This enables to use low speed ADCs which can have much higher dynamic range and are much cheaper. But periodicity of the sounding signal leads to range ambiguity and high sensitivity to monochromatic interference. The proposed approach consists in generation of narrowband noise signal with step-like variation of its central frequency. Sounding signal and radar return are fed to mixer and then digitized. The digitized signal is processed like conventional stepped frequency one. This gives range profile, but radar is sensitive to targets only within the correlation range of noise signal. The obtained range profile contains phase information which enables to use it for SAR imaging. In the paper, the proposed approach is experimentally tested using noise radar based upon digital arbitrary waveform generator.

Keywords: SAR, stepped frequency, noise radar.

INTRODUCTION

Ground Based Synthetic Aperture Radar (SAR) are used for microwave coherent imaging of an area of interest and may be applied for detection of small objects, Ground Penetrating Radar, through-the-wall vision and many others. Stepped frequency technique is a common technique for SAR design. Transmission of single frequency signal enables application of ADC with rather slow sampling rate, which may provide rather high dynamic range since they have up to 36 bits of amplitude resolution. However, this technique also has some drawbacks, such as: ambiguity in range measurements; high level of range sidelobes; and low resistance against narrowband coherent interferences. We suggest application of *random* waveforms [1] with synthesized spectrum to go around these drawbacks.

In the paper we realize step-like increase of the central frequency of a narrow band random signal using fast Arbitrary Waveform Generator (AWG) from EUVIS Company. In this approach the target range can be measured within the range limited by correlation function width of the transmitted noise signal. Because of continuity of probing signal spectrum the use of this approach enables eliminating ambiguity in range measurements, which is inherent drawback of conventional stepped frequency radar. Part of the processing is to be done in analog way using a wideband phase detector. The phase detector output should be sampled with a slow multi-bit ADC and transferred to a PC for further processing consisting in performing Fourier transform over whole frequency mesh. This gives a range profile [2]. After that the azimuth compression technique for generation of the SAR image may be applied.

In the paper, the developed stepped frequency noise radar (SFNR) and results of SAR imaging experiments using this approach have been described.

1. LABORATORY TESTS OF UWB AWG-BASED STEPPED FREQUENCY NOISE RADRAR

We elaborated a prototype of the stepped frequency noise radar based upon digital generation of signals in arbitrary waveform generator (AWG). Sounding signal shape is digitally formed in a PC in advance. This signal is uploaded to AWG memory. After uploading it can be used for generation of analog signal with the waveform specified by the digital signal. This device is used in radar scheme shown as block diagram in fig. 1. Output of the AWG is fed to power amplifier unit where it is being filtered and amplified. Part of the sounding signal is coupled to be used as a reference and other part is transmitted through antenna. Radar return signal is received by the same antenna. It goes to a mixer where it is mixed with the reference. Output of the mixer is low pass filtered and sampled with comparatively low sampling rate. AWG enables to generate signal of any shape. In current series of experiments we generated two types of signal: stepped frequency and stepped frequency with narrowband noise modulation. Stepped frequency signal was generated as 500 frequency steps with 1 MHz spacing. Phase changed smoothly between the steps. Signal repetition period was 1 ms. Noise stepped frequency signal was generated as a narrowband random signal with constant bandwidth and varying in steps central frequency. Central frequency varied with the same step as in the case of free of noise stepped frequency regime. At the output of phase detector signal in spectral domain is obtained. Fig. 2. shows example of such signal realization. If stepped frequency signal is used, the output corresponding to each frequency step is supposed to be constant within the step. If noise modulation is present the output has random structure and can be averaged out to certain mean level using low pass filter. Step-like linear variation of frequency in time enables to obtain data in frequency domain, where complex amplitude of product of sounding

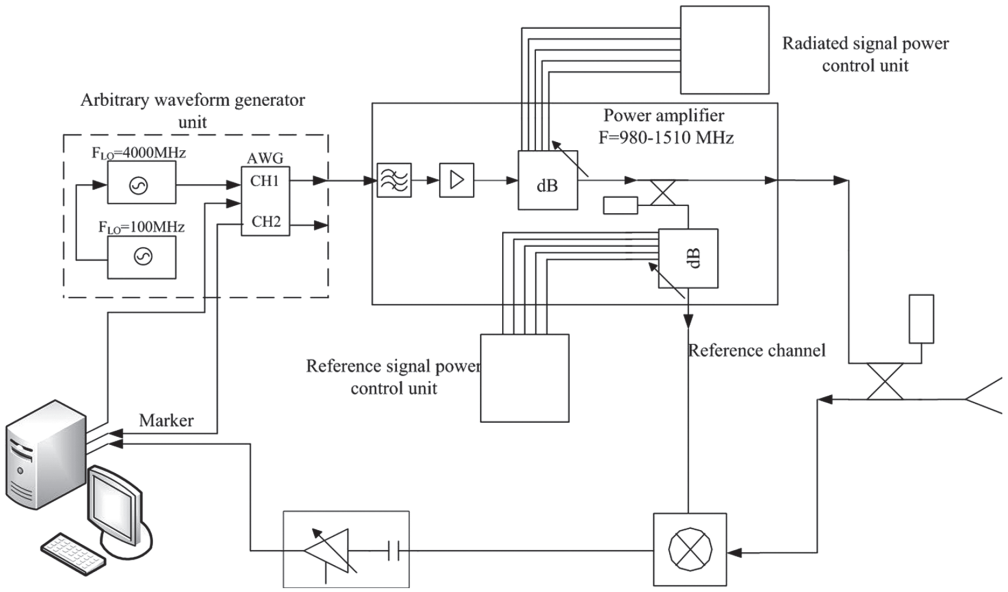

Fig. 1. Block diagram of experimental setup of stepped frequency noise radar

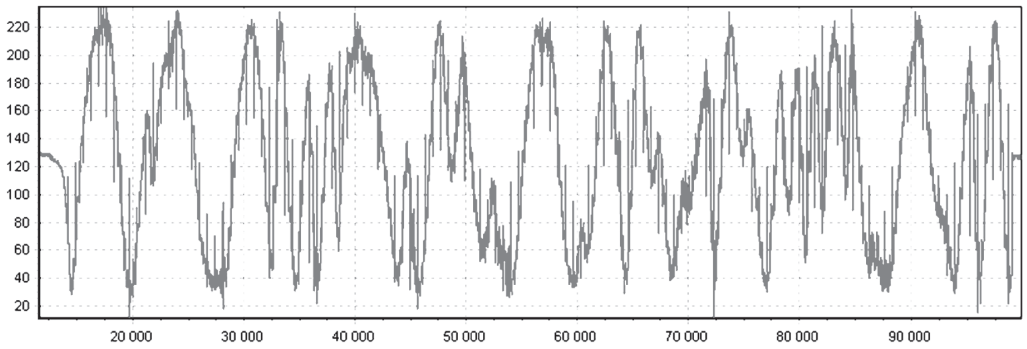

Fig. 2. Realization of signal acquired at the output of stepped frequency noise radar

and reference signals is a function of frequency. Inverse Fourier transform of such signal produces range profile of the scene. We have carried out experiment aimed on generation of range profile of scene containing a spherical target. High RCS sphere covered by aluminum foil was placed in a room in front of Tx-Rx antennas of the SFNR. Obtained in experiment range profile is shown in fig. 3. This range profile has been obtained by performing two scans – with and without target and subtraction of range profiles in order to decrease effects of antenna cross-talk and multiple targets in the room.

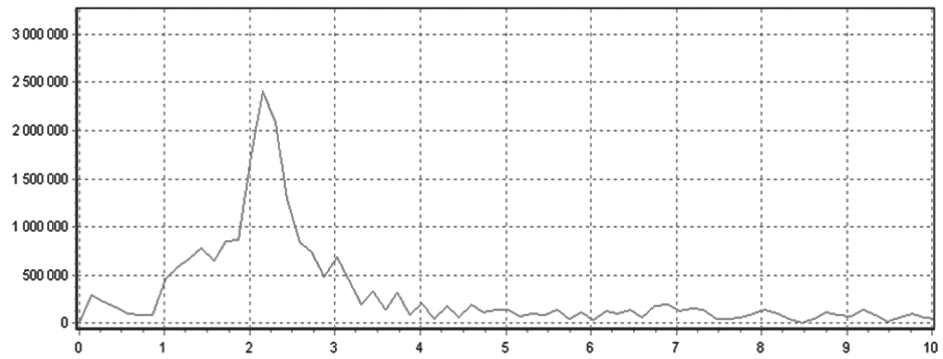

Fig. 3 Range profile obtained by subtraction of one image from another. Target was placed at distance of 2 m from the radar

2. DOPPLER FREQUENCY SHIFT MEASUREMENTS IN UWB SFNR

SAR imaging is based upon phase sensitivity of the radar. In order to confirm ability of the designed radar to generate SAR images we have tested phase sensitivity of the system via Doppler frequency measurement. Experiments were carried our using the AWG – based SFNR. The setup of the experiment was following: the radar was placed in a laboratory room. In front of its Tx/Rx antenna a vibrating target was placed. Sphere covered by aluminum foil was used as a vibrating reflector. Special mechanism was used for its sinusoidal movement. The target had high RCS but amplitude of the vibration was much lower than wavelength of the signal. This lead to low Doppler signal output from such target. Obtained range-Doppler map for the case of distance to target of 3 m is shown in fig. 4.

Next experiment was carried out in the same situation but distance to the vibrating target was 6.5 m. Corresponding range-

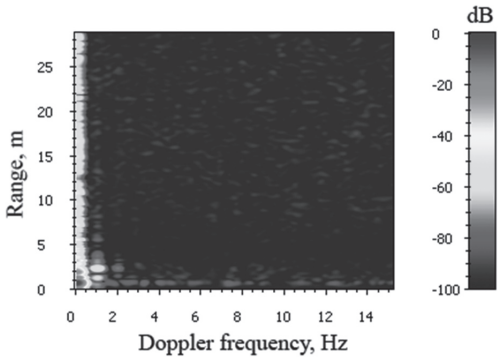

Fig. 4. Range-Doppler map of 1 Hz vibrating target at distance of 3 m obtained using stepped frequency signal with 30 MHz noise modulation

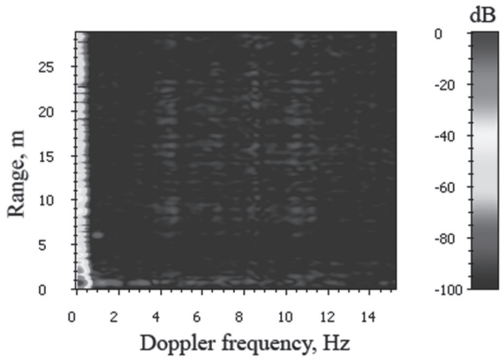

Fig. 5. Range-Doppler map of 1 Hz vibrating target at distance of 6.5 m obtained using stepped frequency signal with 10 MHz noise modulation

Doppler map is shown in fig. 5. When the target is placed at higher distance, influence of noise modulation is much more significant: it can be seen that in the second experiment at bandwidth 10 MHz the response from the target is weak. Increasing of bandwidth to 30 MHz leads to disappearing of the response because of low correlation interval of such noise signal. Thus it is possible to isolate the area of radar sensitivity by choosing proper noise signal bandwidth and adding delay to the reference channel. Combination of such isolation with stepped frequency radar concept enables obtaining range profiles within the observable ranges. Stepped frequency radar concept can be realized with comparatively low speed ADCs. The obtained range-Doppler maps show that the system has good phase sensitivity even if noise modulation with high bandwidth is used.

3. 3D SAR IMAGING WITH UWB SFNR

UWB SNFR radar enables obtaining range profiles using the described above approach. After performing of Fourier transform of the acquired signals one obtains information not only about amplitude, but also about phase of reflected signals. This enables using UWB SNFR with concept of synthetic aperture radar. In order to use this approach one needs to perform operation of UWB SFNR with variable position with respect to the scene. One can achieve this by moving of the antenna or all the radar on special positioning system. All positions of antenna phase center with respect to the scene form synthetic aperture. It can be either one dimensional either two dimensional. In the first case obtaining of 2D images in range-azimuth plane is possible, in the second case one can obtain 3D image with additional cross-range axis resolution.

Principle of SAR operation is based on processing of signal obtained by radar at various positions of transceiver antenna with respect to observed objects. Antenna positions form certain virtual antenna aperture. The range resolution in our case is obtained by processing of stepped frequency data. The range resolution is determined by bandwidth of the signal. Angular resolution is obtained by processing of signals from the antenna positions and depends on length of antenna path rather than dimensions of antenna.

Experiments were carried out in the laboratory room. In order to provide scanning transmitter and receiver antennas were moved mechanically with respect to the scene. Example of SAR image of laboratory room and complex target is shown in fig.6. It can be seen that increasing of noise modulation bandwidth limits the operation range of the radar.

We have considered linear scanning. This approach is valid for two-dimensional apertures as well. In this case scanning is performed in such a way that antenna is moved over a two-dimensional array forming a 2D aperture. As the result of such processing a 3D image can be formed.

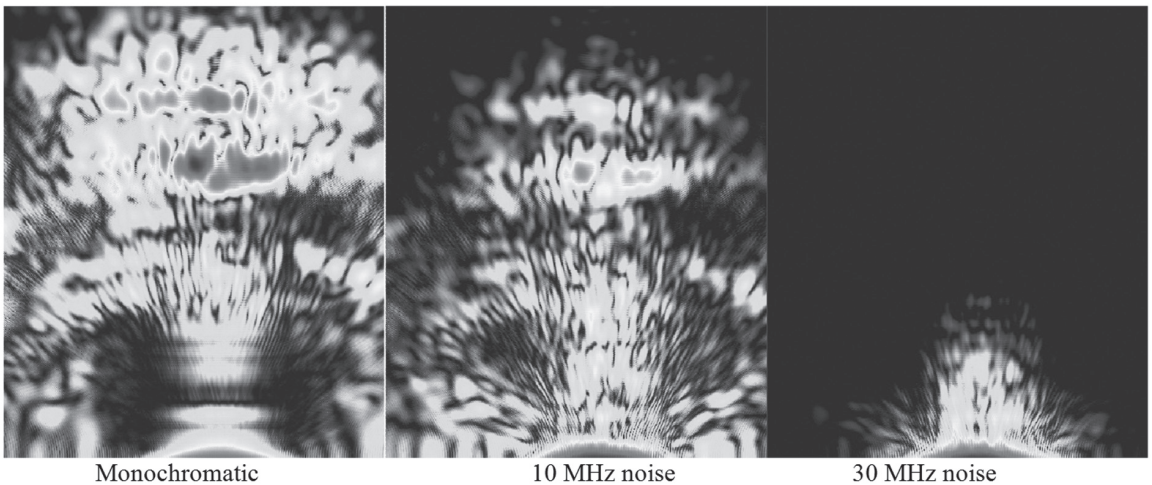

Fig. 6 SAR images obtained with stepped frequency noise radar with three values of noise modulation bandwidth

CONCLUSIONS

In the work, stepped frequency noise radar approach has been tested. This approach combines solutions of stepped frequency radar and noise radar in the following way: noise signal is radiated by the radar in the same way as in noise radar, but its central frequency is varied in stepped-like manner. This approach provides such benefits as low instant bandwidth of the signal, high dynamic range, high electromagnetic compatibility and resistance to interference. Main principles of the approach have been described. Experimental tests have shown that the approach works well for both Doppler processing and SAR imaging and that variation of noise modulation bandwidth enables to choose size of the observable area.

References

[1] Lukin K.A. Noise Radar Technology. Radiophysics and Electronics, Kharkiv, Institute for Radiophysics and Electronics of NASU, 1999, vol.4, #. 3, pp.105-111 (In Russian). Translation is published in Telecommunications and Radio Engineering, V.55, #12, 2001, pp.8-16.

[2] A.A.Mogyla, K.A. Lukin, V.V.Kulyk. Statistical error of measurement made using double spectral analysis method with noise signals. 6th International Conference "Radars, navigation and telecommunications ", 25-27 April 2000, Proc. V.1, pp. 420-428.

Manuscript received December, 12, 2012

Konstantin A. Lukin, for photograph and biography, see this issue, p. 24.

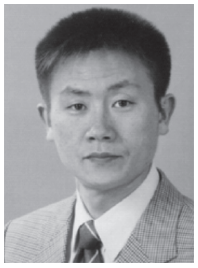

Jeong Phill Kim, professor of Chung-Ang University, Seoul, Korea. Current research interests include the design of antennas, RF and microwave components, on-chip tunable filters RFID systems applications and various communication applications of true random signals.

Vyplavin Pavel Leonidovich, for photograph and biography, see this issue, p. 94.

Palamarchuk Vladimir Petrovich, leading engineer of Laboratory for Nonlinear Dynamics of Electronic Systems of Usikov Institute for Radiophysics and Electronics NAS of Ukraine. The field of scientific interests: radar microwave technology.

УДК 621.37

Формирование РСА изображений с помощью шумового радара со ступенчатой перестройкой центральной частоты / К.А. Лукин, Дж. Ф. Ким, П.Л. Выплавин, В.П. Паламарчук // Прикладная радиоэлектроника: науч.-техн. журнал. – 2013. – Том 12. – № 1. – С. 141–144.

В данной работе рассматривается система, комбинирующая достоинства шумовых сигналов и сигналов со ступенчатым изменением частоты. Шумовые сигналы обеспечивают лучшие характеристики электромагнитной совместимости, низкой вероятности перехвата, устойчивости к шуму. С другой стороны, создание обычных шумовых радаров требует использования дорогих высокоскоростных АЦП. Радары со ступенчатой перестройкой частоты излучают узкополосные сигналы. Это позволяет использовать низкоскоростные АЦП с большим динамическим диапазоном и меньшей ценой. Но периодичность излучаемого сигнала приводит к наличию неопределенности по дальности и высокой чувствительности к монохроматическим помехам. В работе предлагается подход, заключающийся в генерации узкополосных шумовых сигналов со ступенчатой перестройкой центральной частоты. Излучаемый сигнал и радарный отклик подаются на смеситель и оцифровываются. Цифровой сигнал обрабатывается аналогично обычному радару со ступенчатой перестройкой частоты. Это позволяет сформировать профиль дальности, но чувствительность радара ограничена зоной корреляции шумового сигнала. Получаемые профили дальности содержат фазовую информацию, позволяющую использовать их для формирования РСА изображений. В данной работе предлагаемый подход экспериментально исследован с использованием шумового радара, основанного на цифровом генераторе произвольных сигналов.

Ключевые слова: РСА, ступенчатая перестройка частоты, шумовой радар.

Ил. 6. Библиогр.: 2 назв.

УДК 621.37

Формування РСА зображень за допомогою шумового радара із ступінчастою зміною центральної частоти / К.О. Лукін, Дж. Ф. Кім, П.Л. Виплавін, В.П. Паламарчук // Прикладна радіоелектроніка: наук.-техн. журнал. – 2013. – Том 12. – № 1. – С. 141–144.

У роботі розглядається система, що комбінує переваги шумових сигналів і сигналів зі ступінчастою зміною частоти. Шумові сигнали забезпечують кращі характеристики електромагнітної сумісності, низької ймовірності перехоплення, стійкості до шуму. З іншого боку, створення звичайних шумових радарів вимагає використання дорогих високошвидкісних АЦП. Радари зі ступінчастою перебудовою частоти випромінюють вузькосмугові сигнали. Це дозволяє використовувати низькошвидкісні АЦП з великим динамічним діапазоном і меншою ціною. Але періодичність випромінюваного сигналу призводить до наявності невизначеності за дальністю і високої чутливості до монохроматичних перешкод. У роботі пропонується підхід, який являє собою генерацію вузькосмугових шумових сигналів зі ступінчастою перебудовою центральної частоти. Випромінюваний сигнал і радарний відгук подаються на змішувач і оцифровуються. Цифровий сигнал обробляється аналогічно звичайному радару зі ступінчастою перебудовою частоти. Це дозволяє сформувати профіль дальності, але чутливість радара обмежена зоною кореляції шумового сигналу. Одержувані профілі дальності містять фазову інформацію, що дозволяє використовувати їх для формування РСА зображень. У даній роботі пропонований підхід експериментально досліджено з використанням шумового радара, заснованого на цифровому генераторі довільних сигналів.

Ключові слова: РСА, ступінчаста зміна частоти, шумовий радар.

Іл. 6. Бібліогр.: 2 найм.

UDC 621.37

KA-BAND GROUND-BASED NOISE SAR TRIALS IN VARIOUS CONDITIONS

K.A. LUKIN, A. G. STOVE, K. KULPA, D. CALUGI, V.P. PALAMARCHUK, P.L. VYPLAVIN

Interest to noise radars is growing because they provide good electromagnetic compatibility, the best Low Probability of Interception (LPI) and Probability of Exploiting (LPE) characteristics and other desirable features whilst current progress in electronics makes them more and more affordable. One of the noise radar applications is SAR imaging. Correct operation of SAR requires high stability of radar parameters including the parameters of the probing signal. This paper is devoted to experimental investigation of Ka-band ground based noise SAR and estimation of noise level, dynamic range, range resolution, residual fluctuations and sidelobe levels. In the paper, we briefly describe design of the Noise Waveform SAR and present the trials results.

Keywords: noise radar, SAR, interferometry.

I. INTRODUCTION

Currently, noise radars (NR) is gaining more interest from engineers and researchers. Progress in analog and digital electronics enables their design to be simpler and cheaper and, thus, increases NR affordability. Noise signals provide high robustness to interference, good electromagnetic compatibility, low probability of interception (LPI), simple generation of signals with low range sidelobes and having a highly stable frequency spectrum shape. The presence of so called residual fluctuations in range profiles is a well known effect of using noise signals. They appear in the compressed signals as random fluctuations of the cross-correlation function related to the randomness of sounding signal. Their level is dependent on time-bandwidth product of the signal. Proper choice of the integration time and the signal bandwidth enables the negative effects of residual fluctuations to be reduced to a level where they have only a minor effect on the dynamic range of the radar[1-3].

In the Laboratory of Nonlinear Dynamics of Electronic Systems of IRE NASU a Ka-band Ground Based noise waveform Synthetic Aperture Radar (GB NW-SAR) has been designed for imaging of illuminated areas and detection of small structural changes in buildings, constructions or environmental formations using differential SAR interferometry technique [4,5]. The SAR principle in this radar is realized using a novel design of Antennas with Beam Synthesis (ABS) [6-8]. Two such antennas can be used in this system providing operation in bistatic and monostatic regimes. A truly random Ka-band signal with bandwidth up to 480 MHz provides high range resolution of the SAR images. A series of experiments with the aimof testing this SAR system have been carried out against various backgrounds such as: on asphalt and ground areas with low incidence angles and on the water surface of a wide pond.

In the paper, we shortly describe main performance of the Noise Waveform SAR, the trials results, and discuss its future applications.

2. KA-BAND GROUND BASED NOISE WAVEFORM SAR

The GB NW-SAR operates at (36.0 – 36.5) GHz. To obtain good angular resolution and coverage without turning the whole system, scanning is achieved by moving a single slot along the desired antenna aperture and forming the angular resolution by the equivalent of focused synthetic aperture processing [6-8]. Physically, the scanner is a length of waveguide with its broad wall removed and a piece of copper sheet containing the resonant radiating/receiving slot and some matching structures is pulled along its front face. The elevation pattern is formed with a 2D horn structure [6-8]. The GB NW-SAR is shown in fig. 1.

Fig. 1. The Ka-band noise SAR photo

The system can either be used as a short-baseline bistatic system with identical transmit and receive antennas, or monostatically with a small horn transmit antenna directly above the receive antenna which is used to form the narrow synthesized beam [6-8]. This synthetic aperture mode of operation gives the advantage that the SAR imagery provides an indication of the close-to-carrier noise, but it did mean that any movement of a target during the 20 seconds or so which it took to form an image led to its being defocused in azimuth. The farther unit is the receiver; the vertical green waveguide feed to the monostatic transmit transmitter can be seem attached to this unit. The nearer unit is the transmitter. The box with the heat sink is the control unit with the power supply. The copper band with the radiating slot in it can be seen at the near end of the transmitter. It is designed

to fit standard 35mm film sprockets. The unit below the baseplate contains the stepper motor which drives the. The scan is indexed by an optical sensor on the back on the copper tape but the system also uses an absolute-position shaft encoder above which can be seen above the motor unit. The main performance of the system is summarized in Table 1.

Table 1

Main performance of Ka-band Noise Waveform SAR

Operational mode	Bistatic
Waveform	CW Noise
Working frequencies, GHz	36-37
Power Spectrum Bandwidth at -3 dB level, GHz	0.45
Antenna pattern width in elevation, deg	20
Antenna pattern width in azimuth, deg	80
Maximal transmitted power, W	0.15
Nominal Power spectrum shape	"Gaussian" or "Rectangular"
Receiver frequency response width, GHz	0.5 or 1.0
Receiver Noise Figure, dB	< 7
ADC Sampling rate, GSamples/sec	1.0 or 2.0
Synthetic aperture length, m	0.7
Cross-range resolution at 50 m distance, m	0.3
Range resolution, m	0.35
Precision of displacement detection, mm	0.03
Single scan duration, s	≈ 22

3. EXPERIMENTAL INVESTIGATIONS

The trials were planned to concentrate on proving the resolution, dynamic range and stability of the radar. The noise limited sensitivity was estimated based on the return from a corner reflector. Other trial aims were to measure returns from water, which led to the SAR image of the lake being obtained. This trial provided an illustration of the capabilities of the GB NW-SAR and a comparison with some of the more tightly-controlled trials. In all, a comprehensive set of tests were able to be carried out during the week of the trials.

The antenna took up 237 discrete positions during the scan. At each of the antenna positions signals were transmitted, received and recorded at 1GHz rate. Thus, each data set consists of 237 subsets of data. Each data subset consists of 1 940 480 samples, representing just under 1.95ms of data. The data was recorded for every half wavelength of the movement of the real aperture along the line of the synthetic aperture. The first step in the analysis was to correlate the signal with the reference for each data set. For the 'lake' data set the correlation was performed out to 10000 range cells (1500m at 1GHz sample rate) but nothing was seen beyond about 4350 cells (about 650m). Correlation estimation yielded only real data, since both inputs to the correlation were real. Further processing requires analytic signals with complex values. The imaginary part for these signals may be obtained using a Hilbert transform.

Two algorithms were used for obtaining angular resolution. First images were generated using simple FFT-based approach. The successive samples at each range cell were stacked together, zero-filled to 256 points and Fourier transformed to give the angular resolution. This is in fact a beam-forming rather than a SAR process. The data was given a cosine-squared weighting to control the azimuth sidelobes. The angular resolution of the data was 0.24°, determined by the synthetic aperture length. The azimuth cell width was slightly less, 0.22°, determined by the FFT size.

At this stage, the image of the lake was examined, to get a 'feel' of the performance of the radar in a relatively simple scene, i.e. one which was known to have a relatively 'clear' area (the lake itself) at short range. Fig. 2 is a SAR image of the lake, fig. 3 is a 'Google Earth' picture of the area

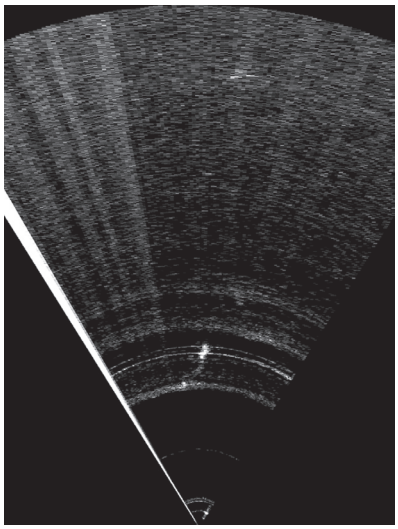

Fig. 2. SAR image of the Lake

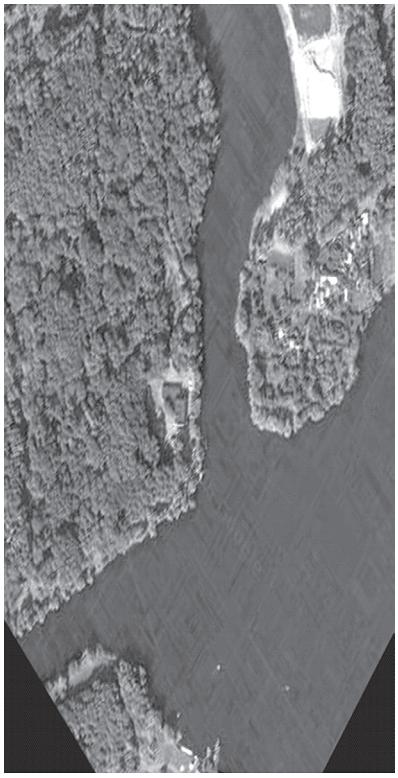

Fig. 3. Satellite image of the Lake

The arcs in the SAR image are caused by failure of the target to focus perfectly in bearing, because part of it has decorrelated (i.e., moved) during the relatively long time taken for the antenna to travel across the synthetic aperture.

The prominent white line at the upper edge of the limit is due to the d.c. offsets in the signal and reference, which, having no bandwidth, produces a return at all ranges, but, being always present, focuses up at broadside (the 'end' of the image around which the SAR image 'folds'). It can be removed by calculating the mean value of each data set and subtracting this value from each element before performing the correlations. Since the mean value of any finite number of normally-distributed random values will not be exactly zero, this process introduces a small bias into the data, equivalent to a high-pass filtering of the data. In practice, the noise bandwidth would not go exactly down to zero, so this is not an issue.

Fig. 4 shows an example of a SAR image of the same area obtained with removal of DC offset and using a straightforward SAR imaging algorithm rather than FFT-based one. This algorithm requires more processing time but takes into account detailed information about movement of the antenna's phase centers and gives results with higher precision. Main features of the scenario are marked in the image. The most distant target is at a range of about 640m, which is believed to have been a record for a noise waveform radar at the time when the trials were done. The brightness is scaled using a range-squared 'sensitivity time control' on the image to avoid the barge dominating the dynamic range and have then increased the contrast to help detection.

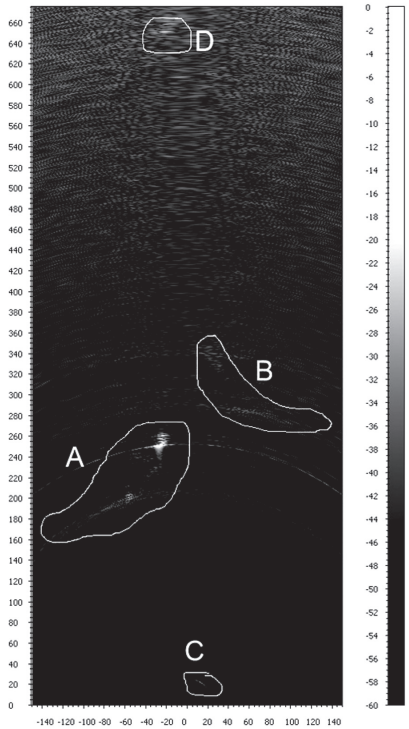

Fig. 4. SAR image of the Lake with main features marked: A) Lake shore and the little building; B) Shore of the island; C) Barge very close to position of radar; D) Obvious distant target

It can be seen that the signal/background on the target in the middle of the SAR image is between 50 dB and 60 dB. The dynamic range against some of the targets at short range exceeds 60 dB. The general level of the azimuth sidelobes is about 40 dB, which is good for a one-way antenna pattern. Another image was also obtained in another direction at the same site, one which contained more targets. This is the scene at the boat club which is shown in fig. 5. Fig. 6 shows its SAR image. SAR images generated from this area enable clear detection of such objects as fence, car (labeled 'auto'), trees, and corner reflectors (labeled 'scatteratori'). Fig. 7 shows SAR image of two corner reflectors spaced by 1 m and placed in the walking path (fig. 5) at the distance of 31 m from the GB NW-SAR.

Fig. 5. Photo of the measurements area

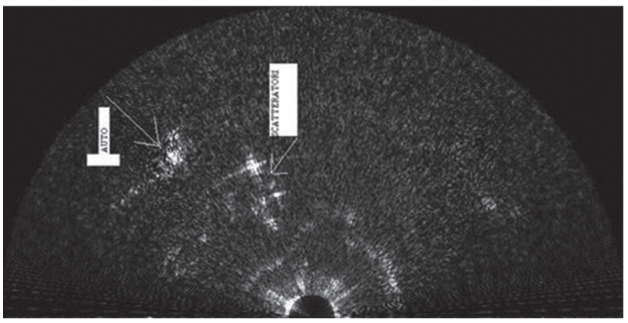

Fig. 6. SAR image generated from the area shown in fig 5

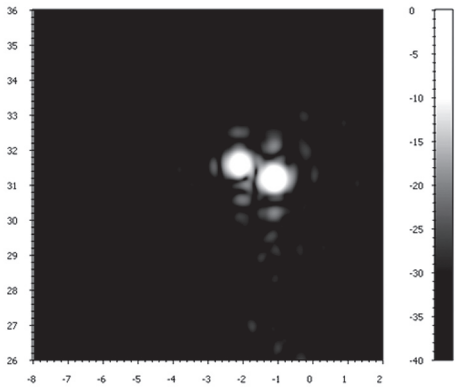

Fig. 7. Zoomed in image of two corner reflectors at area shown in Fig.5. Distance between the reflectors is 1m

This image clearly shows that the radar is capable of achieving its expected resolution of about 50 cm in both down-and cross-range.

3.1. Image of the Asphalted Court

A series of SAR images of an area covered by asphalt were obtained at low grazing angles. Figure 8 shows the scene of measurements and figure 9 shows the SAR image obtained in a straightforward manner and adds labels to indicate some of the features which can be seen in this image. This image extends out to a maximum range of 100m.

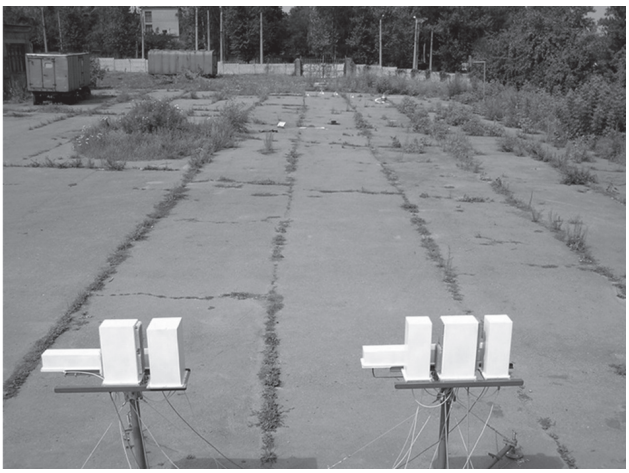

Fig. 8. Asphalted court and GB NW-SAR in bistatic configuration

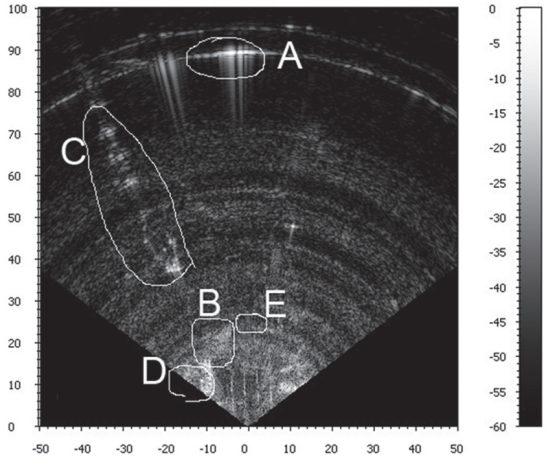

Fig. 9. SAR image of asphalted court with main features of the scene marked: A) gate at the end of the area; B) region of vegetation seen on the left of the photograph; C) building at the edge of the area; D) some vehicles at the left side of the radar; E) the region containing the corner reflectors

A significant feature of this image is that the noise floor is similar to that of the SAR image of the lake, and so is the dynamic range of the image.

3.2. Indoor measurements

In order to characterize operation of the GB-NW SAR on an indoor scenario measurements have been performed during NRT 2012 conference in Yalta Crimea. The experiments were done inside a conference hall with concrete walls and some chairs on the floor. A SAR image was obtained with the best specialist in noise radar sitting on the chairs in front of the noise GB NW SAR. Figure 10 shows photograph of the scene and the obtained SAR image of the room with people and with empty chairs. The measurement was perfectly safe because radiated power was as low as 1 mW. It can be seen that the room, radar community and empty chairs are well resolved and clearly seen in the obtained SAR images. The strongest reflection in the image corresponds to the mirror reflection from the far wall in front of the radar.

Fig. 10. Photograph of the indoor scenario

4. SENSITIVITY

The power budget of the radar at maximum sensitivity when using synthetic-aperture antennas on both transmit and receive was estimated theoretically using the known specifications of the radar system and taking into account the integration time. The integration is performed in the signal processing by performing range compression and synthetic aperture processing.

For the tests in the asphalted court, the signal to noise ratio expected for the largest corner reflector (a tridehral 30cm long on the sides) was 97.5dB. The measured signal to noise ratio was 39dB.

The results for all four corner reflectors are summarized below

Table 2

Expected Sensitivities

Side	Expected SNR	Observed SNR	Discrepancy
30 cm	97.5dB	39dB	58.5dB
15 cm	85.5dB	42dB	43.5dB
		51dB	34.5dB
10 cm	78.4dB	45dB	33.4dB

If we assume that any uncontrolled factors will only reduce the signal to noise ratio, and noting that the latter two rows of the table both show discrepancies of about 34dB, we may conclude that the sensitivity of the radar is about 30dB less than simple theory would suggest.

One cross-check is to use the assumption that the transmit-receive isolation is of the order of -100dB, so the leakage power for 7dBm transmit power would be -92dBm. In contrast, the power returned from the smallest corner reflector would be expected to be -71.5dBm, i.e. about 20dB above the leakage signal. The measured ratio is +25dB. This suggests that the signal levels are as expected, implying that the source of the discrepancy in the signal to noise ratios would be

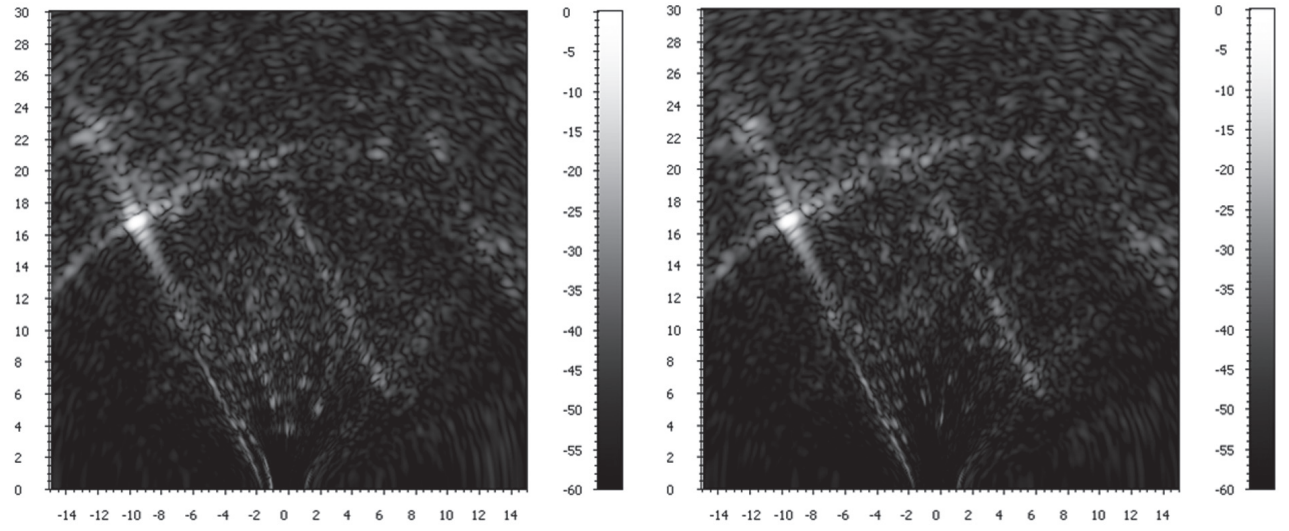

a) b)

Fig. 11. SAR images of scenario shown in fig.10 obtained (a) with people on the chairs and (b) without them

expected to be found in the background noise levels. The most likely explanation of this mismatch is that the measurements at the asphalted court were done during windy conditions and vegetation around the radar was moving during the scanning. This led to losing of coherence of its responses in the SAR image and spreading out in azimuth. This is proven by the noisy arcs visible in the image at the ranges corresponding to the areas with highest vegetation amounts.

The sensitivity may also be limited by the far-out sidelobes of the targets.

5. RANGE AND DOPPLER RESOLUTION

Fig. 12 shows the down-range cut through the return from the largest corner reflector

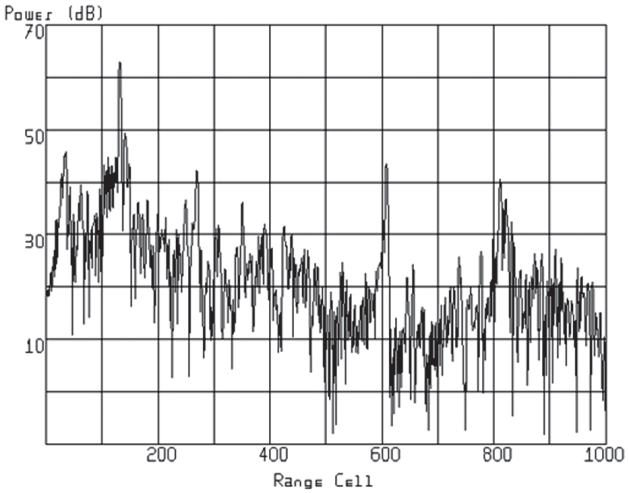

Fig. 12. Range cut through 30cm corner reflector

The corner reflector is at range cell 131. It is clear that other targets at longer range limit the ability to see the noise floor. It can be seen, however, that the dynamic range is at least 60dB and so the far-out sidelobe level must be below -60dB. Fig. 13 shows the cut 'zoomed in' around the target.

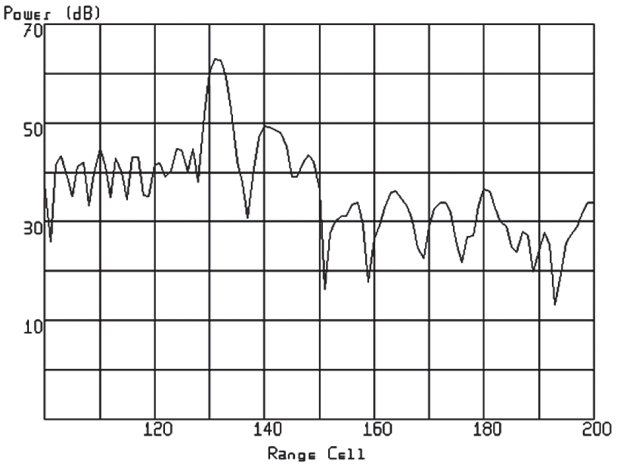

Fig. 13. Range cut near the corner reflector

This shows that the down-range sidelobes are probably at least 30dB below the peak. However, the second peak around cell 140, 13dB below the peak, is probably part of the same return. The difference in range between them is about 1.35m which is compatible with the physical size of the radar equipment, so this return may be due to internal reflections within the radar. The signal in cell 149 may also be due to another internal reflection, but this is more speculative. It might be a separate return, but the range extent of all the targets on the SAR image suggests that it is present on all the targets. The range sidelobes could probably be improved by weighting the spectrum of the received signal. The 3dB width of the signal is about 3 cells (0.45m) which is compatible with the signal bandwidth of about 400MHz. Figure 14 shows the cut of the data from the corner reflector in the bearing domain.

In this image the corner reflector is in cell -100. The dynamic range is limited by instability in the return from the bushes, around cells 50 and 60. Examination of the return from the gate in figure 12, however, suggests that the cross-range dynamic range is also limited to about this level.

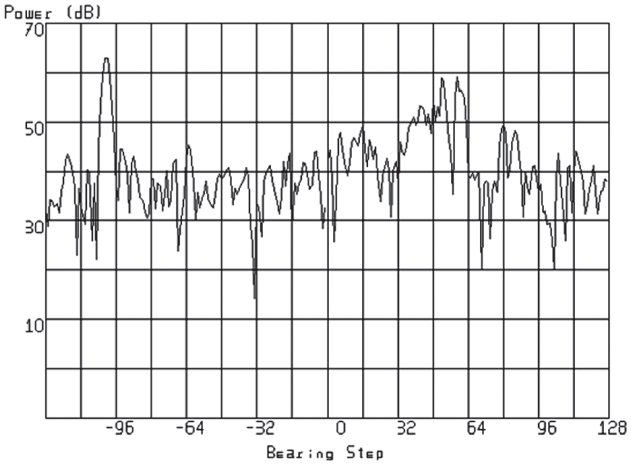

Fig. 14. Cross-range profile of the corner reflector

6. CONCLUSION

The Ka-band GB NW-SAR is capable of producing high resolution imagery, with close-to-ideal resolution and a demonstrated dynamic range of at least 60dB. It is capable of seeing navigational features at ranges out to about 650m. The experiment showed certain mismatch between the theoretical and measured signal-to-noise ratio which may be explained by losing of radar returns coherence due to objects randomly moving during measurement and by the bistatic angles being too high for correct operation of corner reflectors. It is therefore important to investigate signal-to-noise ratio by further experiments, may be to reveal other sources of the above mismatching between theory and the experiments.

The far-out sidelobes in range are at least 60dB below the peak, but in Doppler they are probably only 30dB down. This may happen due to instabilities of the scene and radar during the measurements on windy day. Apart from the features described above, the remaining sidelobe pattern appeared to be roughly elliptical in the range-Doppler.

ACKNOWLEDGEMENT

The authors are very much thankful to LNDES staff for carrying out the trial campaign in Kharkov.

References

[1] K.A.Lukin, "Noise Radar Technology", Radiophysics and Electronics, Kharkiv, Institute for Radiophysics and Electronics NASU, 1999, vol.4, #. 3, pp.105-111. *Translated to English*: Lukin, K.A. *Noise Radar Technology*, Telecommunications and Radio Engineering, V.55(2001), #12, pp.8-

[2] Lukin, K.A. *Noise Radar Technology: the Principles and Short Overview,* Applied Radio Electronics, V.4, #1, pp. 4-13, (2005).

[3] A.A. Mogyla, K.A.Lukin, Y.A.Shiyan, "Ambiguity Function of Noise Pulses Train and its Distortions in Noise Radar Receiver", Proc. of IRS 2004, International Radar Symposium, 19-21 May 2004, Warszawa, Poland, 2004, pp. 37 – 42.

[4] Lukin, K. A., Mogyla, A. A., Palamarchuk, V. P., Vyplavin, P. L. Zemlyaniy, O. V., Shiyan, Y. A. and Zaets, M., 'Ka-band Bistatic Ground-Based Noise Waveform SAR for Short-Range Applications,' IET Proc. Radar Sonar & Navig., **2**, pp 233-243, August 2008.

[5] D. Tarchi, K.Lukin, J.Fortuny-Guasch, A. Mogyla, P.Vyplavin, A. Sieber, SAR imaging with noise radar, IEEE Transactions on Aerospace and Electronic Systems, vol. 46, no.3, July 2010.

[6] K.A. Lukin, "A Novel Approach to Scanning Antenna Design", Proceedings 4th Int. Conf. on Antenna Theory and Techniques, Sevastopol, Vol. 11, pp. 290-293, 2003.

[7] K.A. Lukin, "Sliding Antennas for Noise Waveform SAR" // Applied Radio Electronics, 2005, Vol. 4, No. 1, pp. 103-106.

[8] K.A. Lukin, "Scanning Antennae with Beam Synthesis." // Radioelectronics. 2010,vol.53, No. 4, pp. 58-64.

Manuscript received December, 12, 2012

Konstantin A. Lukin, for photograph and biography, see this issue, p. 24.

Andy Stove, for photograph and biography, see this issue, p. 121.

Krzysztof S. Kulpa (M'1991, SM'2010), Ph.D in electronics. Since 1990 he is Associate Professor at Institute of Electronic Systems (WUT). He is now the head of Digital Signal Processing Laboratory, and head of Radar Technology Research Group at WUT. Since 2011 he is the Scientific Director of Defense and Security Research Center of Warsaw University of Technology. His research interests involve radar signal and data processing including detection, tracking, PCL, SAR, ISAR and noise radars. He is a senior member of IEEE and a member of EUMA and AOC. He is the vice-chairman of the joint Polish chapter IEEE AESS/AP/MTT.

David Calugi Since 1986 works at Radar Department of Selex – ES (Ex SMA) – Florence, Italy. He participated in development the first Italian radar for air combat airplanes. Scientific interests are in avionic radars, noise radars, SAR imaging, tracking algorithms as TWS systems, applied Polarimetric radar to detection and classification of target. He is a member of IEEE and AI AA.

Palamarchuk Vladimir Petrovich, for photograph and biography, see this issue, p. 144.

Vyplavin Pavel Leonidovich, for photograph and biography, see this issue, p. 94.

УДК 621.37

Испытания наземного шумового РСА 8-мм диапазона в различных условиях / К.А. Лукин, А.Г. Стоув, К. Кульпа, Д. Калуджи, В.П. Паламарчук, П.Л. Выплавин // Прикладная радиоэлектроника: науч.-техн. журнал. – 2013. Том 12. № 1. – С. 145–151.

Интерес к шумовым радарам растет, поскольку они обеспечивают наилучшую электромагнитную совместимость, малую вероятность перехвата и использования сигналов и другие положительные свойства, в то время как прогресс в электронике делает их все более доступными. Одной из сфер применения шумовых сигналов являются радары с синтезированной апертурой (РСА). Для правильной работы РСА требуется высокая стабильность параметров радара, включая параметры зондирующего сигнала. Данная работа посвящена экспериментальному исследованию 8-мм наземного шумового РСА и оценке уровня шума, динамического диапазона, разрешения по дальности, остаточных флуктуаций и боковых лепестков. В работе мы кратко описываем устройство шумового наземного РСА и представляем результаты измерений.

Ключевые слова: шумовой радар, РСА, интерферометрия

Ил.14. Библиогр.: 8 назв.

УДК 621.37

Випробовування наземного шумового РСА 8-мм діапазону у різних умовах / К.О. Лукін, А.Г. Стоув, К. Кульпа, Д. Калуджі, В.П. Паламарчук, П.Л. Виплавін // Прикладна радіоелектроніка: наук.-техн. журнал. – 2013. Том 12. № 1. – С. 145–151.

Інтерес до шумових радарам росте, оскільки вони забезпечують найкращу електромагнітну сумісність, малу ймовірність перехоплення і використання сигналів та інші позитивні властивості, в той час як прогрес в електроніці робить їх все більш доступними. Однією зі областей застосування шумових сигналів є радари з синтезованою апертурою (РСА). Для правильної роботи РСА потрібна висока стабільність параметрів радара, включаючи параметри сигналу. Дана робота присвячена експериментальному дослідженню 8-мм наземного шумового РСА та оцінці рівня шуму, динамічного діапазону, розрізнення по дальності, залишкових флуктуацій і бічних пелюсток. У роботі ми коротко описуємо пристрій шумового наземного РСА і представляємо результати вимірювань.

Ключові слова: шумовий радар, РСА, інтерферометрія.

Іл. 14. Бібліогр.: 8 найм.

UDC 621.396.962.25

TOMOGRAPHIC IMAGING USING NOISE RADAR AND 2D APERTURE SYNTHESIS

K.A. LUKIN, P.L. VYPLAVIN, V.V. KUDRIASHOV, V.P. PALAMARCHUK, O.V. ZEMLYANIY, S.K. LUKIN JONG-MIN LEE, JONG-SOO HA, SUN-GU SUN, YOUN-SIK KANG, KYU-GONG CHO, BYUNG-LAE CHO

Implementation of 2D aperture synthesis enables obtaining of 2D angular resolution which in combination with range resolution gives tomographic 3D images. Tomographic 3D radar images can give detailed and precise information about spatial distribution of semitransparent objects or other area of interest. Radar tomography may be realized with the help of any type of high resolution radar; however this paper is focused on *noise radar tomography*. We describe simulation of wideband noise radar operation combined with 2D aperture synthesis and present some results of tomographic SAR imaging experiments using continuous noise waveform and 2D aperture synthesis carried out in S-band.

Keywords: noise waveform, radar tomography, 3D SAR imaging, noise waveform SAR, antenna with beam synthesis.

INTRODUCTION

There are many applications of radar imaging and radar tomography. For instance, such systems can be used for intrusion detection, concealed weapons detection, monitoring of bridges, buildings, towers, etc. 3D microwave or millimeter wave imaging of partially transparent objects may be realized via generation of a series of 2D images as cross-range slices at different range gates [1] which is possible when applying a high resolution radar. Actually this technique is a combination of 2D aperture synthesis and wideband radar ranging with high enough resolution. Hereinafter, this technique will be called as *Radar Tomography* which is in agreement with general definition of the tomography. Microwave or millimeter wave radar tomography may be realized with the help of any type of high resolution radar; however in this paper we will be focused on *Microwave noise radar tomography* [2,3]. To demonstrate this capability of noise radar we have carried out computer simulation of noise radar operation in combination with 2D aperture synthesis. Indoor experiments aimed on obtaining of 3D tomographic images of a laboratory room interior have been carried out using S-band noise radar. Besides, we have shown tomographic 3D images generated experimentally and have estimated the coordinates of some strong scatterers measured from these images. Bisatic Ka-band Noise waveform SAR using antennas with beam synthesis [3,4] may be applied for tomographic imaging as well, but the related results are presented in another paper by the authors.

I. 2D IMAGE GENERATION USING NOISE WAVEFORM AND 2D APERTURE SYNTHESIS

Consider, first, simulation of 2D imaging using 2D aperture synthesis along two cross-range coordinates with the help of wideband Noise Radar. The required noise waveform with Gaussian shape of its power spectrum has been obtained from white noise sequence via application of three transformations: 1. Fast Fourier Transform (FFT), 2. Gaussian windowing in frequency domain, and 3. Inverse FFT [2,3] to obtain the required random signal in time domain.

We have simulated 2D aperture synthesis for the case of *rectangular* aperture shape. We suppose mechanical motion of transmit/receive (Tx/Rx) antenna or proper electronic switching between elements of 2D Tx/Rx antenna array. Rectangular aperture is realized via line by line scanning consisting in radiation and reception of noise signal at each discrete position of the antennas. The scene consists of point-like scatterers which don't have mutual electromagnetic interaction.

SAR imaging can be considered as matched filtration of the signals received by Rx antenna at different positions. Reference function for such filtration is obtained as a signal from a point-like scatterer placed at the point of interest. Such matched filtration can be described in spectral domain as follows. Relation for a Fourier component of the received signals from a point-like scatterer can be described as a harmonic of probing signal with factors which describe its distortions due to propagation and backscattering:

$$E_m(f,\chi_1,\chi_2) = \\ = E_0(f,\chi_1,\chi_2)\cdot\zeta(x,y,z)h(f,\chi_1,\chi_2,x,y,z), \quad (1)$$

where $E_0(f,\chi_1,\chi_2)$ is a Fourier component of the signal radiated at the antenna position described by two coordinates on the plane of the synthetic aperture (χ_1,χ_2); f is frequency; $\zeta(x,y,z)$ is reflection coefficient of the scene element with coordinates (x,y,z); $h(f,\chi_1,\chi_2,x,y,z)$ is a factor describing propagation of the signal from antenna at the position (χ_1,χ_2) towards the target with coordinates (x,y,z) and back.

Relation for estimation of the reflectivity ξ of the given point (x,y,z) of the 3D scene using matched filter concept will have the form of convolution between measured signals and theoretical return from the point-like scatterer [6]:

$$\xi(x,y,z) = \\ = \iint_S \int_{-\infty}^{\infty} E_{rec}(f,\chi_1,\chi_2)\cdot E_m^*(f,\chi_1,\chi_2)dfd\chi_1 d\chi_2, \quad (2)$$

where $E_{rec}(f,\chi_1,\chi_2)$ is a Fourier component of the signal received by the radar receiver at the given

antenna coordinates; S is the surface of antenna aperture, superscript * denotes complex conjugation.

Reference signal from idealistic scatterer $E_m(f,\chi_1,\chi_2)$ is to be substituted from (1) taking $\zeta(x,y,z)=1$. The propagation factor $h(f,\chi_1,\chi_2,x,y,z)$ is to be obtained from geometrical consideration of relative positions of antenna and scatterer and model of propagation. Let us denote for simplicity the coordinates of Tx/Rx antenna as radius-vector $\vec{R}_\chi$ and coordinates of the point of interest as $\vec{R}_{xyz}$. For the far zone of the antenna the propagation factor can be written as follows:

$$h\left(f,\vec{R}_\chi,\vec{R}_{xyz}\right)=\frac{P\left(\vec{R}_\chi,\vec{R}_{xyz}\right)^2 e^{-\frac{4\pi i\left|\vec{R}_\chi-\vec{R}_{xyz}\right|}{c}}}{\left|\vec{R}_\chi-\vec{R}_{xyz}\right|^2}, \quad (3)$$

where $P\left(\vec{R}_\chi,\vec{R}_{xyz}\right)$ is pattern of the physical antenna; c is propagation velocity of radio frequency in the medium. Low variation of amplitude part of (3) enables to leave only phase part of the signal propagation factor.

When SAR antennas move with low velocity and transmitting-receiving is carried out at certain positions, it is possible to substitute integral over χ_1 and χ_2 by a sum over all antenna positions. Besides, due to the limited duration of signal, integration over frequencies can be substituted by sum over frequency spectrum components.

The cross-range resolution in both angular directions is defined by the corresponding dimensions of synthetic aperture and wavelength of the probing waveform. For simulation of 2D imaging via 2D aperture synthesis an object has been formed as a set of scattering points, which are shown in Fig. 1. The image of this object generated with rectangular scanning geometry is shown in Fig. 2.

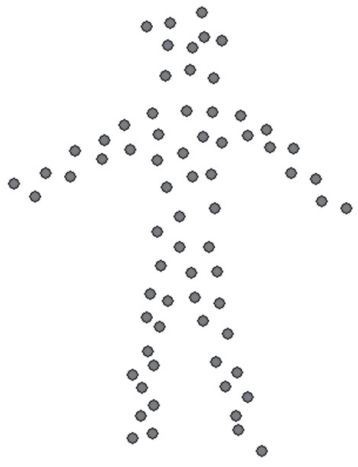

Fig. 1. 2D model formed by a number of point-like scatterers

Simulation was done for the following parameters: carrier frequency 3.6 GHz; power spectrum bandwidth 200MHz; range 1m; synthetic aperture dimensions 0.6x0.6 m; size of radar field of view 2.4x2.4m; spacing between antenna positions 2.5cm.

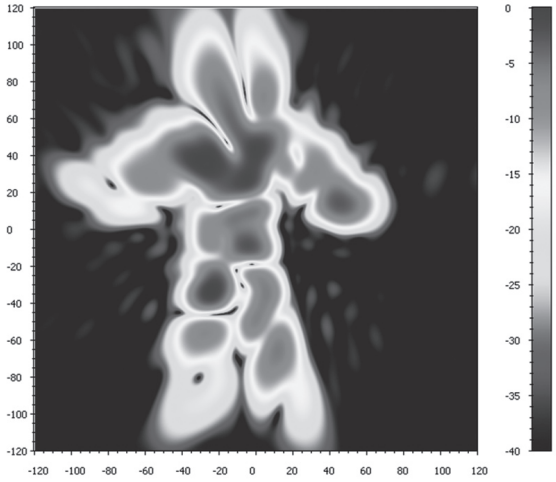

Fig. 2. 2D coherent image generated with the help of 2D aperture synthesis and noise waveform. Modeled taget is shown in Fig.1

II. 3D IMAGE GENERATION USING NOISE WAVEFORM AND 2D APERTURE SYNTHESIS

Microwaves are reflected by human body and by metals. The principle of tomographic 3D imaging consists in illumination of the object of interest with a broadband signal enabling to get high enough range resolution and in formation of 2D image for providing the angular resolution required. This is based on the fact that microwaves can penetrate through many artificial and natural media which are optically opaque. Dielectric materials such as plastics and organic materials will cause partial reflection of the waves and partial transmission so they will be seen as partially transparent. Having the reference signal we can vary its delay and thereby perform range focusing which enables generation of 2D image (tomographic slice) from certain range inside transparent object, separately. In this way, application of noise waveform with wide enough power spectrum bandwidth enables layer-by-layer visualization of a semitransparent object and, therefore, generation of its tomographic 3D image.

The Noise Radar system uses illumination by random signal and coherent detection (both amplitude and phase) of the scattered wave. Noise waveform with a variable power spectral density width enables controlling the resolution in depth of the 2D Imaging. The range resolution is defined by the power spectrum bandwidth, as

$$\Delta z = c/2\Delta f,$$

where Δf is power spectrum bandwidth, c is the velocity of light.

Use of random waveform delivers such benefits as absence of range ambiguity and improving immunity against external electromagnetic interferences [1-3]. Thus imaging with 2D aperture synthesis and noise waveform enables tomographic 3D imaging through the range resolution of the wideband radar.

III. EXPERIMENT FOR INDOOR 3D SAR IMAGING

Experiment was carried out using 3.5GHz transceiver. Noise continuous waveform (CW) with 300MHz bandwidth and 20mW transmit power was used for sounding. 2D rectangular SAR scanning was implemented by moving a receive antenna on special supplement construction. Transmit antenna remained the same position during the measurements which lead to loss of half of the angular resolution but enabled to overcome high crosstalk between antennas and simplify the construction. Synthetic aperture dimensions of 0.6x0.6m defined angular resolution in both cross range axis of about 8°. Radar return and reference signals were down converted to intermediate frequency band and digitized with a 1Gs/s 8bit ADC and then processed in a PC using the proposed algorithm. Dynamic range of the generated 2D and tomographic images reaches 42dB which is determined by 7bit effective vertical resolution of the ADC.

Fig. 3 shows a picture of the experiment scenario.

Fig. 3. Scenario for tomographic 3D SAR imaging

The scheme of the experiment includes position of the SAR receive aperture and two test targets shown on the Fig. 4. The measurements were carried out in a laboratory room with concrete walls and floor. Inside the room, there were several tables with equipment, metal chairs and multiple metal objects.

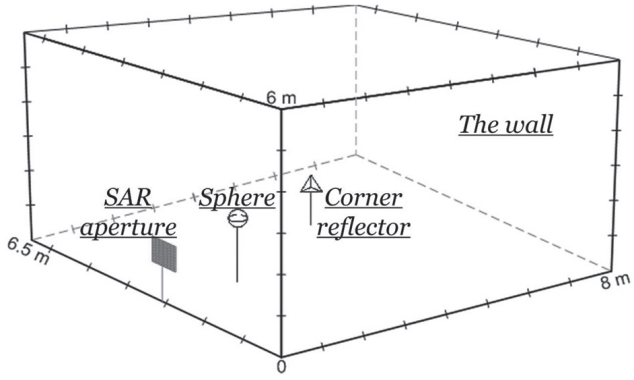

Fig. 4. Scenario for the experiment (see picture of the scene in fig. 3)

Two targets having rather strong reflectivity were placed in the radar field of view inside the room: a duralumin corner reflector and a polyethylene sphere covered with aluminum foil (Table 1). The targets positions were measured from the SAR aperture center.

Table 1

Details of the experimental setup

Features of the targets	Sphere	Corner reflector
Range, m	1.6	4.8
Cross range, m	-0.5	0.8
Elevation, m	-0.1	-0.4
Size, m	radius=0.1	length=0.3
Radar cross section, m^2	$31.4 \cdot 10^{-3}$	19.7
Size of the angular resolution cell at the distance of the target, m	0.5	1.3

Fig. 5 shows a 2D SAR image obtained using the data from these tomographic measurements (top view). The sphere and the corner reflector are clearly seen in the image. Besides, the back wall of the room, tables and chairs could be easily recognized in the image as well.

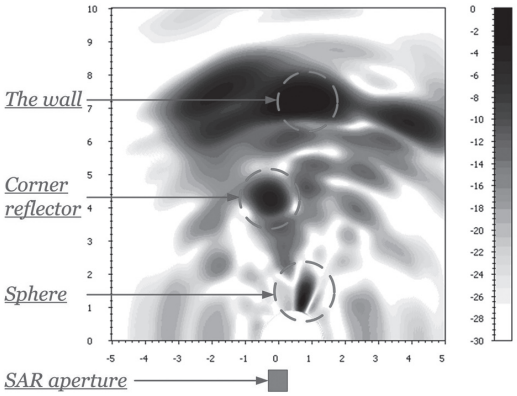

Fig. 5. 2D 'range'-'cross range' SAR image of laboratory room; top view (see picture of the scene in Fig. 3)

Fig. 6 shows vertical slice of tomographic 3D SAR image at the distance of 1.6m which corresponds to the sphere position. The target is clearly seen in the image.It has to be noted that at this distance from the radar synthetic aperture all the resolutions along all three coordinate axis (elevation, azimuth and range) are comparable (Table 1).

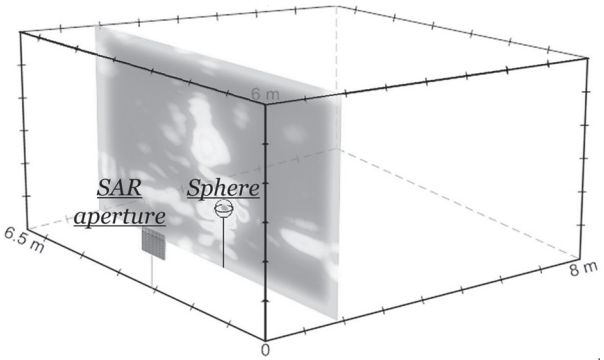

Fig. 6. Vertical slice of tomographic 3D SAR image at the distance corresponding to the sphere position

Fig. 7 shows vertical slice of tomographic 3D SAR image at the distance of 4.8m which corresponds to position of the corner reflector. The latter is also focused well. Besides, responses from chairs and tables can be also found in this image. Fig. 8 shows vertical slice of tomographic 3D SAR image at the distance of 8m which corresponds to the back wall of the room and shows strong reflection from this wall. Magnitudes of the responses are in a good agreement with the known RCS values of the reflectors. Positions of the detected peaks are in a good agreement with the placement of the radar targets (listed in Table 1). Range and angular resolutions obtained are close to their theoretical values. Application of Noise waveform and coherent reception of the radar returns enabled performing tomographic radar measurements inside the room containing high number of reflectors and, also, at the presence of multiple reflections from the walls. Experimental results have shown high repeatability of the measurements.

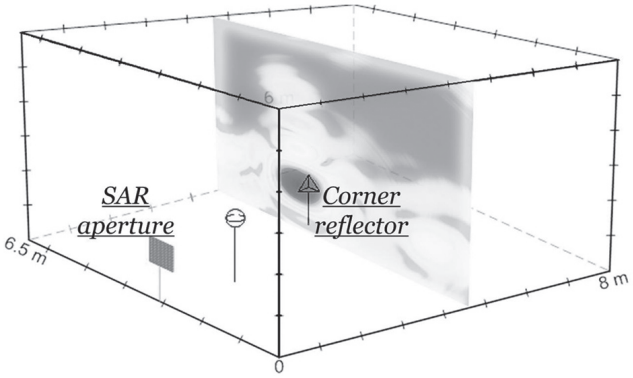

Fig. 7. Vertical slice of tomographic 3D SAR image at the distance corresponding to position of the corner reflector

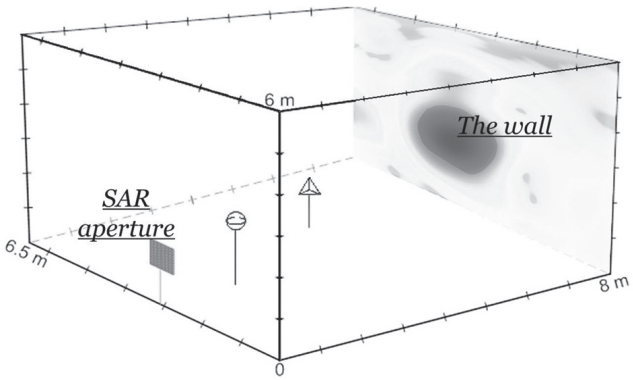

Fig. 8. Vertical slice of tomographic 3D SAR image at the distance corresponding to the back wall position

CONCLUSIONS

A method for generation of tomographic 3D microwave images based upon 2D Aperture Synthesis and Noise Radar Technology has been considered theoretically and validated experimentally.

We have carried out computer modeling of noise radar operation in 2D aperture synthesis mode. The code developed gives a possibility to simulate: (1) tomographic 3D image generation for various 2D synthetic aperture geometries; (2) simulation of the response from point scatterer and (3) perform space-time processing. Besides, this code can be used for processing of realistic radar data and for generation of tomographic 3D SAR images.

We have analyzed resolution and sidelobes of various configurations of synthetic aperture through the modeling of 1D and 2D aperture synthesis. Besides, we have carried out experiment for tomographic 3D SAR imaging using S-band (3.5 GHz) continuous waveform noise radar and 2D rectangular synthetic aperture. In these experiments we have shown possibility to generate tomographic 3D SAR images and to measure positions of strong scatterers in these images. The method is promising for many applications, in particular for homeland security and covert terrorist detection inside buildings.

References

[1] *Lukin K.A. et. al.* 2D and 3D imaging using S-band noise waveform SAR // Proceedings of 3rd International Asia-Pacific Conference on Synthetic Aperture Radar (APSAR), 2011. pp. 1-4.

[2] *Lukin, K.A.* Noise Radar Technology // Telecommunications and Radio Engineering, Vol.55 (2001), No. 12, pp.8-16.

[3] *Lukin, K.A.* Noise Radar Technology: the Principles and Short Overview // Applied Radio Electronics, Vol. 4, No. 1, pp. 4-13, (2005).

[4] *Lukin K.A. et. al.* Ka–Band Bistatic Ground-Based Noise Waveform SAR for Short-Range Applications // IET Radar, Sonar & Navigation 2008. Vol.2. No. 4, pp. 233–243

[5] *Trachi D., Lukin K.A., Fortuny-Guasch J., Mogyla A., Vyplavin P., Sieber A.* SAR Imaging with Noise Radar // IEEE transactions on Aerospace and Electronic Systems AES 2010, Vol. 46, No. 3, pp.1214-1225.

[6] *Curlander J., McDonough R.* Synthetic Aperture Radar: Systems and Signal Processing. – John Wiley & Sons, 1991. - 672 p.

Manuscript received January, 29, 2013

Konstantin A. Lukin, for photograph and biography, see this issue, p. 24.

Pavlo L. Vyplavin, for photograph and biography, see this issue, p. 94.

Volodymyr V. Kudriashov, Ph.D. student, researcher in Laboratory for Nonlinear Dynamics of Electronic Systems (LNDES), O.Ya. Usikov Institute for Radiophysics and Electronics of the National Academy of Sciences of Ukraine. Field of scientific interests: radiometric measurements, radar signal processing, SAR imaging.

Vladimir P. Palamarchuk, for photograph and biography, see this issue, p. 144.

Oleg V. Zemlyaniy, for photograph and biography, see this issue, p. 36.

Sergiy K . Lukin, for photograph and biography, see this issue, p. 36.

Jong-Min Lee, Ph. D., principal researcher in Agency for Defense Development (ADD) in Korea. Field of scientific interests: radar system design & analysis; antenna design; and sensor fusion & fire controls.

Jong-Soo Ha, M. S., senior researcher in Agency for Defense Development (ADD) in Korea. Field of scientific interests: radar signal processing; M&S of radar system; image processing; and forward looking SAR.

Sun-Gu Sun, Ph. D., principal researcher in Agency for Defense Development (ADD) in Korea. Field of scientific interests: radar signal processing; image processing; robot vision and sensor fusion

Youn-Sik Kang, Ph. D., principal researcher in Agency for Defense Development (ADD) in Korea. Field of scientific interests: electro-optical system design; adaptive control.

Byung-Lae Cho, Ph. D., senior researcher in Agency for Defense Development (ADD) in Korea. Field of scientific interests: synthetic aperture radar (SAR); interferometric SAR; forward-looking SAR; and FMCW radar.

Kyu-Gong ChoPh. D., principal researcher in Agency for Defense Development (ADD) in Korea. Field of scientific interests: active protection; missile & rocket defense for platforms & localized areas; and sensor fusion & fire controls.

УДК 621.396.962.25

Формирование томограмм с помощью шумового радара и двумерного апертурного синтеза / К.А. Лукин, П.Л. Выплавин, В.В. Кудряшев, В.П. Паламарчук, Джонг-Мин Ли, Джонг-Су Ха, Сан-Гу Сан, Юн-Сик Канг, Кью-Гонг Чо, Бьюньг-ла Чо // Прикладная радиоэлектроника: науч.-техн. журнал. – 2013. – Том 12. – № 1. – С. 152–156.

Реализация двумерного апертурного синтеза позволяет получить двумерное угловое разрешение, которое в комбинации с разрешением по дальности позволяет формировать томографические трехмерные изображения. Томографические трехмерные изображения могут дать детальную и точную информацию о пространственном распределении полупрозрачных объектов или других зондируемых областей. Радарная томография может быть реализована с помощью любого типа радара с высоким разрешением; однако эта статья сфокусирована на *шумовой радарной томографии*. Мы приводим результаты моделирования работы широкополосного шумового радара в комбинации с двумерным апертурным синтезом и представляем некоторые результаты эксперимента по получению томографических изображений, используя непрерывные шумовые сигналы S-диапазона и двумерный апертурный синтез.

Ключевые слова: шумовой сигнал, радарная томография, формирование трёхмерных РСА изображений, шумовой РСА.

Табл. 1. Ил. 8. Библиогр. 4 назв.

УДК 621.396.962.25

Формування томограм за допомогою шумового радара та двовимірного апертурного синтезу / К.О. Лукін, П.Л. Виплавін, В.В. Кудряшов, В.П. Паламарчук, Джонг-Мін Лі, Джонг-Су Ха, Сан-Гу Сан, Юн-Сік Канг, К'ю-Гонг Чо, Б'юньг-ла Чо // Прикладна радіоелектроніка: наук.-техн. журнал. – 2013. – Том 12. – № 1. – С. 152–156.

Реалізація двовимірного апертурного синтезу дозволяє отримати двовимірну кутову роздільну здатність, яка в комбінації з роздільною здатністю за дальністю дає змогу формувати томографічні тривимірні зображення. Томографічні тривимірні зображення можуть дати детальну та точну інформацію про просторовий розподіл напівпрозорих об'єктів або інших областей, що зондуються. Радарна томографія може бути реалізована за допомогою будь-якого типу радара з високою роздільною здатністю; проте ця стаття сфокусована на шумовій радарній томографії. Ми описуємо результати моделювання роботи широкосмугового шумового радара в комбінації з двовимірним апертурним синтезом і представляємо деякі результати експерименту з отримання томографічних зображень, використовуючи безперервні шумові сигнали S-діапазону і двовимірний апертурний синтез.

Ключові слова: шумовий сигнал, радарна томографія, формування тримірних РСА зображень, шумовий РСА.

Табл. 1. Іл. 8. Бібліогр. 4 найм.

UDK 621.396

DESCRIPTIVE EXPERIMENT DESIGN FRAMEWORK FOR HIGH RESOLUTION IMAGING WITH MULTIMODE ARRAY RADAR SYSTEMS

V. ESPADAS AND Yu. SHKVARKO

We address a descriptive experiment design (DED) regularization approach for enhanced resolution imaging of multiple targets via space-time processing of multimode array radar (MAR) data. The multiple frequency-polarization signal processing (SP) mode is employed to provide necessary DED redundancy that is next exploited to enhance the MAR imaging resolution performances in different operational environments including harsh scenarios with imperfect array calibration, partial sensor failure and/or uncertain noise statistics. The proposed DED framework provides robust extension of the Van-Zittert — Zernike approach based on the matched spatial filter bank SP for such realistic operational scenarios. The DED-based MAR employs the robust regularized matched spatial filter bank SP for image formation, in which the shape of the MAR resulting point spread function is optimized applying the new proposed DED-inspired quality metrics constructed to optimally balance the resolution-over-noise-suppression performances adapted to harsh multiple target sensing scenarios. Numerical simulations verify the effectiveness of the proposed DED-SP method for MAR imaging in harsh sensing environments.

Keywords: antenna ray, descriptive experiment design, multimode imaging radar, regularization.

INTRODUCTION

Sensor array signal processing (SP) for imaging radars has been the focus of tremendous theoretical advances and application developments in the last decades and many sophisticated techniques are now available (see, for example [1]–[6] and the references therein). In the imaging radar science, new trends relate to employment of multiple processing modes that provide the necessary data redundancy that can be next exploited to enhance the overall multimode array radar (MAR) imaging resolution performances. Crucial still unresolved MAR-SP issues relate to robust enhanced imaging in harsh operational scenarios characterized by possible imperfect array calibration, partial sensor failure and/or uncertain noise statistics.

In this study, we address a new descriptive experiment design regularization approach for enhanced resolution imaging of multiple targets via space-time processing of MAR system data. The multiple frequency-polarization SP mode is employed to provide necessary DED redundancy in the considered harsh operational scenarios. At the hardware (HW) design level, the crucial problem relates to optimization of the sensor array configuration aimed at approaching the desired resulting point spread function (PSF) performances, e.g., the lowest possible side-lobes level balanced over the minimum effective width of the main PSF beam. At the software (SW) design level, the further problem is to develop the robustified matched spatial filter (MSF) bank image formation techniques aimed at approaching the overall high-resolution MAR imaging performances. To approach these HW-SW co-design goals, we propose the descriptive experiment design (DED) framework constructed via robust extension of the Van-Zittert-Zernike approach based on the MSF bank SP. The shape of the MAR system PSF is optimized applying the new proposed DED-inspired quality metrics constructed to satisfy the balanced resolution-over-noise suppression requirements adapted to high resolution multiple target sensing scenarios. We analyze the achievable PSFs for a variety of admissible MAR-SP mode specifications [4], [5], that is, different inter-sensor distance and various carrier frequencies and polarization modes. This study establishes a DED framework for MAR imaging HW system design in terms of new resolution metric that controls the minimization of the resolution cells balanced over the suppression of the PSF grating sidelobes. Next, the DED-based SW level SP performs the robust regularized image formation with the optimized PSF shape. Last, the numerical simulations verify the effectiveness of the proposed DED-SP method for MAR imaging in harsh sensing environments.

I. GEOSTAR-CONFIGURED MAR SYSTEM SPECIFICATIONS

The so-called GeoSTAR (Geo synthesized thinned array radiometer) imaging sensor system has been originally addressed in [1] as a concept to provide high resolution imaging of distributed RS scenes with passive microwave and mm waveband radiometers. Nevertheless, the celebrated GeoSTAR array configuration is also well adapted for active MAR systems as it was demonstrated in [6], [11].The particular imaging MAR system under consideration in this study is a multimode array sensor system of [6], [11]. Such MAR operates at two separate yet concurrent frequencies of 24.5 GHz and 35 GHz with dual polarization (V – vertical and H – horizontal). At one instant, radio frequency (RF) pulses of a specified pulse width (PW) are transmitted concurrently at 24.5 and 35 GHz in either V polarization or H polarization. These pulses are "calibrated" to maintain coherency so that their amplitudes and phases are constant for different pulses. The transmitting antenna is switched between vertical (V) and horizontal (H) polarizations, i.e., V and H transmitted pulses are delayed by a certain time. For each frequency (24.5 GHz or 35 GHz), transmitted V polarized and H polarized RF

pulses are separated by a half of the fixed pulse repetition time (PRT/2) as illustrated in Fig.1.

The antenna array is composed of 24 elements as in [1], [6]; each sensor element receives signals at V and H polarizations. The received signals are spread over time duration of N PWs, where N is the number of range resolution cells used to process the received signals for each transmitted pulse. In every PRT corresponding to one frequency band (24 GHz or 36 GHz), one time delay vector $\mathbf{T_d}$ and 4 measurement data vectors, $\mathbf{U_{VV}}$, $\mathbf{U_{VH}}$, $\mathbf{U_{HV}}$, $\mathbf{U_{HH}}$, are provided for further processing. That is, for each polarization modes (VV, VH, HV or HH) there is no time delay between receiving antenna elements since they are spaced close to each other, so $\mathbf{T_d}$ has only one value for all 24 elements for each received signal. Each data vector $\mathbf{U_{VV}}$ ... $\mathbf{U_{HH}}$ contains the relevant in phase (I) and quadrature (Q) components that compose 24 rows data ($i = 1 \rightarrow 24$) collected for $2N$ measurement time instants ($n = 1 \rightarrow N$). The transmit-receive format is explained in Fig. 2. The operation range of the MAR system is in the interval from 1m to 50m, with a range resolution cell of 0.3m, so at the SP level the observer controls 165 overall range processing gates.

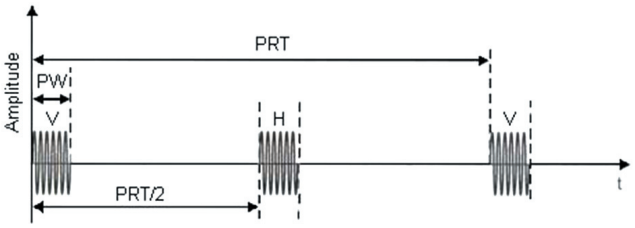

Fig. 1. Transmit RF pulse format

The crucial SP issue relates to the formation of the empirical estimate $\mathbf{Y}_r = \underset{i}{aver}\{\mathrm{U}_r(i)\mathrm{U}_r^+(i)\}$ of the sensor data true correlation matrix $\mathbf{R}_r = <\mathrm{U}_r\mathrm{U}_r^+>$ for each range gate $r = 1, ..., R_r = 165$. The independent realizations $\{\mathrm{U}_r(j);\ j = 1,...,J\}$ in the averaging procedure for formation of $\mathbf{Y}_r$ are to be recorded over J transmitted pulses for each range gate $r = 1, ..., R_r = 165$. To guarantee the full-rank sensor data covariance matrices $\{\mathbf{Y}_r, r = 1,..., R\}$ the minimal number of independent recordings J should be not less than the number of sensors ($M = 24$), thus $J > 24$ independent realizations are to be recorded for each range gate $r = 1, ..., R_r = 165$. In the opposite case, $J < 24$, the data covariance matrices are rank-deficient. This means that for $J < 24$ the robust MSF-based beamforming for sensor focusing inevitably faces the problem of huge artifacts (so called ghosts on the speckle corrupted scene images [5], [8]). At the target detection SP stage, such artifacts inevitably increase the false alarm rate [8]. That is why, in all SP developments in this study, the redundancy guaranteed SP mode $J > 24$ is considered.

To compare different HW designs, in this study we analyze three feasible sensor array configurations. Fig. 3(a) shows the conventional X-shaped equally-spaced antenna array layout for the inter-element spacing $d_{A(1)} = 0.5\,\lambda_o$, where λ_o specifies the employed wavelength, in this case $f_o = 24$ GHz. The corresponding so-called *uv* spatial samples in the *visibility* domain are presented in Fig. 3(b). In Fig. 4(a), a circular-shaped (O-shaped) antenna array layout with the same parameters is depicted. The related *uv* spatial visibility samples are shown in Fig. 4(b). The GeoSTAR Y-shaped antenna array is presented in Fig. 5(a) with the corresponding *uv* samples in Fig 5(b), respectively. In all cases, u and v samples specify the normalized (so-called *visibility* domain) coordinate representation format, i.e., $u = x/\lambda_o$, and $v = y/\lambda_o$.

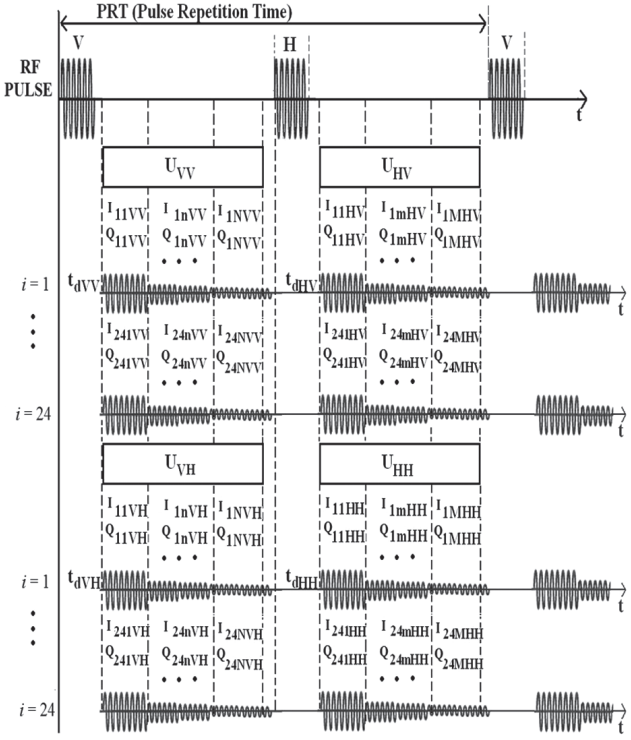

Fig. 2. Transmit-receive signal format

II. MSF IMAGE FORMATION TECHNIQUE

The proposed MSF-based image formation algorithm comes directly from the celebrated Van-Zittert-Zernike theorem from radio astronomy [6], [8] according to which, the noise-free data visibility function $R(u,v)$ (constructed directly from the noise free data true covariance function $R(x,y)$ at each range gate via its scaling to the visibility domain [6]) and the related spatial spectrum pattern (SSP) or angular brightness distribution $b(\theta_x,\theta_y)$ over the 2-D angular observation space $(\theta_x,\theta_y) \in \Theta$ are related through the 2-D spatial inverse Fourier transform:

$$R(u,v) = c\Im_\theta^{-1}\left\{b(\theta_x,\theta_y)\right\} = c\int_\Theta b(\theta_x,\theta_y)\exp\left[+i2\pi(u\theta_x + v\theta_y)\right]d\theta_x\,d\theta_y, \quad (1)$$

where c is the normalizing constant [6] (not critical for image formation and analysis) and the visibility function arguments (u, v) represent the x–y projections of the normalized sensor *baseline* vectors (normalized to the wavelength λ_o) in the visibility domain $(u, v) \in P/\lambda_o$ [6], [8].

The robust MSF-based method [4], [5] for RS image formation implies, first, formation of the

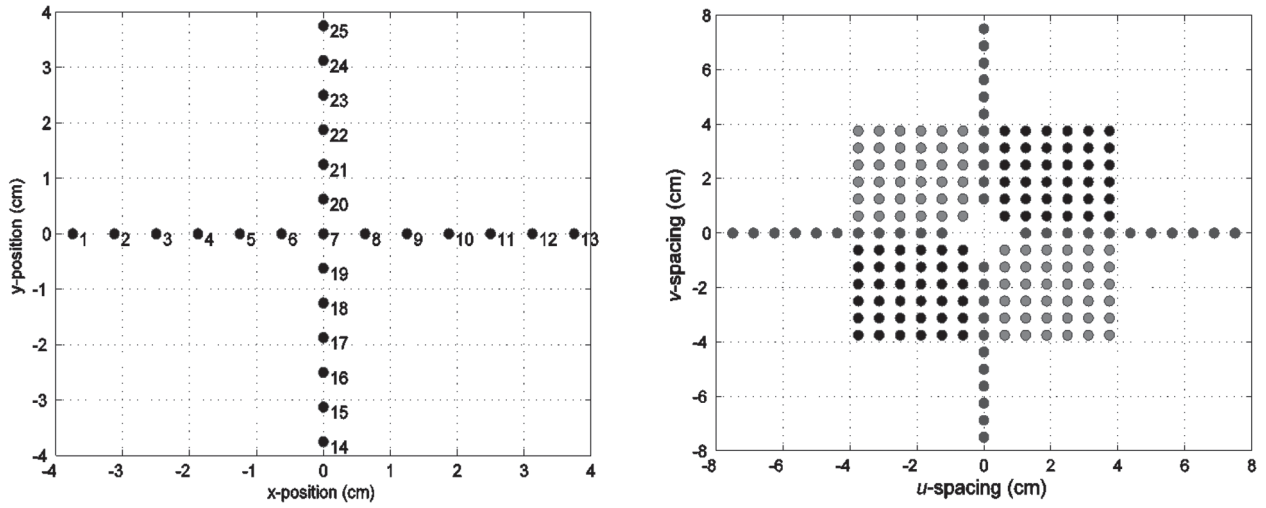

(a) (b)

Fig. 3. (a) Antenna array layout with sensor numbering for X-shaped configuration;
(b) corresponding *uv* samples for inter-element spacing $d_{A(1)} = 0.5\lambda_o$; carrier frequency $f_o = 24$GHz

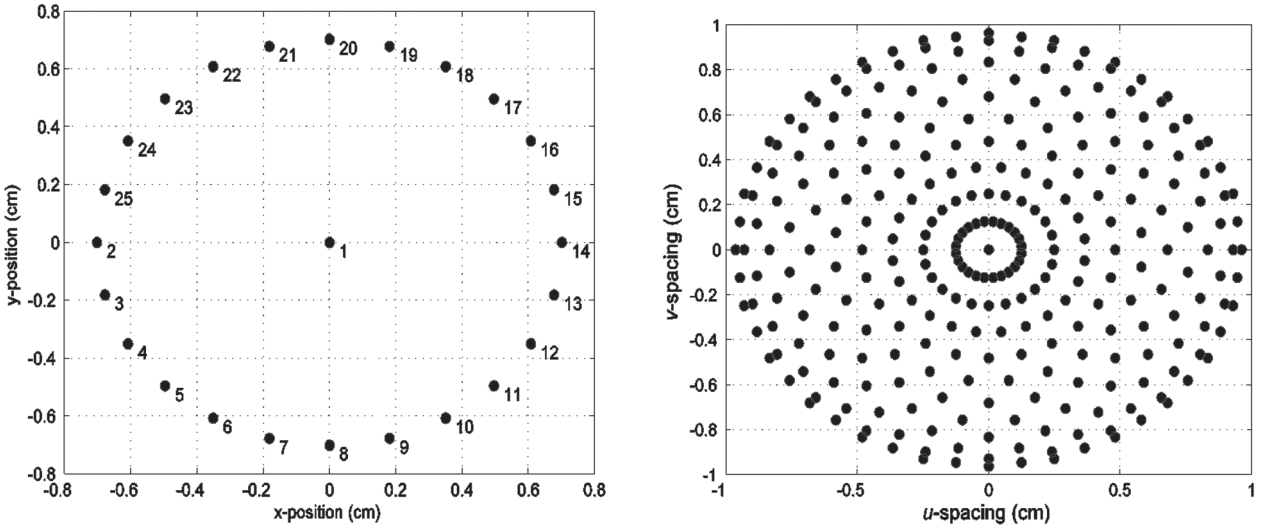

(a) (b)

Fig. 4. (a) Antenna array layout with sensor numbering for O-shaped configuration;
(b) corresponding *uv* samples for inter-element spacing $d_{A(1)} = 0.5\lambda_o$; carrier frequency $f_o = 24$GHz

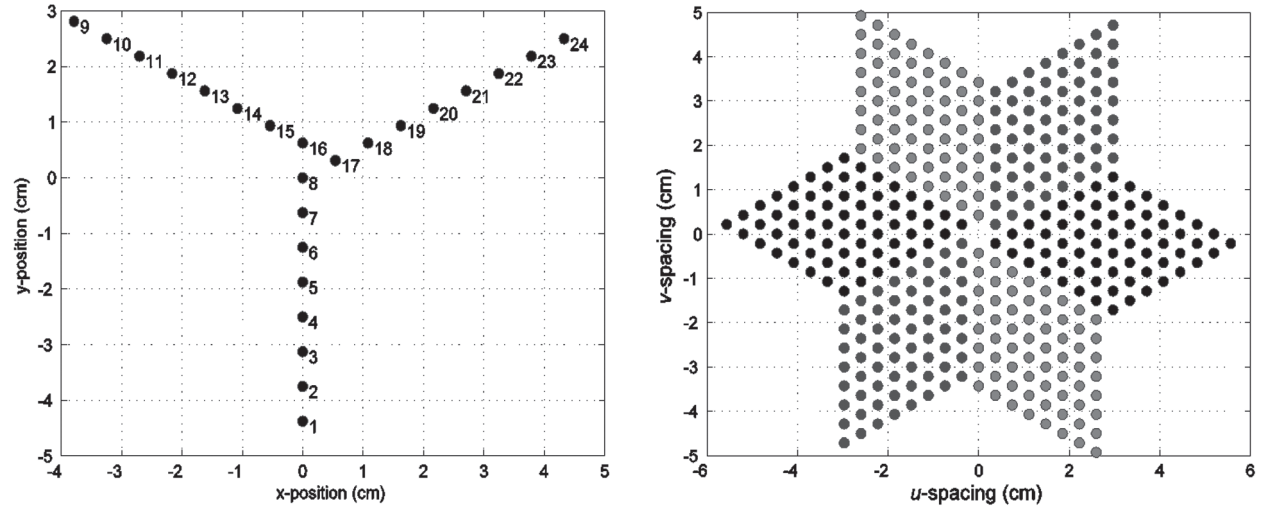

(a) (b)

Fig. 5. (a) Antenna array layout with sensor numbering for Y-shaped GeoSTAR configuration;
(b) corresponding *uv* samples for inter-element spacing $d_{A(1)} = 0.5\lambda_o$; carrier frequency $f_o = 24$GHz

observed noised visibility function $\hat{R}(u,v)$ via scaling the estimated correlation matrix $\mathbf{Y}_r$ to the visibility domain (over a range of normalized visibility spacings $(u,v)\in P/\lambda_o$) followed, second, by the 2-D Fourier transform that yields the MSF image of the scene

$$\hat{b}(\theta_x,\theta_y)=\Im_{u,v}\left\{\Pi_{A(u,v)}\,\hat{R}(u,v\,|\,r)\right\}= \int_R \Pi_{A(u,v)}\,\hat{R}(u,v\,|\,r)\exp\left[-i2\pi(u\theta_x+v\theta_y)\right]d\theta_x\,d\theta_y \quad (2)$$

at a particular rth range gate from the range observation domain $R\ni r$ [2]. Here, the projector $\Pi_{A\{u,v\}}$ specifies the particular employed sensor array configuration resulting in different resolution performances attainable with the MSF-based imaging technique (2). In the pursued here nonparametric problem treatment, such resolution quality is assessed by the shape of the resulting system PSF associated with the image (2) of a single point-type target located at the scene origin at the corresponding range gate $r\in R$. In particular, the desired system PSF is associated with the shape that provides the lowest possible side lobes (and grating lobes) level balanced over the minimum achievable effective width of the PSF main beam [7], [9], [10].

Based on (2), let us next analyze the PSFs of the MAR imaging systems attainable with the employment of the conventional X-shaped, O-shaped array and the celebrated GeoSTAR-configured Y-shaped array. In Figures 6 thru 8, we present the PSFs related to the MSF-based single target (TAG) imaging procedure (2) employing the cross-shaped (X-shaped) [6], circular-shaped (O-shaped) [10] and the GeoSTAR-configured Y-shaped sensor array [1], [11] geometries in the terms of the attainable angular PSF of the corresponding MAR imaging systems. The PSF cross-sections in the x-y imaging scene provide explicit information on the spatial resolution cells achievable with such differently configured imaging sensor arrays that employ the conventional 2-D MSF method (2) for RS image formation. In Fig. 6, we present the PSF for the conventional X-configured imaging array with the inter-element spacing $d_{A(6)} = 2\lambda_o$, i.e., equal to the double of the carrier wavelength (for the carrier frequency f_0 = 24 GHz), while in Fig. 7 the PSF for the O-configured array with the same parameters is depicted. Next, in Fig. 8, the PSF for the Y-shaped (GeoSTAR-configured) imaging array with the same parameters as the previous two PSFs is presented. Note that the most important characteristics of these PSFs are the width of the main beam and the maximum level of the secondary lobes (including the suppressed grating lobes). The simulations were next performed using the elaborated virtual remote sensing laboratory (VRSL) software [6], which are indicative of the usefulness of the HW-level DED-optimization of the multi-target scene imaging tasks via configuring the multi-mode sensor arrays employed in the particular RS array radar imaging systems. Fig. 9 shows the results of simulations of the DED-optimized multiple target scene imaging performed applying the 2-D MSF technique (2). The multiple target scene is composed of 5 targets (5 TAGs) in the particular simulated range gate (r = 30m) and the corresponding scene images are depicted in the x-y plane for the employed X, O and the Y (GeoSTAR) imaging sensor array configurations. The particular MAR operational sensing parameters employed in the reported simulations are specified in the figure captions.

III. OPERATIONAL UNCERTAINTIES

In this section, we treat two types of operational scenario uncertainties, in particular, possible sensor displacements and data failure due to some disabled sensors. We present a brief description of these operational uncertainties as well as an analysis of the image degradations that may suffer the MSF-based MAR-SP procedure (2) assuming such harsh scenarios.

A. Displaced Sensors

In Fig. 5(a) the MAR antenna layout was depicted; at this point it is important to fix the locations and the spacing between the elements of the antenna array. These positional characteristics are vital to compose the visibility function as shown in Fig. 5(b).

The sensor displacements (shifts) may occur due to damage or manufacturing errors. A sensor shift implies that the sensor's centroid is not in the correct coordinate position specified by the HW design. Assuming that a sensor is displaced at a quantity between the interval $[-\lambda_0/4, \lambda_0/4]$ for both coordinates x and y, we define now a vector $\tilde{p}_m$ wich characterizes the position of such displaced sensor

$$\tilde{p}_m=(x_m,y_m)+(x_{\Delta m},y_{\Delta m}) \quad (3)$$

where (x_m, y_m) are the correct (HW calibrated) coordinates of the sensor and $(x_{\Delta m},y_{\Delta m})$ represents the coordinate shifts. When adding these new parameters to the original procedure (2), we obtain the following MSF imaging result

$$\hat{b}(\theta_x,\theta_y\,|\,r)= \int_R \Pi_{A(u,v)}\,\hat{R}(u,v\,|\,r)\exp\left[-i2\pi(u\theta_x+v\theta_y)\right]\exp\{i2\pi[\tilde{\rho}_m,\theta]\}du\,dv \quad (4)$$

which contains the phase shift error term $\exp\{i2\pi[\tilde{\rho}_m,\theta]\}$ dependent on the inner product $[\tilde{\rho}_m,\theta]$. When a sensor is not shifted, this phase factor is equal to 1, that results in the original undistorted imaging procedure (2).

B. Disabled Sensors

As we mentioned in the previous section, the certain operational scenario presumes active functioning of all array sensors, i.e., all sensors must provide the measurement signal data signals needed to form the sensor data cross-correlation matrices ($\mathbf{Y}_r$ at all R range gates) and the related visibility functions. If one or more sensors in the array are disabled, the loss of data would cause a malformation of the matrix $\mathbf{Y}_r$, hence, inevitably distorted imaging via the MSF procedure (2). To relax the influence of such distortions, we perform the DED-based robustification of the

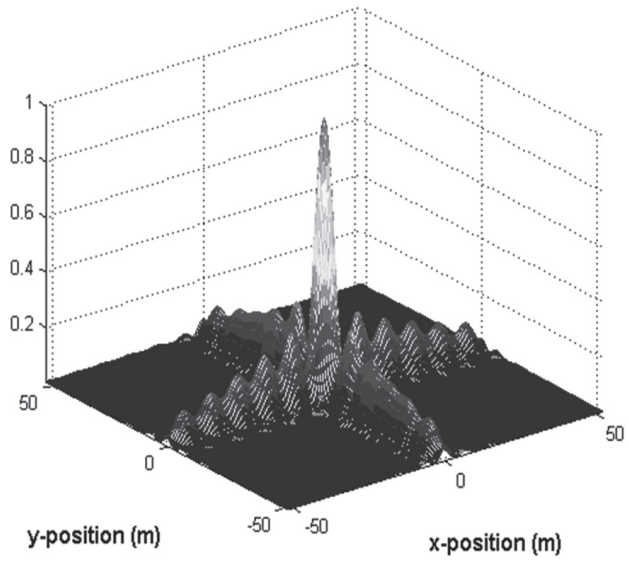

Fig. 6. Point Spread function (PSF) for 24 element X-shaped configured imaging array with $2\lambda_o$ inter-element spacing for 30m range gate

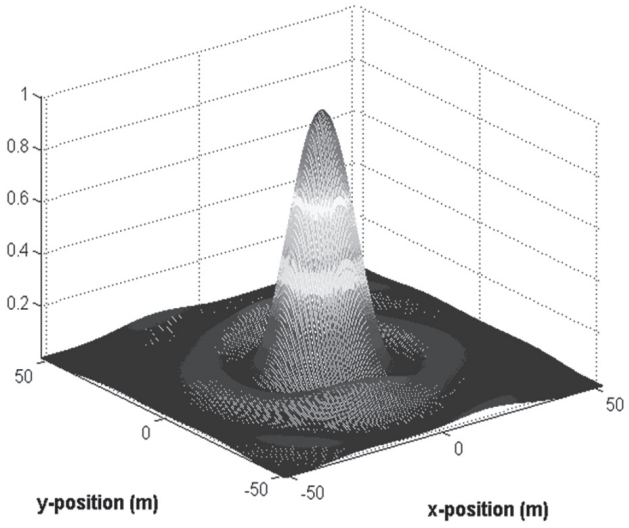

Fig. 7. Point Spread function (PSF) for 24 element O-shaped configured imaging array with $2\lambda_o$ inter-element spacing for 30m range gate

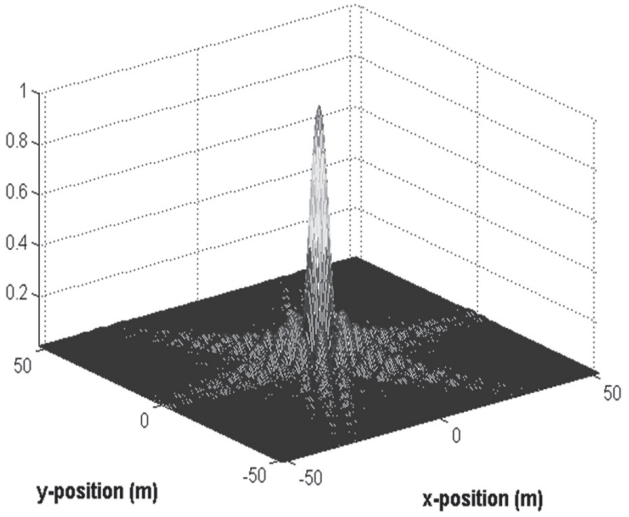

Fig. 8. Point Spread function (PSF) for 24 element Y-shaped configured imaging array with $2\lambda_o$ inter-element spacing for 30m range gate

covariance matrix $\mathbf{Y}_r$ at all R range gates following the sparse diagonal structuring regularization [11]. Fig. 10 shows the DED sparsified [11] structure of matrix $\mathbf{Y}_r$ for a fixed ($r = 30$m) range gate.

This sparse signal correlation matrix is composed of six active data blocks of 8-by-8 matrices and three zero-structured diagonal blocks $\underline{\mathbf{0}}_{(8x8)}$ composed of zeros. Three upper data blocks (sector S1, sector S2 and sector S3) relate to the sectors that correspond to the GeoSTAR unique baselines. The three lower data blocks (sector S4, sector S5 and sector S6) correspond to the symmetrical (virtual) GeoSTAR baselines composed by correlations between sensors of different arms of the antenna array. Last, three zero blocks $\underline{\mathbf{0}}_{(8x8)}$ located along the principal diagonal of the DED-sparse matrix $\mathbf{Y}_r$ correspond to the baselines between arms A1-A1, A2-A2 and A3-A3 that are *not* incorporated in the DED regularized processing algorithm (2) [11]. The complete set of measurements that compose matrix $\mathbf{Y}_r$ are applied in (2), but when one sensor or more are disabled, the DED-sparse matrix $\mathbf{Y}_r$ with the structure of Fig. 10 cannot be composed yielding possible undesirable processing results. In an illustrative interpretation, if sensor 1 of arm 1 is disabled, the first row of the sub matrices S1 and S2 (see Fig. 10) will be completely lost, along with their corresponding symmetric virtual elements in sub matrices S5 and S5.

To tackle with such harsh operational scenario uncertainties we address two DED inspired proposals. The first one is to perform an interpolation between the rows and the columns next to the missing elements in the matrix $\mathbf{Y}_r$ in a sparse form as shown in Fig. 10. When the sensor $m' = k$ presents a signal failure, the following interpolation is to be performed

$$\tilde{\mathrm{Y}}_r(k,m') = \frac{\mathrm{Y}_r(k+1,m') + \mathrm{Y}_r(k-1,m')}{2} \quad (5)$$

$$\text{for } m' = 1, \ldots, M;\ M = 24.$$

This new interpolated matrix $\tilde{\mathrm{Y}}_r(k,m')$ is constructed for replacing the distorted matrix $\mathbf{Y}_r$, and next, the DED-MSF image formation procedure (2) is performed.

The second DED inspired approach is based on the 4-nearest neighbor interpolation (4-NNI) technique [11]. This technique is applied to fill in the lost data directly in the visibility function domain related to the distorted matrix $\mathbf{Y}_r$ (see Fig. 5(b)). In Fig. 11, we explain the 4-NNI procedure in a graphical form in the visibility domain. The lost data row is displayed as empty dots in the visibility function, and the applied 4-NNI technique consists in averaging four nearest sensors data measurements to interpolate the concerned empty data slot (u-v sample). This is done performing the following

$$\tilde{\mathrm{Y}}_r(k,m') = \frac{1}{4}\big(\mathrm{Y}_r(k-1,m'+1) + \mathrm{Y}_r(k-1,m') + \\ + \mathrm{Y}_r(k+1,m') + \mathrm{Y}_r(k+1,m'-1)\big) \quad (6)$$

$$\text{for } m' = 1, \ldots, M;\ M = 24.$$

Our next objective is to determine the maximal number of disabled sensors with which the DED

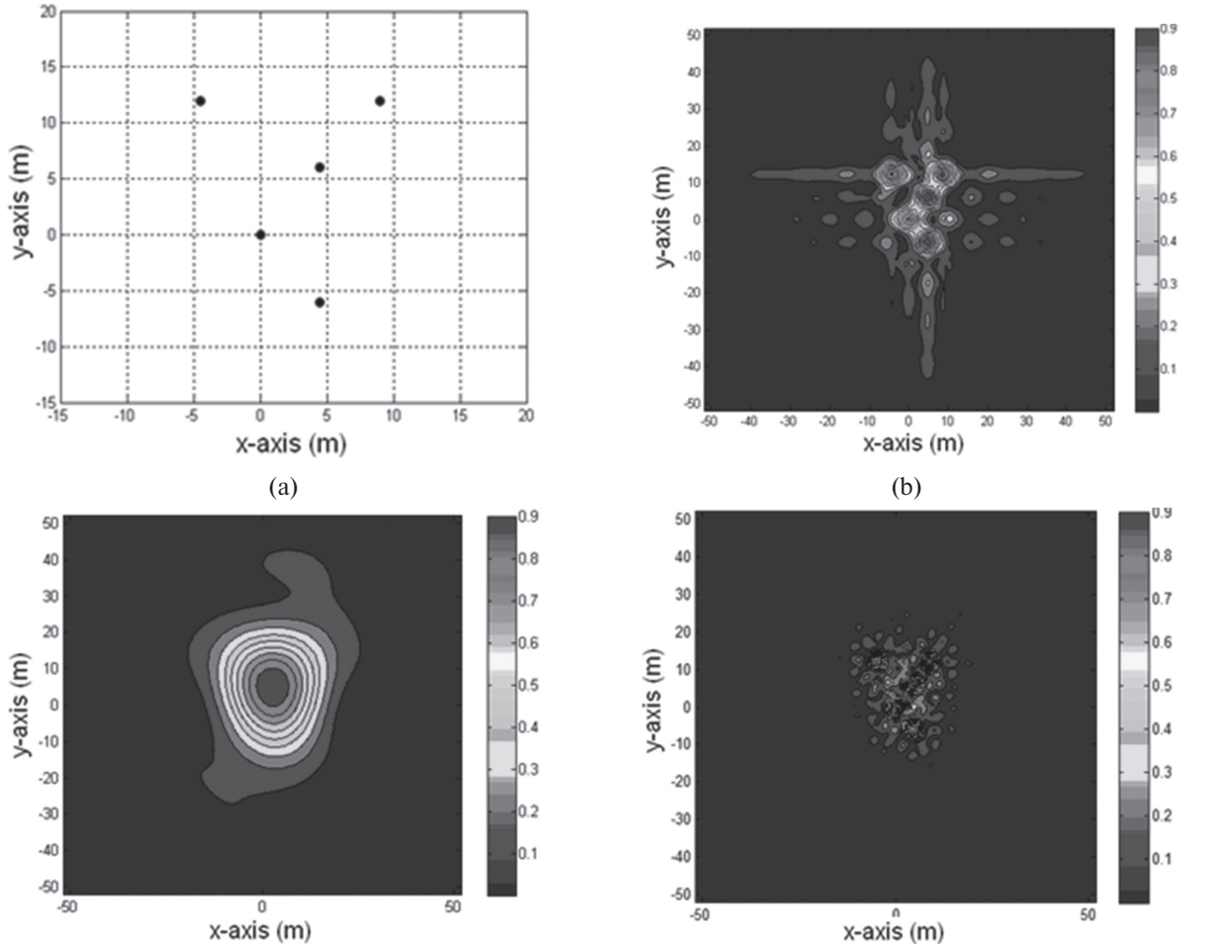

Fig. 9. Multiple target scene imaging protocols: (a) multiple target scene specification; (b) scene image in the *x-y* plane formed with the X-configured imaging array via implementing the technique (2); (c) the same scene image formed with the O-configured imaging array system; (d) the same scene image formed with the Y-configured (GeoSTAR) imaging array system. In all reported simulations, the images have been reconstructed from the data contaminated with additive zero-mean Gaussian noise with the same signal-to-noise ratio, SNR = 20 dB

regularized MSF procedure (2) (DED-MSF) can still operate within some admissible performance degradation level. In Fig. 12, the related simulation results are shown for the 4-NNI method (6).

IV. OPTIMIZATION OF GEOSTAR ARRAY CONFIGURATION

At the HW design level, three configuration "degrees of freedom" that we denote as $\{\gamma, d_A, D_s\}$ influence the overall PSF performances. In particular, parameter γ specifies the adopted array geometry (X, O or Y); d_A is the inter-element spacing, and D_s represents the effective aperture width of a single sensor. Unfortunately, no unique criterion exists for balanced optimization of $\{\gamma, d_A, D_s\}$ aimed at minimization of the resolution cell width over the balanced suppression of the PSF side lobes [6], [11].

That is why, in this study, we perform the solution to the HW-level optimization problem employing a new quality metric that we construct following the general DED framework [4], [5] for minimization of the energy of the main beam (E_M) of the PSF balanced over the normalized energy of the PSF side lobes (E_S). That is, we construct the PSF shape metrics μ_1 (that characterizes the quality of spatial resolution) to be proportional to the energy of the main beam E_M and

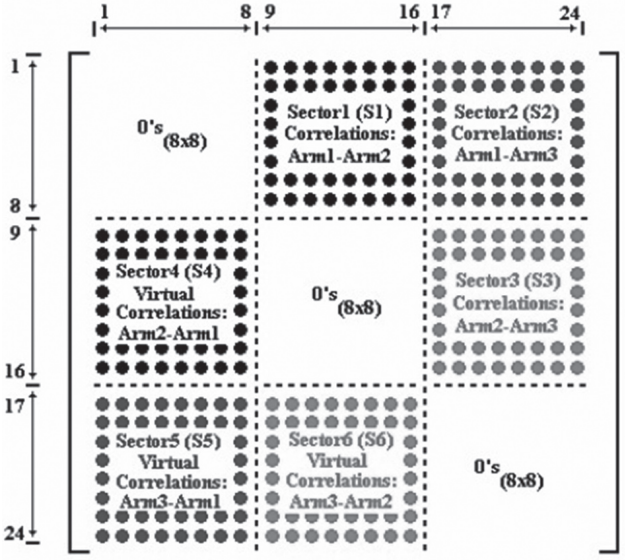

Fig. 10. Illustrating the structure of the DED-sparse GeoSTAR-configured MAR system data correlation matrix $\mathbf{Y}_r$ (collected data signal visibilities)

inversely proportional to the energy of the PSF side lobes energy norm E_S scaled by the factor C_M, i.e.,

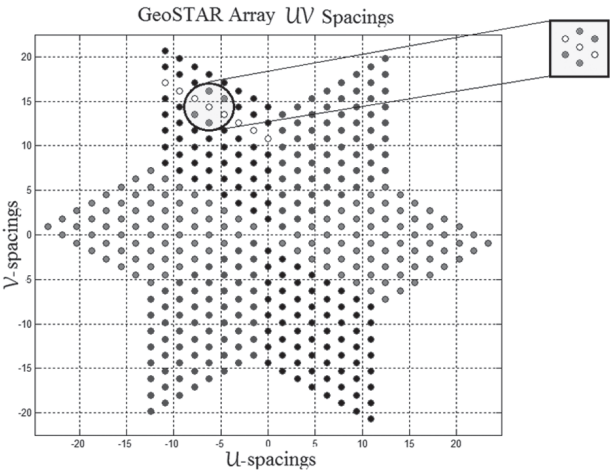

Fig. 11. Graphical description of the 4-NNI algorithm for reconstruction of matrix $\mathbf{Y}_r$ (in the visibility function domain)

$$\mu_1(\gamma, d_A, D_s) = \frac{E_M(\gamma, d_A, D_s)}{E_S(\gamma, d_A, D_s) C_M(\gamma, d_A, D_s)} \quad (7)$$

where the scaling factor

$$C_M(\gamma, d_A, D_s) = \frac{mes_{(0.5)} MB(\gamma, d_A, D_s)}{mes._{(0.1)} SL(\gamma, d_A, D_s)} \quad (8)$$

is calculated by measuring the main beam area $mes_{(0.5)}$ (MB) at 0.5 threshold from its maximum level normalized by the corresponding side lobes area $mes_{(0.1)}$ (SL) measured at 0.1 threshold from the PSF maximum level. We address this metric (7) as an indicator of the efficiency of the employed array configuration subject to three controllable geometrical degrees of freedom (interelement spacing, antenna array geometry and the effective aperture width of a single sensor). In Fig. 13, the performance metric (7) is presented for 10 possible tested inter-element spacings, in particular, $d_{A(1)} = 0.5\lambda_o$, $d_{A(2)} = 0.8\lambda_o$, $d_{A(3)} = 1\lambda_o$, $d_{A(4)} = 1.5\lambda_o$, $d_{A(5)} = 1.8\lambda_o$, $d_{A(6)} = 2\lambda_o$, $d_{A(7)} = 2.5\lambda_o$, $d_{A(8)} = 3\lambda_o$, $d_{A(9)} = 3.5\lambda_o$, and $d_{A(10)} = 4\lambda_o$, with a field of view of 60°. This metric can be also referred to as a normalized probability of target detection [11]. From the analysis of these data of Fig. 13, it follows that the best imaging and detection performances evaluated via metric (7) is achieved with $d_{A(6)} = 2\lambda_o$ as it was previously previsioned in [11].

To quantify the imaging performance in the harsh operational scenarios, we also employed the conventional signal-to-noise improvement (SNI) metric

$$\mu_2 = \frac{\sum_{(x_i, y_j)} |picId - picN|^2}{\sum_{(x_i, y_j)} |picId - picOb|^2} \quad i, j = 1, \ldots, N \quad (9)$$

where N represents the number of pixels in the image scene (at a particular range gate), $picId$ is the hypothetical ideal image, $picN$ is the MSF image formed

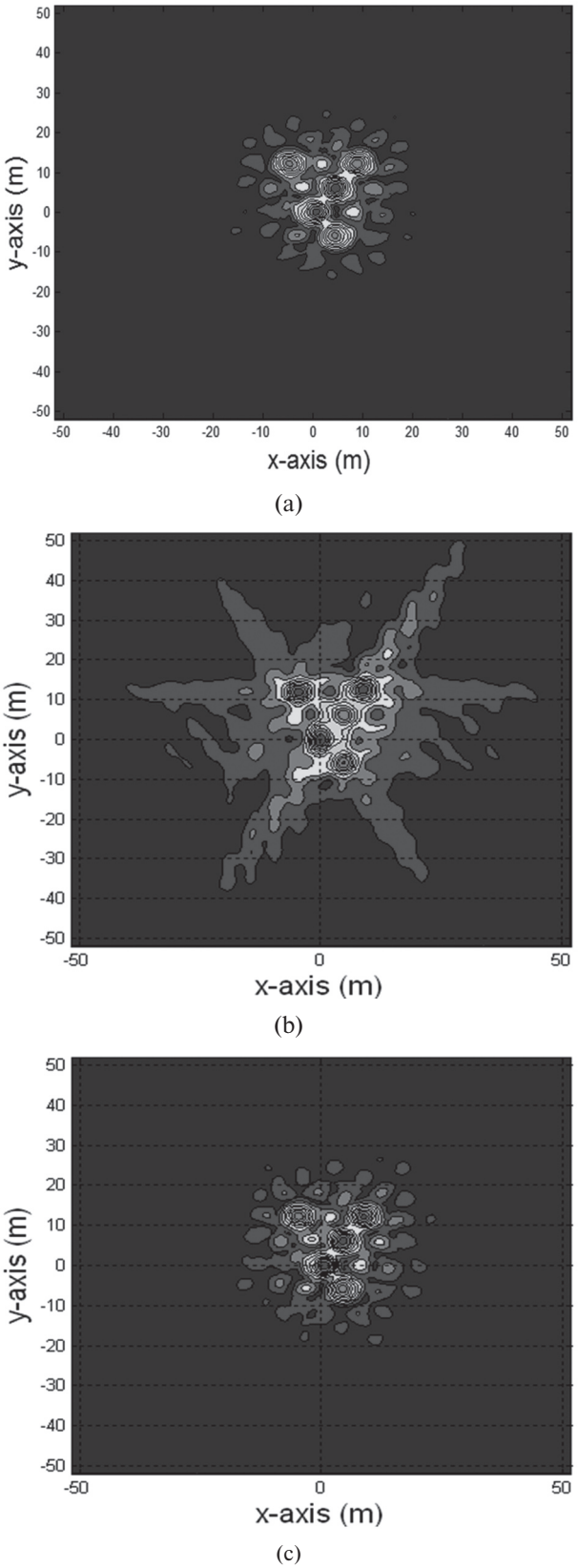

Fig. 12. Multiple target scene imaging protocols for 2λ inter-element spacing: (a) TAGs scene image in the x-y plane formed with the Y-configured imaging array via implementing the MSF technique (2) for 30m range gate (scenario without operational uncertainties); (b) scene image formed for the same range gate with 5 disabled sensors (without employing any correcting algorithm); (c) the same scene image with the same 5 disabled sensors formed via aggregating the MSF technique (2) with the 4-NNI method (6). All scene images have been reconstructed from the data contaminated with additive zero-mean Gaussian noise with the same signal-to-noise ratio, SNR = 20 dB

in a scenario without operational uncertainties and *picOb* is the corresponding DED-MSF image formed in a harsh (uncertain) scenario. The difference between the desired image and the actually formed distorted image is calculated via (9). In Fig. 14 the SNI values (9) are presented in a graphical format.

As it was mentioned before, one of the goals of the undertaken analysis is to determine the maximal number of disabled sensors with which the MAR that employs the DED-MSF method (2) can still operate within some performance degradation tolerance level. It is reasonably to specify such the level via the admissible SNI losses, e.g., –3 dB SNI losses.

Based on the analysis of the performances reported in Fig. 14, one may conclude that at the admissible –3 dB SNI loss threshold level, the DED-MSF (2) can still operate with up to 7 disabled sensors when aggregated with the DED regularized 4-NNI technique (6).

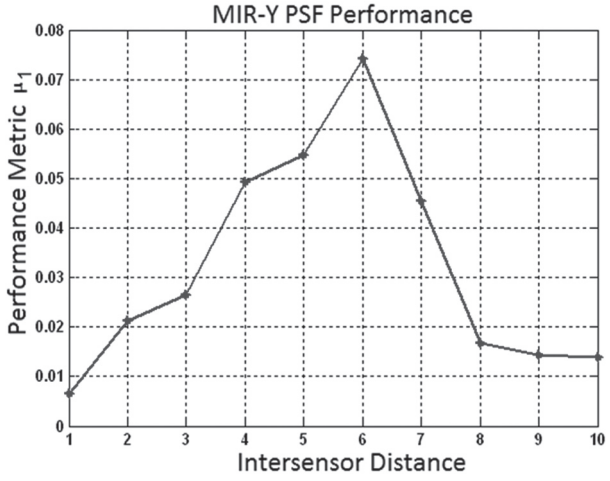

Fig 13. μ_1 metric for the MAR-MSF technique (2) for Y-configured MAR

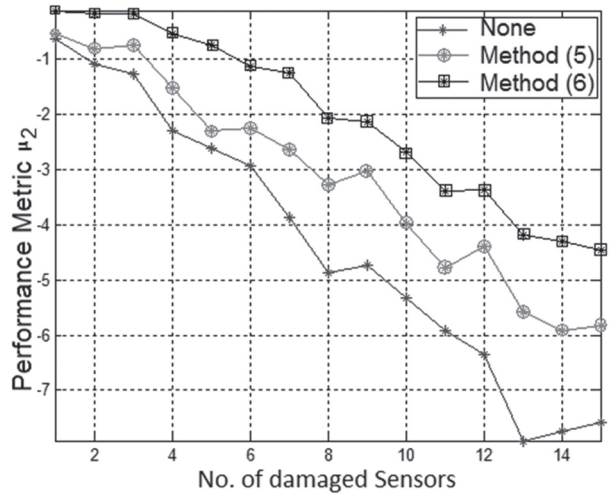

Fig 14. μ_2 metric for the MAR-MSF technique (2) for Y-configured MAR. The μ_2 metric characterizes the SNI loses dependent of the number of disabled sensors

DISCUSSIONS AND CONCLUDING REMARKS

We have addressed the new robust DED approach for enhanced imaging of multiple target scenes in harsh operational environments directly adapted to MAR imaging systems with different array configurations. We have also presented the detailed analysis of operational performances for uncertain operational scenarios, in particular, with antenna array sensor displacement due to damage or manufacturing errors and/or some possibly disabled sensors. The reported performance analysis establishes the tolerance to such harsh operational uncertainties admissible with the proposed robust DED-MSF imaging procedure.

The presented high-resolution target localization protocols are indicative of the superior operational efficiency of the Y-configured multimode imaging MAR system with the adopted GeoSTAR array geometry. The reported PSFs provide explicit information on the spatial resolution achievable with such MAR system that employs the proposed DED-robustified MAR-MSF image formation technique. We demonstrated via the analysis of behavior of μ_1 quality metric that the inter-element sensor spacing $d_{A(6)} = 2\lambda_o$ yields the best imaging performances for the 60° adopted field of view; the larger inter element spacings ($d_A > 2\lambda$) result in undesirably high artifacts (inadmissibly high grating sidelobes level) that is strongly undesirable for the target localization problems. For the purpose of precise multiple target localization, we established an admissible SNI loss threshold of –3 dB and found that the robustified DEDR-MSF technique admits operating for up to 7 disabled sensors. In future studies, we intend to focus on the HW-SW co-design aimed at the resolution enhancement of the DED-MSF imagery and approaching the super-resolution imaging performances with MAR systems.

REFERENCES.

[1] A.B. Tanner *et al*, "Initial Results of the Geosynchronous Synthetic Thinned Aperture Radiometer (GeoSTAR)", *IEEE Inern. Symposium on Geoscience and Remote Sensing, IEEE IGARSS 2006*, ISBN 0-7803-9510-7/06, pp. 3951-3954, 2006.

[2] Y. Shkvarko, "Estimation of wavefield power distribution in the remotely sensed environment: Bayesian maximum entropy approach", *IEEE Trans. Signal Proc.*, vol. 50, No. 9, pp. 2333-2346, 2002.

[3] Y. Shkvarko, "Unifying regularization and Bayesian estimation methods for enhanced imaging with remotely sensed data—Part I: Theory", *IEEE Trans. Geoscience and Remote Sensing*, vol. 42, No. 5, pp. 923-931, (2004).

[4] Y. Shkvarko, "From matched spatial filtering towards the fused statistical descriptive regularization method for enhanced radar imaging", *EURASIP J. on Applied Signal Processing*, vol. 2006, Article ID 39657, pp. 1-9. (2006).

[5] Y. Shkvarko, "Unifying experiment design and convex regularization techniques for enhanced imaging with uncertain remote sensing data—Part I: Theory", *IEEE Trans. Geoscience and Remote Sensing*, vol. 48, No. 1, pp. 82-111, 2010.

[6] Y. Shkvarko and V. Espadas, "Experiment Design Framework For Super-High Resolution Imaging With The GeoSTAR Configured Sensor Array Data", *The Seventh International Kharkov Symposium on Physics and engineering of Microwaves, Milimiter and Submilimiter Waves MSMW'10, ,* ISBN 978-1-4244-7898-9/10, 2010.

[7] *Principles and Applications of Imaging Radar*, *Manual of Remote Sensing*, 3d ed., F.M. Henderson and A. V. Lewis, Eds., vol. 3, NY: Willey, 1998.

[8] H.H. Barrett and K.J. Myers, *Foundations of Image Science*, NY: Willey, 2004.

[9] J.C. Curlander and R. McDonough, *Synthetic Aperture Radar––System and Signal Processing.* NY: Wiley, 1991..

[10] D.R. Wehner, *High-Resolution Radar*, 2nd ed., Boston, MA: Artech House, 1994.

[11] Y. Shkvarko, V. Espadas, and D. Castro, "Descriptive Experiment Design Optimization of GeoSTAR Configured Multisensor Imaging Radar", *4th International Radio Electronics Forum* (4th IREF'2011), Kharkov, Ukraine, Vol. I, pp. 76-81, Oct. 2011

Manuscript received February, 14, 2013

V. E. Espadas (S'10) was born in Merida, Yucatan, Mexico, on May 17, 1985. He received his Bachelor of Science degree in Electronic Engineering from the Institute of Technology of Merida (ITM), Merida, Mexico, in 2008 and the M.Sc. degree in Electrical Engineering from the Centro de Investigaciyn y de Estudios Avanzados del Instituto Politйcnico Nacional (Superior Education and Research Center of the National Polytechnic Institute of Mexico, CINVESTAV-IPN), Guadalajara, Mexico, in 2011. He is currently working towards the Ph.D. degree at the Department of Electrical Engineering, Communications Division, at the CINVESTAV-IPN. His research interests are in applications of signal processing of remote sensing, radar imagery, statistical sensor array data processing and communications.

Yuriy V. Shkvarko (M'95–SM'04) received the Dip. Eng. (Hon.) degree in electrical engineering, the Ph.D. degree in radio engineering, and the Dr. Sci. degree in radio physics, radar, and navigation from the Kharkov Aviation Institute, Kharkov, Ukraine, in 1976, 1980, and 1990, respectively. From 1976 to 1991, he was with the Scientific Research Department of the Kharkov Aviation Institute (presently National Airspace University of Ukraine), as a Research Fellow, a Senior Fellow, and a Chair of the Research Laboratory in information technologies for radar and navigation. From 1991 to 1999, he was a Full Professor with the Department of System Analysis and Control, Ukrainian National Polytechnic Institute, Kharkov. From 1999 to 2001 he was an Invited Professor with the Guanajuato State University at Salamanca, Mexico. Since 2001, he has been with the "Centro de Investigaciyn y de Estudios Avanzados del Instituto Politйcnico Nacional" (Superior Education and Research Center of the National Polytechnic Institute of Mexico), Guadalajara, Mexico, as a Full Titular Professor. He holds 12 patents and has published two books and some 160 journal and conference papers. His research interests are in applications of signal processing to remote sensing, imaging radar, navigation, and communications, particularly in inverse problems, random fields estimation, adaptive spatial analysis, statistical sensor array and multimode remote sensing data processing, and system fusion.

УДК 621.396

Метод регуляризации на основе дескриптивного планирования экспериментов для формирования высокоразрешающих радиоизображений в мультимодальных РЛС с антенными решетками / В.Э. Эспадас, Ю.В. Шкварко // Прикладная радиоэлектроника. – 2013. Том 12. № 1. – С. 157-165.

Предложен новый метод регуляризации обратных задач формирования радиолокационных (РЛ) изображений с улучшенным разрешением на основе теории дескриптивного планирования экспериментов (ДПЭ) дистанционного зондирования. Для необходимой избыточности РЛ измерений используется многомодовая поляризация, позволяющая комплексировать РЛ изображения отдельных мод и обеспечить робастность обработки сигналов в различных операционных сценариях. Предложенный ДПЭ-подход осуществляет робастную модификацию метода Ван-Циттерта — Цернике для РЛС с антенными решетками. Метод реализуется в форме банка согласованных фильтров формирования РЛ изображений на различных модах. Форма результирующей вещественной функции неопределенности оптимизируется на основе метода ДПЭ-регуляризации, который реализует оптимальный баланс между повышением разрешения и фильтрации помех, адаптированный к сценариям визуализации множественных целей в условиях статистической априорной неопределенности. Численное моделирование подтверждает эффективность предложенного метода формирования высокоразрешающих РЛ изображений множественных целей в статистически неопределенных операционных сценариях.

Ключевые слова: антенная решетка, дескриптивное планирование экспериментов, многомодовая РЛС формирования изображений, регуляризация.

Ил. 14. Библиогр.: 11 назв.

УДК 621.396

Метод регулярізації на основі дескриптивного планування експериментів для формування високорозрізняючих радіозображень в мультимодальних РЛС з антенними решітками / В.Е. Еспадас, Ю.В. Шкварко // Прикладна радіоелектроніка. – 2013. Том 12. № 1. – С. 157-165.

Запропоновано новий метод регуляризації обернених задач формування радіолокаційних (РЛ) зображень з покращеним розрізненням на основі теорії дескриптивного планування експериментів (ДПЕ) дистанційного зондування. Для забезпечення необхідної надмірності РЛ вимірювань використовується багатомодова поляризація, що дозволяє скомплексувати РЛ зображення окремих мод і забезпечити робасність обробки сигналів у різних операційних сценаріях. Запропонований ДПЕ-підхід здійснює робастну модифікацію методу Ван-Циттерта — Церніке для РЛС з антенними решітками. Метод реалізується у формі банку узгоджених фільтрів формування РЛ зображень на різних модах. Форма результуючої дійсної функції невизначеності оптимізується на основі методу ДПЕ-регуляризації, який реалізує оптимальний баланс між підвищенням розрізнення та фільтрації перешкод, адаптований до сценаріїв візуалізації множини цілей в умовах статистичної апріорної невизначеності. Кількісне моделювання підтверджує ефективність запропонованого методу формування високорозрізняючих РЛ зображень множини цілей у статистично невизначених операційних сценаріях.

Ключові слова: антенна решітка, дескриптивне планування експериментів, багатомодова РЛС формування зображень, регуляризація.

Іл. 14. Бібліогр.: 11 найм.

NOISE RADAR TECHNIQUE IN OPTICS AND SEISMOLOGY

UDC 681.785.57

NANO-DISTANCE MEASUREMENTS USING SPECTRAL INTERFEROMETRY BASED ON LIGHT-EMITTING DIODES

K.A. LUKIN, M.B. DANAILOV, Yu.P. MACHEKHIN, AND D.N. TATYANKO

The paper presents some results of the optical interferometry investigations based on the noise spectral interferometry method with use of low-coherent optical sources beyond their coherence zone. It is shown that when the path difference of arms in Michelson interferometer exceeds the coherence length of light-emitting diode radiation, the interference pattern in spectral domain enables to perform absolute measurements of micro- and nanodistances due to its dependence on both time delay and relative phase of the signals.

Keywords: spectral interferometry method, optical coherence tomography, Michelson interferometer, light-emitting diode, optical noise signal.

INTRODUCTION

Interferometry based on application of lasers with highly stabilized frequency provides precise measurements of linear shifts within the range of few millimeters up to tens of meters. Real application of existing laser interferometers for nano-scale measurements, i.e. for the scale much smaller of the laser wavelength, suffers of insufficient short-term stability of the laser frequency. The latter does not allow carrying out interferometric measurements of micro and nano distances. Which considerably limits applications of laser interferometers for nano distances measurements.

Therefore the search of alternative methods for optical interferometry methods has resulted at the end of the last century in development of optical coherence tomography (OCT) [1]. OCT performs cross-sectional imaging by measuring the magnitude and echo time delay of backscattered light [1]. OCT has found applications in such areas of medicine as ophthalmology, stomatology, dermatology, cardiology, etc. OCT is used in an industry for studying of material surface characteristics, surface roughness and other applications. In particular, in the paper production industry it is used for paper quality inspection.

The spectral interferometry method are researched and developed in radio-frequency region at Laboratory for Nonlinear Dynamics of Electronic Systems (LNDES) of Usikov Institute for Radiophysics & Electronics, NASU (Kharkov, Ukraine) long time [2-5]. Now, LNDS, Kharkov National University of Radio and Electronics (KHNURE, Kharkov, Ukraine) and Laser Laboratory of Synchrotron (Trieste, Italy) in common begin investigations of the spectral interferometry in an optical band for a nanometrology [6, 7].

In the papers, theoretical and experimental results on further elaborations of the noise spectral interferometry method for the micro-distances measurements are presented. In particular it has been found, which kind of optical sources can be used for such measurements, and which limit of measurement accuracy has been achieved.

1. THEORETICAL BASICS OF SPECTRAL INTERFEROMETRY METHOD

The method of noise spectral interferometry (or a method of double spectral processing) is based on a linear interference of spectral components of the noise probing and reflected signals [2-7] provided the distance to probing object exceeds the coherence length of the radiated signal:

$$l_c = \frac{c}{\Delta f}, \qquad (1)$$

where Δf is the width of the frequency spectrum of the noise probing signal, c is the speed of light in vacuum.

The method can be realized with the help of a classical Michelson interferometer.

In case of a single reflector, the power spectrum, $F_\Sigma(f)$, of the signal at the interferometer output (at the photodetector input) may be represented as follows:

$$F_\Sigma(f,\tau_0) = 2F(f)\{1+\cos(2\pi f\tau_0+\theta)\}, \qquad (2)$$

where θ is the phase difference between reference and reflected signals, t is current time, τ_0 is time of propagation of the signal up to the reflector and back, f – the frequency of harmonic spectral components of the broadband spectrum of optical radiation.

The analysis [3] of the power spectrum, $F_\Sigma(f)$, of the total (probing and reflected) signal allows to obtain the information about the distance to the reflector placed at the range L_0.

The power spectrum (2) is valid for infinite number of averaging, which is not achievable in practice. That is why we will suppose that in the measurements we are dealing with ergodic random signals, and averaging over ensemble of realizations may be substituted with averaging over time. The average interval is to be long enough to minimize scattering in the power spectrum estimation due to random nature of the probing signal. A large enough time-bandwidth product $\Delta f T_{mes} >> 1$ normally be used as criterion for choosing of an appropriate measurement/integration time T_{mes}.

It is seen that power spectrum (2) contains periodic alternations of maxima and minima along the

frequency (wavelength) axis, which are (as it is shown in [3]) the results of constructive, distractive and intermediate interferences of harmonic spectral components of the stationary signals being summed in the output arm of the interferometer. The period of these alternations is inversely proportional to the time-delay τ_0 of the reflected signal with respect to the reference one which enables estimating the reflector distance. For this purpose the difference Δf_m of frequencies f_1 and f_2 is to be measured, corresponding to positions of two neighboring extrema (maximum or minimum) in the power spectrum (2) and the distance are tied via the following formula [2-7]:

$$L_0 = \frac{c}{2\Delta f_m} = \frac{c}{2(f_1 - f_2)}. \quad (3)$$

2. EXPERIMENTAL SETUP

For realization of the noise spectral interferometry method for nanodistance measurement an experimental setup of the optical Michelson interferometer (hereinafter - the interferometer) was assembled. The block diagram of the setup is showed in fig. 1.

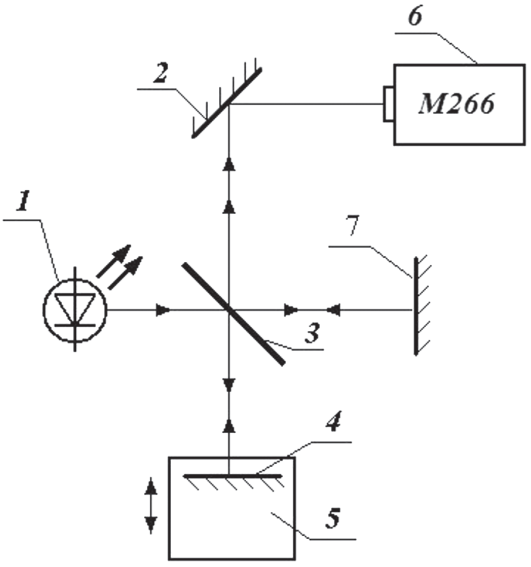

Fig. 1. Block diagram of the experimental setup. The Michelson interferometer. 1 – the source of random optical radiation (Toshiba TLRH190P LED); 2 – mirror, 4, 7 – Ag mirrors (Metal Mirror Ag: Er2, Newport); 3 – beam-splitting plate 50/50 (10RQ00UB.2, Newport); 5 – translation stage (F1-055/721299 Magini and C firms with micrometric screw TESA with 2 μm grating period); 6 – spectrum analyzer (on the basis of "M266 Solar Laser Systems" monochromator/spectrograph, made in Byelorussia)

The period of alternation of the spectrum extrema increases, when reducing the measured distance, therefore it is required to use not only wideband sources of radiation, but also wideband optical spectrum analyzers. "M266 Solar Laser Systems" monochromator/spectrograph (Byelorussia) has been used as the spectrum analyzer. It has a diffraction grating of 1200 lines/mm and a photodiode array with 2048 channels. Average value of a spectrum resolution of the M266 is less than 0.22 nm.

Investigation of the spatial interference has been carried out with the aim of estimation of the coherence length. Interference fringes in cross-section of a beam are visible within the limits of the coherence length of the radiation source. Hence, we can find the coherence length of the source if we determine visibility of the interference fringes.

3. OPTICAL NOISE SIGNALS SOURCES

Several methods may be applied to obtain band limited noise optical signals with various size of a spectrum width [6, 7]. One of them is noise modulation of the optical signal generated in a single-frequency and a single mode He-Ne laser using an acousto-optic modulator. At all advantages of this method it is very expensive. Other method is to use a single-mode radiation of semiconductor lasers. Semiconductor lasers being based on usual technology, work with a Lorentz radiation line-width up to 200 MHz. This width depends on a working current of the semiconductor laser, therefore it is possible to provide its increase or small reduction depending on the selected operating mode of the semiconductor laser.

Another perspective source of random optical radiation which can be used in optical noise radar or OCT is a femtosecond laser (PL) which works in a mode of generation of white light (supercontinuum) [8, 9]. PL have an extremely wide range of light (hundreds of nanometers) in the infrared region with central wavelengths of 800 nm, 1000 nm, 1300 nm. These wavelengths semiconductor PL emit, for example, Ti:Al2O3, Nd:Glass or Yb fiber, and Cr:Forsterite lasers. Axial image resolution in OCT systems based on these lasers reaches 4.1 microns. The main disadvantage of the PL is their relatively high cost, which imposes a limit on the scope of their application.

In the literature on measurements of nano-distances researches in which were used low-coherence radiation sources with a wide spectrum width were already described [10, 11]. Due to this feature of the used optical radiation sources, the given area of measurements refers to as a low-coherence interferometry or a white-light spectral interferometry.

In industrially released measuring devices (microscopes, profilometers, etc.) and in researches described in a scientific literature, as the sources of optical radiation so-called superluminescent diodes, various kinds of lamps (tungsten- and quartz lamps) are usually used [12, 13]. But the lamps have low power spectral density.

The most frequently used radiation sources for the spectral interferometry, for example, for the OCT, are superluminescent diodes due to their high spectral power and relatively low cost. Superluminescent diode (SLD) is a light-emitting diode operating in a superluminescence mode. The SLD has characteristics which is necessary to implement OCT inherent in LEDs and lasers. The SLD is similar to semiconductor lasers which amplifies spontaneous emission pn-junction. But, unlike a laser, SLD has no reflecting mirror surfaces, ie, there is no cavity. So, resulting

radiation output of SLD is not monochromatic like a laser radiation and contains all wavelengths in the band of gain. Thus, it has a wide band, like LEDs, which is necessary for the implementation of OCT.

Positive qualities of the SLD are high power radiation (tens of milliwatts), like lasers and broad spectral band, like LEDs, tens of nanometers. For greater tissue penetration now SLD with a wavelength of 1300 nm are used, which can reach an axial resolution of 10 microns. For OCT applications SLD with greater spectral width are required. Therefore the rapid development of technology has led to the emergence of a composite SLD. Spectral width of the source exceeds the 150 nm and, therefore, it has a better axial resolution (5.3 microns).

The most cost-effective source of noise optical radiation, which could provide distances measurements from one micron and less, is an ordinary light-emitting diode (LED), the spectrum width of which exceeds that of a semiconductor laser. It allows expanding the range of measured distances towards its reduction.

In the present paper we suggest to use the LEDs which are released serially for indication and illumination needs, namely Toshiba TLRH190P InGaAlP LED and OSHR5111P LED from OptoSupply.

The researched Toshiba TLRH190P LED has the following characteristics: a central wavelength of the LED radiation is 645 nm with spectrum width at half is about 15 nm; Radiation level from the LED output diverges within the 40 angle only. Due to these properties, radiation of the LED has been used in interferometer without additional collimation and beam focusing.

The manufacturer positions the given type of LEDs as «LED Lamp» by virtue of high brightness of radiation which is 19 cd. The example of spectral characteristic of TLRH190P LED radiation is shown in fig. 2.

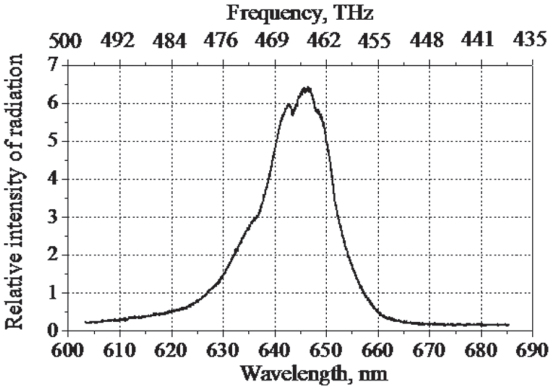

Fig. 2. Radiation Spectrum of the Toshiba TLRH190P LED

Also second type of LED named OSHR5111P from OptoSupply Company was investigated. Light intensity of the OSHR5111P LED is 50 cd, a radiation wavelength under LED manual is 625 nm (at an experimental sample it is about 637 nm), a divergence angle at 3dB level of the maximal radiation intensity is 15 degrees; a width of a spectrum is about 20 nm. The example of spectral characteristic of the OSHR5111P LED radiation is shown in fig. 3.

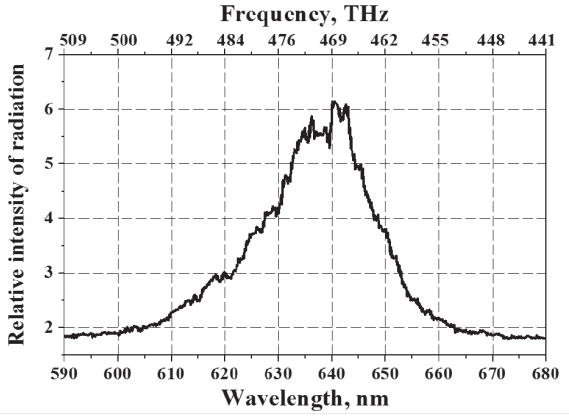

Fig. 3. Radiation Spectrum of the OptoSupply OSHR5111P LED

4. THE MEASUREMENT METHOD AND MEASUREMENTS RESULTS

After the interferometer has been checked up in conditions of the spatial interference in the coherence zone of radiation, its tuning has been done. Then the difference of the interferometer arms has been increased more than the coherence length. After that the spatial fringes vanished and a periodical structure appeared in the spectral area, i.e. in the noise radiation spectrum which has been registered at the interferometer output, the spectral interference was observed which is well described by the equation (2). If the mounted difference of the interferometer arms is more than the coherence length of the LED noise radiation the periodic structure has been observed in the registered radiation spectrum. The radiation spectrum at the interferometer output for the case of the arms difference exceeds the LED coherence length is shown in fig. 4a. Fig. 4b shows result of Fourier analysis of the Toshiba TLRH190P LED spectrum that is shown in fig. 4a [7].

Fig. 5 shows the radiation spectrograms and the result of Fourier analysis of the OptoSupply OSHR5111P LED.

Estimated value of a spectral fringes contrast is 0.27 for the Toshiba TLRH190P LED and 0.45 for the OptoSupply OSHR5111P LED. For example, the spectral fringes contrast of the superluminescent diode used in the work [11] and shown in Fig. 6 equal 0.6. So it has similar value with the researched LEDs.

The considered spectra have a similar periodic channels structure with a good contrast of spectral fringes (lines). Due to this Fourier-processing of the spectra in these cases enables to determine unequivocally a time delay of signals between interferometer arms and hence the difference of interferometer arms lengths, i.e. allows to determine distances.

Fig. 7 shows the dependencies of the time delay between the signals, which are distributed in the arms of the interferometer (signals of the interferometer arms) based Toshiba TLRH190P LED (that is proportional to the measured distance), on the position of the measure arm mirror of the interferometer near the coherence zone [7].

Scanning began outside of the coherence zone, passed through the coherence zone (the interferometer arms are equal), and came to an end behind the

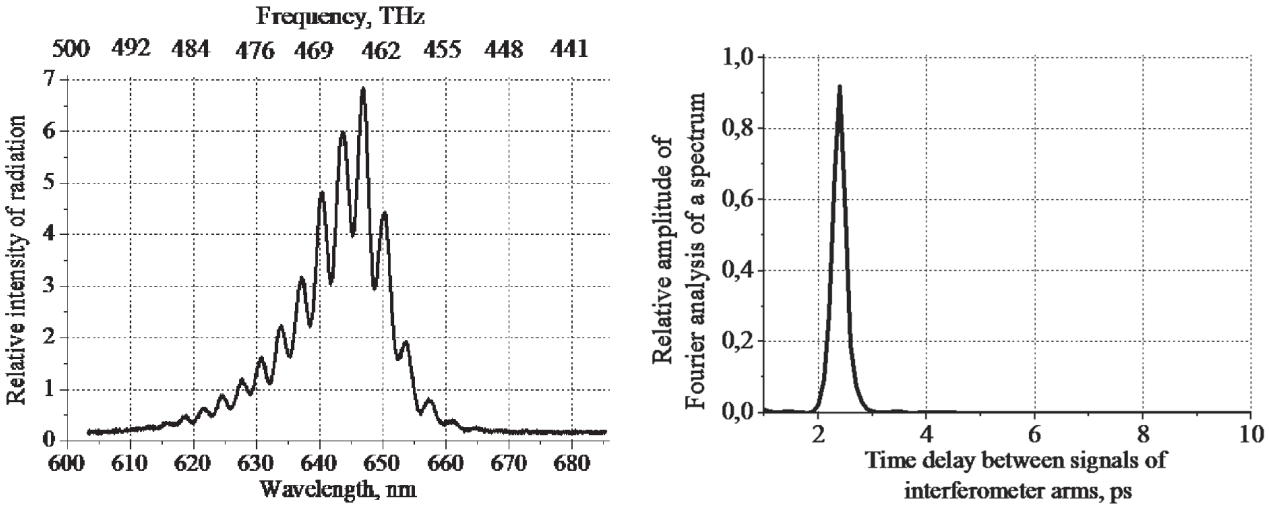

a *b*

Fig. 4. *a* — Power spectrum of noise optical radiation of the Toshiba TLRH190P LED at the output of the Michelson interferometer: the arms difference exceeds the coherence length of the LED noise radiation; *b* — the result of the second Fourier transform being applied to the spectrogram of fig. 4a

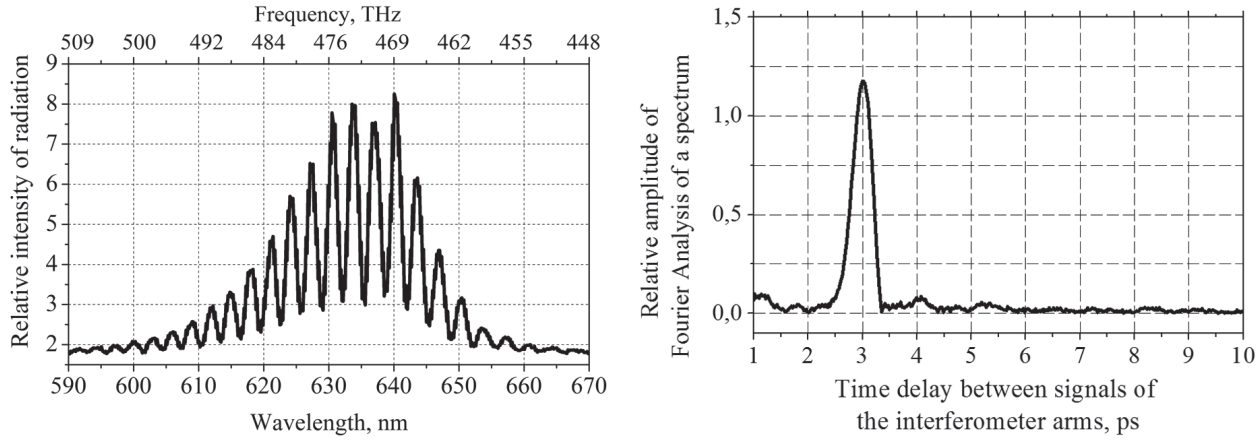

a *b*

Fig. 5. *a* — Power spectrum of noise optical radiation of the OptoSupply OSHR5111P LED at the output of the Michelson interferometer: the arms difference exceeds the coherence length of the LED noise radiation; *b* — the result of the second Fourier transform being applied to the spectrogram of fig.5a.

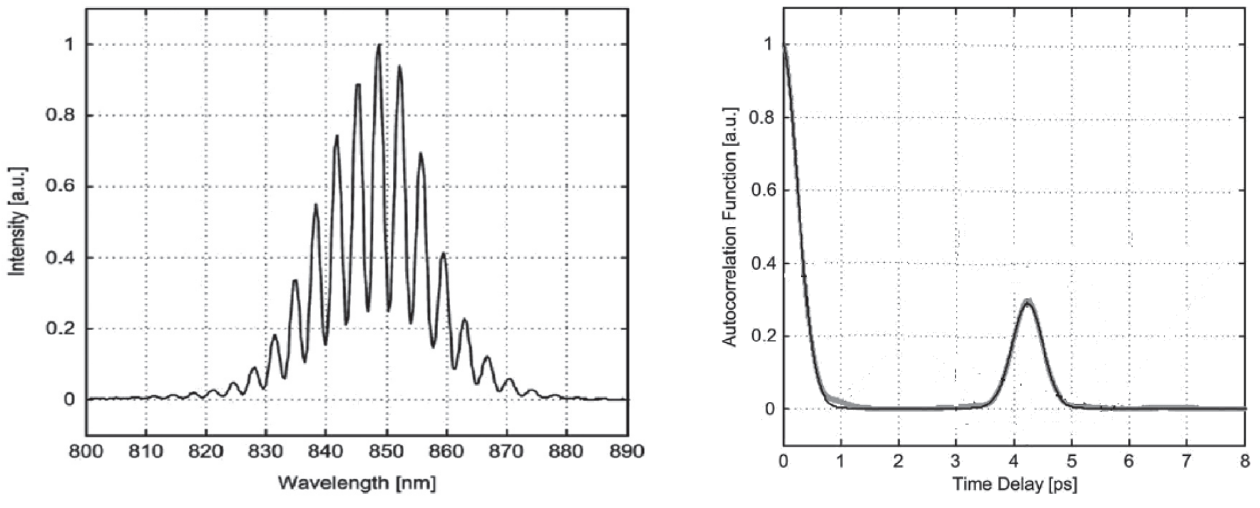

a *b*

Fig. 6. SLD characteristics: *a* — the output channelled spectrum from the SLD based optical-fiber Fabry-Perot interferometer [11]; b — the autocorrelation function of the spectrum in Fig. 6a.

coherence zone. As a result it is possible to observe behavior of the radiation spectrum from the output of the interferometer on borders of the coherence zone.

The interferometer arms difference was changed with a step 1 μm. On the abscissa axis of the diagrams of fig. 7 and 8, position of the mirror of the measuring interferometer arms at begin of scanning was accepted as zero value for simplicity of perception.

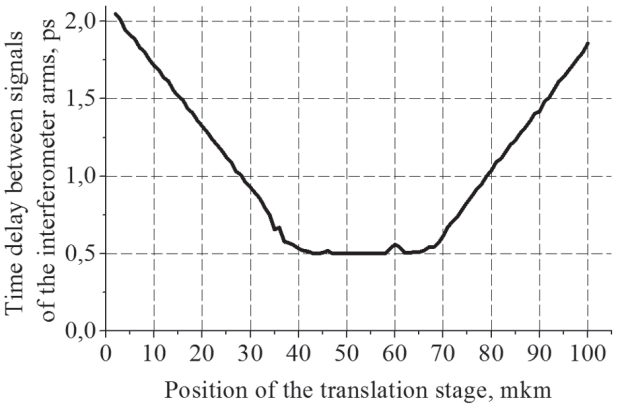

Fig. 7. The experimental dependencies the time delay between the signals of the Toshiba TLRH190P LED based interferometer arms on the position of the measure arm mirror of the interferometer near the coherence zone.

At position of the measuring interferometer arm mirror 4 (fig. 2) in a range ~35-69 μm (fig. 7) the periodicity of the structure of the LED spectrum is practically not observed, i.e. the spectral interference in the given area is absent. The given range is ~34 μm, i.e. about ±17 μm from a point of interferometer arms equality. Meanwhile, as it has been told earlier, the experimental researches of the spatial interference have shown that the radiation coherence length from the output of the interferometer is ~16-18 μm. Thus, it is possible to draw a conclusion that the spectral interference effect begins to be shown abroad the coherence zones i.e. on the distance exceeding the coherence length.

The relative error of the measurement presented in fig. 7, corresponding to the maximal absolute error at confidence probability 0.95 is 1.5-3 %.

The result of the measurements for the interferometer arms difference within the range more than 1 mm is shown in fig. 8. The interferometer arms difference was changed with step 10 μm. The top border of a distance range was limited to resolution of the measuring equipment, i.e. the Solar M266 monochromator/spectrograph. Fig. 8 presents the experimental dependence of inversely of the period of the radiation spectrum non-uniformity of the Toshiba TLRH190P LED on the interferometer arms difference in ranges more than 1 mm [7].

The diagram in fig. 8 shows linear dependence of the period in the radiation spectrum pattern on the interferometer arms difference. Thus, knowing the period of the spectrum pattern of the LED, we can determine the interferometer arms difference, i.e. in case of use of the given circuit in a distancemeter, we can determine the distance up to the object the above accuracy.

The relative error of the measurement presented in fig. 8 is about 0.5% for the maximal absolute error at the 0.95 confidence probability.

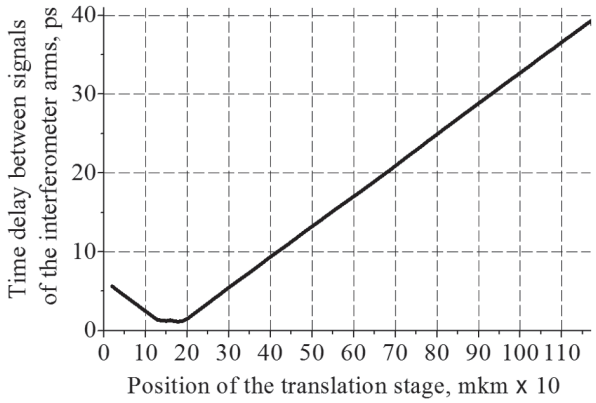

Fig. 8. The experimental dependencies the time delay between the signals of the Toshiba TLRH190P LED based interferometer arms on the position of the measure arm mirror of the interferometer.

At change of the interferometer arms difference by 1 μm (minimally possible step for the used mechanics) the period of the spectrum structure changes on the average by 2.5 nm. The spectrum analyzer has its 0.22 nm wavelength resolution, which gives a distance resolution of the measuring setup under consideration to be not less than 100 nm.

CONCLUSIONS

The paper describes the theoretical model of the noise spectral interferometry in an optical band. As the result of experimental test of the method of optical spectral interferometry the possibility of periodic modulation of the radiation spectrum of the Toshiba TLRH190P LED and OptoSupply OSHR5111P LED have been shown. This is shown possibility of use of the low-cost industrial-produced low-coherent optical radiation sources for measure the micro- and nanodistances using the method of spectral interferometry. The authors suggest and see the perspectives of using such LEDs in OCT devices, as they are much cheaper superluminescent diodes commonly used in the OCT. This will reduce the cost of devices based on them.

It was investigated the capability of the application of the noise spectral interferometry for the micro- and nanodistances measurements. Minimum measuring distance is the coherence length of the radiation source. This is due to the fact that the periodicity of structure spectrum is appeared at the distance exceeding the coherence length [7]. So, the minimum measured distance can be down to tens of micrometers or less. For Toshiba TLRH190P LED minimum measured distance determined by its coherence length and is equal ~18 μm [7]. The value of the maximal measured distance is mainly determined by the resolution of measurement equipment.

The work has been carried out within the frameworks of Sandwich Training Educational Programme (STEP) of The Abdus Salam International Centre for Theoretical Physics (ICTP, Trieste, Italy) at Laser

laboratory of Sinhrotron (Elettra, Trieste, Italy) and Laboratory of Nonlinear Dynamics of Electron systems (LNDES) IPE NASU, Kharkov, Ukraine. It has been also supported by the STCU Project 3377.

REFERENCES

[1] W. Drexler and J. Fujimoto. Optical Coherence Thomography: Technology and Applications. Springer Berlin Heidelberg New York, 2008, 1346 p.

[2] B.P. Efimov, K.A. Lukin, V.A. Rakityansky. About transformation of a spectrum of stochastic fluctuations of the auto-oscillator under action of reflections. // Techn. Physics. Journal - 1988. - 58, № 12. - With. 2398-2400(In Russian).

[3] K.A. Lukin. Noise Radar Technology // Radiophysics and electronics. – Kharkov: Institute of Radiophysics and Electronics NASU, 1999.-4, №3.- pp.105-111 (In Russian).

[4] V.V. Kulik, K.A. Lukin, V.A. Rakityansky. Modification of the method of double spectral processing of noise signals. // Ukrainian Metrological Journal. - 1997. - 4. - pp. 28-32 (In Russian).

[5] K.A. Lukin, V.V. Kulyk and A.A. Mogyla. Spectral Interferometry method and autodyne (self-mixing) effect for Noise Radar Application / Proc. Int. Workshop on the Noise Radar Technology, Sept., 18-20, 2002, Yalta, Cremea, Ukraine, pp.179-186.

[6] K.A. Lukin, Yu.P. Machekhin, A.A. Mogila, D.N. Tatyanko, V.M. Babich, A.S. Litvinenko. Laser distance meter on the basis of spectral interferometry method / Applied Radio Electronics: Sci. Mag. – 2010. Vol. 9. № 2. – P. 240-245 (In Russian).

[7] K. A. Lukin, Yu. P. Machekhin, M. B. Danailov, D. N. Tatyanko. Application of the spectral interferometry method for micro- and nanodistances measurement. // Radiophysics and electronics. – Kharkov: Institute of Radiophysics and Electronics NASU, 2011.-2(16), №1.- pp.39-45 (In Russian).

[8] W. Drexler and J. Fujimoto. Optical Coherence Thomography: Technology and Applications. Springer Berlin Heidelberg New York, 2008, 1346 p..

[9] Friedrich Dausinger, Friedemann Lichtner, Holger Lubatschowski. Femtosecond technology for technical and medical applications. Springer Berlin Heidelberg New York, 2004 –326 p.

[10] U. Schnell, E. Zimmermann and R. Dдndliker. Absolute distance measurement with synchronously sampled white-light channelled spectrum interferometry. Pure Appl. Opt. 4, 1995, pp. 643-651.

[11] Lazo M.Manojlović. A simple white-light fiber-optic interferometric sensing system for absolute position measurement. Optics and Lasers in Engineering, 48 (2010) pp. 486–490.

[12] Maruthi M. Brundavanam, Nirmal K. Viswanathan, and D. Narayana Rao. Nanodisplacement measurement using spectral shifts in a white-light interferometer. Applied optics / Vol. 47, No. 34 / 1 December 2008, pp. 6334-6339.

[13] P. Hlubina. Dispersive white-light spectral interferometry to measure distances and displacements / Optics Communications 212 (2002) pp. 65–70.

Manuscript received January, 23, 2013

Konstantin A. Lukin, for photograph and biography, see this issue, p. 24.

Yuri Pavlovich Machekhin, Dr. Sci., winner of the State Prize of Ukraine in Science and Technology, honored metrologist Ukraine, academician of the Academy of Sciences of Applied Radio Electronics, Chair PFEE KNURE. Research interests: laser measuring equipment and optoelectronic devices.

M.B. Danailov, PhD, head of Laser Laboratory of Synchrotron, Trieste, Italy. Research interests: Lasers, laser measuring equipment and optoelectronic devices.

Dmytro Nikolayevich Tatyanko, Junior research worker of LNDES of IRE NASU. Field of research: spectral interferometry for precision distance measurement, precision measurement of energy and spectral characteristics of coherent and noise optical radiation.

УДК 681.785.57

Измерение нано-расстояний с использованием спектральной интерферометрии на основе светодиодов / К.А. Лукин, М.Б. Данаилов, Ю.П. Мачехин, Д.Н. Татьянко // Прикладная радиоэлектроника. – 2013. – Том 12. – № 1. – С. 166–171.

В работе представлены результаты исследований оптической интерферометрии на основе низкокогерентных источников излучения вне зоны когерентности. Показано, что когда разность плеч интерферометра Майкельсона превышает длину когерентности излучения светодиода, явление спектральной интерференции обеспечивает абсолютные измерения микро- и нано-расстояний в соответствии со временем задержки и относительной фазой между опорным и зондирующим сигналами.

Ключевые слова: метод спектральной интерферометрии, томография оптической когерентности, интерферометр Майкельсона, светодиод, шумовой оптический сигнал.

Ил. 08. Библиогр.: 13 наимен.

УДК 681.785.57

Вимірювання нано-відстаней з використанням спектральної інтерферометрії на основі світлодіодів / К.О. Лукін, М.Б. Данаїлов, Ю.П. Мачехін, Д.М. Татьянко // Прикладна радіоелектроніка. – 2013. – Том 12. – № 1. – С. 166–171.

У роботі наведено результати досліджень оптичної інтерферометрії на основі низько-когерентних джерел випромінювання поза межами зони когерентності. Показано, що коли різниця пліч інтерферометра Майкельсона перевищує довжину когерентності випромінювання світлодіода, явище спектральної інтерференції забезпечує абсолютні вимірювання мікро- та нано-відстаней згідно з часом затримки та відносною фазою між опорним та зондуючим сигналами.

Ключові слова: метод спектральної інтерферометрії, томографія оптичної когерентності, інтерферометр Майкельсона, світлодіод, шумовий оптичний сигнал.

Іл. 08. Бібліогр.: 13 найм.

UDC 537.8

ON SEISMIC SIDE-LOOKING LOCATION WITH ANTENNA APERTURE SYNTHESIS

G.Ya. SHAIDUROV, V.V. SUHOTIN, D.S. KUDINOV AND M.A. KOPYLOV

This article has given an assessment of implementation possibilities of the method of seismic location using pulsed non-explosive sources and receivers that are placed in one transport base during the side looking of the geological environment and the synthesis of an equivalent aperture of transceiver antennas.

Keywords: seismic, location, aperture, synthesis, interface.

Nowadays radiolocation method of side looking (RMSL) with the synthetic antenna aperture is the classic way to increase the resolving power of the mapping systems with the location of transmitter and receiver on one carrier - airplane or satellite. [1] This method is also used in the technique of mapping of the sea floor, but with the usage of acoustic excitation and reception with the placement of all the complex on the submarine or surface vessel.

Essence of the method RMSL (Fig. 1) consists in the probing of the ground surface or sea floor with the sequence of pulses and receiving of the reflected signals from the profile plane relative to the transport base. As the transport base is moving, the received signals are stored and summarized, so that along the line of motion there is a synthesis of virtual antenna with the length equal to the summarized section of the transport base trajectory.

Since the length of the section of this trajectory is much higher than the base of transport base, as a result the equivalent length of the synthesized antenna determines the high resolving of the method RMSL.

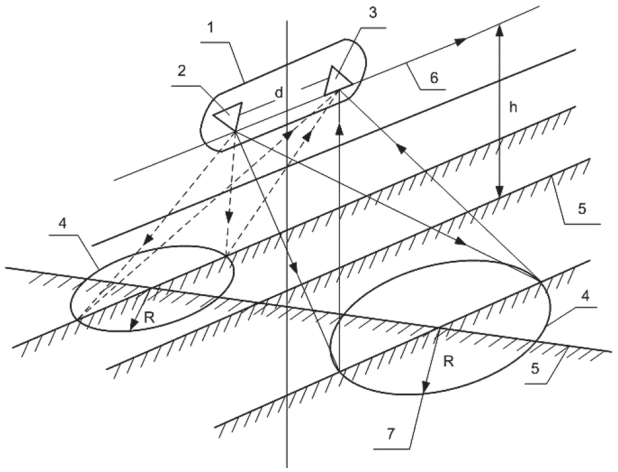

Fig. 1. Scheme of implementation of the method RMSL on one transport carrier: 1 – the transport base (carrier); 2 – the pulse non-explosive emitter; 3 – the geological receiver; 4 – the reflective spot; 5 – the surface of the reflective layer; 6 – the motion line of carrier; 7 – the radius of the first Fresnel zone; h – the depth of the reflective layer position; d – the system base

It is known that during the synthesis of the antenna aperture with the length L, the resolving power of the mapping of soil elements increases by $(L/\lambda)^2$ times, where λ – the length of the used wave.

Concerning the exploration seismology, this method is equivalent to the interference method of signal processing using groups of emitters (sources) and seismic receivers, but with the difference that both of them move together with a fixed distance between them.

This method is known in seismic exploration [2] of the high resolution as the term seismic locator of side looking (SLSL) with the usage of scattered waves. It's advantage is in the opportunity to study the fissuring of geological environment.

Implementation of the method RMSL in motion is possible both on land and water. In the first case, the aperture synthesis is performed simultaneously with the ordinary signal-processing technique, with the difference that geological profile is based on the indications of the seismic receiver or their "cables" that are the nearest to the source.

This technology is particularly relevant for marine exploration seismology with the work of one ship-carrier without the usage of seismometer cable assemblies under tow, as well as with the work on the rivers.

It is known that the work of exploration seismology in the mountain and taiga areas like East Siberia, is very difficult because of the need for heavy equipment, so the implementation of the method RMSL in the motion would solve many problems of exploration seismology that are not realized by other technologies.

For the scientific and technical justification of the method it is necessary to solve the following problems:

- To evaluate the loss in the ratio signal/interference by reduction of the frequency of processing;
- To determine the optimal length of the synthetic aperture taking into account the heterogeneity of the geological environment;
- To solve the technical problem of the simultaneous work of the source and seismic receivers on one transport base;
- To design the project of hardware complex of seismic locator and create a prototype of the water version;
- To carry out experimental and methodological work in the field conditions on the ground, as well as by the cameral treatment of prepared records on well-known deposits.

We will consider the problem of geological mapping in motion by the method RMSL of the two-layer profile including some heterogeneity in the first layer (Fig. 2).

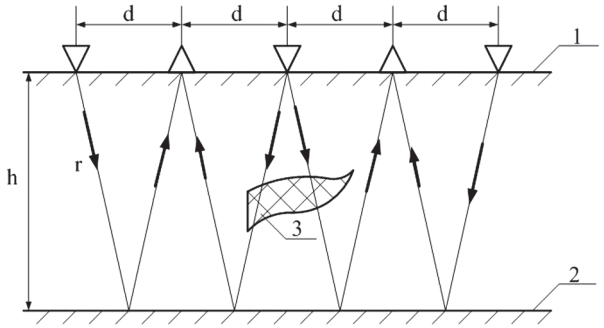

Fig. 2. The problem of geological mapping of the two-layer profile by the method RMSL: 1 – the first layer boundary; 2 – the second layer boundary; 3 – geological heterogeneity

Reflected signals along the line of motion can be written as the following:

$$u_i(t) = U_{mi} e^{-\alpha_i t} \sin(\omega t_i + \varphi_i) \quad (1)$$

where i = 1,2,3 ... – the serial numbers of points of reflection; U_{mi} – the initial amplitude; α_i – the attenuation factor; ω – the operating frequency; t_i – the delay time on the path 2 r_i; φ_i – the initial phase.

Remembering and summation gives the following:

$$u\Sigma(t) = \sum_{i=1}^{n} U_{0i} e^{-\alpha_i t_i} \cdot \sin(\omega t_i + \varphi_i) \quad (2)$$

If in the section of the synthetic aperture L there is m acoustic inhomogeneities with the speed of seismic waves v_j, while the average speed of homogeneous sections is v_{i-j}, then the total signal (2) can be written as the following:

$$u\Sigma H(t) = \sum_{i=1}^{n-j} U_{0i-J} e^{-\alpha_i - jt_i - j} \cdot \sin(\omega t_{i-j} + \varphi_{i-j}) + \\ + \sum_{i=1}^{m} U_{0j} e^{-\alpha_j t_j} \cdot \sin(\omega t_j + \varphi_j). \quad (3)$$

Assuming that the parameters of the inhomogeneities are random, then the sum (3) will have the following limit:

$$u\Sigma(t) = (n-j) U_{0i-J} e^{(n-j)\alpha_{i-j} t_{i-j}} \cdot \sin(\omega t_{i-j} + \varphi_{i-j}) + \\ + \sum_{i=1}^{n} \sqrt{U_{0j}^2 e^{-2\alpha_j t_j} \cdot \sin^2(\omega t_j + \varphi_j)}, \quad (4)$$

i.e. the second term (3) is summarized by the law of random quantities.

In this case, the ratio signal/interference will be the following:

$$\frac{u_c(t)}{u\ (t)} = \frac{(n-m) U_{0c-m} e^{-(n-m)\alpha_{i-m} t_{im}} \cdot \sin(\omega t_{i-m} + \varphi_{i-m})}{\sqrt{m} \sqrt{U_{0j}^2 e^{-2\alpha_j t_j} \cdot \sin^2(\omega t_j + \varphi_j)}} \quad (5)$$

The ratio of the initial amplitudes:

$$\frac{u_{c0}}{u_{n0}} = \left(\frac{n-m}{\sqrt{m}} \right) \cdot \frac{U_{0i-m}}{U_{0j}} \quad (6)$$

If n >> m, then:

$$\frac{u_{c0}}{u_{n0}} = \frac{n}{\sqrt{m}} \cdot \frac{U_{0i-m}}{U_{0j}}. \quad (7)$$

Noises (microseisms) that are uncorrelated with the signal will be summarized despite of their independence also as the random quantities, i.e. there will be summarization of their two dispersions:

$$u\Sigma N = n \cdot U_{Nn}. \quad (8)$$

If the total length of the synthetic aperture L will contain $n = \frac{L}{d}$ signal reference points, then the multiplicity of the method RMSL will match this quantity.

Next, we will give an assessment of the reasonable length of the synthesized amplitude L, based on the spherical symmetry of the diagram of the radiation source direction (Fig. 3).

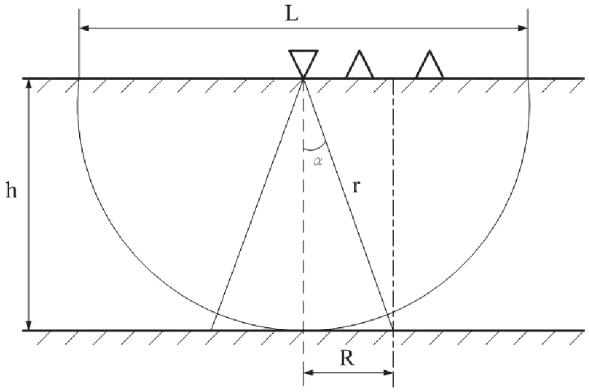

Fig. 3. For the assessment of the reasonable length of the synthesized aperture

We will assume that the area of the active zone of the reflective layer is determined by the radius of the Fresnel zone:

$$R = \sqrt{\frac{\lambda h}{\cos\alpha}}, \quad (9)$$

where λ – the average length of the radiated seismic wave.

In this case, the length of the coherent section of the reflective layer will be the following:

$$L = 2R. \quad (10)$$

For example, when h =4000 m; λ=100 m; cos α=1:

$$L = 2\sqrt{4 \cdot 10^5} \approx 1400\,\text{m}.$$

When h=100 m; λ=100 m ; L=200 m.

During the motion of carrier at a speed v and the count interval between the operating points Δt, the number of summarized signals on the section of aperture L will be the following:

$$h = \frac{L}{v \cdot \Delta t}. \quad (11)$$

For example, during the motion of the ship at a speed of $v = 10$ km/ $h \approx 3$ m/s , the number of counts for L=1400 m will be the following:

$$n = \frac{1400}{3 \cdot 10} \approx 46 . \qquad (12)$$

This quantity will be the summation factor, and the ratio signal/interference increases in amplitude by $\sqrt{h} \approx 7$ times.

The given calculations are made for the case of specular reflection.

With the small transport base, i.e. separation between emitter and receiver, it is difficult to implement the alternative of reflection specularity because of the influence of reverberations. For this reason, it is necessary to use the side looking that naturally reduces the level of useful signal. The problems of the method implementation for solving problems of exploration seismology in the Arctic basin are presented in [3].

It should be noted that with the small separation between emitter and receivers there is elimination of the problem of low-speed interference reduction, because they disappear almost instantly after the generation of the next pulse of radiation. However, in this case, at the moment of radiation it is necessary to damp, i.e. to "brake" the seismic receivers in order to avoid their damage and the nonlinear saturation.

With a significant linear dimension of the vehicle, in particular ships or submarines, the emitters and receivers can be placed in various parts of the ship, i.e. at the stern and the bow. It is equivalent to the realization of the method of scattered waves with side looking that is used in the practice of land exploration seismology.

CONCLUSION

- For the work in the mountain and taiga area of East Siberia one of the options of exploration seismology is the usage of rivers and other water basins as the exploration profiles using water options of the pulsed non-explosive sources "Yenisei".
- The estimations given in the article substantiate the reasonability of the technology development of side looking with the synthesized aperture and deployment of all the seismic complex, including the source and receiver based on one transport base without the usage of seismographs.

ACKNOWLEDGMENTS

The article was published with financial support of the Ministry of education and science of the Russian federation (government decree №218).

References

[1] *Reutov A.P., Mikhailov B.A., Kondratenko G.S., Boikov B.V.* 1970, 'Radiolocation stations of side looking'. Moscow, Soviet Radio. 360.

[2] *Bondarev Yu.* Exploration seismology.

[3] *Levitsky N.V., Detkov V.A., Megera V.M., Shaidurov G.Ya.* 2010, 'On the technology of seismic studies of the deep seabed of the Arctic Ocean', *Technologies of exploration seismology*, No. 3. 75-79.

Manuscript received January, 31, 2013

Shaidurov George Yakovlevich, the honored worker of a science and technics RF, Doctor of Engineering, Professor, Professor Radio-electronic systems department Siberian Federal University. Area of scientific interests: electromagnetic methods, search, seismic exploration, subsurface radar.

Suhotin Vitaly Vladimirovich, PhD of Engineering, Associate professor Radio-electronic systems department Siberian Federal University. Area of scientific interests: radiodalnometriya, the radio direction finding, the protected systems of a radio communication.

Kudinov Danil Sergeevich, PhD of Engineering, Associate professor Radio-electronic systems department Siberian Federal University. Area of scientific interests: parametrical methods, search methods, defectoscopy, diagnostics, seismic exploration.

Kopylov Mikhail Aleksandrovich, Director of Minusinsk branch JSC Evenkiyageofizika, Area of scientific interests: seismic exploration, pulse non-explosive seismic sources, methods of multiwave seismic exploration.

УДК 537.8

Сейсмическая локация бокового обзора с использованием синтеза апертуры антенны / Г.Я. Шайдуров, В.В. Сухотин, Д.С. Кудинов, М.А. Копылов // Прикладная радиоэлектроника: науч.-техн. журнал. – 2013. – Том 12. – № 1. – С. 172–174.

В статье дана оценка возможности реализации метода сейсмической локации с помощью импульсных невзрывных источников и приемников, которые расположены на единой транспортной базе во время бокового обзора геологической среды и синтеза эквивалентной апертуры антенны трансивера.

Ключевые слова: сейсмическая локация, апертура, синтез, интерфейс.

Ил. 03. Библиогр.: 03 назв.

УДК 537.8

Сейсмічна локація бокового огляду з використанням синтезу апертури антени / Г.Я. Шайдуров, В.В. Сухотін, Д.С. Кудінов, М.О. Копилов // Прикладна радіоелектроніка: наук.-техн. журнал. – 2013. – Том 12. – № 1. – С. 172–174.

У статті дана оцінка можливості реалізації методу сейсмічної локації за допомогою імпульсних невибухових джерел і приймачів, які розташовані на єдиній транспортній базі під час бокового огляду геологічного середовища та синтезу еквівалентної апертури антени трансивера.

Ключові слова: сейсмічна локація, апертура, синтез, інтерфейс.

Іл. 03. Бібліогр.: 03 найм.

UDC 681.785

PHASE SHIFT MEASUREMENT OF OPTICAL NOISE WAVEFORM MODULATION ENVELOPE

J.P. KIM, O.V. ZEMLYANIY, D.N. TATYANKO, K.A. LUKIN

The paper presents investigation results of a single-beam anemometer, in which the only one optical beam is used. The principle of operation of single-beam anemometer is based on the fact that the frequency shift due to Doppler effect appears both on a carrier frequency (optical band) and on the frequency of any oscillation, which can be distinguished from the signal by means of linear or nonlinear transformations. Such system is less dependent on destabilizing factors such as temperature fluctuations, mechanical impact of system components, vibration, etc. The extraction of information from the modulating signal, but not directly from the signal of the optical range allows using slow-speed and therefore less expensive components (photodetectors, ADC's). The approach used in the work ultimately simplifies the measuring device and makes it more reliable.

Keywords: Doppler effect, anemometer, single-beam optical speed meter, modulator, photodetector.

1. INTRODUCTION

At the present time, measurement of a speed of objects by metrological instrumentation is the actual task. Laser anemometers based on an effect of Doppler frequency shift are used as the optical speed meters for measuring the velocity of both solid objects and flows of gases and liquids [1]. The range of measured velocities is quite broad: from 1 mm/s for the study of near-wall flows with low velocities up to 1000 m/s for a hypersonic gas flows in large wind tunnels.

The operation of the laser Doppler anemometer (LDA) is based on the following. The moving object is irradiated by laser beam illuminated from a stationary source. This radiation is detected by a stationary receiver after reflection from the object. The frequency of the waveform at the receiver input due to the Doppler effect is shifted with respect to the radiated waveform frequency. This frequency shift is proportional to the radial velocity of the object having motion with respect to the source and receiver.

The oscillation frequency of the light wave is very large; for visible light it is of the order of 460 THz. At present time, direct measuring of such a high frequency with sufficient accuracy for detecting the Doppler frequency shift (DFS) is practically almost impossible. Therefore, to determine the Doppler shift the method of optical mixing is used. Two light waves with different frequencies are simultaneously sent to the photodetector input pad. As a result of the interference of these waves, the light intensity on the surface of a sensor varies with frequency which is equal to the difference between the frequencies of these waves.

The photodetector converts the light beam into an alternating electrical signal, the magnitude of which is directly proportional to the intensity of light on the photodetector surface. Thus, the frequency of the electrical signal at the photodetector output is equal to the DFS and directly proportional to the radial velocity of the object. For measuring the frequency of the photodetector output in laser Doppler anemometer modern digital techniques are used.

Measuring the speed of moving objects with laser anemometers requires very precise alignment of the measuring apparatus. This is due to the fact that two beams are used, which are intersect at one point, through which an object or a stream of gas or liquid moves. The change of interference pattern of two interfering beams at the point of intersection determines the frequency shift caused by object movement due to the Doppler effect. The interference occurs in the optical band, and then the resultant optical signal is received by a photodetector and then processed.

2. DETECTION OF DOPPLER SHIFT VIA MODULATION WAVEFORM MEASUREMENT

In general case, an amplitude-modulated waveform is given by

$$u_{AM} = U(t)\cos(\omega_0 t + \varphi_0), \quad (1)$$

where $U(t) = U_m\left[1 + M\,s(t)\right]$ is the envelope, U_m is the amplitude of un-modulated waveform, M represents the modulation constant, $s(t)$ is the modulating signal. For simplicity, in future consideration the respective values of U_m and φ_0 can be set to 1 and 0. For the case, when the amplitude of the optical radiation of wavelength $\lambda_0 = 2\pi c / \omega_0$ is modulated by sine waveform the expression (1) takes the following form:

$$u_{AM}(t) = \left[1 + M\cos(\Omega t + \Phi_0)\right]\cos(\omega_0 t) = \\ = u_0(t) + \frac{M}{2}u_1(t) + \frac{M}{2}u_2(t), \quad (2)$$

where Ω is the frequency of sine waveform, Φ_0 is the initial phase of modulating waveform, $u_0(t)$, $u_1(t)$ and $u_2(t)$ are the carrier wave, lower and upper sideband components, respectively. After reflection from the moving object, each of three spectral components of the sum (2) due to the Doppler effect takes the frequency shift, which is proportional to $K = 2V_R / c$, where V_R is the object radial velocity, c is the speed of light. Therefore, the reflected AM waveform is expressed as

$$u_{AM}^{D}(t)=\left[1+M\cos(\Omega t+\Phi_0)\right]\cos\omega_0 t=$$
$$=\cos\omega_0 t+\frac{M}{2}\cos\left(\Omega_1^D t-\Phi_0\right)+\frac{M}{2}\cos\left(\Omega_2^D t+\Phi_0\right), \quad (3)$$

where $\omega_0^D=\omega_0(K+1)$, $\Omega_1^D=(\omega_0-\Omega)(K+1)$, $\Omega_2^D=(\omega_0+\Omega)(K+1)$ are the shifted frequencies of carrier, lower and upper sideband components of reflected AM waveform, respectively. After algebraic transformations, we have

$$u_{AM}^{D}(t)=\left[1+M\cos\left(\left(1+\frac{2V_R}{c}\right)\Omega t+\Phi_0\right)\right]\times$$
$$\times\cos\left(\left(1+\frac{2V_R}{c}\right)\omega_0 t\right). \quad (4)$$

It is obvious from this, that envelope of amplitude-modulated waveform, reflected from the moving object, takes frequency shift, proportional to the object radial velocity V_R.

3. SINGLE-BEAM OPTICAL ANEMOMETER. SETUP AND EXPERIMENT

The authors propose a single-beam anemometer, in which the only one optical beam is used and a result of the Doppler shift frequency caused by the moving object is processed in digital form. Experimental setup which simulates Doppler frequency shift is shown in Fig. 1.

To simplify the experiment the model that emulates the object movement at different speeds was created.

It is difficult to implement experimentally the high speed motion of the object during the time required for recording the results of measurements. As the Doppler frequency is characterized by the phase changing velocity of the modulated signal reflected from the object, the motion of an object was emulated by recording signals reflected from the object (mirror), placed in three different fixed positions with following estimation of the phase shift of the modulating waveform in these positions.

Two mirrors were used. One mirror was placed at various distances along the direction of propagation of the optical beam. Another mirror was fixed. The beam was modulated by a low frequency. The mirrors reflected the beam onto one photodetector. Beam was incident onto each of the mirrors alternately and thus emulated the movement of the reflecting object. With placing one of the mirrors at different distances from another mirror we emulated motion of the object.

The path difference in reflection from the distant and near mirror is

$$L=L_3+L_4-L_2. \quad (5)$$

The setup uses the semiconductor red laser (its wavelength is ~640 nm) and an electro-optical modulator/shutter ML-5 whose operation is based on the Pockels effect [2]. The Pockels effect is the linear electro-optic effect, where the refractive index of a medium is changing proportionally to the applied electric field strength. This effect can occur only in non-centrally symmetric materials. The most important materials of this type are crystal materials such as lithium niobate ($LiNbO_3$), lithium tantalate ($LiTaO_3$), potassium di-deuterium phosphate (KD^*P), β-barium borate (BBO), potassium titanium oxide phosphate (KTP), and compound semiconductors such as gallium arsenide (GaAs) and indium phosphide (InP). The modulator ML-5 based on the metaniobate lithium.

The intensity of laser beam was modulated by sine waveform of frequency 27 MHz having this electro-optical modulator. Using sine wave as modulation signal was not principal. A range ΔL within which the phase shift is measured unambiguously can be defined for any periodic signal by the following way:

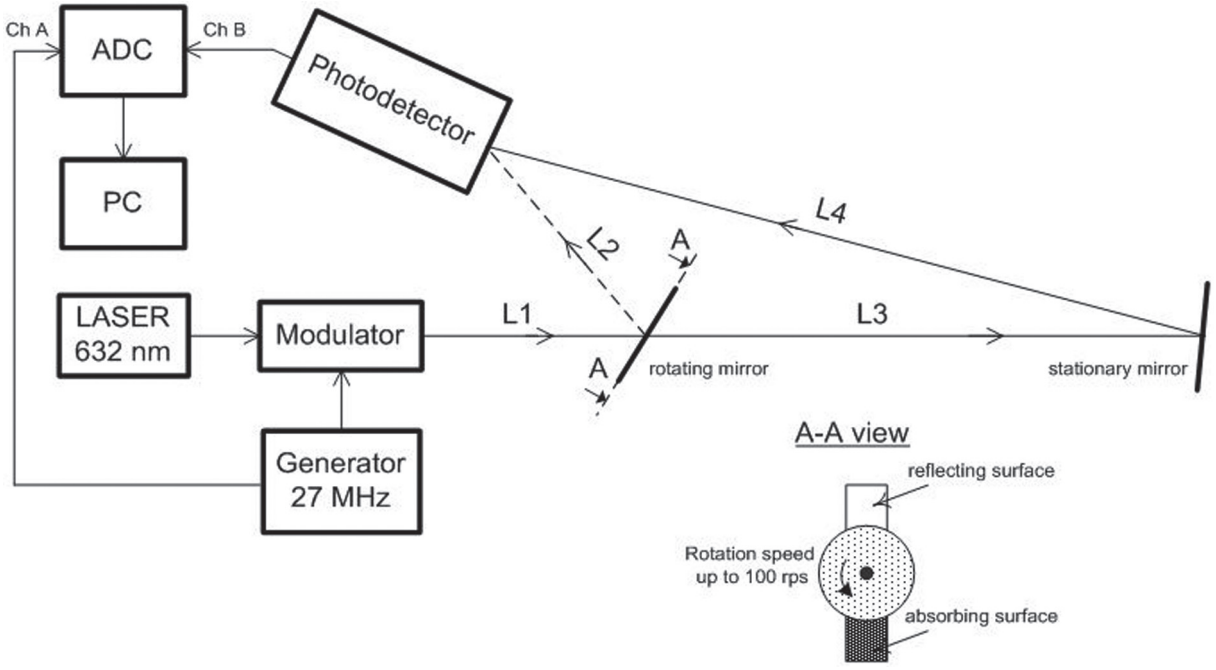

Fig. 1. The experimental setup

$$\Delta L = 2\pi c / \Omega, \quad (6)$$

where Ω is the frequency of modulating waveform.

Alternately rotating mirror reflects the beam onto the photodetector and the beam passes to the stationary mirror. Stationary mirror also reflects the beam onto the photodetector. Value of the signal at the output of the photodetector over time is shown in Fig. 2. From the output of the photodetector the measuring signal arrives to the input of an analog-to-digital converter (ADC). High-speed double-channel CS82G ADC of Gage Applied Technology Company was used [3]. The 1 GHz CompuScope 82G widens the precision and range of applications of fast digitizers. The enhanced bandwidth minimizes the distortion of high frequency components, improving the characterization of very fast transients from laser pulses and high-speed electronic signals. The CompuScope 82G-1GHz allows undersampling, all the way up to the Nyquist frequency, of continuous periodic signals to extract important spectral information. The CompuScope 82G is the tool of choice for the critical test and measurements applications, such as optical anemometers.

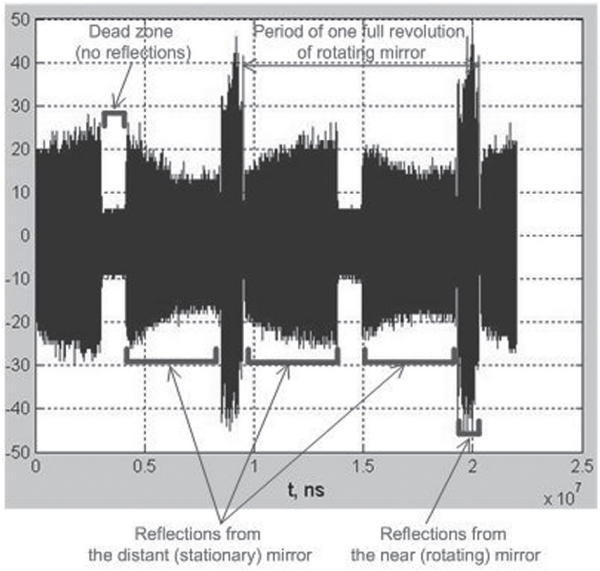

Fig. 2. The signal structure at the photodetector output during the rotation of the near mirror. The rotation speed is about 90 rps

From the generator of modulating waveform the signal is fed to the second input of the ADC. This signal serves as the reference signal of the measurement system. The digitized signals are then processed in the computer.

So, if the optical radiation modulated by amplitude is directed to a moving object or a flux, and the reflected from the object radiation is received by a photodetector, the modulated signal comes out at its output. Its frequency shift equals to

$$f_c = 2FV_R / c, \quad (7)$$

where F is the frequency of modulating signal.

The signal structure at the photodetector output during the rotation of the near mirror is shown in Fig. 2. The rotation speed is about 90 rps.

Shifted in frequency modulating signal is then compared with the modulation generator output. The frequency difference of these two signals in accordance with the Doppler effect is proportional to the velocity of a moving object or flux under investigation.

4. RESULTS OF THE EXPERIMENTAL DATA PROCESSING

For evaluation of the phase shift between two sine waveforms we calculated the cross-correlation function between them:

$$R_{uv}(\tau) = \int_{-\infty}^{\infty} u(t)v(t-\tau)dt, \quad (8)$$

where $u(t)$ is modulating signal from the generator, $v(t)$ is the optical radiation envelope, distinguished by photodetector on reflection from the mirror. Calculation of $R_{uv}(t)$ was performed by means of numerical methods after digitizing of both signals.

The cross-correlation function between the modulating signal from the generator and the optical radiation envelope, distinguished by photodetector on reflection from the near mirror (solid line) and from the distant mirror (dashed line) with different path differences are shown in Fig. 3-5.

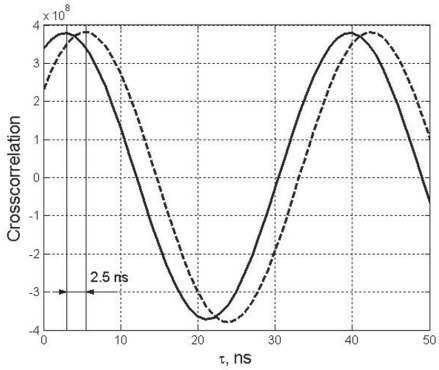

Fig. 3. The cross-correlation function between the modulating signal from the generator and the optical radiation envelope, distinguished by photodetector on reflection from the near mirror (solid line) and from the distant mirror (dashed line) when the path difference is L=0.75 m

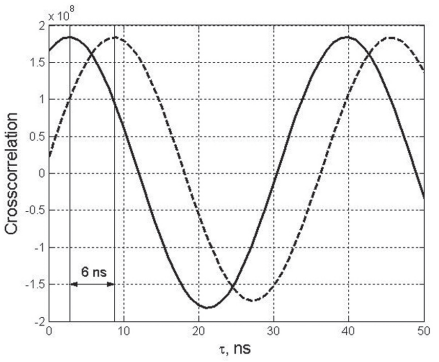

Fig. 4. The cross-correlation function between the modulating signal from the generator and the optical radiation envelope, distinguished by photodetector on reflection from the near mirror (solid line) and from the distant mirror (dashed line) when the path difference is L=1.8 m

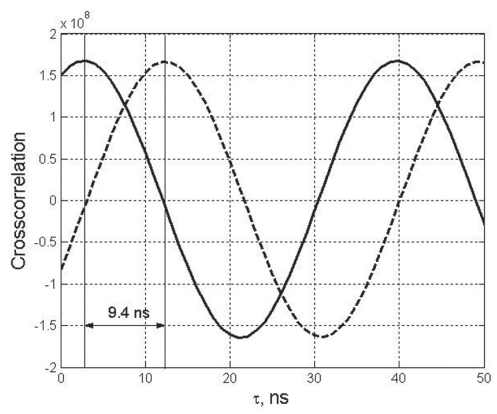

Fig. 5. The cross-correlation function between the modulating signal from the generator and the optical radiation envelope, distinguished by photodetector on reflection from the near mirror (solid line) and from the distant mirror (dashed line) when the path difference is L=2.82 m

Fig. 3-5 show that when the distance between the mirrors was changed, the phase of modulated optical signal also was changed. The change of phase shift signal is proportionally to the distance between the mirrors.

Thus, when the object moves the phase of the reflected signal will change at a rate proportional to the velocity of the object. As a result, the frequency of the reflected from the object signal will change accordingly to the phase change. When an object moves from the photodetector the phase change velocity will be reduced, so the signal frequency will be reduced. When the object approaches to the photodetector the value of the phase change velocity will be increased so the frequency will be increased.

5. CONCLUSIONS

Theoretical and experimental studies of speed measuring of moving objects were carried out. The experimental method of the Doppler frequency shift measurement, which simulates the moving of objects, was proposed and realized.

We developed and evaluate the single-beam speed meter (anemometer), the principle of operation of which is based on the fact that the Doppler effect appears both on a carrier frequency of the optical signal and on the frequency of any oscillation, which can be distinguished from the signal by means of a linear or nonlinear transformations. That is, if the signal is not monochromatic, the Doppler effect causes changes in the frequencies of all spectral components of the signal.

One of the advantages of using such velocity meter is a single-beam system which can be adjusted easier than double-beam system. Such system is less dependent on destabilizing factors such as temperature fluctuations, mechanical stress of system components, vibration, etc. The extraction of information from the modulating signal, but not directly from the signal of the optical range allows using slow-speed and therefore less expensive components (photodetectors, ADC's). The approach used in the work ultimately simplifies the measuring device and makes it more reliable.

REFERENCES

[1] Rinkevichus B.S. Laser anemometry. - M.: Energy, 1978. - 160 p.

[2] William K. Pratt. Laser Communication Systems. Transl. from Engl., edited by A.G. Sheremetyev. M., "Communication", 1972. - 232 p.

[3] www.gage-applied.com

Manuscript received February, 23, 2012

Jeong Phill Kim, for photograph and biography, see this issue, p. 144.

Konstantin A. Lukin, for photograph and biography, see this issue, p. 24.

Oleg V. Zemlyaniy, for photograph and biography, see this issue, p. 36.

Dmytro N. Tatyanko, for photograph and biography, see this issue, p. 171.

УДК 681.785

Измерение фазового сдвига огибающей оптического шумового сигнала. / Д. Ф. Ким, О. В. Земляный, Д. Н. Татьянко, К. А. Лукин. // Прикладная радиоэлектроника: науч.-техн. журнал. – 2013. – Том 12. – № 1. – С. 175–179.

Представлены результаты исследования однолучевого анемометра, в котором используется только один оптический луч. Принцип работы однолучевого анемометра основан на том, что сдвиг частоты в соответствии с эффектом Доплера появляется как на несущей частоте (оптический диапазон), так и на частоте любого колебания, которое можно выделить из сигнала с помощью линейного или нелинейного преобразования. Таким образом, если модулированное по амплитуде оптическое излучение направлено на движущийся объект или поток и отраженное излучение регистрируется фотоприемником, сдвиг частоты сигнала на выходе фотоприемника пропорционален скорости движения объекта и частоте модуляции. Сдвинутый по частоте сигнал, выделенный фотодетектором, затем сравнивается с модулирующим сигналом с выхода генератора. Разность частот этих двух сигналов в соответствии с эффектом Доплера пропорциональна скорости движения исследуемого объекта или потока. В экспериментальной установке были использованы полупроводниковый красный лазер (с длиной волны 640 нм) и электро-оптический модулятор/затвор, действие которого основано на эффекте Поккельса. Одним из преимуществ использования такого измерителя скорости является то, что система однолучевая, и поэтому ее проще юстировать, чем двухлучевую систему. Такая система является менее зависимой от дестабилизирующих факторов, таких как колебания температуры, механические воздействия на компоненты системы, вибрации и т.д. Получение информации из модулирующего сигнала, а не непосредственно из сигнала в оптическом диапазоне, позволяет использовать меньшие скорости и, следовательно, менее дорогие

компоненты (фотоприемники, АЦП). Подход, используемый в работе, в конечном итоге, упрощает измерительное устройство и делает его более надежным.

Ключевые слова: эффект Доплера, анемометр, однолучевой оптический измеритель скорости, модулятор, фотоприемник.

Ил. 05. Библиогр.: 03 наимен.

УДК 681.785

Вимірювання фазового зсуву огинаючої оптичного шумового сигналу. / Д. Ф. Кім, О. В. Земляний, Д. М. Татьянко, К. О. Лукін // Прикладна радіоелектроніка: наук.-техн. журнал. – 2013. – Том 12. –№ 1. – С. 175–179.

Представлено результати дослідження однопроменевого анемометра, в якому використовується тільки один оптичний промінь. Принцип роботи однопроменевого анемометра заснований на тому, що зсув частоти у відповідності з ефектом Доплера з'являється як на несучій частоті (оптичний діапазон), так і на частоті будь-якого коливання, яке можна виділити з сигналу за допомогою лінійного або нелінійного перетворення. Таким чином, якщо модульоване по амплітуді оптичне випромінювання спрямоване на рухомий об'єкт або потік, і відбите випромінювання реєструється фотоприймачем, зсув частоти сигналу на виході фотоприймача пропорційний швидкості руху об'єкта і частоті модуляції. Зсунутий за частотою сигнал, виділений фотодетектором, потім порівнюється з модулюючим сигналом з виходу генератора. Різниця частот цих двох сигналів у відповідності з ефектом Доплера пропорційна швидкості руху досліджуваного об'єкта або потоку. В експериментальній установці були використані напівпровідниковий червоний лазер (з довжиною хвилі 640 нм) і електро-оптичний модулятор / затвор, дія якого заснована на ефекті Поккельса. Однією з переваг використання такого вимірювача швидкості є те, що система однопроменева, і тому її простіше юстувати, ніж двопроменеву систему. Така система є менш залежною від дестабілізуючих факторів, таких як коливання температури, механічні дії на компоненти системи, вібрації тощо. Отримання інформації з модулюючого сигналу, а не безпосередньо з сигналу в оптичному діапазоні, дозволяє використовувати менші швидкості і, отже, менш дорогі компоненти (фотоприймачі, АЦП). Підхід, який використовується в роботі, зрештою, спрощує вимірювальний пристрій і робить його більш надійним.

Ключові слова: ефект Доплера, анемометр, однопроменевий оптичний вимірювач швидкості, модулятор, фотоприймач.

Іл. 05. Бібліогр.: 03 найм.

APPLIED RADIO ELECTRONICS

Scientific and technical journal

Senior Editor

Electronic Publishing Manager

Elena B. Isaieva

Рекомендовано засіданням Бюро Президії Академії наук прикладної радіоелектроніки
(протокол № 1 від 29.03.2013 р.).

Рекомендовано Вченою радою Харківського національного університету радіоелектроніки
(протокол № 20 від 29.03.2013 р.).

Свідоцтво про державну реєстрацію КВ № 6037 від 09.04.2002 р.

Журнал включений у список фахових видань ВАК України
з технічних наук
(постанова президії ВАК України № 1-05/2 от 10.03.2010),
з фізико-математичних наук (фізика)
(постанова президії ВАК України № 1-05/5 от 1.07.2010)

Підписано до друку 29.03.2013. Формат 60 × 84 $^{1}/_{8}$.
Папір офсет. Друк офсет. Умов.-друк. арк. 21. Облік.-вид. арк. 20,6.
Тираж 300 прим. Ціна договірна.

Віддруковано в ТОВ «ДРУКАРНЯ МАДРИД»
61024, м. Харків, вул. Ольмінського, 8. Тел.: (057) 717-41-79
www.madrid.in.ua, e-mail: info@madrid.in.ua